Modulation of Porosity, Melting and Glass Formation in Zeolitic Imidazolate Frameworks

Dissertation

Wenlong Xue

August 2024

Modulation of Porosity, Melting and Glass Formation in Zeolitic Imidazolate Frameworks

Department of Chemistry and Chemical Biology
Technische Universität Dortmund

Dissertation

Submitted by

Wenlong Xue

August 2024

This work has been performed in the time between February 2021 and August 2024 in the Inorganic Chemistry Section of Department of Chemistry and Chemical Biology – Technische Universität Dortmund.

1st referee: Prof. Dr. Sebastian Henke

2nd referee: Prof. Dr. Guido Clever

Date of submission: 12.08.2024

Date of examination: 06.09.2024

Knowledge from books is superficial, true understanding comes from hands-on practice.

纸上得来终觉浅，绝知此事要躬行。

– *Lu You (1125-1210)*

I am deeply grateful to my supervisor

Prof. Dr. Sebastian Henke

for accepting me as his student and affording me the opportunity to delve into this fascinating topic. His exceptional teaching, unwavering support, and motivating guidance have been instrumental throughout the course of this dissertation.

I also thank Prof. Dr. Guido Clever for being the second referee of this dissertation.

Furthermore, I would like to thank the following people for their help with synchrotron experiments, without them it would not have been possible to realize major parts of this work:

- Dr. Christian Sternemann and Dr. Michael Paulus for their tremendous help during numerous beamtimes at Dortmunder Elektronenspeicherringanlage (DELTA, Germany).
- Dr. Philip A Chater for data collection and processing and fruitful discussions on X-ray total scattering at Diamond Light Source (DLS, UK)
- Dr. Volodymyr Baran and Dr. Martin Etter for their help during beamtimes at Deutsches Elektronen-Synchrotron (DESY, Germany).

I would also like to acknowledge Prof. Dr. Rasmus Linser, Dr. Suresh Vasa, Dr. Alexander Klein, and Hanna Aucharova for conducting the solid-state NMR experiments.

I am also grateful to Prof. Dr. Mirijam Zobel and Felix Müller for the inhouse X-ray total scattering measurements at RWTH Aachen University.

Many thanks to the current and former members of the *Henke Group* for the pleasant working atmosphere, the fun group events, and all the business/conference trips:

Dr. Louis Frentzel-Beyme, Dr. Roman Pallach, Dr. Chinmoy Das, Dr. Athanasios Koutsianos, Dr. Jianbo Song, Pascal Kolodzeiski, Kai Terlinden, Jan-Benedikt Weiß, Farzad Mamusy, Guoqiang Li, Dagmar Schürmann, Christian Nelle, Nuttaporn Krittametaporn, Tim Krokowski, Elizaveta Stoliarova, Katrin Vollmari, Denise Zickler, and Leandro Straeter.

I would like to give a special thanks to my colleague Jannik Engel for the fast processing for all chemicals and consumables orders.

I would also like to give another special thanks to my colleague Kai Terlinden, who organised various activities during the Chinese New Year and Mid-Autumn Festival, eating dumplings and mooncakes together and playing table tennis, making me feel the warmth of a family.

I also thank my students and trainees Jack Szymanski, Frodewin Brumshagen, and Sebastian Brandenburg for choosing me as a supervisor and for synthesizing the samples and performing the characterizations.

Furthermore, I would like to thank my colleagues in the neighbouring groups (Clever group, Steffen group, Strohmann group, Hansmann group, and etc.) or in other departments for their help and valuable discussions in research and life.

Last but not least, I am grateful to my family for their unconditional and constant support and the selfless love through the screens. My parent, my sister's family and myself.

Wenlong Xue, August 2024

For Linyang

Abstract

The phase transition of metal–organic frameworks (MOFs) from a crystalline to a liquid and a glassy state represents a promising avenue for the development of a novel class of amorphous materials. In contrast to their crystalline counterparts, liquid and glassy MOFs exhibit excellent processability, a highly advantageous property for industrial applications where the formation of specific shapes, such as pellets or thin films, is often a prerequisite. Furthermore, unlike conventional glasses, the utilization of coordination chemistry allows for the implementation of rational design concepts, thereby facilitating the fine-tuning of the desired properties.

In this thesis, *Solvent-assisted linker exchange (SALE)* as a versatile method for the preparation of melt-quenched MOF glasses from proto typical MOFs, such as ZIF-8. Two additional organic linkers are incorporated into the non-meltable ZIF-8, yielding high-entropy linker-exchanged ZIF-8 derivatives that undergo a phase transition from crystalline to liquid and glassy states upon thermal treatment. This strategy opens new pathways for creating meltable and glass-forming MOFs from the extensive pool of non-meltable MOFs documented in the literature.

Moreover, *Post-synthetic ball-milling (PSBM)* is explored as a suitable alternative to melt-quenching in MOF glass formation. MOFs can be transformed into glasses in just 5 minutes by mechanical milling at room temperature. This PSBM method can also transform crystalline MOFs in the glassy state that do not melt due to low thermal stability. This approach broadens the spectrum of potential applications, paving the way for the development of multifunctional MOF glass composites and expanding their use into more diverse fields.

Additionally, *Single-component glass-ceramics (SCGC)* explored from a Cd-based MOF exhibit unique structural and thermal properties. Upon reheating the Cd-based MOF glass, it undergoes partial recrystallization into a single component glass-ceramic state with potentially enhanced mechanical properties — a feature not observed in previous melt-quenched MOF glasses.

Overall, this thesis offers new insights into the porosity of MOF glasses, their formation mechanism, the preparation of MOF glass-ceramics and a generic method for the mechanochemical preparation of MOF glasses.

Kurzfassung

Der Phasenübergang von metallorganischen Gerüstverbindungen (MOFs) von einem kristallinen in einen flüssigen und glasartigen Zustand stellt einen vielversprechenden Ansatz für die Entwicklung einer neuartigen Klasse amorpher Materialien dar. Im Gegensatz zu ihren kristallinen Analoga weisen flüssige und glasartige MOFs eine hervorragende Verarbeitbarkeit auf, eine für industrielle Anwendungen äußerst vorteilhafte Eigenschaft, bei denen die Formgebung, wie etwa zu Pellets oder dünnen Filmen, oft eine Voraussetzung ist. Darüber hinaus ermöglicht die Nutzung der Koordinationschemie im Gegensatz zu herkömmlichen Gläsern die Umsetzung rationaler Designkonzepte und damit die Feinabstimmung der gewünschten Eigenschaften.

In dieser Arbeit wird der *lösungsmittelunterstützte Ligandenaustausch (English: Solvent-assisted linker exchange, SALE*) als vielseitige Methode zur Herstellung von Schmelzen-quenchen MOF-Gläsern, die durch das Quenchen des Schmelzes entstehen, aus prototypischen MOFs wie ZIF-8 untersucht. Zwei zusätzliche organische Liganden werden in das nicht schmelzbare ZIF-8 eingebaut, wodurch hochentropische ligandenausgetauschte ZIF-8-Derivate entstehen, die bei thermischer Behandlung einen Phasenübergang von kristallin zu flüssig und schließlich glasartig durchlaufen. Diese Strategie eröffnet neue Wege zur Herstellung schmelzbarer und glasbildender MOFs aus dem umfangreichen Pool nicht schmelzbarer MOFs, die in der Literatur dokumentiert sind.

Post-synthetisches Kugelmahlen *(English: Post-synthetic ball-milling, PSBM).* Darüber hinaus wird das nachsynthese Ballmahlen als geeignete Alternative zum Schmelzen-quenchen bei der MOF-Glasbildung untersucht. MOFs können durch mechanisches Mahlen bei Raumtemperatur innerhalb von nur 5 Minuten in Gläser umgewandelt werden. Diese PSBM-Methode kann auch kristalline MOFs in einen glasartigen Zustand überführen, die aufgrund ihrer geringen thermischen Stabilität nicht schmelzen. Dieser Ansatz erweitert das Spektrum potenzieller Anwendungen, ebnet den Weg für die Entwicklung multifunktionaler MOF-Glaskomposite und erweitert deren Nutzung in vielfältigere Bereiche.

Zusätzlich zeigen *einkomponenten Glaskeramiken (English: Single-component glass-ceramics, SCGC)* aus einem Cd-basierten MOF einzigartige strukturelle und thermische Eigenschaften. Beim erneuten Erhitzen des Cd-basierten MOF-Glases erfolgt eine teilweise Rekristallisation in einen einkomponenten Glaskeramikzustand mit potenziell verbesserten mechanischen Eigenschaften – ein Merkmal, das bei Schmelzen-quenchen MOF-Gläsern zuvor nicht beobachtet wurde.

Insgesamt bietet diese Arbeit neue Einblicke in die Porosität von MOF-Gläsern, ihren Bildungsmechanismus, die Herstellung von MOF-Glaskeramiken und eine generische Methode zur mechanochemischen Herstellung von MOF-Gläsern.

Contents

Contents i

List of Abbreviations v

1 Motivation and Aims 1

2 General Introduction 3

2.1 Metal-Organic Frameworks 3

2.1.1 General preparation of MOFs 3

2.1.2 Postsynthetic modification methods of MOFs 5

2.2 Zeolitic Imidazolate Frameworks 7

2.3 MOF Glasses 9

2.4 MOF Glass Characterization 12

2.3.1 Structural identification via X-ray diffraction and total scattering 12

2.3.2 Thermal analysis 14

2.3.3 Porosity determination 17

2.3.4 Gas Separation 19

3 Highly Porous ZIF-8 Glasses 23

Abstract 24

3.1 Introduction 25

3.2 Preparation and characterization of ZIF-8 derivatives 27

3.3 Thermal behavior 29

3.4 Constructing a triangular phase diagram 33

3.5 NMR and Far-IR spectroscopy 35

3.6 Porosity determination 37

3.7 Kinetic separation of hydrocarbons 40

3.8 Conclusion 41
4 Mechanically Induced ZIF Glasses 43
Abstract 44
4.1 Introduction 45
4.2 Crystalline ZIF synthesis and structural characterization 48
4.3 Amorphization by post-synthetic ball milling 50
4.4 CO_2 physisorption data and porosity analysis 51
4.5 Thermal properties 54
4.6 Conclusion 60
5 Cadmium-based ZIF Glasses 63
Abstract 64
5.1 Introduction 65
5.2 Preparation and characterization of $Cd(im)_2$ 66
5.3 Thermal behavior 68
5.4 Local structural analysis 73
5.5 Fragility determination 79
5.6 Conclusion 79
6 Summary and Outlook 81
7 Experimental Section 87
7.1 X-ray diffraction techniques 87
7.1.1 In-house X-ray powder diffraction 87
7.1.2 Variable temperature XRPD (VT-XRPD) 87
7.1.3 X-ray total scattering 87
7.2 FTIR spectra spectroscopy 88
7.3 Nuclear magnetic resonance (NMR) spectroscopy 89
7.4 Thermal analysis 89
7.5 Isothermal gas physisorption 90
7.6 Scanning electron microscopy (SEM) 91
7.7 Synthesis 92

Appendix 99
Appendix to Section 3 99
A.3.1 – Compositional analysis by ^{1}H NMR spectroscopy 99
A.3.2 – X-ray powder diffraction data 111
A.3.3 – X-ray total scattering 129
A.3.4 – Solid state 2D spin diffusion NMR spectroscopy 134
A.3.5 – FTIR spectra 136
A.3.6 – Thermal analysis 139
A.3.7 – Micrography 152
A.3.8 – Gas physisorption studies 157
Appendix to Section 4 167
A.4.1 – X-ray powder diffraction data and X-ray total scattering data 167
A.4.2 – ^{1}H NMR spectroscopy data 187
A.4.3 – Fourier-transform infrared (FTIR) spectroscopy data 192
A.4.4 – CO_2 physisorption studies 204
A.4.5 – Thermal analysis 213
A.4.6 – Scanning electron microscopy and optical microscopy 235
Appendix to Section 5 239
A.5.1 – X-ray powder diffraction data and variable temperature XPDF 239
A.5.2 – H NMR spectroscopy data 245
A.5.3 – Fourier-transform infrared (FTIR) spectroscopy data 251
A.5.4 – Thermal analysis 254
A.5.5 – Thermal analysis CO_2 physisorption studies 259
A.5.6 – Optical Microscopy 259
Bibliography 261
List of Publications 273
List of Presentations 275

List of Abbreviations

E	Young's modulus
T_{g}	glass transition temperature
T_{m}	melting temperature
T_{am}	amorphization temperature
T_{rc}	recrystallization temperature
T_{d}	decomposition temperature
V_{pore}	pore volume
abim$^-$	5-Amino-benzimidazolate
bim$^-$	benzimidazolate
Clbim$^-$	5-Chloro-benzimidazolate
CNim$^-$	4-Cyanoimidazolate
CSD	Cambridge Structural Database
DSC	differential scanning calorimetry
GFA	glass forming ability
HDL	high-density liquid

HK	Horvath-Kawazoe
im^-	Imidazolate
IUPAC	International Union of Pure and Applied Chemistry
LDL	low-density liquid
MAF	metal azolate framework
$mbim^-$	5-Methyl-benzimidazolate
MD	molecular dynamics
MIG	mechanically induced Glass
mim^-	methylimidazolate
MOF	metal-organic framework
MQG	melt-quenched glass
NLDFT	nonlocal density functional theory
PALS	positron annihilation lifetime spectroscopy
PDF	pair distribution function
PSD	pore size distributions
QSDFT	quenched solid density functional theory
RMC	reverse Monte Carlo

SAXS	small-angle X-ray scattering
SEM	scanning electron microscopy
STEM	scanning-transmission electron microscopy
TGA	thermogravimetric analysis
VT	variable temperature
WAXS	wide-angle X-ray scattering
XRPD	X-ray powder diffraction
ZIF	zeolitic imidazolate framework

1 Motivation and Aims

Metal-organic framework (MOF) glasses categorized as the fourth-generation of coordination polymers (CPs), are an emerging area. The interest in glass materials has grown rapidly in recent times, due to the advantages offered by their processing and shaping. The advanced processability and grain-boundary-free nature of isotropic liquid and glassy MOF phases, in comparison to their crystalline counterparts, has opened up new avenues for applications ranging from gas separation to solid-state ionics.

Zeolitic imidazolate frameworks (ZIFs), known as a subclass of MOFs, are constructed from divalent metal cations with tetrahedral coordination geometry and imidazolate-based linkers (e.g., imidazolate, benzimidazolate, or 5-Chlorobenzimidazolate). Among the family of ZIFs, ZIF-8 is the most extensively studied ZIF material, both from a fundamental and an applied perspective. ZIF-8 is a high-porosity zeolitic imidazolate framework (ZIF) comprising approximately 50% porosity. It is composed of zinc cations (Zn^{2+}) and 2-methylimidazolate (mim^{-}) linkers connected to a framework with large spherical cavities of approximately 1 nm in diameter and sodalite (**sod**) topology. Recently, some ZIFs have been reported to melt at high temperature and form glassy materials upon cooling to room temperature. These glassy monolithic ZIF materials have better processability than crystalline ZIF particles and can be easily prepared into films and bulk materials for gas separation and ion conduction applications. Nevertheless, only a limited number of glass-forming ZIFs (e.g., ZIF-4, ZIF-62, and their derivatives) have been identified thus far, and these have only been observed in the **cag** and **zni** topologies and only in handful metal ions (e.g., Zn^{2+}, Co^{2+}, or Fe^{2+}). Some of the most researched **sod** (sodalite) topology ZIFs in common use (e.g., ZIF-8 and ZIF-67) are unable to form MOF glasses. Secondly, the MOF glasses obtained thus far feature only very small porosities and very small pore sizes, which limits its application to gas storage and separation. Moreover, melting a ZIF requires relatively high temperatures (usually > 400 °C), it limits the scope of development of new materials based on MOF glasses,

i.e., additional molecules that are not resistant to high temperatures cannot be added to the matrix of MOF glasses to obtain composites with better properties.

Thus, the central goal of this thesis is to develop new universal methods to prepare new MOF glasses, not only from meltable MOFs but also from unmeltable MOFs, as well as to apply more metal ions for the MOF glass family, and gain a deeper understanding of the porosity of ZIF glasses and the fundamentals of ZIF melting. The following questions will be addressed in order to gain insight into the aforementioned aspects.

(i) Is the commercial material ZIF-8 meltable? If it cannot be melted, is it because of its composition or because of its highly porous topology? (Section 3)
(ii) If so, how is the porosity of the ZIF-8 glass? Can it be used for efficient separation of hydrocarbon molecules? (Section 3)
(iii) Is it possible to bypass the high-temperature melting process and employ other protocols for the vitrification of ZIFs at room temperature? (Section 4)
(iv) Is it possible to obtain ZIF glasses with metal cations other than Zn^{2+}, Co^{2+} and Fe^{2+} ions as the inorganic building unit? (Section 5)

In the following chapters, these questions will be systematically explored, providing insights into the potential and limitations of MOF glasses. The goal is to establish new methodologies for creating MOF glasses and develop MOF glasses with enhanced properties and broader application perspectives.

2 General Introduction

2.1 Metal-Organic Frameworks

Metal-organic frameworks (MOFs), also revered to as porous coordination polymers (PCPs), belong to the subclass of coordination networks (CNs), which, in turn, fall under the category of coordination polymers (CPs).[1-3] This hierarchical classification was proposed by a task force of the International Union of Pure and Applied Chemistry (IUPAC) in 2013.[4] As per the IUPAC definition, MOFs are characterized as potentially porous framework structures created through the connection of inorganic and organic building units. At present, nearly 100,000 crystalline MOFs have been reported in the literature[5] and many of them exhibit great potential for applications in various fields, like gas storage, gas separation, or catalysis, previously only suited for conventional purely inorganic or purely organic porous materials, e.g., zeolites and activated carbons.

2.1.1 General preparation of MOFs

MOFs are built from two parts, i.e. inorganic building units, such as metal ions or metal-(oxo) clusters, and organic building units, typically multitopic organic molecules (see **Figure 2.1**).[6-8]

The most commonly used synthesis method for MOFs is known as solvothermal synthesis.[9] This method typically involves dissolving metal salts and organic linkers in a solvent, then heating the mixture in a sealed vessel, often referred to as an autoclave. The choice of solvent is critical in solvothermal synthesis as it can influence the solubility of the reactants and the stability of the resulting MOF structure. In the synthesis of some MOFs, the solvent also acts as a templating agent to support the highly porous structure of the MOF.[10] Common solvents include water, alcohols (such as methanol and ethanol), dimethylformamide (DMF), and dimethyl sulfoxide (DMSO).[11] Many stable MOFs exhibit the retention of permanent pores following the removal of the solvent (i.e. activation).[12]

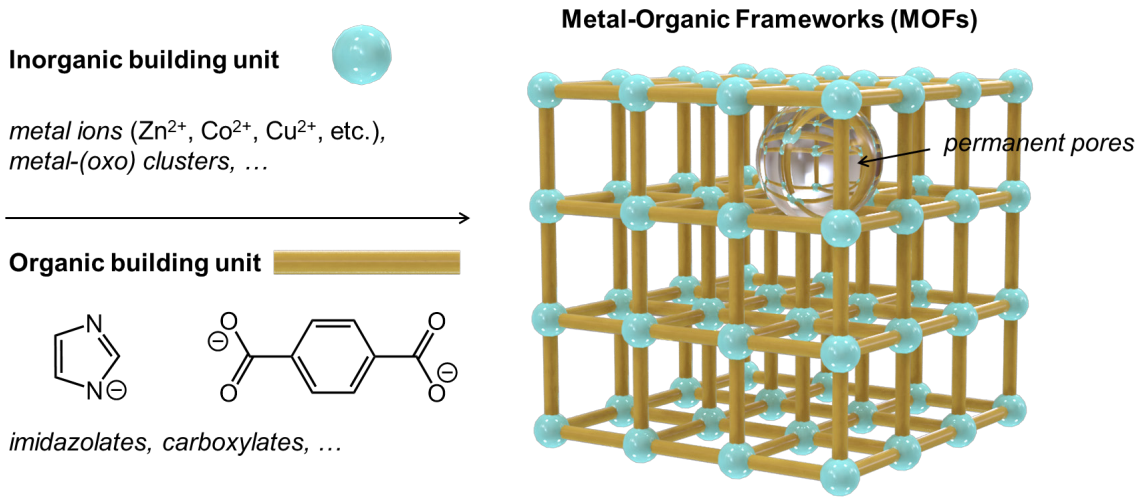

Figure 2.1. Schematic representation of a MOF with inorganic and organic building units (left) and an assembled metal-organic framework with permanent pores (right).

A canonical MOF is the highly porous MOF-5 reported by the group of O. M. Yaghi group in 1999 (**Figure 2.2**).[8] The structure of MOF-5 employs octahedral $Zn_4O(–COO)_6$ clusters as nodes, which are connected by the 1,4-benzenedicarboxylate ($BDC^{2–}$) linkers. MOF-5 exhibits a cubic **pcu** topology with a typical scaffold-like framework.

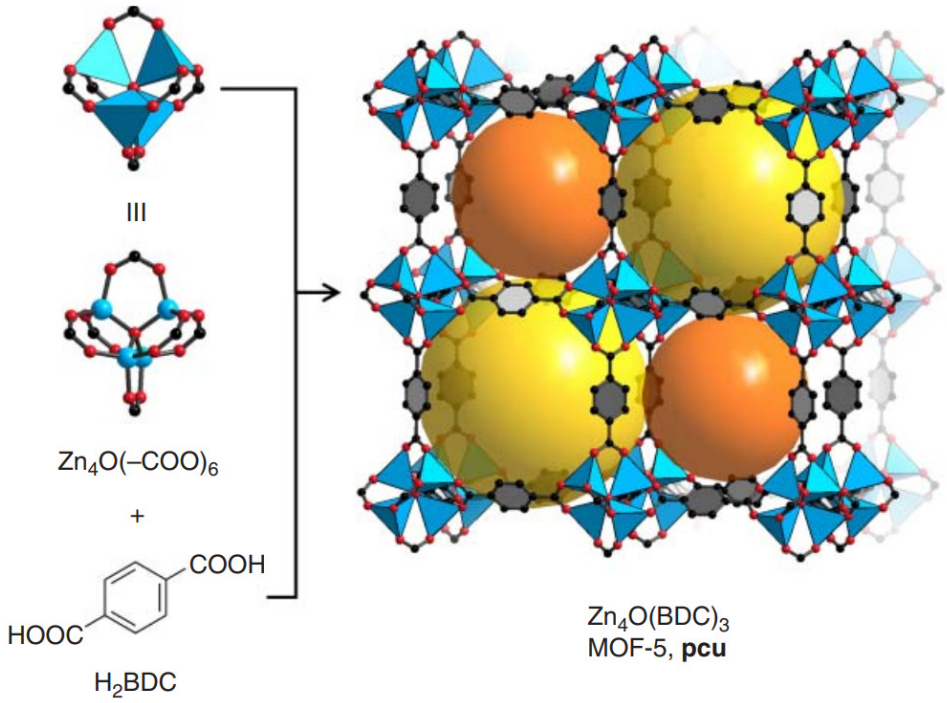

Figure 2.2. The three-dimensional structure of MOF-5. The two types of cavities are highlighted in yellow and orange, respectively. Color code: black, C; red, O; and blue tetrahedra, Zn. Reprinted with permission from *John Wiley and Sons*, copyright @ 2016.

The introduction of different functional groups into MOFs is a relatively straightforward process when compared to that of other inorganic solids. This is because MOFs possess an organic component that is suitable for installing any number of chemical moieties. Indeed, MOF-5 can be made that mix 1,4-benzenedicarboxylate and up to eight of its derivatives in a random fashion (**Figure 2.3**), which have been coined as multivariate MOFs (MTVMOFs).[13]

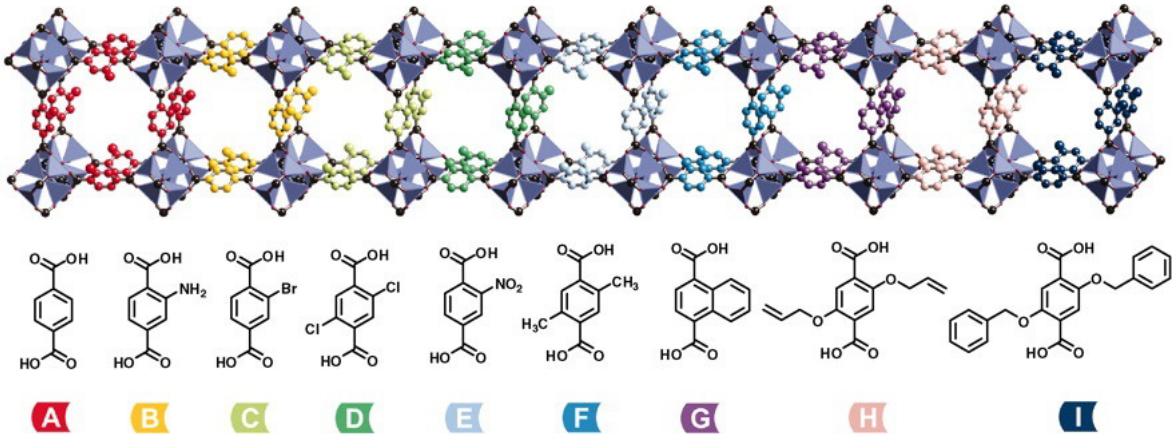

Figure 2.3. Illustration of multiple linkers coexisting in MOF-5. Reprinted with permission from *American Association for the Advancement of Science.* Copyright © 2010.

2.1.2 Postsynthetic modification methods of MOFs

Nevertheless, the preparation of highly functionalized MOFs has been significantly constrained by the solvothermal synthetic methodologies employed in the synthesis of the majority of MOFs. In the context of solvothermal conditions, ligands are typically unable to accommodate functional groups that are susceptible to thermal instability, exhibit problematic solubility, or engage in coordination with metal ions. In any of these instances, the synthesis of the MOF will be rendered unfeasible or will require a significantly more complex process.

Fortunately, there is an alternative method, postsynthetic modification (PSM),[14] which can be employed for the introduction of functional groups into MOFs, which are incompatible with the solvothermal MOF synthesis. This means that the chemical modification can be carried out on the MOF (micro)crystals, rather than on the molecular precursor (i.e., the monomer). In this way, the newly introduced functional groups (and the reaction conditions required for their introduction) need

only be compatible with the final material, while incompatibility with the synthesis method required to obtain the material can be avoided.

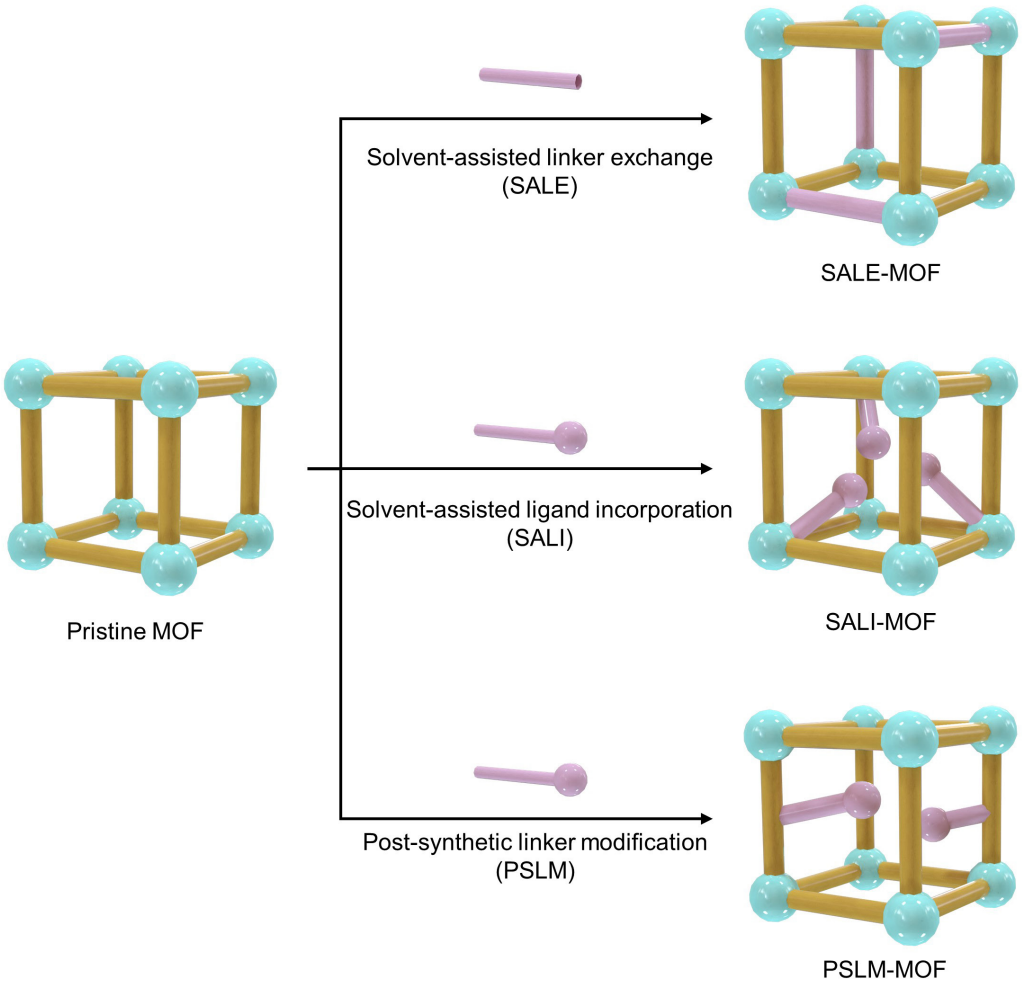

Figure 2.4. Summary of postsynthetic methods of linker engineering of MOFs.

In general, there are three typical approaches to PSM of MOFs, with each form of modification altering the physical and chemical properties of the framework. The aforementioned typical items are referred to as solvent-assisted linker exchange (SALE), solvent-assisted ligand incorporation (SALI), and post-synthetic linker modification (PSLM) (**Figure 2.4**). Most notably, the utilization of the SALE technique has become a valuable addition to the methodologies employed in MOF chemistry. The SALE technique can be applied to some of the most stable MOFs known, for example ZIF-8 (Zeolitic Imidazolate Framework - 8)[15-16] and UiO-66 (Universitetet i Oslo - 66)[17-18], and is capable of controlling pore volume, functionality and pore size.

2.2 Zeolitic Imidazolate Frameworks

Zeolitic imidazolate frameworks (ZIFs) represent an important subclass of MOFs. The designation ZIF was introduced on the grounds that the materials in question exhibit structural similarities to zeolites, which gives rise to MOF structures with zeolitic topologies. The inorganic building units of ZIFs are mostly zinc(II), cobalt(II), iron(II), or cadmium(II) ions, while the organic building units are based on imidazolate or imidazolate derivatives. The bond angles of M–im–M (ca. 144°) in the ZIF building block is similar to that of Si–O-Si (ca. 145°) in the silicates/zeolites (**Figure 2.5**).

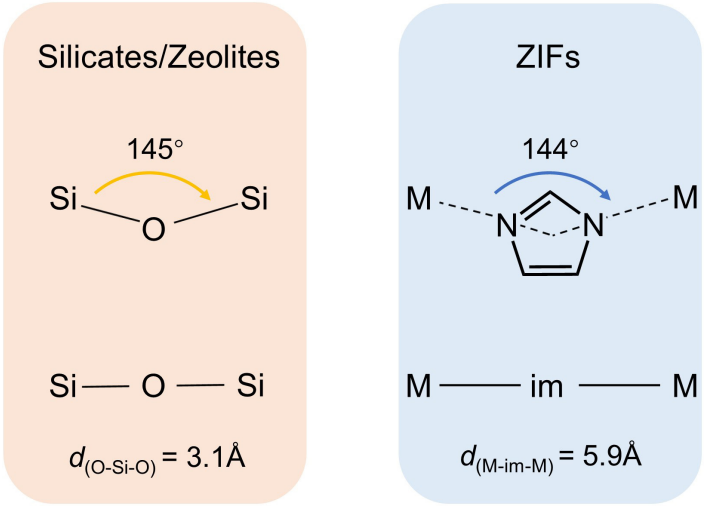

Figure 2.5. Representative scheme showing the similarities between the bond angles and building block geometry between zeolites/silicates and ZIFs. Both exhibit an approximate bond angle of ~145°, but the Si–O–Si distance is 3.1 Å, in comparison to the M–im–M distance of 5.9 Å, which results in expansion of pore sizes for identical topologies in ZIFs. Adapted from Reference[19].

As a consequence of this geometrical similarity, a considerable number of ZIFs display the topologies characteristic of zeolite minerals. The most common topologies observed in ZIFs are **sod** (ZIF-8, ZIF-65, and ZIF-67) and **lta** (ZIF-20, ZIF-21, and ZIF-76), as well as other topologies, as illustrated in **Figure 2.6**.[20] It is noteworthy that ZIFs can also be synthesized using mechanochemical synthesis. In some cases, mechanochemical synthesis has been shown to yield target ZIFs that cannot be synthesized by solvothermal synthesis, and tends to result in smaller particle sizes.[21-23]

Today, ZIFs have been synthesized and structurally characterized with above 50 of different topologies.[24] The open and permanently porous structure of these materials has prompted significant research interest in the field of ZIFs. This is largely due to the potential for enlarging the pore size, functionalizing the pores, and investigating new adsorption, separation and catalytic properties.[25-28]

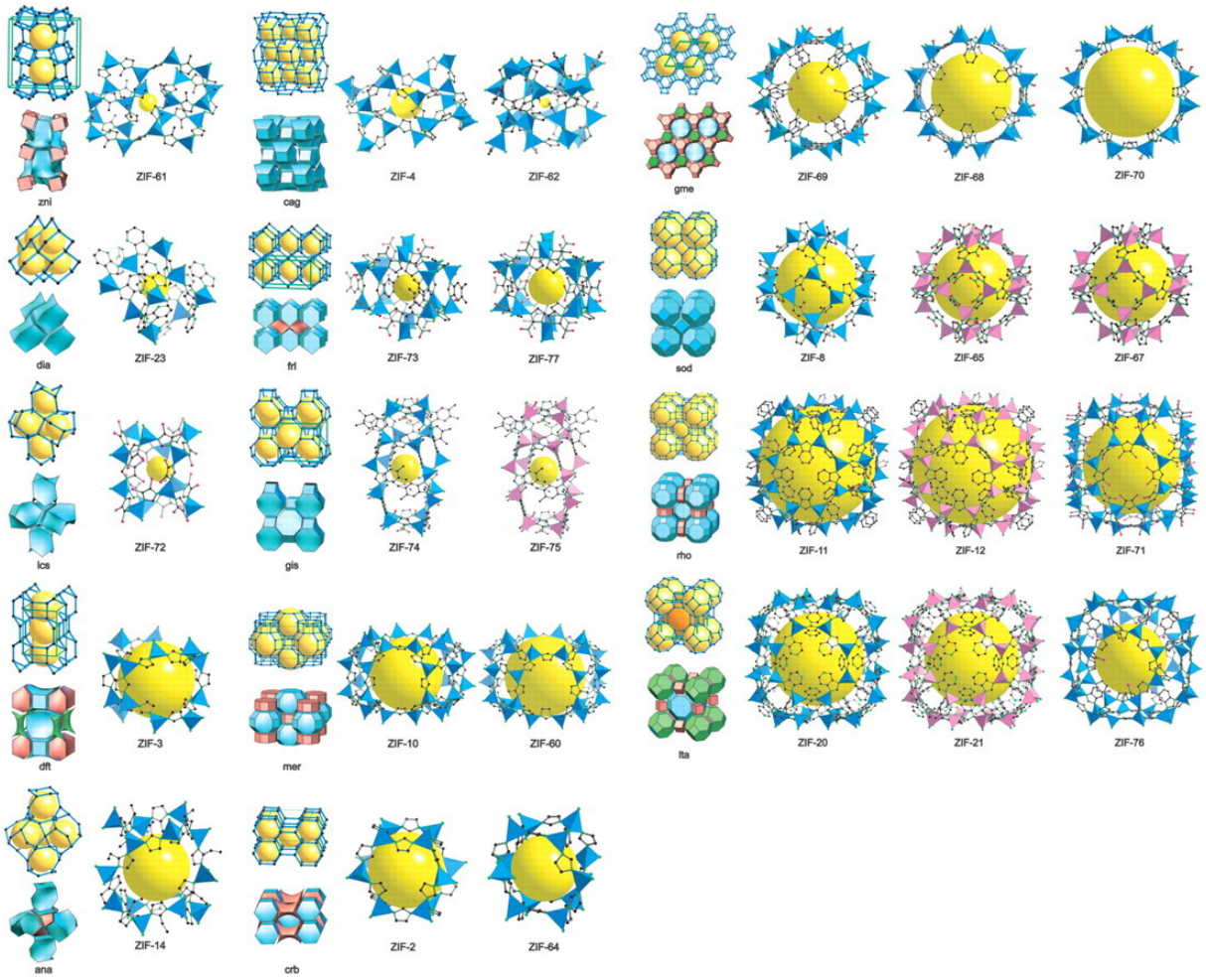

Figure 2.6. The representation of selected ZIFs as reported in the literature. Each row has the nets (blue line and black dot drawings) shown stacked on top of the tiles representing the subdivision of space (variously colored polyhedral shapes) in the net labeled with the three-letter net symbol, followed by the single-crystal XRD structures of ZIFs corresponding to each of the nets. The largest cage in each ZIF is shown with ZnN_4 tetrahedra in blue and CoN_4 in pink. The yellow ball is placed in the structure for clarity and to indicate the open space in the cage. H atoms have been omitted [imidazolate-based links are shown in ball-and-stick representation (C, black; N, green; O, red; Cl, pink)]. From Reference[20]. Reprinted with permission from *American Association for the Advancement of Science.* Copyright © 2008.

2.3 MOF Glasses

Recently, meltable MOFs have garnered significant attention due to their ability to form glasses upon melting. Specifically, crystalline ZIFs can be heated above their melting temperature (T_m) to achieve a molten state. Rapid cooling (vitrification) of the melt, faster than the rate of crystallization, then results in a glassy state (**Figure 2.7**). [1, 29-33] Noteworthy, glasses always are a metastable state that relaxes towards the crystalline state, i.e., in ultimate fate, in the limit of infinite time, is to crystallize.[34]

Nevertheless, the glassy state of MOFs is a fascinating and complex state characterized by its amorphous, non-crystalline structure similar to that of conventional SiO_2 glass. However, unlike SiO_2 glass, MOF glasses typically inherit remarkable porosity from their crystalline counterparts. Furthermore, unlike crystalline MOFs, which usually exist as microcrystalline particles, MOF glasses are highly processable due to their liquid nature at high temperatures. This processability allows MOF glasses to be formed into large monolithic materials without grain boundary effects, enhancing their mechanical integrity and functional properties.[35-37] Therefore, this unique structure imparts several interesting properties and potential applications, particularly in the fields of membranes and solid-state ionics.[38-39]

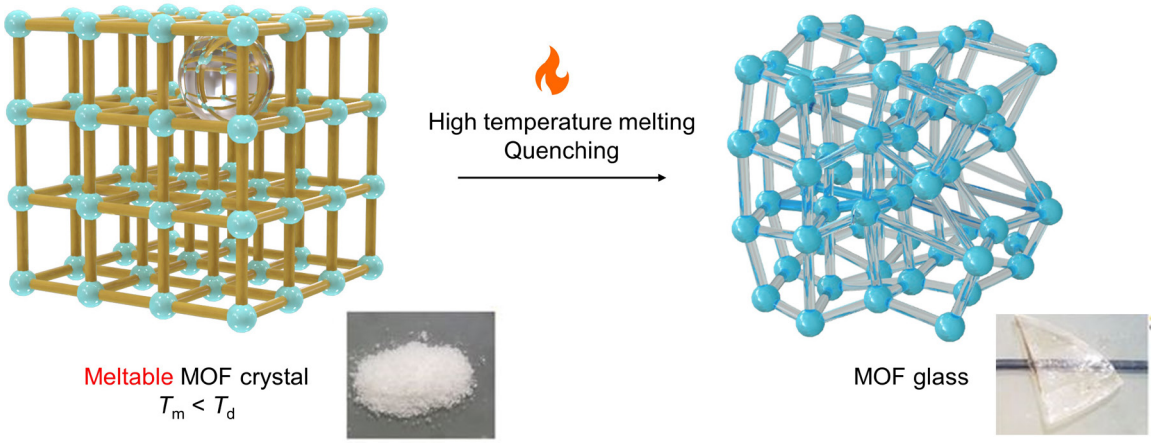

Figure 2.7. Schematic representation of a typical preparation process from meltable MOF to MOF glass via melt-quenching. Inserts were adapted with permission from *American Association for the Advancement of Science*. Copyright © 2020.

It is worth noting that the majority of the meltable MOFs belong to its subset ZIFs, including ZIF-4, ZIF-zni, and ZIF-62.[33, 40] For the ZIF-4 and ZIF-zni, they share the same chemical composition $Zn(im)_2$ (im^- = imidazolate), but differ in their topologies, with ZIF-4 having a **cag** topology and ZIF-zni having a **zni** topology. ZIF-62 is a derivative of ZIF-4, i.e. a small portion of imidazolate (im^-) is replaced by benzimidazolate (bim^-) (**Figure 2.8**).[41] They are three of the first reported meltable ZIF materials in the literature.[33, 40] Due to the high thermal stability and porosity inherited from their pristine crystals, these ZIF glasses inherit this porous nature and have become the most studied MOF glasses to date. Notably, despite the inevitable reduction in porosity after formation of the glassy state, ZIF glasses still exhibit notable porosity and selectivity for gas storage and separation. This makes them promising candidates for applications in energy conversion, gas purification and carbon capture. [38, 42-43]

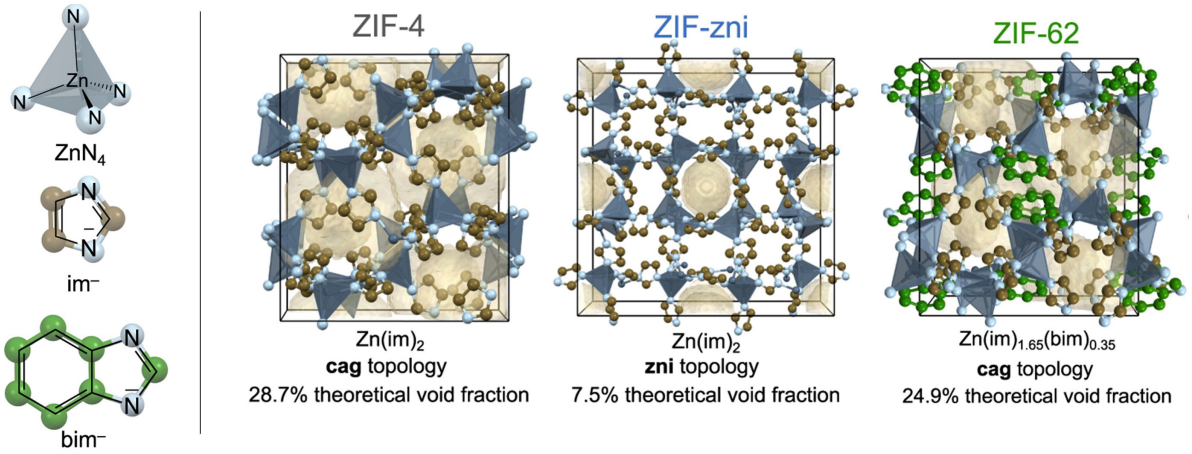

Figure 2.8. (Left) Building units of the investigated ZIF glass formers. (Right) Crystal structures of the ZIF glass formers. ZIF-4 and ZIF-62 are viewed along the crystallographic *b*-axis. ZIF-zni is viewed along the crystallographic *c*-axis. Hydrogen atoms are omitted for clarity. The theoretical void fraction was calculated with a probe radius of 1.6 Å and is shown in pale yellow. From reference[41]. Adapted with permission from *Springer Nature*. Copyright © 2022.

The formation mechanism of MOF glasses aligns with that of traditional glasses, as illustrated in **Figure 2.9**, Initially, the MOF crystal is heated, causing an increase in enthalpy until the melting temperature (T_m) is reached. At this point, the crystalline MOF transitions to a liquid state, characterized by a significantly higher enthalpy. If the liquid is rapidly cooled, it bypasses crystallization and forms a supercooled liquid. Further cooling below the glass transition temperature (T_g) results in the formation of MOF glass, following an enthalpy change distinct from the crystalline state.[34, 44-46]

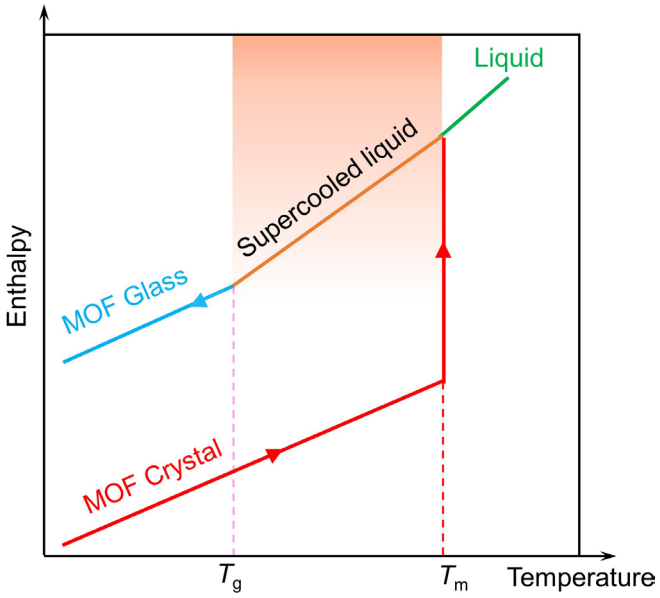

Figure 2.9. Enthalpy versus temperature plot depicting the process from crystalline MOFs to MOF glasses.

The melting mechanism of ZIFs has been elucidated through density functional theory (DFT) based molecular dynamics (MD) simulations, corroborated by X-ray and neutron scattering data.[47] The proposed mechanism involves Zn–N bond breakage, resulting in the Zn^{2+} ion being temporarily three-fold coordinated, followed by the coordination of another imidazolate (im^-) group, ultimately yielding the porous ZIF liquid. This process is illustrated in **Figure 2.10**.

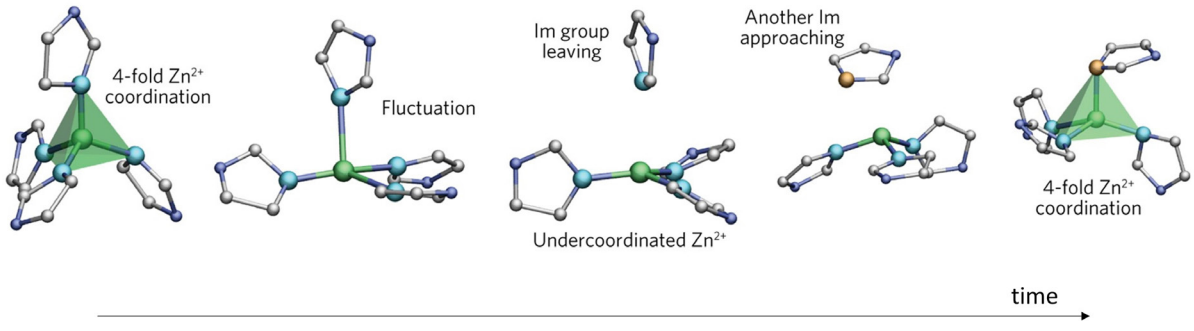

Figure 2.10. Visualization of representative imidazolate exchange events in meltable ZIFs. From reference[47]. Reprinted with permission from *Springer Nature*. Copyright © 2017.

2.4 MOF Glass Characterization

2.3.1 Structural identification via X-ray diffraction and total scattering

X-ray powder diffraction

X-ray powder diffraction (XRPD) is one of the most widely used techniques for the structural characterization of crystalline MOF materials. In the crystalline MOFs, XRPD patterns are characterized by distinct, sharp Bragg peaks. These peaks correspond to the regular, periodic arrangement of atoms within the crystal lattice. Each peak's position, intensity, and shape provide detailed information about the unit cell dimensions, symmetry, and atomic positions. XRPD is a powerful way of structuring the MOF, which can usually be done using profile fitting. Beyond structure fitting by Rietveld refinement[48], there are two common methods for structureless profile fitting, the Pawley[49] and Le Bail[50] method. The Pawley method is employed throughout the course of this thesis.

However, when the MOF is transformed into an amorphous or liquid/glassy state, XRPD is unable to determine its structure, even though it is still an important tool for studying *in-situ* changes in its structural properties. In the case of MOF liquids and glasses, the long-range periodicity is lost, resulting in the disappearance of sharp Bragg peaks and the emergence of broad, diffuse scattering signals.

X-ray total scattering and PDF analysis

Total scattering includes both Bragg and diffuse scattering, capturing information from both long-range periodicity (if present) and local structural arrangements. In the case of MOF glasses, where the material lacks long range order, the focus is on the diffuse scattering component. The total scattering data is collected over a wide range of scattering angles to ensure that both the high and low Q[†] regions are adequately sampled. High Q data are essential to probe short range interactions, while low Q data can provide insight into medium range order.[51-53]

Pair distribution function (PDF) analysis is a powerful methodology based on X-ray total scattering data that provides a real-space representation of atomic pair

[†] Scattering vector $Q = [4\pi sin(\theta)]/\lambda$, with the scattering angle θ and the experimental X-ray wavelength λ.

correlations.[54] A hypothetical PDF is shown in **Figure 2.11**. In the simple case, the PDF represents a radial distribution function ($R(r)$) with peaks appearing at the distances of neighboring atoms from the reference atom at the origin. The area under these peaks corresponds to the number of neighboring atoms at each distance. This suggests that $R(r)$ can provide valuable information for understanding the arrangement of atoms in a lattice. For real materials, the XPDF is the sum of all interatomic distances, allowing us to understand the local structure, even in amorphous materials.

In the data processing, the obtained scattering intensity $I(Q)$ is normalized to yield $S(Q)$ the 'total-scattering structure factor' given in absolute of scattering per atom. The $S(Q)$ is then further transformed into real space via Fourier transformation. This results in the function $G(r)$ being obtained as follows:

$$G(r) = \frac{2}{\pi}\int_0^\infty Q[S(Q) - 1]\sin(Qr)dQ$$

The function $G(r)$ describes the change in density as a function of interatomic distances in the material what is called the XPDF.[53] It has to be noted that $G(r)$ makes the peaks at low r prominent. Therefore, $D(r)$[52] is often used in literature:

$$D(r) = 4\pi r\rho_0 G(r)$$

with $\rho_0 = N/V$ the average number density of the material. In the case of MOF glasses, PDF analysis is not only a powerful tool for distinguishing the long-range order of crystalline and glassy states, but is also of particular value in revealing the local atomic structure. The PDF provides insight into the coordination environments around metal nodes and the connectivity of organic linkers.

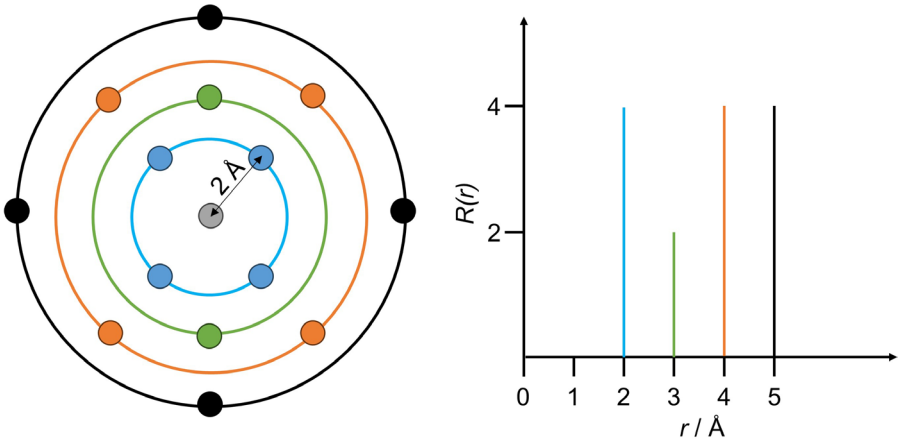

Figure 2.11. Schematic illustration of the hypothetical generation of a PDF in $D(r)$ from a two-dimensional arrangement of atoms. The coloured rings indicate the distance of neighbouring atoms to the atom in the origin (left). The integral of the peaks is proportional to the number of respective distances. The same colours are assigned to the corresponding peaks (right).

2.3.2 Thermal analysis

Thermal analysis of glass-forming MOFs typically involves two key methods. The first method is thermogravimetric analysis (TGA), which examines the relationship between temperature and residual weight. A rapid decline in TGA traces generally signals the onset of decomposition temperature (T_d) of MOFs (**Figure 2.12**, grey line of TGA). Once T_d is obtained, the validation of the subsequent phase transition should be carried out in the temperature interval below T_d. In addition to assessing the decomposition temperature of glass-forming MOFs, it is important to evaluate the thermal stability of the MOF glasses themselves. This is demonstrated by examining the TGA traces of the MOF glasses (**Figure 2.12**, red line of TGA), which show the thermal stability of the glass as it undergoes a transformation into a supercooled liquid when heated.

Additionally, differential scanning calorimetry (DSC) is a powerful tool for investigating the detailed thermodynamic and kinetic parameters of glass-forming MOFs, as well as identifying the glass transition of the MOF glasses.[55] In DSC, heat flow is measured by comparing the heat absorbed or released by MOF sample with that of an empty aluminum reference crucible under identical temperature conditions. This technique identifies exothermic and endothermic transitions by detecting changes in heat flow associated with phase transitions. In this thesis, an exothermic transition releases heat, resulting in a downward peak, while an endothermic transition absorbs heat, leading to an upward peak in the DSC curve. Specifically, the DSC profile of a glass-forming MOF typically features an endothermic solid-liquid phase transition at the melting temperature (T_m) and a glass transition temperature (T_g), at which the vitrified glass transitions to the supercooled liquid state in the second upscan (**Figure 2.12**).

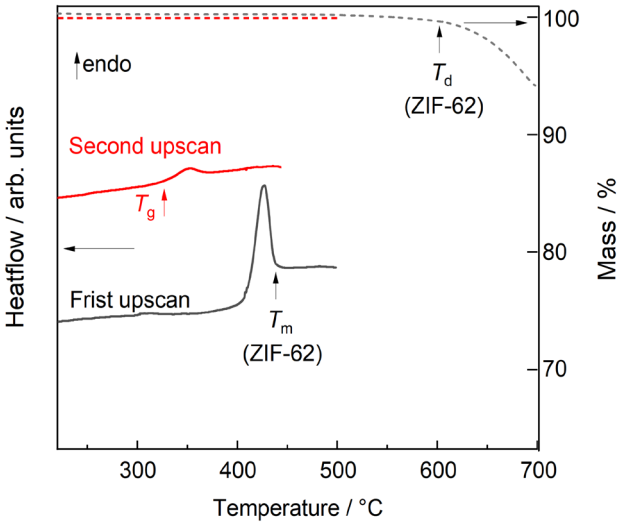

Figure 2.12. Two upscans (first: grey lines, second: red lines) of the combination data of TGA (dotted lines) and DSC (solid lines) of the representative meltable MOF ZIF-62.

Additionally, the fragility index of a glass can be extracted from the DSC experiments with heating rates (q_h) and cooling rates (q_c) varying (between ±5 and ±25 °C min^{-1} in this thesis). From these experiments, the heating/cooling-rate-dependent fictive temperature T_f of the glasses is obtained. T_f can be envisioned as the temperature at which the supercooled liquid is vitrified (i.e., frozen in).[56] Based on the variation of T_f with q_c, the dimensionless calorimetric fragility index (m) of the corresponding supercooled liquids is extracted.[55] m is a measure for the activation energy ($E_{a,vis}$) of the viscosity (η) at T_g, while T_g is defined as the temperature where η is equal to 10^{12} Pa · s.[57] Small values of m (<30) indicate strong liquids which vitrify into brittle glasses (e.g., for silica, $m = 20$), while large values of m (>50) specify fragile liquids that form ductile glasses.[40]

Moreover, DSC is able to detect the change in heat capacity (ΔC_p) of MOF glasses at their T_g. ΔC_p is a crucial parameter in the study of MOF glasses, as it provides insight into the level of connectivity in MOF glass materials. In this thesis, ΔC_p is also measured by comparing the heat flow to the sample with that of an empty aluminum reference crucible, but by applying a sinusoidal modulation to the temperature profile, called modulated DSC (MDSC), an example of which is shown in **Figure 2.13**. This modulation allows for the separation of overlapping thermal events and provides a more accurate measurement of specific heat capacity. MDSC can distinguish between reversible and non-reversible transitions, offering detailed insight into the thermodynamic and kinetic properties of glass-forming MOFs. By using MDSC, it is possible to obtain a clearer understanding of the complex thermal behavior of MOF glasses, which is not achievable through conventional DSC alone.

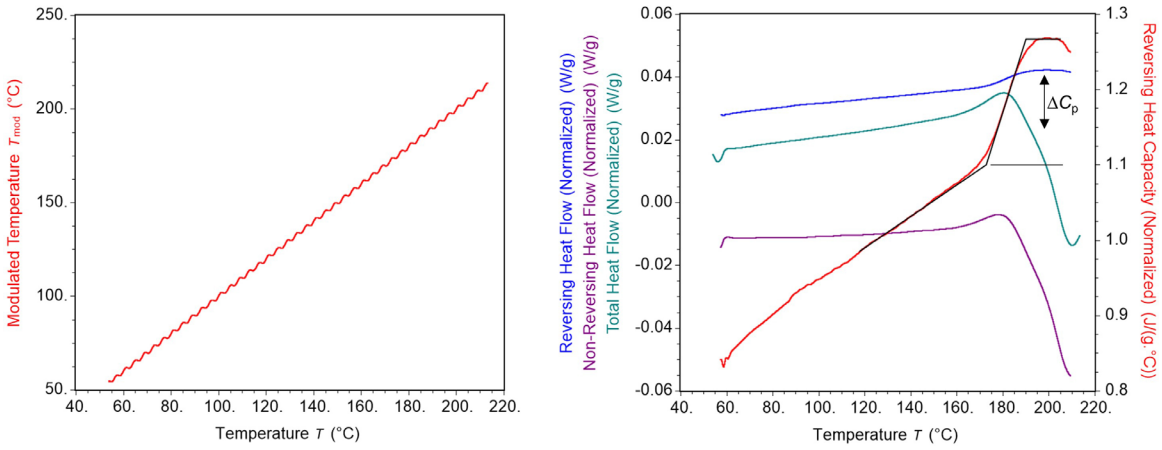

Figure 2.13. An exemplary MDSC data of a coordination network glass. (Left) Example of a sinusoidal temperature profile used in MDSC. (Right) The total heat flow, reversing and non-reversing heat flow, and heat capacity curve (C_p) and ΔC_p obtained from MDSC.

Overall, the DSC provides valuable information and additional insights into materials. Un a fundamental level, DSC allows technique to distinguish between simply amorphous MOF materials and MOF glasses, information which cannot be deduced from X-ray diffraction methods. While X-ray diffraction is effective at identifying crystalline structures, it cannot provide detailed information about the amorphous state. Amorphous materials can exist in various forms, including disordered solids that do not exhibit the characteristics of glasses, examples include amorphous carbons and many amorphous MOFs and porous polymers.[58-60] Glasses are a specific type of amorphous material that undergo a glass transition, characterized by a distinct T_g.[34] This transition is detectable by DSC, allowing for the differentiation between general amorphous materials and true glasses. The presence of a glass transition is of highest relevance for the processability of these compounds. Above the glass transition the material is in a supercooled liquid state allowing for shaping and molding, processes which are not possible in the vitrified state. Therefore, DSC provides critical insight into the thermal properties and phase transitions of MOF glasses, which are not discernible through X-ray related methods alone.

2.3.3 Porosity determination

Positron annihilation lifetime spectroscopy (PALS) is a non-destructive analytical technique used to determine the porosity and free volume of materials. The investigation of the porosity of MOF glasses using PALS was first performed by Thornton *et al.*,[61] on a_gZIF-4(Zn) as well as its crystalline phase ZIF-4(Zn) and dense crystalline phase ZIF-zni(Zn). a_gZIF-4(Zn) exhibits both the smallest and largest pore sizes, with voids estimated at 6.9 Å and 2.6 Å, respectively (**Figure 2.14a**).

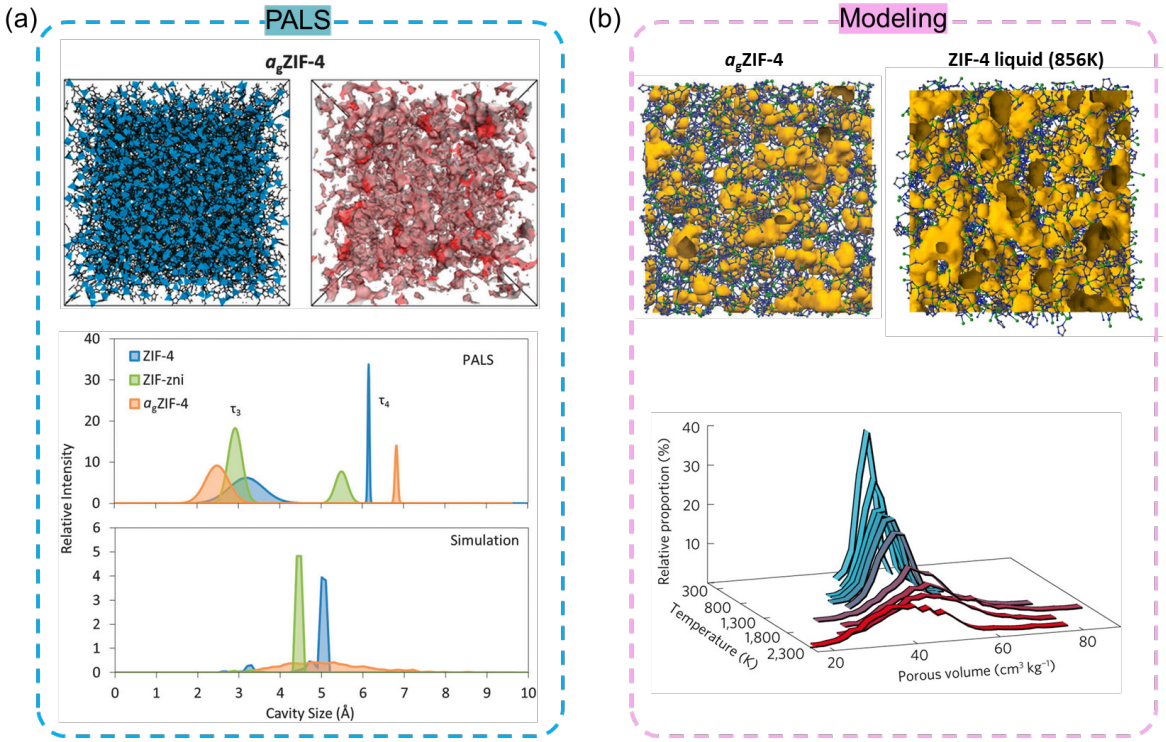

Figure 2.14. (a) The structure and porosity models of a_gZIF-4 constructed by PALS method, and the pore size distributions of related samples. Reprint with permission from *Royal Society of Chemistry*. Copyright © 2016. (b) The structure model of a_gZIF-4 and liquid ZIF by Reverse Monte Carlo (RMC) simulation. Pore size distribution calculated using molecular dynamics (MD) method. Reprinted with permission from *Springer Nature*. Copyright © 2017.

Modeling based on Reverse Monte Carlo (RMC) and molecular dynamics (MD) simulations can also be used to perform similar structural simulations and visualize porosity, as the simulated results can be exported as crystallographic files (**Figure 2.14b**). The porosity can be represented as voids or empty spaces between the atoms in the model and can be quantified using Zeo++ software[62] or visualized using

software such as Mercury[63]. By visualizing the porosity, the RMC simulation results can provide information about the distribution and size of voids in the material. It is worth mentioning that these methods are also able to provide intramolecular and intermolecular interactions that are not available with classical methods, but they are computationally expensive.

In addition to the aforementioned unconventional characterization techniques, gas adsorption is a classical method commonly employed for the characterization of porosity in porous materials. Unlike crystalline MOFs, where the pores are uniform, the pores in MOF glass are not only complex but also tiny. This limits the access of gas molecules with large kinetic diameters to the interior of the glass frameworks for quantification of porosity. Consequently, the selection of an appropriate gas probe and temperature is of utmost importance. The measurement of porosity and surface area of porous materials is commonly performed using isothermal physisorption of N_2 at 77 K or Ar at 87 K, which is a widely adopted technique applicable to both crystalline and amorphous porous materials. Regrettably, the use of N_2 and Ar physisorption is not feasible for quantifying the porosity and surface area of ZIF glasses.[41] This is ascribed to diffusion limitations of N_2 and Ar gas into the narrow pores of the MOF glasses at this low temperature.[64-65] The most effective method for detecting porosity in MOF glasses was determined to be CO_2 physisorption at 195 K (**Figure 2.15**). In this context, CO_2 is considered to be in its supercooled liquid state, filling the micropores effectively with fluid CO_2 instead of solid CO_2.[66-67] As a result, the maximum p/p_0 (p_0 denotes saturation pressure) achievable in a CO_2 sorption experiment of microporous materials at 195 K is up to approximately 0.5, and all pores up to a width of 50 Å are completely filled.[41] Furthermore, the density of the CO_2 supercooled liquid of at 195 K is estimated to be 1.258 g cm^{-3}.[41] This allows all micropore volumes to be optimally quantified and porosity calculated (See **Appendix 3.8** in this thesis for details.).

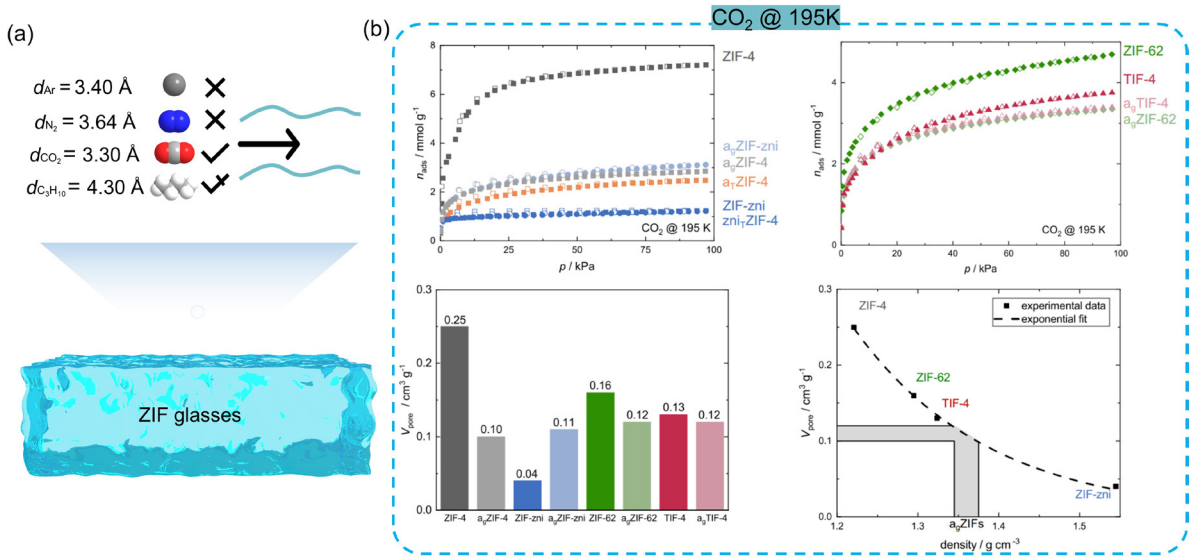

Figure 2.15. (a) Schematic diagram of the diffusion of four gases in ZIF glass. i.e. CO_2 at 195K, N_2 at 77k, Ar at 87K, and C_3H_{10} at 273K. The d_{gas} values are the kinetic diameters the gases. (b) Quantification of the pore volume and density of ZIF glasses by CO_2 at 195K. Adapted with permission from *Springer Nature*. Copyright © 2022.

2.3.4 Gas separation

Gas separation is a critical process in various industrial applications, including natural gas purification, carbon capture and storage, and air quality control. The objective of gas separation is to isolate specific components from a mixture of gases, which can be essential for further processing or environmental protection. Porous materials, including zeolites, activated carbons, and metal-organic frameworks (MOFs), are highly effective in these processes due to their unique structural properties. Two primary phenomena are critical for gas separation using porous materials: thermodynamic adsorption and kinetic diffusion.[68]

2.3.4.1 Thermodynamic Gas Separation

Thermodynamic adsorption occurs when gas molecules are adsorbed onto the surface or within the voids of the porous material. This process depends on the interaction between the gas molecules and the material's surface, which is influenced by factors such as surface area, pore size, and surface chemistry. Materials with high surface areas and appropriate surface functionalities can selectively adsorb certain gases more effectively than others. The advantages of thermodynamic gas separation are as follows: (i) high selectivity for specific gases based on interactions with the material's surface, (ii) effective for separating gases with significantly different

adsorption affinities. However, there are some drawbacks of the adsorptive separation technology. (i) It is limited by the capacity of the adsorbent, leading to saturation (ii) It requires regular regeneration of the adsorbent material to restore its capacity. The main application of thermodynamic gas separation is the adsorber columns, where gas mixtures pass through a packed bed of adsorbent material and specific gases are selectively removed.

Semi-quantitative estimation of thermodynamic gas separation can be achieved directly from single-component gas isotherms. This allows for comparison of the adsorption capacities of relevant gases under identical and ideal conditions. In this context, the ideal adsorbed solution theory (IAST) has been developed, enabling a more detailed investigation of the thermodynamic gas separation ability of a porous material in regard to a gas mixture.[69-70] It is worth noting that IAST is suitable for calculating separation constants when the adsorbed capacities of different gases are very different. For a two-component gas mixture (gas A and B) the IAST selectivity (S_{IAST}) can be calculated from these values which is defined as:

$$S_{IAST} = \frac{x_i}{y_i}$$

here $x_i = x_A/x_B$ is the molar ratio of the adsorbed fluids and $y_i = y_A/y_B$ is the chosen molar ratio of the fluids in the gas phase. The values of x_A, x_B, y_A, and y_B are determined experimentally. The molar ratios x_A and x_B are obtained from adsorption isotherms, which are measured at equilibrium conditions over a range of pressures.

2.3.4.1 Kinetic Gas Separation

Kinetic diffusion relies on the different rates at which gas molecules diffuse through the pores of the material. This process is governed by the size and shape of the pores, as well as the size and shape of the gas molecules. Smaller or lighter molecules typically diffuse faster through the pores, enabling separation based on molecular size or mass. The advantages of kinetic gas separation are as follows: (i) It can separate gases with similar adsorption properties but different diffusion rates. (ii) It is a continuous process with potential for high throughput. However, the disadvantages are as follows: (i) It typically provides lower selectivities compared to thermodynamic adsorption for gases with similar sizes. (ii) Pore clogging or fouling can drastically affect performance. This type of separation is commonly used in (polymer)membrane separations, where a mixture of gases is passed through a membrane with selective permeability so that some gases diffuse faster than others. The separation process of microporous membranes (such as MOF membranes or

MOF-based mixed matrix membranes) is typically based on both adsorption and diffusion processes in parallel.

The kinetic separation selectivity of porous materials can be assessed by sorption measurements. In these experiments, a certain amount of gas at a certain pressure is added to the porous material and the adsorbed volume of the gas is measured over time until equilibrium is reached. Subsequently the separation constants can be further quantified from the kinetic adsorption curves. The derived kinetic adsorption curves can be fitted to suitable kinetic models (e.g. equations for pseudo-first order, or stretched exponential reactions) to determine the rate constants of adsorption for a given material and gas combination. The method has for example been applied on a coordination polymer (CP) crystal/glass composite (**Figure 2.16**).[71]

The specific calculation in the literature is as follows:

The equation describing the relationship between the normalized uptake (corresponding to $(P_i - P)/(P_i - P_e)$) and time by the pseudo-first order model is given as follows:

$$\text{normalized uptake} = \frac{(P_i - P)}{(P_i - P_e)} = 1 - e^{-kt}$$

And the stretched exponential model is given as follows:

$$\text{normalized uptake} = \frac{(P_i - P)}{(P_i - P_e)} = 1 - e^{-(kt)^{\beta}}$$

where P_i is the initial pressure, P is the pressure at time t (in s), P_e is the pressure at equilibrium, k is the rate constant of gas adsorption (in s^{-1}), and β is the exponent parameter related to the width of the distribution of diffusion rate constants.

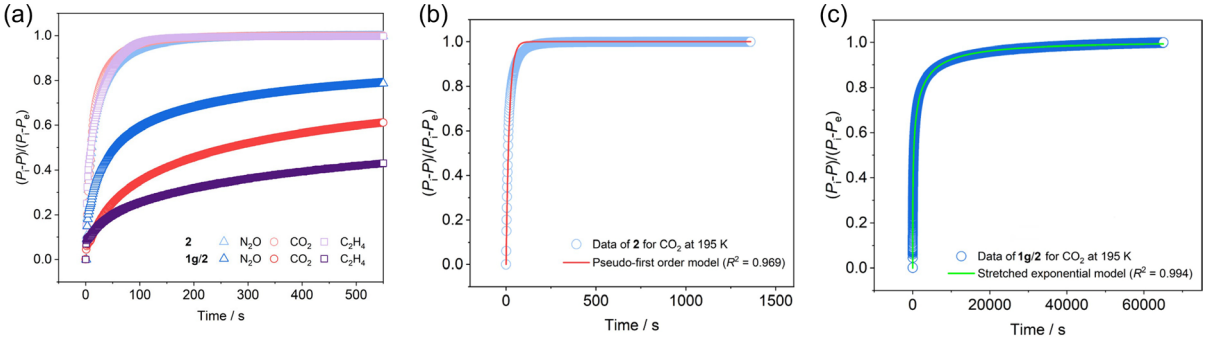

Figure 2.16. (a) Normalized kinetic sorption profiles of a crystalline CP (**2,** $[Cu_2(pzdc)_2(pyz)]$) (pzdc = 2,3-pyrazinedicarboxylate and pyz = pyrazine), and CP crystal/glass composite (**1g/2,** $[Cu(bib)_{2.5}] \cdot 2NTf_2$ glass/$[Cu_2(pzdc)_2(pyz)]$), where bib and NTf_2 are 1,4-bisimidazole butane and bis(trifluoromethylsulfonyl)amide, respectively. (b) First order fitting of the CO_2 kinetic adsorption profile for **2**. (c) pseudo-first order fitting of the CO_2 kinetic adsorption profile for **1g/2**. Reprinted with permission from *American Chemical Society*. Copyright © 2023.

3 Highly Porous ZIF-8 Glasses

The work presented in this chapter has been published in a peer-reviewed research article. Herein, text and figures of this publication are reprinted or adapted (licensed under a Creative Commons Attribution 4.0 International License, https://creativecommons.org/licenses/by/4.0/legalcode). Adaptions involve changes in compound nomenclature and rearrangements of figure parts. Reference to the publication and author contributions are given below.

Wen-Long Xue, Pascal Kolodzeiski, Hanna Aucharova, Suresh Vasa, Athanasios Koutsianos, Roman Pallach, Jianbo Song, Louis Frentzel-Beyme, Rasmus Linser, Sebastian Henke*., "Highly Porous Metal-Organic Framework Liquids and Glasses via a Solvent-Assisted Linker Exchange Strategy of ZIF-8", *Nat. Commun.* **2024**, 15, 4420.

Publisher: Springer Nature
Date: May 25, 2024

Author contributions:

S.H. and W.-L.X. designed the project. W.-L.X. synthesized the materials and performed and analyzed XRPD, FTIR spectroscopy, ^{1}H NMR spectroscopy and thermal analysis and gas sorption experiments. J.S. contributed to the preparation of ZIF-8. W.-L.X. performed the synchrotron XRPD experiments with the help of P.K., A.K., R.P. and L.F-B. P.K., A.K., and R.P. collected X-ray total scattering data. W.-L.X. processed and analyzed all the synchrotron radiation data with the help of J.S. H.A. and S.V. performed the solid-state NMR experiments with R.L. contributing to data analysis and interpretation. W.-L.X and S.H. wrote the manuscript with contributions from all the authors. All authors have given approval of the final manuscript.

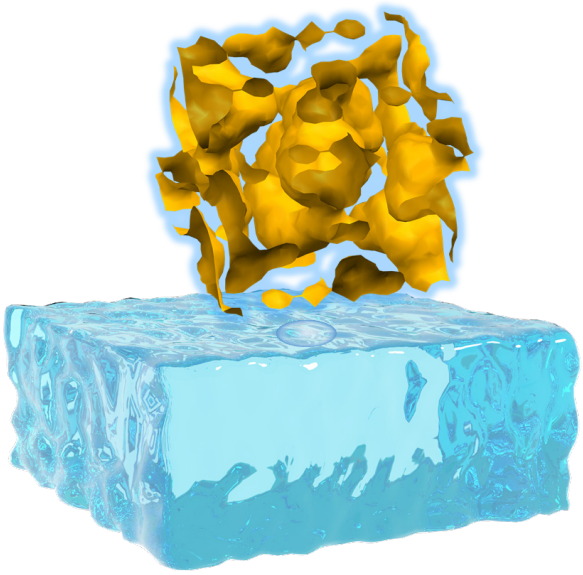

Abstract

By combining the porosity of crystalline MOFs with the unique processability of the liquid state, melt-quenched MOF glasses offer exciting opportunities for molecular separation. However, progress in this field is limited by two factors. Firstly, only very few MOFs melt at elevated temperatures and transform into stable glasses upon cooling the corresponding MOF liquid. Secondly, the MOF glasses obtained thus far feature only very small porosities and very small pore sizes. Here, in this chapter, the solvent-assisted linker exchange (SALE) is demonstrated as a versatile method to prepare highly porous melt-quenched MOF glasses from the canonical ZIF-8. Two additional organic linkers are incorporated into the non-meltable ZIF-8, yielding high-entropy, linker-exchanged ZIF-8 derivatives undergoing crystal-to-liquid-to-glass phase transitions by thermal treatment. The ZIF-8 glasses demonstrate specific pore volumes of about $0.2\,cm^3\,g^{-1}$, adsorb large amounts of technologically relevant C_3 and C_4 hydrocarbons, and feature high kinetic sorption selectivities for the separation of propylene from propane.

3.1 Introduction

As described in the previous chapter, MOFs are network structures composed of organic linkers interconnecting inorganic building units (metal ions or (oxo)-clusters) via coordination bonds.[72-74] At present, nearly 100,000 unique MOFs have been reported, mainly in the form of small single crystals and polycrystalline powders.[5] Although MOFs in crystalline form have been used for various applications, their lack of processability and grain boundary effects limit their utility for the fabrication of homogeneous membranes for gas separation and efficient solid-electrolytes. ZIFs[20] are an important subset of MOFs and major formers of the fourth generation of MOFs[1-2, 29] (i.e. liquid MOFs[47] and their corresponding glasses[33, 43]), offering processable bulk shapes which still retain the advantageous chemical functionality of crystalline MOFs. The advent of fourth-generation MOFs is proposing an elegant solution for the processing of these materials in bulk shapes of specific geometries, as required for most practical applications, by moulding them in their (supercooled) liquid state.[35, 75]

However, only very few ZIFs have been observed to melt at elevated temperatures and to form glasses by melt-quenching. This is because the materials' decomposition temperature (T_d) is typically lower than their melting temperature (T_m). In most cases, the imidazolate-based organic linkers decompose before the metal-linker coordination bonds break and reorganize – the prerequisite for ZIF melting.[40, 43, 47, 76] So far, only ZIFs with the relatively dense **cag**, **zni** and **gis** network topologies have been reported to melt, whereas ZIFs exhibiting more porous topologies (i.e. **sod** or **lta**) do not melt on their own but can be flux melted in the liquid of a meltable ZIF.[40, 77-78] The most critical issue, however, is that the gas-accessible porosity of the known melt-quenched ZIF glasses is rather low and ranges between 14% and 16% of the bulk glass volume.[41] Moreover, the pores of the ZIF glasses are very narrow, so that N_2 molecules (kinetic diameter 3.6 Å) do not enter the intrinsic pore network of the glasses at 77 K, whereas the diffusion of the larger *n*-butane (kinetic diameter 4.3 Å) is kinetically hindered at 273 K, resulting in very low gas uptakes and strongly hysteretic sorption behaviour.[43] This greatly limits their application in gas adsorption and separation, guest molecule loading and transport, so the development of MOF glasses, especially melt-quenched MOF glasses with high porosity, remains an important task.

The aim of this chapter is to make ZIF-8[79] ($Zn(mim)_2$) melt and form a glassy material. ZIF-8 is also known as MAF-4[80], is a high-porosity MOF (about 50% of the crystal volume is void) consisting of Zn^{2+} and 2-methylimidazolate (mim^-) connected to a framework with large spherical cavities of about 1 nm diameter and **sod** (sodalite) topology. ZIF-8 is the single most extensively studied ZIF material, both from a fundamental[15, 81-82] and an applied[83-86] perspective. Nevertheless, ZIF-8 cannot be directly formed into a glass by melt-quenching as the free-energy barrier for melting is too high due to its high porosity.[87] Thus, crystalline ZIF-8 decomposes at about 540 °C before reaching the liquid state. It has been demonstrated, however, that infiltration of an ionic liquid (IL) into the pores of ZIF-8 yields a meltable and glass-forming IL@ZIF-8 composite.[29] Unfortunately, the composite partially decomposes during melting while the porosity of the derived IL@ZIF-8 glass is even smaller than the porosity of the prototypical ZIF-62 glass.

In this chapter, two additional organic linkers, im^- and bim^- (benzimidazolate) are incorporated into ZIF-8 by solvent-assisted linker exchange (SALE) at varying ratios. The two additional linkers are supposed to play distinct roles in enabling the melting of ZIF-8 crystals. The im^- linker is known to exhibit weaker binding to Zn^{2+} compared to the original mim^- linker.[87] Conversely, the bulky bim^- linker is essential for inhibiting the crystallization into a dense ZIF phase with the **zni** topology.[43] Depending on the precise chemical composition (i.e. the molar ratio of the three different linkers), some of the derived linker-exchanged ZIF-8 derivatives undergo crystal-to-liquid-to-glass phase transitions by thermal treatment. By analyzing altogether 50 linker-exchanged ZIF-8 samples with varying compositions, a triangular phase diagram is generated, depicting regions of (i) congruent melting, (ii) incongruent melting and (iii) decomposition before melting in the available phase space. The porosity of a representative congruent melting and glass-forming ZIF-8 derivative is quantified for the crystal and glass forms by CO_2 and N_2 gas sorption measurements. The ZIF-8 glass exhibits a substantially higher specific pore volume than the prototypical ZIF-62 glass. Moreover, gas physisorption experiments establish that the ZIF-8 glass adsorbs rather large amounts of technologically relevant C_3 and C_4 hydrocarbons and features the ability to kinetically separate propylene from propane. This demonstrates an unanticipated potential of linker exchange for the generation of high-porosity MOF glasses for a broad range of technical applications. Importantly, the present work also reveals that MOF melting is not limited to crystalline precursors having rather dense network topologies (e.g.

cag or **zni**), but can be extended to more porous MOF phases through targeted linker engineering and linker mixing.

3.2 Preparation and characterization of ZIF-8 derivatives

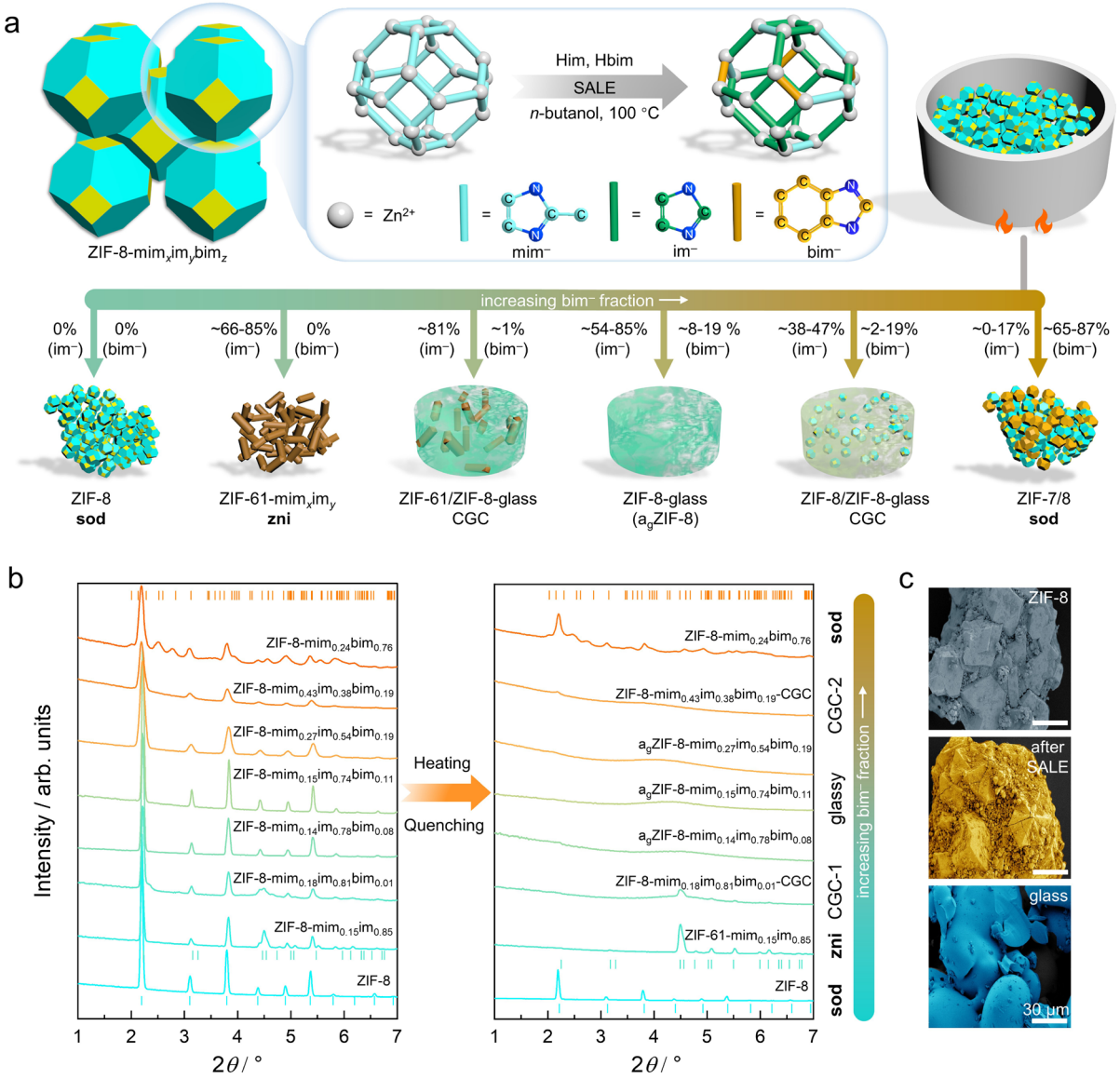

Figure 3.1. Representation of the SALE process to derive various linker-exchanged ZIF-8 derivatives and their crystallographic and microscopic analysis. a Schematic of the SALE process leading to the incorporation of im^- and bim^- linkers in ZIF-8 and the thermal phase behaviour of the derived linker-exchanged ZIF-8 derivatives. **b** Synchrotron radiation XRPD patterns of selected ZIF-8 derivatives before (left) and after (right) heating to 414 °C (λ = 0.45920 Å). Tick marks represent the characteristic Bragg reflection positions of ZIF-7 (orange tick marks, CCDC code RIPNOV01), ZIF-61 (upper cyan tick marks, CCDC code GITTAF) and ZIF-8 (lower cyan tick marks, CCDC code FAWCEN). **c** False colour SEM images of crystalline ZIF-8, crystalline ZIF-8-$mim_{0.15}im_{0.74}bim_{0.11}$ (after SALE) and glassy a_gZIF-8-$mim_{0.15}im_{0.74}bim_{0.11}$ (a_g = amorphous glass), all scale bars are 30 µm.

ZIF-8 was synthesized by an established solvothermal procedure.[88] Subsequently, the SALE method was used to exchange a fraction of the mim^- linkers for im^- and bim^- (**Figure 3.1a and Experimental Section**). By running the SALE reactions for different times (between 1 and 7 days) and with varying molar ratios of the linkers in *n*-butanol, 49 unique linker-exchanged ZIF-8 samples with the general composition $Zn(mim)_{2x}(im)_{2y}(bim)_{2z}$ ($x + y + z = 1$), here denoted ZIF-8-$mim_xim_ybim_z$ (**Table A3.1** and **Figure A3.1-2**) were prepared.

Fourier transform (FT) IR spectra recorded on the activated ZIF-8 derivatives (heated at 100 °C under vacuum for 12 h) prove that neither *n*-butanol nor protonated linkers (i.e. Hmim, Him and Hbim) remain in the pores of the linker-exchanged ZIF-8 derivatives after activation (**Figure A3.60**). The molar ratio of the three linkers in the ZIF-8-$mim_xim_ybim_z$ derivatives was determined by solution ^1H nuclear magnetic resonance (NMR) spectroscopy of acid-digested samples (**Figure A3.4-15**, **Table A3.1**). Noteworthy, the mim^- linkers in all the SALE products were intentionally not completely exchanged in any of the samples, so that a wide variety of sample compositions was generated by the described approach (**Figure A3.2**).

X-ray powder diffraction (XRPD) was used to investigate the phase identity of the ZIF-8-$mim_xim_ybim_z$ derivatives (**Figure 3.1b**, **Figure A3.17-28**). Based on the diffraction data, the following conclusions can be drawn:

(i) The **sod** structure of ZIF-8 is maintained after the SALE process, even though at some compositions a second minority phase is formed in parallel.

(ii) If only im^- is incorporated (i.e. if Hbim is not present in the exchange solution and $z = 0$) a small amount of a denser ZIF phase with **zni** topology is formed. The formed phase is related to ZIF-61, a dense ZIF with the nominal chemical composition Zn(mim)(im).[20]

(iii) With increasing amounts of bim^- incorporation the fraction of the ZIF-61-like minority phase formed during the SALE reaction is decreasing.

(iv) If larger amounts of bim^- are incorporated ($z > 0.65$) a phase mixture of the cubic **sod** phase (typical for ZIF-8) and the heavily distorted rhombohedral or triclinic **sod** phase (typical for ZIF-7, $Zn(bim)_2$)[79, 89] is present.

These main conclusions are supported by structure-less profile fitting (Pawley method[90]) of XRPD patterns using reference data from the literature (**Figure A3.29-35**, **Table A3. 2**). The profile fits further reveal that the unit cell volume

of the cubic ZIF-8-mim$_x$im$_y$bim$_z$ phases is between 0.7% and 2.5% smaller than the unit cell volume of conventional ZIF-8, indicating that the lack of the methyl group in position 2 of the im$^-$ and bim$^-$ linkers allows for a slightly denser packing of the building units in the **sod** structure. It is worth noting that the SALE reaction mixtures must remain undisturbed throughout the linker exchange process. Notably, when the reaction mixture is stirred for 15 minutes per day during a 3-day SALE procedure, the original ZIF-8 crystals transition to the denser ZIF-62 phase, with only 5% of the linkers being mim$^-$ (yielding a composition of Zn(mim)$_{0.10}$(im)$_{1.60}$(bim)$_{0.30}$; **Figure A3.29** and **Figure A3.35**). This finding underscores the critical role of slow linker exchange under static conditions for preserving the ZIF-8 structural integrity.

3.3 Thermal behavior

The thermal behaviour of the materials was comprehensively analyzed by differential scanning calorimetry (DSC), thermogravimetric analysis (TGA), variable temperature (VT)-XRPD and VT X-ray total scattering. Pair distribution functions (PDFs) in the form $D(r)$, providing information about the characteristic atom-atom correlations in the materials, were obtained from the corrected X-ray total scattering functions $S(Q)$ via Fourier transformation.[52-53] Similar to pristine ZIF-8, all linker-exchanged ZIF-8 derivatives have very high thermal stability with minimal weight-loss up to 500 °C and decomposition temperatures (T_d) above 500 °C as proven by TGA under N_2 atmosphere (**Figure A3.63a-74a**). Cyclic DSC measurements (two upscans, one downscan) were performed from room temperature to 430 °C or 450 °C to screen for potential melting (first upscans) and glass transition signals (second upscans) (**Figure A3.63b-74b**).

As expected, pristine ZIF-8 does not show any phase change up to at least 530 °C, which was confirmed by the retention of the Bragg peaks in VT-XRPD, the absence of thermal events in two consecutive DSC upscans (**Figure 3.2a left**) and the persistence of long-range order in the VT-PDFs (**Figure 3.2b**). However, ZIF-8 loses its high thermal stability after most of the mim$^-$ linkers are exchanged by im$^-$. Starting from around 310 °C, ZIF-8-mim$_{0.15}$im$_{0.85}$ undergoes an exothermic solid-state transition to a phase called ZIF-61-mim$_{0.15}$im$_{0.85}$ exhibiting the dense **zni** topology (**Figure 3.2a middle**, **Figure 3.2c**). The thermally triggered reconstructive phase transition of ZIF-8-mim$_{0.15}$im$_{0.85}$ from the **sod** to the **zni** phase indicates that the

inclusion of im^- facilitates metal-linker bond breaking;[87] the essential element of MOF melting. It is known that the thermally triggered reconstruction of **zni** phases can be prevented and direct melting facilitated by including larger linkers in the frameworks, i.e. linkers that are too large to be incorporated in the **zni** topology[43]. As expected, several ZIF-8-$mim_xim_ybim_z$ derivatives (represented by ZIF-8-$mim_{0.15}im_{0.74}bim_{0.11}$ in **Figure 3.2**) possess well-defined melting points (T_m) in the range from 360 °C to 399 °C in the first DSC upscan (**Figure A3.64-66**, **Figure A3.74** and **Table A3.4**), corroborated by the complete loss of Bragg scattering above 310 °C in VT-XRPD experiments (**Figure 3.2a right** and **Figure A3.41-44**) and the loss of long-range order in the VT-PDFs (**Figure 3.2d Figure A3.53-54**). The congruently melting ZIF-8-$mim_xim_ybim_z$ derivatives lie in a range of compositions featuring large fractions of im^- ($0.54 \leq y \leq 0.85$) and small fractions of bim^- ($0.08 \leq z \leq 0.19$). Importantly, crystallization is not detected upon cooling the liquid ZIF-8-$mim_xim_ybim_z$ derivatives to room temperature (**Figure 3.2e, f, g**), while a second DSC upscan displays clear glass transition events with glass transition temperature (T_g) values in the range from 334 °C to 361 °C, establishing the formation of a_gZIF-8-$mim_xim_ybim_z$ (a_g = amorphous glass).

The influence of the linker ratios on the thermal behaviour of the ZIF-8 derivatives is also evident from the morphological changes during heat treatment (**Appendix A.3.7**). Pristine ZIF-8 and ZIF-8-$mim_{0.15}im_{0.85}$ remain as polycrystalline powders after heating to 450 °C. In contrast, the particles of ZIF-8-$mim_{0.15}im_{0.74}bim_{0.11}$ fuse into a monolithic glassy structure when heated to 430 °C (**Figure 3.2a inserts**). Scanning electron microscopy (SEM) imaging (**Figure 3.1c**) reveals that the microcrystals of pristine ZIF-8 develop some cracks on the crystal facets after the formation of ZIF-8-$mim_{0.15}im_{0.74}bim_{0.11}$ via SALE. The cracks originate from chemical stress upon linker substitution via the solid-liquid reaction.[15] Conversely, a_gZIF-8-$mim_{0.15}im_{0.74}bim_{0.11}$ derived from melt-quenching exhibits the morphological characteristics of a typical ZIF glass, showing particle coalescence to a fused structure which evidently experienced significant flow while in the liquid state.

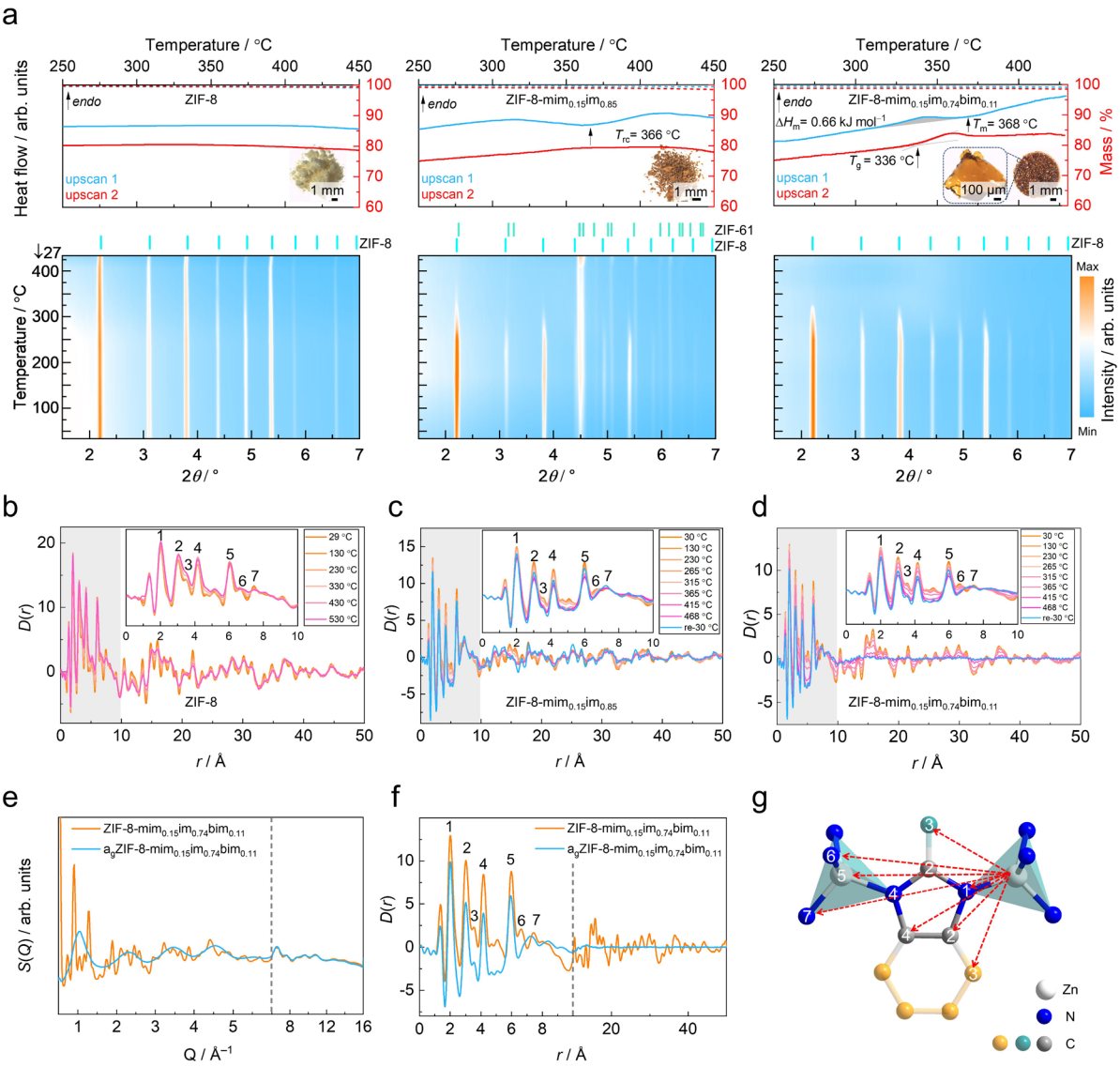

Figure 3.2. ***In situ*** **and** ***ex situ*** **synchrotron X-ray diffraction and scattering data. a** TGA (dotted lines, right vertical scale) and DSC (solid lines, left vertical scale) traces of ZIF-8 (left), ZIF-8-mim$_{0.15}$im$_{0.85}$ (middle) and a$_g$ZIF-8-mim$_{0.15}$im$_{0.74}$bim$_{0.11}$ (right, the grey shaded region highlights the integrated area for the determination of ΔH_m). The samples were cycled from 50 °C to 450 °C or 430 °C with a heating/cooling rate of ±10 °C min^{-1} twice. The insets show micrographs of ZIF-8, recrystallized ZIF-61-mim$_{0.15}$im$_{0.85}$, glassy a$_g$ZIF-8-mim$_{0.15}$im$_{0.74}$bim$_{0.11}$ derived by cooling the materials from 450 °C or 430 °C to room temperature. Contour maps of the VT-XRPD patterns are shown below the TGA/DSC data. Each map is generated from 11 XRPD patterns recorded at temperatures between 27 °C and 414 °C, containing 10 patterns recorded during heating and one additional pattern recorded after returning to room temperature. **b-d** VT-PDF data of ZIF-8 (**b**), ZIF-8-mim$_{0.15}$im$_{0.85}$ (**c**) and ZIF-8-mim$_{0.15}$im$_{0.74}$bim$_{0.11}$ (**d**) derived from VT X-ray total scattering experiments. The insets highlight changes in the local structure ($r < 10$ Å, grey-shaded region). **e** Room temperature X-ray total scattering data in the form $S(Q)$ of ZIF-8-mim$_{0.15}$im$_{0.74}$bim$_{0.11}$ and a$_g$ZIF-8-mim$_{0.15}$im$_{0.74}$bim$_{0.11}$. The latter was prepared by melt-quenching from 430 °C in the DSC apparatus. **f** PDFs in the form $D(r)$ obtained from the $S(Q)$ data shown in **e**. **g** Visualization of the relevant short-range atomic distances present in the ZIFs and their assignment to the peaks in the PDFs. Since mim$^-$, im$^-$ and bim$^-$ are statistically distributed throughout the materials, the carbon atoms shown in cyan and orange are only partially occupied and thus have only a minor contribution to the PDFs.

The ZIF-8 derivatives that are close to but not in the compositional region required for congruent melting display incongruent melting, thus leading to crystal-glass-composites (CGCs) after cooling the solid-liquid mixture to room temperature (**Table A3.4**). For example, ZIF-8-$mim_{0.18}im_{0.81}bim_{0.01}$ forms a CGC of crystalline ZIF-61 and glassy a_gZIF-8 (**Figure 3.1b**, **Figure A3.45** and **Figure A3.74**b) due to the deficiency of bim^-, while ZIF-8-$mim_{0.43}im_{0.38}bim_{0.19}$ forms a CGC of crystalline ZIF-8 and glassy a_gZIF-8 (**Figure 3.1b**, **Figure A3.46** and **Figure A3.67b**) due to the deficiency of im^-. Moreover, ZIF-8-$mim_{0.17}im_{0.34}bim_{0.49}$ maintains the crystalline ZIF-8 phase during thermal treatment, although most of its linkers are exchanged (**Figure A3.48**). We conclude that the fraction of im^- in this material is too small to cause framework collapse/melting, while the large fraction of bim^- supports the crystalline framework.

To investigate if the thermal treatment leads to any chemical alterations of the organic linkers, ^{1}H NMR (**Figure A3.16**) and FTIR spectra were recorded for representative heat-treated ZIF-8 derivatives (**Figure A3.61**). Both types of spectroscopic data establish the integrity of the organic linkers after heat treatment and the absence of any organic decomposition products.

The most notable of the above samples is ZIF-8-$mim_{0.15}im_{0.74}bim_{0.11,}$ which features a low T_m of 368 °C in the first DSC upscan, a T_g of 336 °C in the second DSC upscan and the highest T_g/T_m ratio[91-92] of 0.95 (calculated with absolute temperatures) ever reported[93] (**Figure 3.2a**, **Figure A3.74b**). The melting point of the linker-exchanged ZIF-8 derivative is drastically lower than the previously predicted "virtual" melting point of 1377 °C for conventional ZIF-8.[33] The enthalpy of melting (ΔH_m) determined by integration of the DSC melting peak is only about 0.7 kJ/mol and thus approximately seven times lower than ΔH_m of the prototypical ZIF-62[41]. A comparison with the melting enthalpies and entropies of other reported meltable ZIFs can be found in **Table A3.3**. The very low ΔH_m of ZIF-8-$mim_{0.15}im_{0.74}bim_{0.11}$ can be ascribed to its higher porosity, which allows for a more substantial densification during the transition from the crystalline to the liquid state as will be shown by gas sorption data below. Due to increased dispersion interactions in the denser liquid phase, the enthalpy difference between the crystal and the liquid is small. An additional DSC experiment with five heating/cooling cycles in the range from 100 to 430 °C was performed to verify the stability of the glass of ZIF-8-$mim_{0.15}im_{0.74}bim_{0.11}$ (**Figure A3.76**). The fact that T_g only varies between 336 °C and 338 °C in the consecutive upscans implies that a_gZIF-8-$mim_{0.15}im_{0.74}bim_{0.11}$ has

excellent robustness during temperature cycling. Heat capacity (C_p) measurements demonstrate that the heat capacity change around the glass transition (ΔC_p) of a_gZIF-8-$mim_{0.15}im_{0.74}bim_{0.11}$ is 0.12 J g^{-1} K^{-1} (**Figure A3.82**); a value comparable to that of a_g(IL@ZIF-8) (ΔC_p = 0.11 J g^{-1} K^{-1}) and other ZIF glasses (**Table A3.5**).[33, 93] Moreover, the fragility index (m) of a_gZIF-8-$mim_{0.15}im_{0.74}bim_{0.11}$ obtained from DSC is 21 (**Figure A3.83**), a value almost identical to that of fused silica (m = 20),[40, 93-94] and smaller compared to that of a_gZIF-62 (m = 23)[93]. The low fragility is characteristic of a strong liquid that vitrifies to a brittle glass and is in agreement with the extraordinarily high glass-forming ability (T_g/T_m = 0.95) of the material.

To exhibit that the SALE approach is not restricted to the im^-/bim^- linker system, we employed the same linker exchange protocol but substituted bim^- with $Clbim^-$ (5-chlorobenzimidazolate), the derived ZIF-8-$mim_{0.20}im_{0.70}Clbim_{0.10}$ is again a phase pure ZIF-8 derivative (**Figure A3.36**) and can also be transformed into a glass exhibiting a T_g of 322 °C by thermal treatment (**Figure A3.80** and **Figure A3.81**). Furthermore, with the aim to demonstrate that the SALE approach can also be used to make non-meltable cobalt-based ZIFs meltable, we applied the same linker exchange protocol to ZIF-67, $Co(mim)_2$, which is isostructural to ZIF-8. The derived ZIF-67-$mim_{0.18}im_{0.68}bim_{0.14}$ is also a phase-pure crystalline framework with **sod** topology, melts at 399 °C and forms a glass with a T_g of 344 °C upon melt-quenching (T_g/T_m = 0.92; **Figure A3.50**, **Figure A3.55** and **Figure A3.78**). This finding suggests that the SALE approach may be a universal tool for the preparation of glasses based on other highly porous ZIFs with other topologies.

3.4 Constructing a triangular phase diagram

Based on the thermal analysis and XRPD data of 50 ZIF-8-$mim_xim_ybim_z$ derivatives, a ternary phase diagram to visualize the melting and glass-forming properties is constructed (**Figure 3.3a**). The dark orange area highlights the compositional range showing congruent melting and glass formation upon cooling the melt. The blue area marks the compositional range of ZIF-8-$mim_xim_ybim_z$ derivatives, which do not melt. In the region between the two dashed lines, we observe incongruent melting, leading to a heterogeneous mixture of a liquid ZIF with either a crystalline ZIF with **zni** topology (if the fraction of im^- is large) or a crystalline ZIF with **sod** topology (if the fraction of im^- is rather small). When the liquid-solid mixtures from the region of incongruent melting are quenched to room temperature, CGCs are formed. This

introduces a path for the preparation of CGCs as previously CGCs were formed either from heterogeneous mixtures of two or more MOFs containing a meltable and a non-meltable MOF[95-96] or via physically mixing a crystalline MOF with a prefabricated MOF-glass of the same composition[97]. By contrast, the CGCs are formed from a single phase of mixed-linker ZIF-8 derivatives via thermally triggered phase segregation here.

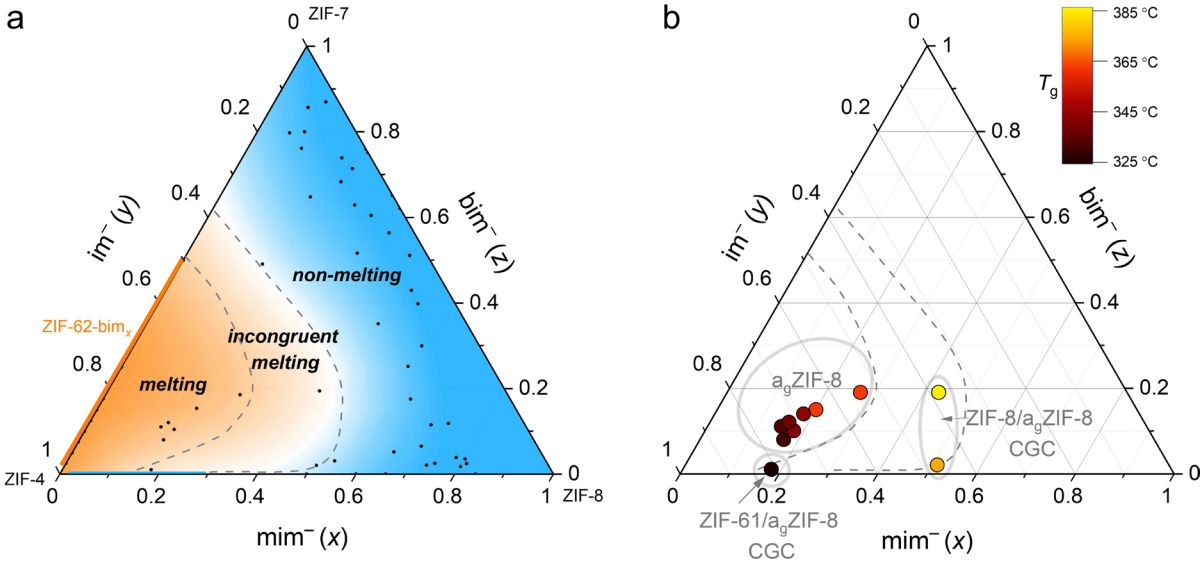

Figure 3.3. Ternary phase diagrams of ZIF-8-mim$_x$im$_y$bim$_z$ displaying the melting and glass transition properties. a Ternary phase diagram based on thermal analysis and XRPD data of 50 derivates of ZIF-8-mim$_x$im$_y$bim$_z$ along with literature data of ZIF-4[33] and ZIF-62-bim$_x$ (orange line)[43],[98], with the blue area being the non-melting region, the area between the two dashed lines being the incongruent melting region, and the orange area being the melting region (excluding the blue line of ZIF-8-mim$_x$im$_y$). **b** Visualization of the glass transition temperatures of the glass forming ZIF-8-mim$_x$im$_y$bim$_z$ derivatives in the ternary phase diagram.

Besides the compositional influence on the melting behaviour, the relative molar fractions of the linkers also have a considerable influence on the T_g of the corresponding glass or CGC (**Figure 3.3b**, details in **Table A3.4**). Depending on x, y and z, T_g ranges between 328 °C and 383 °C. Generally, T_g is lower when the fractions of mim⁻ and bim⁻ are low.

3.5 NMR and Far-IR spectroscopy

With the aim of obtaining further insights into the distribution of the three different linkers within the crystal and glass phases of the linker-exchanged ZIF-8 derivatives, 2D ^{1}H-^{13}C spin-diffusion magic angle spinning (MAS) NMR spectroscopy measurements[†] were recorded on crystalline ZIF-8-$mim_{0.15}im_{0.74}bim_{0.11}$ and glassy a_gZIF-8-$mim_{0.15}im_{0.74}bim_{0.11}$ with mixing times between 90 and 5000 µs to track the polarization transfer from the methyl protons of mim^- (resonance at 1.5 ppm) to the various ^{13}C atoms in the sample (**Figure 3.4a**, **Figure A3.58-59**). Variations in the rate of polarization transfer provide information about the proximity of different organic linkers in the solid.[96, 99] With increasing mixing times, polarization transfer from the $–CH_3$ protons to the ^{13}C atoms **C1** and **C2** of the three linkers is observable. The resonance of the **C1** atom of mim^- is isolated at 150 ppm, while **C1** of im^- overlaps with **C1** and **C2** of bim^- (~141 ppm) and **C2** of mim^- and im^- overlap with each other at ~123 ppm. The peak areas of the $–CH_3$ resonances were normalized to 1 for both samples to facilitate a comparison of the relative polarization transfer rates to the aromatic carbons. The differences in the rates of fast intra-linker transfers of mim^- (from $–CH_3$ to **C1** of mim^-) are insignificant when comparing crystal and glass samples (**Figure 3.4b, left**). In contrast, the inter-linker polarization transfer rate (from $–CH_3$ to **C1**/**C2** of im^- and bim^-) in the glass (second panel) is much faster than in the crystalline state. Consistently, the peak representing mixed intra- and inter-linker transfer (third panel) shows a behaviour in between these two cases. This implies that the collapse of the framework structure upon melting, followed by vitrification, leads to a closer intermolecular proximity of the three linkers on average. Although the polarization transfer in the crystalline material is slower compared to the corresponding glass, its high transfer efficiencies suggest that the SALE procedure leads to a rather homogeneous distribution of im^- and bim^- throughout the bulk microcrystals even before melting and not just a clustering of these linkers on the crystal surface.

[†] MSA NMR experiments have been done by Hanna Aucharova and Dr. Suresh Vasa from the gorup fo Prof. Rasmus Linser, Physical Chemistry, TU Dortmund.

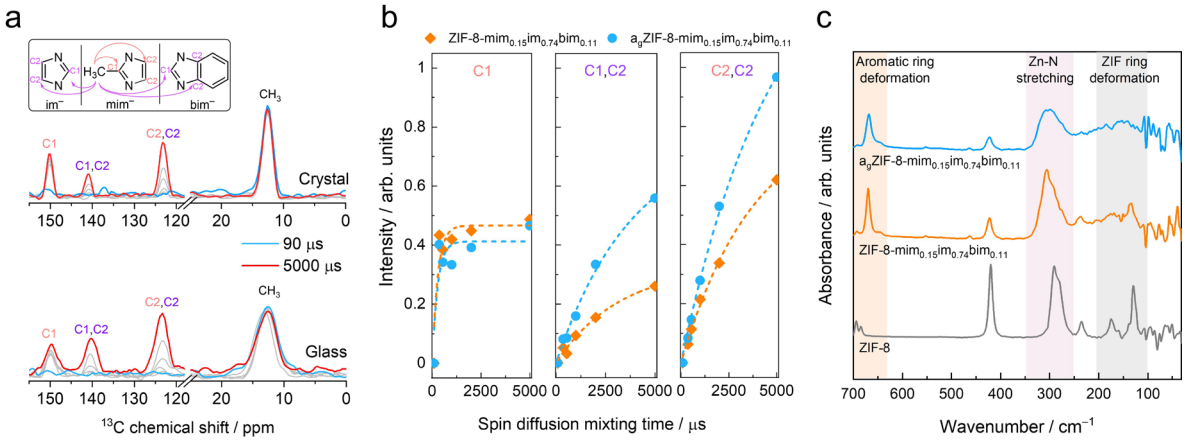

Figure 3.4. MAS NMR and far-IR spectroscopic characterization. a Slices along the indirectly detected dimension through the 2D ^{1}H-^{13}C spin-diffusion solid state NMR spectra of crystalline ZIF-8-mim$_{0.15}$im$_{0.74}$bim$_{0.11}$ (top) and glassy a$_g$ZIF-8-mim$_{0.15}$im$_{0.74}$bim$_{0.11}$ (bottom). Slices were taken at a ^{1}H chemical shift of 1.5 ppm and normalized to the peak area of –CH$_3$. The slices show the polarization transfer from the protons of the –CH$_3$ groups of mim$^-$ to all ^{13}C atoms in the samples as a function of the mixing time. Blue lines represent the slices obtained with a spin-diffusion mixing time of 90 µs, red lines correspond to a mixing time of 5000 µs, and gradually increasing grey lines correspond to mixing times of 360, 540, 1000 and 2000 µs. **b** Comparison of the spin-diffusion polarization transfer processes in the crystalline and glassy states. Peach-colored labels in a and b represent intramolecular polarization transfers within mim$^-$, while purple labels represent inter-linker polarization transfers from mim$^-$ to im$^-$ or bim$^-$. Dashed lines are exponential fits to the data. **c** Far-IR spectra of ZIF-8, ZIF-8-mim$_{0.15}$im$_{0.74}$bim$_{0.11}$ and a$_g$ZIF-8-mim$_{0.15}$im$_{0.74}$bim$_{0.11}$.

Far-IR spectroscopy data show that with the partial exchange of mim$^-$ against im$^-$ and bim$^-$, the vibrational bands associated to mim$^-$ (420 cm^{-1} and 677-700 cm^{-1}) reduce in intensity, while new bands associated to im$^-$ and bim$^-$ (636-681 cm^{-1}) emerge in crystalline ZIF-8-mim$_{0.15}$im$_{0.74}$bim$_{0.11}$ (**Figure 3.4c**). Moreover, the band for the stretching vibration of the ZnN$_4$ tetrahedron centred at 291 cm^{-1} in ZIF-8 becomes broader and shifts to 305 cm^{-1} upon linker exchange. This is in agreement with results from a previous far-IR spectroscopy study on crystalline ZIF-4, ZIF-7 and ZIF-8,[100] and further supports reasoning of this study that the im$^-$ and bim$^-$ linkers are rather homogeneously distributed in ZIF-8-mim$_{0.15}$im$_{0.74}$bim$_{0.11}$. For the melt-quenched a$_g$ZIF-8-mim$_{0.15}$im$_{0.74}$bim$_{0.11}$ the stretching band of the ZnN$_4$ tetrahedron is even broader and the characteristic low-energy phonon modes in the region from 100-200 cm^{-1}, which are associated with collective distortions of the four- and six-membered rings of the **sod** structure, vanish to a broad continuum.[100] Both observations establish the non-crystalline and highly disordered structure of a$_g$ZIF-8-mim$_{0.15}$im$_{0.74}$bim$_{0.11}$.

3.6 Porosity determination

Isothermal N_2 physisorption at 77 K is an established method for the quantification of the specific pore volume and the specific surface area of crystalline MOFs. All the reported melt-quenched ZIF glasses, however, feature very narrow micropores, which are inaccessible for N_2 at 77 K.[41] In contrast to this, a_gZIF-8-$mim_{0.15}im_{0.74}bim_{0.11}$ adsorbs comparatively large amounts of N_2 (~108 $cm^3\,g^{-1}$ (STP) at $p/p_0 = 0.95$) at 77 K and displays a Type I isotherm typical for microporous materials (**Figure 3.5a**, **Table A3.6**). Although the N_2 adsorption capacity near saturation is substantially lower for this ZIF-8 glass compared to ZIF-8 (~411 $cm^3\,g^{-1}$ (STP)) and its crystalline glass-former counterpart ZIF-8-$mim_{0.15}im_{0.74}bim_{0.11}$ (~304 $cm^3\,g^{-1}$ (STP)), this is the first instance of a ZIF glass adsorbing N_2 at 77 K. Pore size distributions (PSDs) calculated from the N_2 sorption data (quenched-solid density functional theory, QSDFT model[101]) not only confirm that ZIF-8-$mim_{0.15}im_{0.74}bim_{0.11}$ has a narrower pore size distribution than ZIF-8, but also indicate that a small number of likely disordered sodalite cages still exist in a_gZIF-8-$mim_{0.15}im_{0.74}bim_{0.11}$ (**Figure 3.6**).

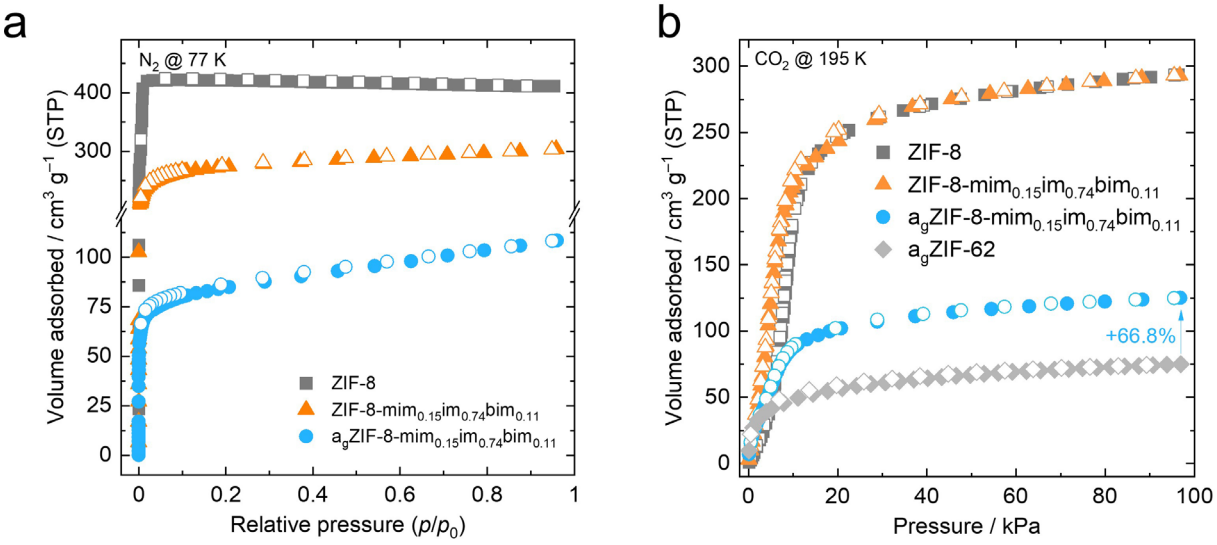

Figure 3.5. N_2 and CO_2 gas sorption analysis. a N_2 sorption isotherm at 77 K and **b** CO_2 sorption isotherm at 195 K of ZIF-8, ZIF-8-$mim_{0.15}im_{0.74}bim_{0.11}$ and a_gZIF-8-$mim_{0.15}im_{0.74}bim_{0.11}$. The CO_2 sorption isotherm of a_gZIF-62 recorded at 195 K (taken from reference[41]) is shown for comparison. The solid and hollow circles represent adsorption and desorption, respectively.

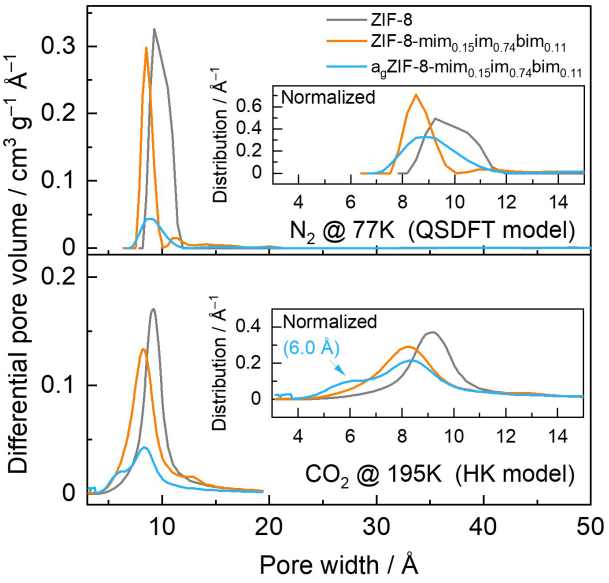

Figure 3.6. Pore size distributions for ZIF-8, ZIF-8-$mim_{0.15}im_{0.74}bim_{0.11}$ and a_gZIF-8-$mim_{0.15}im_{0.74}bim_{0.11}$ calculated from the N_2 adsorption data (QSDFT model, carbon equilibrium transition kernel at 77 K based on a slit-pore model) and the CO_2 adsorption data (HK model, isotherms recorded at 195 K, p_0 = 191 kPa, slit-like pore). The insets show normalized pore size distributions for easier visual comparison of the pore widths.

Additional CO_2 (kinetic diameter 3.3 Å) sorption measurements recorded at 195 K were performed to get information about the smaller micropores in the materials, which are inaccessible for N_2 at 77 K (kinetic diameter 3.6 Å), and so to quantify the full micropore volume (V_{pore}).[41] ZIF-8 and ZIF-8-$mim_{0.15}im_{0.74}bim_{0.11}$ exhibit the same CO_2 adsorption capacity of ~293 $cm^3\,g^{-1}$ (STP) at 100 kPa (**Figure 3.5b** and **Table A3.6**). Naturally, a_gZIF-8-$mim_{0.15}im_{0.74}bim_{0.11}$ adsorbs lower amounts of CO_2, however, the capacity at 100 kPa amounts to ~125 $cm^3\,g^{-1}$ (STP), which is about 67% higher than the CO_2 capacity of the prototypical glass a_gZIF-62 under identical conditions (**Figure 3.5b**). The BET area (S_{BET}) calculated from the CO_2 sorption isotherm is 403 $m^2\ g^{-1}$, about twice as large as the BET area of a_gZIF-62 (S_{BET} = 200 $m^2\ g^{-1}$).

Noteworthy, supporting CO_2 sorption isotherms recorded on the cobalt-based a_gZIF-67$mim_{0.18}im_{0.68}bim_{0.14}$ highlight a similarly high CO_2 adsorption capacity of ~293 $cm^3\,g^{-1}$ (STP) and pore volume of 0.19 $cm^3\,g^{-1}$ for this glass (**Figure 3.7**, **Figure A3.98** and **Table A3.6**).

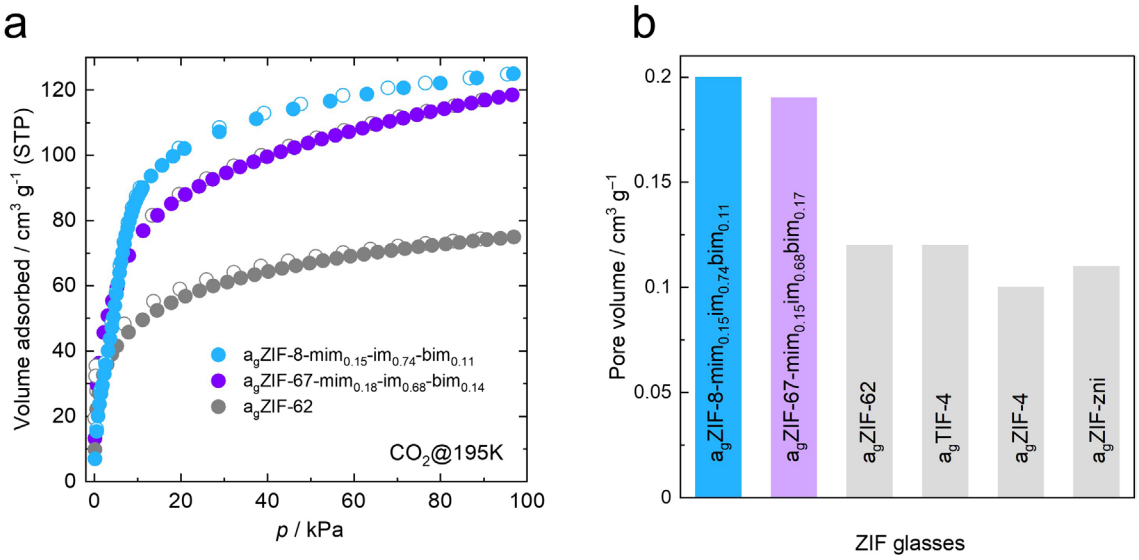

Figure 3.7. a CO_2 sorption isotherms recorded at 195 K for a_gZIF-8-mim$_{0.15}$im$_{0.74}$bim$_{0.11}$, a_gZIF-67-mim$_{0.18}$im$_{0.68}$bim$_{0.14}$ and a_gZIF-62 (data taken from previous work reference[41]). **b** Bar plot representing the specific pore volumes calculated from the CO_2 sorption capacity at 195 K and 95 kPa for a_gZIF-8-mim$_{0.15}$im$_{0.74}$bim$_{0.11}$, the Co-based a_gZIF-67-mim$_{0.18}$im$_{0.68}$bim$_{0.14}$ and prototypical literature-known ZIF glasses (data taken from reference[41]).

PSDs calculated from the CO_2 isotherms via the Horvath–Kawazoe (HK) model[102] underline that a_gZIF-8-mim$_{0.15}$im$_{0.74}$bim$_{0.11}$ also features a considerable amount of smaller micropores with a diameter of 5-6 Å, which are not present in the crystalline ZIF-8-mim$_{0.15}$im$_{0.74}$bim$_{0.11}$ (**Figure 3.6**). These smaller pores likely result from the collapse of the framework upon melting and glass formation. The specific pore volume of a_gZIF-8-mim$_{0.15}$im$_{0.74}$bim$_{0.11}$ calculated from the CO_2 sorption data is 0.20 $cm^3\,g^{-1}$, which is by far the highest among ZIF glasses (**Figure 3.7**). The higher porosity and thus lower density of a_gZIF-8-mim$_{0.15}$im$_{0.74}$bim$_{0.11}$ compared to the prototypical a_gZIF-62 is also confirmed by the position of the first scattering peak at smaller Q in the X-ray total scattering data (**Figure A3.57**).[103]

The largely improved porosity of a_gZIF-8-mim$_{0.15}$im$_{0.74}$bim$_{0.11}$ compared to previously reported melt-quenched ZIF glasses is further evident by propylene, propane and *n*-butane sorption experiments (**Figure 3.8** and **Table A3.7**). Even though the glass adsorbs significantly smaller amounts of these gases than their crystalline relatives, the hydrocarbon sorption capacities are about 3 to 5 times higher compared to other ZIF glasses[41]. Moreover, the hysteresis between adsorption and desorption is small, suggesting negligible diffusion limitations for the larger hydrocarbon molecules.

3.7 Kinetic separation of hydrocarbons

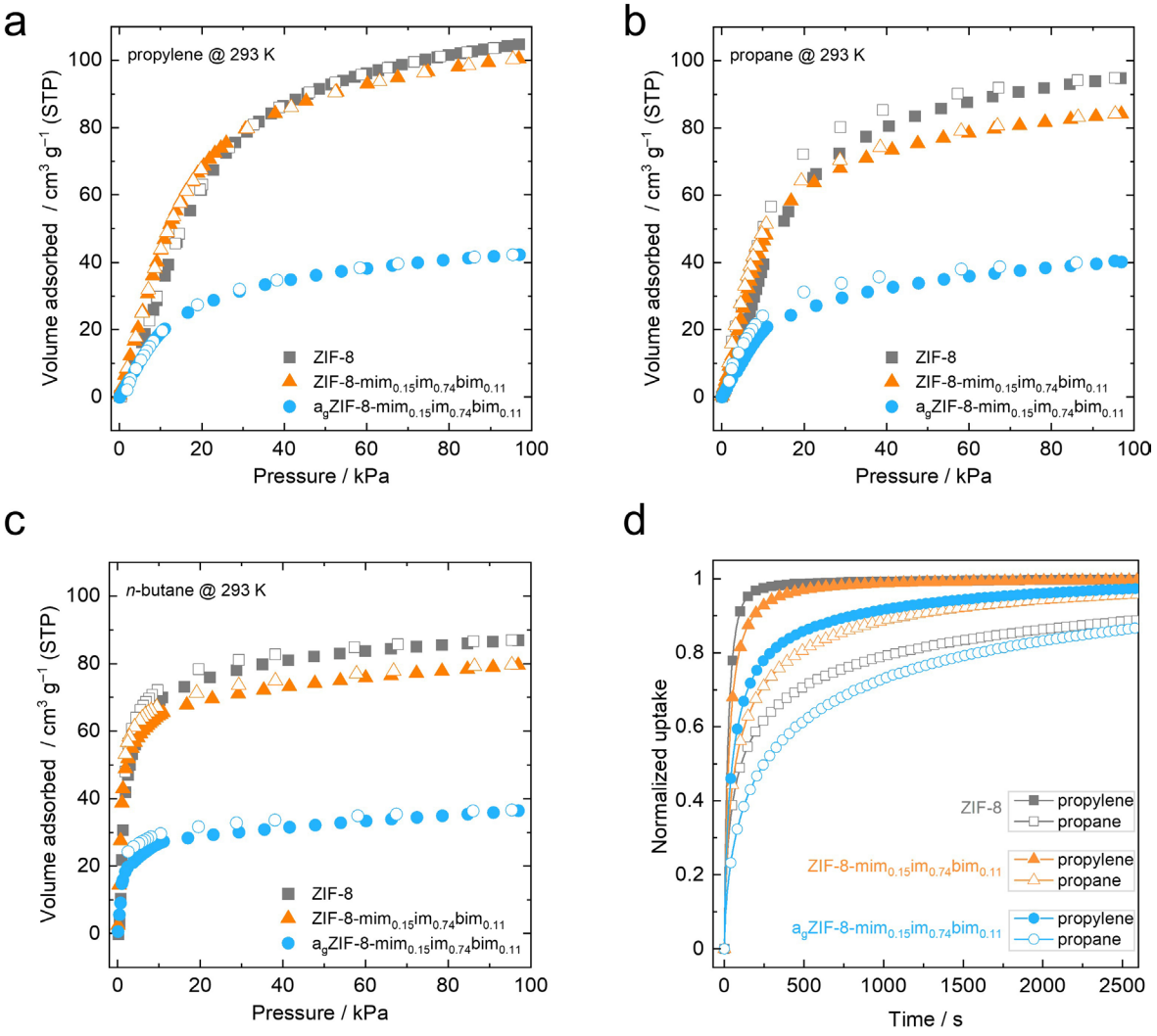

Figure 3.8. Hydrocarbon sorption studies. a Propylene sorption isotherms collected at 293 K. **b** Propane sorption isotherms collected at 293 K. **c** *n*-Butane sorption isotherms collected at 293 K. In all panels, adsorption and desorption branches are shown as closed and open symbols, respectively. **d** Kinetic adsorption data of propylene and propane for ZIF-8, ZIF-8-mim$_{0.15}$im$_{0.74}$bim$_{0.11}$ (crystal) and a$_g$ZIF-8-mim$_{0.15}$im$_{0.74}$bim$_{0.11}$ (glass) recorded at 293 K with an equilibrium pressure of about 80 kPa.

Kinetic adsorption data showcase that propylene is adsorbed much faster than propane in a$_g$ZIF-8-mim$_{0.15}$im$_{0.74}$bim$_{0.11}$, similar to the crystalline ZIF-8 and ZIF-8-mim$_{0.15}$im$_{0.74}$bim$_{0.11}$ (**Figure 3.8d**). Fitting the kinetic data using stretched exponential models (**Figure A3.101-109**) yielded the corresponding rate constants (k, **Table A3.9**). For crystalline ZIF-8, $k_{propylene}$ and $k_{propane}$ are 3.26 × 10^{-2} s^{-1} and 3.18 × 10^{-3} s^{-1}, resulting in a high kinetic propylene/propane selectivity (S_{kin} = $k_{propylene}/k_{propane}$) of 10.3, as expected from previous reports.[104] By contrast, $k_{propylene}$

and $k_{propane}$ are more similar for ZIF-8-$mim_{0.15}im_{0.74}bim_{0.11}$ (2.14×10^{-2} and 6.21×10^{-3} s^{-1}), resulting in a much lower S_{kin} of just 3.5. Hence, the structural complexity of the pores caused by the three imidazolate-type linkers present after SALE seems to reduce the selectivity. Strikingly, the corresponding glass a_gZIF-8-$mim_{0.15}im_{0.74}bim_{0.11}$ features a significantly improved selectivity (S_{kin} = 5.4) even though the rate constants are slightly lower than for its crystalline relative ($k_{propylene} = 9.37 \times 10^{-3}$ s^{-1} and $k_{propane} = 1.73 \times 10^{-3}$ s^{-1}) as expected due to the lower porosity and narrower pore sizes. These findings highlight that glass formation can be a beneficial tool not only for materials processing but also for improving the functional sorption characteristics of a porous material.

3.8 Conclusion

This research made significant advances in the field of MOFs glasses: (i) enabling the melting of unmeltable MOF with good processing properties. (ii) significantly increased porosity of MOF glasses.

The dual-linker exchange strategy developed in this work is crucial for the successful modification of ZIF-8. The exchange of the mim^- linker with a smaller im^- linker facilitates the weakening of the coordination bonds, thereby promoting the melting process. Simultaneously, the introduction of a larger bim^- linker plays a pivotal role in stabilizing the liquid phase, preventing the crystallization of dense ZIFs that could hinder the formation of a homogeneous glass. This dual mechanism highlights the importance of a balanced approach in linker substitution, where both the size and coordination strength of the linkers must be carefully considered to achieve the desired material properties. Moreover, the construction of a ternary phase diagram was a key outcome of this research, providing a visual representation of the compositional phase space and delineating the conditions under which ZIF-8 derivatives exhibit congruent melting, incongruent melting, or no melting. This phase diagram serves not only as a tool for understanding the melting behavior of these materials but also as a predictive model for the design of new MOFs with tailored thermal properties. The ability to systematically explore and manipulate the phase behavior of MOFs marks a significant advancement in the field, offering a pathway to the rational design of materials with specific thermal and structural characteristics.

Among the derivatives studied, some exhibited ultra-high glass-forming ability (GFA), with a T_g/T_m ratio reaching 0.95. This high GFA, combined with the substantial specific pore volumes, positions these ZIF-8 glasses as superior to previously reported MOF glasses in terms of porosity and potential applications. Furthermore, their excellent sorption capacities for hydrocarbon gases, underscores the utility of these materials in gas separation applications. The grain-boundary-free structure of MOF glasses, which minimizes diffusion barriers, further enhances their performance, particularly in the kinetic separation of propylene from propane—a critical process in the petrochemical industry.

Furthermore, the success of this strategy provides a roadmap for future research. The principles established here can be applied to other MOFs, particularly those with higher inherent porosity than ZIF-8, potentially leading to the discovery of new MOF glasses with even more remarkable properties. The possibility of achieving porosity levels in glasses comparable to those in their crystalline counterparts is particularly exciting, as it could revolutionize the use of MOF glasses in applications that demand high porosity and high pore size. Looking ahead, the exploration of other solvent-assisted linker exchange processes, potentially involving different solvent systems and well-designed linkers, could yield new classes of MOF glasses with tailored properties for specific industrial applications.

In conclusion, this research advances the development of meltable and glass-forming MOFs through compositional engineering. By employing the solvent-assisted linker exchange method, this work effectively transforms non-meltable highly porous ZIFs into meltable derivatives, thereby expanding the limited repertoire of MOFs capable of transitioning to a glassy state and greatly increase the porosity of ZIF glasses. These findings provide a foundation for new insights into the melting of MOFs and the fabrication of highly porous MOF glasses.

4 Mechanically Induced ZIF Glasses

The work presented in this chapter has been published in a peer-reviewed research article. Herein, text and figures of this publication are reprinted or adapted (licensed under a Creative Commons Attribution 4.0 International License, https://creativecommons.org/licenses/by/4.0/legalcode). Adaptions involve changes in compound nomenclature and rearrangements of figure parts. Reference to the publication and author contributions are given below.

Wen-Long Xue, Chinmoy Das, Jan-Benedikt Weiß, Sebastian Henke*., "Insights into the Mechanochemical Glass Formation of Zeolitic Imidazolate Frameworks", *Angew. Chem. Int. Ed.,* **2024**, e202405307.

Wen-Long Xue, Chinmoy Das, Jan-Benedikt Weiß, Sebastian Henke*., "Insights into the Mechanochemical Glass Formation of Zeolitic Imidazolate Frameworks", *Angew. Chem.,* **2024**, e202405307.

Publisher: Wiley
Date: June 14, 2024

Author contributions:

S.H. designed this project. W.-L.X synthesized the materials and performed all experiments as well as data analysis. J.-B.W. conducted the initial exploration of the thermal properties of ZIF-62 and ZIF-Cu-1. W.-L.X., C.D. and S.H. wrote the manuscript with contributions from J.-B.W. All authors have given approval of the final manuscript

Abstract

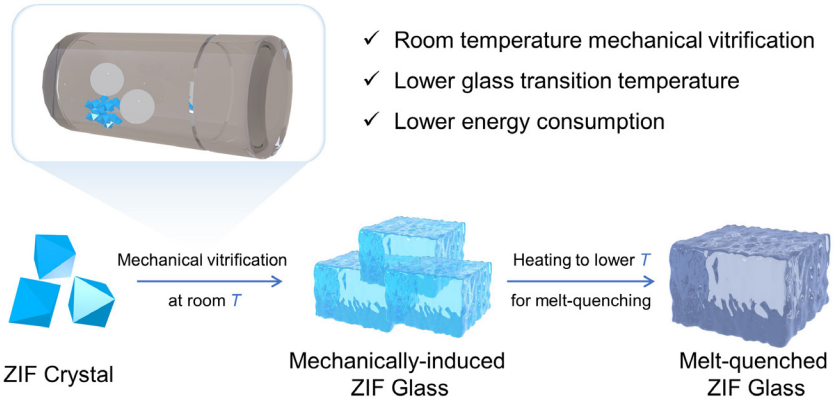

Traditionally, MOF glasses are produced by heating MOF crystals to their melting point and then cooling the liquid MOF to room temperature under an inert atmosphere. While effective, this melt-quenching technique requires high energy due to the high temperatures involved. It also limits the scope of new material development by restricting the compositional range to only those combinations of metal ions and linkers that are highly thermally stable. An alternative, mechanical milling at room temperature, has demonstrated its capability to transform MOF crystals into amorphous phases. However, the specific conditions under which these amorphous phases exhibit glass-like behavior remain uncharted. In this study, the mechanochemical amorphization and vitrification of a variety of zeolitic imidazolate frameworks (ZIFs) with diverse linkers and different metal ions (Zn^{2+}, Co^{2+} and Cu^{2+}) are explored at room temperature. The findings in this study demonstrate that ZIFs capable of melting can be successfully converted into glasses through ball-milling. Remarkably, some non-meltable ZIFs can also be vitrified using the ball-milling technique, as highlighted by the preparation of the first Cu^{2+}-based ZIF glass.

4.1 Introduction

As discussed in the previous chapters, the advanced processability and grain-boundary-free nature of isotropic liquid and glassy MOF phases compared to their crystalline relatives opens new routes for applications ranging from gas separation[105] to solid-state ionics[106-107]. MOF glasses have been proposed as attractive materials for utilization as phosphors[108] and in radioactive waste storage[109]. The family of zeolitic imidazolate frameworks (ZIFs) represents the most investigated subset of meltable and glass-forming MOFs. ZIFs are based on tetrahedrally coordinated transition metal ions (e.g. Zn^{2+} or Co^{2+}), which are linked by imidazolate linkers creating a typically three-dimensional network.[20] Interestingly, among the plethora of MOFs, just a few ZIFs transform into stable liquids when heated under an inert atmosphere before they undergo thermal decomposition.[22, 33] During melting, the metal-linker bonds are dynamically broken and reformed, giving rise to ZIF liquids.[47] When the ZIF liquids are cooled down, they vitrify, forming melt-quenched glasses (MQGs).[110]

Practically, melting a ZIF requires relatively high temperatures (usually > 400 °C) and thus a significant energy consumption.[33] Moreover, the necessity to obtain ZIF glasses via the liquid ZIF phase, drastically limits the choice of ZIF glass former, as many of the functional groups utilized in substituted imidazolate linkers are sensitive to high temperature (e.g. halide substituents or nitro groups[20, 111]). The prototypical glass former ZIF-4, for example, requires a very high melting temperature of 590 °C,[40, 47] resulting in a partially decomposed MQG.[33, 41]

Ball-milling is an established technique for synthesizing microcrystalline MOF powders. In this method, typically, a metal oxide is milled in a vibratory mixer mill alongside the organic linker in its acid form in the presence of a small quantity of additives and templating solvent molecules.[23, 112-113] Conversely, post-synthetic ball-milling (PSBM) of MOF microcrystals, conducted without solvent, leads to the rapid amorphization of the materials. The mechanical impact during PSBM aids in breaking and reforming coordination bonds, ultimately resulting in the formation of amorphous solids.[114] For a variety of dense coordination polymers (CPs) and networks (CNs) based on triazolate, dicyanamide, or cyanide linkers the amorphous phases obtained by PSBM were shown to exhibit a glass transition.[115-116] For ZIFs, different methods of mechanical perturbation[45] were shown to have a facilitative effect on ZIF melting and glass formation. Applying high hydrostatic pressure[117] or

high-frequency vibration[118], for example, promotes ZIF melting (i.e. dynamic metal-linker bond breaking). Previous research has shown that PSBM can cause rapid amorphization of crystalline ZIFs, including ZIF-4 ($Zn(im)_2$; **cag** topology; im^- = imidazolate), ZIF-zni ($Zn(im)_2$; **zni** topology) and ZIF-8 ($Zn(mim)_2$; **sod** topology; mim^- = 2-methylimidazolate).[119-122] However, it is unclear whether the amorphized ZIFs exhibit glassy behavior. Recently, a mechanochemical synthesis by ball-milling has been employed to prepare ZIF-62 ($Zn(im)_{2-x}(bim)_x$; **cag** topology when crystalline; bim^- = benzimidazolate) by reaction of ZnO with imidazole and benzimidazole in the presence of small amounts of *N,N*-dimethylformamide (DMF).[21, 123] Depending on the composition of the reaction mixture, the derived material was either crystalline (for $0.05 \leq x \leq 0.30$) or amorphous (for $0.35 \leq x \leq 1$).[98] Interestingly, the amorphous ZIF-62 prepared by ball-milling showed a calorimetric glass transition, showcasing that glassy ZIF-62 can be prepared mechanochemically at room temperature by increasing the bim^- concentration in the ball-milling synthesis. However, the technique of preparing a ZIF-62 glass by ball-milling via a considerable increase in the bulky linker fraction (i.e. $0.35 \leq x(bim^-) \leq 1$) has constraints, such as the possibility of porosity blockage in the glasses and a significant rise of the glass transition temperature (T_g), necessitating a higher processing or working temperature.

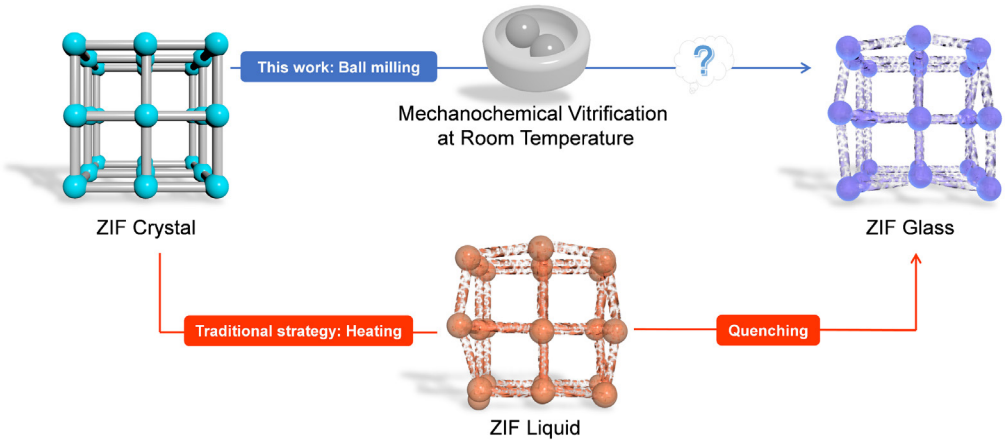

Figure 4.1. Schematic representation of the traditional route to ZIF glass formation (red line) and the mechanochemical vitrification approach followed in this work (blue line).

While ball-milling is commonly employed for the synthesis of crystalline ZIFs or their transformation into amorphous states, its capacity for enabling direct vitrification of ZIFs at room temperature remains uncharted. Herein, this work reports a detailed study of the utility of solvent-free PSBM for the vitrification of crystalline ZIFs of varying chemical composition, network topology and porosity at ambient temperatures (**Figure 4.1**). To evaluate the potential of PSBM for ZIF glass formation, we investigate several meltable and glass-forming ZIFs,[41, 65, 124] namely ZIF-4(Zn/Co), ZIF-zni(Zn/Co), ZIF-62(Zn/Co), ZIF-UC-5 and TIF-4, but also ZIFs known not to melt when in pure form, i.e. ZIF-76[77] and ZIF-8[33, 87], and ZIFs which were previously not studied in terms of glass formation, i.e. ZIF-70[20] and ZIF-Cu-1 ($Cu(im)_2$)[125] (**Figure 4.2**). These materials comprise representatives with Zn^{2+} and Co^{2+} tetrahedral building units typical for ZIFs, as well as a Cu^{2+}-based ZIF featuring drastically flattened pseudo-tetrahedral units. It is important to note that Cu^{2+}-based ZIFs have not been studied in terms of melting and glass formation so far. X-ray powder diffraction (XRPD), differential scanning calorimetry (DSC), simultaneous thermogravimetric and differential thermal analyses (TG/DTA), X-ray total scattering and its deduced pair distribution functions (PDFs), scanning electron microscopy (SEM), and CO_2 gas sorption measurements provide important insights into the thermal, structural, and textural features of the ZIFs after varying PSBM times (between 5 and 60 min). This stury find that PSBM transforms several of these ZIFs into glasses (MIGs = milling-induced glasses), highlighted by the preparation of the first ZIF glass with Cu^{2+} building units, while

other ZIFs amorphize but show no glassy behavior. The results in this study provide a first guide for preparing ZIF glasses by mechanical milling at ambient temperature but also expose some limitations of the method.

4.2 Crystalline ZIF synthesis and structural characterization

Firstly, twelve different ZIF crystals were synthesized by adapting established solvothermal reaction procedures (see **Experimental section**).[20, 43, 77, 125] Among these ZIF-4(M), ZIF-zni(M) and ZIF-62(M) were prepared using either Zn^{2+} or Co^{2+} as metal centers (M^{2+}), whereas TIF-4, ZIF-UC-5, ZIF-76, ZIF-8 and ZIF-70 avail Zn^{2+} as inorganic building unit, and ZIF-Cu-1 was prepared with Cu^{2+} as the metal center (**Figure 4.2**). The ZIFs comprise a variety of functionalized linkers as well as network topologies of diverse porosities. The theoretical void fractions (tVFs) of the ZIFs calculated based on reported crystal structures range from about 7% (ZIF-zni and ZIF-Cu-1) up to about 67% (ZIF-70). After washing and solvent exchange procedures, the desolvated Zn- and Co-ZIF materials were obtained by heating to 170 °C under a dynamic vacuum for 6 h, while ZIF-Cu-1 was activated at 110 °C because of its lower decomposition temperature. The identity and purity of the crystalline ZIFs were verified by structureless profile fits (Pawley method) of XRPD patterns using reference data from the literature (**Figure A4.1-12, Table A4.1**). All compounds are phase-pure except for ZIF-UC-5, which contained about 5 wt% of ZIF-76 as a parasitic phase according to a dual-phase Rietveld refinement of the XRPD pattern (**Figure A4.7**). The latter sample is therefore referred to as ZIF-76/UC-5. Complete removal of solvents from the pores of the ZIFs is demonstrated by ^{1}H nuclear magnetic resonance (^{1}H NMR) and Fourier-transform infrared (FTIR) spectroscopy data (see **Appendix A4.2-4.3**). ^{1}H NMR spectroscopy of acid-digested samples was performed to determine the linker ratios of the mixed-linker materials ZIF-62(M), TIF-4, ZIF-70, ZIF-76 and ZIF-76/UC-5, leading to the chemical compositions given in **Figure 4.2** (**Figure A4.35-36** and **Figure A4.41-44**).

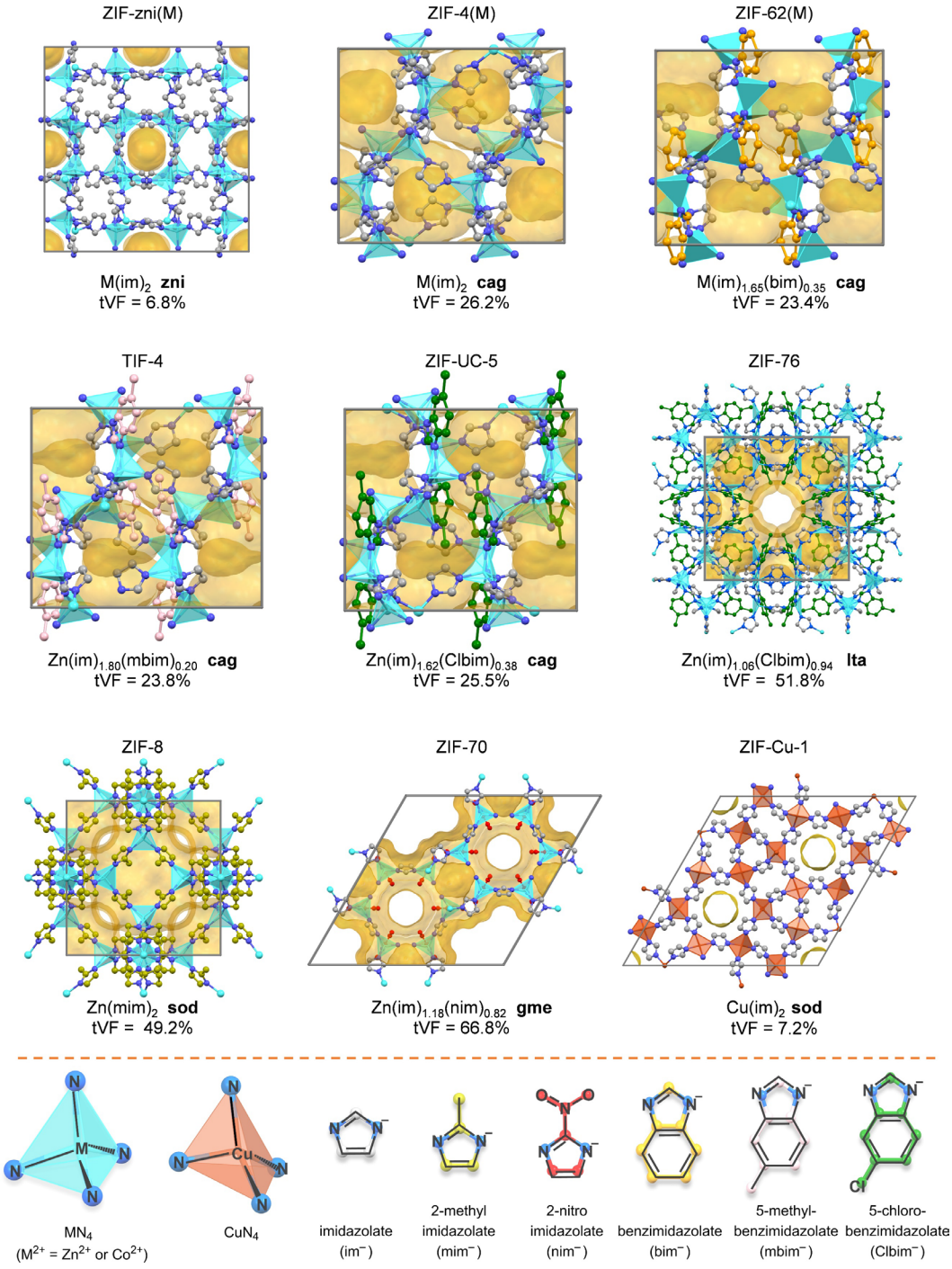

Figure 4.2. TOP: Crystal structures of the ZIFs investigated in this work. ZIF-zni (CCDC code IMIDZB) viewed along the crystallographic *c* axis, ZIF-4 (CCDC code IMIDZB11), ZIF-62 (CCDC code SIWJAM), TIF-4 (CCDC code QOSYAZ) and ZIF-UC-5 (CCDC code GULVIV) viewed along the crystallographic *b* axis. ZIF-76 (CCDC code GITWEM) and ZIF-8 (CCDC code FAWCEN03) viewed along the crystallographic *a* axis. ZIF-70 (CCDC code GITVEL) and ZIF-Cu-1 (CCDC code CUIMDZ01) viewed along the crystallographic *c* axis. Hydrogen atoms are omitted for clarity. The theoretical void fractions (tVFs) were calculated using Mercury software with a probe radius of 1.6 Å and a grid spacing of 0.2 Å and are shown in pale yellow. Solvent molecules were removed and linker disorder was resolved as far as possible without changing the space group symmetry before the calculation of the tVFs. If H atoms were not included in the reported crystal structures, they were positioned at geometrical positions before the calculation of the tVF. The compositions of the ZIFs were obtained by ^{1}H NMR spectroscopy of acid-digested samples. Bottom: Building units of the investigated ZIFs.

4.3 Amorphization by post-synthetic ball milling

The activated microcrystalline ZIFs were treated with PSBM at 25 Hz in a vibratory shaker mill for 5, 10, and 15 minutes, respectively, using a 10 mL stainless steel grinding jar with two 8 mm stainless-steel balls and ca. 50 mg ZIF. The derived PSBM materials are denoted by ZIF-*X*-5min/10min/15min according to the corresponding PSBM time. Additional 30 min and 60 min ball milled samples were prepared for ZIF-8 (ZIF-8-30min and ZIF-8-60min). The XRPD patterns of almost all ball-milled ZIFs show only diffuse scattering without sharp Bragg reflections already after 5 min of PSBM proving rapid amorphization of the materials (**Figure 4.3** and **Figure A4.14-20**). The only exceptions are the ZIF-zni(M) samples, which still contain reflections assigned to the crystalline ZIF-zni phase after 5 min PSBM, even though the reflections are of diminished intensity and increased peak width (**Figure 4.3** and **Figure A4.16**). Upon increasing the PSBM times, the Bragg reflections of the ZIF-zni phases decrease further in intensity, but the samples are still not fully amorphized after 15 min PSBM. The residual crystallinity of the ZIF-zni(Zn) samples was estimated from profile fitting of the XRPD data (**Figure A4.21-24**). It is observed that within the first 10 min PSBM, the degree of crystallinity of the sample gradually reduces to 49%, while after 15 min PSBM, a degree of crystallinity of 36% remains. The higher resistance of ZIF-zni towards amorphization by PSBM can be explained by the higher density of ZIF-zni (ρ = 1.56 g cm^{-3})[126] compared to the other Zn- and Co-based ZIFs studied here (0.78 g cm^{-3} ≤ ρ ≤ 1.32 g cm^{-3})[41], as it is known that a higher density correlates well with increased elastic moduli and hardness[127].

In agreement with previous structural investigations of amorphized ZIFs,[119, 128] PDFs derived from X-ray total scattering data of selected pristine and 5-min-ball-milled ZIF samples show that the short-range structure (< 6 Å) of the crystalline phase (i.e., metal ions surrounded by four imidazolate-based linkers) is preserved in the amorphous PSBM samples (**Figure A4.30-34**). Hence, the PDFs of the amorphous PSBM-derived ZIFs are largely identical to those of the literature-known ZIF MQGs. In line with the loss of long-range order, increased structural heterogeneity and distortions in the ball-milled ZIFs are evident from the broadening of various vibrational bands in the FTIR spectra relative to the bands of the crystalline parent materials (**Figure A4.47-58**). In particular, the asymmetric stretching vibrational bands of the MN_4 polyhedra (M^{2+} = Zn^{2+}, Co^{2+}, Cu^{2+}) located at 300 cm^{-1} in the

far-IR spectra exhibit notably broader profiles in the PSBM samples compared to their crystalline counterparts, observable as early as 5 minutes into the ball-milling process. These bands mirror the widths seen in the corresponding MN_4 vibrations of MQG reference samples (**Figure A4.59-67** and **Table A4.2**). An exception is again observed with ZIF-zni(Zn), which shows a gradual broadening over the course of PSBM, consistent with the gradual decline in crystallinity discussed above. SEM images reveal that the solvothermally synthesized ZIFs, initially characterized by large crystals (up to several hundred micrometers in size), undergo significant fragmentation into smaller particles ranging from 1 to 10 µm in size following a 5-min PSBM treatment (**Figure A4.106-108** and **Table A4.8**). Prolonged ball-milling times result in only marginal further reductions in particle size.

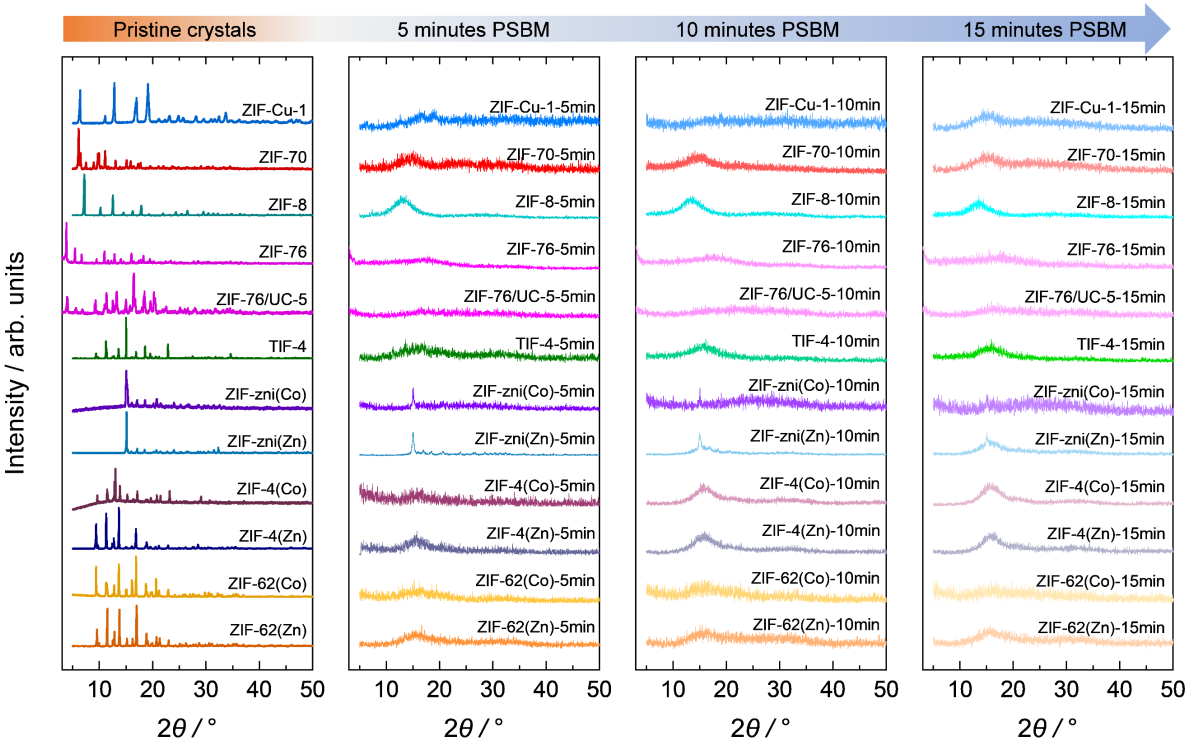

Figure 4.3. XRPD patterns of the pristine ZIF polycrystalline materials and after 5, 10 and 15 min PSBM.

4.4 CO_2 physisorption data and porosity analysis

Since it is established that N_2 is hardly adsorbed at 77 K in some of the ZIFs studied here,[22, 41, 129] the evolution of the ZIFs' porosity with PSBM time was studied by isothermal CO_2 sorption at 195 K (**Figure A4.68-75** and **Table A4.3**). CO_2 has a smaller kinetic diameter than N_2 and can enter very narrow micropores.[41] The

maximum gas pressure used for the data collection is 95 kPa, corresponding to a relative pressure p/p_0 of about 0.50, ensuring the complete filling of the materials' micropores. The maximum adsorbed gas capacities at 95 kPa (V_{ads}^{max}) of CO_2 of all studied ZIFs progressively decrease with increasing PSBM time except for ZIF-zni(Zn) (**Figure 4.4a**). The reduced CO_2 capacities indicate that the materials densify during the PSBM-induced amorphization. As expected, the rate of densification decreases with increasing ball-milling-time, indicating that the most significant structural changes under amorphization appear during the first few minutes of milling. The more porous ZIFs (i.e., ZIF-4(M), ZIF-8 and ZIF-76) undergo stronger densification (stronger loss of porosity) with increased ball-milling time than the less porous ZIF-62(M) (**Figure 4.4b**). This is in accordance with the larger bulk moduli and increased mechanical resistance of ZIF-62(M) compared to the isoreticular but more porous ZIF-4(M).[130] Surprisingly, the porosity of ZIF-zni(Zn) increases with PSBM. V_{ads}^{max} progressively reaches 181% of the capacity of pristine ZIF after 10 min of PSBM and then settles at 171% of the original capacity after 15 min of PSBM. This unusual behavior likely is because the **zni** topology is one of the densest ZIF topologies known, and the increase in its disorder by PSBM leads to an increase in its porosity[131].

Except for ZIF-8 and ZIF-Cu-1, the CO_2 capacity is very similar for the samples treated with 15 min PSBM, signifying that they all form amorphous MOFs of similar porosity and density. Notably, the CO_2 capacities at 95 kPa are in the range from 50 to 65 $cm^3\ g^{-1}$ (STP), which is very similar to the CO_2 capacity of the MQGs of ZIF-4, ZIF-62 and TIF-4 determined under the same conditions[41]. ZIF-8 is more resistant to a framework collapse than the other ZIFs, so a substantially higher porosity is observed after 15 min of PSBM (V_{ads}^{max} = 82 $cm^3\ g^{-1}$). Even after 60 min of PSBM, the amorphized ZIF-8 has a substantially higher sorption capacity than the other ZIFs subjected to only 15 min PSBM (V_{ads}^{max} = 70 $cm^3\ g^{-1}$). We speculate that the methyl groups present at position 2 of the mim^- linker might be the reason for the formation of a more open amorphous network structure in the case of ball-milled ZIF-8 compared to the other ZIFs, which use linkers that are not substituted at position 2.[129]

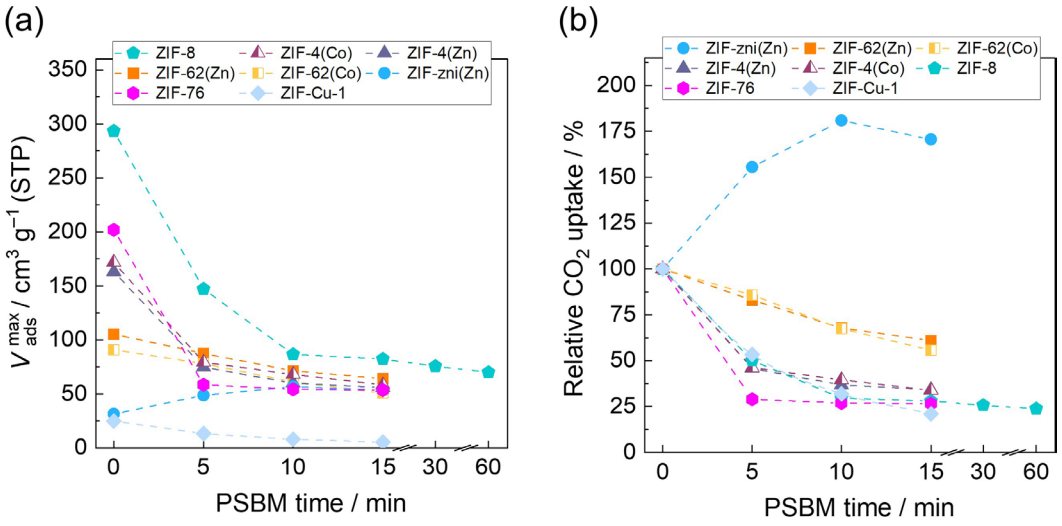

Figure 4.4. (a) Absolute CO_2 uptake (V_{ads}^{max}) recorded at 195 K, 95 kPa and (b) the corresponding relative CO_2 uptake ($V_{ads}^{max}(t)/V_{ads}^{max}(t=0)$) as a function of PSBM time of the studied ZIF samples. The lines are just a guide to the eyes.

ZIF-Cu-1 is very different to all the other materials investigated here. As expected from its low tVF, the gravimetric CO_2 capacity (V_{ads}^{max} = 25 cm^3 g^{-1} (STP)) of the crystalline ZIF-Cu-1 is on the same scale as the capacity of crystalline ZIF-zni (V_{ads}^{max} = 31 cm^3 g^{-1} (STP)). In contrast to ZIF-zni(Zn), milling does not increase the porosity of ZIF-Cu-1 but progressively densifies the material so that V_{ads}^{max} amounts to only about 5 cm^3 g^{-1} (STP) after 15 min PSBM, rendering the amorphous ZIF-Cu-1-15min essentially non-porous. Since the dense ZIF-zni(Zn) and ZIF-Cu-1 both contain the same im$^-$ linkers, the drastic difference in milling-induced structural evolution between these two materials may be ascribed to their inorganic building units. The almost perfectly tetrahedral Zn^{2+} centers of ZIF-zni(Zn) (geometry index τ_4 = 0.97 and 0.95 for the two crystallographically independent Zn^{2+} ions; τ_4 = 1 for tetrahedral and τ_4 = 0 for square planar[132], **Appendix A.5.7**) seem to facilitate a looser packing of the building units in the amorphous frameworks compared to the severely flattened pseudo-tetrahedron of Cu^{2+} in ZIF-Cu-1 (τ_4 = 0.47; **Figure 4.5**).

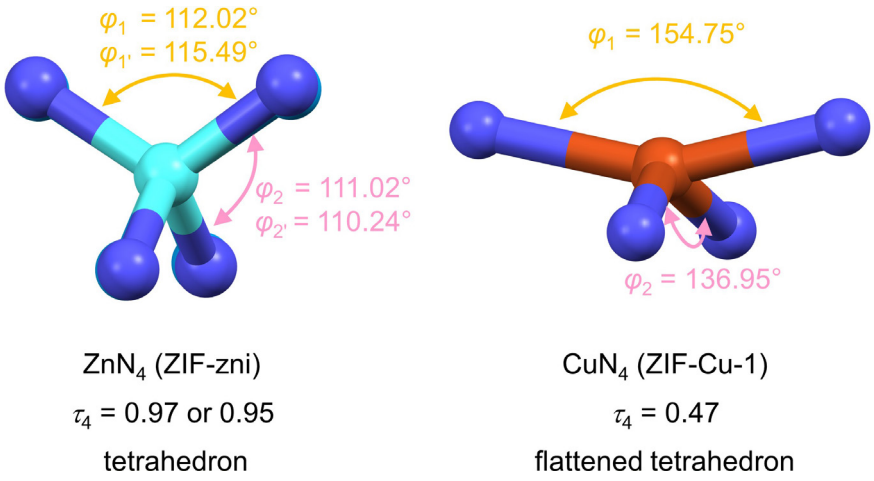

Figure 4.5. Coordination environments of Zn^{2+} in ZIF-zni (left, CCDC code IMIDZB) and Cu^{2+} in ZIF-Cu-1 (right, CCDC code CUIMDZ01). The two largest N-M-N angles (φ_1 and φ_2) utilized to calculate the geometry index (τ_4) are shown in both diagrams. Note, ZIF-zni has two crystallographically independent Zn^{2+} ions exhibiting slightly different angles.

4.5 Thermal properties

To examine the thermal stability and possible phase/glass transitions of the pristine ZIFs and the corresponding PSBM samples, simultaneous thermogravimetric and differential thermal analyses (TG/DTA) were carried out between 40 and 800 °C under N_2 atmosphere (**Figure A4.76-87**). The decomposition temperature (T_d) of all ZIFs generally decreases slightly with increasing PSBM time (**Table A4.6**). The reduced thermal stability may be due to increased defect concentrations and unfavorable structural distortions caused by PSBM.

To screen the samples for thermal phase changes, additional cyclic DSC experiments (two upscans, one downscan) were performed between ambient temperature and T_d also under N_2 atmosphere (**Figure 4.6**, **Figure A4.88-91** and **Figure A4.99**). Excitingly, the ZIFs which are known glass formers (ZIF-62(M), ZIF-4(M), ZIF-zni(Zn), ZIF-76/UC-5 and TIF-4) exhibit a well-defined glass transition signal in the first upscan of the DSC already after only 5 minutes of PSBM (**Figure 4.6** and **Figure A4.88**). Hence, these PSBM-amorphized materials represent ZIF MIGs that transition to a supercooled liquid upon heating.[34] This proves that the vitrification of these compounds can be achieved by ball milling at room temperature instead of heating across the materials' melting points, followed by melt-quenching. We believe that the mechanical energy generated by compression and shear, together with potential instantaneous temperature hotspots, achieves the glass transition process through PSBM.[133-134] Notably, the T_g values of the MIGs are lower than the T_g

values of the corresponding glasses prepared by conventional melt-quenching methods (MQGs). Interestingly, the T_g values of the MIGs decrease further with increasing PSBM time, which can be rationalized by an increasing number of structural defects (i.e. undercoordinated Zn^{2+} ions, linkers with dangling bonds) with longer milling times (**Figure 4.6** and **Figure A4.88**).[115, 135] The lower T_g values of the MIGs imply that these glasses could be molded and shaped at a lower temperature than the corresponding MQGs. Moreover, the MIGs transform into the supercooled liquid state at T_g, while the MQGs must first be obtained by heating the crystalline precursors to the higher T_m.

In the second DSC upscan of the MIGs, the T_g values converge to the values known for the corresponding MQGs. This is likely because most of the structural defects arising from PSBM are healed by thermal relaxation in the supercooled liquid state. Broad exothermic features in the DSC traces of the first upscans of the PSBM samples of ZIF-62(Zn) at temperatures between 400 °C and 500 °C support this reasoning.

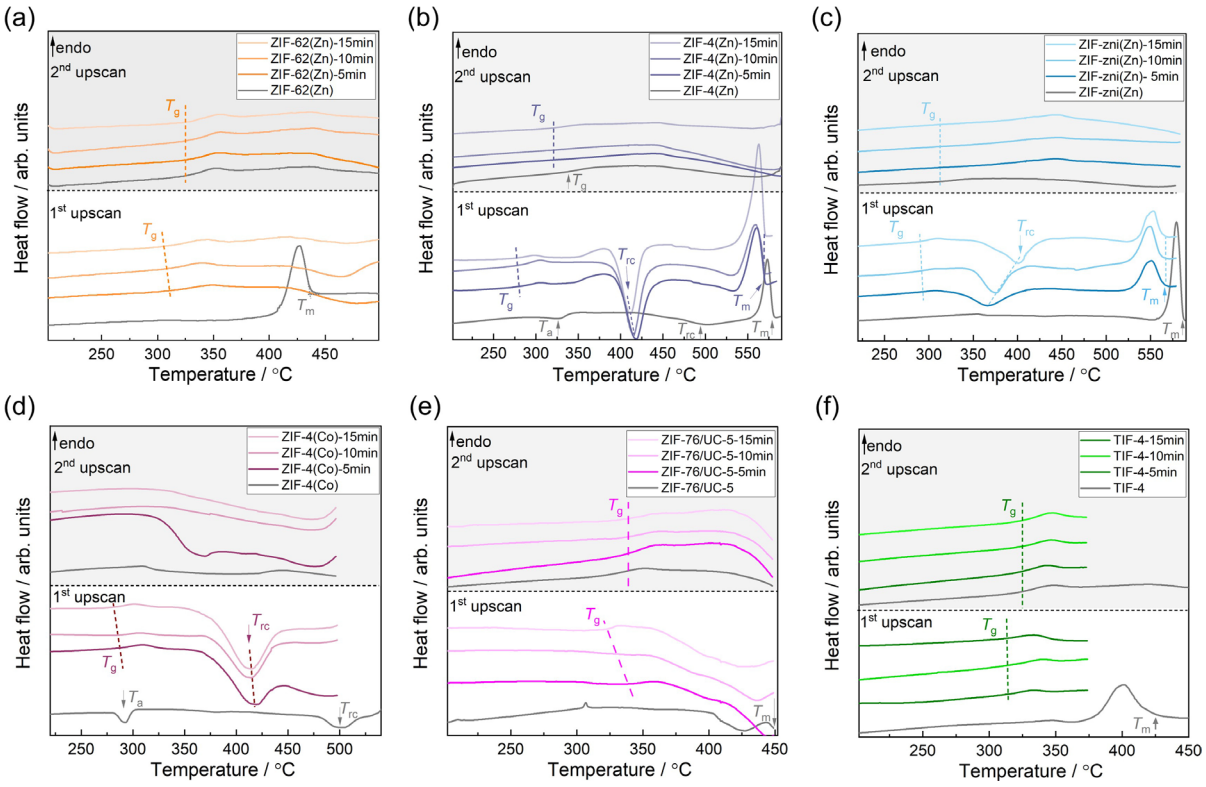

Figure 4.6. First and second upscans of DSC measurements of (a) ZIF-62(Zn), (b) ZIF-4(Zn), (c) ZIF-zni(Zn), (d) ZIF-4(Co), (e) ZIF-76/UC-5, (f) TIF-4, and the corresponding samples after 5, 10 and 15 min PSBM. The heating rate for all measurements was +10 °C min^{-1}. The colored arrows and dotted lines indicate the amorphization temperature (T_a), glass transition temperature (T_g), recrystallization temperature (T_{rc}), and melting temperature (T_m) of the ZIFs. The gray regions represent the second upscans.

The DSC data of both ZIF-4(Zn/Co) and ZIF-zni(Zn/Co) reveal distinct thermal characteristics (**Figure 4.6b** and **c**). Similar to crystalline ZIF-4(Zn), which recrystallizes to ZIF-zni(Zn) after thermal amorphization, the MIGs ZIF-4(Zn)-5min, -10min and -15min, also recrystallize to the ZIF-zni(Zn) polymorph after passing through their glass transition (confirmed by variable temperature XRPD, **Figure A4.27-29**). Interestingly, the recrystallization temperature (T_{rc}) and the corresponding enthalpy ($\triangle H_{rc}$) decrease slightly with increased milling time (**Table A4.6** and **Table A4.7**). The PSBM samples derived from ZIF-zni(Zn) also recrystallize to the same phase after passing through the glass transition; however, here, T_{rc} and $\triangle H_{rc}$ increase with milling time. These thermal variations align with the milling-induced changes in the porosity and density, where ZIF-zni(Zn) experiences an increase in porosity and a decrease in density with milling, while ZIF-4(Zn) shows the opposite trend. Additionally, ZIF-zni(Zn) does not fully amorphize even after 15 min of PSBM. Consequently, the remaining crystalline grains of the ZIF-zni phase in the ball-milled materials aid in recrystallization, as they serve as nucleation sites for crystal growth when subjected to elevated temperatures.

It can generally be stated that $\triangle H_{rc}$ for all ball-milled ZIF-4(Zn) and ZIF-zni(Zn) materials ($\triangle H_{rc}$ = –7.2 to –10.2 kJ mol^{-1}) is slightly smaller than that of pristine ZIF-4(Zn) ($\triangle H_{rc}$ = –10.6 kJ mol^{-1}). This finding indicates incomplete recrystallisation in the PSBM samples so that a substantial proportion of the amorphous phase remains. This hypothesis is reinforced by the observation that the melting enthalpy ($\triangle H_m$) of the recrystallized ZIF-zni(Zn) phases from the PSBM materials ($\triangle H_m$ = 5.0 to 7.7 kJ mol^{-1}) is ca. 35 to 58% lower than that of pure ZIF-zni(Zn) ($\triangle H_m$ = 11.9 kJ mol^{-1}). Correspondingly, these recrystallized phases from the PSBM materials also exhibit substantially lower melting temperatures (T_m = 570 °C and 565 °C) compared to their pristine counterparts (T_m ≥ 581 °C). The lower T_m and $\triangle H_m$ of the PSBM samples can be attributed to the presence of a considerable amount of residual amorphous content, a higher concentration of structural defects in the recrystallized phases, and the smaller particle sizes induced by PSBM (**Figure A4.107-108**).[136-138] Noteworthy, similar variations in the glass transition and recrystallization behavior are observed for the Co^{2+}-derivatives ZIF-4(Co) and ZIF-zni(Co), even though the ZIF-zni(Co) phases derived by recrystallization thermally decompose before they melt. (**Figure 4.6d** and **Figure A4.89**)[124, 139].

Excitingly, the PSBM samples of phase-pure ZIF-76 demonstrate clear T_g signals between 278 °C (15 min PSBM) and 347 °C (5 min PSBM) in the first DSC upscans

(**Figure 4.7**). Similar to the behavior observed for the other ZIF glass formers discussed earlier, T_g converges to 357 °C in the second upscans due to thermal relaxation during the first heating-cooling cycle. Note that the glassy state of ZIF-76 is unattainable by the melt-quenching technique when the material is in phase-pure form because the ZIF-76 microcrystals reach their decomposition temperature (T_d) before they can melt (**Figure A4.83**).[77] Consequently, ZIF-76 can only be melted in a flux of a meltable ZIF, such as the chemically similar but topologically different ZIF-UC-5.[77, 99, 140] The inability of phase-pure ZIF-76 to melt can be attributed to its substantially higher porosity compared to the ZIFs with **cag** or **zni** topology, which results in an increased activation energy for the dissociation of the metal-linker bond.[87] The strong densification experienced by ZIF-76 during PSBM (**Figure 4.4**a) appears to be the key to observing glassy behavior and forming a supercooled liquid state at elevated temperatures. This development is advantageous as it expands the range of chemical compositions available for ZIF glasses. Notably, the fraction of the bulky Clbim$^-$ linker in ZIF-76 accounts for approximately 50%, whereas it is only around 20% in ZIF-UC-5. This is relevant because the fraction of the bulky linker in ZIF glasses has been shown to influence important material properties, including the viscosity of the ZIF liquids and the gas sorption selectivity of the corresponding glasses[41, 43].

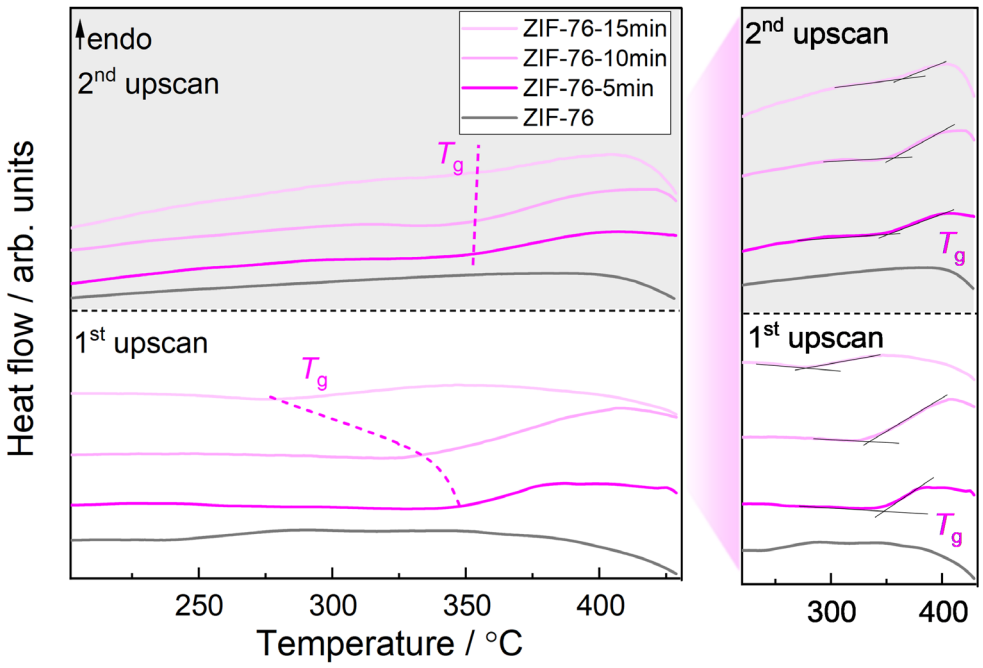

Figure 4.7. First and second upscans of DSC measurements of phase-pure ZIF-76 and the corresponding samples after 5, 10 and 15 min PSBM. The heating rate for all measurements was +10 °C min^{-1}. The graph on the right is used to highlight the glass transition signals.

Inspired by the finding that the non-melting ZIF-76 can be transformed into a glass by PSBM, we embarked on an investigation into the thermal characteristics of ZIF-8, ZIF-70 and ZIF-Cu-1. We aimed to explore the possibility of observing glass transitions and attaining supercooled liquid states for these ZIFs following PSBM treatment as well. Crystalline ZIF-8 has already been investigated in terms of melting from an experimental and theoretical perspective,[33, 87] while the thermal phase behavior of ZIF-70 and ZIF-Cu-1 is unexplored.

It is established that crystalline ZIF-8 is resistant to melting at elevated temperatures, which has been explained by the stronger Zn–N bond of the mim^- linker compared to the non-substituted im^- linker as well as the larger activation energy for Zn–N bond breaking originating from the large porosity of ZIF-8.[33, 87, 129] In agreement with these facts, none of the ball-milled ZIF-8 samples exhibits a calorimetric glass transition, although the amorphous ZIF materials possess rather high thermal stability (T_d > 486 °C) (**Figure A4.85** and **Figure A4.90**). It becomes evident that the densified amorphous ZIF-8 phases resulting from PSBM do not undergo the dynamic dissociation and association of Zn–N bonds, required for the transition from a vitrified glass to a supercooled liquid state. This observation underscores the critical role played by the non-substituted and smaller im^- linker, which is an integral building block common to all reported glass-forming ZIFs.

ZIF-70 possesses a chemical composition with about 59% of the small im^- linker and about 41% of the bulkier nim^- linker. TG/DTA reveals that the crystalline ZIF-70 has a low T_d of 325 °C. In contrast to all the other ZIFs investigated in this work, ZIF-70 displays a strongly exothermic decomposition, which can be associated with the low thermal stability of the nim^- linker. No melting signal can be observed in the DSC before the exothermic decomposition. The rather large fraction of the im^- linkers, however, suggests that the material has the potential for glass formation by PSBM, akin to ZIF-76. Nevertheless, the amorphous ZIF-70 derivatives obtained through PSBM also exhibit a strongly exothermic decomposition starting already at around 300 °C (**Figure A4.86**). This low thermal stability of the amorphous ZIF-70 renders it incapable of showing a glass transition signal in DSC analysis, as T_g would be expected somewhere above 300 °C (**Figure A4.91**). Thus, the amorphized and densified ZIF-70 shows no glassy behavior, presumably due to its poor thermal stability.

The thermal properties of the Cu^{2+}-based ZIF-Cu-1 have not yet been investigated, although the material with the **sod** topology was reported more than 20 years ago.[125]

TG/DTA experiments reveal that crystalline ZIF-Cu-1 experiences a two-step decomposition process, with the first step starting at only 258 °C (**Figure 4.8a**). Hence, T_d of ZIF-Cu-1 is much lower compared to the previously discussed Zn^{2+}- and Co^{2+}-based ZIFs. The heat flow signature at the first decomposition step is strongly endothermic, and heating ZIF-Cu-1 just past the first decomposition step (i.e. to 270 °C) followed by cooling the material to room temperature results in a dark-colored, glassy material exhibiting a glass transition with a T_g of 172 °C upon reheating (**Figure A4.99**). The fact that the particles of the pristine microcrystalline ZIF-Cu-1 fuse to form a millimeter-sized glassy structure indicates that ZIF-Cu-1 melts and decomposes in parallel at around 258 °C. Since the weight-loss is about 22% for the first decomposition step, the glassy phase of ZIF-Cu-1 derived by melt-quenching suffers from severe decomposition. Excitingly, the ZIF-Cu-1 samples amorphized by PSBM display glass transition temperatures between 166 °C and 170 °C in DSC experiments, classifying them as MIGs. In contrast to the Zn- and Co-based MIGs, the ZIF-Cu-1 samples processed for 5 - 15 min exhibit a slight increase in T_g with longer PSBM durations. This distinctive behavior could be attributed to the unique coordination chemistry of Cu^{2+} (**Figure 4.5**). Upon further heating, the MIGs recrystallize to the original ZIF-Cu-1 phase with **sod** topology, demonstrated by exothermic signals with an onset around 202 °C (**Figure 4.8b**) and the reappearance of characteristic diffraction peaks in the XRPD patterns (**Figure A4.20**). The recrystallization is followed by thermal decomposition around 220 °C. However, if the MIGs are only heated to 200 °C, recrystallization does not occur, and glass transitions are again observed in the second DSC upscans (**Figure 4.8c**). Importantly, the MIGs of ZIF-Cu-1 are the first Cu^{2+}-based ZIF glasses, enhancing the compositional variety of the ZIF glass family beyond the materials with Zn^{2+}, Co^{2+} and Fe^{2+} metal centers[141] reported so far. Given the unique catalytic, electronic and redox properties of Cu^{2+}-based MOFs,[142-144] the finding that PSBM gives access to Cu^{2+}-based MOF glasses significantly expands the range of potential applications of this family of materials.

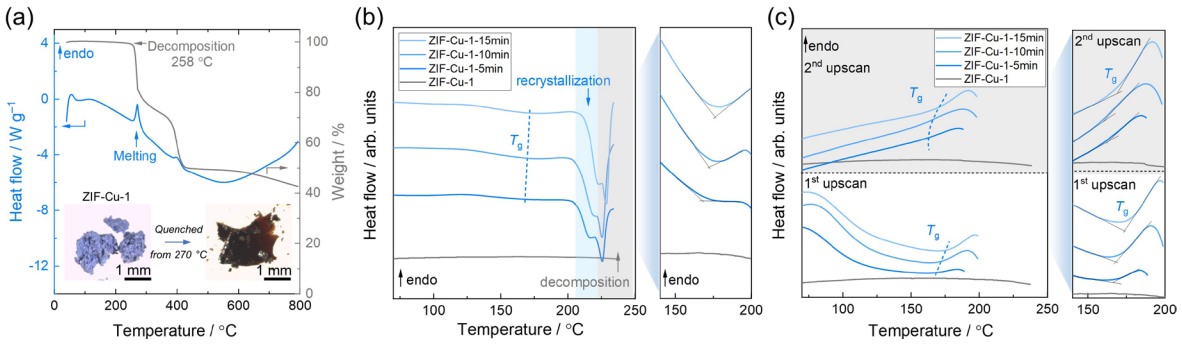

Figure 4.8. (a) TG/DTA data of ZIF-Cu-1. The inset is microscopic images of the neat ZIF-Cu-1 microcrystalline powder and the glassy phase derived by heating ZIF-Cu-1 to 270 °C under N_2 atmosphere (i.e. to the offset of the endothermic DTA signal) followed by cooling to room temperature. (b) DSC measurements of ZIF-Cu-1 and its PSBM derivatives recorded to a maximum temperature of 235 °C. (c) Cyclic DSC scans of ZIF-Cu-1 and its PSBM derivatives. To avoid recrystallization of the PSBM samples, the first upscan was heated to only 190 or 200 °C. The heating rate for all measurements was +10 °C min^{-1}. The zoom on the right in panels (b) and (c) is to highlight the glass transition signals.

Among the known ZIF glass formers of the composition $M(im)_2$, with M^{2+} = Zn^{2+} (ZIF-4), Co^{2+} (ZIF-4), Fe^{2+} (MUV-24) and Cu^{2+} (ZIF-Cu-1), the Cu-derivative is unique. The metastable ZIF-4 (**cag** topology) and MUV-24 (*lla1* topology) recrystallize to polymorphs with **zni** topology upon thermal treatment, and the $M(im)_2$ phases with **zni** topology melt (decompose in the case of Co^{2+}) at temperatures between 482 and 590 °C.[141] The liquids of $Zn(im)_2$ and $Fe(im)_2$ can be quenched to room temperature to derive their glasses with glass transition temperatures of 292 °C (Zn^{2+}) or 190 °C (Fe^{2+}). ZIF-Cu-1 possesses the **sod** topology, which is already quite dense because of the unique flattened tetrahedral coordination geometry of the Cu^{2+} ion (**Figure 4.2**). A solid-solid transition to a polymorph with **zni** topology is not observed for $Cu(im)_2$, likely because the **zni** topology cannot be realized with the flattened tetrahedral Cu^{2+} geometry. Instead, ZIF-Cu-1 melts at a much lower temperature (~260 °C) and decomposes in parallel. Nevertheless, employing the PSBM technique, a non-decomposed, glassy form of ZIF-Cu-1 can be obtained, exhibiting a T_g of ~166 °C. Therefore, the T_g, T_m and T_d of ZIF-Cu-1 are the lowest in the $M(im)_2$ series. This indicates a greater lability of the Cu–N bond compared to the bonds involving the other M^{2+} ions.

4.6 Conclusion

In this chapter, the amorphization and glass formation of twelve distinct ZIFs featuring a range of imidazolate-type linkers and metal ions (Zn^{2+}, Co^{2+} and Cu^{2+})

through solvent-free PSBM were investigated. ZIFs capable of melting and forming melt-quenched glasses also vitrify via PSBM was observed. Conversely, ZIFs that decompose thermally before melting exhibit varied responses to ball milling; some display glass-like properties, while others do not. The absence of glassy behavior in ZIF-8 and ZIF-70 can be attributed to the exceptionally strong Zn–N bond with the mim^- linker in ZIF-8 and the very limited thermal stability of the nim^- linker in ZIF-70. In the case of the non-melting ZIF-76, vitrification through PSBM is achievable since the imidazolate-type linkers in this material have adequate thermal stability and sufficient Zn–N bond lability. The significance of PSBM in forming ZIF glasses is particularly evident in the case of ZIF-Cu-1. The lower thermal stability of ZIF-Cu-1 likely originates from the labile Cu–N bonds and the redox activity of the Cu^{2+} centers, leading to simultaneous melting and thermal decomposition of the crystalline ZIF-Cu-1 phase. However, amorphization by PSBM enables the attainment of a glassy state in ZIF-Cu-1 while maintaining material integrity, marking the creation of the first Cu^{2+}-based ZIF glass.

This research underscores the vast potential of PSBM in developing new glassy ZIFs. While the small particle size of the PSBM-derived glasses may limit their direct application, the process of sintering or remelting by heating the materials above their T_g facilitates particle fusion and enables the formation of bulk glasses.[145-146]

Looking forward, future studies should explore the applicability of PSBM for producing glassy MOFs utilizing alternative linker chemistries, such as dicarboxylates[147-148]. This expansion could be pivotal in broadening the scope of MOF glasses, traditionally constrained by the necessity for MOFs to be meltable – a characteristic that only a limited number of MOFs exhibit. Thus, we envisage that several non-meltable ZIFs and other MOFs can also be vitrified by PSBM. Moreover, creating MOF glasses through ball-milling at room temperature may not only be more energy-efficient[21] but also enable the integration of thermally sensitive materials, such as organic or organometallic molecules, into versatile MOF glass composites[149]. This approach broadens the spectrum of potential applications, paving the way for developing multifunctional MOF glass composites, thereby venturing into more diverse application fields.

5 Cadmium-based ZIF Glasses

The work presented in this part is currently being written up to a manuscript:

Cadmium-based Zeolitic Imidazolate Framework Glass and Glass-Ceramics

Wen-Long Xue, Alexander Klein, Jan-Benedikt Weiß, Suresh Vasa, Felix Müller, Mirijam Zobel, Rasmus Linser, Sebastian Henke*

Author contributions:

S.H. and W.-L.X designed this project. W.-L.X synthesized the materials and performed all basic experiments as well as data analysis. W.-L.X. performed the synchrotron XRPD experiments. F.M. and M.Z. performed X-ray total scattering experiments. W.-L.X. analyzed the XPDF data. A.K. performed the solid-state NMR experiments with S.V. and R.L. contributing to data analysis and interpretation. W.L.X. and S.H. wrote the manuscript with contributions from all the authors. All authors have given approval of the final manuscript.

Abstract

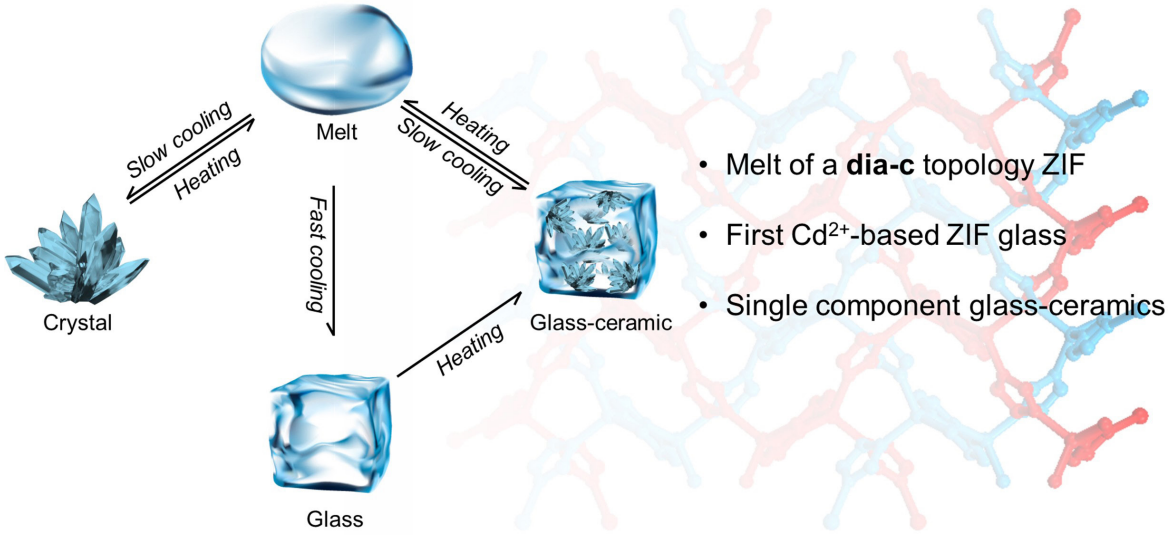

This work demonstrates the first cadmium imidazolate (im^-) glass obtained from a mechanochemically synthesized meltable cadmium-based zeolitic imidazolate framework (ZIF). The mechanochemically synthesized $Cd(im)_2$ microcrystals have a lower melting temperature (T_m) than solvent-synthesized crystals, thus largely avoiding decomposition during melting. The crystalline $Cd(im)_2$ framework, composed of tetrahedral Cd^{2+} cations and im^- linkers, exhibits an two-fold interpenetrated diamondiod topology (**dia-c**). Mechanochemically synthesized $Cd(im)_2$ melts at approximately 455 °C and transitions to a glass upon rapid cooling to room temperature. Remarkably, upon reheating, the material undergoes partial recrystallization into a single component, monolithic glass-ceramic state — a phenomenon not observed in previous melt-quenched ZIF glasses. Our results pave the way for the development of metal-organic framework glasses and glass-ceramics from second-row transition metal ions, with promising applications in energy storage, optics and semiconductors. The transfer of functionality from glass to glass-ceramics points toward new routes to tunable, functional ZIF glass-ceramics.

5.1 Introduction

As previously discussed, ZIF glasses[22, 33, 40] possess continuous random network structures based on Werner-type coordination chemistry.[150] ZIF glasses not only retain the advantageous chemical functionality of crystalline ZIFs, but also exhibit excellent processability[35, 75] combined with intrinsic microporosity[41, 129, 151], even allowing for the preparation of micro-optical elements[152]. These attributes make them attractive for various applications, ranging from gas separation[38, 43], ionic conductivity[148] to optoelectronics[108]. Once again, it is worth noting that despite the large number of crystalline ZIFs already reported,[20, 27] only very few can be melted and transformed into ZIF glasses by melt-quenching. So far, the portfolio of meltable ZIFs is limited to structures based on the first-row transition metal ions Zn^{2+}, Co^{2+}, and Fe^{2+} and only a few network topologies (**cag**, **zni**, **gis**, and **sod**, for the latter see Chapter 3).[40, 124, 129, 141] For most other crystalline ZIFs, the imidazolate-based organic linkers decompose before or during the melting process, characterized by dynamic breaking and reorganization of the metal–imidazolate coordination bonds. Even though it is possible to prepare a Cu^{2+}–based glass by the mechanochemical methods, i.e. a_gZIF-Cu-1, see Chapter 4 of this thesis, crystalline ZIF-Cu-1 cannot be melted without decomposition.

In this chapter, driven by the goal of expanding the as-of-yet very small family of meltable ZIFs, the first meltable cadmium-based zeolitic imidazolate frameworks based on the literature known $Cd(im)_2$ with the catenated diamondoid topology (**dia-c**) is demonstrated. Solution-synthesized $Cd(im)_2$ thermally decomposes in parallel to melting, whereas the mechanochemically synthesized $Cd(im)_2$ features a larger separation of the melting and decomposition temperatures, allowing for the preparation of a melt-quenched $Cd(im)_2$ glass with only very little decomposition. Compared to the reported solution-synthesized $Cd(im)_2$, the smaller particle size of the mechanically synthesized $Cd(im)_2$ makes it possible to melt at lower temperature, thereby minimize the decomposition during melting. Remarkably, after rapid quenching to form a ZIF glass, the material undergoes partial recrystallisation to form a transparent single component glass-ceramic state upon reheating. The controlled partial recrystallization in the glass matrix resulting in the formation of ZIF glass ceramics is so far unique to the $Cd(im)_2$ system and has not been observed for the previously reported ZIF glases based on first-row transition metals. This study opens up new opportunities for the family of meltable MOFs potentially

allowing control over the phase fraction of crystalline and amorphous phases in glass-ceramic-like complex and multifunctional MOF materials.

5.2 Preparation and characterization of $Cd(im)_2$

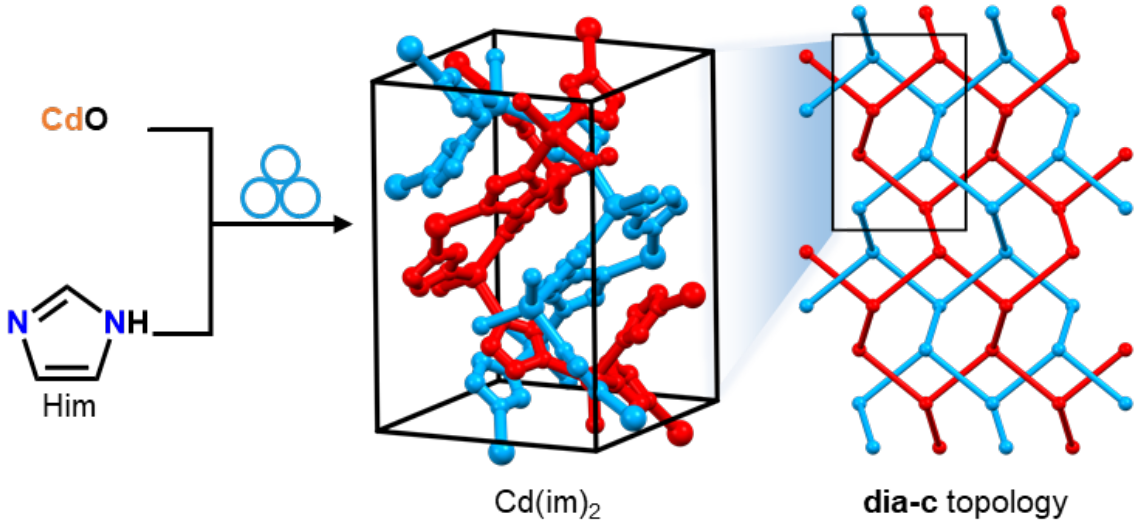

Figure 5.1. Mechanosynthetic route for $Cd(im)_2$ and an illustration of the **dia-c** topology of $Cd(im)_2$.

Crystalline $Cd(im)_2$ was prepared via two routes: the solution-chemistry route as previously documented[153] and the newly developed mechanochemical ball-milling approach (**Figure 5.1** and **Experimental Section**). The ZIF compounds are designated as $Cd(im)_2$-*sol*, and $Cd(im)_2$, respectively. The $Cd(im)_2$ ZIF compounds exhibit the same crystal structure with the two-fold interpenetrated diamondoid topology (**dia-c**, catenated diamondoid) and the same composition, comprising Cd^{2+} as the inorganic building unit and the imidazolate (im^-) as the organic building unit. After washing procedures, the dried $Cd(im)_2$ ZIF materials were obtained by heating to 170 °C under a dynamic vacuum for 6 h. The identity and purity of the crystalline $Cd(im)_2$ ZIFs were verified by structureless profile fits (Pawley method) of XRPD patterns using reference crystallographic data from the literature[153] (**Figure 5.2**, **Figure A5.1-2** and **Table 5.2**). Additionally, a Gaussian peak shape model based on Scherrer's equation was employed to ascertain the particle size of the $Cd(im)_2$ ZIFs from the peak widths in the profile fitting process, resulting in the conclusion that $Cd(im)_2$ has a much smaller particle size than $Cd(im)_2$-*sol* (74±2 nm *vs.* 217±4 nm). Complete removal of solvents of the $Cd(im)_2$ ZIFs is demonstrated by Fourier-

transform infrared (FTIR) spectroscopy and ^1H nuclear magnetic resonance (^1H NMR) data (see **Appendix A.5.2-A5.3**).

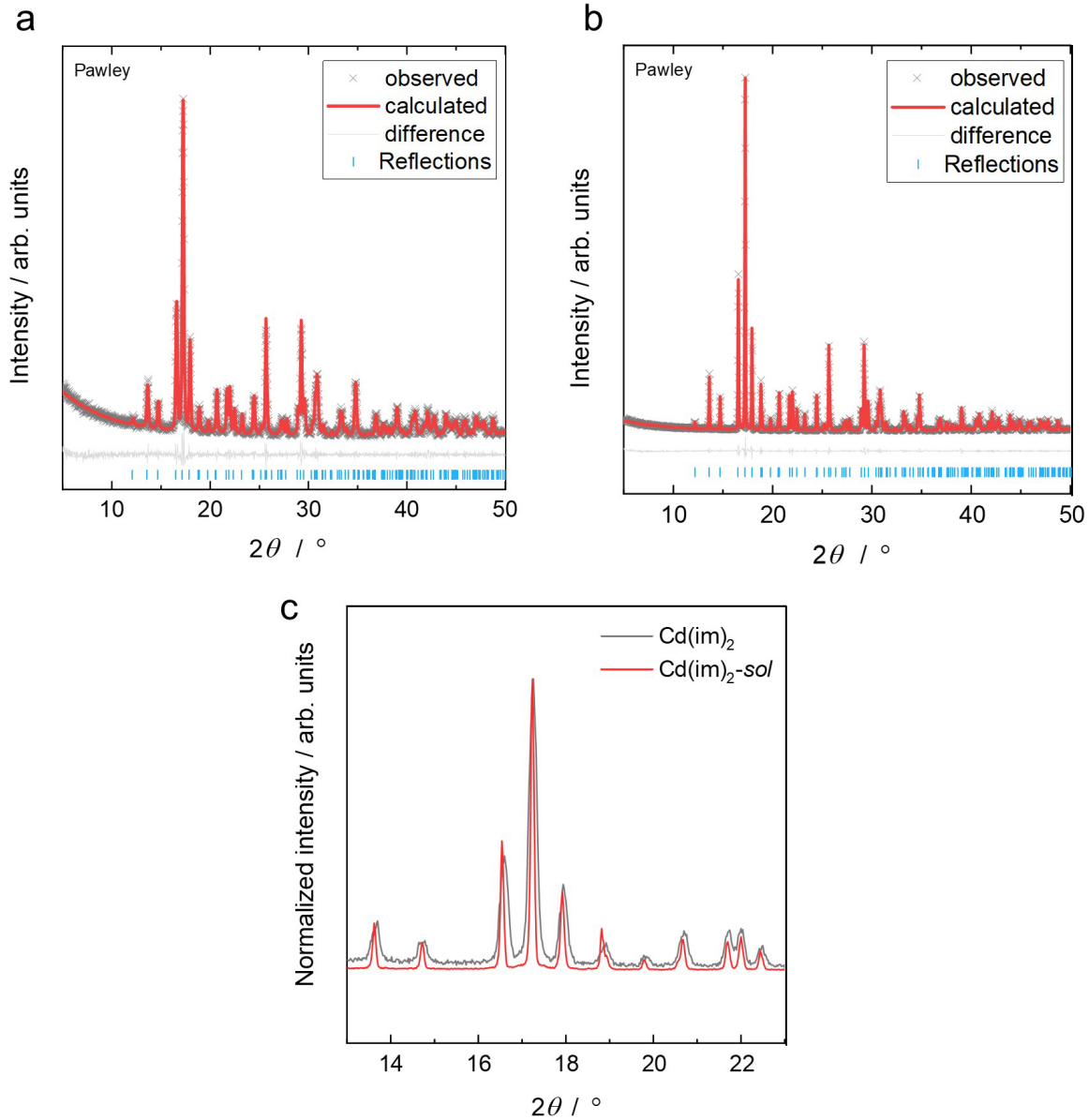

Figure 5.2. Profile fit (Pawley method) performed on the XRPD pattern of (a) $Cd(im)_2$ and (b) $Cd(im)_2$-*sol*. The initial crystallographic parameters are taken from crystalline structure (CCDC code BAYQAU11).[153] (c) Magnified view of the normalized XRPD of $Cd(im)_2$ and $Cd(im)_2$-*sol* showing the fraction from 13° to 23°. The peaks width of $Cd(im)_2$ is broader, indicating a smaller particle size.

It is worth mentioning that even though $Cd(im)_2$ possesses a denser **dia-c** topology structure compared to ZIF-zni (**zni** topology), they possess similarly "perfect" coordination tetrahedral (**Appendix A.5.7**). The Zn^{2+} centers of ZIF-zni feature geometry indices τ_4 of 0.97 or 0.95 for the two crystallographically independent Zn^{2+}

ions, whereas the Cd^{2+} center of $Cd(im)_2$ possesses a geometry index τ_4 of 0.93) (τ_4 = 1 for tetrahedral and τ_4 = 0 for square planar[132]) (**Figure 5.3**).

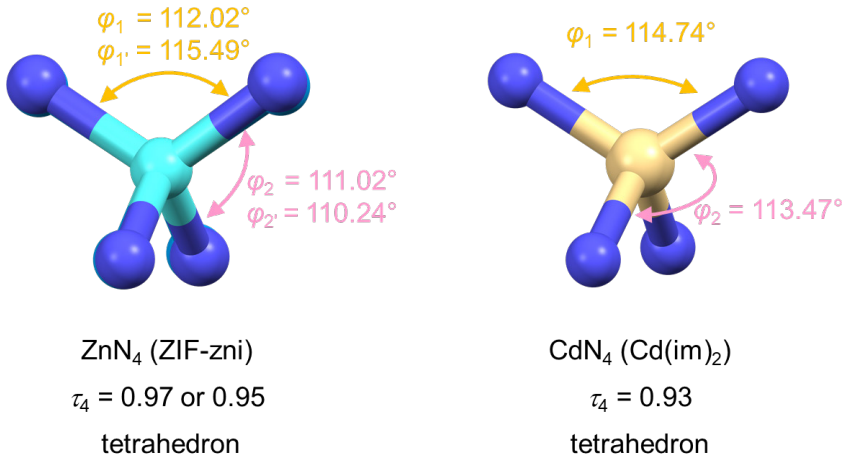

Figure 5.3. Coordination environments of Zn^{2+} in ZIF-zni (left, CCDC codeIMIDZB) and Cd^{2+} in $Cd(im)_2$ (right, CCDC code BAYQAU11). The two largest N-M-N angles (φ_1 and φ_2) utilized to calculate the geometry index (τ_4) are shown in both diagrams.

5.3 Thermal behavior

Simultaneous TG/DTA measurements of the $Cd(im)_2$ and $Cd(im)_2$-*sol* materials were performed under an N_2 atmosphere with a heating rate of +10 °C min^{-1}. TG data show that decomposition of the $Cd(im)_2$ and $Cd(im)_2$-*sol* starts at 473 °C and 455 °C respectively (**Figure 5.4**), which is significantly lower than the start of decomposition observed for ZIF-4(Zn) ($Zn(im)_2$, 605 °C)[154], ZIF-4(Co) ($Co(im)_2$, 546 °C)[154] and MUV-24(zni) ($Fe(im)_2$, 530 °C)[141]. The DTA trace of $Cd(im)_2$ exhibits a pronounced endothermic signal associated with the melting of the framework (**Figure 5.4**). Although $Cd(im)_2$-*sol* also displays a pronounced melting signal, it basically coincides with its decomposition temperature (T_d) (**Figure 5.4b**).

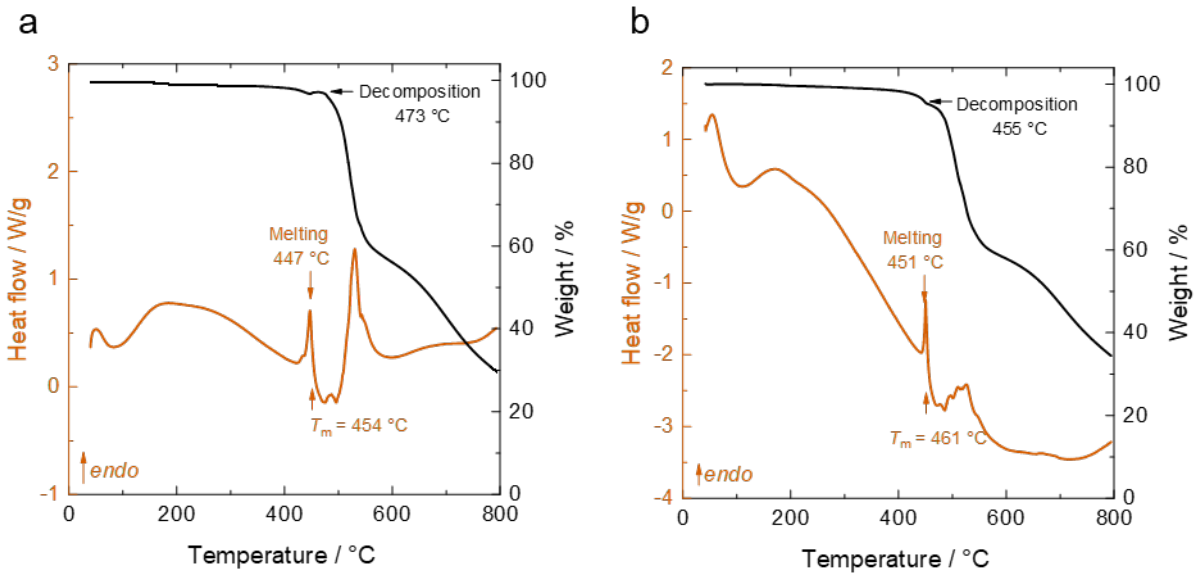

Figure 5.4. TG/DTA data of (a) $Cd(im)_2$ and (b) $Cd(im)_2$-*sol* with heating rate of +10 °C min^{-1}.

To obtain more precise information on the thermal phase changes occurring during the heating and cooling cycles, additional cyclic DSC experiments were conducted between ambient temperature and T_d also under an inert N_2 atmosphere. During the cooling process to room temperature with a rate of −10 °C min^{-1}, the liquid $Cd(im)_2$ undergoes partial recrystallisation and does not form a fully glassy state (**Figure 5.5**). It further completely recrystallized back to $Cd(im)_2$ when reheating again to 300 °C (rate of +10 °C min^{-1}), based on the measured two recrystallization enthalpies and melting enthalpy. The fully recrystallized sample obtained after reheating to 300 °C is termed as frcCd(im)$_2$ (frc denotes fully recrystallized crystalline).

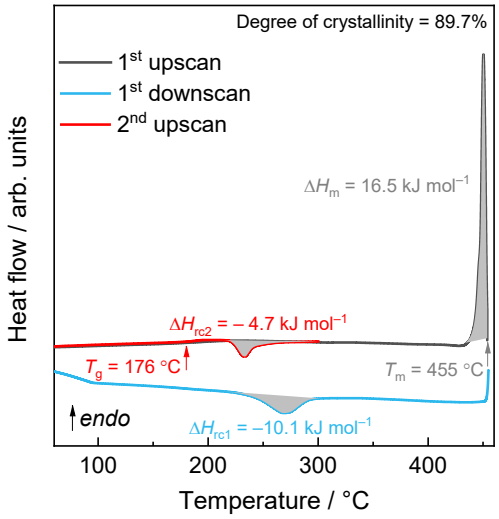

Figure 5.5. DSC data for preparation of the fully recrystallized fr$_c$Cd(im)$_2$. The heating and cooling rates for both scans were ±10 °C min^{-1}.

Importantly, Faster cooling rates prevent recrystallization. When a cooling rate of –100°C min^{-1} is set (the actual average rate from T_m to T_g is approximately –42 °C min^{-1} due to instrumental limitations), $Cd(im)_2$ forms a compact monolithic amorphous glass (**Figure A5.21** and **Figure 5.7**), as evidenced by the loss of Bragg scattering of crystalline $Cd(im)_2$ compounds (**Figure 5.7b** and **Figure A5.7**) and a glass transition temperature (T_g) at 175 °C during a subsequent heating scan (**Figure 5.7a** and **Figure A5.21**). The fact that T_g only varies between 175 °C and 176 °C in five consecutive upscans, implies that $a_gCd(im)_2$ (a_g denotes amorphous glass) has excellent robustness during temperature cycling (**Figure A5.20**). Heat capacity (C_p) measurements demonstrate that the heat capacity change around the glass transition (ΔC_p) of $a_gCd(im)_2$ is 0.16 J K^{-1} g^{-1} (**Figure 5.6**); a value comparable to that of other reported ZIF glasses (**Table 5.1**).

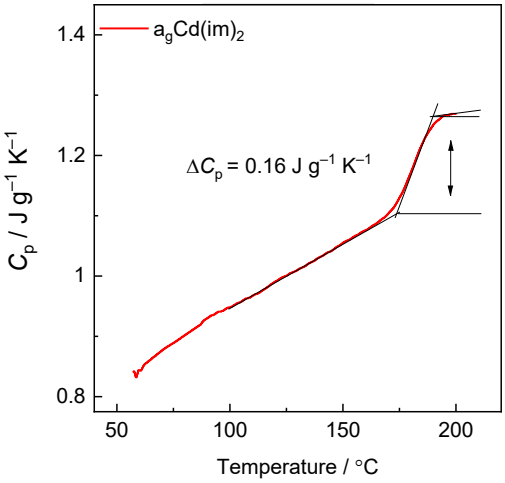

Figure 5.6. Heat capacity (C_p) scan of $a_gCd(im)_2$. The heat capacity change around the glass transition (ΔC_p) was determined using the difference between the two intersections of the onset and offset tangent lines of the glass transition signal

Table 5.1. Comparison of the heat capacity change (ΔC_p) around the glass transition of $a_gCd(im)_2$ and other reported ZIF glasses.

Material	Composition	T_g (°C)	ΔC_p (J K^{-1} g^{-1})	References
$a_gCd(im)_2$	$Cd(im)_2$	176	0.16	This work
a_gZIF-62	$Zn(im)_{1.75}(bim)_{0.25}$	322	0.19	*Sci. Adv.* 4, eaao6827 (2018)
a_gZIF-4 (HDA)	$Zn(im)_2$	292	0.16	*Nat. Commun.* 6, 8079 (2015)
a_gZIF-4 (LDA)		316	0.11	
a_gZIF-8-$mim_{0.15}im_{0.74}bim_{0.11}$	$Zn(mim)_{0.30}(im)_{1.48}(bim)_{0.22}$	336	0.12	*Nat Commun* **15**, 4420 (2024)

Notably, a_gCd(im)$_2$-*sol*, which was prepared at a higher temperature due to its higher T_m, contains visible metallic cadmium, as detected by XRPD (**Figure A5.6**). We suppose some im^- linkers decompose during Cd(im)$_2$-*solv* melting and their decomposition products initiate reductive formation of metallic Cd. A similar phenomenon was previously observed for a Co-based ZIF glass.[124] However, the mechanically synthesized Cd(im)$_2$ effectively reduces this undesirable situation during melting, producing only a negligible amount of metallic Cd in a_gCd(im)$_2$ according to XRPD data (**Figure 5.7b** and **Figure A5.7**). This may be explained by the smaller particle size of Cd(im)$_2$ compared to Cd(im)$_2$-*sol* resulting from mechanical synthesis and leading to a lower melting temperature of Cd(im)$_2$ compared to Cd(im)$_2$-*sol*. Noteworthy, unlike other M(im)$_2$ compounds, which undergo a transition to the **zni** topology before melting, Cd(im)$_2$ shows no signs of transitioning to a polymorph with the **zni** topology before melting, consistently maintaining the **dia-c** topology up to its melting point (**Figure 5.9**).

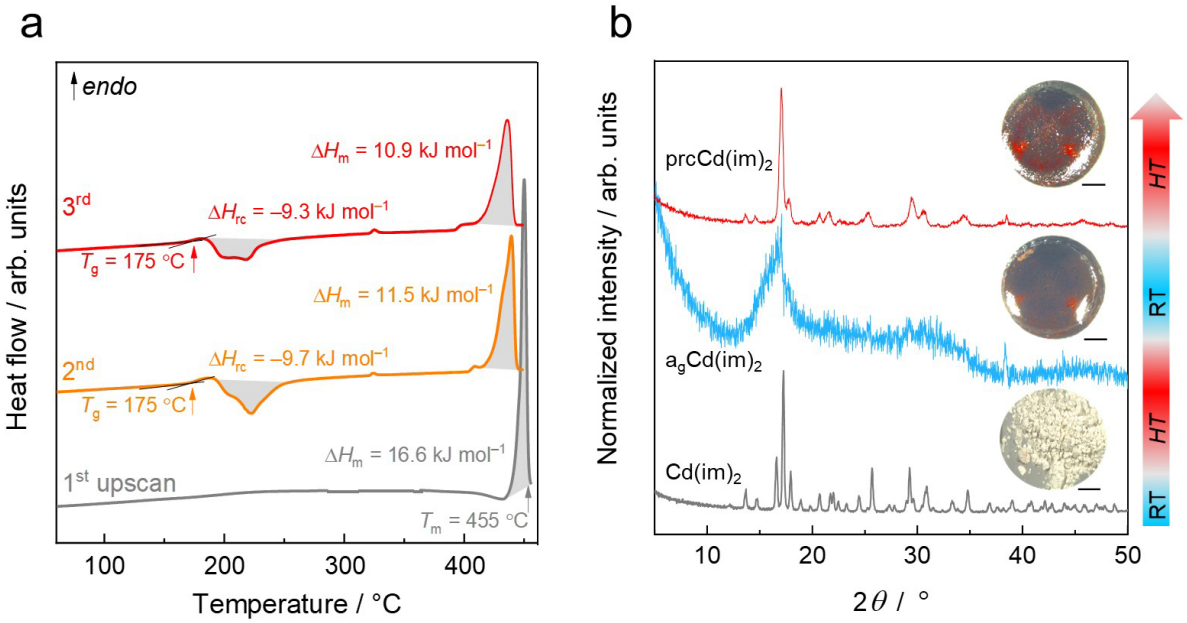

Figure 5.7. (a) Three cyclic DSC with +10 °C min^{-1} heating and about –42 °C min^{-1} (average) cooling rate of Cd(im)$_2$. The weak reproducible endothermic signal at 325° is associated to the melting of metallic cadmium. (b) Normalized XPRD patterns of Cd(im)$_2$, a_gCd(im)$_2$, and prcCd(im)$_2$. The insets show micrographs of the corresponding samples, all scale bars are 1 mm.

Strikingly, upon reheating the a_gCd(im)$_2$, a partial recrystallization occurs, whereby the supercooled liquid partially crystallizes to the original Cd(im)$_2$ structure with **dia-c** topology. The material derived after reheating a_gCd(im)$_2$ to 300 °C is denoted prcCd(im)$_2$ (prc expressed partially recrystallized), as confirmed by DSC, in-situ and ex-situ XRPD (**Figure 5.7** and **Figure A5.5**). The proportion of recrystallized

phase of prcCd(im)$_2$ is estimated to be 59% based on the measured recrystallization enthalpy (**Figure 5.7** and **Figure A5.21**). Nonetheless, prcCd(im)$_2$ maintains the monolithic semitransparent morphology of a$_g$Cd(im)$_2$ despite a large fraction of the sample is composed of crystalline particles. (**Figure 5.7** and **Figure A5.25**). This indicates that prcCd(im)$_2$ is in a semi-crystalline state, in which crystalline grains of sub-micrometer size are embedded in a glassy matrix of the same composition. The transparent nature of the monolithic structure implies that the interfacial contact between the crystalline grains and the amorphous glass matrix is strong. A material wich such a microstructural characteristic and strong interfacial contact between amorphous and crystalline regions is typically referred to as a glass-ceramic.[155] Furthermore, the transitions from the crystalline to the liquid and the partially crystallized glass-ceramic phase are observed over multiple heating and cooling cycles demonstrating good repeatability of the involved processes (**Figure 5.7a**).

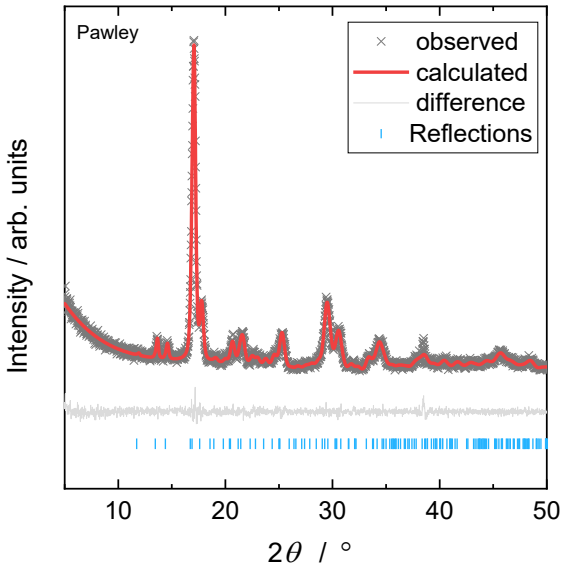

Figure 5.8. Profile fit (Pawley method) performed on the XRPD pattern of prcCd(im)$_2$. The initial crystallographic parameters are taken from crystalline structure (CCDC code BAYQAU11).[153]

Interestingly, the crystalline Cd(im)$_2$ phase in this recrystallized glass-ceramic prcCd(im)$_2$ after cooling down to room temperature is in the expanded high-temperature configuration (unit cell volume 1610 Å^3) and not in the conventional room temperature configuration of Cd(im)$_2$ (unit cell volume 1566 Å^3) (**Figure 5.8**, **Figure A5.3** and **Table 5.2**)[153]. This is associated with the glassy matrix surrounding the recrystallized grains, which inhibits the contraction of the recrystallized phase to the more compact configuration which is the stable one at room temperature if the material is not embedded in a glass matrix.[96, 108] This distinctive and exceptional transition from the glassy state to the glass-ceramic state has not been observed in ZIF glasses in previous studies (**Figure 5.9**).

Table 5.2. Unit cell parameters and corresponding R_{wp}, R_{exp} and χ values determined by the above displayed structureless profile fits (Pawley method).

Compound	$Cd(im)_2$	$Cd(im)_2$-*sol*	prc$Cd(im)_2$	frc$Cd(im)_2$
crystal system	orthorhombic	orthorhombic	orthorhombic	orthorhombic
space group	*Pbca*	*Pbca*	*Pbca*	*Pbca*
a / Å	14.6585(15)	14.619(4)	15.088(19)	14.748(6)
b / Å	10.7536(9)	10.759(2)	10.594(13)	10.669(4)
c / Å	9.9405(0)	9.935(2)	10.071(11)	9.935(4)
α / °	90	90	90	90
β / °	90	90	90	90
γ / °	90	90	90	90
V / Å^3	1566.9(3)	1562.6(6)	1610(3)	1563.3(10)
crystal size / nm	73.9(2)	216.8(4)	50.9(9)	83.3(12)
R_{wp} / %	9.58	18.40	8.38	11.17
R_{exp} / %	8.44	16.66	7.53	7.14
χ	1.13	1.10	1.11	1.56

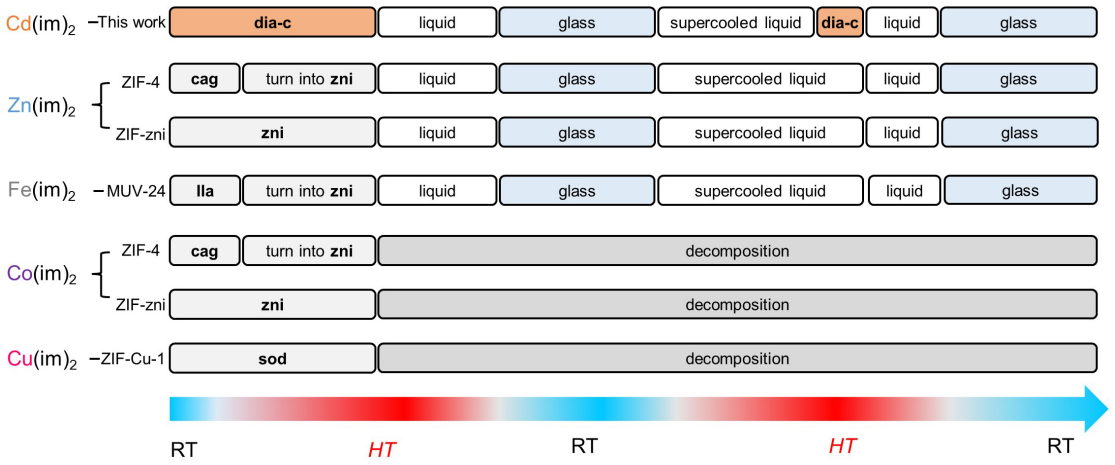

Figure 5.9. Schematic representation of the phase behaviour of the $M(im)_2$ ZIFs during cyclic heating and cooling. The bold letter codes represent the topologies of the crystalline phases present.

5.4 Local structural analysis

To gain insights into the structural similarities and differences between the crystalline and glassy state of $Cd(im)_2$, X-ray total scattering experiments were performed on $Cd(im)_2$ and $a_gCd(im)_2$ (**Figure A5.8**). The total scattering structure factors, $S(Q)$, show that the Bragg peaks at low-Q from the crystalline phases are not present in the glassy phase of $a_gCd(im)_2$ (**Figure 5.10**). Nevertheless, the appearance of additional Bragg peaks is observed in the $a_gCd(im)_2$ at higher-Q is attributable to the small amounts of generated metallic Cd, which is consistent with that observed in XRPD.

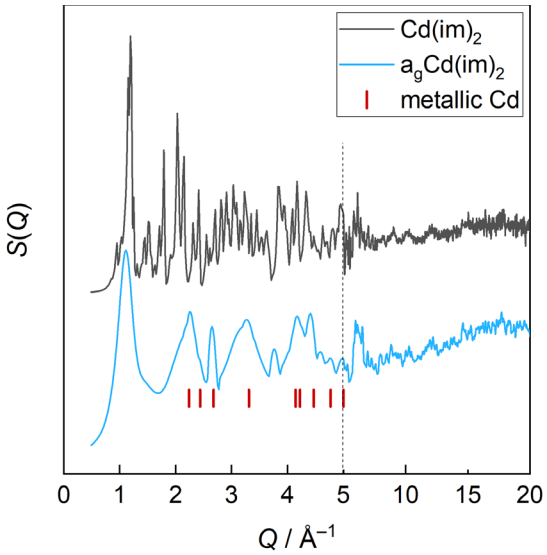

Figure 5.10. X-ray total scattering data in the form of $S(Q)$ of $Cd(im)_2$ and $a_gCd(im)_2$. The pronounced diffraction positions ($Q < 5$ Å^{-1}) of metallic Cd are marked.

The PDFs in the form of $D(r)$ were further calculated from the X-ray total scattering data. In order to designate the peaks in the PDFs, the assignment of the eight physical sharp features below 8 Å was carried out by using the PDFgui software[156] to calculate the partial and total PDFs for the constituent atom pairs of $Cd(im)_2$ (**Figure 5.11**).

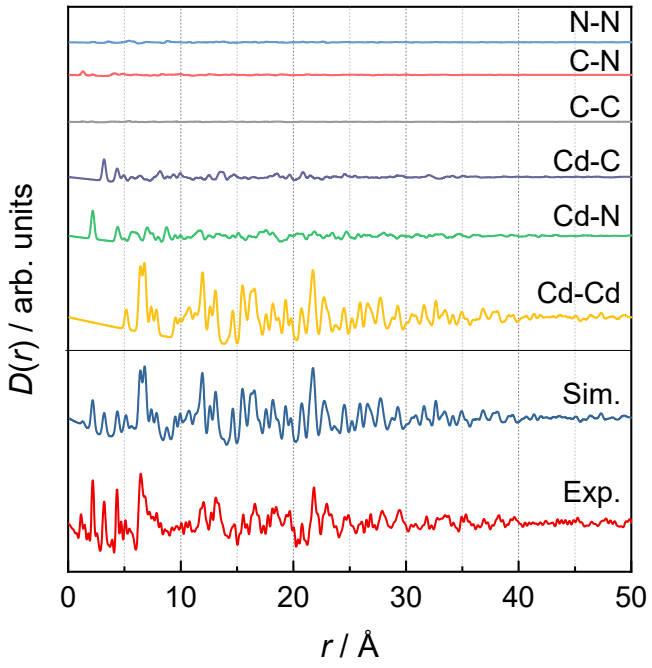

Figure 5.11. Partial pair distribution functions (upper plots), simulated total PDF for $Cd(im)_2$ calculated from the published crystalline structure (CCDC code BAYQAU11)[153] using PDFGui[156], and experimental PDF for $Cd(im)_2$

Surprisingly, a PDF peak representing Cd···Cd distance r = 5.2 Å in $Cd(im)_2$ was observed (**Figure 5.11** and **Figure 5.12**), which is not been observed in other reported ZIFs (**Figure 3.2** and **Figure A4.30-34**).[40, 129] This is attributed to the unique two-fold interpenetrated diamondoid structure of $Cd(im)_2$, which results in a closer intermolecular (i.e. inter-network) Cd···Cd distance (5.2 Å) compared to the longer intramolecular (i.e. intra-network) Cd···Cd distance (6.4 Å). Moreover, this interpenetrated structure also features PDF peaks at 6.8 Å and 7.4 Å, which are also related to intermolecular Cd···Cd distances (**Figure 5.11** and **Figure 5.12**). Interestingly, the PDF of $a_gCd(im)_2$ illustrates that the intramolecular short-range order of the $Cd(im)_2$ (i.e., the Cd–im⁻–Cd connectivity at 6.4 Å) remains intact in the glassy phases, while the characteristic intermolecular Cd···Cd correlations significantly reduce in intensity (**Figure 5.12**). This indicates that the interpenetrated structure is completely disrupted after the glass formation, and also suggests that $a_gCd(im)_2$ is likely to exhibit short-range disorder. (**Figure 5.12**).

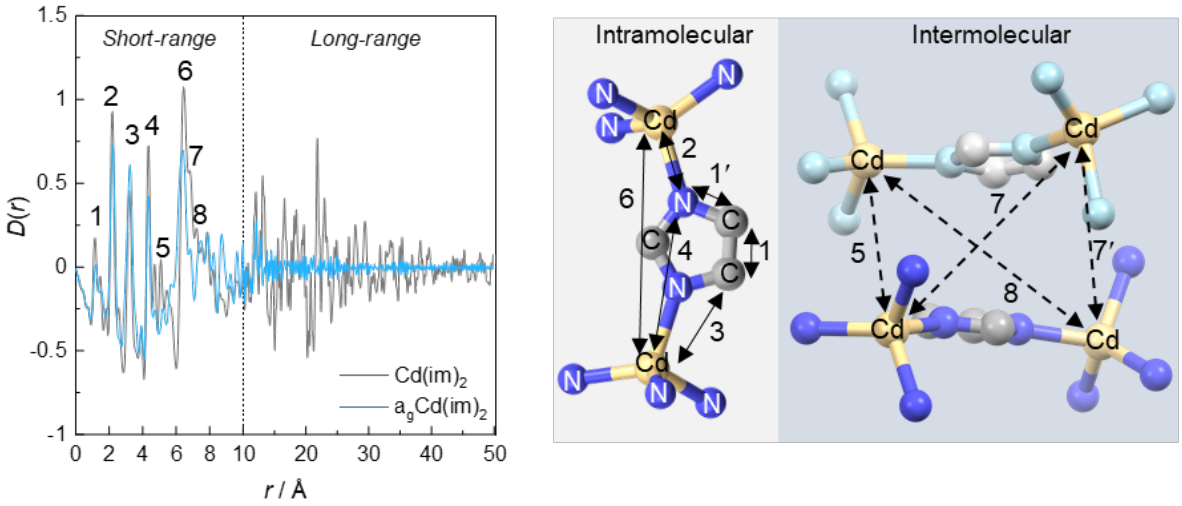

Figure 5.12. (Left) Comparison of PDF data of $Cd(im)_2$ and $a_gCd(im)_2$, derived from X-ray total scattering experiments. (Right) Visualization of the relevant short-range atomic distances (intramolecular and intermolecular) present in the $Cd(im)_2$ taken from the reported crystal structure (CCDC code BAYQAU11). The Assignment of the eight physical sharp features below 8 Å was carried out by using the PDFgui software[156] to calculate the partial and total PDFs for the constituent atom pairs of $Cd(im)_2$. The colour of the second independent network is lightened for better discrimination.

In line with the loss of long-range order, increased structural heterogeneity and distortions in the $a_gCd(im)_2$ are evident from the broadening of various vibrational bands in the FTIR spectra relative to the bands of the crystalline parent $Cd(im)_2$ (**Figure A5.17**). This is especially reflected in the out-of-plane ring bending

vibrations[41, 100] of im^- between 800 and 850 cm^{-1} (**Figure 5.13a**) and the the band for the asymmetric stretching vibration of the CdN_4 tetrahedra centered at 252 cm^{-1} (**Figure 5.13b**). The vibrational bands become broader after melt-quenching, and then gradually sharpen when going from $a_gCd(im)_2$ over $prcCd(im)_2$ to $frcCd(im)_2$. Notbly, the stretching vibration of CdN_4 is located at a much lower frequency than that of ZnN_4 (301 cm^{-1} in ZIF-4(Zn)) and CoN_4 (331 cm^{-1} in ZIF-4(Co)).[154] This can be explained by the higher mass of Cd^{2+} and may also indicate a weaker Cd–N bond strength compared to the Zn–N and Co–N bond strengths. With the aim of getting qualitative insights into relative M–N bond strength for Cd^{2+} and the previously used first-row transition metals Fe^{+2}, Co^{2+}, Cu^{2+} and Zn^{2+}, DFT calculations‡ were performed on molecular model systems of the type $[M(imH)_4]^{2+}$, where one M^{2+} cation is bound to four N atoms of the imidazole ligands (**Appendix A.5.8**). The energy required for heterolytic M–imH bond dissociation for each $[M(Him)_4]^{2+}$ was calculated. Not surprisingly, Cd–im exhibits the lowest bond energy $E_{Cd–im}$ of 197.9 kJ mol^{-1} (**Figure 5.13c**), significantly lower than $E_{Zn–im}$ (220.6 kJ mol^{-1}) and those of the other divalent metals previously used in ZIF glasses. The lower heterolytic bond dissociation energy of Cd–im is in agreement with the lower melting temperature (T_m) and the lower glass transition temperature (T_g) of $Cd(im)_2$ compared to the derivatives of the first-row transition metal ions.

Solid-state magic angle spinning (MAS) NMR is considered a powerful tool for studying the structure of disordered and amorphous materials. Experiments involving an NMR active nucleus of the materials metal centers are particularly valuable, as this yields information on short-range order and disorder of the coordination entities. MAS NMR investigations with NMR-active metal centers is only possible for the Zn^{2+}-derivatives of the glass forming ZIFs from the first-row transition metals. The Fe^{2+}-, Co^{2+}- and Cu^{2+}-derivatives are all paramagnetic, thus preventing high resolution NMR (besides other issues such as low sensitivity, low resonant frequency and low natural abundance). With ^{67}Zn MAS NMR such investigations are possible for the diamagnetic Zn^{2+}-based ZIF glass formers, however, ultra-high magnetic fields are usually required for ^{67}Zn to obtain a good resolution.[36] Moreover, ^{67}Zn also has a rather low sensitivity and natural abundance while it is a quadrupolar nucleus (spin 5/2) yielding extremely broad lines over a very wide chemical shift range, making data collection and analysis challenging. In contrast to ^{67}Zn, ^{113}Cd (spin 1/2) has no quadrupolar effect, providing the opportunity for high

‡ DFT calculations were performed by Jan-Benedikt Weiß, Henke Group, TU Dortmund.

resolution spectra with sharp resonances. Consequently, ^{113}Cd MAS NMR spectroscopy measurements were recorded on crystalline $Cd(im)_2$, glassy $a_gCd(im)_2$, partially-recrystallized $prcCd(im)_2$, and fully-recrystallized $frcCd(im)_2$.[§] Additionally, ^{13}C MAS NMR spectroscopy measurements were conducted in order to provide further insight (**Figure 5.13d-e**). The ^{113}Cd MAS NMR spectra of $Cd(im)_2$ features one sharp and highly symmetrically distributed resonance at 433 ppm, which is in agreement with the presence of only one crystallographically independent Cd site in crystalline $Cd(im)_2$. The ^{113}Cd spectrum of $a_gCd(im)_2$ features an asymmetric and much broader line shape, which is indicative of the short range structural heterogeneity in the $a_gCd(im)_2$ glass. A similar observation has been made previously in ^{29}Si MAS NMR studies of silicate glasses.[157] The structural heterogeneity can be ascribed to the presence of varying bond angles in the glass sample. This finding shows a notable correlation with the ^{13}C MAS NMR data. The ^{13}C MAS NMR spectrum of crystalline $Cd(im)_2$ shows five sharp resonances, which is in good agreement to the presence of six independent carbon atoms in its crystal structure. The five sharp resonances converge to two broad signals after glass formation. In both ^{113}Cd and ^{13}C MAS NMR spectra, the signals get sharper after partial recrystallisation to $prcCd(im)_2$, while after fully recrystallisation to $frcCd(im)_2$ the signals in both spectra are sharp again and almost identical to those of the pristine crystalline $Cd(im)_2$ (**Figure 5.13d-e**).

[§] MSA NMR experiments have been done by Dr. Alexander Klein and Dr. Suresh Vasa from the gorup fo Prof. Rasmus Linser, Physical Chemistry, TU Dortmund.

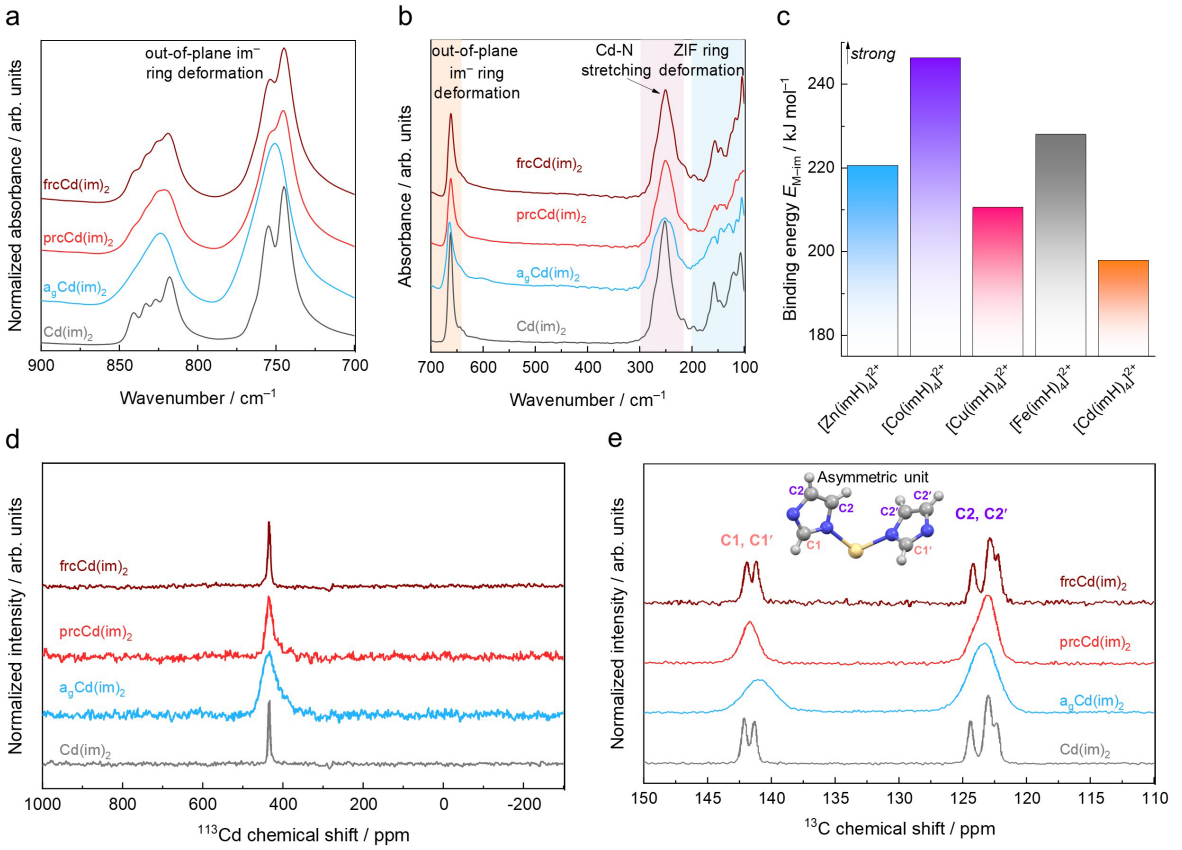

Figure 5.13. FTIR spectra in the range of (**a**) mid-IR (zoomed in 700 – 900 cm^{-1}) and (**b**) far-IR (100 - 700 cm^{-1}) of $Cd(im)_2$, $a_gCd(im)_2$, $prcCd(im)_2$, and $frcCd(im)_2$. (**c**) The binding energies ($E_{M–im}$) of M–im calculated by DFT based on the dissociation of a $[M(im)_4H]^{2+}$ model complexes. (**d**) ^{113}Cd MAS NMR and (**e**) ^{13}C MAS NMR of $Cd(im)_2$, $a_gCd(im)_2$, $prcCd(im)_2$, and $frcCd(im)_2$. The inset shows the asymmetric unit of $Cd(im)_2$, taken from the reported crystal structure (CCDC code BAYQAU11).

5.5 Fragility determination

To deepen our understanding of the physical properties of the a_gCd(im)$_2$ glass, DSC experiments with heating rates and cooling rates varying between ±5 and ±25 °C min^{-1}. These experiments provided the fictive temperature (T_f) of the glass, depending on the heating/cooling rates (**Figure A5.23**). By analyzing the variation of T_f with the varying cooling rates, the dimensionless calorimetric fragility index (m) of the corresponding supercooled liquids was determined.[22] The fragility index m quantifies the activation energy of viscous flow. Low values of m (<30) suggest strong liquids that vitrify into brittle glasses (e.g., silica with m = 20), whereas high values of m (>50) indicate fragile liquids that form ductile glasses.[22, 40, 129] Within measurement error, m is about 42 for a_gCd(im)$_2$ glass (**Figure 5.14**), which is much higher than the values of the prototypical Zn^{2+}-based glasses a_TZIF-4 and a_gZIF-62.[22, 93] This indicates that a_gCd(im)$_2$ has the potential to become a ductile glass for specific applications, which are typically governed by organic polymers.

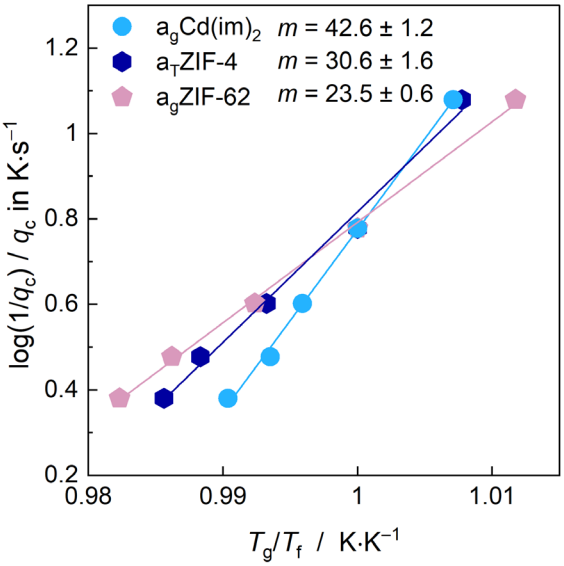

Figure 5.14. Comparison of calorimetric fragility indices of a_gCd(im)$_2$ with selected representative Zn^{2+}-based ZIF glasses. Data of a_TZIF-4 and a_gZIF-62 are taken from the literature.[22]

5.6 Conclusion

In summary, by utilizing Cd^{2+} ions and applying a mechanochemical synthesis strategy for the metal–organic framework Cd(im)$_2$, the first meltable cadmium-based ZIF was synthesised. Cooling this material from above its melting point (T_m =

455 °C) to room temperature results in a monolithic MOF glass. Most importantly, upon reheating, it partially recrystallizes into a single-component glass-ceramic state —an attribute not seen in previous melt-quenched ZIF glasses.

Furthermore, the benefits of mechanochemistry are once again illustrated, not only in the post-synthesis phase for MOF glass formation as discussed in the previous chapter, but also in the synthesis of MOFs, where the utilization of mechanochemistry results in the formation of smaller particles,[21-22] which also reduces the activation temperature required for melting, thus lowering the melting point and preventing decomposition.

These findings represent a substantial advancement in the field of MOF glasses and opens the door for a novel type of MOF-based glass-ceramics. The successful creation of Cd^{2+}-based ZIF glasses and glass-ceramics not only broadens the scope of meltable MOFs but also suggests new pathways for developing tunable, multifunctional materials. The transformation from the glass state to the glass-ceramic state observed in this study highlights the potential for fine-tuning the physical and chemical properties of these materials, thereby expanding their applicability in various high-tech fields, including energy storage, optics, and semiconductors.

6 Summary and Outlook

Glassy metal-organic frameworks (MOFs) are a promising class of amorphous porous materials with enormous potential for a wide range of applications. The presence of a reversible solid-liquid transition in MOF glasses makes them malleable and capable of producing grain boundary free monoliths. In this thesis, a thorough investigation has been carried out into the modulation of the porosity of MOF glasses, the prerequisites for melting highly porous ZIFs with **sod** topologies, the development of alternative methods for MOF vitrification without high temperature treatment and the introduction of novel metal ions (Cu^{2+} and Cd^{2+}) as the central building units in ZIF glasses.

(i) Highly Porous MOF Glasses by Compositional Engineering

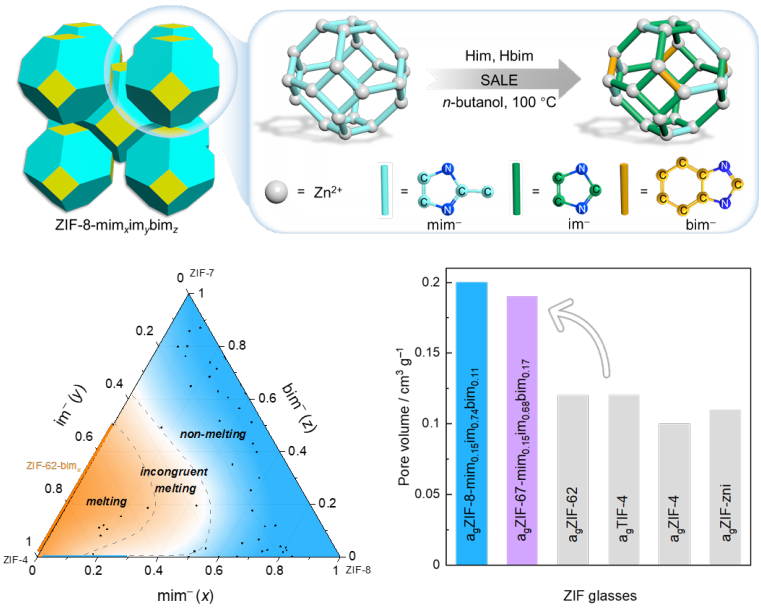

Figure 6.1. (Top) Representation of the SALE process in this thesis to derive various linker-exchanged ZIF-8 derivatives. (bottom left) Ternary phase diagrams constructed in this thesis to demonstrate the intervals of meltable ZIF-8 derivatives. (bottom right) The significantly improved porosity of ZIF-8 glass and ZIF-67 glass.

In order to increase the porosity of MOF glasses and to break the constraints imposed on MOF melting by topological concepts, the solvent-assisted linker exchange (SALE) has been effectively utilized in the chapter 3 of this thesis to modify highly porous MOFs with **sod** topology (i.e. ZIF-8 and ZIF-67) by partially replacing their organic linkers with others that possess weaker metal-linker bond strengths. This alteration enables the MOF derivatives to transition through crystal, liquid, and glass phases upon thermal treatment. A comprehensive series of 50 modified ZIF-8 derivatives was produced, and detailed thermal and crystallographic analyses were conducted. These efforts led to the construction of a ternary phase diagram that delineates the compositional range for melting and glass formation. Notably, the resulting ZIF-8 and ZIF-67 glasses demonstrated a significantly increased specific pore volume (approximately 0.20 cm^3/g of ZIF-8 glass and 0.19 cm^3/g for ZIF-67 glass) compared to previous MOF glasses. Additionally, gas physisorption tests revealed that these glasses adsorb substantial amounts of technologically relevant C3 and C4 hydrocarbons and can effectively separate propylene from propane based on their different adsorption kinetics.

The limited number of meltable MOFs known to date underscores the potential of the linker exchange strategy, opening new pathways for creating meltable and glass-forming MOFs from the extensive pool of non-meltable MOFs documented in the literature. This breakthrough not only advances the science of MOF glasses but also paves the way for future investigations into the development of highly porous, moldable materials for diverse technological uses.

(ii) Creating Porous Glasses at Room Temperature Through Mechanochemistry

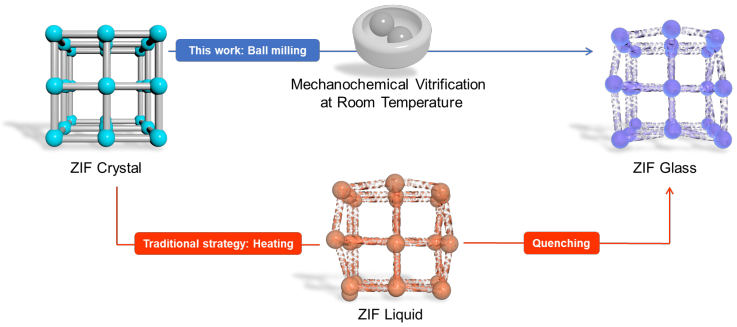

Figure 6.2. The new mechanochemical strategy for fabricating MOF glasses proposed in this thesis.

Traditionally, MOF glasses are produced by heating MOF crystals to their melting point and then cooling the liquid to room temperature under an inert atmosphere. While effective, this melt-quenching technique is energy-intensive due to the high temperatures required. Additionally, it limits the development of new materials to combinations of metal ions and linkers that are highly thermally stable.

To address these challenges, in the chapter 4 of this thesis has demonstrated that some crystalline ZIFs, can be transformed into glasses by mechanical milling at room temperature in just 5 minutes. This milling method can also transform crystalline ZIFs into a glassy state that do not melt due to low thermal stability. Notably, this technique enabled the preparation of the first thermally sensitive Cu-based ZIF glass via mechanochemistry.

Furthermore, the ZIF glasses produced by the milling process feature relatively small particle sizes compared to the ZIF glasses made by melt-quenching process. The melt-quenched ZIF glasses benefit from the fusion of the ZIF particles while the material is in the liquid state. However, bulk ZIF glasses can still be produced from the ball-milled microparticulate ZIF glasses by heating them to a temperature above their glass transition temperature (lower than the melting temperature of crystalline ZIF) to reach the supercooled liquid state in which particle fusion takes place (a process known as remelting).

Creating MOF glasses through mechanical milling at room temperature is potentially not only more energy-efficient but will also allow for the incorporation of thermally sensitive materials, such as organic or organometallic molecules, into versatile MOF glass composites. This approach broadens the spectrum of potential applications, paving the way for the development of multifunctional MOF glass composites and expanding their use into more diverse fields.

(iii) Melting of a Cadmium-based MOF, and the fabrication of its glass and glass-ceramic

With the aim of expanding the family of meltable ZIFs, the first meltable cadmium-based ZIF, $Cd(im)_2$, was synthesized using a mechanochemical approach. Compared to the reported solution-synthesized $Cd(im)_2$-*sol*, the mechanochemically synthesized version features a smaller crystal size, thus melting at lower temperature and minimizing decomposition during melting. Remarkably, after rapid cooling to form a glass, it undergoes partial recrystallization upon reheating. This yields transparent

single-component monoliths composed of a nanocrystalline phase that is embedded in a matrix of a glassy phase of the identical composition. Such a partially amorphous and partially crystalline single component material is strongly related to inorganic glass-ceramics and thus could be classified as the very first metal-organic glass-ceramic.[158] The opportunity to control the degree of crystallization in such kind of metal-organic glass ceramics is exciting for the application of these materials in various fields. It is envisaged that important optical, mechanical, thermal and electronic materials properties can be tuned by controlling the crystalline phase fraction and the grain size of the crystalline particles in the glass-ceramic.

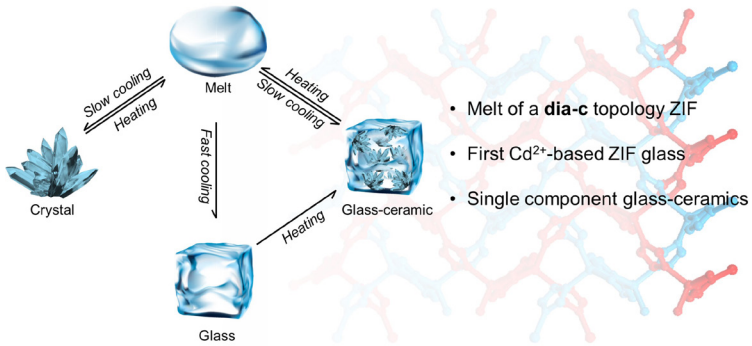

Figure 6.3. Phase transition diagram of the Cd-based ZIF shown in this thesis.

The development of Cd-based ZIF glasses and glass-ceramics also highlights the potential for exploring other less commonly used metal ions in the creation of MOF glasses. Future research could investigate the use of heavier transition metals or even rare earth elements to create MOF glasses with unique optical, electronic, or magnetic properties. The ability to control the degree of crystallization and the size of crystalline domains within the glass matrix offers a powerful tool for fine-tuning material properties, which could lead to breakthroughs in fields such as photonics and advanced ceramics.

(iv) Future Directions of MOF glasses

The studies presented in this thesis lays a strong foundation for the continued development and expansion of the MOF glass field, yet several challenges and opportunities remain. One of the most pressing issues is the relatively low porosity of current MOF glasses compared to their crystalline counterparts, the porosity of ZIF-8 glass in this thesis is just approximately 25%, which is considerably lower

than that of highly porous crystalline MOFs. Achieving higher porosity while retaining the desirable properties of glasses will require innovative approaches, potentially involving the integration of new materials, such as the integration of MOF glasses into composites with other lightweight porous materials (such as COFs), to create hybrid MOF glasses with enhanced porosity.

Another critical area for future exploration is the processing and shaping of MOF glasses for industrial and commercial applications. Recent advances, such as the development of micro-optical lenses from MOF glasses by the Wondraczek group,[152] highlight the potential for these materials in precision optics related high-tech fields. However, scaling these processes and ensuring the reproducibility and uniformity of MOF glass components is essential for their commercial viability. Developing robust, scalable methods for processing MOF glasses into complex shapes and ensuring their stability under operational conditions will be key to unlocking their full potential.

7 Experimental Section

7.1 X-ray diffraction techniques

7.1.1 In-house X-ray powder diffraction

XRPD patterns were recorded at room temperature on a Siemens D5005 diffractometer or a Bruker D8 Advance diffractometer. Data were collected with CuKα radiation in the range from 5° to 50° 2θ with a step size of 0.02°. Finely ground samples (crystalline or glassy) were deposited on a glass holder or a single crystal zero background sample holder made of silicon (cut along the (610) plane). For phase identification, structureless profile fits (Pawley method[90]) were performed with the TOPAS academic v6 software.[159]

7.1.2 Variable temperature XRPD (VT-XRPD)

X-ray powder diffraction data at various temperatures were collected at BL9 of DELTA (Dortmunder Elektronenspeicherring-Anlage, Dortmund, Germany) with a monochromatic X-ray beam ($\lambda = 0.45920$ or 0.61992 Å) using a MAR345 image plate detector. Finely ground samples were sealed in quartz capillaries (diameter 1 mm) in an N_2-filled glovebox and heated using an Anton Parr heating stage covered with a graphite dome from 27 °C to a temperature before T_d (previously determined via TGA). Temperature calibration of the heating stage was performed by reference XRPD measurements of α-quartz. Data were integrated using the DAWN[160] software package.

7.1.3 X-ray total scattering

Synchrotron radiation X-ray total scattering data were collected at beamline P02.1 at Deutsches Elektronen-Synchrotron (DESY, Germany) using a monochromatic X-ray beam (λ = 0.20734 Å, 60 keV) and a Perkin Elmer XRD1621 (2048 x 2048

pixels active area) detector. The finely ground samples were placed in a 1 mm (outer diameter) quartz glass capillary. For the VT experiments, a hot air blower was used to heat the samples from room temperature to a maximum of 530 °C. The heating rate between the various set temperatures was 20 °C min^{-1}. After reaching the set temperatures, 10 consecutive diffraction patterns were collected with continuous rotation of the sample and an exposure time of 60 s. These 10 diffraction patterns were averaged for data analysis. For all datasets, background subtraction was performed with scattering data collected from an empty capillary. Background subtraction and corrections for multiple, container and Compton scattering, as well as for absorption, were done with the GudrunX program. The normalized scattering functions ($S(Q)$) were Fourier transformed to yield the pair distribution functions (PDFs) in the form of $D(r)$.[52-53]

In house X-ray Total Scattering were collected on a STOE powder diffractometer with an Ag X-ray beam ($\lambda = 0.5614$ Å) using a MYTHEN2 4K detector at institute of crystallography, RWTH Aachen University. PDF data are collected in a moving PDF mode about 6 h.

7.2 FTIR spectra spectroscopy

Fourier transform infrared (FTIR) spectroscopies of both MIR (mid IR, $\tilde{\boldsymbol{\nu}}$ = 4000 cm^{-1} - 400 cm^{-1}) and FIR (far IR, $\tilde{\boldsymbol{\nu}}$ = 700 cm^{-1} – 100 or 30 cm^{-1}) were performed on a Spectrum 3 FTIR spectrometer from Perkin Elmer equipped with a Gladi ATR-300 unit from Pike Technologies (ATR = attenuated total reflectance). After scanning the background, powdered samples were placed on the diamond ATR unit and carefully compressed with a stamp for the measurement.

7.3 Nuclear magnetic resonance (NMR) spectroscopy

Solid-state NMR experiments in Section 3 were carried out on a 700 MHz NMR spectrometer system equipped with a 1.3 mm probe. For two-dimensional ^{1}H–^{13}C spin-diffusion measurements, the number of scans was 56, and the number of increments in indirectly detected dimensions was 888, with a spectral width of 27.777 kHz for ^{1}H dimension, and 55.555 kHz for ^{13}C dimension. Repetition delay between scans was 0.8 s. The data were processed with the TopSpin (v4.1.4) software. Solution ^{1}H NMR spectroscopy was performed on digested crystalline and glassy ZIF samples with Bruker DPX-300, DPX 500 or Agilent DD2 500 spectrometers. The solid samples were digested before the measurement using DMSO-d_6 (0.5 mL) and DCl/D_2O (35 wt%, 0.015 mL) as solvents. The data were processed with the MestReNova (v14.2.0) software. Data were referenced to the residual proton signal of DMSO.

For the Solid-State ^{113}Cd and ^{13}C Nuclear Magnetic Resonance (NMR) spectroscopy in section 5. All spectra were recorded on a Bruker Avance NEO spectrometer with a 1H Larmor frequency of 700 MHz in a 2.5 mm rotor at a magic angle spinning (MAS) frequency of 24 kHz. For ^{113}Cd measurements the carbon channel was tuned to the respective Larmor frequency of ^{113}Cd. Without external referencing the signal appears at around –230 ppm, which was chosen as the carrier frequency. External referencing was done after acquisition, using $Cd(NO_3)_2 \cdot 4H_2O$ set to –100 ppm. After referencing the $Cd(im)_2$ signals appear around 430 ppm. For the crystalline $Cd(im)_2$ and partially recrystallized $prcCd(im)_2$, the number of scans was 4096 scans, the spectral width was 1609 ppm. For the fully recrystallized $frcCd(im)_2$, the number of scans was 4096, the spectral width was 3218 ppm. For the glassy $a_gCd(im)_2$, the number of scans was 8192, the spectral width was 1609 ppm.

7.4 Thermal analysis

Differential scanning calorimetry (DSC) measurements were performed on a DSC 25 from TA Instruments under a constant nitrogen flow (50 mL min^{-1}). For all measurements, a heating/cooling rate of ±10 °C min^{-1} was applied (except for the variable heating/cooling rate measurements for the determination of the fragility and the determination of heat capacity by modulated DSC; see Supplementary

Information). Before the measurement, the samples were ground and placed in a hermetically sealed aluminium crucible, and a hole was pinched into the lid of the sealed crucible. Thermogravimetric analysis (TGA) measurements were conducted on an SDT 650 from TA Instruments under a constant nitrogen flow (100 mL min^{-1}). Ceramic alumina crucibles (90 µL) were used for the TGA measurements. The heating rate was 10 °C min^{-1}. All thermal analysis data were processed and evaluated using the TRIOS (v5.1.0.46403) software from TA instruments. According to previous studies, the melting point (T_m) is defined as the offset temperature of the calorimetric melting peak in the first DSC upscan and the glass transition temperature (T_g) is specified as the onset point of the endothermic step in the second DSC upscan, whereas all other derived temperatures are defined as the peak temperature.[33, 40, 43, 93]

7.5 Isothermal gas physisorption

Experiments were performed with a Quantachrome iQ MP porosimeter. Sample quantities of about 100 mg (for crystals) and at least 40 mg (for all others) were used for the experiments. Prior to the first measurement, the ground samples were degassed under a dynamic vacuum ($p \approx 10^{-5}$ kPa) at 100 °C for 2 h. Gas sorption isotherms were measured with N_2 (77 K, gas purity > 99.999%), CO_2 (195 K, dry ice/iso-propanol bath, gas purity > 99.995%) and *n*-butane (273 K and 293 K, gas purity > 99.95%), propane and propylene (293 K, gas purity > 99.95%). Between measurements, samples were degassed under a dynamic vacuum ($p \approx 10^{-5}$ kPa) at ambient temperature for approximately 2 h. After adsorption measurements with *n*-butane, the samples were again heated to 100 °C for 30 min under a dynamic vacuum ($p \approx 10^{-5}$ kPa). Pore size distributions were determined from the N_2 adsorption data (QSDFT model, carbon equilibrium transition kernel at 77 K based on a slit-pores model) and the CO_2 adsorption data (HK model, isotherms recorded at 195 K, $p_0 = 191$ kPa, slit-like pore model) using the ASiQwin software package. Kinetic hydrocarbon gas adsorption data were also recorded with a Quantachrome iQ MP porosimeter at 293 K with an equilibrium pressure of about 80 kPa.

7.6 Scanning electron microscopy (SEM)

SEM imaging was performed with a Hitachi S-4500 instrument. For measurements, samples were placed on a conductive adhesive pad. Imaging was done with 1 kV accelerating voltage on a secondary electron detector. All investigated samples were ground and taken from the sorption tubes after conduction of physisorption measurements before imaging.

7.7 Synthesis

All chemicals were purchased from commercial suppliers (Sigma-Aldrich, BLDpharm, Tokyo Chemical Industry, etc.)

ZIF-62(Zn)/(Co): $Zn(NO_3)_2 \cdot 6H_2O$ (4.0 mmol, 1.2 g) or $Co(NO_3)_2 \cdot 6H_2O$ (4.0 mmol, 1.2 g), imidazole (11.55 mmol, 786 mg) and benzimidazole (1.660 mmol, 196 mg) were dissolved in DMF to yield a total volume of 90 mL. After the reactants were fully mixed by ultrasound for 5 min, the reaction mixture was transferred to a 250 mL screw-capped vial. The reaction vial was sealed tightly and heated in an oven for 7 d at 100 °C (for ZIF-62(Zn)) and 130 °C (for ZIF-62(Co)). After cooling to room temperature, the reaction volumes were recombined, filtered, and washed three times with 20 mL DMF. ZIFs were obtained as large, truncated octahedrally shaped single crystals. Subsequently, the crystals were soaked in dichloromethane (DCM) (40 mL) for 2 days. After filtration, the crystals were dried at 170 °C under dynamic vacuum ($p \approx 10^{-4}$ kPa) overnight to obtain the evacuated materials in the form of crystals.

ZIF-4(Zn)/(Co): $Zn(NO_3)_2 \cdot 6H_2O$ (4.0 mmol, 1.2 g) or $Co(NO_3)_2 \cdot 6H_2O$ (4.0 mmol, 1.2 g) and imidazole (13.22 mmol, 900 mg) were dissolved in DMF to yield a total volume of 90 mL. After the reactants were fully mixed by ultrasound for 5 min, the reaction mixture was transferred to a 250 mL screw-capped vial. The reaction vial was sealed tightly and heated in an oven for 7 d at 100 °C (for ZIF-4(Zn)) and 130 °C (for ZIF-4(Co)). After cooling to room temperature, the obtained truncated octahedrally shaped single crystals went through the same activation process as described for ZIF-62.

ZIF-zni(Zn): $Zn(NO_3)_2 \cdot 6H_2O$ (4.0 mmol, 1.2 g) and imidazole (13.22 mmol, 900 mg) were dissolved in EtOH to yield a total volume of 90 mL. After the reactants were fully mixed by ultrasound for 5 min, the reaction mixture was transferred to a 250 mL screw-capped vial. The reaction vial was sealed tightly and heated in an oven for 7 d at 100 °C. After cooling to room temperature, the obtained rod-shaped single crystals went through the same solvent exchange and activation process as described for ZIF-62.

ZIF-76/UC-5 phase mixture: $Zn(NO_3)_2 \cdot 6H_2O$ (0.84 mmol, 250 mg), imidazole (1.76 mmol, 120 mg) and 5-chlorobenzimidazole (0.85 mmol, 130 mg) were mixed together in a solution of DMF (8.28 ml) and *N,N*-diethylformamide (5.73 mL), along

with aqueous NaOH (0.52 ml, $c = 2.5$ mol L^{-1}). The turbid solution was then heated to 90 °C for 5 days. After cooling to room temperature, the obtained microcrystalline powder went through the same solvent exchange and activation process as described for ZIF-62.

Pure-phase ZIF-76: $Zn(NO_3)_2 \cdot 6H_2O$ (0.87 mmol, 260 mg), imidazole (1.76 mmol, 120 mg) and 5-chlorobenzimidazole (0.85 mmol, 130 mg) were mixed together in a solution of DMF (5.75 mL) and *N,N*-diethylformamide (5.75 mL) along with aqueous NaOH (0.26 mL, $c = 2.5$ mol L^{-1}). The turbid solution was then heated to 90 °C for 5 days. After cooling to room temperature, the obtained microcrystalline powder went through the same solvent exchange and activation process as described for ZIF-62.

TIF-4: $Zn(NO_3)_2 \cdot 6H_2O$ (2.0 mmol, 595 mg,), imidazole (2.0 mmol, 136 mg) and 5-methylbenzimidazole (3.0 mmol, 396 mg) were dissolved in DMF (18.8 mL) and heated at 130 °C for 48 hours. After cooling to room temperature, the obtained truncated octahedrally shaped crystals went through the same solvent exchange and activation process as described for ZIF-62.

ZIF-70: $Zn(NO_3)_2 \cdot 6H_2O$ (1.28 mmol, 380 mg), imidazole (27.0 mmol, 1.84 g) and 2-nitroimidazole (2.0 mol, 226 mg) were dissolved in DMF (50 mL) and heated at 100 °C for 96 hours. After cooling to room temperature, the obtained light brownish microcrystalline powder went through the same solvent exchange and activation process as described for ZIF-62.

ZIF-8: $Zn(NO_3)_2 \cdot 6H_2O$ (7.06 mmol, 2.1 g) and methylimidazole (14.62 mmol, 1.2 g) were dissolved in DMF (80 mL) and heated at 120 °C for 24 hours. After cooling to room temperature, the obtained rhombic-dodecahedral crystals went through the same solvent exchange and activation process as described for ZIF-62.

ZIF-8 SALE samples in section 3 (ZIF-8-$mim_x im_y bim_z$) is based on the exchange method of SALEM-2.[15] Imidazole, benzimidazole, or a mixture of imidazole and benzimidazole (see **Table A3.1**) was placed in a 20 mL microwave vial and dissolved in *n*-butanol (20 mL) by sonication. Activated ZIF-8 crystals (100 mg, 0.44 mmol) were immersed in the resulting solution. The vial was capped and placed in an isothermal oven at 100 °C for 1, 3, 5 and 7 days. After decanting off the solvent and washing with 5 mL of DCM, the samples were transferred to a dynamic vacuum ($p \approx 10^{-4}$ kPa) for activation at 100 °C for 12 hours.

ZIF-Cu-1: $CuSO_4 \cdot 5H_2O$ (10.1 mmol, 2.5 g) was dissolved in 12.5 mL of H_2O with stirring first. Imidazole (20 mmol, 1.36 g) and $NaHCO_3$ (78.56 mmol, 6.6 g) were then placed in 50 ml of water and heated at 80 °C for 3 hours. Then, $CuSO_4$ solution was added dropwise to the hot solution of imidazole. The formation of a violet precipitate was immediately observed. By leaving the mixture under reaction conditions, the violet compound was gradually transformed into blue $Cu(im)_2$. After 2 h the blue compound was filtered off, washed with water, and dried at 110 °C for 6h in vacuum oven.

Mechanical Synthesis of Crystalline $Cd(im)_2$. The synthesis was adapted from previous reports for the mechanochemical synthesis of ZIF-62[21] and ZIF-4 derivatives[22]. CdO (3.9 mmol, 508.5 mg), $Cd(CH_3COO)_2 \cdot 2H_2O$ (0.04 mmol, 10.6 mg) and imidazole (8.2 mmol, 558.3 mg) are mixed in a 20 mL stainless steel grinding jar. Two 10 mm stainless steel grinding balls (4.0 g each) and 200 μL DMF were added to the jar, which was subsequently sealed. Ball milling was performed on a Retsch MM400 mixer mill at 30 Hz for 30 minutes. The resulting powders were washed with DMF (20 mL) followed by washing with dichloromethane (DCM, 20 mL × 2 times). The washed powders were immersed in fresh DCM overnight, followed by drying at 170 °C under dynamic vacuum ($p \approx 10^{-4}$ kPa) overnight.

Solvent Synthesis of Crystalline $Cd(im)_2$-*sol*. The synthesis route is based on the reported method with slight modifications.[153] $Cd(NO_3)_2 \cdot 4H_2O$ (2.0 mmol, 617 mg) and imidazole (4.0 mmol, 272 mg) were dissolved in 10 ml and 20 ml of water, respectively. After adding three drops of ammonia to the aqueous imidazole solution, it was then poured into the aqueous $Cd(NO_3)_2$ solution. The resulting pure white precipitate was washed with water, dried at 170 °C under dynamic vacuum ($p \approx 10^{-4}$ kPa) overnight and then finely ground.

Preparation of glassy $a_gCd(im)_2$ and Glass-ceramic $rcCd(im)_2$. Approximately 10 mg of $Cd(im)_2$ was placed into a ligatured aluminum crucible and the preparation of the relevant derivatives was carried out using the procedure in **Table 7.2**.

Post-synthetic ball milling: The activated microcrystalline ZIFs (ca. 50 mg) were treated by PSBM at 25 Hz in a vibratory shaker mill for 5, 10, and 15 min respectively, using a 10 mL stainless steel grinding jar with two 8 mm stainless-steel balls on Retsch MM 200. The derived PSBM materials are denoted by ZIF-*X*-5min/10min/15min. Additional 30 min and 60 min ball mill samples were prepared for ZIF-8, named ZIF-8-30min and ZIF-8-60min.

Melt-quenched glass formation: The selected MQGs (a_gZIFs and a_gZIFs-5min samples), were prepared by heating the samples in the TG/DTA machine under N_2 protection using the procedures compiled in **Table 7.2**.

Table 7.1. Applied masses of metal salts and imidazole-based ligands as well as solvent volumes for the ZIFs synthesized in this thesis.

Compound	$Zn(NO_3)_2 \cdot 6H_2O$ (mg)	$Co(NO_3)_2 \cdot 6H_2O$ (mg)	$Co(OAc)_2 \cdot 4H_2O$ (mg)	$CuSO_4 \cdot 5H_2O$ (mg)	Him (mg)	Hbim (mg)	HClbim (mg)	Hnim (mg)	Hmim (mg)	$NaHCO_3$ (mg)	DMF (mL)	DEF (mL)	EtOH (mL)	H_2O (mL)	3-methyl-1-butanol (mL)	Quinoline (mL)	NaOH ($c = 2.5$ mol L^{-1}) (mL)
ZIF-4(Zn)	1200	-			900	-	-	-	-	-	80	-	-		-	-	-
ZIF-4(Co)	-	1200			900	-	-	-	-	-	80	-	-		-	-	-
ZIF-62(Zn)	1200	-			786	196	-	-	-	-	80	-	-		-	-	-
ZIF-62(Co)	-	1200			786	196	-	-	-	-	80	-	-		-	-	-
ZIF-zni(Zn)	1200	-			900	-	-	-	-	-	-	-	80		-	-	-
ZIF-zni(Co)	-	-	1245		680	-	-	-	-	-	-	-	-		15	15	-
ZIF-76/UC-5	250	-	-		120	-	130	-	-	-	8.28	5.73	-		-	-	0.52
ZIF-76	260	-	-		120	-	130	-	-	-	5.75	5.75	-		-	-	0.26
TIF-4	549	-	-		136	-	396	-	-	-	18.8	-	-		-	-	-
ZIF-70	380	-	-		1840	-	-	226	-	-	50	-	-		-	-	-
ZIF-8	2100	-	-		-	-	-	-	1200	-	80	-	-		-	-	-
ZIF-Cu-1	-	-	-	2500	1360	-	-	-	-	6600	-	-	-	62.5	-	-	-

Table 7.2. Summary of the temperature programs applied for the preparation of melt-quenched glasses. The programs are designed to heat the sample across their melting points or their glass transition points, followed by quenching them from the (supercooled) liquid.

Compound	Temperature program
a_gZIF-62(Zn)	RT $\xrightarrow{10\,°C/min}$ 500 °C $\xrightarrow{-10\,°C/min}$ RT
a_gZIF-62(Zn)-5min	RT $\xrightarrow{10\,°C/min}$ 500 °C $\xrightarrow{-10\,°C/min}$ RT
a_gZIF-62(Co)	RT $\xrightarrow{10\,°C/min}$ 500 °C $\xrightarrow{-10\,°C/min}$ RT
a_gZIF-62(Co)-5min	RT $\xrightarrow{10\,°C/min}$ 430 °C $\xrightarrow{-10\,°C/min}$ RT
a_gZIF-4(Zn)	RT $\xrightarrow{10\,°C/min}$ 590 °C $\xrightarrow{-10\,°C/min}$ RT
a_gZIF-4(Zn)-5min	RT $\xrightarrow{10\,°C/min}$ 580 °C $\xrightarrow{-10\,°C/min}$ RT
a_gZIF-4(Co)-5min	RT $\xrightarrow{10\,°C/min}$ 340 °C $\xrightarrow{-10\,°C/min}$ RT
a_gZIF-zni(Zn)	RT $\xrightarrow{10\,°C/min}$ 590 °C $\xrightarrow{-10\,°C/min}$ RT
a_gZIF-zni(Zn)-5min	RT $\xrightarrow{10\,°C/min}$ 580 °C $\xrightarrow{-10\,°C/min}$ RT
a_gTIF-4	RT $\xrightarrow{10\,°C/min}$ 450 °C $\xrightarrow{-10\,°C/min}$ RT
a_gTIF-4-5min	RT $\xrightarrow{10\,°C/min}$ 375 °C $\xrightarrow{-10\,°C/min}$ RT
a_gZIF-76/UC-5	RT $\xrightarrow{10\,°C/min}$ 450 °C $\xrightarrow{-10\,°C/min}$ RT
a_gZIF-76/UC-5-5min	RT $\xrightarrow{10\,°C/min}$ 450 °C $\xrightarrow{-10\,°C/min}$ RT
a_gCd(im)$_2$	RT $\xrightarrow{10\,°C/min}$ 456 °C $\xrightarrow{-100\,°C/min}$ RT**
prcCd(im)$_2$	RT $\xrightarrow{10\,°C/min}$ 457 °C $\xrightarrow{-100\,°C/min}$ RT** $\xrightarrow{10\,°C/min}$ 300 °C
frcCd(im)$_2$	RT $\xrightarrow{10\,°C/min}$ 457 °C $\xrightarrow{-10\,°C/min}$ RT $\xrightarrow{10\,°C/min}$ 300 °C
a_gCd(im)$_2$-*sol*	RT $\xrightarrow{10\,°C/min}$ 460 °C $\xrightarrow{-100\,°C/min}$ RT**

** The cooling rate is constrained by the instrumentation, with a maximum average rate of approximately –30 °C min^{-1} between 460 °C and 100 °C. The rate is –80 °C min^{-1} at 460 °C and continuously reduces to –10 °C min^{-1} at 100 °C. Below 100 °C, the cooling rate is further reduced (see Thermal Analysis Section in Appendix Section 5).

Appendix

Appendix to Section 3

A.3.1 – Compositional analysis by ^{1}H NMR spectroscopy

Solution ^{1}H NMR spectroscopy was performed on digested crystalline and glassy ZIF samples. The composition of ZIF-8 derivatives is determined using the integral ratio of the aromatic protons of the different linkers. Note that in a few spectra, there are peaks between 0 and 4 ppm, which are residual traces of *n*-butanol. This is because the materials have not been completely activated prior to the ^{1}H NMR analysis. ^{1}H NMR data of the digested parent material ZIF-8, and *n*-butanol (with DMSO-d_6 and DCl/D_2O) can be found in **Figure A3.3**.

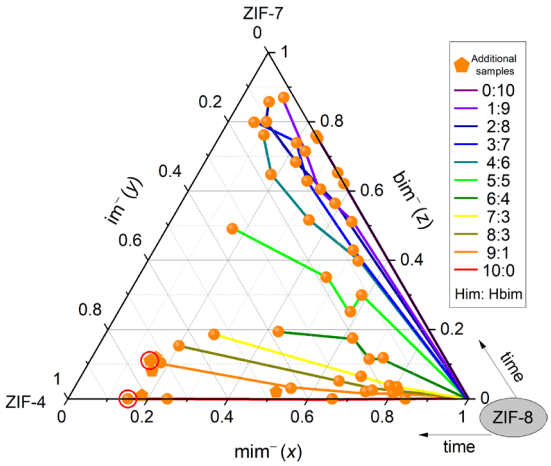

Figure A3.1. Plot of the linker fractions found in the crystalline ZIF-8 derivatives after the various SALE experiments performed in this work. The orange spheres on the coloured lines show the compositions of the materials after 1 day, 3 days, 5 days and 7 days of SALE in *n*-butanol solutions containing Him and Hbim in varying ratios. The lines correspond to a SALE solution with a particular Him:Hbim ratio with the same overall molar linker concentration (i.e. $c_{\mathrm{Him}} + c_{\mathrm{Hbim}} = \mathrm{constant}$). Lines are just a guide to the eye. The pentagons represent additional samples prepared for gathering additional data points to explore the compositional limits of meltability/glassformability in the triangular phase diagram in more detail (**Table A3.1**). The symbols highlighted by the red circles are the most critical samples (ZIF-8-$\mathrm{mim}_{0.15}\mathrm{im}_{0.74}\mathrm{bim}_{0.11}$ and ZIF-8-$\mathrm{mim}_{0.15}\mathrm{im}_{0.85}$) for this work.

Table A3.1. Applied masses and molar amounts of Him and Hbim with 100 mg ZIF-8 (or ZIF-67) in the SALE reaction mixtures for ZIF-8-mim$_x$im$_y$bim$_z$ (ZIF-67-mim$_x$im$_y$bim$_z$) synthesis as well as the corresponding mim$^-$: im$^-$: bim$^-$ ratios found in the corresponding framework (determined by ^{1}H NMR spectroscopy; see later spectrums). Data for an additional linker exchange experiment of ZIF-8 with Him and HClbim (5-chlorobenzimidazole) is included as well. In all exchange experiments except one, the samples have not been stirred over the course of the SALE process. In one SALE experiment, the samples suspension was stirred for 15 min/day with a total reaction time of 3 days. In this process, ZIF-8 is fully converted to a ZIF-62 derivative as proven by XRPD (see **Figure A3.35**).

Applied Him: Hbim	Applied Him (mmol, mg)		Applied Hbim (mmol, mg)		Time (day)	Linkers fractions determined by ^{1}H NMR spectroscopy			Sample name
						mim$^-$ (%)	im$^-$ (%)	bim$^-$ (%)	
10 : 0	2.94	200	0	0	1	84	16	0	ZIF-8-mim$_{0.84}$im$_{0.16}$
					3	66	34	0	ZIF-8-mim$_{0.66}$im$_{0.34}$
					5	25	75	0	ZIF-8-mim$_{0.25}$im$_{0.75}$
					7	15	85	0	ZIF-8-mim$_{0.15}$im$_{0.85}$
9 : 1	2.64	180	0.29	34.7	1	80	18	2	ZIF-8-mim$_{0.80}$im$_{0.18}$bim$_{0.02}$
					3	73	25	2	ZIF-8-mim$_{0.73}$im$_{0.25}$bim$_{0.02}$
					5	54	43	3	ZIF-8-mim$_{0.54}$im$_{0.43}$bim$_{0.03}$
					7	18	72	10	ZIF-8-mim$_{0.18}$im$_{0.72}$bim$_{0.10}$
8 : 2	2.35	160	0.59	69.4	1	82	16	2	ZIF-8-mim$_{0.82}$im$_{0.16}$bim$_{0.02}$
					3	75	23	2	ZIF-8-mim$_{0.75}$im$_{0.23}$bim$_{0.02}$
					5	65	30	5	ZIF-8-mim$_{0.65}$im$_{0.30}$bim$_{0.05}$
					7	20	65	15	ZIF-8-mim$_{0.20}$im$_{0.65}$bim$_{0.15}$
7 : 3	2.06	140	0.88	104.1	1	80	16	4	ZIF-8-mim$_{0.80}$im$_{0.16}$bim$_{0.04}$
					3	78	18	4	ZIF-8-mim$_{0.78}$im$_{0.18}$bim$_{0.04}$
					5	70	24	6	ZIF-8-mim$_{0.70}$im$_{0.24}$bim$_{0.06}$
					7	27	54	19	ZIF-8-mim$_{0.27}$im$_{0.54}$bim$_{0.19}$
6 : 4	1.76	120	1.18	138.8	1	73	15	15	ZIF-8-mim$_{0.73}$im$_{0.15}$bim$_{0.12}$
					3	70	19	11	ZIF-8-mim$_{0.70}$im$_{0.19}$bim$_{0.11}$
					5	62	20	18	ZIF-8-mim$_{0.62}$im$_{0.20}$bim$_{0.18}$
					7	43	38	19	ZIF-8-mim$_{0.43}$im$_{0.38}$bim$_{0.19}$
5 : 5	1.47	100	1.47	173.5	1	58	12	30	ZIF-8-mim$_{0.58}$im$_{0.12}$bim$_{0.30}$
					3	58	17	25	ZIF-8-mim$_{0.58}$im$_{0.17}$bim$_{0.25}$
					5	47	18	35	ZIF-8-mim$_{0.47}$im$_{0.18}$bim$_{0.35}$
					7	17	34	49	ZIF-8-mim$_{0.17}$im$_{0.34}$bim$_{0.49}$
4 : 6	1.18	80	1.76	208.2	1	53	7	40	ZIF-8-mim$_{0.53}$im$_{0.07}$bim$_{0.40}$
					3	34	14	52	ZIF-8-mim$_{0.34}$im$_{0.14}$bim$_{0.52}$

					5	18	17	65	ZIF-8-mim$_{0.18}$im$_{0.17}$bim$_{0.65}$
					7	11	13	76	ZIF-8-mim$_{0.11}$im$_{0.13}$bim$_{0.76}$
3 : 7	0.88	60	2.06	242.9	1	50	7	43	ZIF-8-mim$_{0.50}$im$_{0.07}$bim$_{0.43}$
					3	28	9	63	ZIF-8-mim$_{0.28}$im$_{0.09}$bim$_{0.63}$
					5	20	6	74	ZIF-8-mim$_{0.20}$im$_{0.06}$bim$_{0.74}$
					7	7	13	80	ZIF-8-mim$_{0.07}$im$_{0.13}$bim$_{0.80}$
2 : 8	0.59	40	2.35	277.6	1	39	5	56	ZIF-8-mim$_{0.39}$im$_{0.05}$bim$_{0.56}$
					3	23	9	68	ZIF-8-mim$_{0.23}$im$_{0.09}$bim$_{0.68}$
					5	10	10	80	ZIF-8-mim$_{0.10}$im$_{0.10}$bim$_{0.80}$
					7	7	7	86	ZIF-8-mim$_{0.07}$im$_{0.07}$bim$_{0.86}$
1 : 9	0.29	20	2.64	312.4	1	45	4	51	ZIF-8-mim$_{0.45}$im$_{0.04}$bim$_{0.51}$
					3	33	7	60	ZIF-8-mim$_{0.33}$im$_{0.07}$bim$_{0.60}$
					5	24	5	71	ZIF-8-mim$_{0.24}$im$_{0.05}$bim$_{0.71}$
					7	10	3	87	ZIF-8-mim$_{0.10}$im$_{0.03}$bim$_{0.87}$
0 : 10	0	0	2.94	347.1	1	38	0	62	ZIF-8-mim$_{0.38}$bim$_{0.62}$
					3	35	0	65	ZIF-8-mim$_{0.35}$bim$_{0.65}$
					5	25	0	75	ZIF-8-mim$_{0.25}$bim$_{0.75}$
					7	24	0	76	ZIF-8-mim$_{0.24}$bim$_{0.76}$
8.7 : 1.3	2.35	160	0.34	40	7	15	74	11	ZIF-8-mim$_{0.15}$im$_{0.74}$bim$_{0.11}$
9.3 : 0.7	2.60	177	0.19	23	7	17	75	8	ZIF-8-mim$_{0.17}$im$_{0.75}$bim$_{0.08}$
8.8 : 1.2	2.57	175	0.36	43	7	16	72	12	ZIF-8-mim$_{0.16}$im$_{0.72}$bim$_{0.12}$
9.7 : 0.3	2.79	190	0.08	10	7	18	81	1	ZIF-8-mim$_{0.18}$im$_{0.81}$bim$_{0.01}$
9.3 : 0.7	2.60	177	0.19	23	3.5	51	47	2	ZIF-8-mim$_{0.51}$im$_{0.47}$bim$_{0.02}$
8.7 : 1.3	2.35	160	0.34	40	3 (stirred 15 min/day)	5	80	15	ZIF-62-mim$_{0.05}$im$_{0.80}$bim$_{0.15}$
8.7 : 1.3 (ZIF-67)	2.35	160	0.34	40	7	18	68	14	ZIF-67-mim$_{0.18}$im$_{0.68}$bim$_{0.14}$
8.7 : 1.3 (Him: HClbim)	2.35	160	0.34	52	7	20	70	10	ZIF-8-mim$_{0.20}$im$_{0.70}$Clbim$_{0.10}$

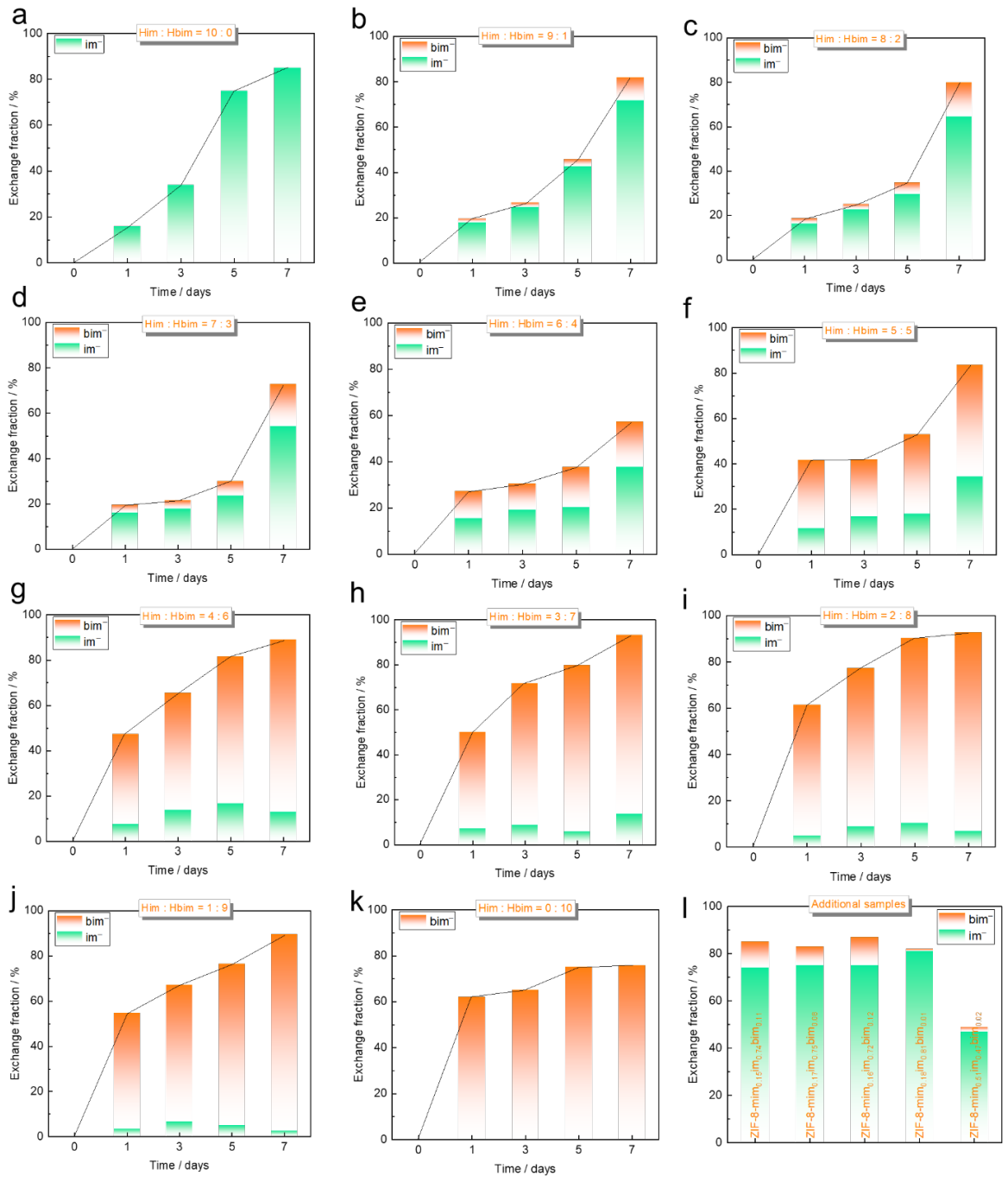

Figure A3.2. Progress of the SALE reactions expressed as the fraction of im^- and bim^- in ZIF-8. The fraction of mim^- can be obtained by subtracting the fractions of im^- and bim^- from 100%. As to be expected, the fraction of exchanged linkers (i.e. the inclusion of im^- and/or bim^- and the removal of mim^-) is increasing with the reaction time. Moreover, bim^- is incorporated preferentially over im^- so that the rate for the incorporation of im^- is much slower than the rate for the incorporation of bim^-. These observations seem counterintuitive at first sight, as Hbim is significantly larger than Him and thus a considerable restriction of diffusion into the pores of ZIF-8 is expected for the former. However, the observations are consistent with the considerably higher acidic strength of Hbim (pK$_a$ = 12.78) compared to Him (pK$_a$ = 14.52)[161].

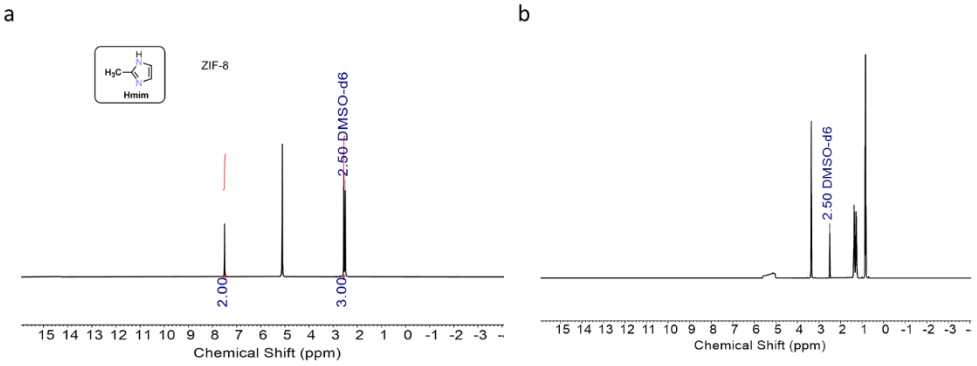

Figure A3.3. ^{1}H NMR data collected for **a** ZIF-8 and **b** *n*-butanol using DMSO-d_6 (0.5 mL) and DCl/D_2O (35 wt%, 0.015 mL) as solvents.

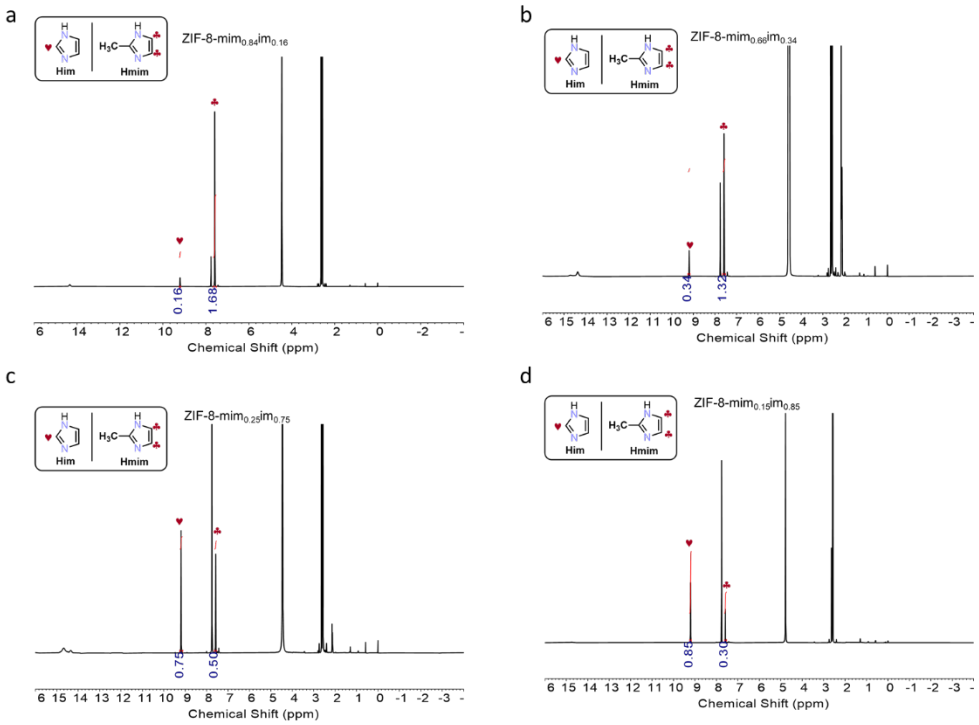

Figure A3.4. ^{1}H NMR data collected for ZIF-8 derivatives after varying SALE reaction times with a solution containing only Him. The SALE time from **a** to **d** is 1, 3, 5, and 7 days, respectively.

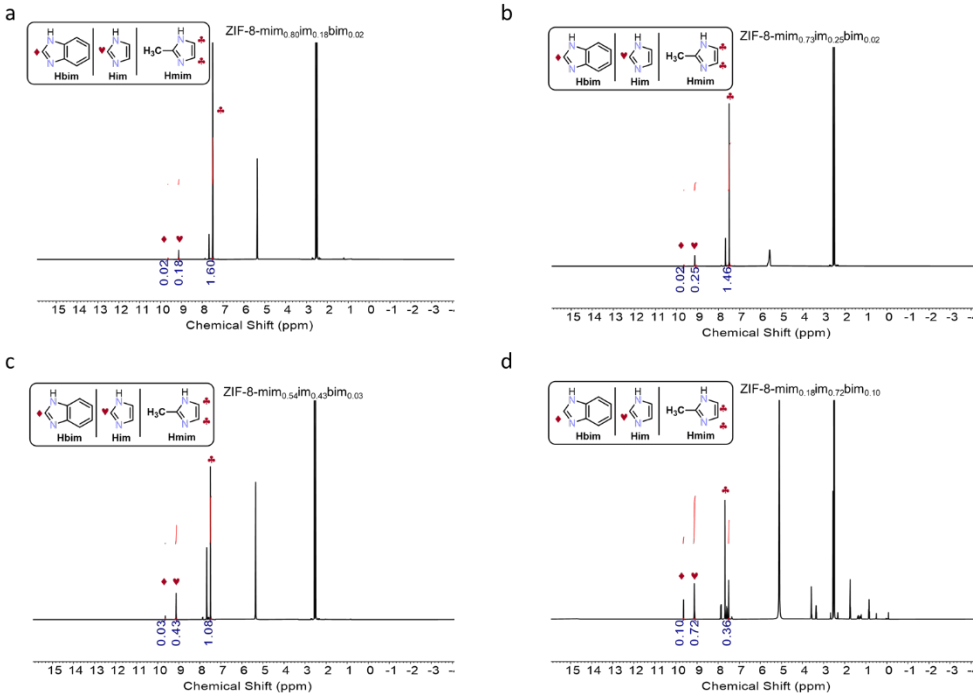

Figure A3.5. ^{1}H NMR data collected for ZIF-8 derivatives after varying SALE reaction times with a solution containing Him and Hbim in a molar ratio of 9:1. The SALE time from **a** to **d** is 1, 3, 5, and 7 days, respectively.

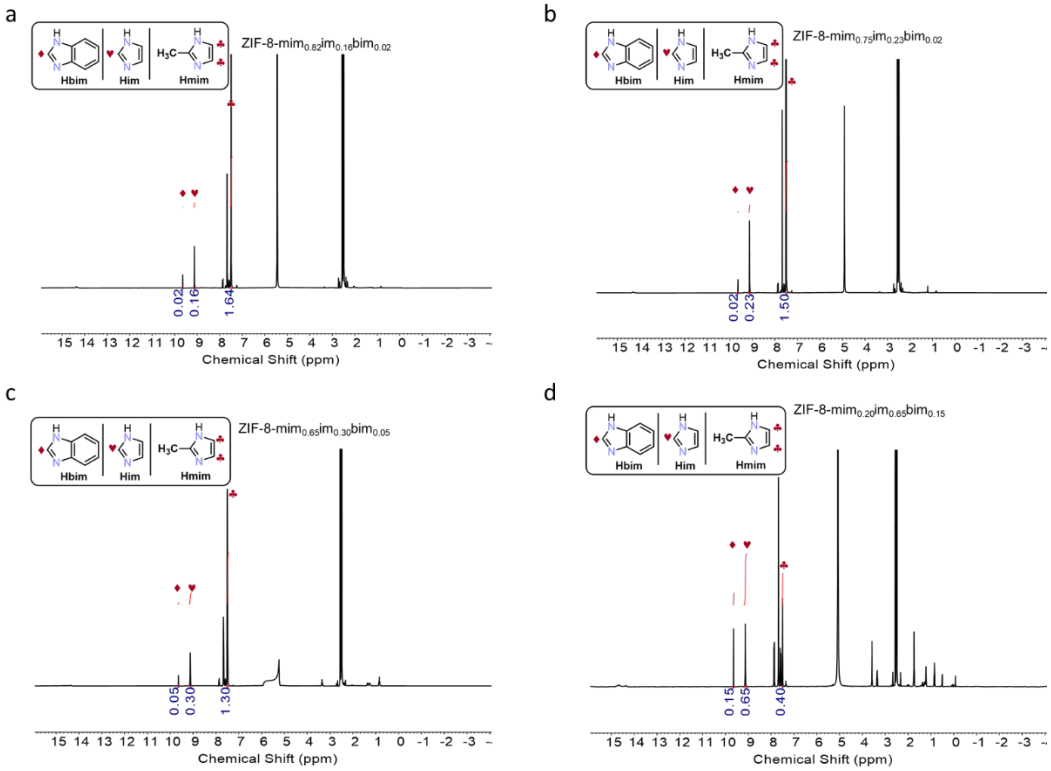

Figure A3.6. ^{1}H NMR data collected for ZIF-8 derivatives after varying SALE reaction times with a solution containing Him and Hbim in a molar ratio of 8:2. The SALE time from **a** to **d** is 1, 3, 5, and 7 days, respectively.

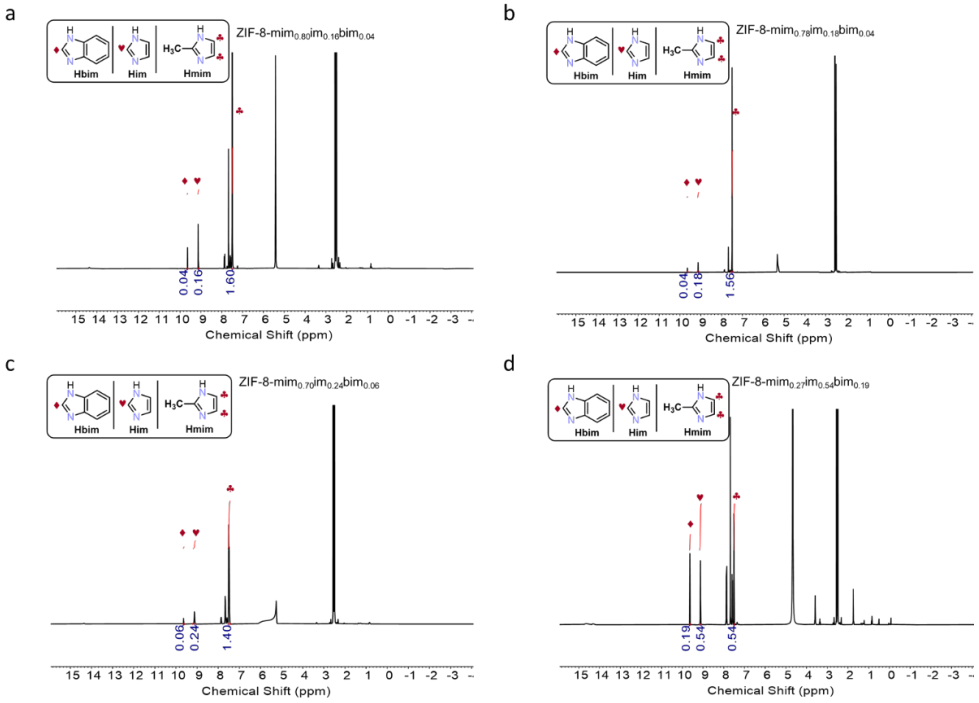

Figure A3.7. ^{1}H NMR data collected for ZIF-8 derivatives after varying SALE reaction times with a solution containing Him and Hbim in a molar ratio of 7:3. The SALE time from a to d is 1, 3, 5, and 7 days, respectively.

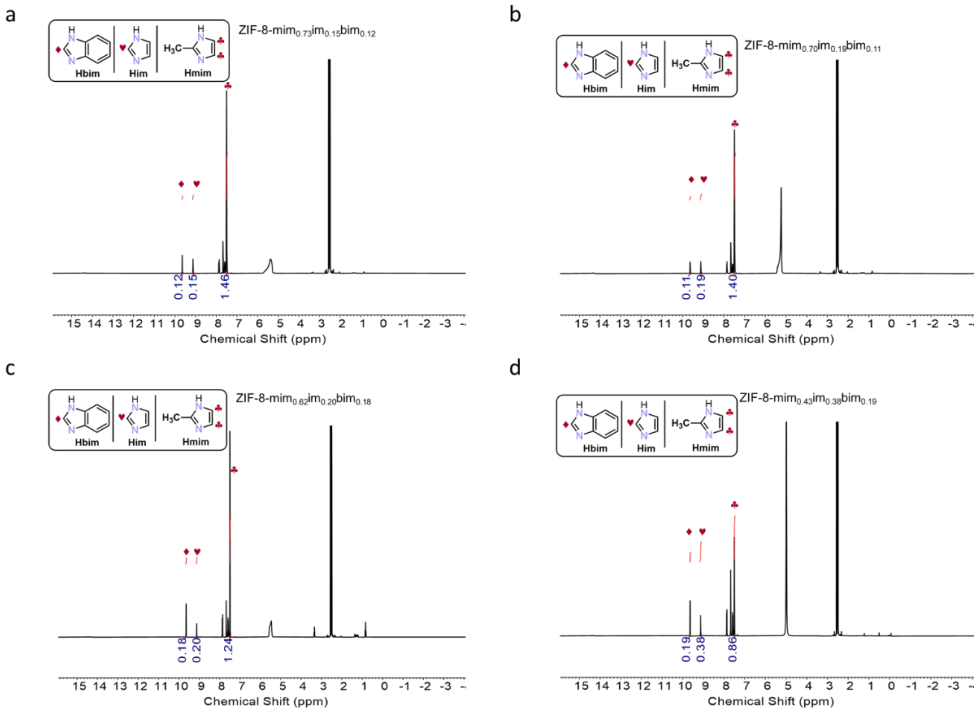

Figure A3.8. ^{1}H NMR data collected for ZIF-8 derivatives after varying SALE reaction times with a solution containing Him and Hbim in a molar ratio of 6:4. The SALE time from **a** to **d** is 1, 3, 5, and 7 days, respectively.

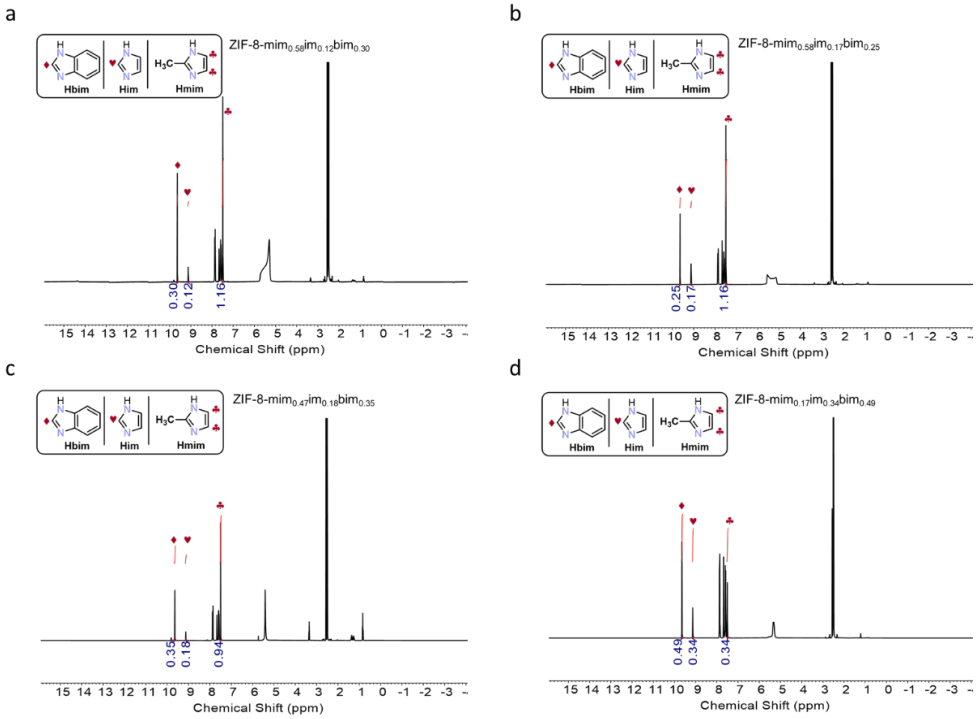

Figure A3.9. ^{1}H NMR data collected for ZIF-8 derivatives after varying SALE reaction times with a solution containing Him and Hbim in a molar ratio of 5:5. The SALE time from **a** to **d** is 1, 3, 5, and 7 days, respectively.

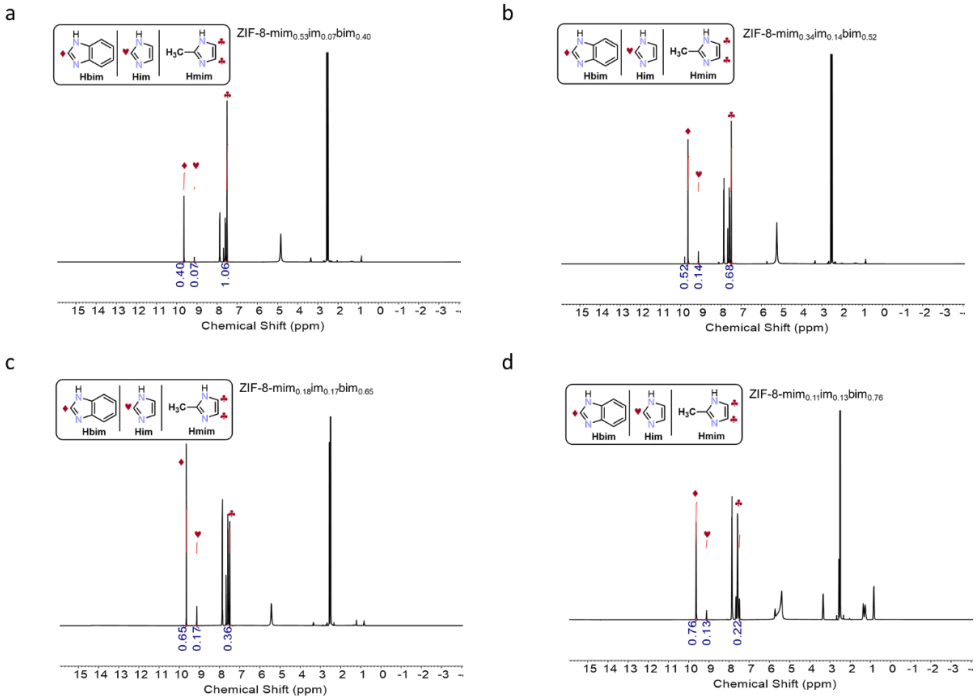

Figure A3.10. ^{1}H NMR data collected for ZIF-8 derivatives after varying SALE reaction times with a solution containing Him and Hbim in a molar ratio of 4:6. The SALE time from **a** to **d** is 1, 3, 5, and 7 days, respectively.

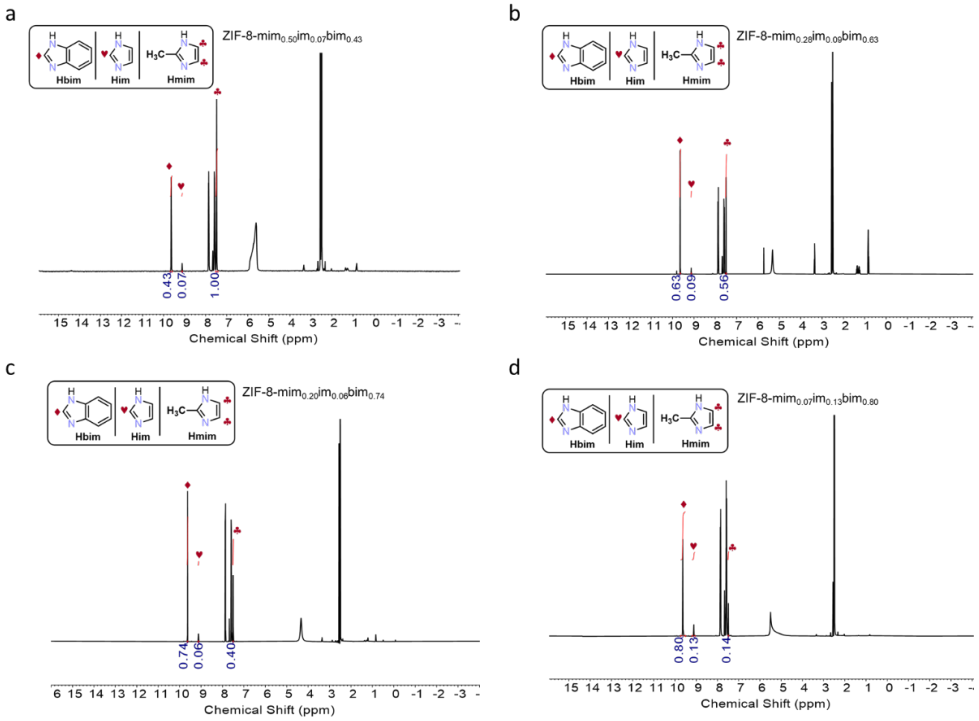

Figure A3.11. ^{1}H NMR data collected for ZIF-8 derivatives after varying SALE reaction times with a solution containing Him and Hbim in a molar ratio of 3:7. The SALE time from **a** to **d** is 1, 3, 5, and 7 days, respectively.

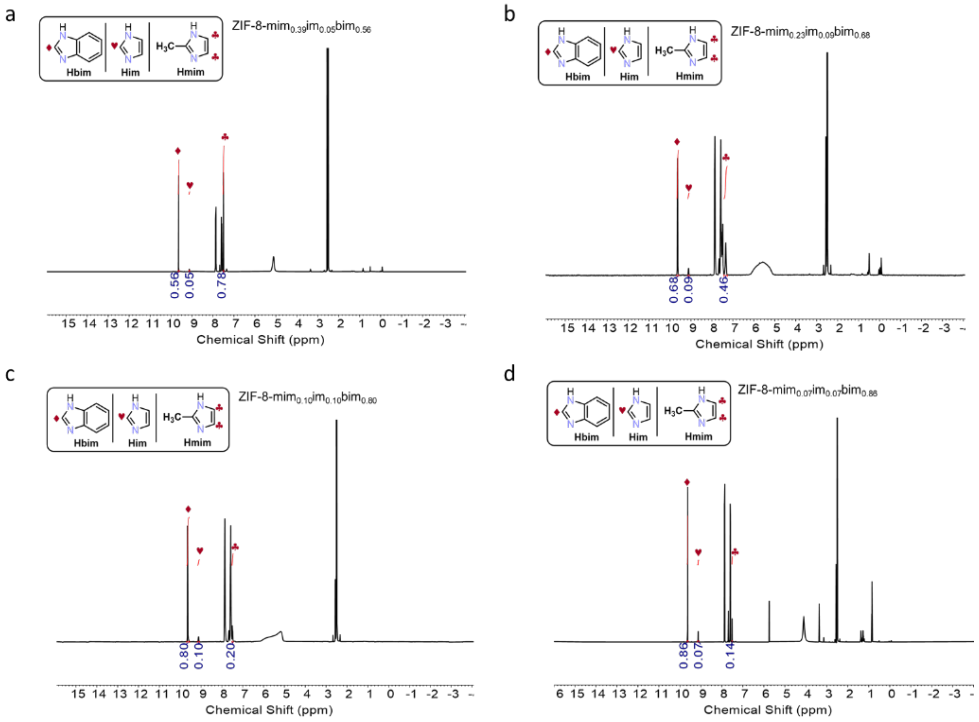

Figure A3.12. ^{1}H NMR data collected for ZIF-8 derivatives after varying SALE reaction times with a solution containing Him and Hbim in a molar ratio of 2:8. The SALE time from **a** to **d** is 1, 3, 5, and 7 days, respectively.

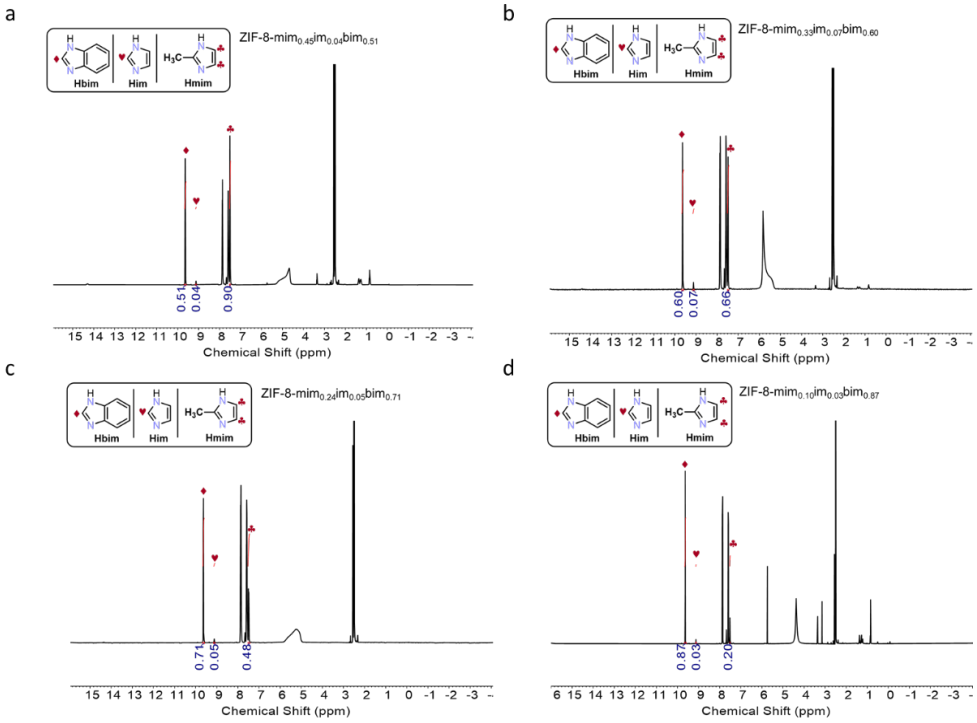

Figure A3.13. [1]H NMR data collected for ZIF-8 derivatives after varying SALE reaction times with a solution containing Him and Hbim in a molar ratio of 1:9. The SALE time from **a** to **d** is 1, 3, 5, and 7 days, respectively.

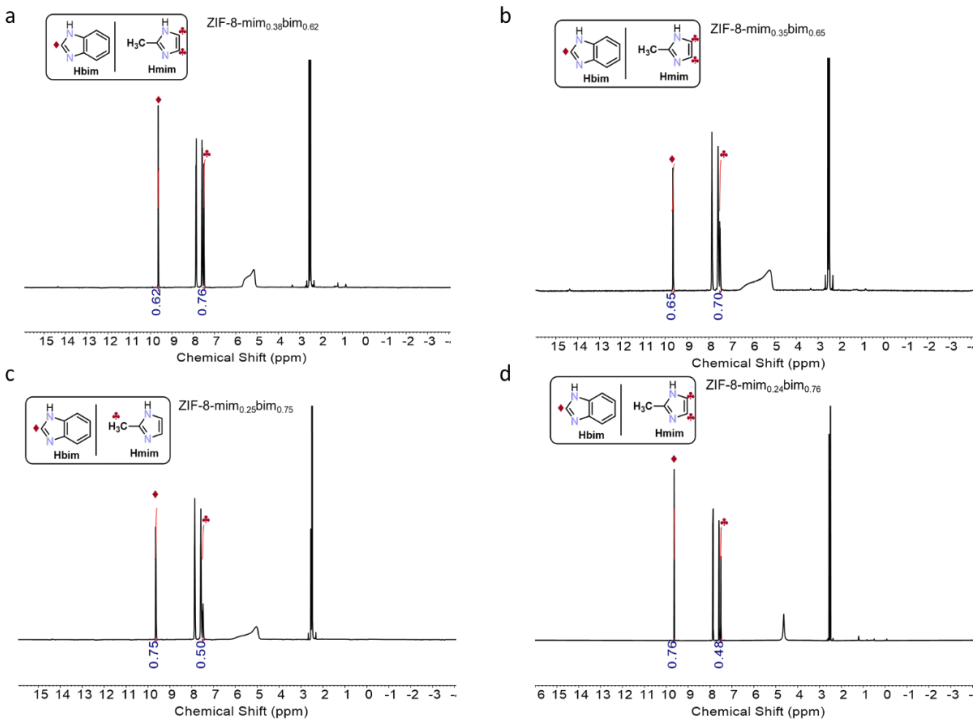

Figure A3.14. [1]H NMR data collected for ZIF-8 derivatives after varying SALE reaction times with a solution containing only Hbim. The SALE time from **a** to **d** is 1, 3, 5, and 7 days, respectively.

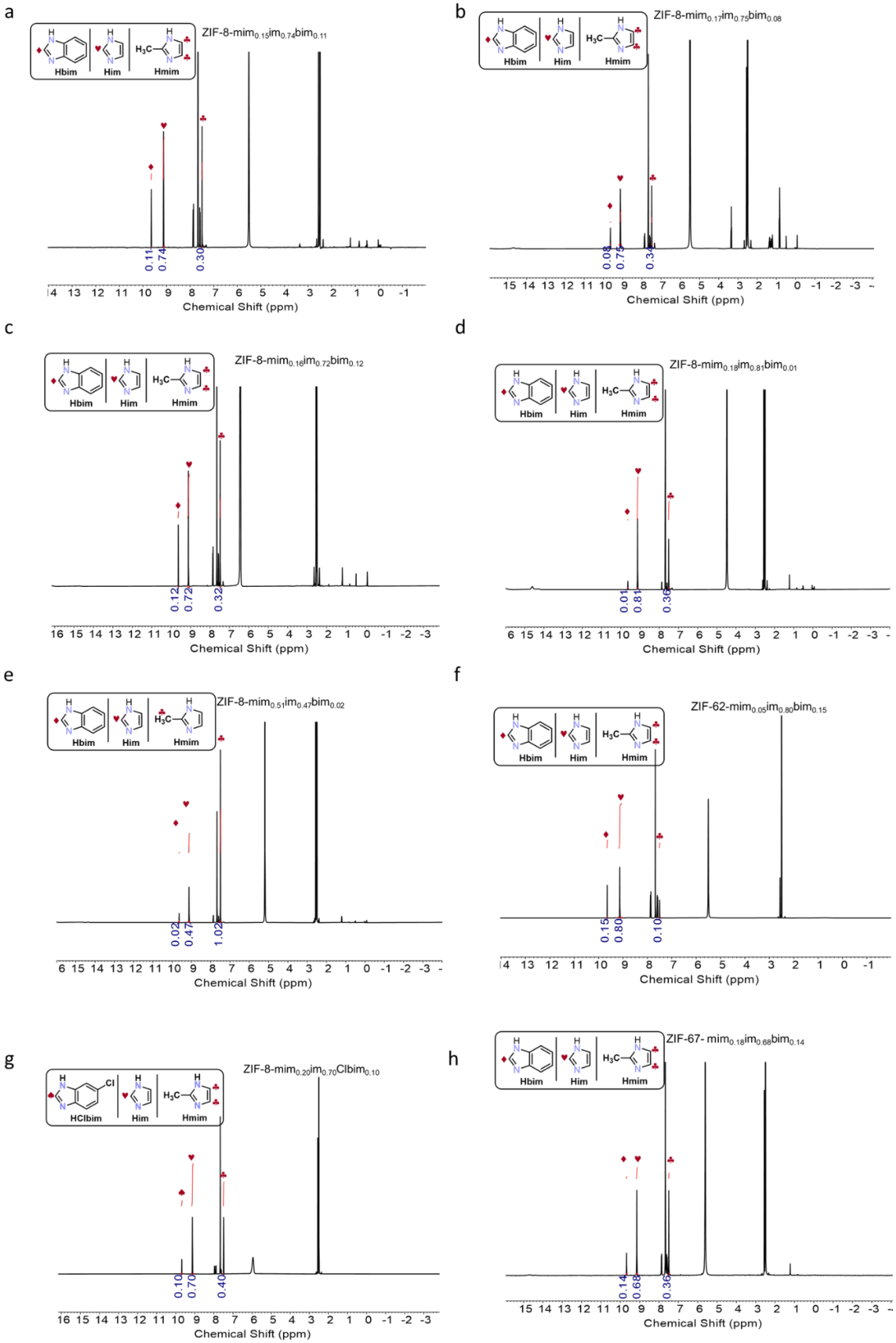

Figure A3.15. ^{1}H NMR data collected for seven additional ZIF-8 derivatives and one ZIF-67 derivative.

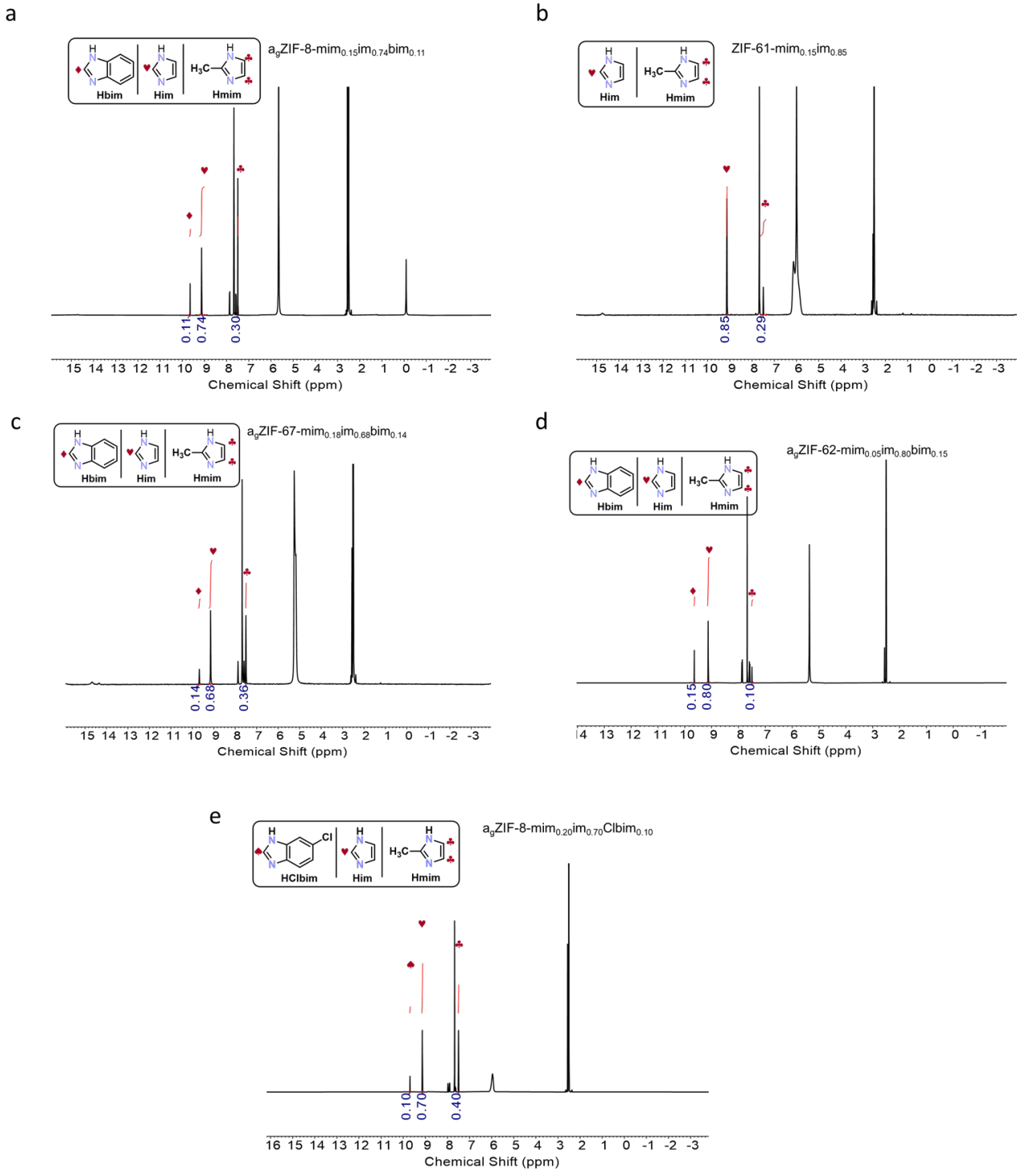

Figure A3.16. ^{1}H NMR data collected for representative ZIF-8 derivatives and ZIF-67 derivative after heat treatment. **a** a_gZIF-8-$mim_{0.15}im_{0.74}bim_{0.11}$. **b** ZIF-61-$mim_{0.15}im_{0.85}$. **c** a_gZIF-67-$mim_{0.18}im_{0.68}bim_{0.14}$. **d** a_gZIF-62-$mim_{0.05}im_{0.80}bim_{0.15}$. **e** a_gZIF-8-$mim_{0.20}im_{0.70}Clbim_{0.10}$.

A.3.2 – X-ray powder diffraction data

A.3.2.1 – Ambient temperature XRPD

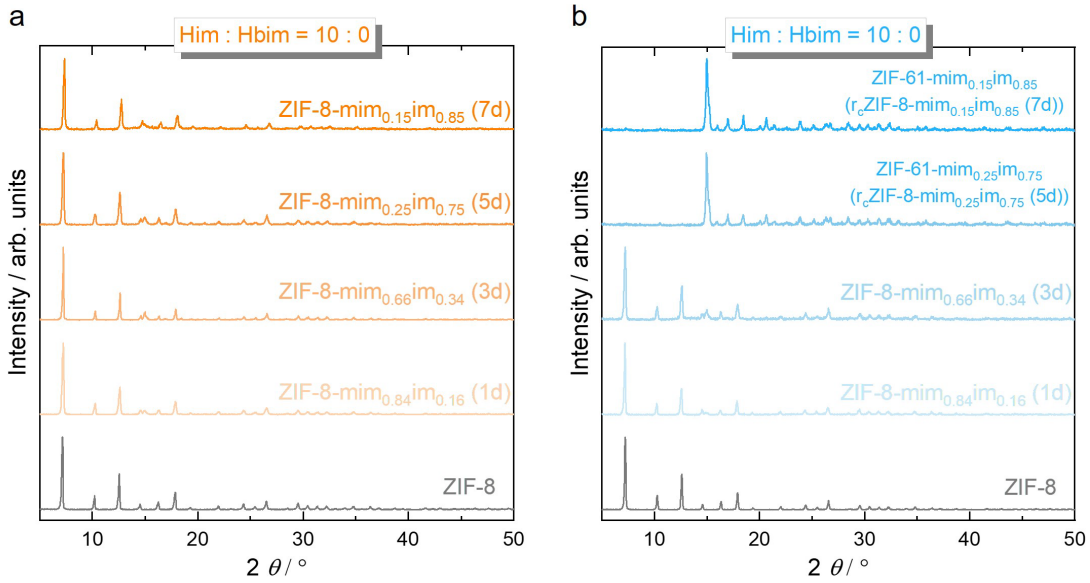

Figure A3.17. **a** XRPD patterns collected for ZIF-8 derivatives after varying SALE reaction times with a solution containing only Him. **b** Corresponding XRPD patterns of samples obtained after heating the materials to 450 °C followed by rapid cooling to room temperature. For the SALE time of 5- and 7- day samples, the presence of a large amount of im^- led to the destabilization of the ZIF-8 **sod** structure and a solid-state transition to a dense **zni** topology (ZIF-61-like) was obtained by heat treatment (validated by Pawley fitting, see **Figure A3.31**).

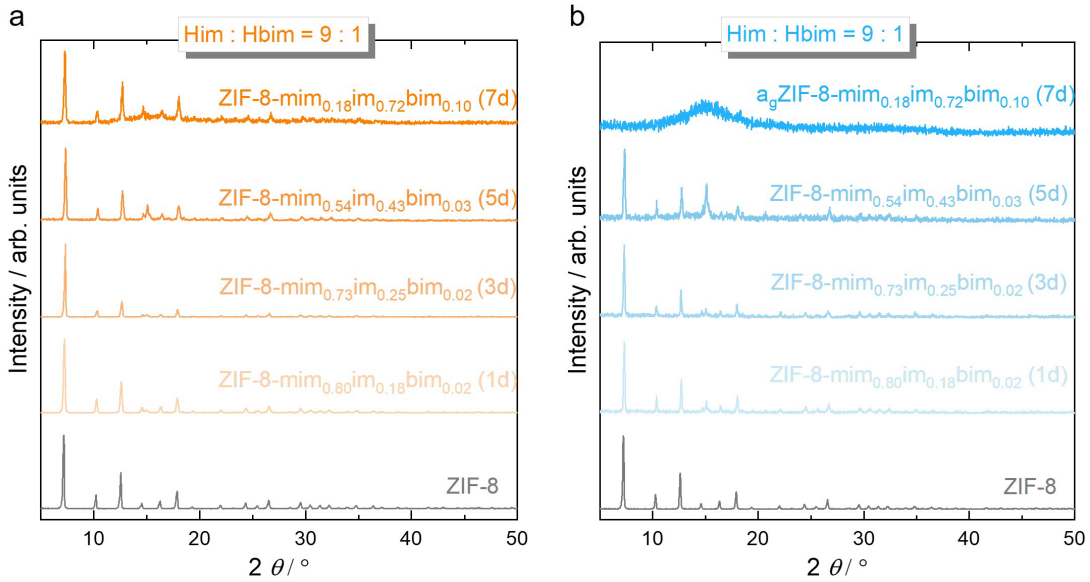

Figure A3.18. **a** XRPD patterns collected for ZIF-8 derivatives after varying SALE reaction times with a solution containing Him and Hbim in a molar ratio of 9:1. **b** Corresponding XRPD patterns of samples obtained after heating the materials to 450 °C followed by rapid cooling to room temperature.

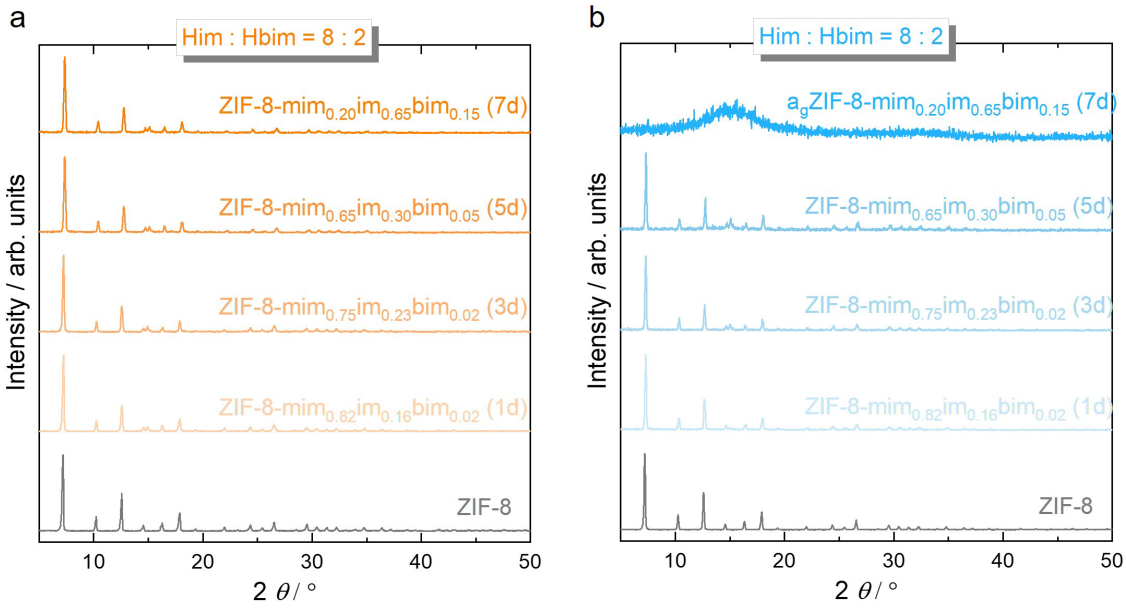

Figure A3.19. **a** XRPD patterns collected for ZIF-8 derivatives after varying SALE reaction times with a solution containing Him and Hbim in a molar ratio of 8:2. **b** Corresponding XRPD patterns of samples obtained after heating the materials to 450 °C followed by rapid cooling to room temperature.

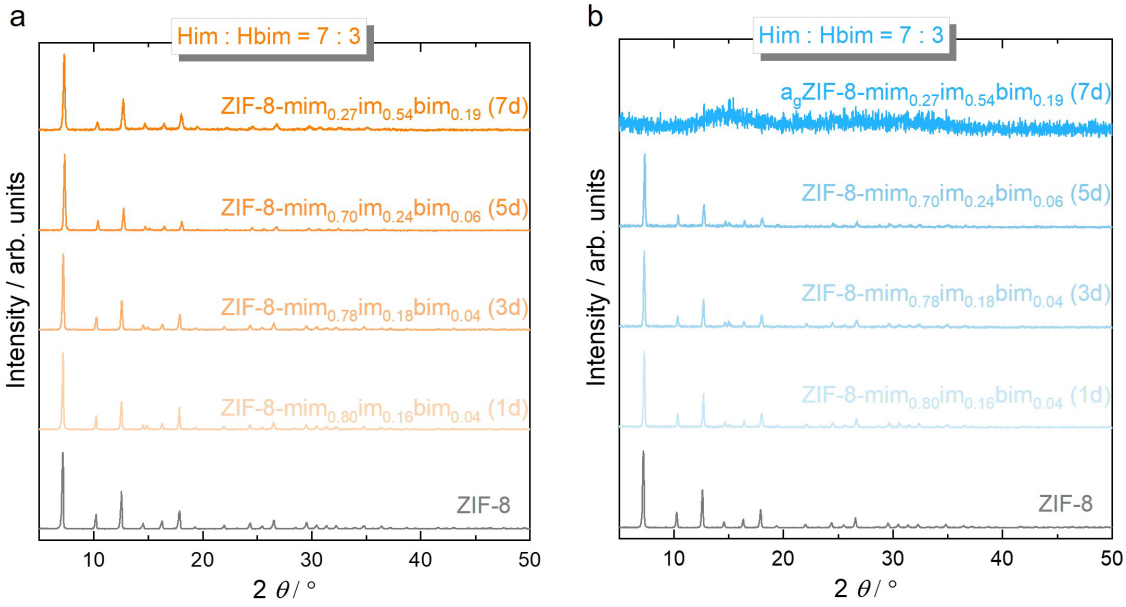

Figure A3.20. **a** XRPD patterns collected for ZIF-8 derivatives after varying SALE reaction times with a solution containing Him and Hbim in a molar ratio of 7:3. **b** Corresponding XRPD patterns of samples obtained after heating the materials to 450 °C followed by rapid cooling to room temperature.

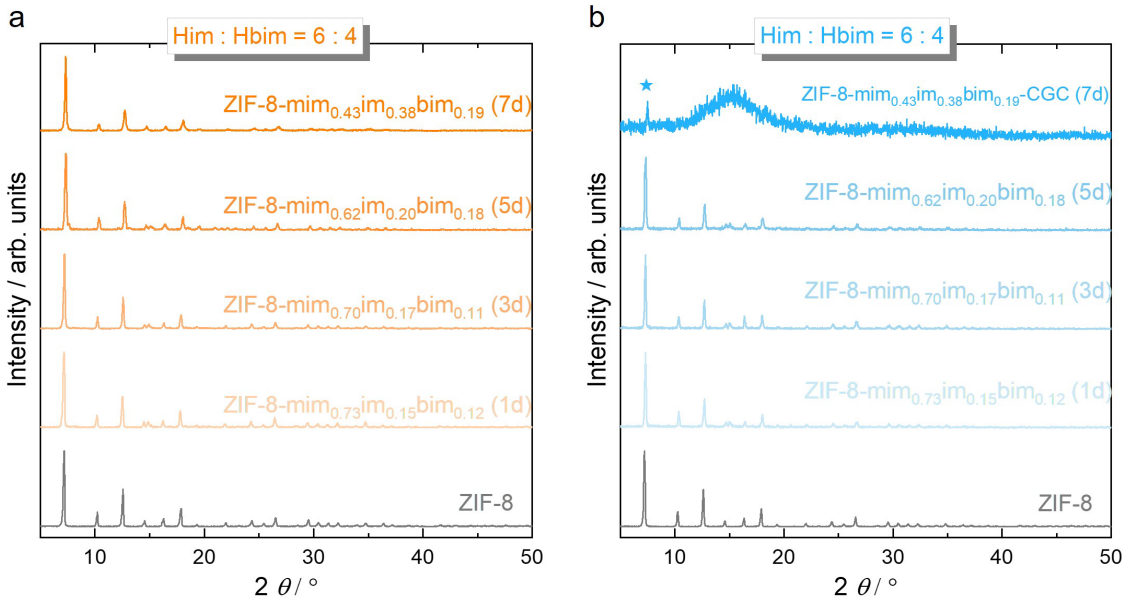

Figure A3.21. a XRPD patterns collected for ZIF-8 derivatives after varying SALE reaction times with a solution containing Him and Hbim in a molar ratio of 6:4. **b** Corresponding XRPD patterns of samples obtained after heating the materials to 450 °C followed by rapid cooling to room temperature.

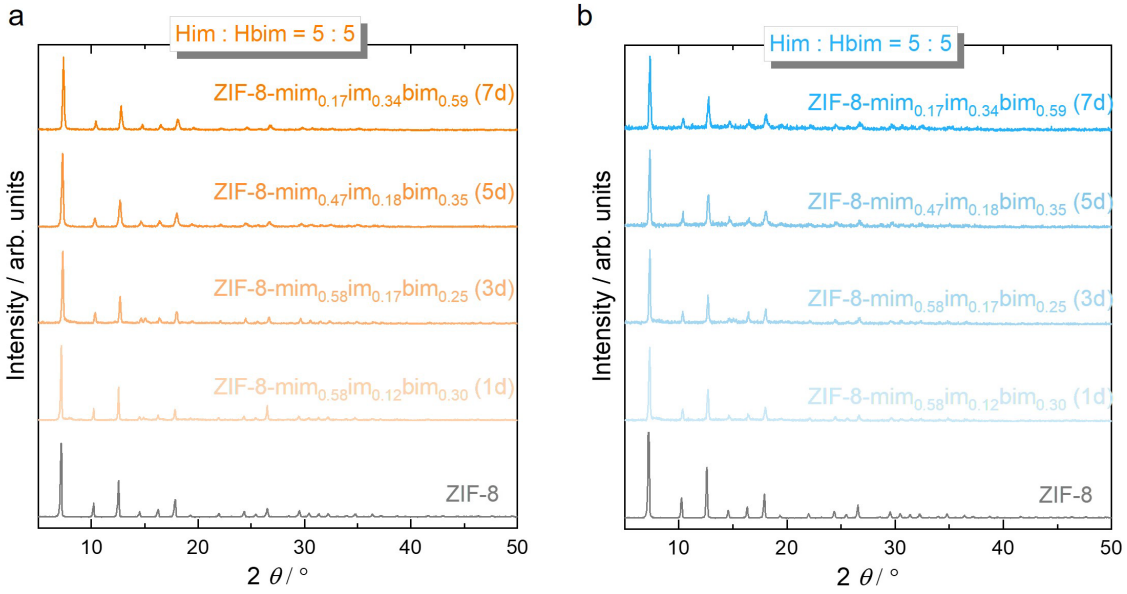

Figure A3.22. a XRPD patterns collected for ZIF-8 derivatives after varying SALE reaction times with a solution containing Him and Hbim in a molar ratio of 5:5. **b** Corresponding XRPD patterns of samples obtained after heating the materials to 450 °C followed by rapid cooling to room temperature.

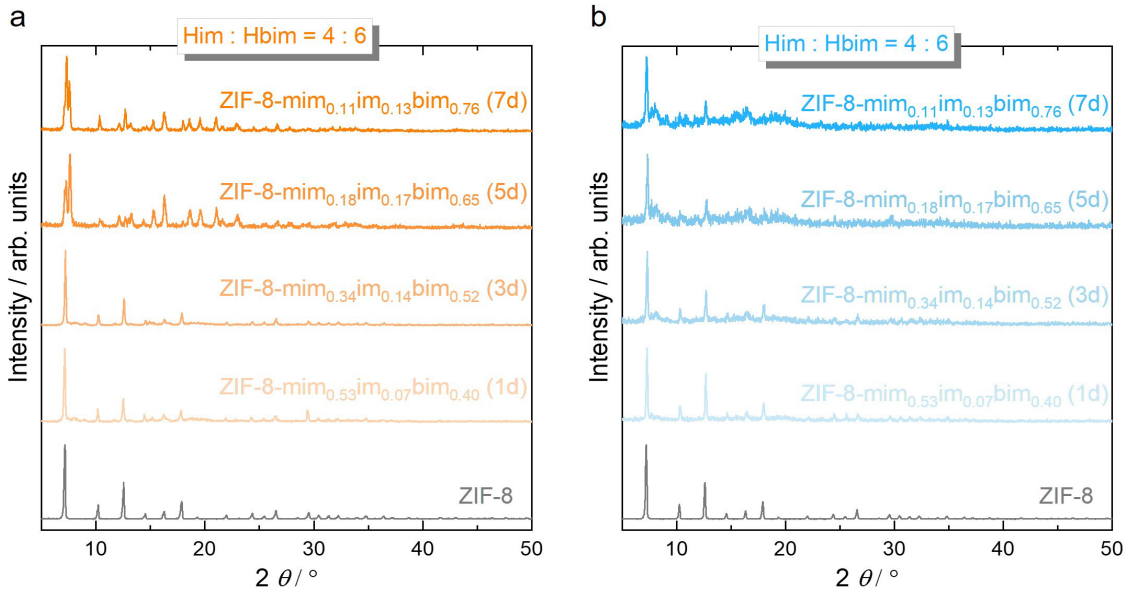

Figure A3.23. a XRPD patterns collected for ZIF-8 derivatives after varying SALE reaction times with a solution containing Him and Hbim in a molar ratio of 4:6. **b** Corresponding XRPD patterns of samples obtained after heating the materials to 450 °C followed by rapid cooling to room temperature. For the samples with 5 and 7 days SALE time, the presence of a large amount of bim^- led to the heavily distorted rhombohedral or triclinic **sod** phase typical for ZIF-7 ($Zn(bim)_2$) (validated by Pawley fitting, see **Figure A3.33Figure A3.32**). The subsequent samples obtained by SALE solutions with higher molar fractions of bim^- were all the ZIF-7/8 mixed phase.

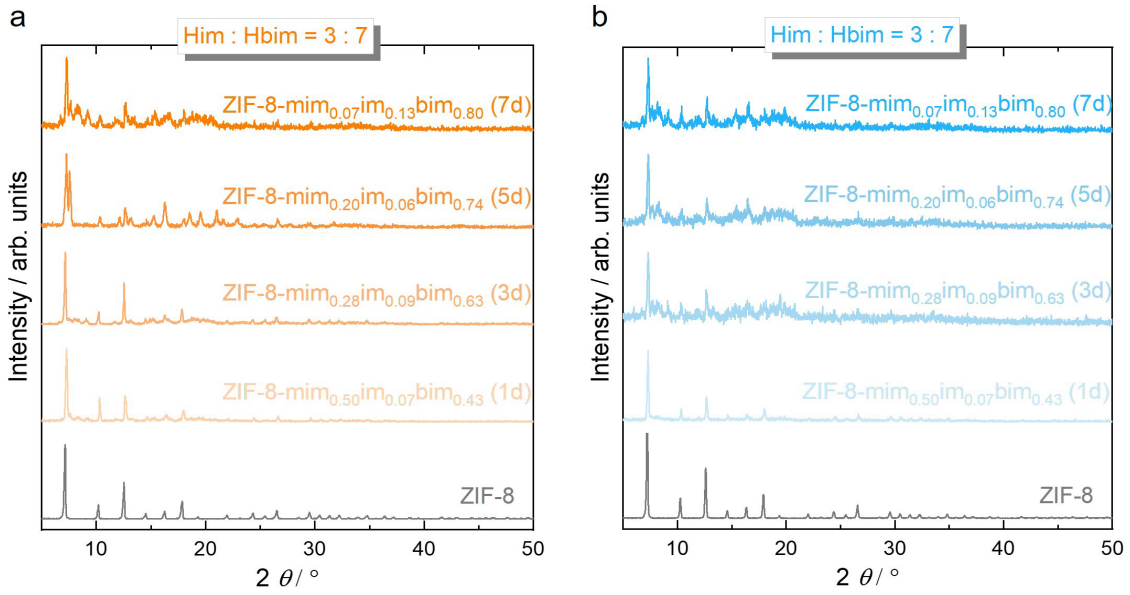

Figure A3.24. a XRPD patterns collected for ZIF-8 derivatives after varying SALE reaction times with a solution containing Him and Hbim in a molar ratio of 3:7. **b** Corresponding XRPD patterns of samples obtained after heating the materials to 450 °C followed by rapid cooling to room temperature. Similar to the above, the samples after 3 and 7 days of SALE are ZIF-7/8 mixed phase.

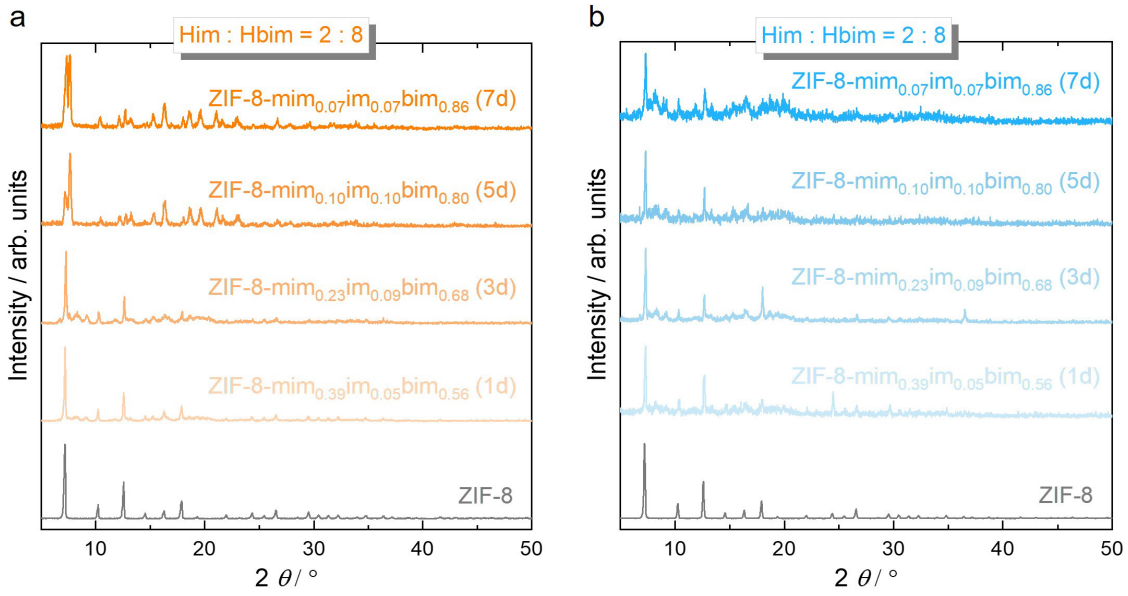

Figure A3.25. a XRPD patterns collected for ZIF-8 derivatives after varying SALE reaction times with a solution containing Him and Hbim in a molar ratio of 2:8. **b** Corresponding XRPD patterns of samples obtained after heating the materials to 450 °C followed by rapid cooling to room temperature. Similar to the above, the samples after 3 and 7 days of SALE are ZIF-7/8 mixed phase.

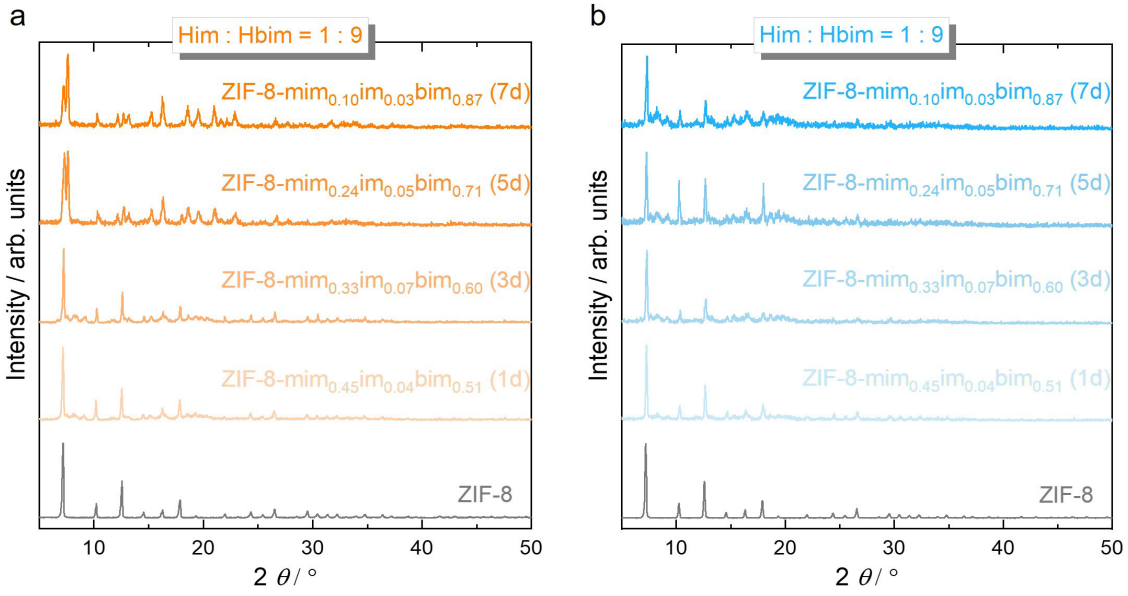

Figure A3.26. a XRPD patterns collected for ZIF-8 derivatives after varying SALE reaction times with a solution containing Him and Hbim in a molar ratio of 1:9. **b** Corresponding XRPD patterns of samples obtained after heating the materials to 450 °C followed by rapid cooling to room temperature. Similar to the above, the samples after 3 and 7 days of SALE are ZIF-7/8 mixed phase.

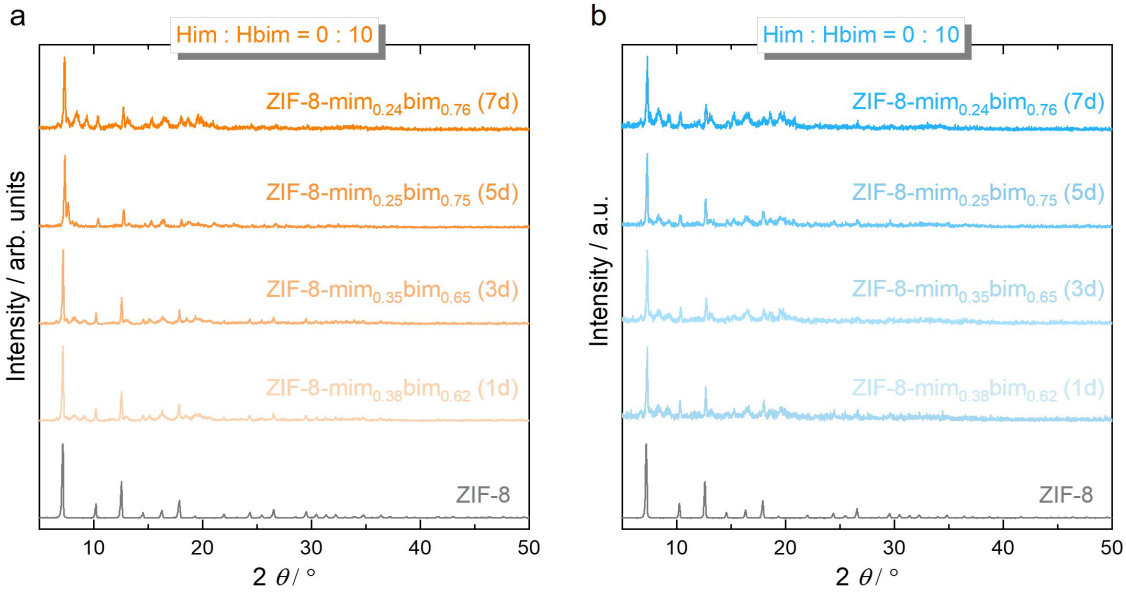

Figure A3.27. a XRPD patterns collected for ZIF-8 derivatives after varying SALE reaction times with a solution containing only Hbim. **b** Corresponding XRPD patterns of samples obtained after heating the materials to 450 °C followed by rapid cooling to room temperature. Similar to the above, all the samples here are ZIF-7/8 mixed phase.

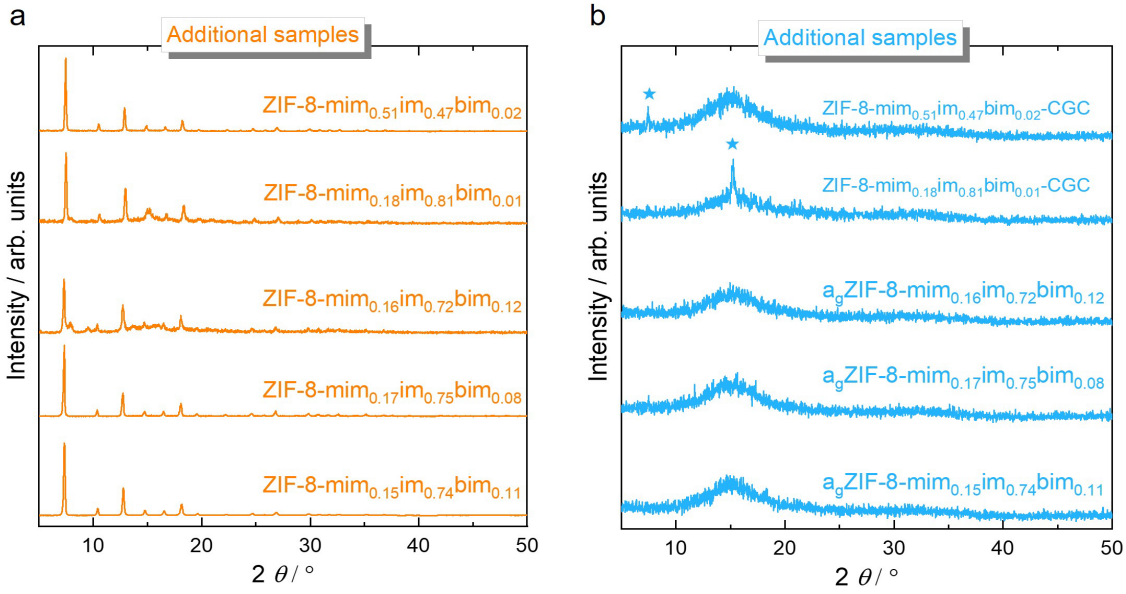

Figure A3.28. a XRPD patterns collected for ZIF-8 derivatives after varying SALE reaction times with a solution containing Him and Hbim in other molar ratios (**Table A3.1**). **b** Corresponding XRPD patterns of samples obtained after heating the materials to 430 or 450 °C followed by rapid cooling to room temperature. The reflections marked with an asterisk stem from crystalline ZIF-8 in the case of ZIF-8-$mim_{0.51}im_{0.47}bim_{0.02}$-CGC and crystalline ZIF-61 in the case of ZIF-8-$mim_{0.18}im_{0.81}bim_{0.01}$-CGC.

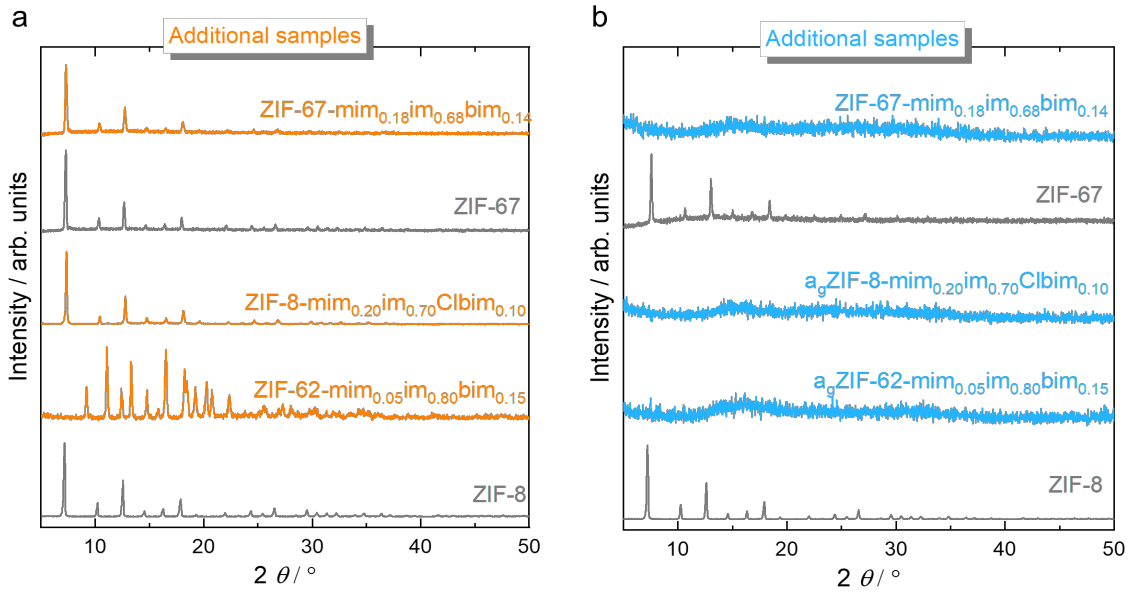

Figure A3.29. **a** XRPD patterns collected for ZIF-8 and ZIF-67 derivatives after varying SALE reaction times with a solution containing Him and Hbim or HClbim in other molar ratios **Table A3.1**). **b** Corresponding XRPD patterns of samples obtained after heating the corresponding samples to 440 or 450 °C followed by rapid cooling to room temperature. ZIF-62-mim$_{0.05}$im$_{0.80}$bim$_{0.15}$ was derived by stirring the SALE solution with ZIF-8 for 15 min per day (total SALE time was 3 days).

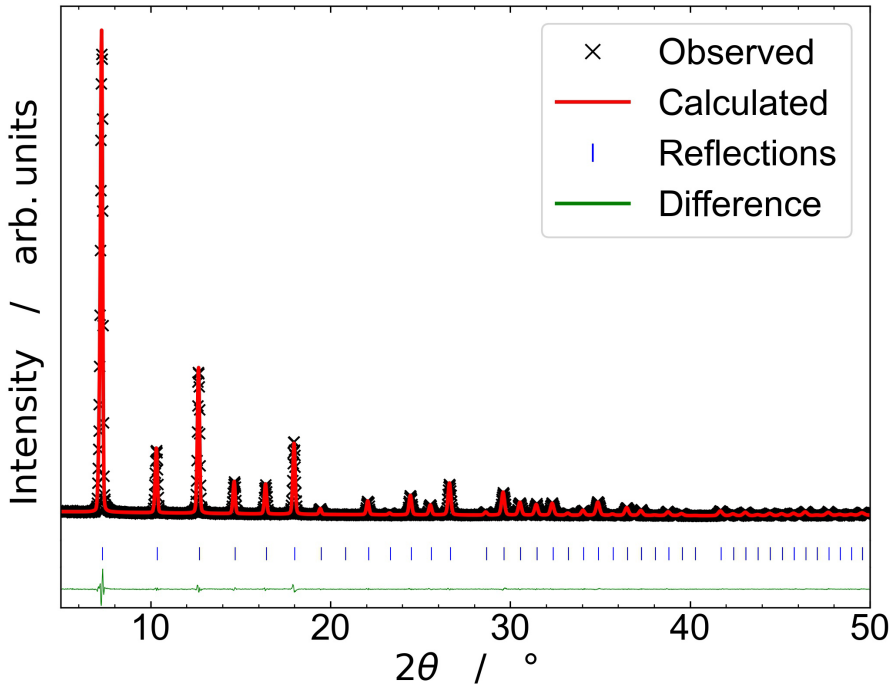

Figure A3.30. Profile fit (Pawley method) performed on the XRPD pattern of ZIF-8. The blue tick marks indicate the positions of allowed Bragg peaks of crystalline ZIF-8.

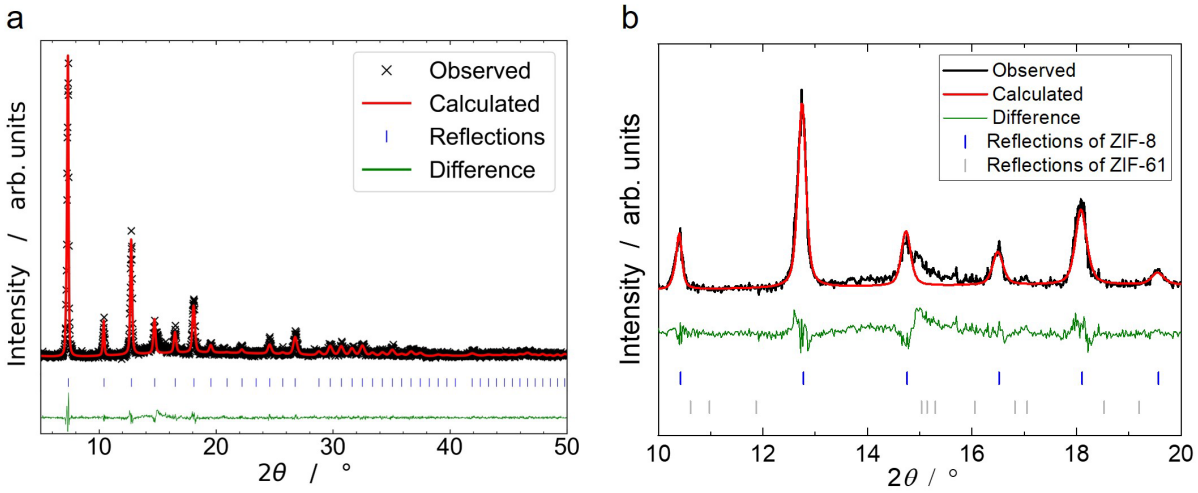

Figure A3.31. a Profile fit (Pawley method) performed on the XRPD pattern of ZIF-8-$mim_{0.15}im_{0.85}$. The blue tick marks indicate the positions of allowed Bragg peaks for ZIF-8. **b** Magnified view of the Pawley fit showing the fraction from 10° to 20°. The part that cannot be fitted is the characteristic peak of the **zni** phase ($2\theta = 15.1°$), i.e. ZIF-61. The blue tick marks indicate the Bragg peak positions of ZIF-8, and the gray tick marks indicate the Bragg peak positions of ZIF-61.

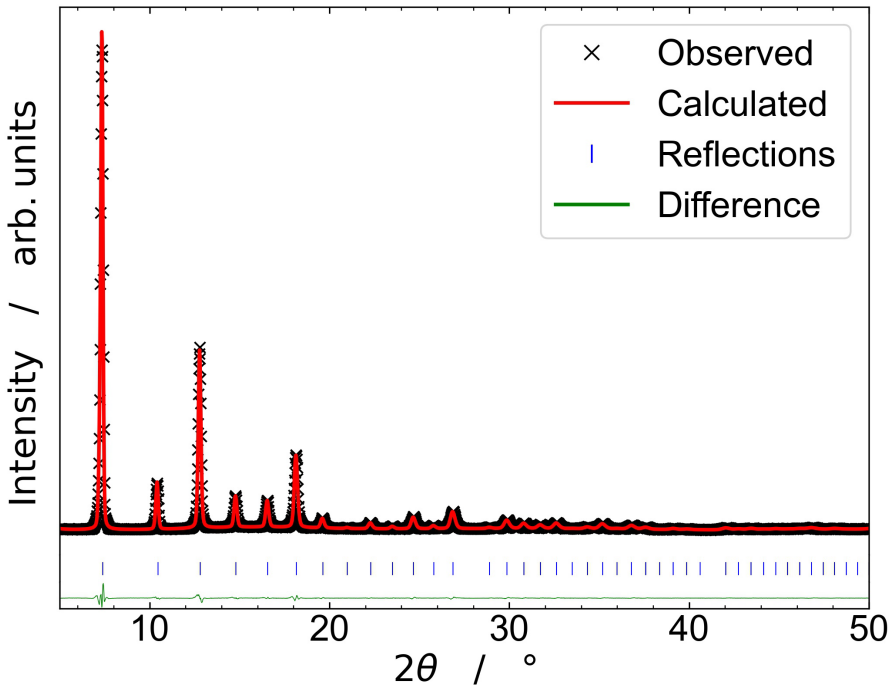

Figure A3.32. Profile fit (Pawley method) performed on the XRPD pattern of ZIF-8-$mim_{0.15}im_{0.74}bim_{0.11}$. The blue tick marks indicate the positions of allowed Bragg peaks of crystalline ZIF-8.

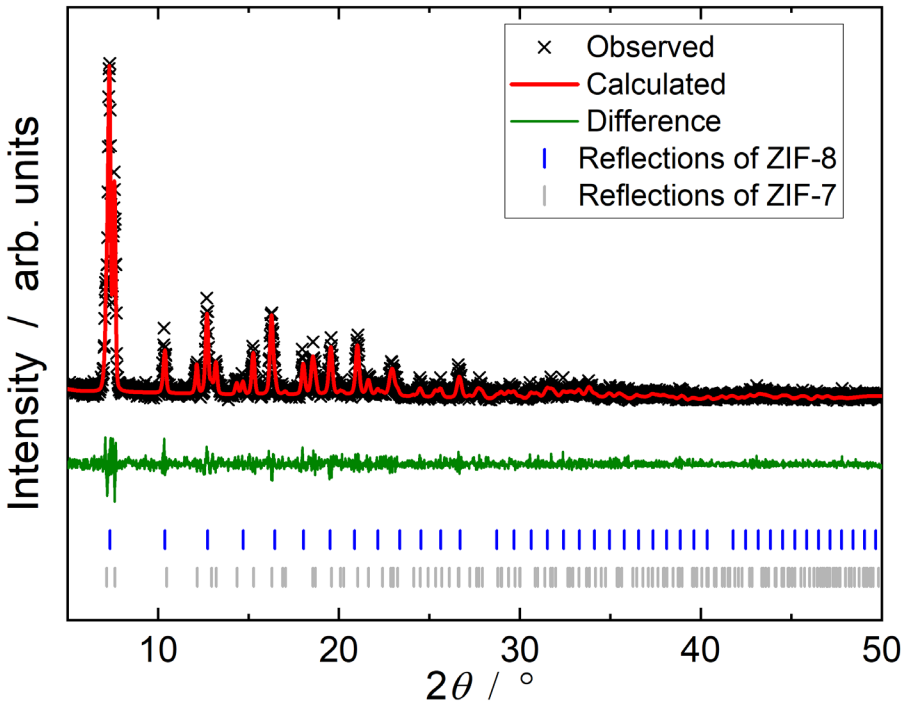

Figure A3.33. Mixed-phase profile fit (Pawley method) performed on the XRPD pattern of ZIF-8-$mim_{0.11}im_{0.13}bim_{0.76}$. The blue tick marks indicate the positions of allowed Bragg peaks. The blue tick marks indicate the Bragg peak positions of ZIF-8, and the gray tick marks indicate the Bragg peak positions of ZIF-7.

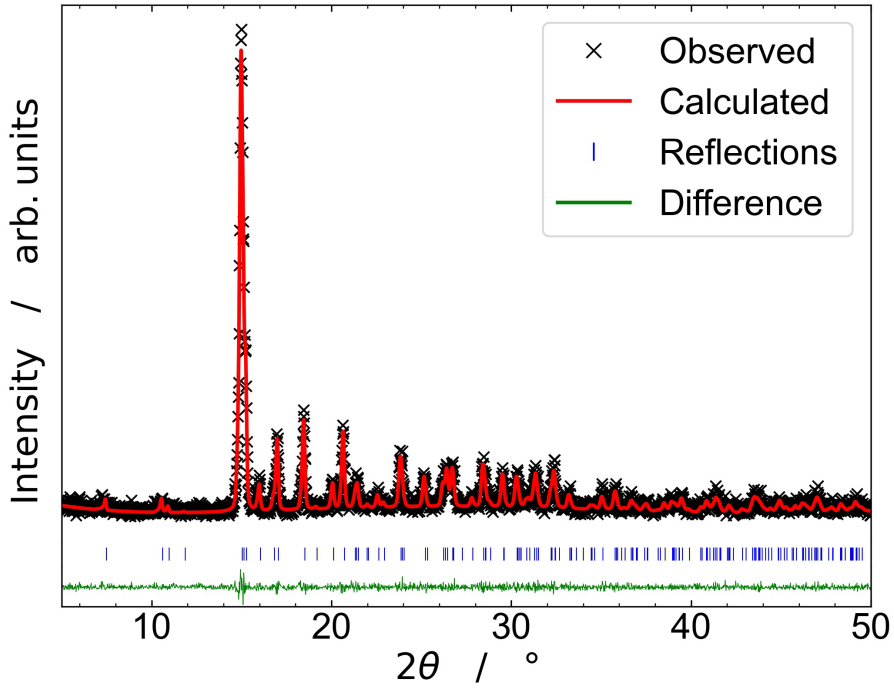

Figure A3.34. Profile fit (Pawley method) performed on the XRPD pattern of ZIF-61-$mim_{0.15}im_{0.85}$ (recrystallized ZIF-8-$mim_{0.15}im_{0.85}$). The blue tick marks indicate the positions of allowed Bragg peaks of crystalline ZIF-61.

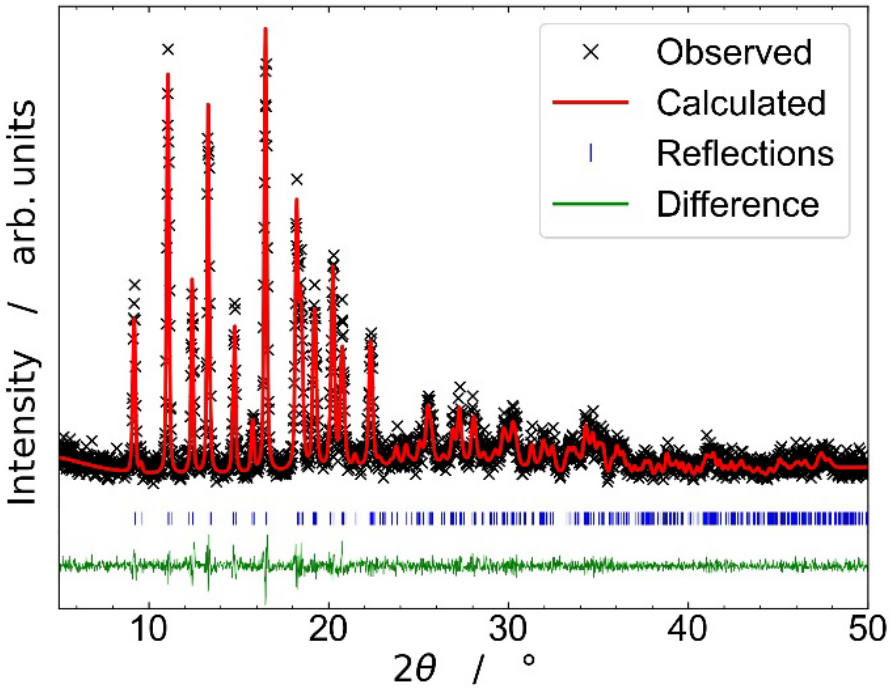

Figure A3.35. Profile fit (Pawley method) performed on the XRPD pattern of ZIF-62-$mim_{0.05}im_{0.80}bim_{0.15}$ (a recrystallized ZIF-8 sample obtained by stirring the SALE reaction mixture for 15 min/day with a total reaction time of 3 days). The blue tick marks indicate the positions of allowed Bragg peaks of crystalline ZIF-62.

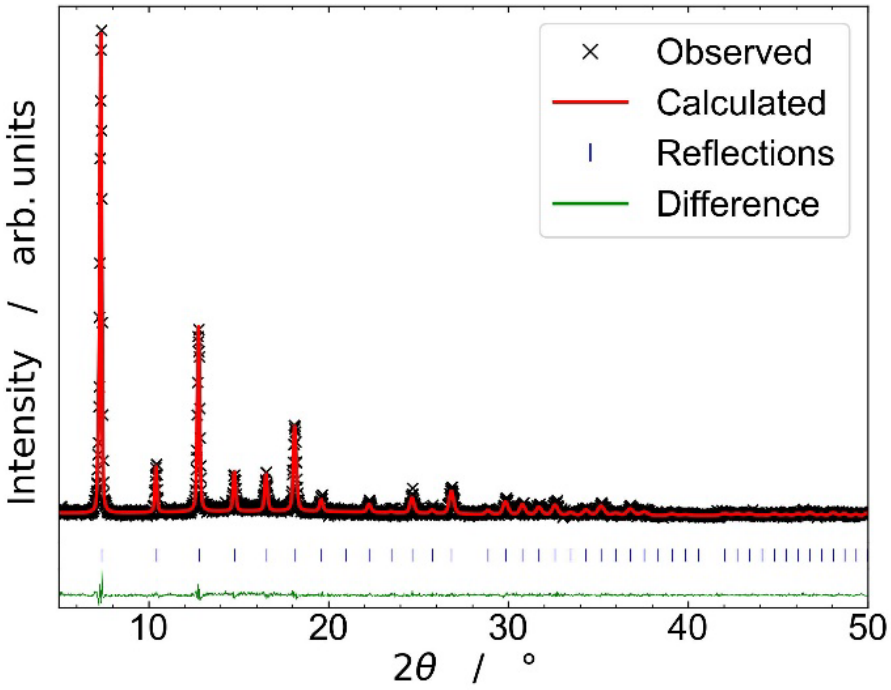

Figure A3.36. Profile fit (Pawley method) performed on the XRPD pattern of ZIF-8-$mim_{0.20}im_{0.70}Clbim_{0.10}$. The blue tick marks indicate the positions of allowed Bragg peaks of crystalline ZIF-8.

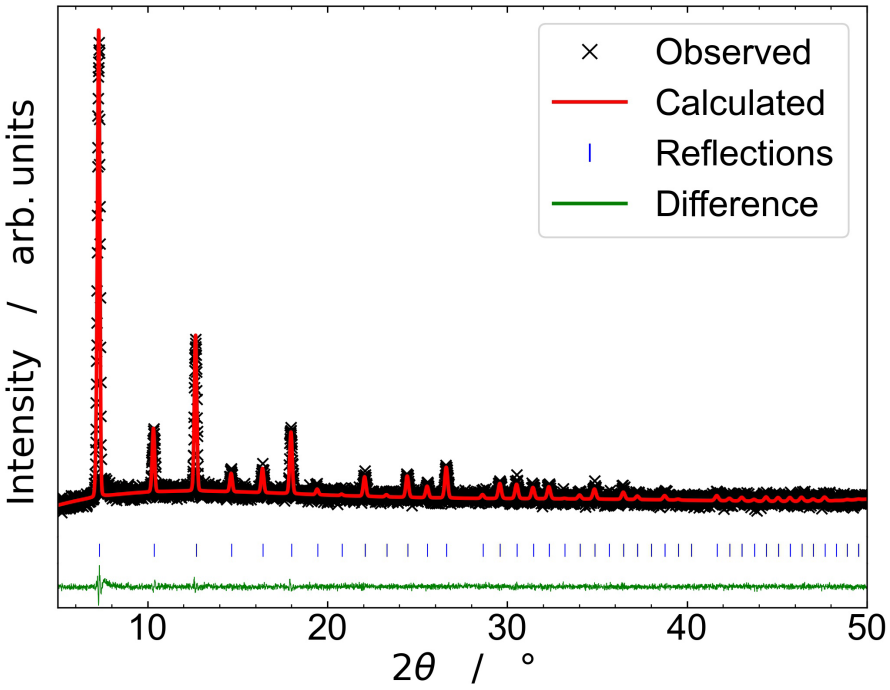

Figure A3.37. Profile fit (Pawley method) performed on the XRPD pattern of ZIF-67. The blue tick marks indicate the positions of allowed Bragg peaks of crystalline ZIF-67.

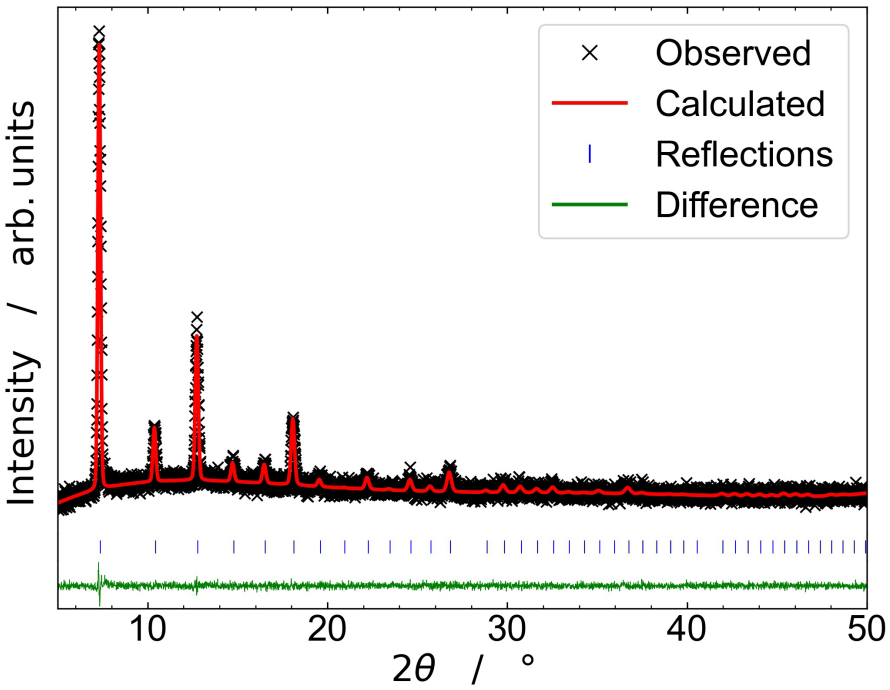

Figure A3.38. Profile fit (Pawley method) performed on the XRPD pattern of ZIF-67-$mim_{0.18}im_{0.68}bim_{0.14}$. The blue tick marks indicate the positions of allowed Bragg peaks of crystalline ZIF-67.

Table A3.2. Unit cell parameters and corresponding R_{wp}, R_{exp} and χ values determined by the above displayed structureless profile fits (Pawley method).

Sample	ZIF-8	ZIF-8-$mim_{0.15}im_{0.85}$	ZIF-8-$mim_{0.15}im_{0.71}bim_{0.11}$	ZIF-8-$mim_{0.11}im_{0.13}bim_{0.76}$		ZIF-61-$mim_{0.15}im_{0.85}$	ZIF-62-$mim_{0.05}im_{0.80}bim_{0.15}$	ZIF-8-$mim_{0.20}im_{0.70}Clbim_{0.10}$	ZIF-67	ZIF-67-$mim_{0.18}im_{0.68}bim_{0.14}$
crystal system	cubic	cubic	cubic	cubic (ZIF-8)	trigonal (ZIF-7)	tetragonal	orthorhombic	cubic	cubic	cubic
space group	*I-43m*	*I-43m*	*I-43m*	*I-43m*	*R-3*	$I4_1cd$	*Pbca*	*I-43m*	*I-43m*	*I-43m*
a / Å	17.0466(10)	16.961(3)	16.9063(8)	17.009(6)	23.170(9)	23.555(8)	15.708(11)	16.913(2)	17.049(3)	16.924(6)
b / Å	17.0466(10)	16.961(3)	16.9063(8)	17.009(6)	23.170(9)	23.555(8)	15.923(10)	16.913(2)	17.049(3)	16.924(6)
c / Å	17.0466(10)	16.961(3)	16.9063(8)	17.009(6)	15.583(7)	12.490(4)	18.329(19)	16.913(2)	17.049(3)	16.924(6)
α / °	90	90	90	90	90	90	90	90	90	90
β / °	90	90	90	90	90	90	90	90	90	90
γ / °	90	90	90	90	120	90	90	90	90	90
V / Å^3	4953.5(9)	4879(3)	4832.2(7)	4921(5)	7245(6)	6930(5)	4585(6)	4838(2)	4956(3)	4848(5)
R_{wp} / %	22.37	25.04	7.75	28.03		25.61	23.30	21.00	5.56	5.47
R_{exp} / %	14.97	19.43	3.10	23.67		23.60	19.82	17.78	5.15	5.20
χ	1.49	1.29	2.50	1.18		1.09	1.18	1.18	1.08	1.05

A.3.2.2 – Variable temperature XRPD

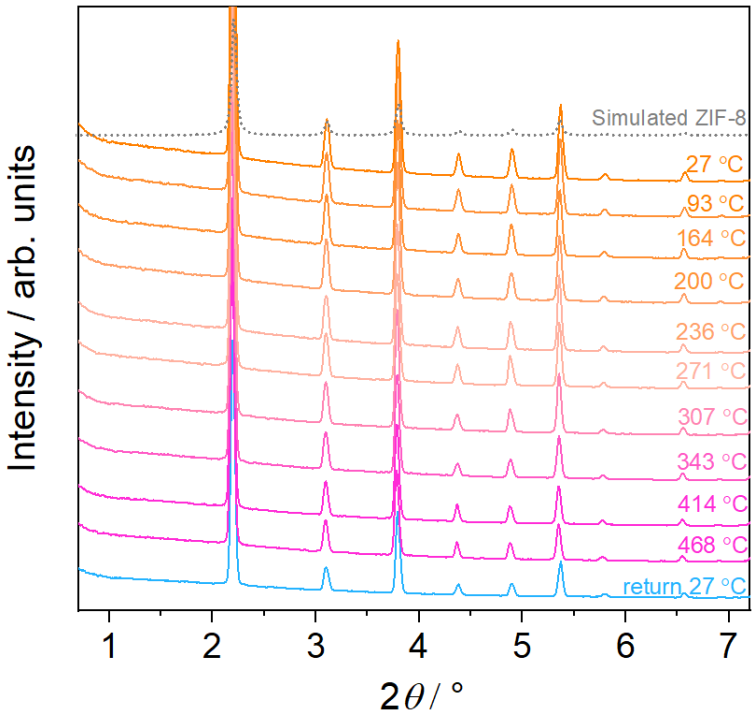

Figure A3.39. Temperature dependent XRPD patterns (λ = 0.45920 Å) of ZIF-8. The patterns are not normalized but vertically offset for clarity. The corresponding contour map is shown in **Figure 3.2a** left.

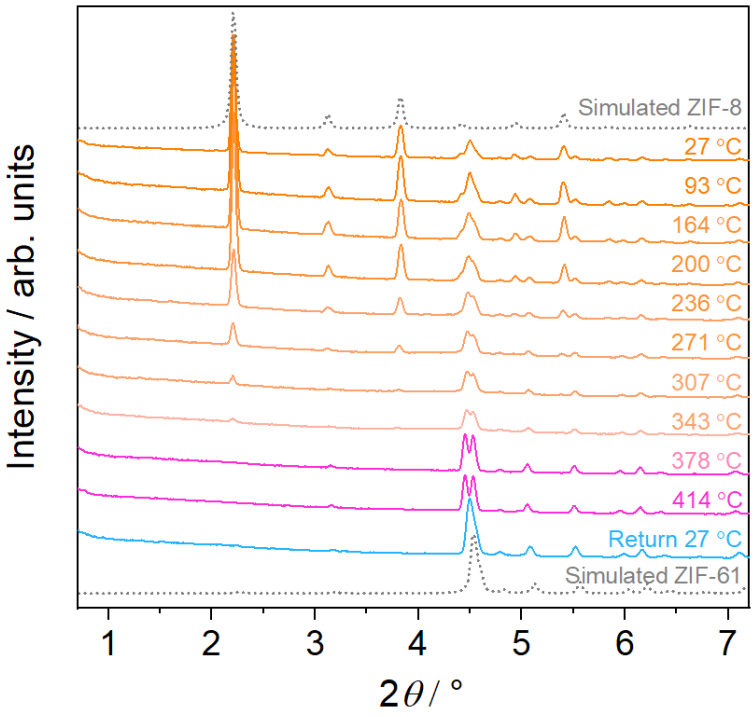

Figure A3.40. Temperature dependent XRPD patterns (λ = 0.45920 Å) of ZIF-8-$mim_{0.15}im_{0.85}$. The patterns are not normalized but vertically offset for clarity. The corresponding contour map is shown in **Figure 3.2a** middle.

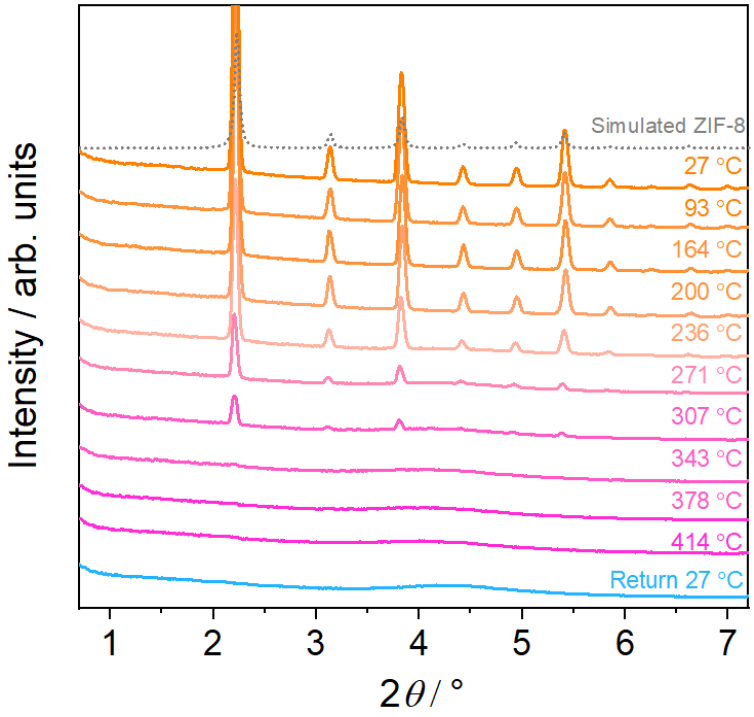

Figure A3.41. Temperature dependent XRPD patterns (λ = 0.45920 Å) of ZIF-8-mim$_{0.15}$im$_{0.74}$bim$_{0.11}$. The patterns are not normalized but vertically offset for clarity. The corresponding contour map is shown in **Figure 3.2a** right.

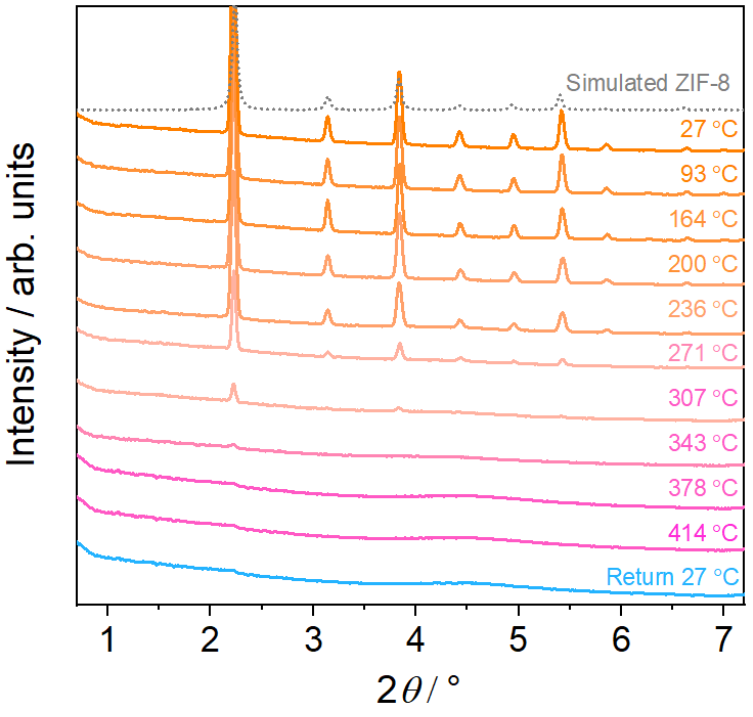

Figure A3.42. Temperature dependent XRPD patterns (λ = 0.45920 Å) of ZIF-8-mim$_{0.17}$im$_{0.75}$bim$_{0.08.}$ The patterns are not normalized but vertically offset for clarity.

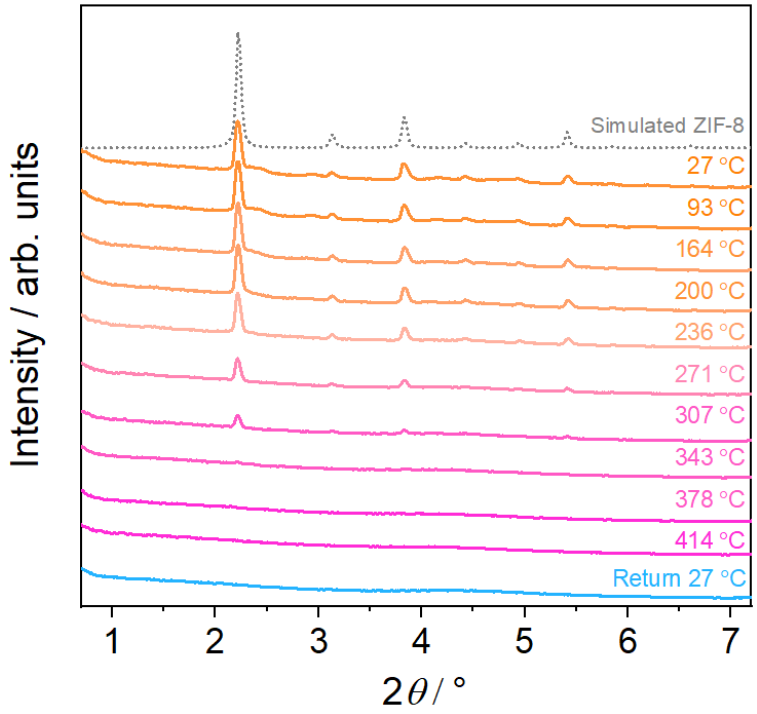

Figure A3.43. Temperature dependent XRPD patterns (λ = 0.45920 Å) of ZIF-8-mim$_{0.16}$im$_{0.72}$bim$_{0.12}$. The patterns are not normalized but vertically offset for clarity.

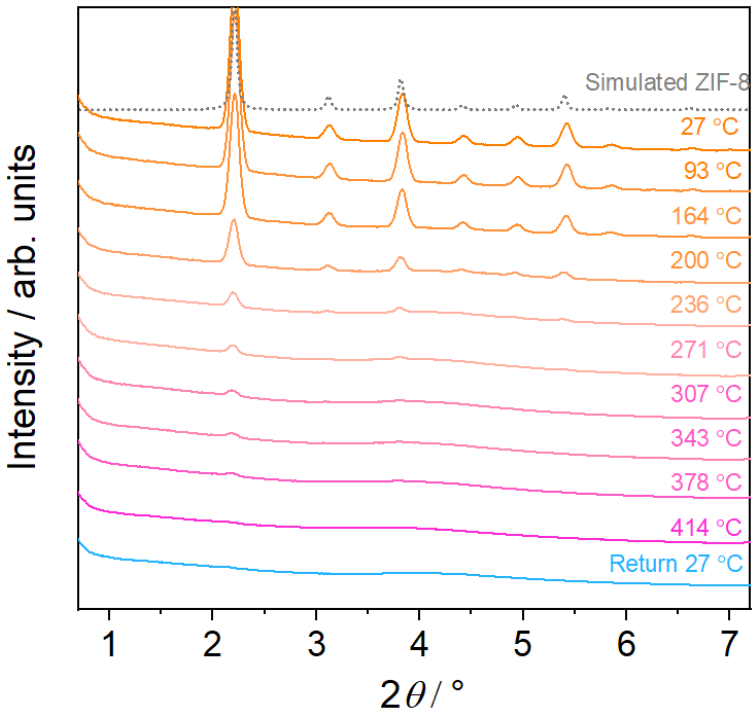

Figure A3.44. Temperature dependent XRPD patterns (λ = 0.45920 Å) of ZIF-8-mim$_{0.27}$im$_{0.54}$bim$_{0.19}$. The patterns are not normalized but vertically offset for clarity.

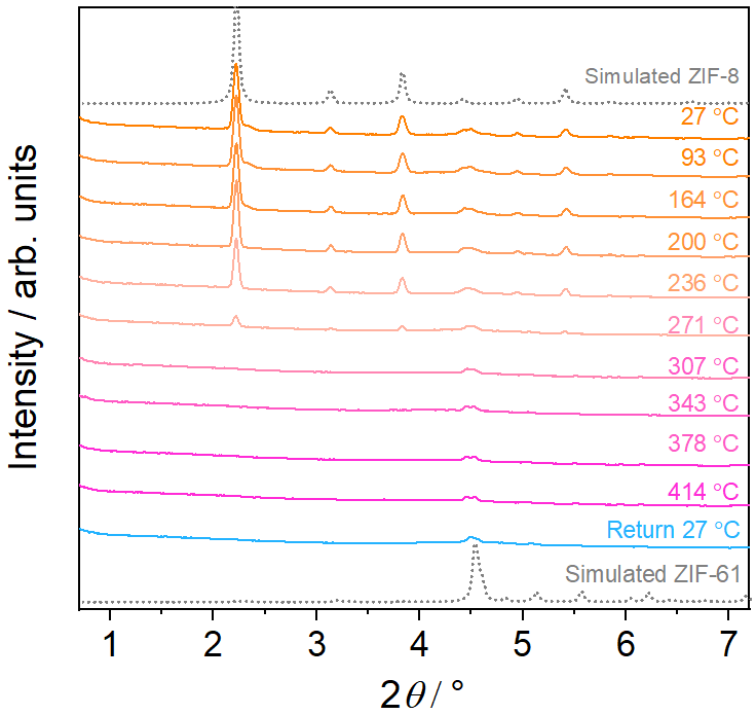

Figure A3.45. Temperature dependent XRPD patterns (λ = 0.45920 Å) of ZIF-8-mim$_{0.18}$im$_{0.81}$bim$_{0.01}$. The patterns are not normalized but vertically offset for clarity.

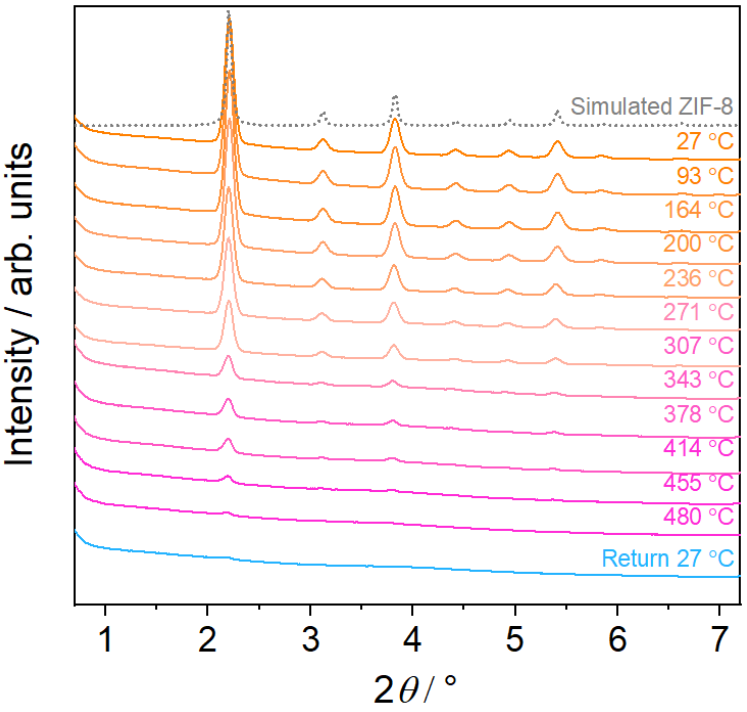

Figure A3.46. Temperature dependent XRPD patterns (λ = 0.45920 Å) of ZIF-8-mim$_{0.43}$im$_{0.38}$bim$_{0.19}$. The patterns are not normalized but vertically offset for clarity.

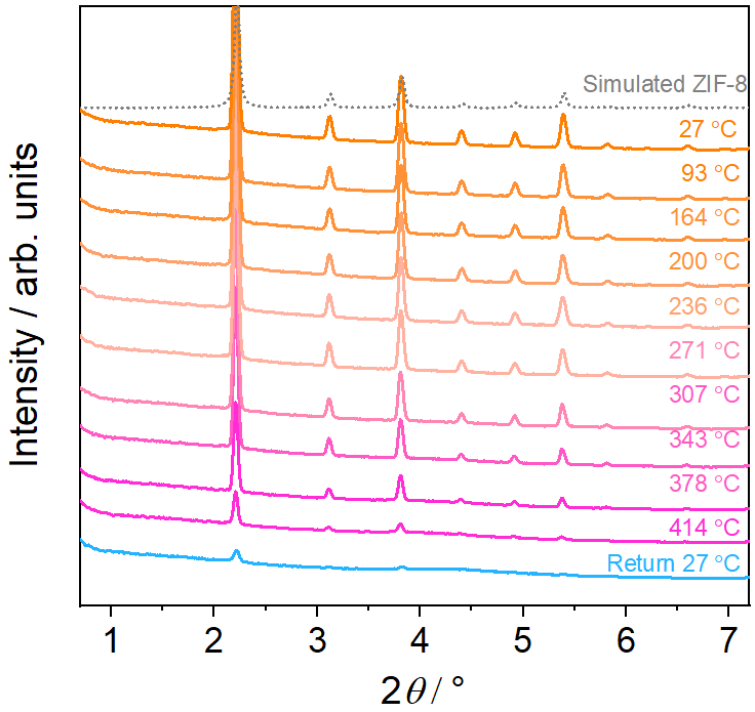

Figure A3.47. Temperature dependent XRPD patterns (λ = 0.45920 Å) of ZIF-8-mim$_{0.51}$im$_{0.47}$bim$_{0.02}$. The patterns are not normalized but vertically offset for clarity.

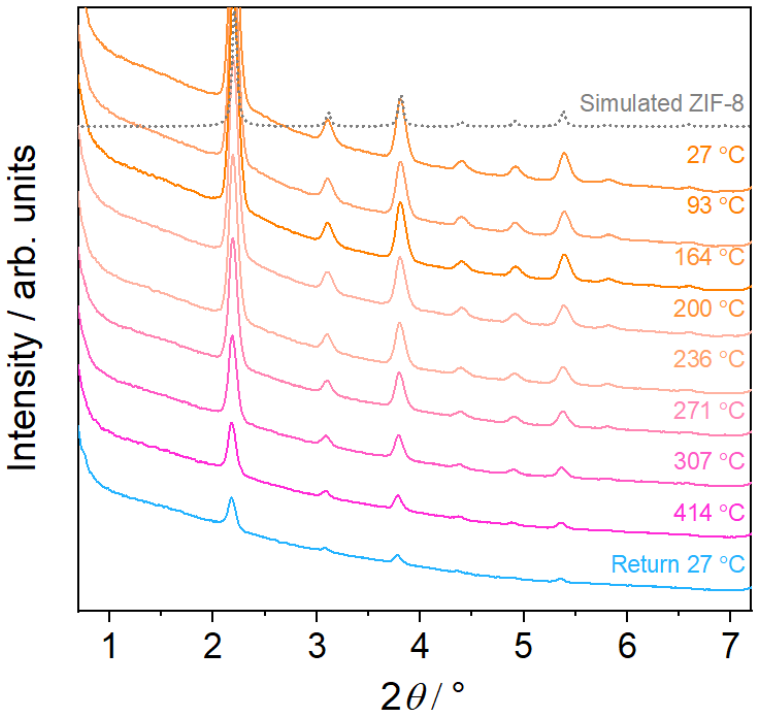

Figure A3.48. Temperature dependent XRPD patterns (λ = 0.45920 Å) of ZIF-8-mim$_{0.17}$im$_{0.34}$bim$_{0.49}$. The patterns are not normalized but vertically offset for clarity.

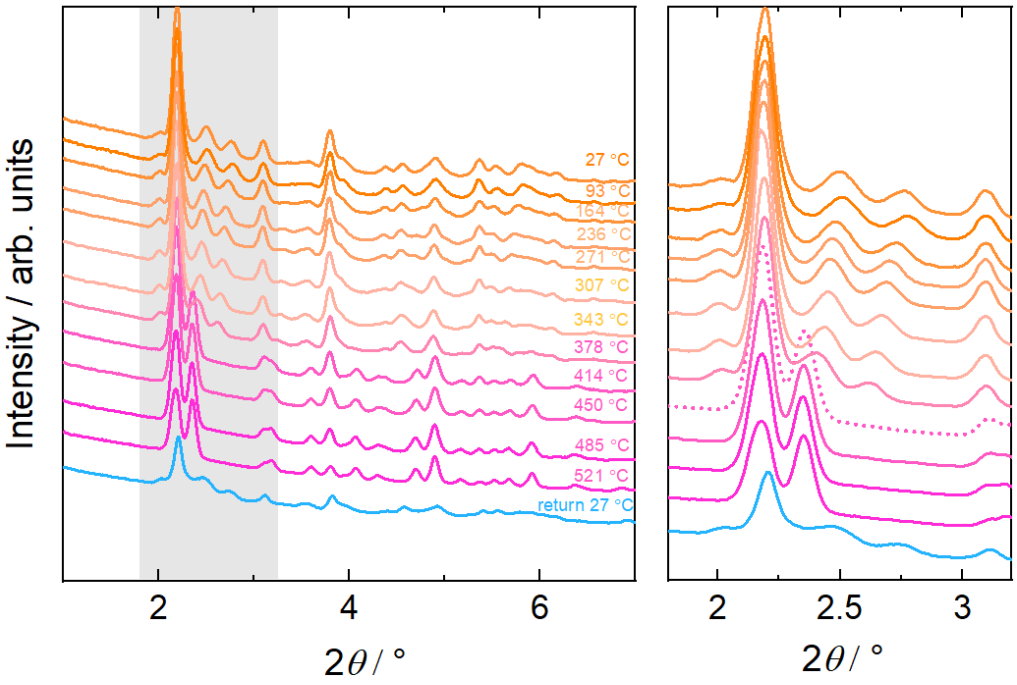

Figure A3.49. Temperature dependent XRPD patterns (λ = 0.45920 Å) of ZIF-8-mim$_{0.24}$bim$_{0.76}$. The patterns are not normalized but vertically offset for clarity. The material clearly consists of a phase mixture of ZIF-8 (i.e. the cubic **sod** phase) and ZIF-7 (i.e. a distorted **sod** phase with triclinic symmetry at low temperature and rhombohedral symmetry at high temperature[162]).

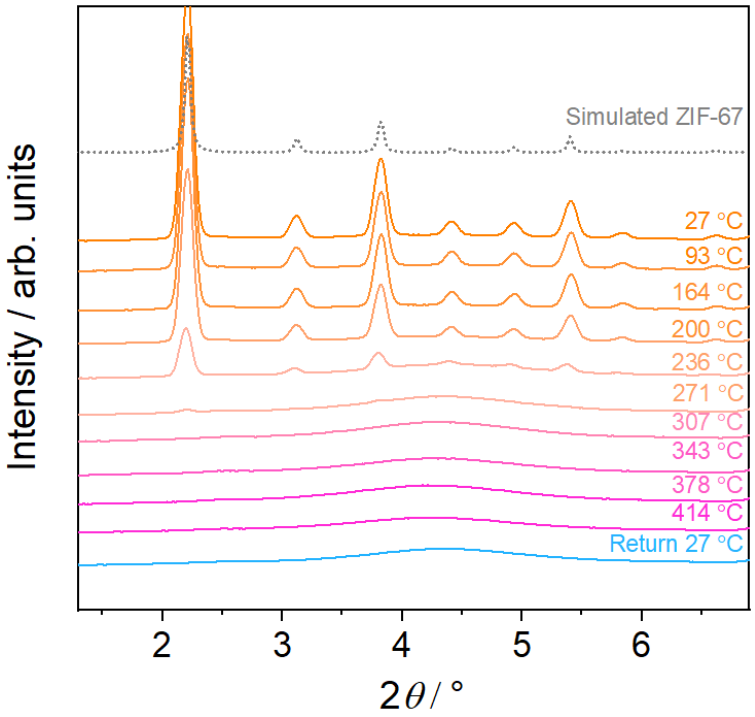

Figure A3.50. Temperature dependent XRPD patterns (λ = 0.45920 Å) of ZIF-67-mim$_{0.18}$im$_{0.68}$bim$_{0.14}$. The patterns are not normalized but vertically offset for clarity.

A.3.3 – X-ray total scattering

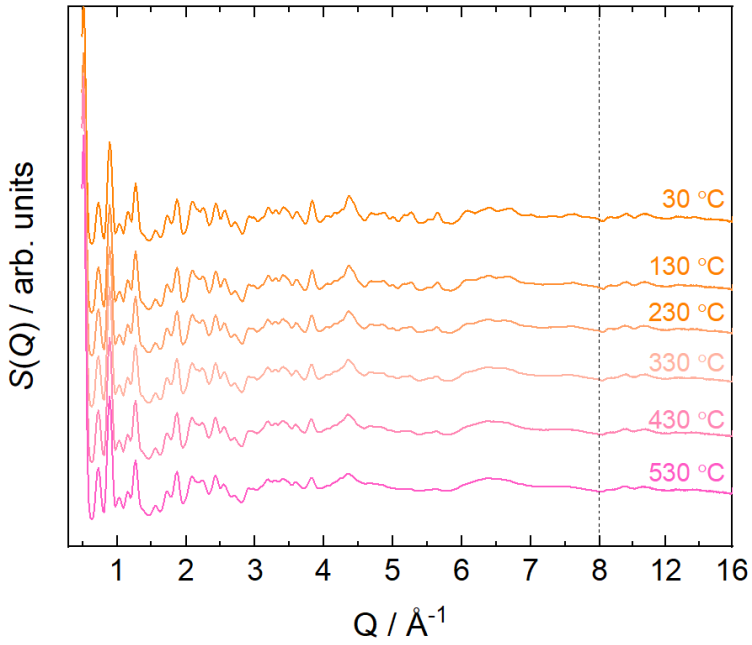

Figure A3.51. Temperature dependent X-ray total scattering data in the form of $S(Q)$ of ZIF-8. The corresponding PDF data in the form of $D(r)$ are shown in **Figure 3.2**. The vertical axis below 8 Å^{-1} is displayed magnified to show the variation of the scattering function in more detail.

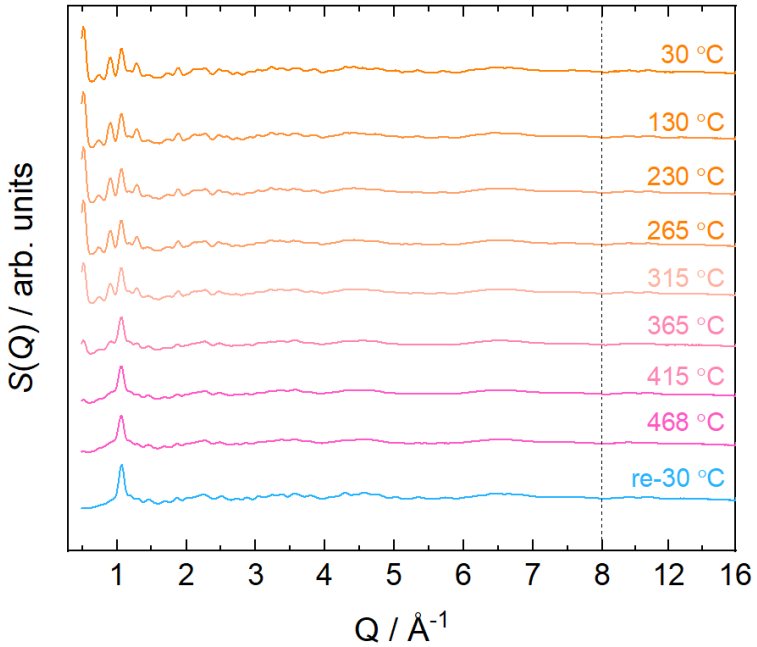

Figure A3.52. Temperature dependent X-ray total scattering data in the form of $S(Q)$ of ZIF-8-mim$_{0.15}$im$_{0.85}$. The corresponding PDF data in the form of $D(r)$ are shown in **Figure 3.2**. The vertical axis below 8 Å^{-1} is displayed magnified to show the variation of the scattering function in more detail.

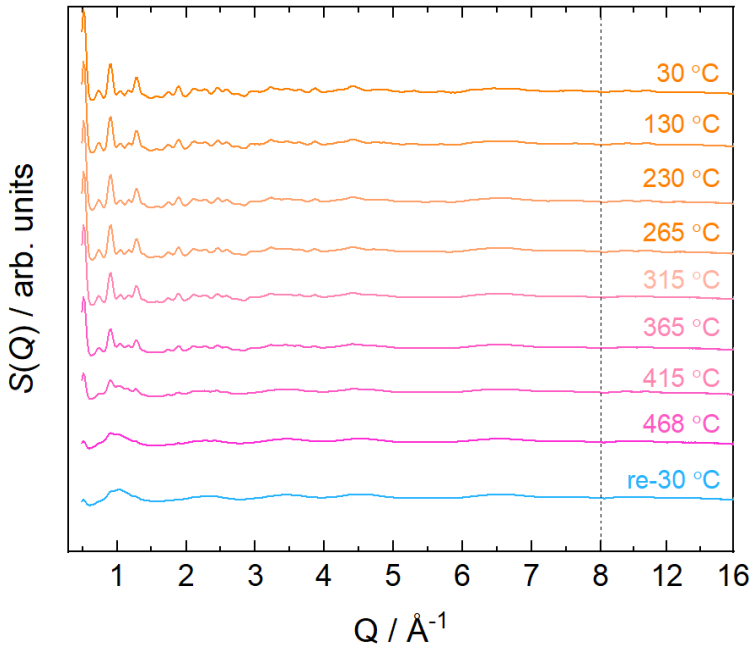

Figure A3.53. Temperature dependent X-ray total scattering data in the form of $S(Q)$ of ZIF-8-mim$_{0.15}$im$_{0.74}$bim$_{0.11}$. The corresponding PDF data in the form of $D(r)$ are shown in **Figure 3.2**. The vertical axis below 8 Å^{-1} is displayed magnified to show the variation of the scattering function in more detail.

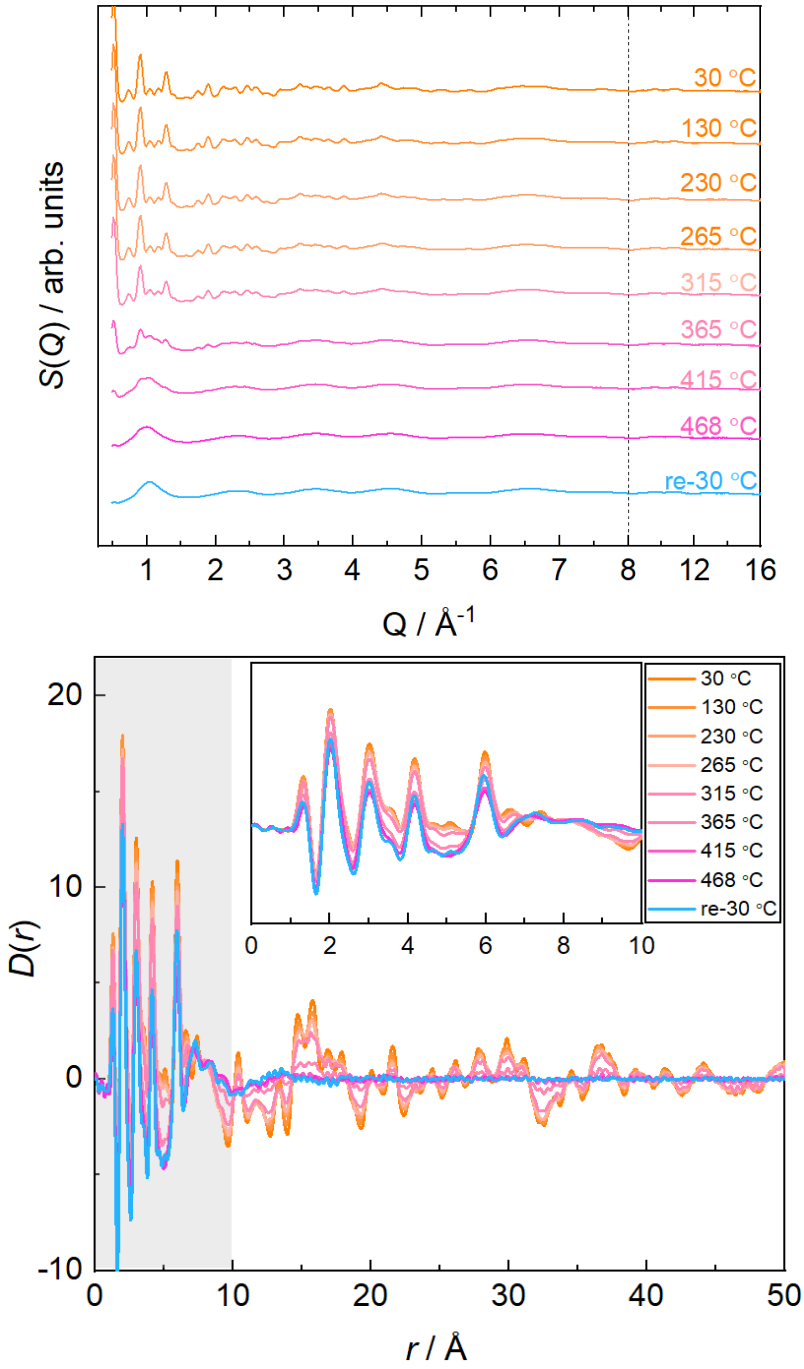

Figure A3.54. Top: Temperature dependent X-ray total scattering data in the form of $S(Q)$ data of ZIF-8-mim$_{0.17}$im$_{0.75}$bim$_{0.08}$. The vertical axis below 8 Å^{-1} is displayed magnified to show the variation of the scattering function in more detail. Bottom: PDF in the form of $D(r)$ of ZIF-8-mim$_{0.17}$im$_{0.75}$bim$_{0.08}$.

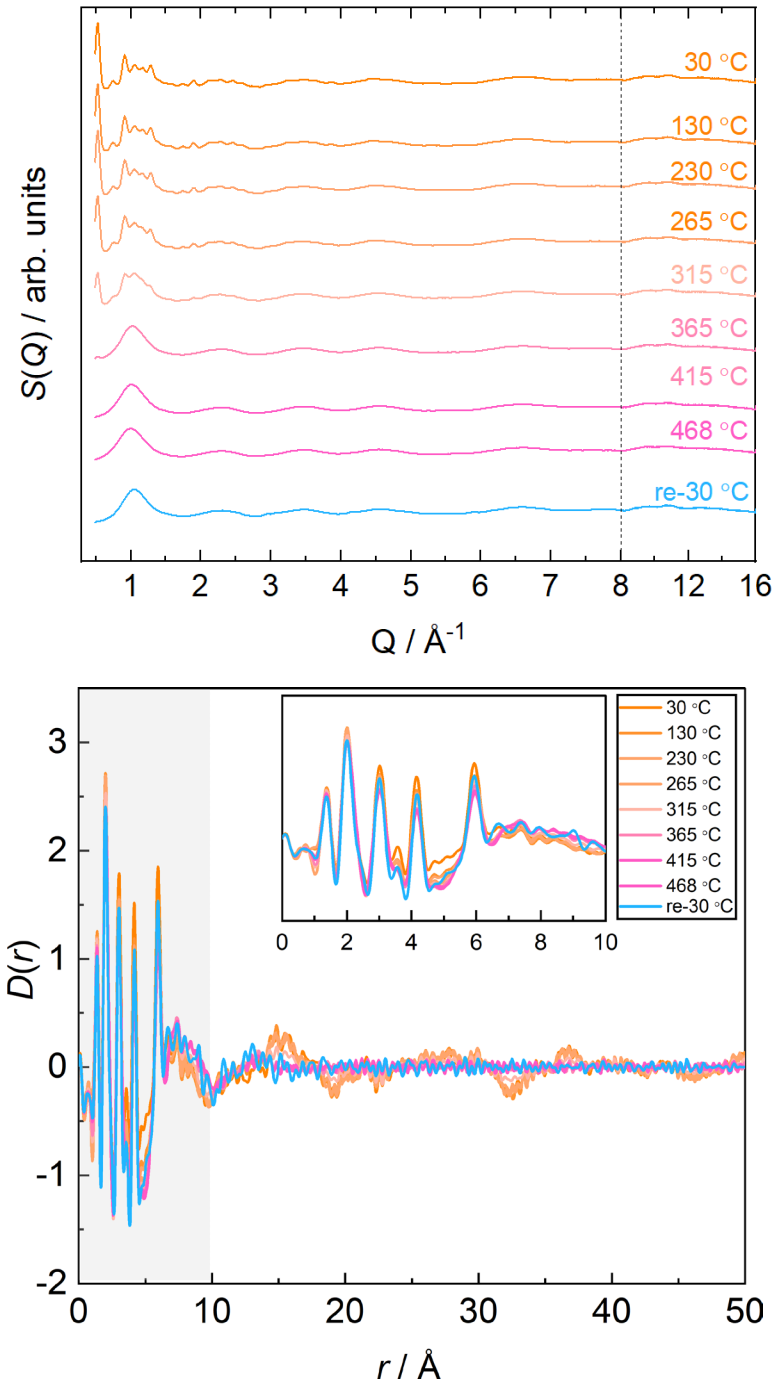

Figure A3.55. Top: Temperature dependent X-ray total scattering data in the form of $S(Q)$ data of ZIF-67-mim$_{0.18}$im$_{0.68}$bim$_{0.14}$. The vertical axis below 8 Å^{-1} is displayed magnified to show the variation of the scattering function in more detail. Bottom: PDF in the form of $D(r)$ of ZIF-67-mim$_{0.18}$im$_{0.68}$bim$_{0.14}$.

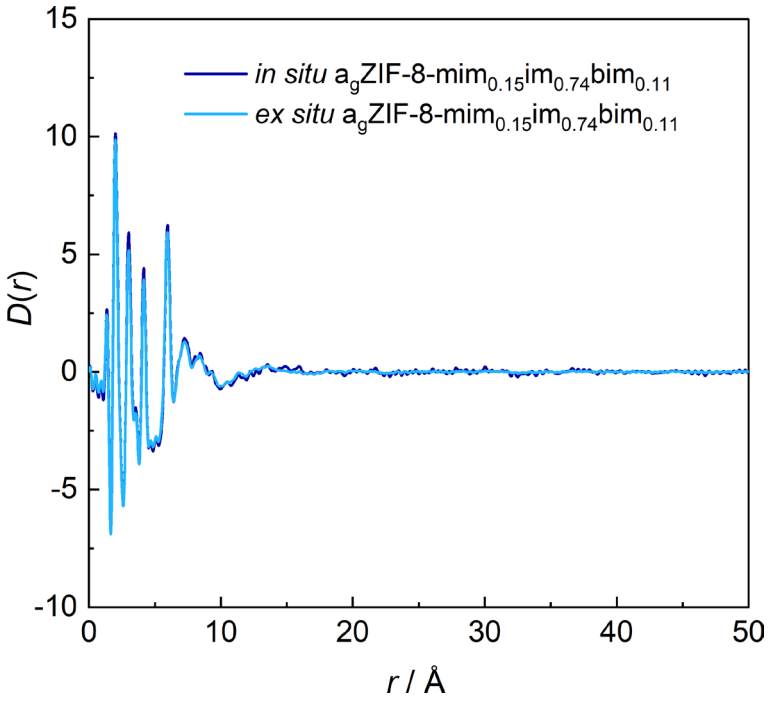

Figure A3.56. Room temperature PDFs in the form $D(r)$ of a_gZIF-8-$mim_{0.15}im_{0.74}bim_{0.11}$. The dark blue function is derived from the VT total scattering experiment by *in situ* heating to 468 °C and returning to room temperature, the light blue sample (*ex situ*) is prepared with the DSC instrument by heating to 430 °C followed by cooling to room temperature under N_2.

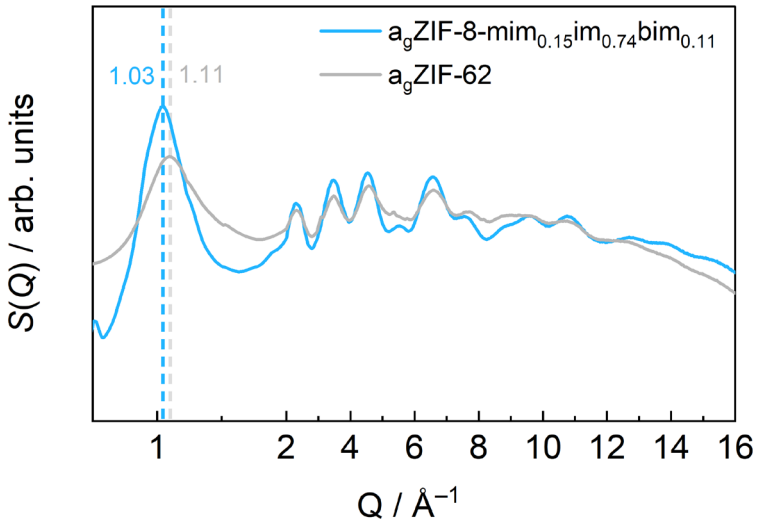

Figure A3.57. Comparison of X-ray total scattering data in the form of $S(Q)$ of a_gZIF-8-$mim_{0.15}im_{0.74}bim_{0.11}$ with a_gZIF-62. The smaller magnitude of the scattering vector for the first sharp scattering peak of a_gZIF-8-$mim_{0.15}im_{0.74}bim_{0.11}$ (1.03 $Å^{-1}$) compared to a_gZIF-62 (1.11 $Å^{-1}$) is an indication for the lower density and higher porosity of the former.

A.3.4 – Solid state 2D spin diffusion NMR spectroscopy

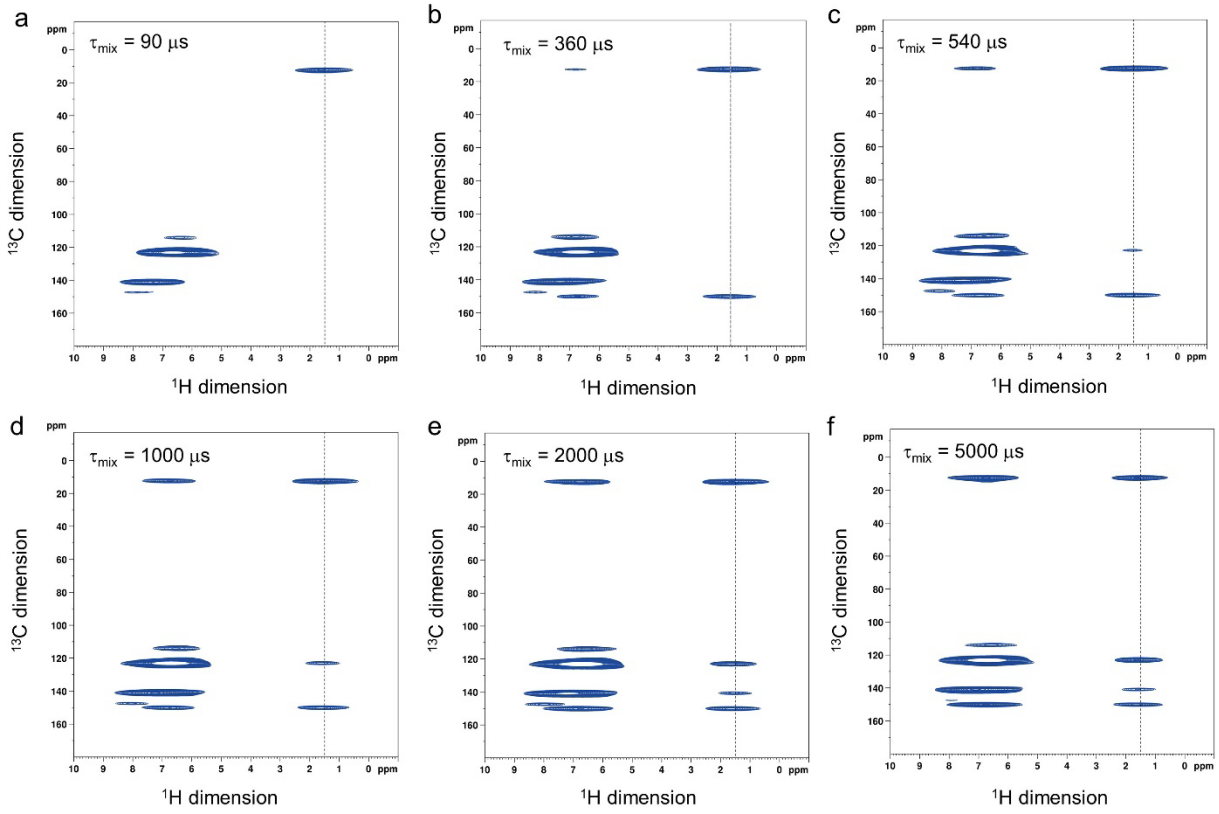

Figure A3.58. ^{1}H–^{13}C proton-detected 2D proton-spin-diffusion spectra of the microcrystalline ZIF-8-$mim_{0.15}im_{0.74}bim_{0.11}$ sample recorded with different CP times. Vertical dashed lines indicate the magnetization transfer from $–CH_3$ group to the imidazolate rings.

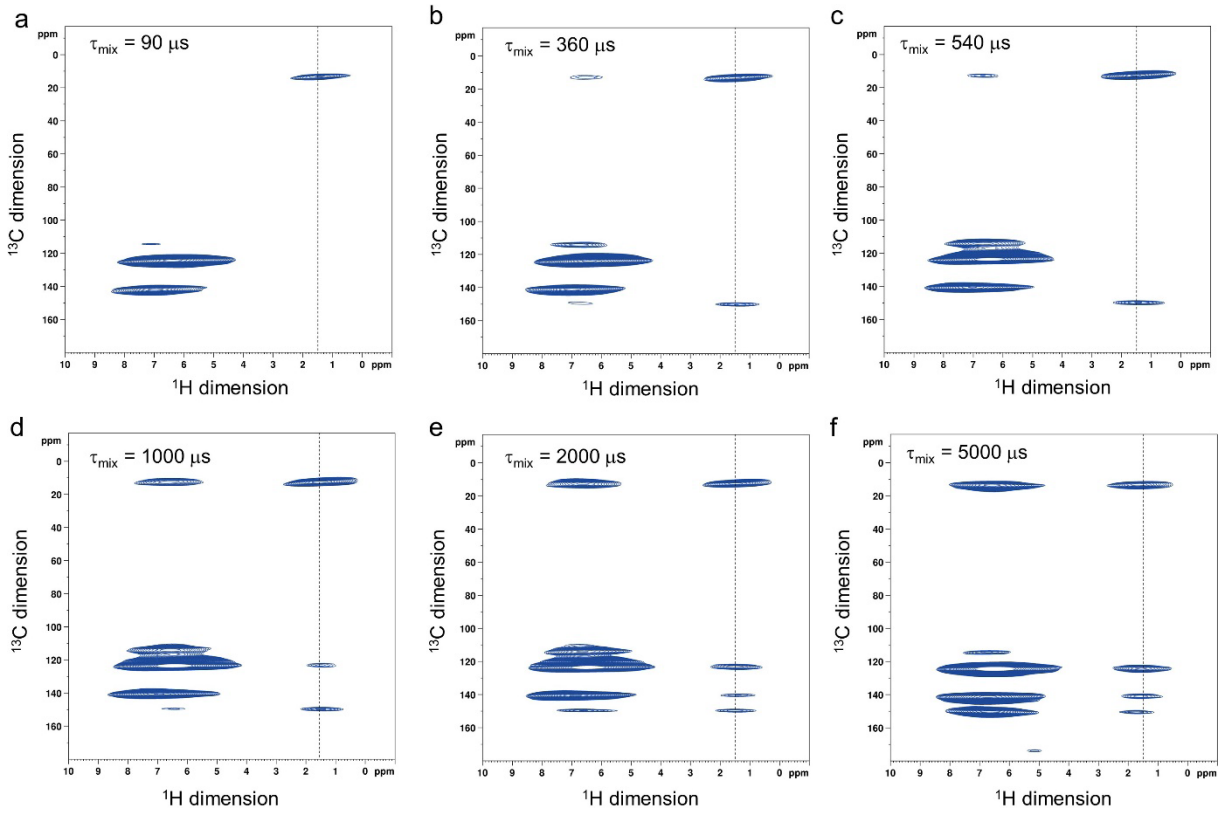

Figure A3.59. ^{1}H–^{13}C proton-detected 2D proton-spin-diffusion spectra of the glassy a_gZIF-8-$mim_{0.15}im_{0.74}bim_{0.11}$ sample recorded with different CP times. Vertical dashed lines indicate the magnetization transfer from $–CH_3$ group to the imidazolate rings.

A.3.5 – FTIR spectra

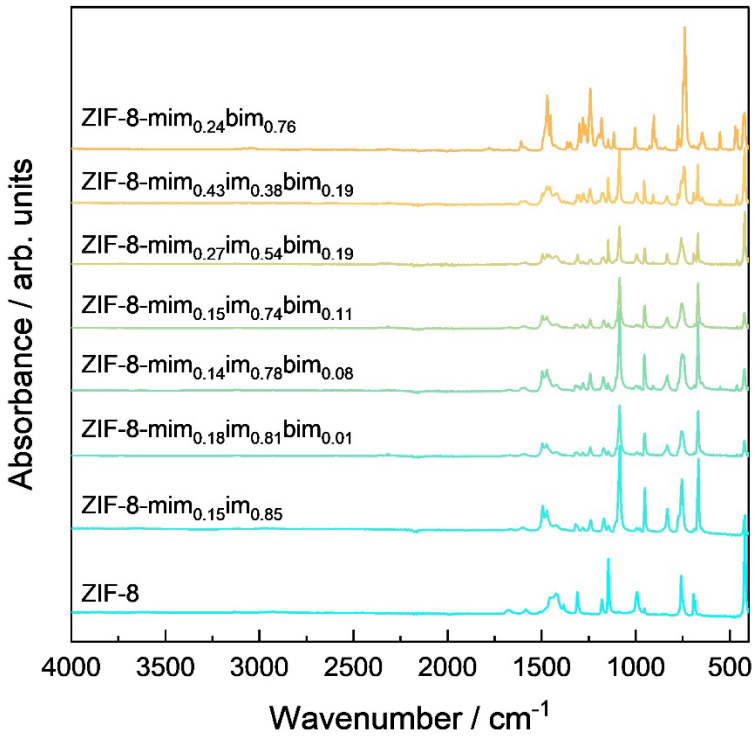

Figure A3.60. FTIR spectra of selected ZIF-8 derivatives after SALE and activation. The selected samples correspond to the ones in **Figure 3.1b**.

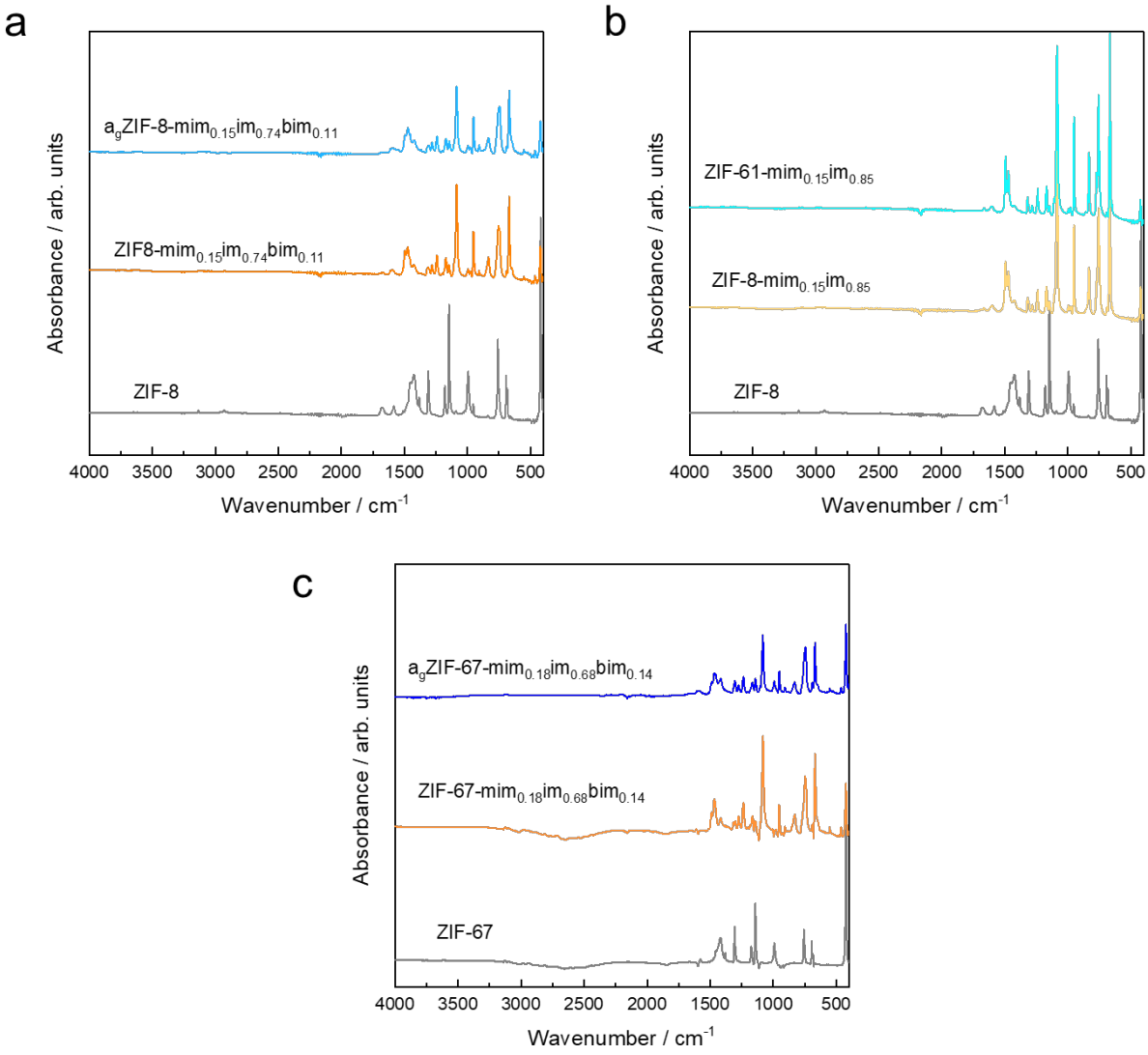

Figure A3.61. Comparison of FTIR spectra of selected ZIF samples. **a** ZIF-8, ZIF-8-$mim_{0.15}im_{0.74}bim_{0.11}$, and a_gZIF-8-$mim_{0.15}im_{0.74}bim_{0.11}$. **b** ZIF-8, ZIF-8-$mim_{0.15}im_{0.85}$, and ZIF-61-$mim_{0.15}im_{0.85}$. **c** ZIF-67, ZIF-67-$mim_{0.18}im_{0.68}bim_{0.14}$, and a_gZIF-67-$mim_{0.18}im_{0.68}bim_{0.14}$.

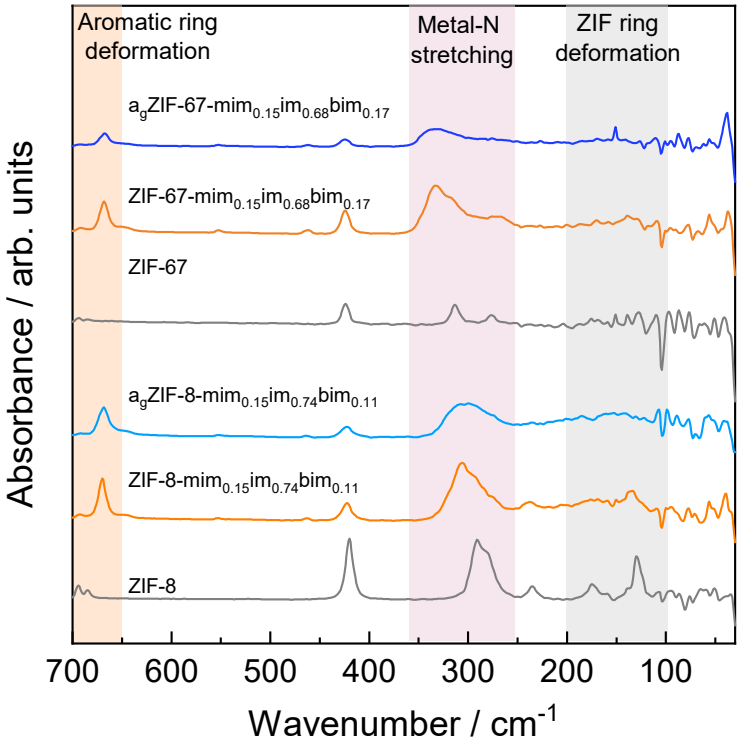

Figure A3.62. Comparison of far-IR spectra data of ZIF-8 derivatives with ZIF-67 derivatives in the crystalline and glassy states.

A.3.6 – Thermal analysis

A.3.6.1 – TGA and DSC

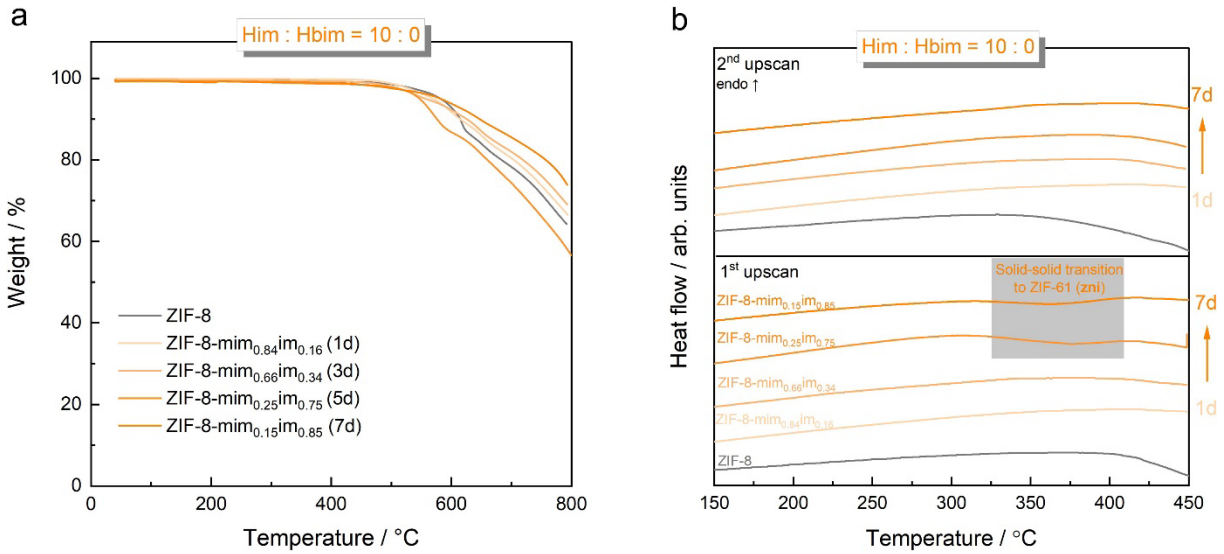

Figure A3.63. a TGA data collected for ZIF-8 derivatives after varying SALE reaction times with a solution containing only Him. **b** DSC data of the same samples showing two consecutive upscans. A weak and broad exothermic signal is visible on the first upscan for the samples containing large im^- concentrations. These signal is assigned to the solid-solid transition of the sample from the **sod** phase (ZIF-8) to the **zni** phase (ZIF-61).

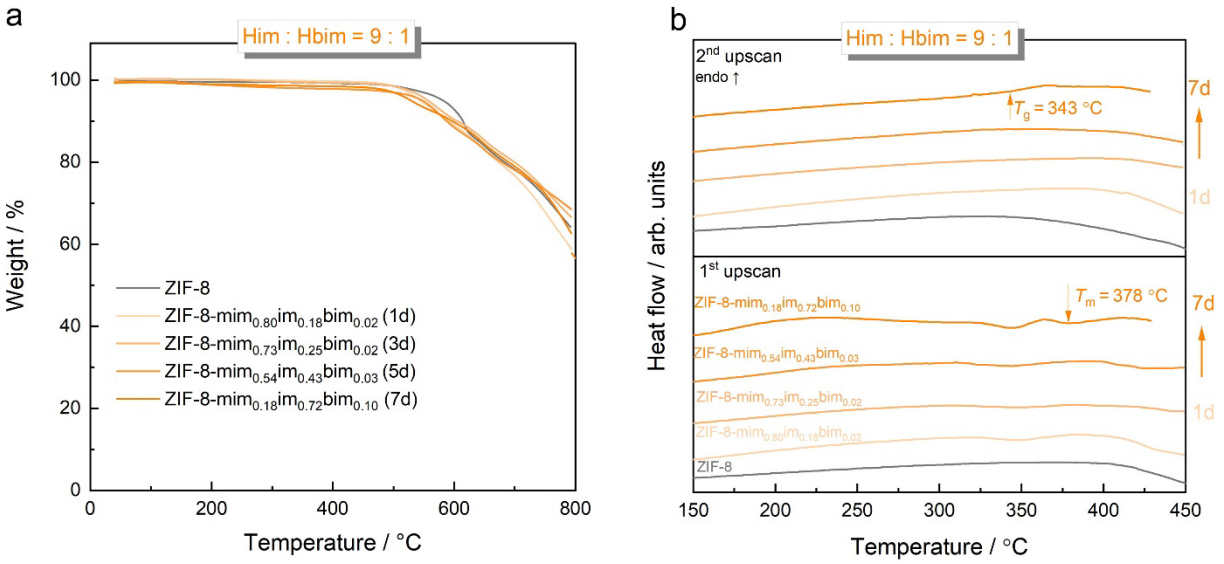

Figure A3.64. a TGA data collected for ZIF-8 derivatives after varying SALE reaction times with a solution containing Him and Hbim in a molar ratio of 9:1. **b** DSC data of the same samples showing two consecutive upscans. An exothermic signal followed by an endothermic signal is visible in the first upscan for the sample containing a large im^- concentration and a small bim^- concentration. The exothermic signal is attributed to the collapse of the frameworks and the endothermic signal is assigned to melting (T_m). A similar thermal behaviour has previously been observed for the liquid- and glass-forming ZIF-4 as well as some functionalized derivatives of ZIF-4.[22, 33] The material that undergoes melting in the first upscan shows a clear glass transition signal (T_g) in the second upscan.

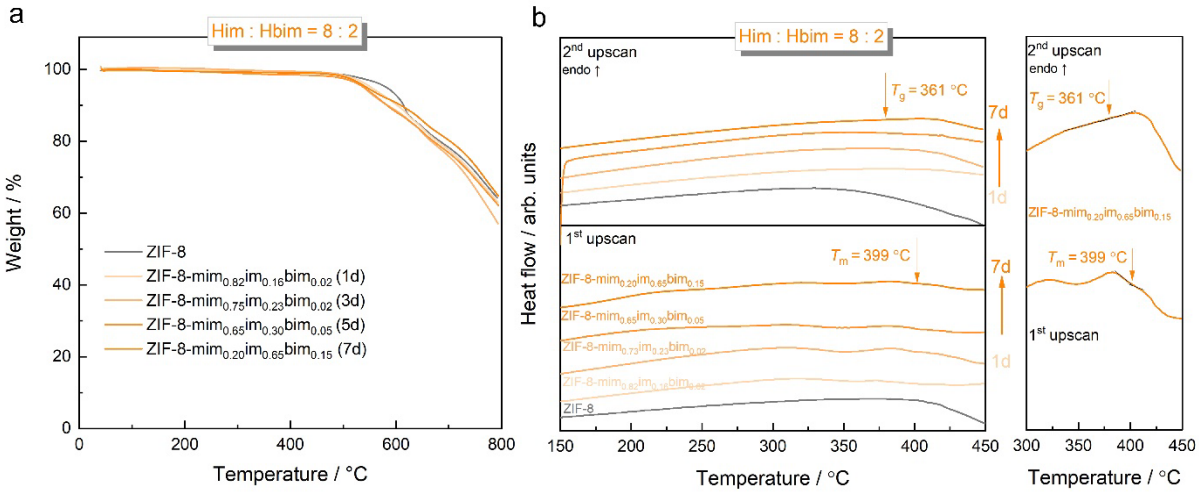

Figure A3.65. a TGA data collected for ZIF-8 derivatives after varying SALE reaction times with a solution containing Him and Hbim in a molar ratio of 8:2. **b** DSC data of the same samples showing two consecutive upscans. The zoomed-in curves on the right are used to demonstrate the determination of T_m and T_g. An exothermic signal followed by an endothermic signal is visible in the first upscan for the sample containing a large im^- concentration and small bim^- concentration. The exothermic signal is attributed to the collapse of the frameworks and the endothermic signal is assigned to melting (T_m). A similar thermal behaviour has previously been observed for the liquid- and glass-forming ZIF-4 as well as some functionalized derivatives of ZIF-4.[22, 33] The material that undergoes melting in the first upscan displays a signal which can be assigned to the glass transition (T_g) in the second upscan.

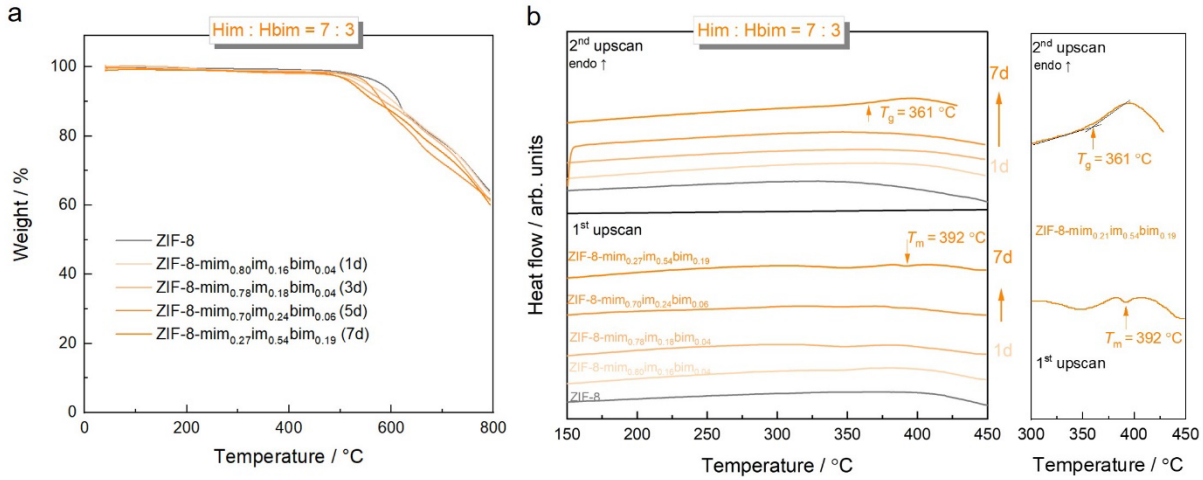

Figure A3.66. a TGA data collected for ZIF-8 derivatives after varying SALE reaction times with a solution containing Him and Hbim in a molar ratio of 7:3. **b** DSC data of the same samples showing two consecutive upscans. The zoomed-in curves on the right are used to demonstrate the determination of T_m and T_g. The exothermic signal is attributed to the collapse of the frameworks and the endothermic signal is assigned to melting (T_m). A similar thermal behaviour has previously been observed for the liquid- and glass-forming ZIF-4 as well as some functionalized derivatives of ZIF-4.[22, 33] The material that undergoes melting in the first upscan displays a signal which can be assigned to the glass transition (T_g) in the second upscan.

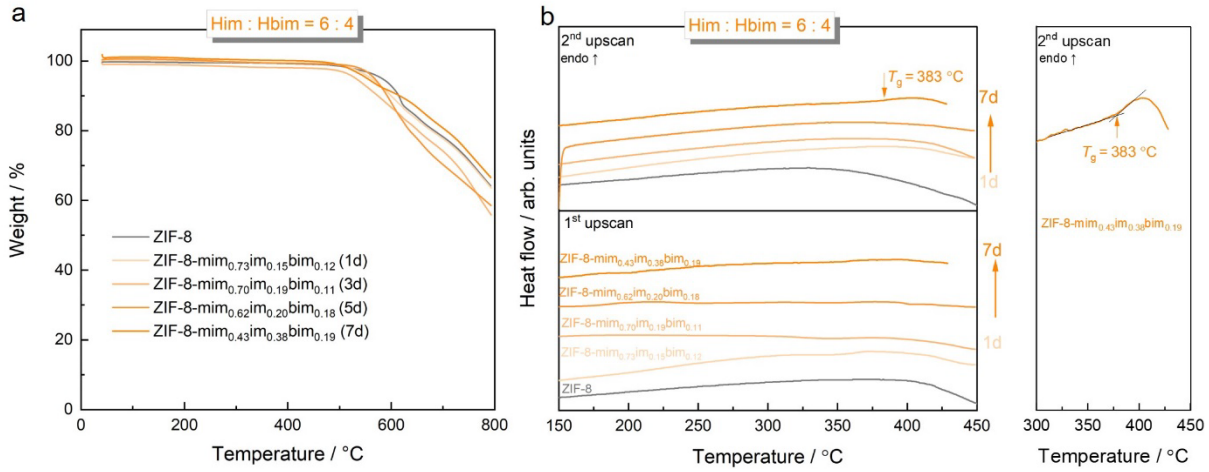

Figure A3.67. a TGA data collected for ZIF-8 derivatives after varying SALE reaction times with a solution containing Him and Hbim in a molar ratio of 6:4. **b** DSC data of the same samples showing two consecutive upscans. The zoomed-in curve on the right is used to demonstrate the determination of T_g. ZIF-8-mim$_{0.43}$im$_{0.38}$bim$_{0.19}$ forms a CGC during the first heating cycle. The formation of the CGC composite appears to be a thermoneutral process, however, glassy behaviour is proven by a glass transition signal (T_g) in the second upscan.

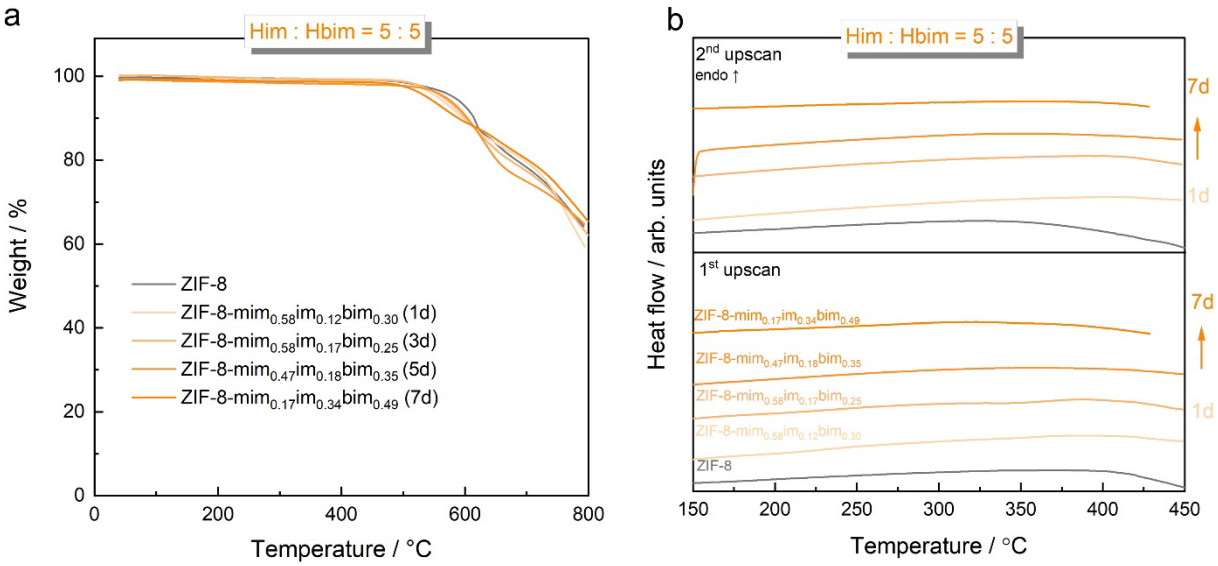

Figure A3.68. a TGA data collected for ZIF-8 derivatives after varying SALE reaction times with a solution containing Him and Hbim in a molar ratio of 5:5. **b** DSC data of the same samples showing two consecutive upscans.

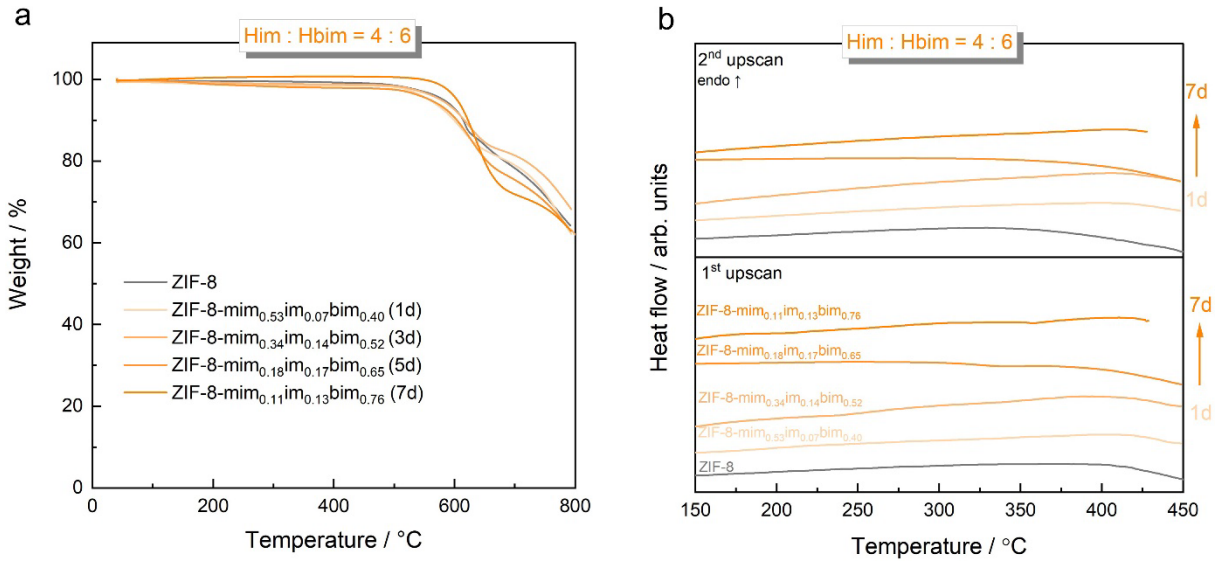

Figure A3.69. a TGA data collected for ZIF-8 derivatives after varying SALE reaction times with a solution containing Him and Hbim in a molar ratio of 4:6. **b** DSC data of the same samples showing two consecutive upscans.

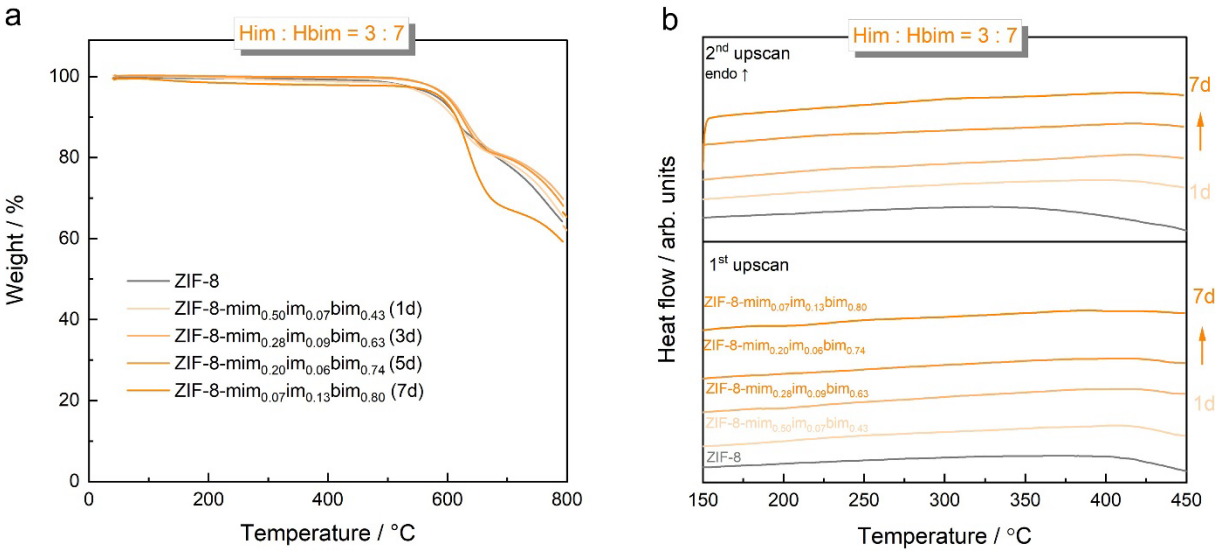

Figure A3.70. a TGA data collected for ZIF-8 derivatives after varying SALE reaction times with a solution containing Him and Hbim in a molar ratio of 3:7. **b** DSC data of the same samples showing two consecutive upscans.

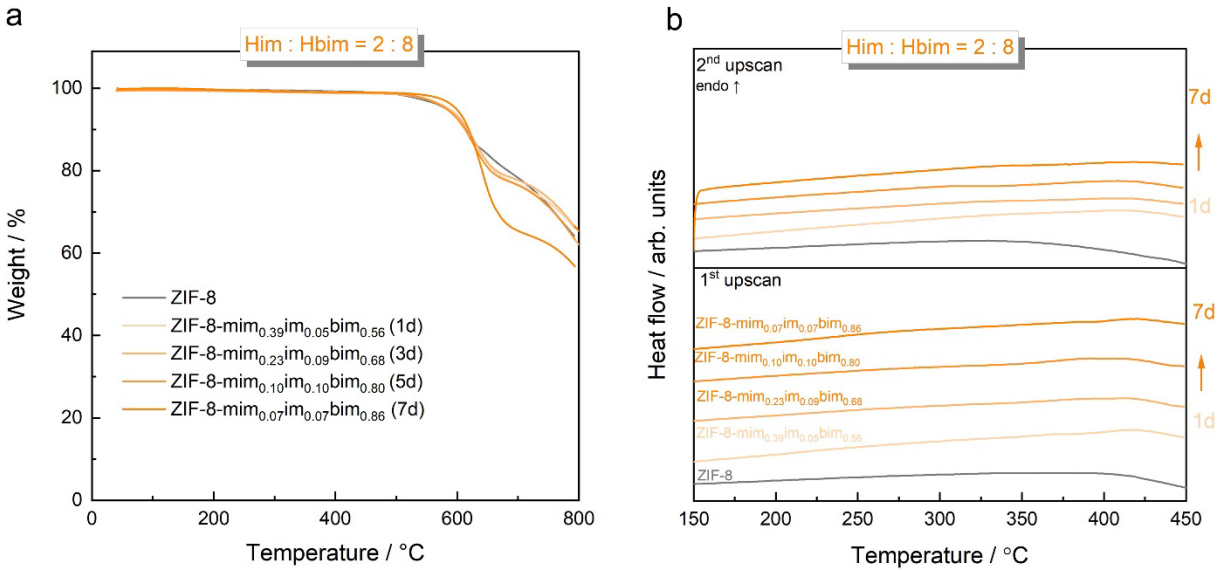

Figure A3.71. a TGA data collected for ZIF-8 derivatives after varying SALE reaction times with a solution containing Him and Hbim in a molar ratio of 2:8. **b** DSC data of the same samples showing two consecutive upscans.

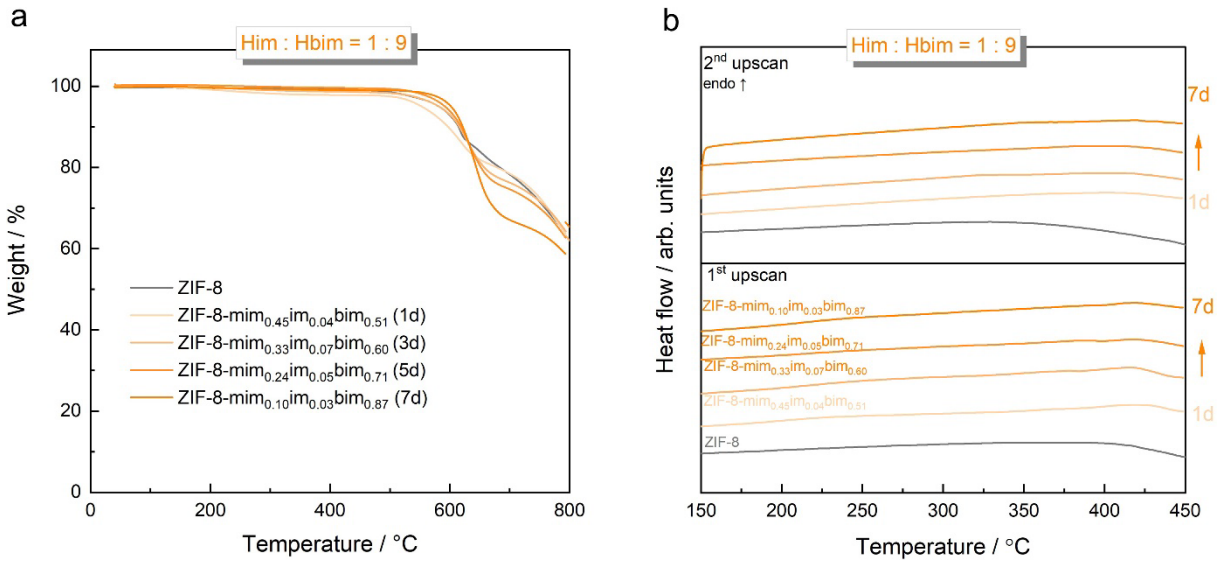

Figure A3.72. a TGA data collected for ZIF-8 derivatives after varying SALE reaction times with a solution containing Him and Hbim in a molar ratio of 1:9. **b** DSC data of the same samples showing two consecutive upscans.

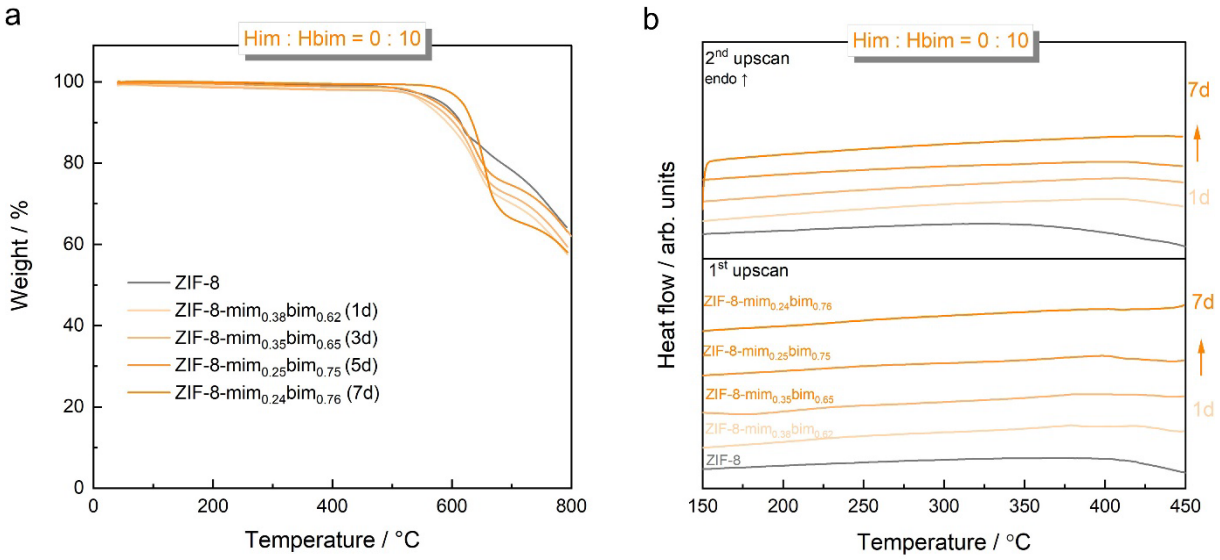

Figure A3.73. a TGA data collected for ZIF-8 derivatives after varying SALE reaction times with a solution containing only Hbim. **b** DSC data of the same samples showing two consecutive upscans.

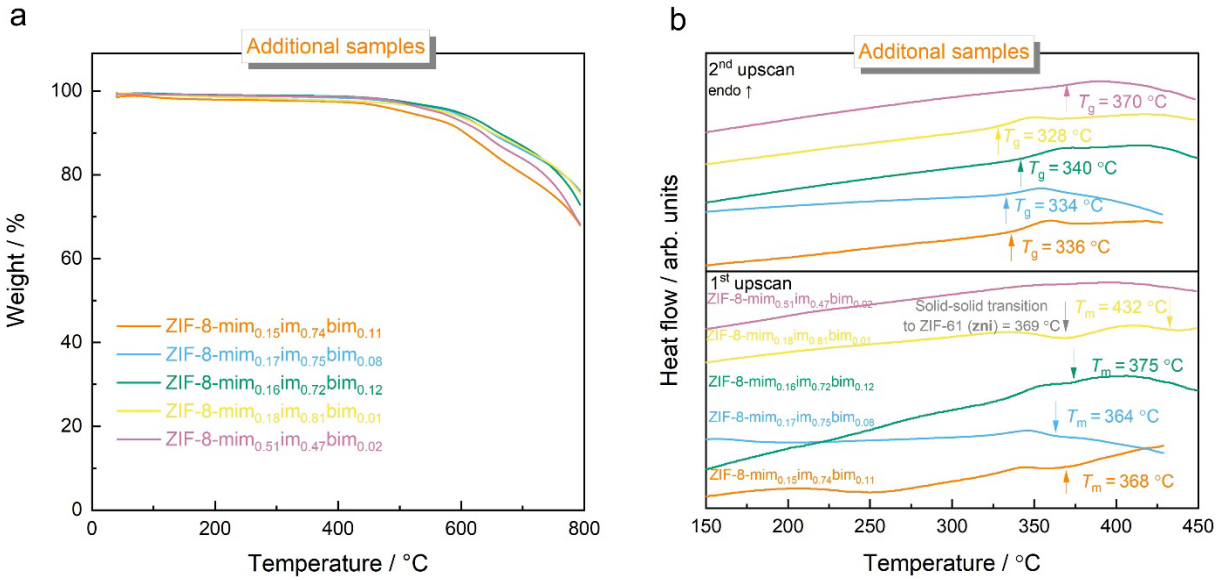

Figure A3.74. a TGA for ZIF-8 derivatives made from a more refined applied exchange ratio of imidazole and benzimidazole. **b** DSC data of the same samples showing two consecutive upscans. An exothermic signal is visible on the first upscan for the sample containing large im^- concentrations and the smallest bim^- concentrations. This signal is assigned to the solid-solid transition of parts of the sample from the **sod** phase (ZIF-8) to the **zni** phase (ZIF-61). In addition, endothermic signals are visible on the first upscan for the samples containing large im^- concentrations and small bim^- concentrations. These signals are assigned to melting (T_m). For all materials, a glass transition signal (T_g) is observed in the second scan.

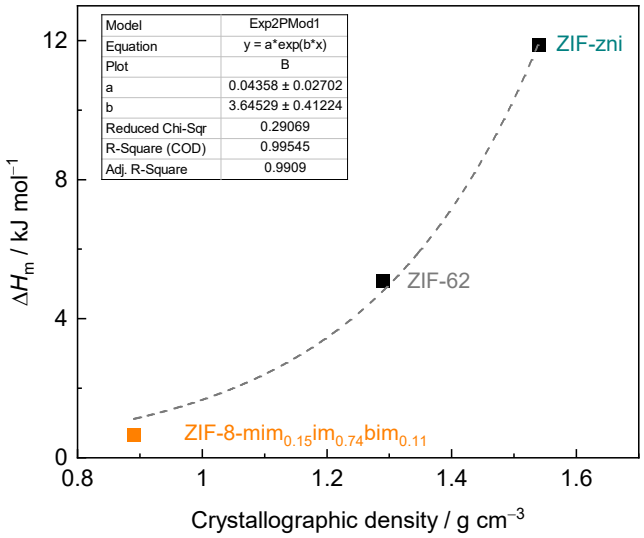

Figure A3.75. Plot of crystallographic density against the molar melting enthalpy (ΔH_m) of ZIF-8-mim$_{0.15}$im$_{0.74}$bim$_{0.11}$, ZIF-62 and ZIF-zni. ΔH_m of ZIF-8-mim$_{0.15}$im$_{0.74}$bim$_{0.11}$ was determined from the integral of the melting signal in the first DSC upscan. For the crystallographic density see Supplementary Table 4. The enthalpies and crystallographic densities of ZIF-62 and ZIF-zni were taken from reference[41]. The dashed curve represents an exponential fit to the data and is provided as a guide to the eye.

Table A3.3. Comparison of thermodynamic melting parameters of ZIF-8-mim$_{0.15}$im$_{0.74}$bim$_{0.11}$ with other reported meltable ZIFs.

Material	Composition	T_m (°C)	T_m (K)	ΔH_m (kJ mol^{-1})	ΔS_m (J K^{-1} mol^{-1})	References
ZIF-8-mim$_{0.15}$im$_{0.74}$bim$_{0.11}$	Zn(mim)$_{0.30}$(im)$_{1.48}$(bim)$_{0.22}$	368	641	0.66	1.03	This work
ZIF-62	Zn(im)$_{1.75}$(bim)$_{0.25}$	435	708	2.92	4.12	*Sci. Adv.* 4, eaao6827 (2018)
ZIF-62-bim$_{0.35}$	Zn(im)$_{1.65}$(bim)$_{0.35}$	438	711	5.08	7.14	*Nat. Commun.* 13, 7750 (2022)
ZIF-4	Zn(im)$_2$	579	852	11.46	13.45	*Nat. Commun.* 13, 7750 (2022)
ZIF-zni	Zn(im)$_2$	585	858	11.88	13.85	*Nat. Commun.* 13, 7750 (2022)
TIF-4	Zn(im)$_{1.68}$(mbim)$_{0.32}$	436	709	2.69	3.79	Nat. Commun. 13, 7750 (2022)
ZIF-UC-5	Zn(im)$_{1.80}$(Clbim)$_{0.20}$	428	701	2.50	3.60	*CrystEngComm*, ,22, 3627-3637 (2020)
ZIF-UC-6	Zn(im)$_{1.82}$(abim)$_{0.18}$	345	618	1.70	2.80	*Chem. Mater.* 34, 2187–2196 (2022)

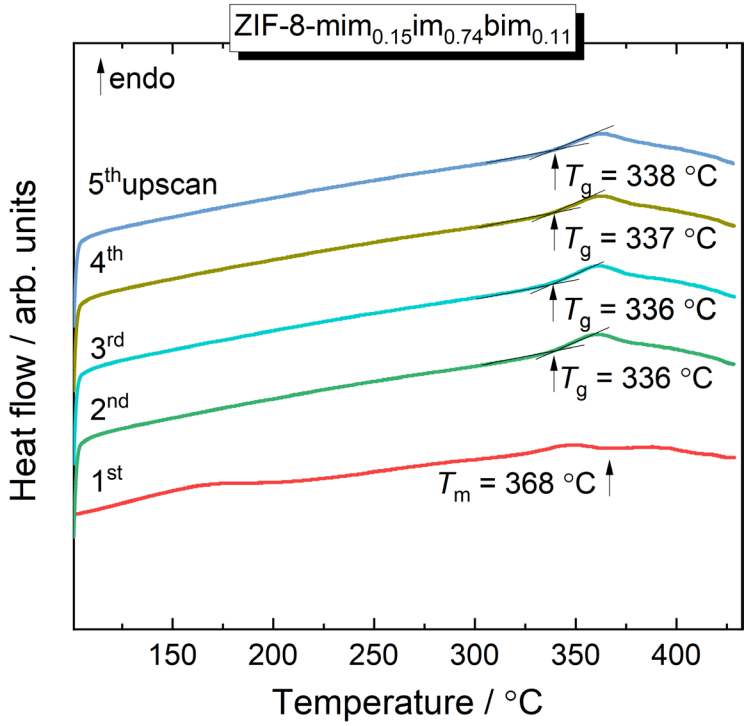

Figure A3.76. Five consecutive DSC cycles for ZIF-8-mim$_{0.15}$im$_{0.74}$bim$_{0.11}$ showcasing the stability of T_g.

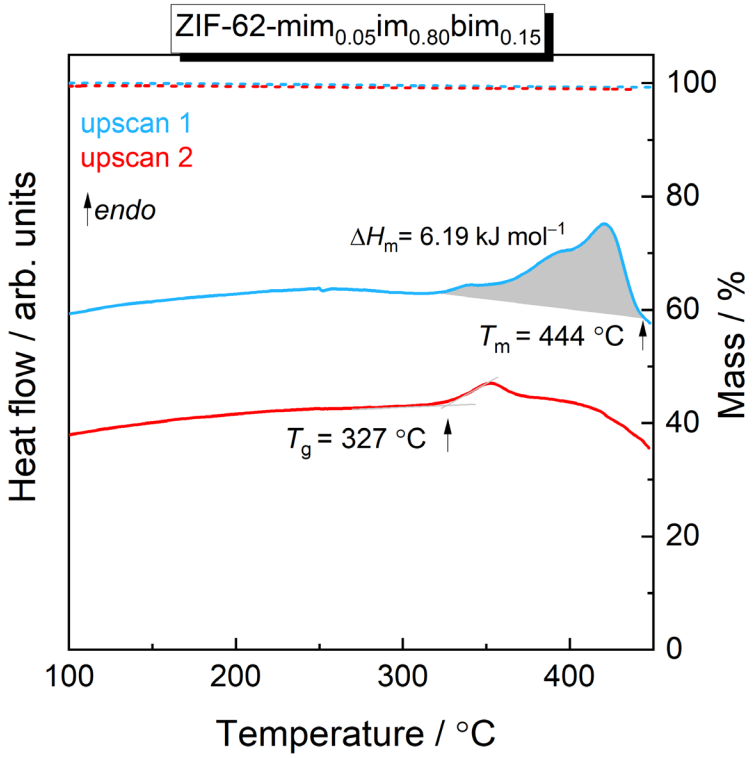

Figure A3.77. TGA (dotted lines) and DSC (solid lines) for ZIF-62-mim$_{0.05}$im$_{0.80}$bim$_{0.15}$. The sample was cycled from 50 °C to 450 °C with a heating/cooling rate of ±10 °C/min for two times. The sample is obtained by a SALE process from ZIF-8 in which the reaction mixture was stirred for 15 min/day (total reaction time is 3 days).

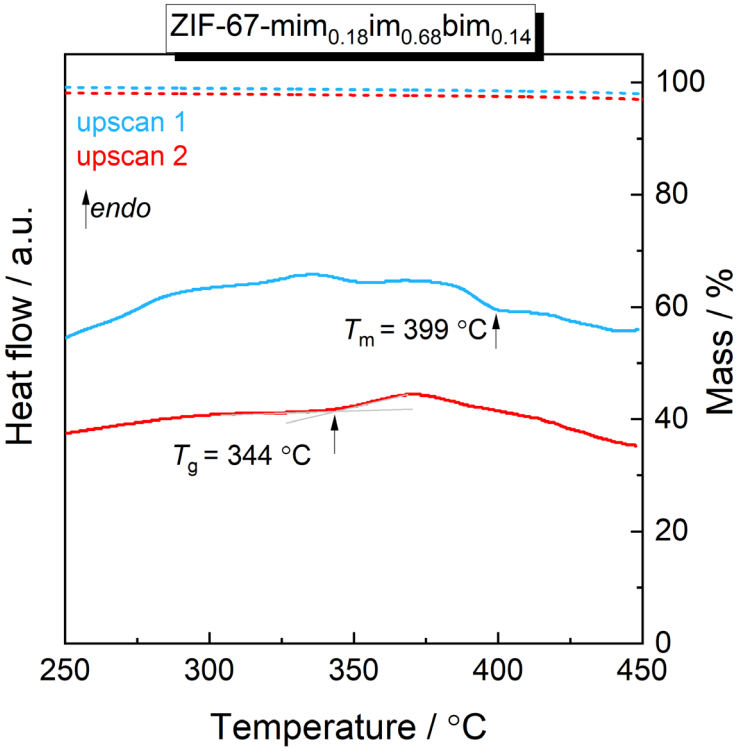

Figure A3.78. TGA (dotted lines) and DSC (solid lines) for ZIF-67-mim$_{0.18}$im$_{0.68}$bim$_{0.14}$. The sample was cycled from 50 °C to 450 °C with a heating/cooling rate of ±10 °C/min for two times.

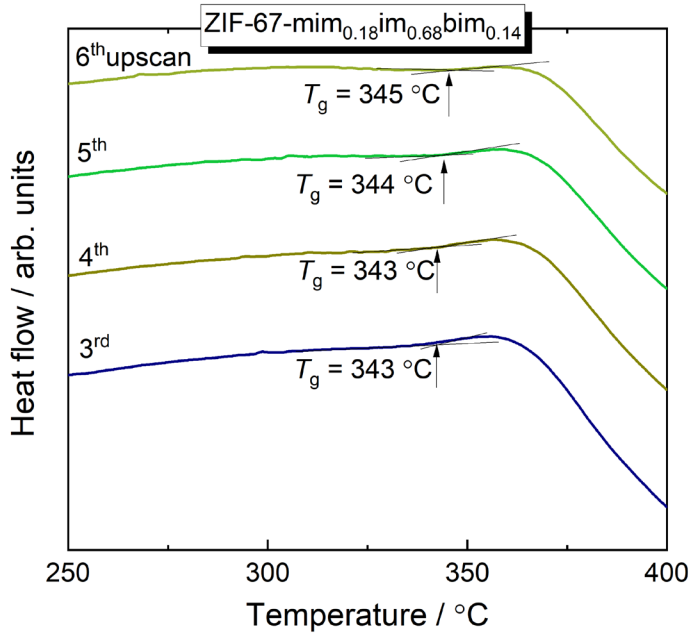

Figure A3.79. The third to sixth consecutive DSC cycles for ZIF-67-mim$_{0.18}$im$_{0.68}$bim$_{0.14}$ showing the stability of T_g.

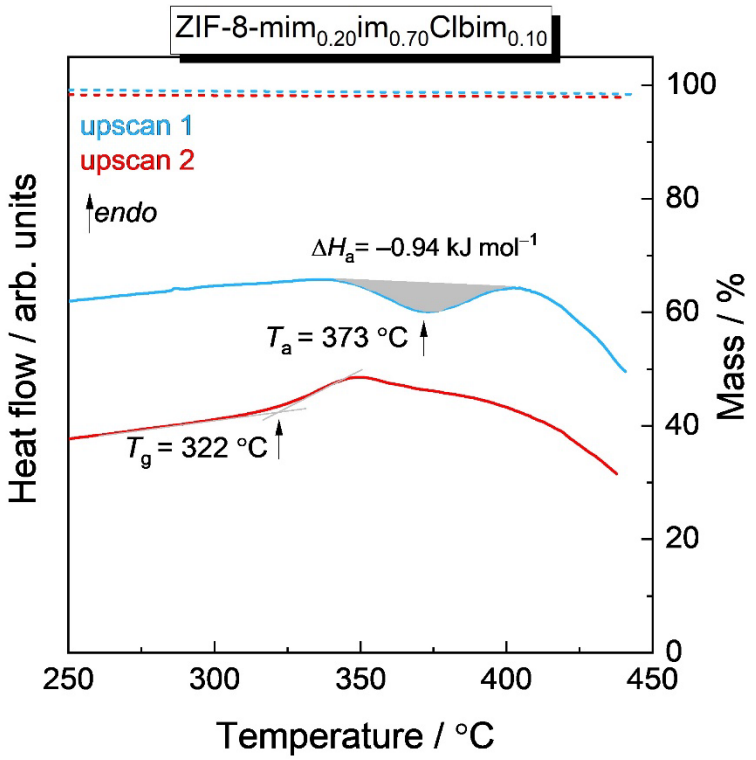

Figure A3.80. TGA (dotted lines) and DSC (solid lines) for ZIF-8-mim$_{0.20}$im$_{0.70}$Clbim$_{0.10}$. The sample was cycled from 50 °C to 440 °C with a heating/cooling rate of ±10 °C/min for two times. The peak in the first upscan is defined as the amorphisation temperature (T_a) due to its exothermic nature. The fact that a glass transition is observable at 322 °C in the second upscan suggests that the amorphization involves a slightly exothermic transition to a liquid phase. Other slightly exothermic transitions to ZIF liquids were previously reported for ZIF-4 and some of its functionalized derivatives.[22, 33]

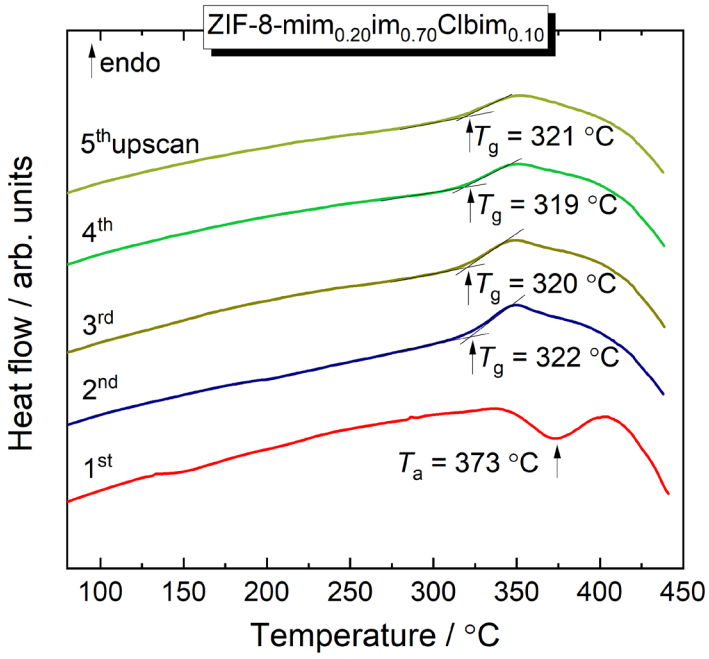

Figure A3.81. Five consecutive DSC cycles for ZIF-8-mim$_{0.20}$im$_{0.70}$Clbim$_{0.10}$ showcasing the stability of T_g.

Table A3.4. Summary of the transition temperatures determined from the DSC data.

Material	T_{rc} / °C	T_m / °C	T_g / °C	Material after heat treatment
ZIF-8-$mim_{0.25}im_{0.75}$	363	/	/	ZIF-61-$mim_{0.25}im_{0.75}$
ZIF-8-$mim_{0.15}im_{0.85}$	374	/	/	ZIF-61-$mim_{0.15}im_{0.85}$
ZIF-8-$mim_{0.18}im_{0.72}bim_{0.10}$	/	378	343	a_gZIF-8-$mim_{0.18}im_{0.72}bim_{0.10}$
ZIF-8-$mim_{0.20}im_{0.65}bim_{0.15}$	/	399	361	a_gZIF-8-$mim_{0.20}im_{0.65}bim_{0.15}$
ZIF-8-$mim_{0.27}im_{0.54}bim_{0.19}$	/	392	361	a_gZIF-8-$mim_{0.27}im_{0.54}bim_{0.19}$
ZIF-8-$mim_{0.43}im_{0.38}bim_{0.19}$	/	/	383	ZIF-8/a_gZIF-8-$mim_{0.43}im_{0.38}bim_{0.19}$ CGC
ZIF-8-$mim_{0.15}im_{0.74}bim_{0.11}$	/	368	336	a_gZIF-8-$mim_{0.15}im_{0.74}bim_{0.11}$
ZIF-8-$mim_{0.17}im_{0.75}bim_{0.08}$	/	360	334	a_gZIF-8-$mim_{0.17}im_{0.75}bim_{0.08}$
ZIF-8-$mim_{0.16}im_{0.72}bim_{0.12}$	/	375	340	a_gZIF-8-$mim_{0.16}im_{0.72}bim_{0.12}$
ZIF-8-$mim_{0.18}im_{0.81}bim_{0.01}$	369	432	328	ZIF-61/a_gZIF-8-$mim_{0.18}im_{0.81}bim_{0.01}$ CGC
ZIF-8-$mim_{0.51}im_{0.47}bim_{0.02}$	/	/	370	ZIF-8/a_gZIF-8-$mim_{0.51}im_{0.47}bim_{0.02}$ CGC
ZIF-62-$mim_{0.05}im_{0.80}bim_{0.15}$	/	444	327	a_gZIF-62-$mim_{0.05}im_{0.80}bim_{0.15}$
ZIF-8-$mim_{0.20}im_{0.70}$Clbim$_{0.10}$	/	373[a]	322	a_gZIF-8-$mim_{0.20}im_{0.70}$Clbim$_{0.10}$
ZIF-67-$mim_{0.18}im_{0.68}bim_{0.14}$	/	399	344	ZIF-67-$mim_{0.18}im_{0.68}bim_{0.14}$

[a] defined as the amorphisation temperature (T_a) due to the exothermic transition into a (supercooled) liquid state.

A.3.6.2 – Heat capacity measurements

The evolution of heat capacity (C_p) of a_gZIF-8-$mim_{0.15}im_{0.74}bim_{0.11}$ in the range from 200 to 415 °C was determined by modulated DSC using a DSC 25 calorimeter (TA Instruments). In this measurement, a sinusoidal modulation with a temperature amplitude of ±1 °C and a modulation period of 120 s was overlaid on a linear heating ramp with an average heating rate of 2 °C min^{-1}. Baseline and sapphire reference scans were collected before the sample scan using the same temperature program.

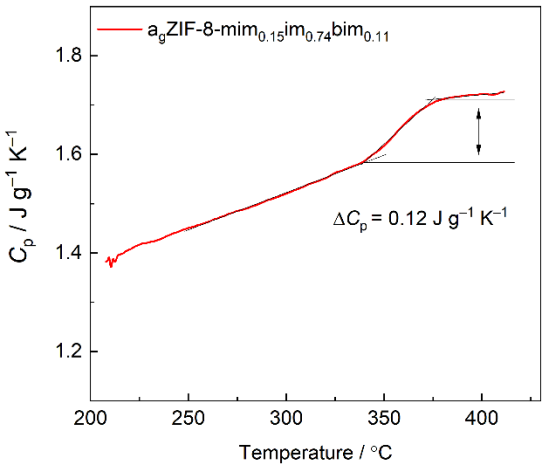

Figure A3.82. Heat capacity (C_p) scan of a_gZIF-8-$mim_{0.15}im_{0.74}bim_{0.11}$. The heat capacity change around the glass transition (ΔC_p) was determined using the difference between the two intersections of the onset and offset tangent lines of the glass transition signal.

Table A3.5. Comparison of the heat capacity change (ΔC_p) around the glass transition of a_gZIF-8-$mim_{0.15}im_{0.74}bim_{0.11}$ and other reported ZIF glasses.

Material	Composition	T_g (°C)	ΔC_p (J g^{-1} K^{-1})	References
a_gZIF-8-$mim_{0.15}im_{0.74}bim_{0.11}$	$Zn(mim)_{0.30}(im)_{1.48}(bim)_{0.22}$	336	0.12	This work
a_gZIF-62	$Zn(im)_{1.75}(bim)_{0.25}$	322	0.19	*Sci. Adv.* 4, eaao6827 (2018)
a_g(IL@ZIF-8)	[EMIM][TFSI]@$Zn(mim)_2$	322	0.11	*Nat. Commun.* 12, 5703 (2021)
a_gZIF-4 (HDA)	$Zn(im)_2$	292	0.16	*Nat. Commun.* 6, 8079 (2015)
a_gZIF-4 (LDA)		316	0.11	

A.3.6.3 – Determination of the calorimetric fragility

The fragility of the a_gZIF-8-$mim_{0.15}im_{0.74}bim_{0.11}$ was determined according to procedures published in previous work[93]. The melt-quenched ZIF glass was cycled from 50 °C to 430 °C, with varying heating and cooling rates from ±25 to ±5 °C/min. T_f is the fictive temperature of the glass sample prepared with different cooling rates (q_c). T_f at a heating/cooling rate of ±10 °C/min corresponds to T_g. The calorimetric fragility index m is determined as the slope of the plot of $\log_{10}(1/q_c)$ versus T_g/T_f (i.e. the T_g scaled reciprocal T_f, absolute temperatures in Kelvin).

$$m = \frac{\partial \log_{10}\left(\frac{1}{q_c}\right)}{\partial\left(\frac{T_g}{T_f}\right)}$$

The fragility index m is a measure for the activation energy of viscous flow at T_g. Glasses with a low fragility are called strong (for example vitreous silica with $m = 20$) while glasses with a fragility higher than about 40 are called fragile.

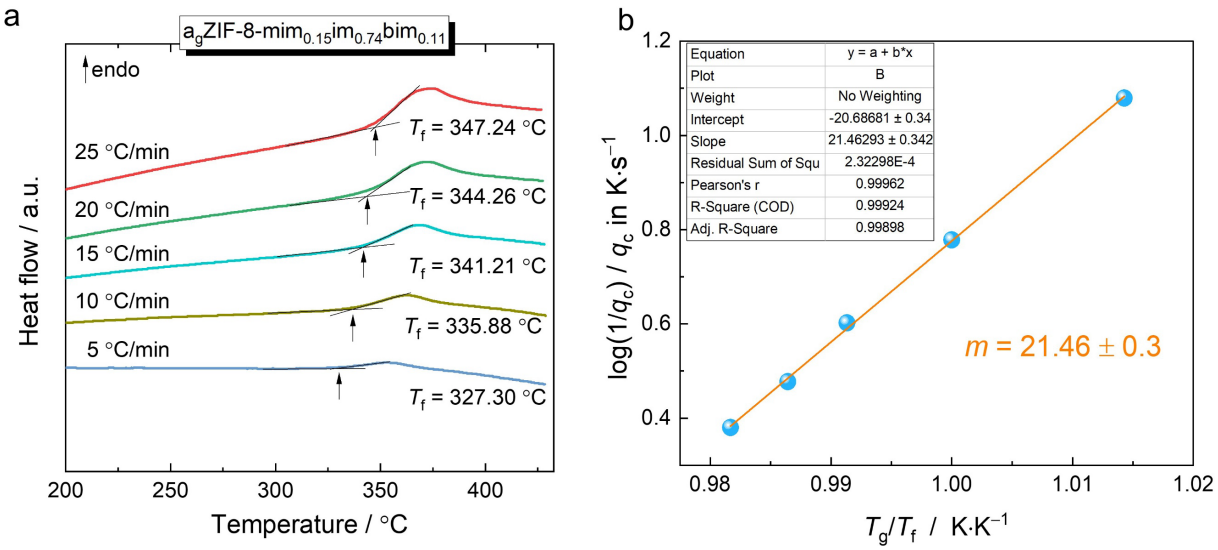

Figure A3.83. a DSC upscans of a_gZIF-8-$mim_{0.15}im_{0.74}bim_{0.11}$ with heating rates from 25 to 5 °C/min. The cooling rate before each of these scans has been identical to its heating rate. **b** Determination of the calorimetric fragility index m by a linear fit of $\log(1/q_c)$ against T_g/T_f.

A.3.7 – Micrography

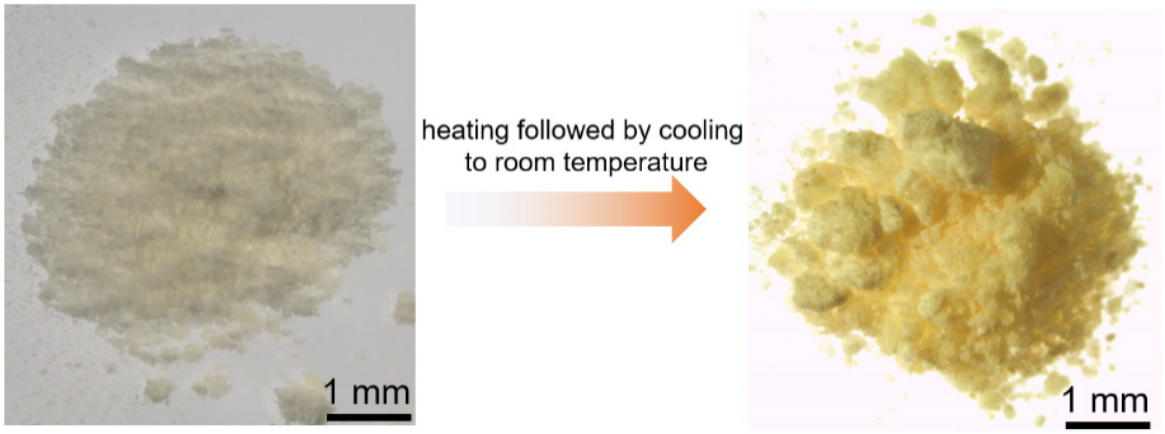

Figure A3.84. Micrographs of ZIF-8 obtained before and after two upscans in the DSC instrument (maximum temperature reached was 450 °C).

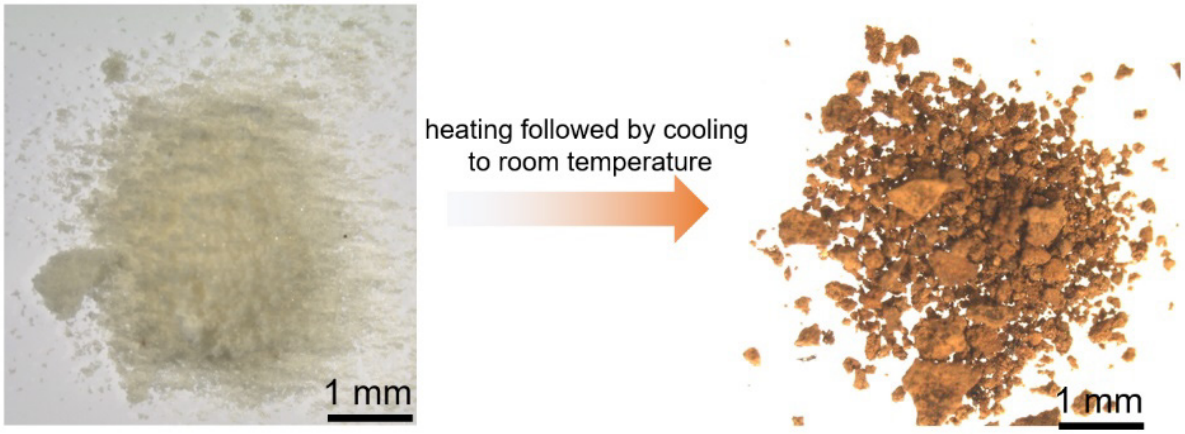

Figure A3.85. Micrographs of ZIF-8-mim$_{0.15}$im$_{0.85}$ obtained before and after two upscans in the DSC instrument (maximum temperature reached was 450 °C).

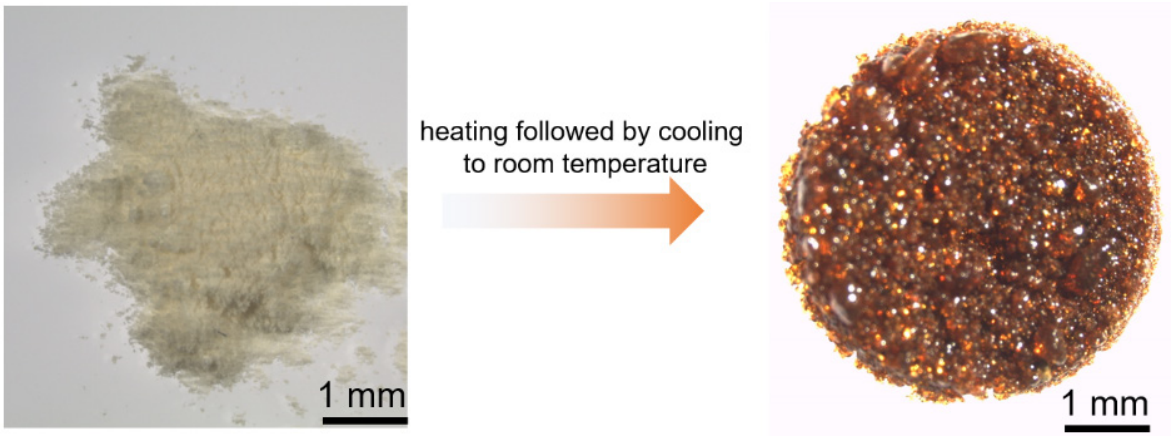

Figure A3.86. Micrographs of ZIF-8-mim$_{0.15}$im$_{0.74}$bim$_{0.11}$ obtained before and after the preparative TGA/DSC experiment (maximum temperature reached was 430 °C).

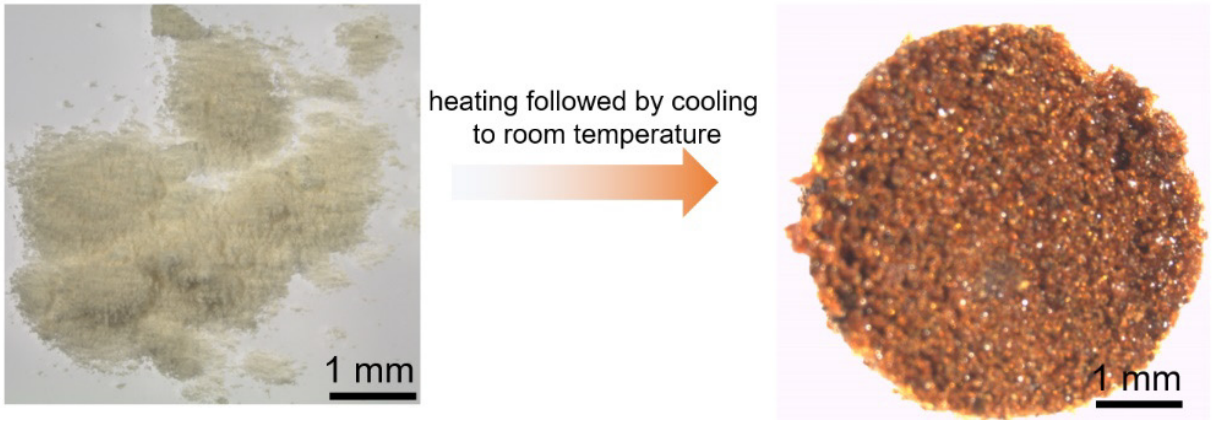

Figure A3.87. Micrographs of ZIF-8-mim$_{0.18}$im$_{0.72}$bim$_{0.10}$ obtained before and after two upscans of DSC experiment (maximum temperature reached was 430 °C).

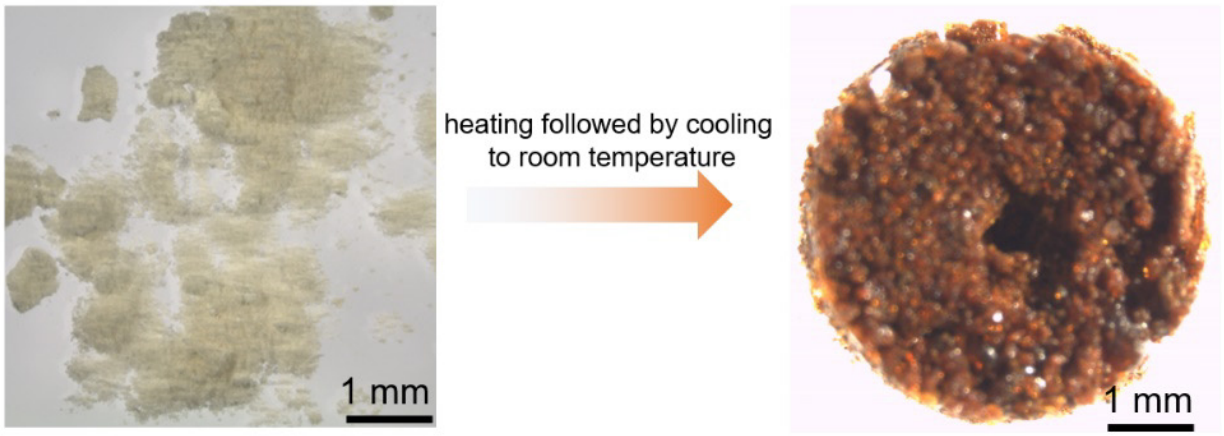

Figure A3.88. Micrographs of ZIF-8-mim$_{0.20}$im$_{0.65}$bim$_{0.15}$ obtained before and after two upscans of DSC experiment (maximum temperature reached was 450 °C).

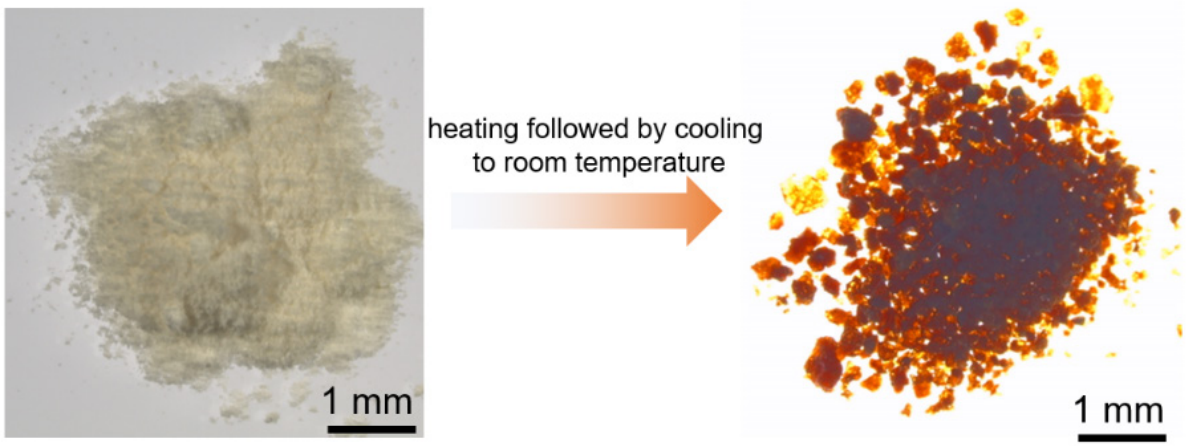

Figure A3.89. Micrographs of ZIF-8-mim$_{0.27}$im$_{0.54}$bim$_{0.19}$ obtained before and after two upscans of DSC experiment (maximum temperature reached was 450 °C).

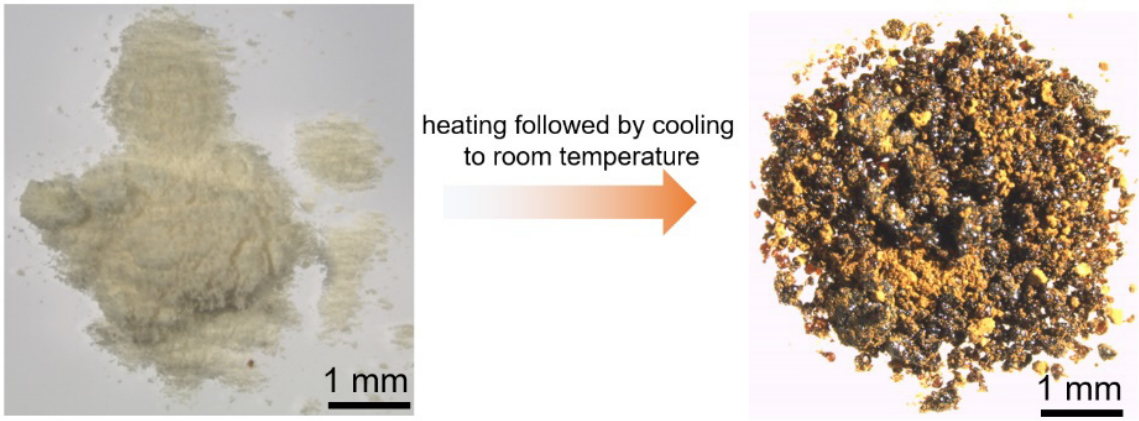

Figure A3.90. Micrographs of ZIF-8-mim$_{0.43}$im$_{0.38}$bim$_{0.19}$ obtained before and after two upscans of DSC experiment (maximum temperature reached was 430 °C).

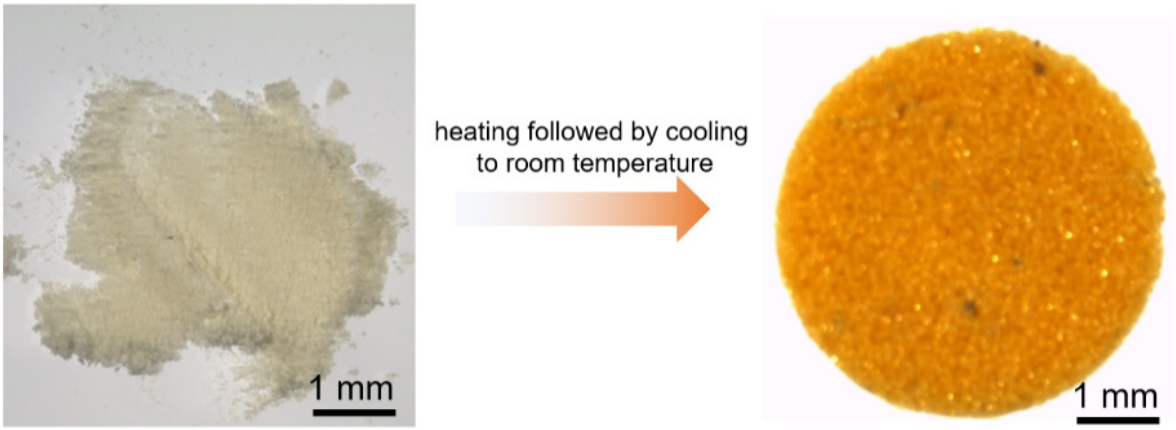

Figure A3.91. Micrographs of ZIF-8-mim$_{0.17}$im$_{0.75}$bim$_{0.08}$ obtained before and after two upscans of DSC experiment (maximum temperature reached was 430 °C).

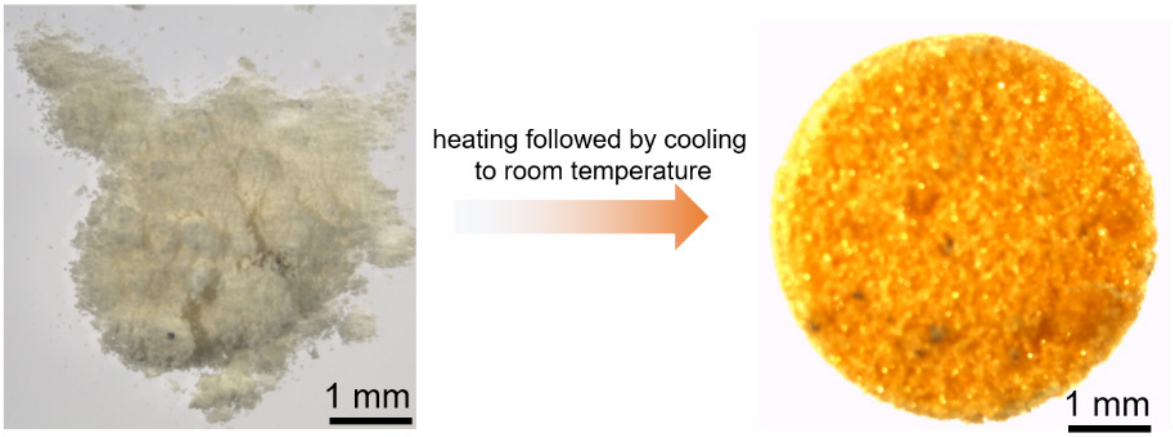

Figure A3.92. Micrographs of ZIF-8-mim$_{0.16}$im$_{0.72}$bim$_{0.12}$ obtained before and after the preparative TGA/DSC experiment (maximum temperature reached was 450 °C).

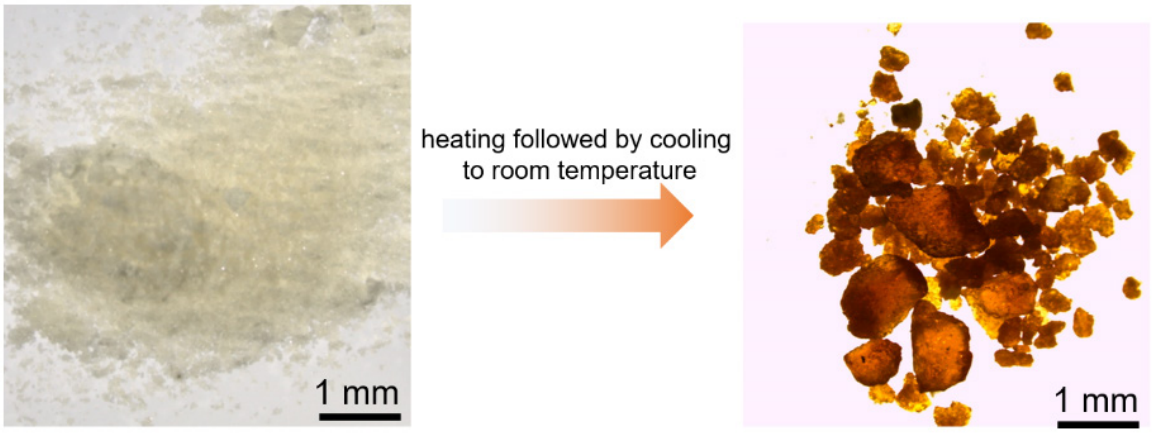

Figure A3.93. Micrographs of ZIF-8-mim$_{0.18}$im$_{0.81}$bim$_{0.01}$ obtained before and after the preparative TGA/DSC experiment (maximum temperature reached was 450 °C).

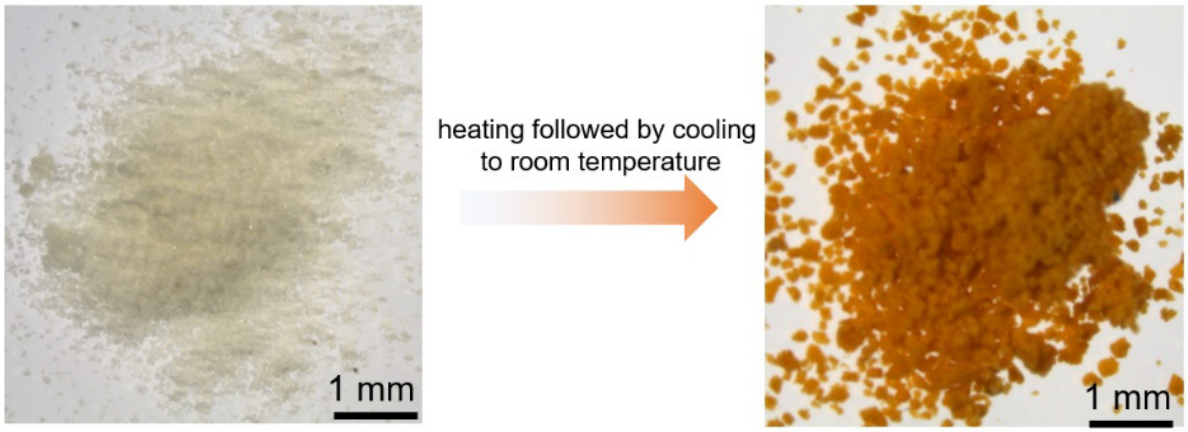

Figure A3.94. Micrographs of ZIF-8-mim$_{0.51}$im$_{0.47}$bim$_{0.02}$ obtained before and after the preparative TGA/DSC experiment (maximum temperature reached was 450 °C).

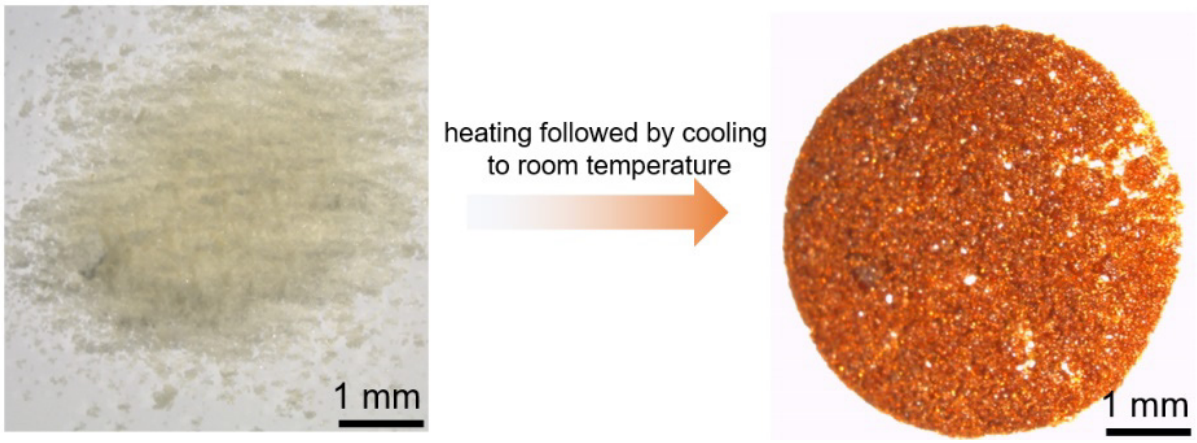

Figure A3.95. Micrographs of ZIF-8-mim$_{0.20}$im$_{0.70}$Clbim$_{0.10}$ obtained before and after the preparative TGA/DSC experiment (maximum temperature reached was 440 °C).

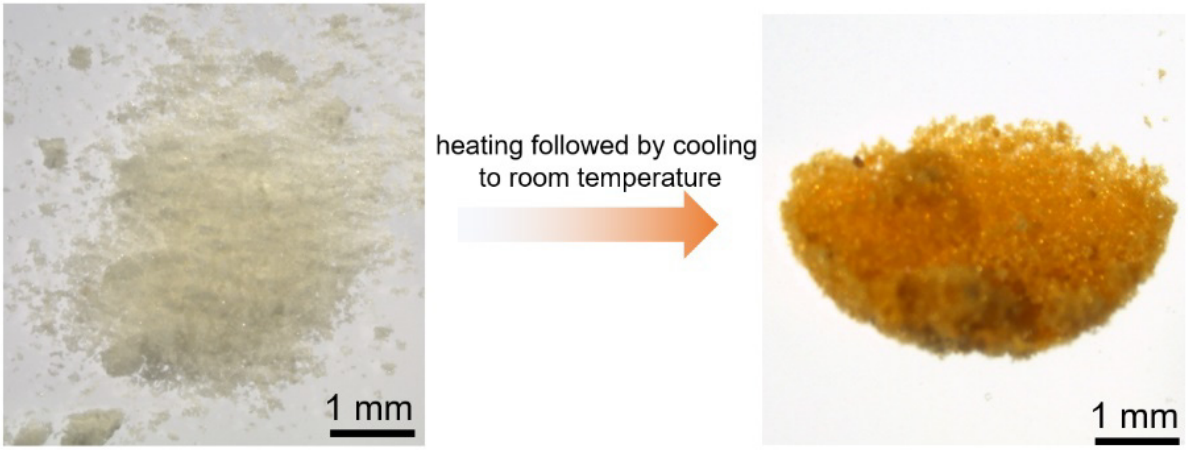

Figure A3.96. Micrographs of ZIF-62-mim$_{0.05}$im$_{0.80}$bim$_{0.15}$ obtained before and after the preparative TGA/DSC experiment (maximum temperature reached was 450 °C).

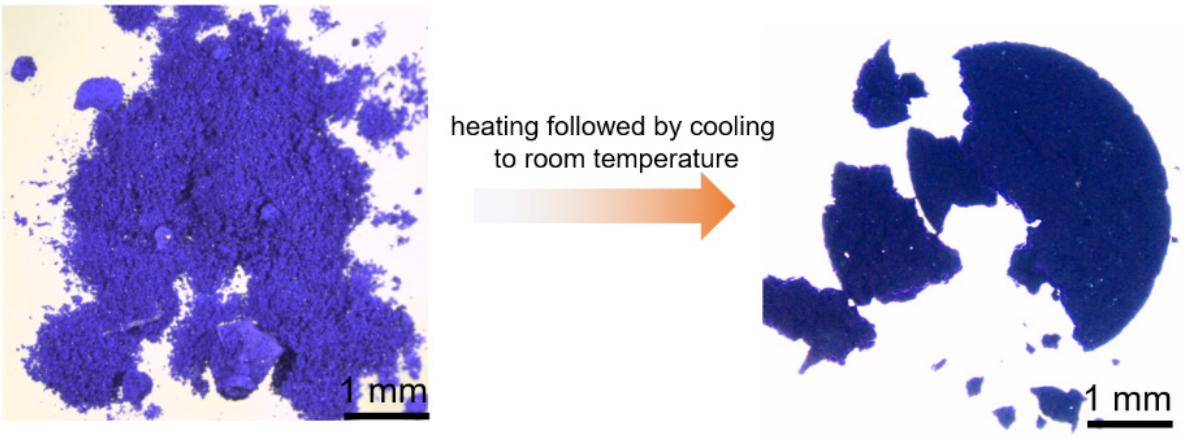

Figure A3.97. Micrographs of ZIF-67-mim$_{0.18}$im$_{0.68}$bim$_{0.14}$ obtained before and after the preparative TGA/DSC experiment (maximum temperature reached was 450 °C).

A.3.8 – Gas physisorption studies

A.3.8.1 – Determination of pore volumes

The specific pore volumes (V_{pore}) were calculated according to previous work[41] with amendments:

$$V_{\text{pore}} = \frac{n_{\text{ads}}^{\text{max}} \cdot M_{\text{CO2}}}{\rho_{\text{sl}}}$$

with $n_{\text{ads}}^{\text{max}}$ the specific molar amount of gas adsorbed (mmol of gas/g material) at 195 K and 95 kPa, M_{CO2} the molar mass of CO_2, and ρ_{sl} the density of the supercooled liquid at 195 K (that is 1.258 g cm^{-3}). For these calculations the implemented routine in the Quantachrome ASiQwin version 5.2 software was used. The obtained values are summarized in **Table A3.6**.

Table A3.6. Summary of maximum gas capacities ($V_{\text{ads}}^{\text{max}}$ and $n_{\text{ads}}^{\text{max}}$), specific pore volumes (V_{pore}) and BET surface area (S_{BET}) obtained from the CO_2 gas physisorption isotherms collected at 195 K or N_2 gas physisorption isotherms collected at 77 K.

Sample	Method	$V_{\text{ads}}^{\text{max}}$ ($cm^3\ g^{-1}$)	$n_{\text{ads}}^{\text{max}}$ (mmol g^{-1})	S_{BET} ($m^2\ g^{-1}$)	V_{pore} ($cm^3\ g^{-1}$)
ZIF-8	CO_2@195K	293.4	13.1	1434	0.46
	N_2@77K	410.9	18.3	1992	0.66
ZIF-8-$mim_{0.15}im_{0.74}bim_{0.11}$	CO_2@195K	293.0	13.1	989	0.46
	N_2@77K	303.7	13.6	1060	0.42
a_gZIF-8-$mim_{0.15}im_{0.74}bim_{0.11}$	CO_2@195K	125.0	5.6	403	0.20
	N_2@77K	108.4	4.8	229	0.16
ZIF-67-$mim_{0.18}im_{0.68}bim_{0.14}$	CO_2@195K	223.9	10.0	897	0.35
a_gZIF-67-$mim_{0.18}im_{0.68}bim_{0.14}$	CO_2@195K	118.5	5.3	316	0.18
a_gZIF-62[a]	CO_2@195K	74.9	3.4	200	0.12

[a] data taken from reference[41].

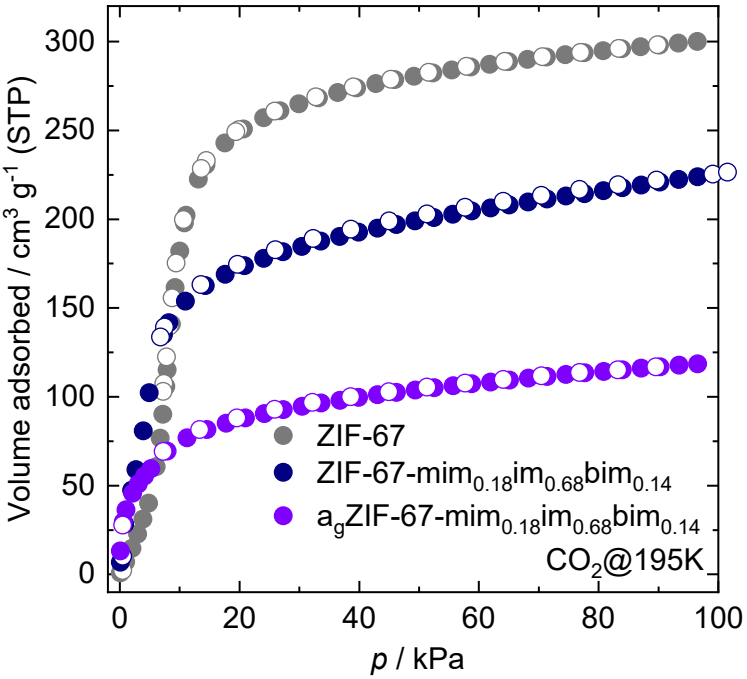

Figure A3.98. CO_2 sorption isotherms recorded at 195 K for ZIF-67, ZIF-67-mim$_{0.18}$im$_{0.68}$bim$_{0.14}$ and a$_g$ZIF-67-mim$_{0.18}$im$_{0.68}$bim$_{0.14}$.

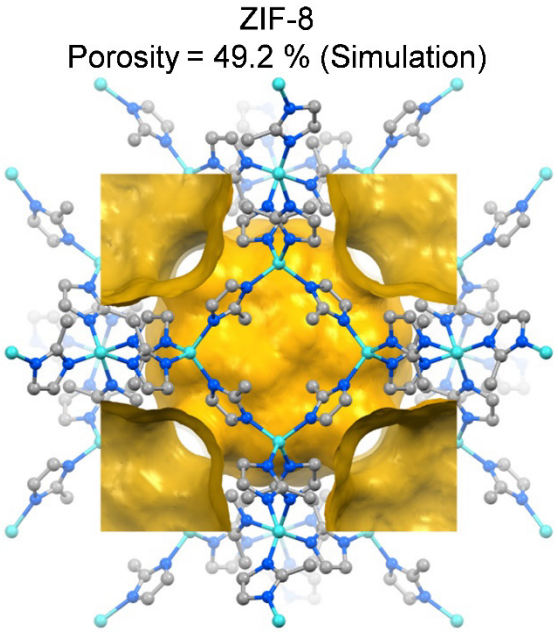

Figure A3.99. Theoretical void fraction of ZIF-8 (CCDC code FAWCEN[163]) was calculated with a probe radius of 1.6 Å and a grid spacing of 0.2 Å by Mercury software V2021.3.0 and is shown in pale yellow. Structure viewed along the crystallographic *a* axis.

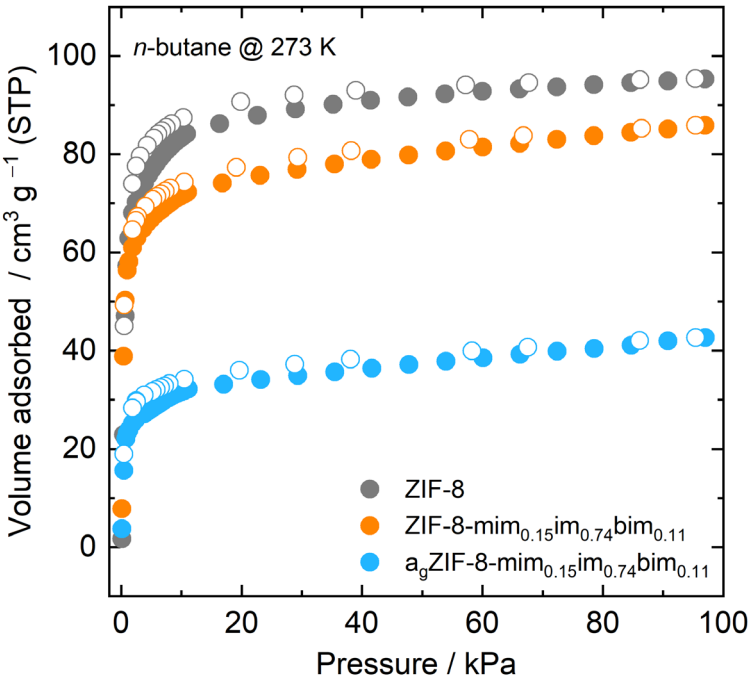

Figure A3.100. *n*-butane sorption isotherms recorded at 273 K for ZIF-8, ZIF-8-mim$_{0.15}$im$_{0.74}$bim$_{0.11}$ and a$_g$ZIF-8-mim$_{0.15}$im$_{0.74}$bim$_{0.11}$.

Table A3.7. Comparison of the hydrocarbon gas capacities (propylene, propane, and *n*-butane) of a_gZIF-8-$mim_{0.15}im_{0.74}bim_{0.11}$ and a_gZIF-62.

Sample	V_{ads}^{max} (propylene) ($cm^3\ g^{-1}$)	V_{ads}^{max} (propane) ($cm^3\ g^{-1}$)	V_{ads}^{max} (*n*-butane) ($cm^3\ g^{-1}$)	
			273K	293K
a_gZIF-8-$mim_{0.15}im_{0.74}bim_{0.11}$	42.2	40.4	42.6	36.4
a_gZIF-62[a]	14.8	6.72	9.9	4.7

[a] data was taken from reference[41].

Table A3.8. Comparison of the specific pore volumes (V_{pore}) of ZIF-8 derivatives obtained from gas sorption isotherms of *n*-butane (@273 K) and CO_2 (@195 K).

Sample	V_{pore} (CO_2)[a] ($cm^3\ g^{-1}$)	V_{pore} (*n*-butane)[b] ($cm^3\ g^{-1}$)	ratio
ZIF-8	0.46	0.41	1: 0.9
ZIF-8-$mim_{0.15}im_{0.74}bim_{0.11}$	0.46	0.41	1: 0.9
a_gZIF-8-$mim_{0.15}im_{0.74}bim_{0.11}$	0.20	0.18	1: 0.9

[a] $p \approx 95$ kPa, applied value for the density of pure liquid adsorbate $\rho_{liq}(CO_2$ @195K) = 1.258 g cm^{-3}.[41]

[b] $p \approx 95$ kPa, applied value for the density of pure liquid adsorbate ρ_{liq}(*n*-butane @273K) = 0.601 g cm^{-3}.[41]

A.3.8.2 – Kinetic gas adsorption

To quantitatively analyze the kinetics for C_3H_6, C_3H_8, and *n*-C_4H_{10} adsorption in ZIF-8, ZIF-8-$mim_{0.15}im_{0.74}bim_{0.11}$ and a_gZIF-8-$mim_{0.15}im_{0.74}bim_{0.11}$, the time-dependent normalized uptake data were fitted using stretched exponential models[71] (pseudo-first-order does not fit the measured curves). The equation describing the relationship between the normalized uptake (corresponding to $(P_i - P)/(P_i - P_e)$) and time by a stretched exponential model is given as follows:

$$\text{normalized uptake} = \frac{(P_i - P)}{(P_i - P_e)} = 1 - e^{-(kt)^{\beta}}$$

where P_i is the initial pressure, P is the pressure at time t (in s), P_e is the pressure at equilibrium, k is the rate constant of gas adsorption (in s^{-1}), and β is the exponent parameter related to the width of the distribution of diffusion rate constants.

Table A3.9. Kinetic parameters for C_3H_6, C_3H_8, and *n*-C_4H_{10} adsorption on ZIF-8, ZIF-8-$mim_{0.15}im_{0.74}bim_{0.11}$ and a_gZIF-8-$mim_{0.15}im_{0.74}bim_{0.11}$ at 293 K.

Sample	Adsorbate	k / s^{-1}	β	R^2
ZIF-8	propylene	3.26×10^{-2}	0.74	0.986
	propane	3.18×10^{-3}	0.39	0.991
	n-butane	3.06×10^{-3}	0.40	0.992
ZIF-8-$mim_{0.15}im_{0.74}bim_{0.11}$	propylene	2.14×10^{-2}	0.59	0.983
	propane	6.21×10^{-3}	0.42	0.996
	n-butane	4.48×10^{-3}	0.38	0.990
a_gZIF-8-$mim_{0.15}im_{0.74}bim_{0.11}$	propylene	9.37×10^{-3}	0.42	0.991
	propane	1.73×10^{-3}	0.49	0.996
	n-butane	1.49×10^{-3}	0.48	0.991

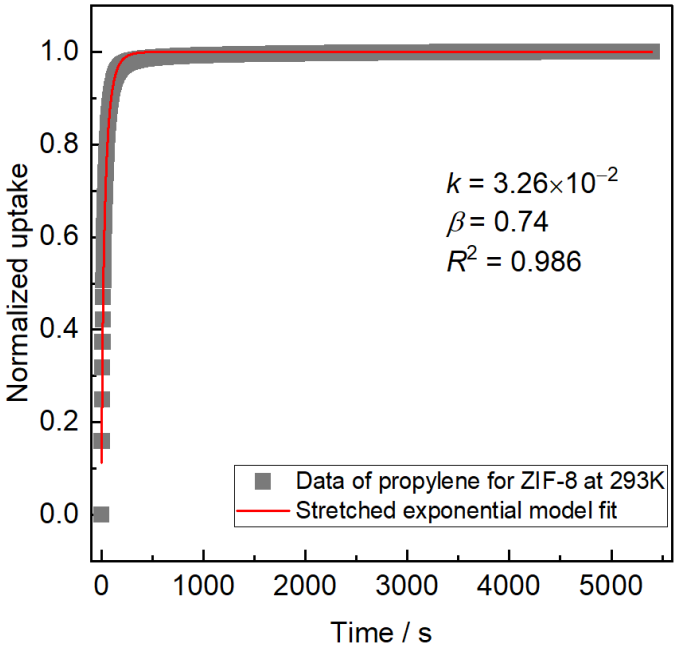

Figure A3.101. Normalized uptake versus time for adsorption kinetic data of ZIF-8 for propylene at 293 K. Stretched exponential fit to the data is shown as a red line.

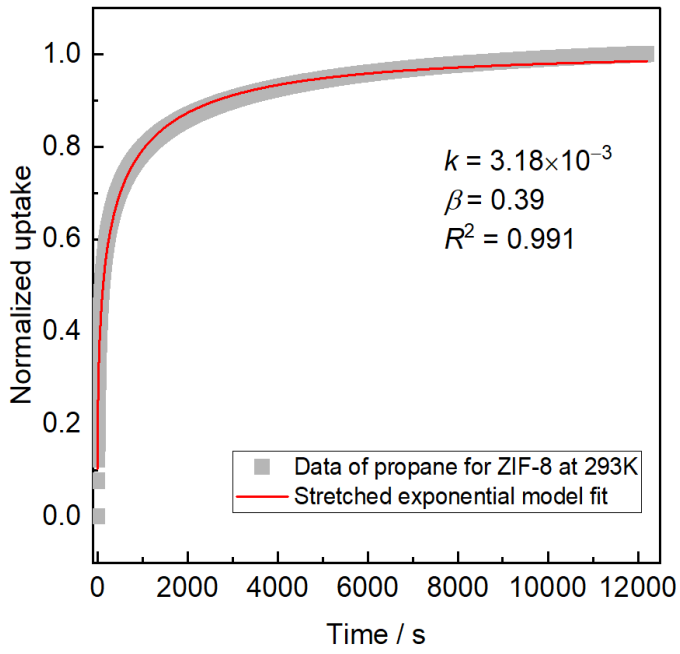

Figure A3.102. Normalized uptake versus time for adsorption kinetic data of ZIF-8 for propane at 293 K. Stretched exponential fit to the data is shown as a red line.

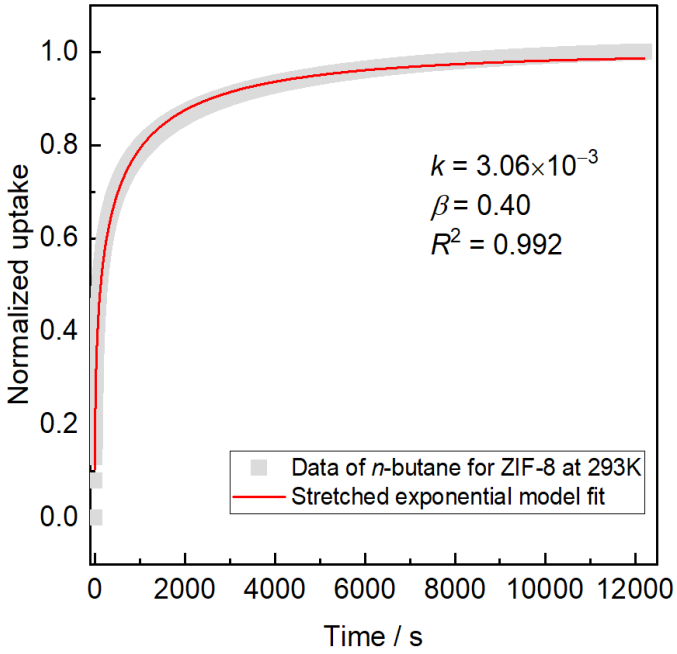

Figure A3.103. Normalized uptake versus time for adsorption kinetic data of ZIF-8 for *n*-butane at 293 K. Stretched exponential fit to the data is shown as a red line.

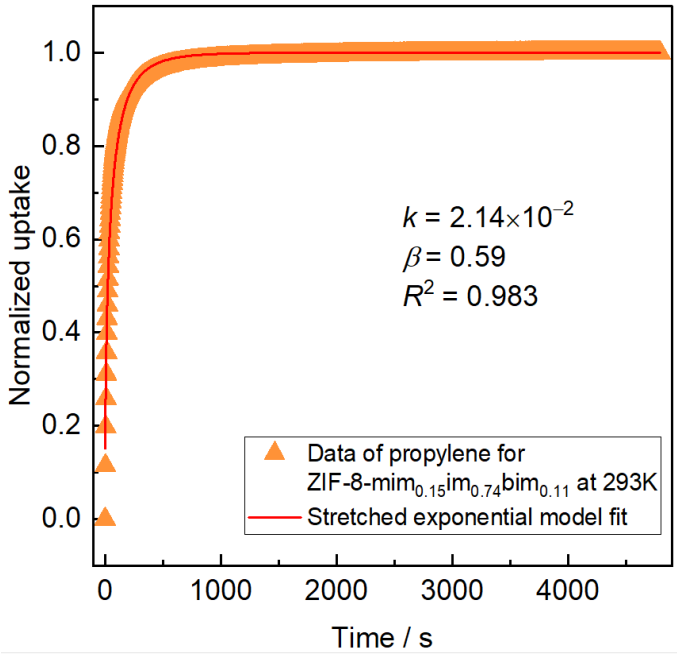

Figure A3.104. Normalized uptake versus time for adsorption kinetic data of ZIF-8-$mim_{0.15}im_{0.74}bim_{0.11}$ for propylene at 293 K. Stretched exponential fit to the data is shown as a red line.

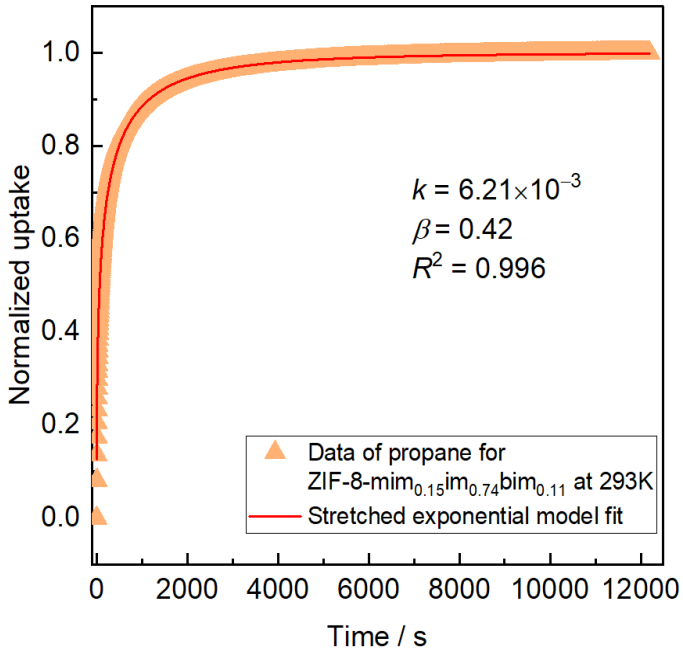

Figure A3.105. Normalized uptake versus time for adsorption kinetic data of ZIF-8-$mim_{0.15}im_{0.74}bim_{0.11}$ for propane at 293 K. Stretched exponential fit to the data is shown as a red line.

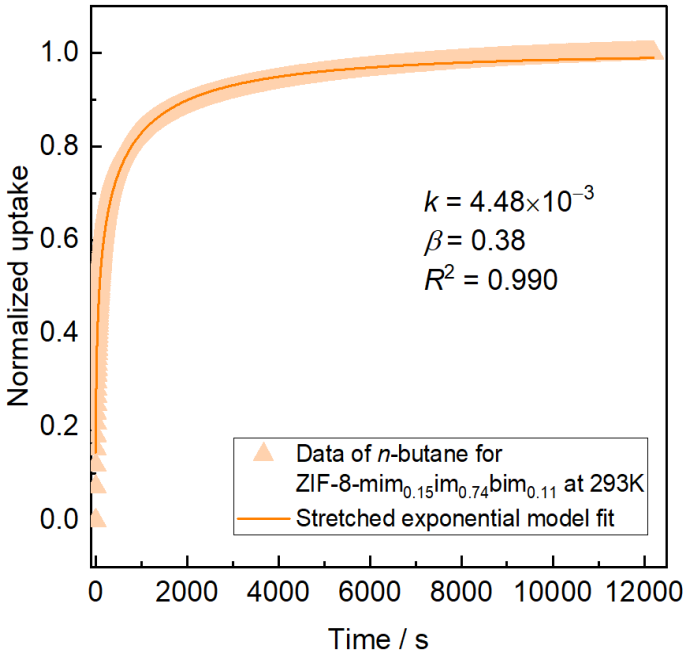

Figure A3.106. Normalized uptake versus time for adsorption kinetic data of ZIF-8-$mim_{0.15}im_{0.74}bim_{0.11}$ for *n*-butane at 293 K. Stretched exponential fit to the data is shown as a red line.

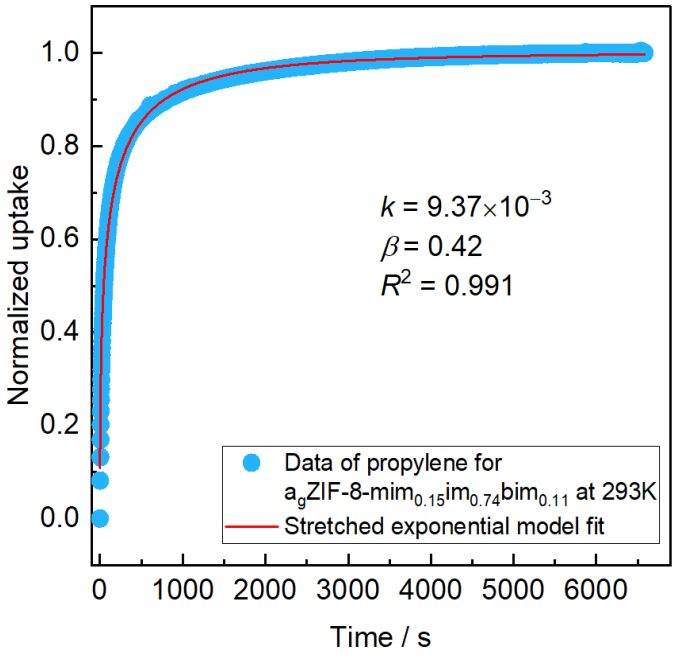

Figure A3.107. Normalized uptake versus time for adsorption kinetic data of a_gZIF-8-$mim_{0.15}im_{0.74}bim_{0.11}$ for propylene at 293 K. Stretched exponential fit to the data is shown as a red line.

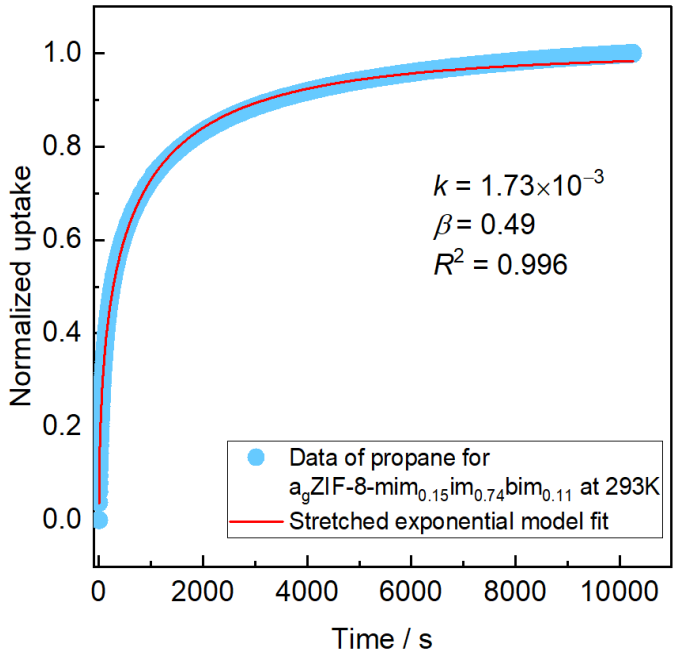

Figure A3.108. Normalized uptake versus time for adsorption kinetic data of a_gZIF-8-$mim_{0.15}im_{0.74}bim_{0.11}$ for propane at 293 K. Stretched exponential fit to the data is shown as a red line.

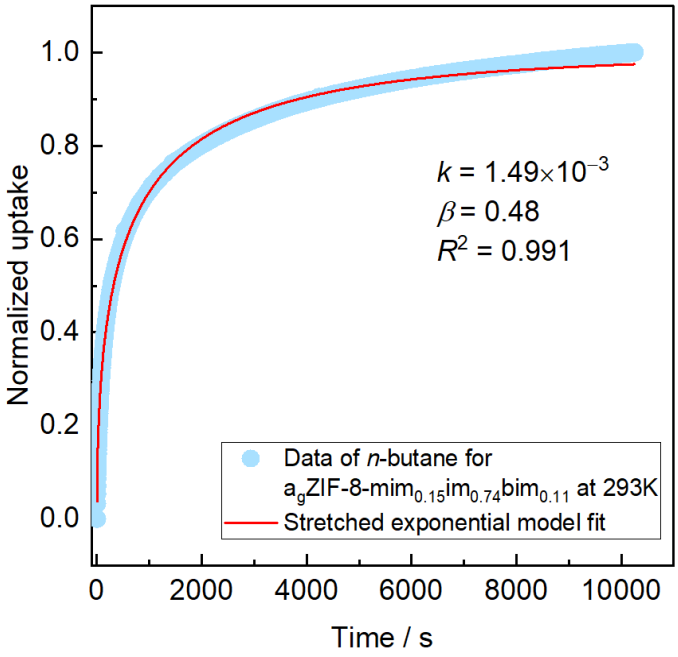

Figure A3.109. Normalized uptake versus time for adsorption kinetic data of a_gZIF-8-$mim_{0.15}im_{0.74}bim_{0.11}$ for *n*-butane at 293 K. Stretched exponential fit to the data is shown as a red line.

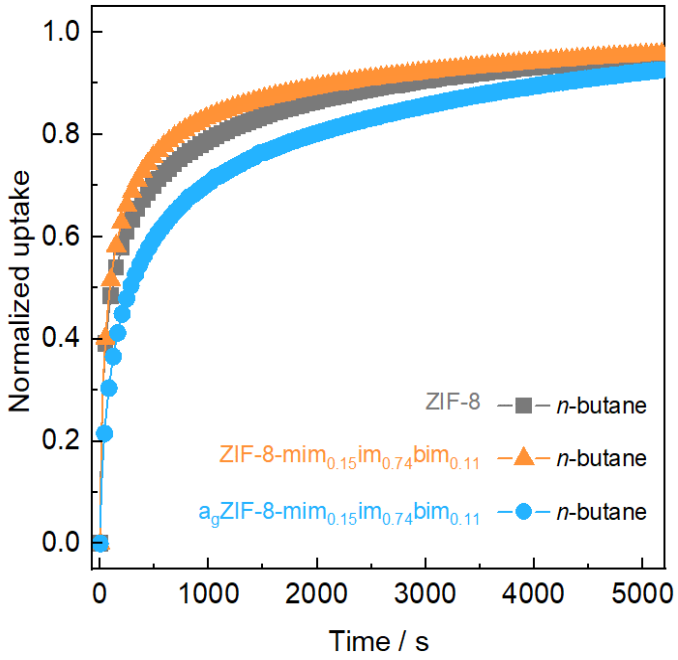

Figure A3.110. Normalized uptake versus time for adsorption kinetic data of *n*-butane for ZIF-8, ZIF-8-$mim_{0.15}im_{0.74}bim_{0.11}$ (crystal) and a_gZIF-8-$mim_{0.15}im_{0.74}bim_{0.11}$ (glass) recorded at 293 K with an equilibrium pressure of about 80 kPa.

Appendix to Section 4

A.4.1 – X-ray powder diffraction data and X-ray total scattering data

A.4.1.1 – Ambient temperature X-ray powder diffraction data

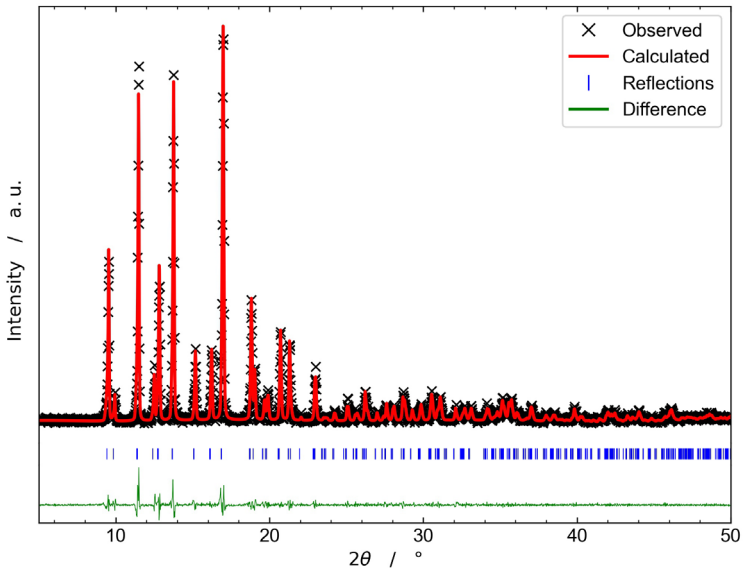

Figure A4.1. Profile fit (Pawley method) performed on the XRPD pattern of ZIF-62(Zn). The blue tick marks indicate the positions of allowed Bragg peaks. The corresponding crystallographic data can be found in **Table A4.1**.

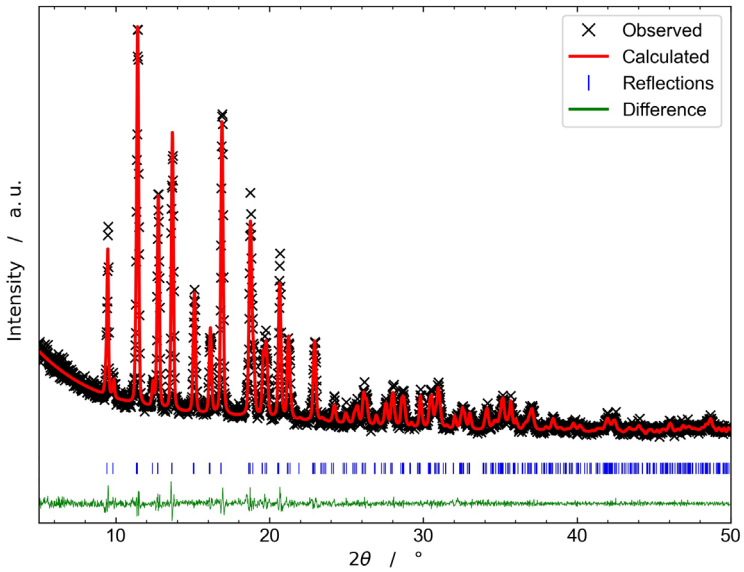

Figure A4.2. Profile fit (Pawley method) performed on the XRPD pattern of ZIF-62(Co). The blue tick marks indicate the positions of allowed Bragg peaks. The corresponding crystallographic data can be found in **Table A4.1**.

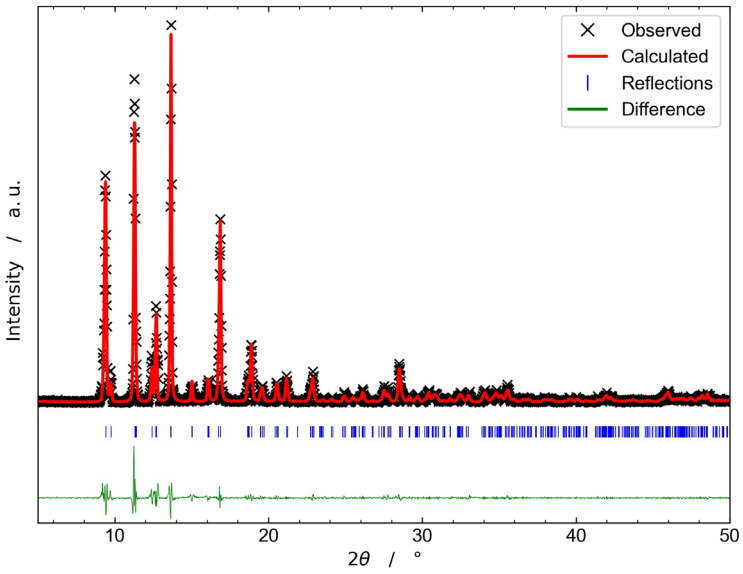

Figure A4.3. Profile fit (Pawley method) performed on the XRPD pattern of ZIF-4(Zn). The blue tick marks indicate the positions of allowed Bragg peaks. The corresponding crystallographic data can be found in **Table A4.1**.

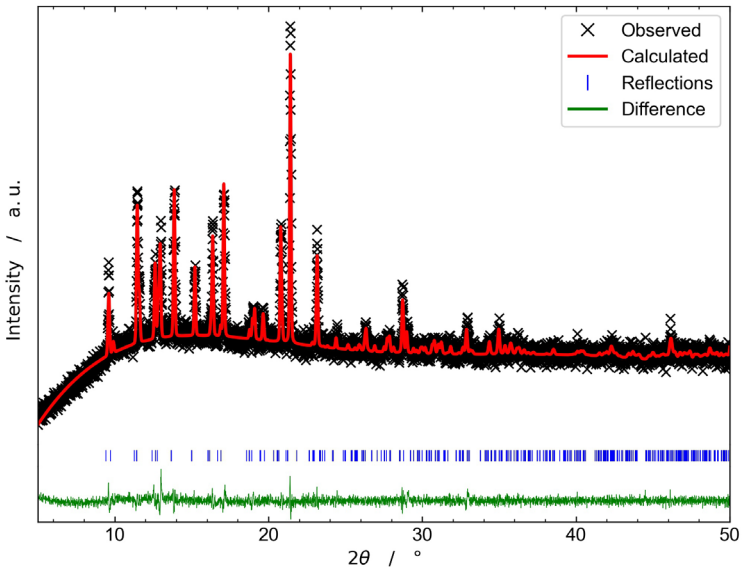

Figure A4.4. Profile fit (Pawley method) performed on the XRPD pattern of ZIF-4(Co). The blue tick marks indicate the positions of allowed Bragg peaks. The corresponding crystallographic data can be found in **Table A4.1**.

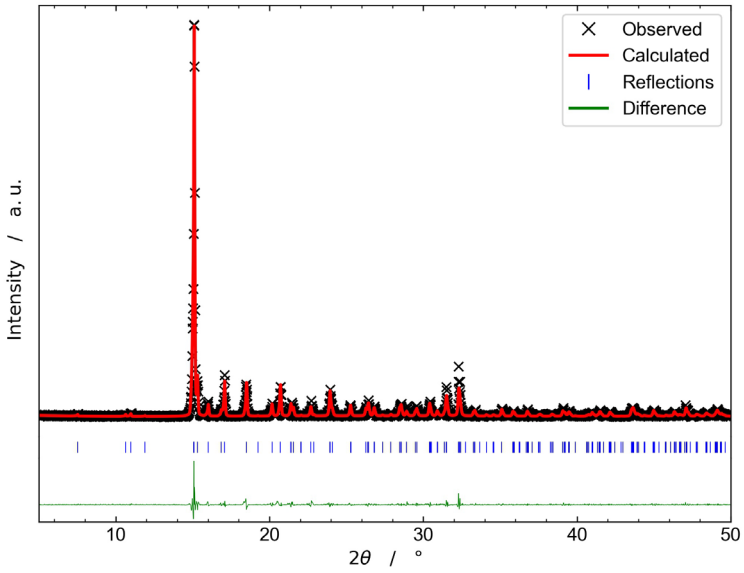

Figure A4.5. Profile fit (Pawley method) performed on the XRPD pattern of ZIF-zni(Zn). The blue tick marks indicate the positions of allowed Bragg peaks. The corresponding crystallographic data can be found in **Table A4.1**.

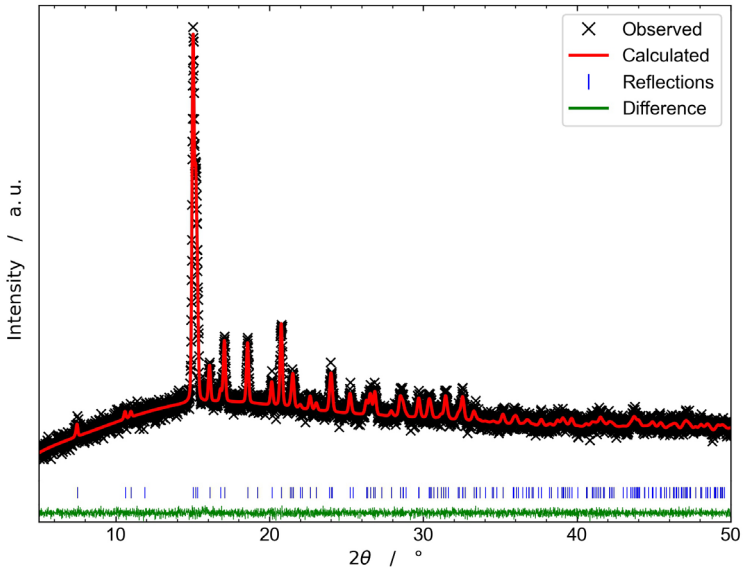

Figure A4.6. Profile fit (Pawley method) performed on the XRPD pattern of ZIF-zni(Co). The blue tick marks indicate the positions of allowed Bragg peaks. The corresponding crystallographic data can be found in **Table A4.1**.

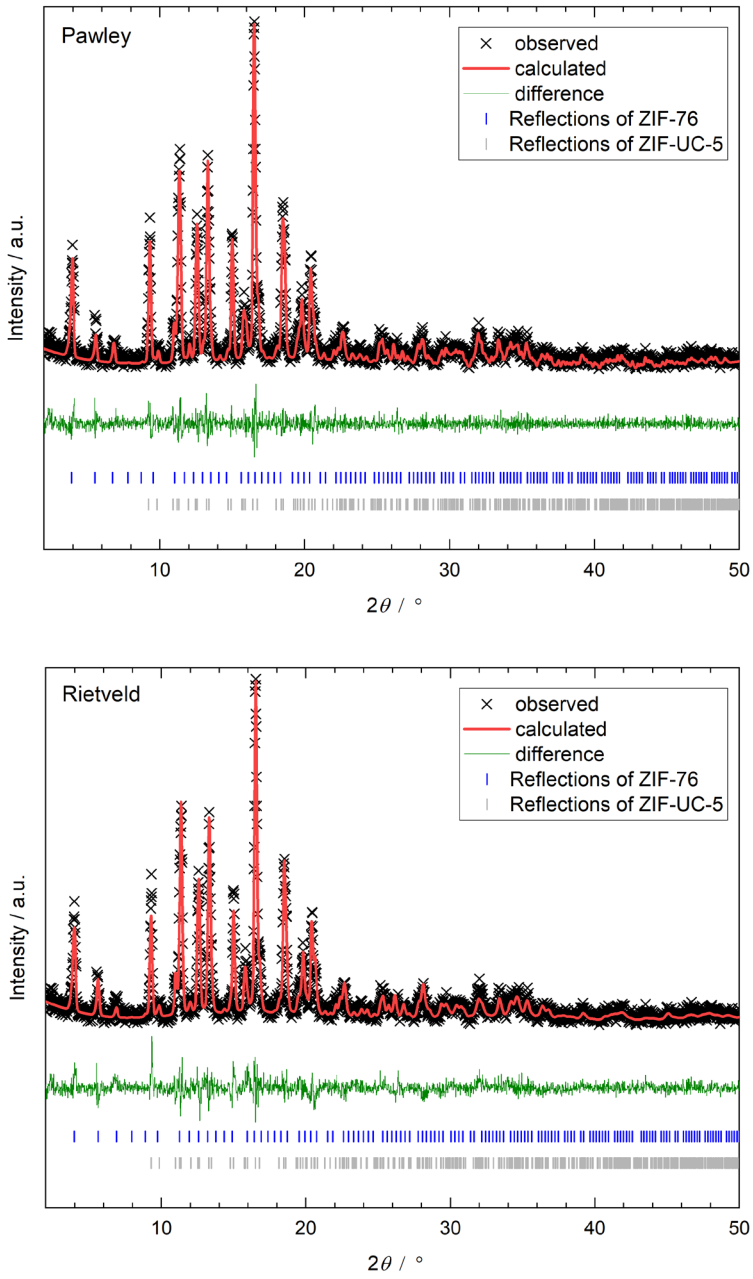

Figure A4.7. TOP: Multiphase profile fit (Pawley method) performed on the XRPD pattern of ZIF-76/UC-5. Bottom: Multiphase Rietveld refinement performed on the XRPD pattern of ZIF-76/UC-5 (CIF files taken from CCDC: GITWEM and GULVIV). The blue and gray tick marks indicate the Bragg positions of ZIF-76 (**lta** topology) and ZIF-UC-5 (**cag** topology), respectively. The results of the Rietveld refinement show that the sample is composed of a phase mixture containing approximately 95 wt% ZIF-UC-5 and about 5 wt% ZIF-76. The corresponding crystallographic data can be found in **Table A4.1**.

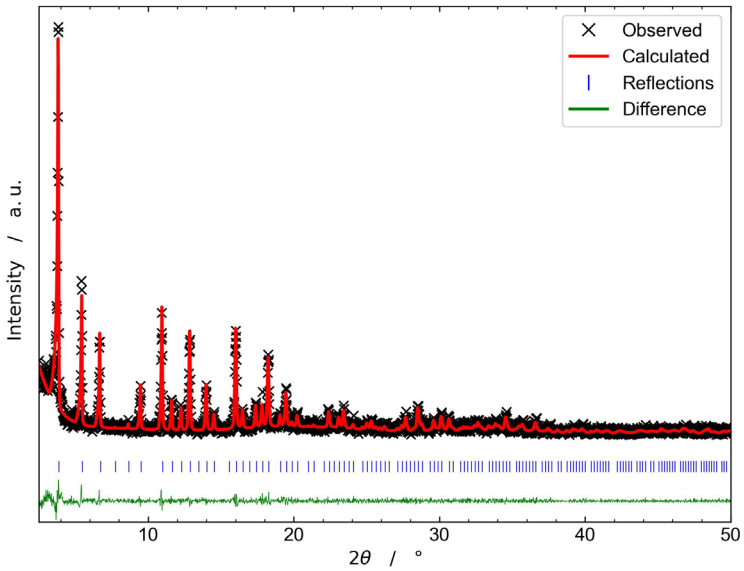

Figure A4.8. Profile fit (Pawley method) performed on the XRPD pattern of pure-phase ZIF-76. The blue tick marks indicate the positions of allowed Bragg peaks. The corresponding crystallographic data can be found in **Table A4.1**.

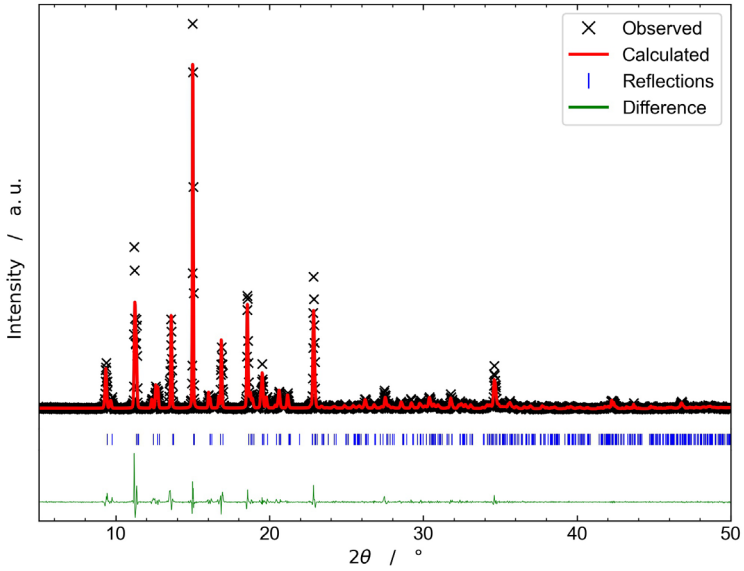

Figure A4.9. Profile fit (Pawley method) performed on the XRPD pattern of TIF-4. The blue tick marks indicate the positions of allowed Bragg peaks. The corresponding crystallographic data can be found in **Table A4.1**.

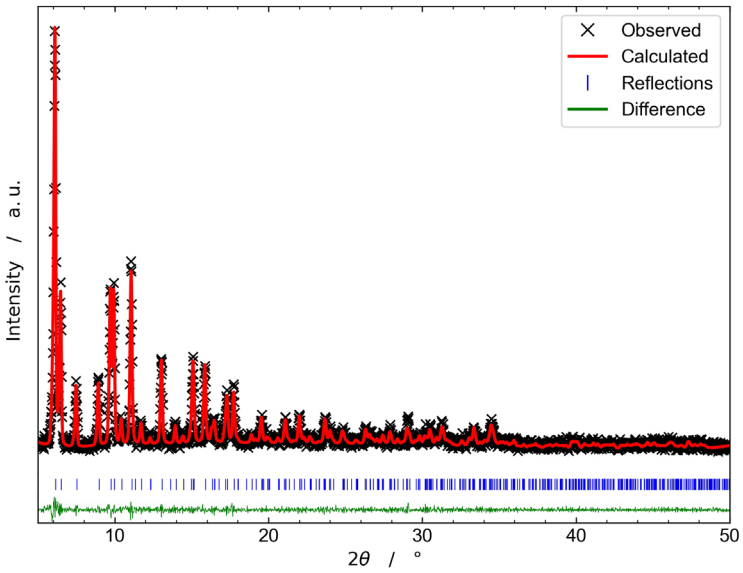

Figure A4.10. Profile fit (Pawley method) performed on the XRPD pattern of ZIF-70. The blue tick marks indicate the positions of allowed Bragg peaks. The corresponding crystallographic data can be found in **Table A4.1**.

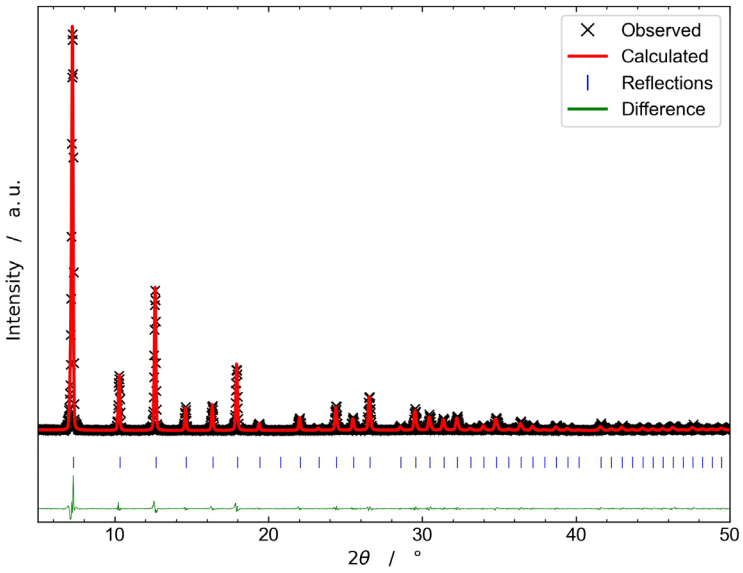

Figure A4.11. Profile fit (Pawley method) performed on the XRPD pattern of ZIF-8. The blue tick marks indicate the positions of allowed Bragg peaks. The corresponding crystallographic data can be found in **Table A4.1**.

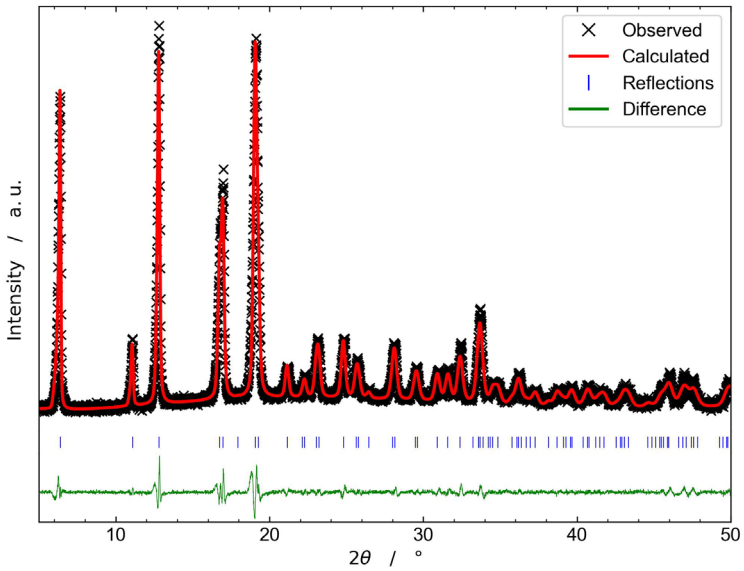

Figure A4.12. Profile fit (Pawley method) performed on the XRPD pattern of ZIF-Cu-1. The blue tick marks indicate the positions of allowed Bragg peaks. The corresponding crystallographic data can be found in **Table A4.1**.

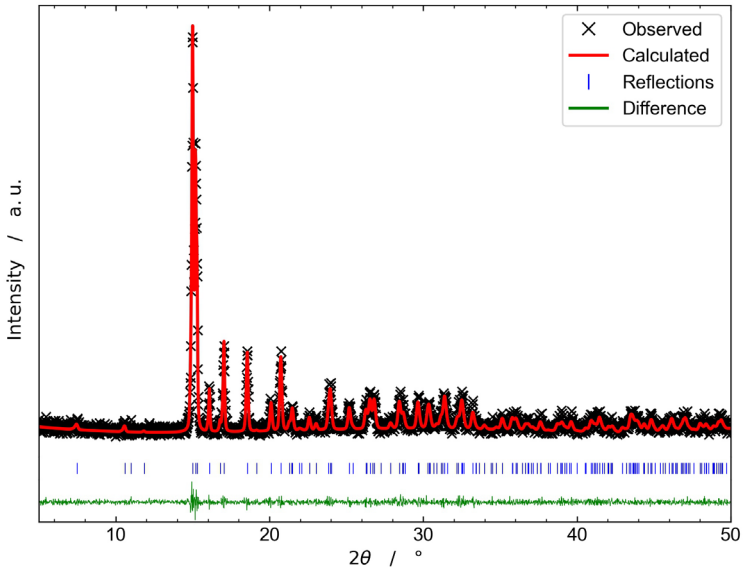

Figure A4.13. Profile fit (Pawley method) performed on the XRPD pattern of ZIF-4(Zn)-5min after heating to 460 °C. The pattern could be very well fit with the crystallographic parameters of ZIF-zni(Zn). The blue tick marks indicate the positions of allowed Bragg peaks of ZIF-zni(Zn). The corresponding crystallographic data can be found in **Table A4.1**.

Table A4.1. Unit cell parameters and corresponding R_{wp}, R_{exp} and χ values determined by the above displayed structureless profile fits (Pawley method) and the multiphase Rietveld refinement of ZIF-76/UC-5 (refinement based on CIF files taken from the CCDC codes GITWEM and GULVIV).

Compound	ZIF-62(Zn)	ZIF-62(Co)	ZIF-4(Zn)	ZIF-4(Co)	ZIF-zni(Zn)	ZIF-zni(Co)	mixed phase ZIF-76/UC-5	
							ZIF-76	ZIF-UC-5
crystal system	orthorhombic	orthorhombic	orthorhombic	orthorhombic	tetragonal	tetragonal	cubic	orthorhombic
space group	*Pbca*	*Pbca*	*Pbca*	*Pbca*	$I4_1cd$	$I4_1cd$	*P*-43*m*	*Pbca*
a / Å	15.491(4)	15.494(7)	15.557(5)	15.47(2)	23.498(4)	23.499(13)	22.71(6)	15.85(4)
b / Å	15.542(3)	15.585(7)	15.484(5)	15.50(2)	23.498(4)	23.499(13)	22.71(6)	16.32(4)
c / Å	17.979(5)	17.995(9)	18.092(7)	18.20(3)	12.534(3)	12.410(6)	22.71(6)	18.10(4)
α / °	90	90	90	90	90	90	90	90
β / °	90	90	90	90	90	90	90	90
γ / °	90	90	90	90	90	90	90	90
V / Å^3	4328.6(17)	4345(4)	4358(2)	4363(11)	6921(3)	6852(8)	11714(88)	4682(19)
R_{wp} / %	21.71	10.78	24.73	4.12	27.79	7.16	21.81	
R_{exp} / %	16.38	8.55	14.51	3.30	18.76	7.09	16.72	
χ	1.33	1.26	1.70	1.25	1.48	1.01	1.30	

Compound	mixed phase ZIF-76/UC-5(Rietveld)		phase pure ZIF-76	TIF-4	ZIF-70	ZIF-8	ZIF-Cu-1	ZIF-4-5min after heating to 460 °C
	ZIF-76 (5.43%)	ZIF-UC-5 (94.57%)						
crystal system	cubic	orthorhombic	cubic	orthorhombic	hexagonal	cubic	trigonal	tetragonal
space group	*P*-43*m*	*Pbca*	*P*-43m	*Pbca*	$P6_3/mmc$	*I*-43*m*	*R*-3	$I4_1cd$
a / Å	22.25(2)	15.721(3)	22.736(2)	15.387(3)	27.036(6)	17.0727(9)	27.617(2)	23.572(7)
b / Å	22.25(2)	16.120(4)	22.736(2)	15.465(3)	27.036(6)	17.0727(9)	27.617(2)	23.572(7)
c / Å	22.25(2)	17.944(6)	22.736(2)	18.078(3)	18.092(5)	17.0727(9)	5.4199(5)	12.424(3)
α / °	90	90	90	90	90	90	90	90
β / °	90	90	90	90	90	90	90	90
γ / °	90	90	90	90	120	90	120	90
V / Å^3	11014(25)	4547(2)	11752(4)	4301.9(12)	11452(6)	4976.3(8)	3580.1(8)	6903(4)
R_{wp} / %	22.26		22.88	28.91	19.18	22.38	7.88	27.44
R_{exp} / %	18.79		19.30	15.59	17.16	14.97	4.09	25.38
χ	1.18		1.19	1.85	1.12	1.49	1.92	1.08

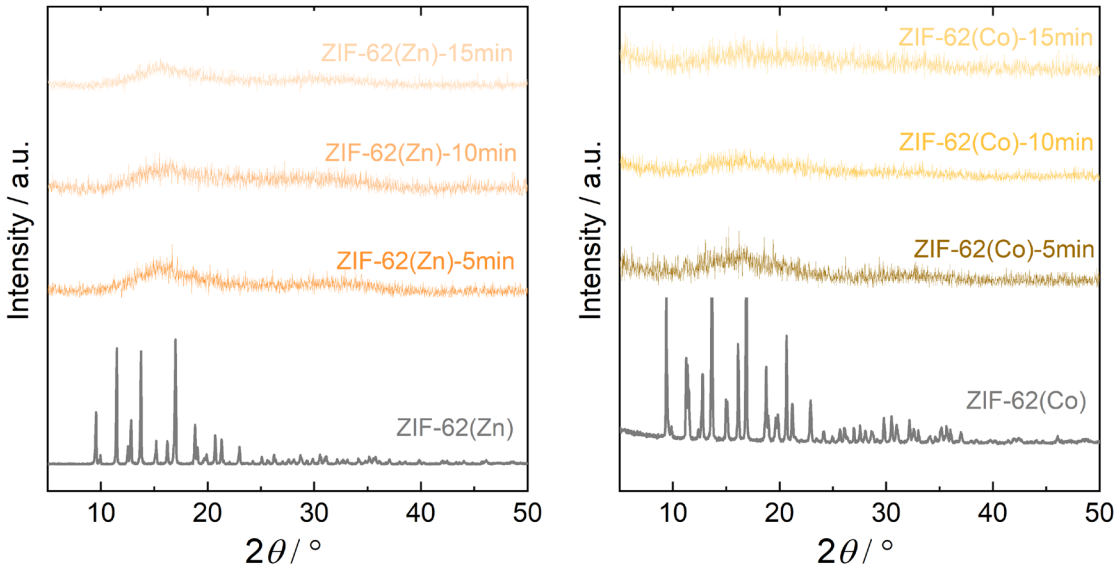

Figure A4.14. Left: XPRD patterns of ZIF-62(Zn) and the corresponding samples derived by PSBM. Right: XPRD patterns of ZIF-62(Co) and the corresponding samples derived by PSBM.

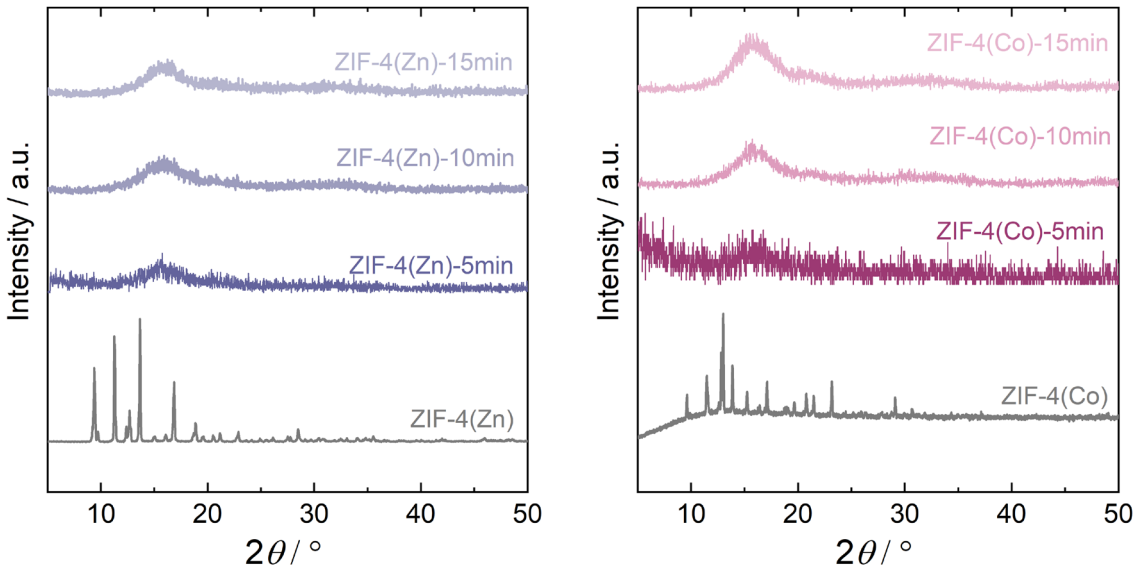

Figure A4.15. Left: XPRD patterns of ZIF-4(Zn) and the corresponding samples derived by PSBM. Right: XPRD patterns of ZIF-4(Co) and the corresponding samples derived by PSBM.

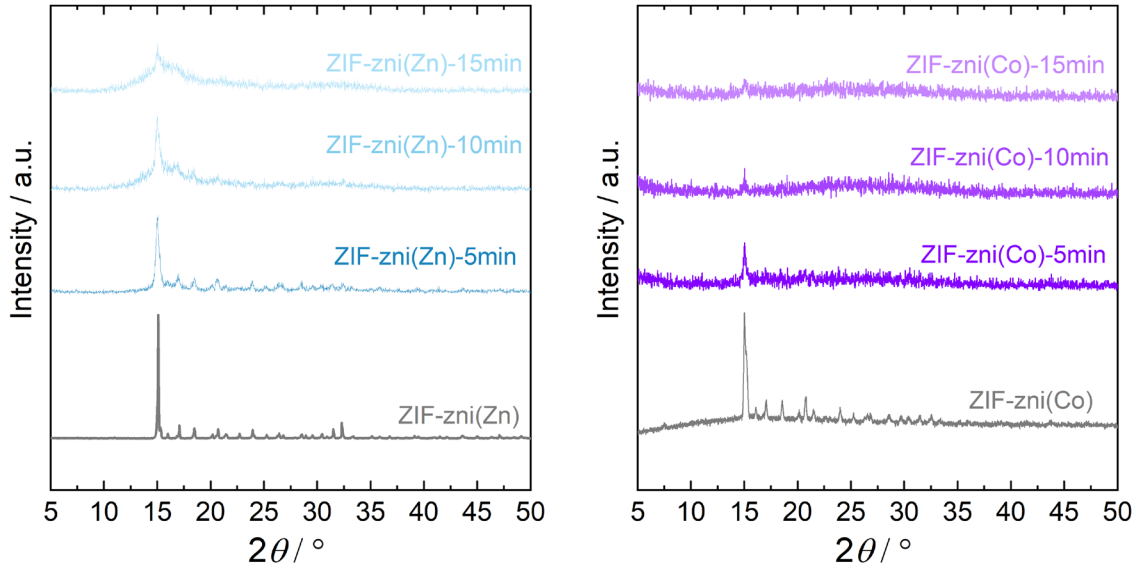

Figure A4.16. Left: XPRD patterns of ZIF-zni(Zn) and the corresponding samples derived by PSBM. Right: XPRD patterns of ZIF-zni(Co) and the corresponding samples derived by PSBM.

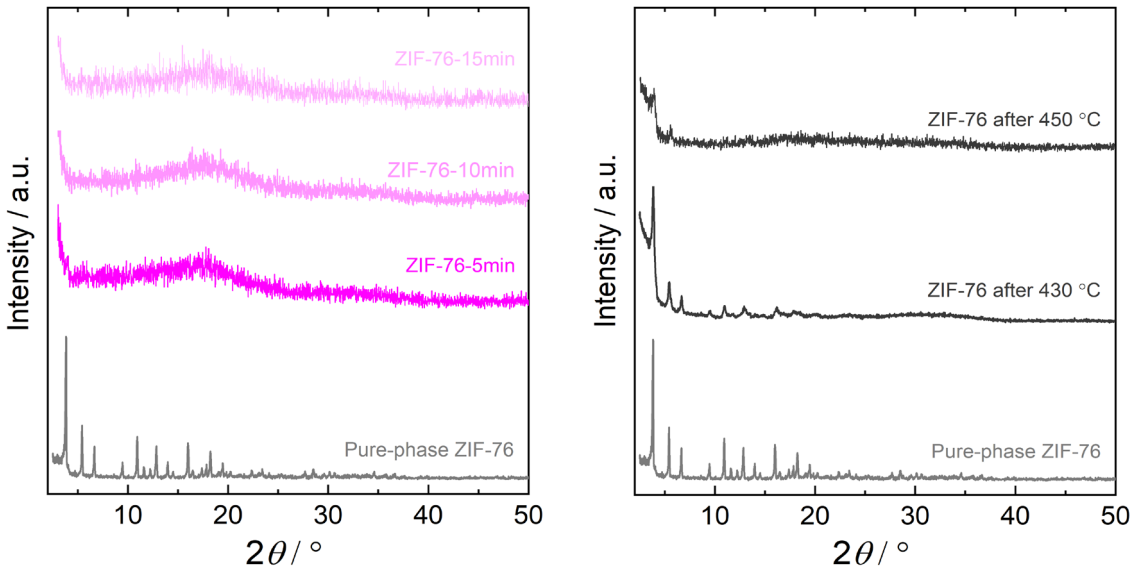

Figure A4.17. Left: XPRD patterns of phase pure ZIF-76 and the corresponding samples derived by PSBM. Right: two XRPD patterns of phase pure ZIF-76 after heating to 430 °C and 450 °C under inert atmosphere. The purpose is to confirm that pure-phase ZIF-76 cannot be melted and only decomposes at 450 °C.

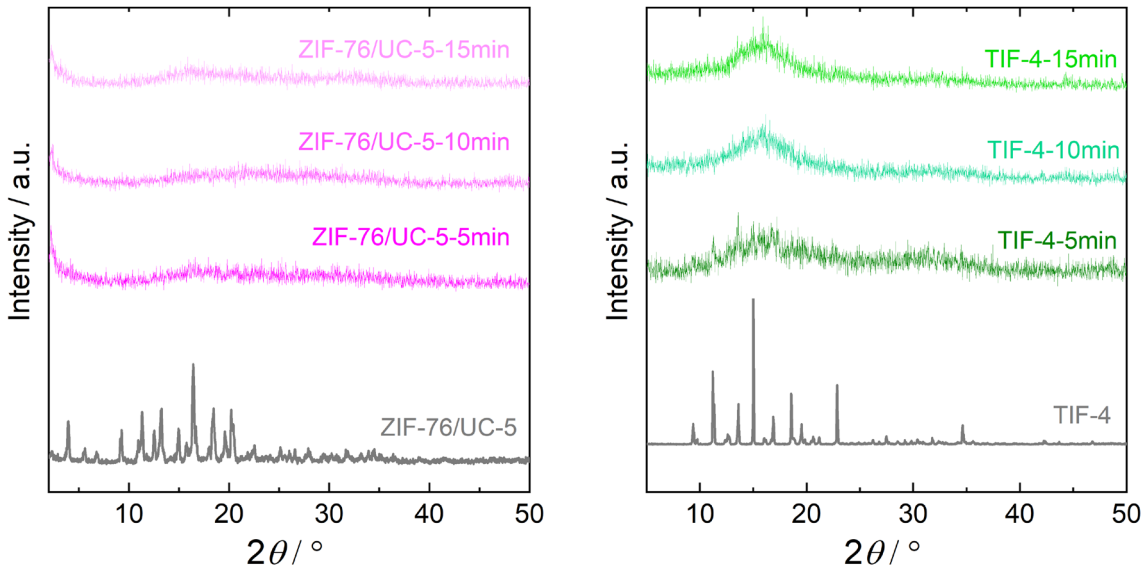

Figure A4.18. Left: XPRD patterns of ZIF-76/UC-5 and the corresponding samples derived by PSBM. Right: XPRD patterns of TIF-4 and the corresponding samples derived by PSBM.

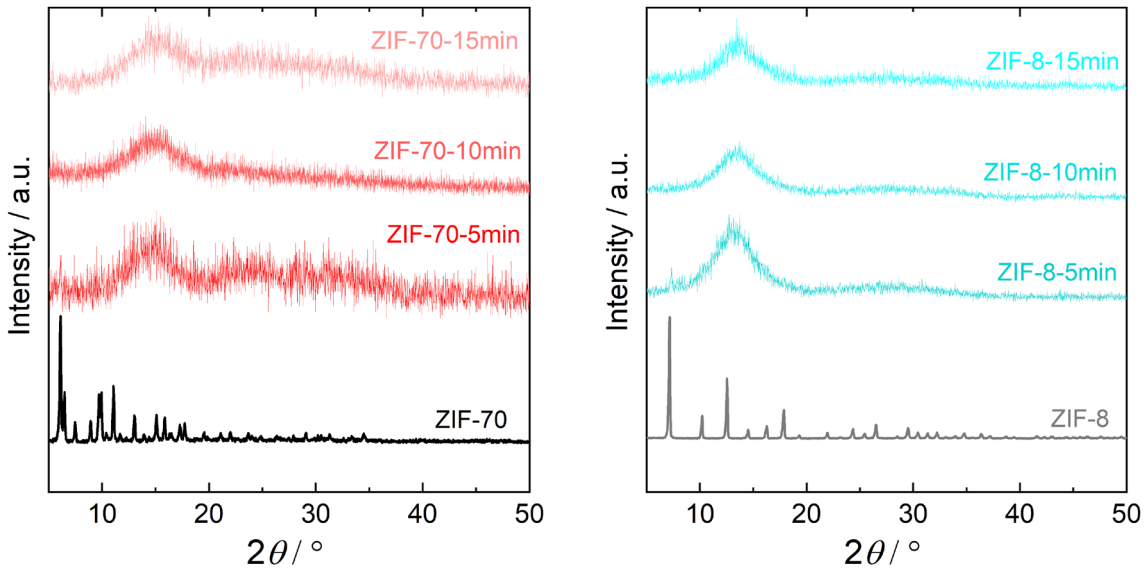

Figure A4.19. Left: XPRD patterns of ZIF-70 and the corresponding samples derived by PSBM. Right: XPRD patterns of ZIF-8 and the corresponding samples derived by PSBM.

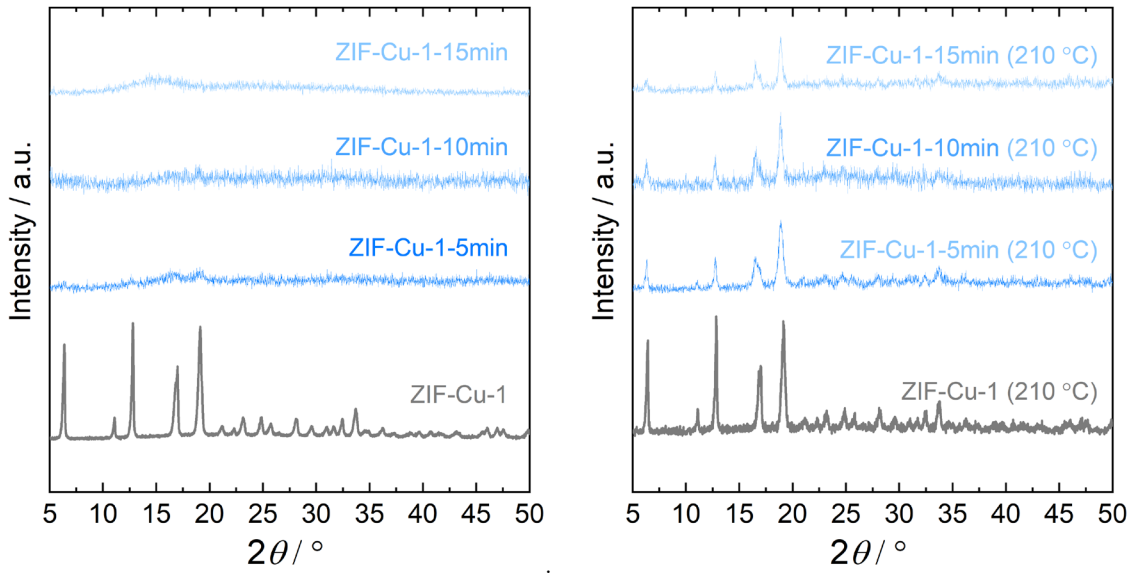

Figure A4.20. Left: XPRD patterns of ZIF-Cu-1 and the corresponding samples derived by PSBM. Right: XPRD patterns of the corresponding samples after heating to 210 °C to check their recrystallization behaviour.

A.4.1.2 – Estimation of crystalline and amorphous weight fractions

The weight fractions of the crystalline and amorphous phases of the ZIF samples, which were not fully amorphous after ball milling, were estimated by using the "degree of crystallinity" approach. The degree of crystallinity is defined according to the following equation[164]:

$$\text{Degree of crystallinity} = \frac{I_c}{I_c + I_a} \times 100\%$$

where I_c is the integrated intensity of the Bragg peaks of the crystalline phase, and I_a is the integrated intensity of diffuse scattering signals of the amorphous phase. Profile fitting was performed using the software TOPAS.[159] The crystalline phase was modelled using the Pawley method, including two parameters to account for both Gaussian and Lorentzian peak broadening due to a reduced crystallite size with increasing ball milling times. The broad diffuse scattering signals of the amorphous/glass phases located at approx. 16° and 32° 2θ were modelled as independent peaks with parameters for Gaussian and Lorentzian peak broadening. We would like to stress that the degree of crystallinity is not to be considered a quantitative measure for the weight fraction of the crystalline phase in a mixture of crystalline and amorphous phases. Instead, it allows for the comparison of the crystallinity of a series of compositionally strongly related materials on a qualitative level.[165]

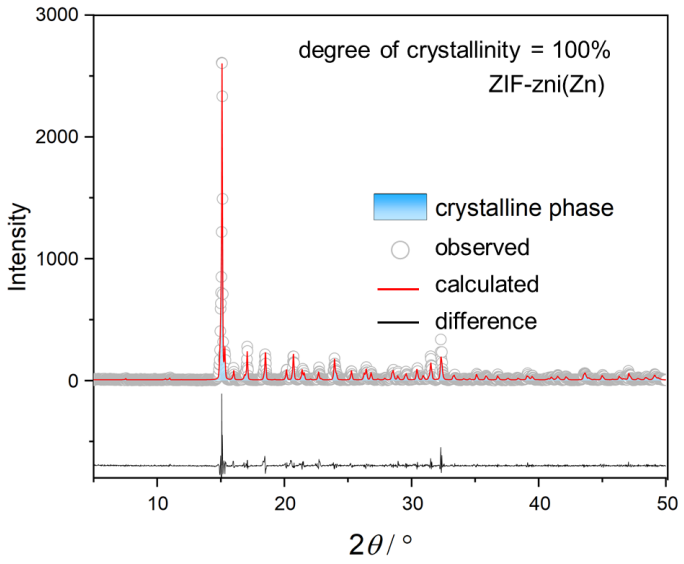

Figure A4.21. Profile fit to the XRPD pattern of ZIF-zni(Zn) (before ball milling). The offset of the difference curve relative to the zero line was set to –700 for clarity. No amorphous phase is detectable, so the degree of crystallinity is 100%.

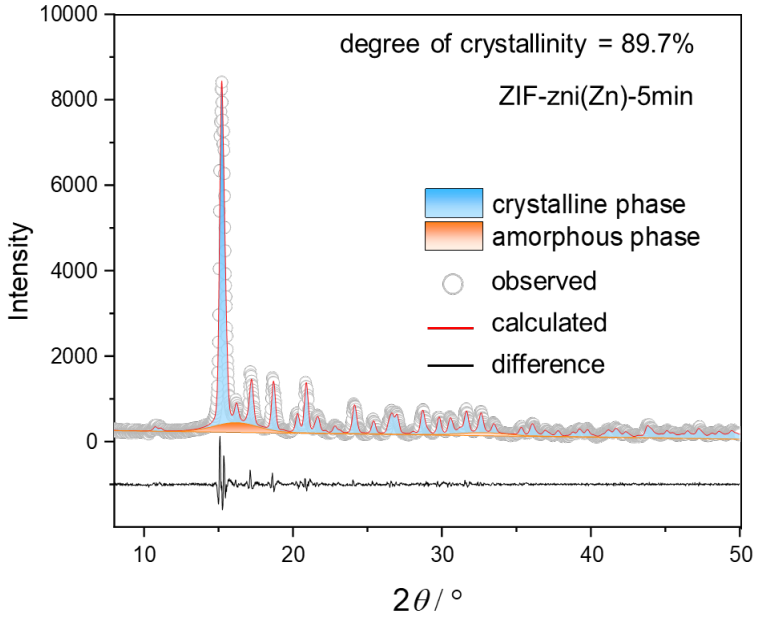

Figure A4.22. Profile fit to the XRPD pattern of ZIF-zni(Zn)-5min where the contribution of the crystalline (blue) and amorphous (orange) phases are highlighted separately. The offset of the difference curve relative to the zero line was set to –1000 for clarity.

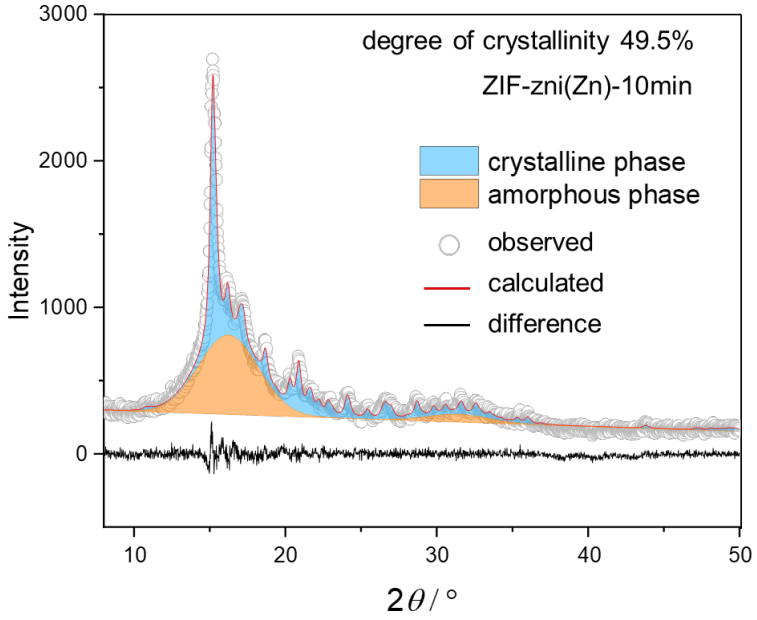

Figure A4.23. Profile fit to the XRPD pattern of ZIF-zni(Zn)-10min, where the contribution of the crystalline (blue) and amorphous (orange) phases are highlighted separately.

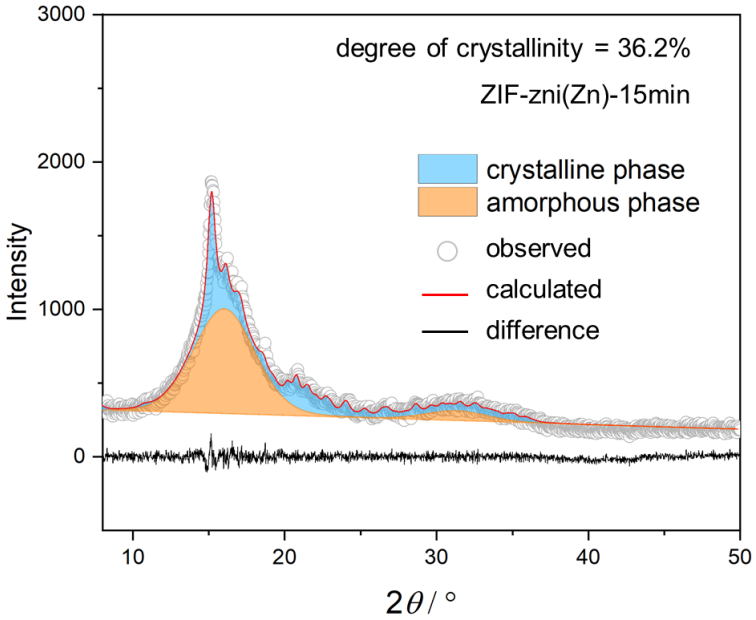

Figure A4.24. Profile fit to the XRPD patterns of ZIF-zni(Zn)-15min, where the contribution of the crystalline (blue) and amorphous (orange) phases are highlighted separately.

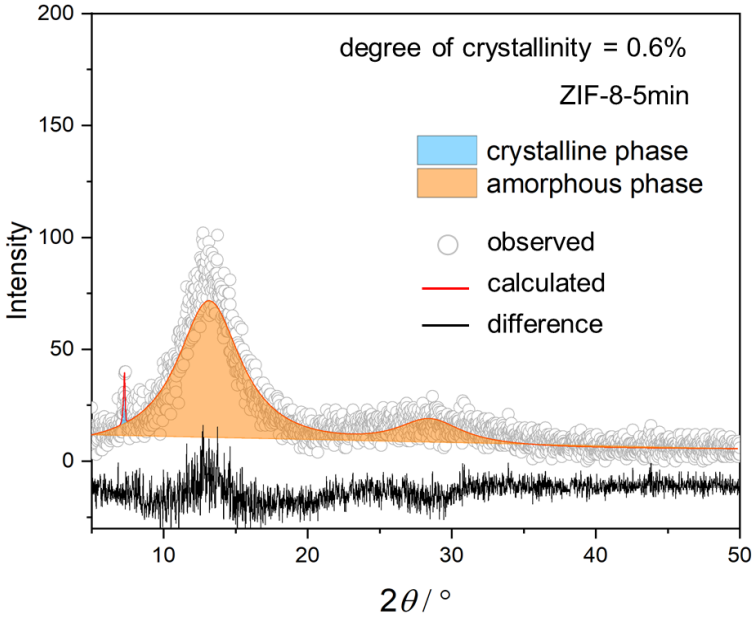

Figure A4.25. Profile fit to the XRPD patterns of ZIF-8-5min, where the contribution of the crystalline (blue) and amorphous (orange) phases are highlighted separately. The offset of the difference curve relative to the zero line was set to –10 for clarity. Due to the poor signal-to-noise ratio of this diffraction pattern, the derived degree of crystallinity may have a rather large error. Anyhow the weight fraction of the amorphous phase is around two orders of magnitude larger than the weight fraction of the residual crystalline phase.

A.4.1.3 – Variable temperature X-ray powder diffraction data

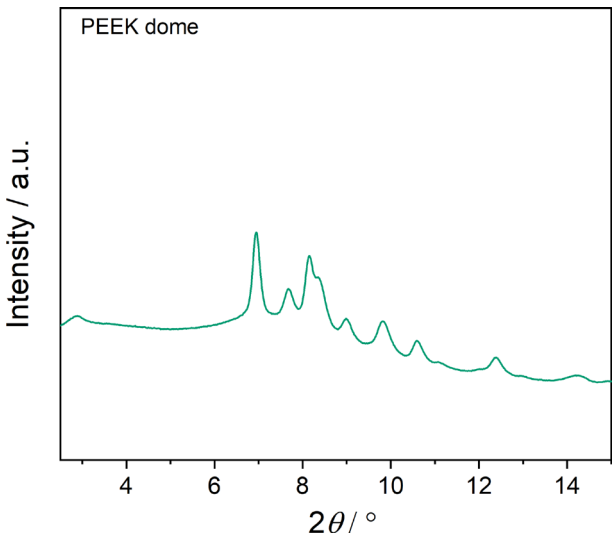

Figure A4.26. XRPD pattern (λ = 0.61992 Å) of the polyether ether ketone (PEEK) dome without sample recorded at 27 °C. The PEEK dome was sealed on the high temperature cell to achieve better uniformity of temperature.

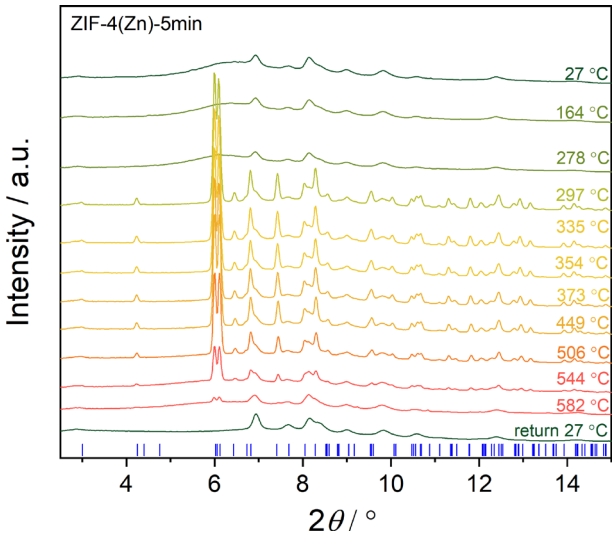

Figure A4.27. VT-XRPD patterns (λ = 0.61992 Å) of ZIF-4(Zn)-5min. The patterns are not normalized but vertically offset for clarity. The residual diffraction peaks on the pattern of return 27 °C originate from the high temperature cell with a PEEK dome. Reflection positions for ZIF-zni (CCDC code IMIDZB) are shown as blue tick marks. ZIF-4(Zn)-5min recrystallizes to ZIF-zni(Zn) at 297 °C. The formed ZIF-zni(Zn) melts around 582 °C.

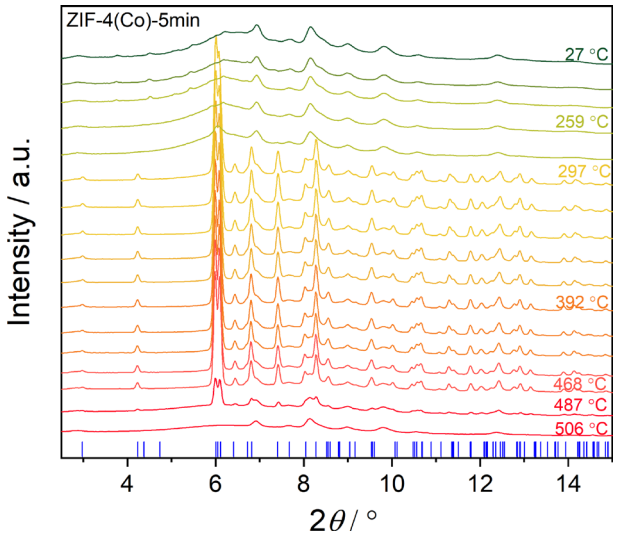

Figure A4.28. VT-XRPD patterns (λ = 0.61992 Å) of ZIF-4(Co)-5min. The patterns are not normalized but vertically offset for clarity. The residual diffraction peaks on the pattern of 506 °C originate from the high temperature cell with a PEEK dome. Reflection positions for ZIF-zni (CCDC code IMIDZB) are shown as blue tick marks. ZIF-4(Co)-5min recrystallizes to ZIF-zni(Co) at 297 °C. The formed ZIF-zni(Co) in parallel melts and decomposes above 487 °C.

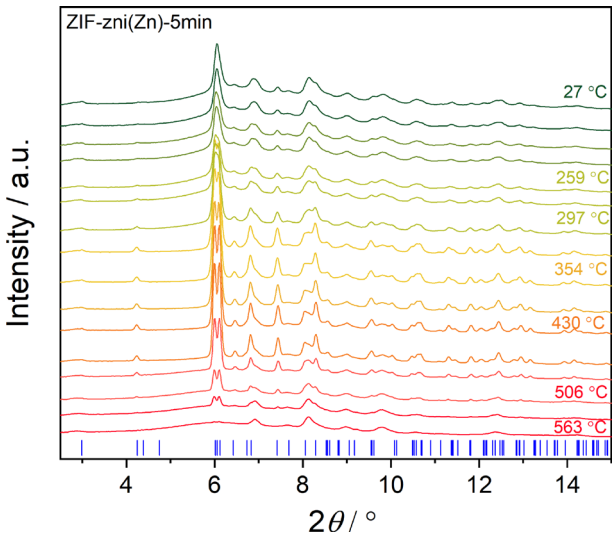

Figure A4.29. VT-XRPD patterns (λ = 0.61992 Å) of ZIF-zni(Zn)-5min. The patterns are not normalized but vertically offset for clarity. The residual diffraction peaks on the pattern of 563 °C originate from the high temperature cell with a PEEK dome. Reflection positions for ZIF-zni (CCDC code IMIDZB) are shown as blue tick marks. ZIF-zni(Zn)-5min contains a large fraction of crystalline ZIF-zni(Zn) at the beginning of the experiment. During heating more ZIF-zni(Zn) forms from the amorphous (glassy) fraction of the sample. The ZIF-zni(Zn) melts around 563 °C.

A.4.1.4 – X-ray total scattering data

It is worth mentioning that $S(Q)$ data for a_gZIF-4(Zn)-5min and a_gZIF-zni(Zn)-5min, which seem to inhibit the generation of ZnO[41] impurity compared to a_gZIF-4(Zn) and a_gZIF-zni(Zn) (**Figure A4.32** and **Figure A4.33**). This is due to their lower melting temperature than the parent material, especially ZIF-zni(Zn)-5min, which is up to 19 °C lower than ZIF-zni(Zn) (**Figure 4.6**), thus the lower melting point prevents the decomposition of the material and the appearance of impurities.

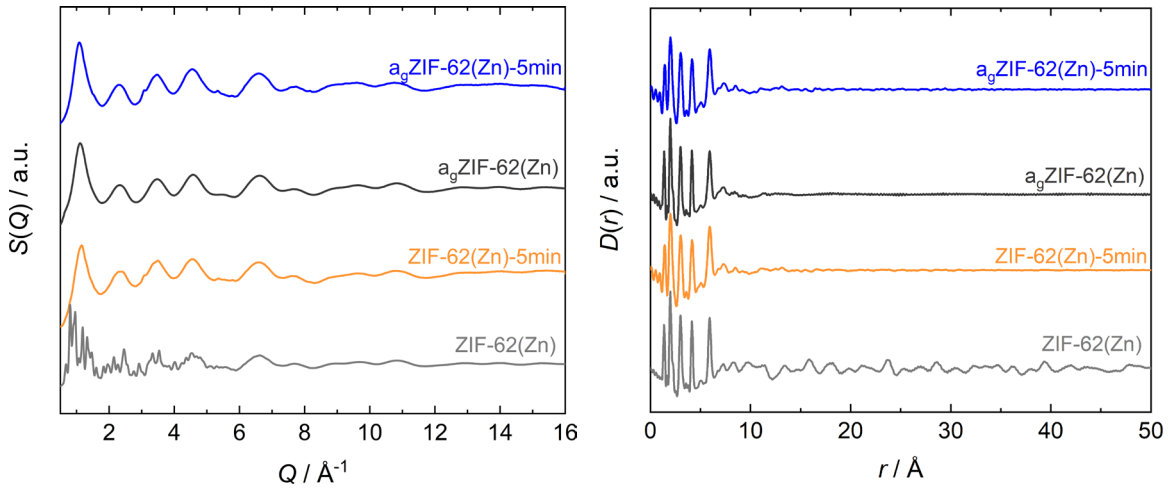

Figure A4.30. X-ray total scattering data in the form of $S(Q)$ and $D(r)$ of ZIF-62(Zn), ZIF-62(Zn)-5min, a_gZIF-62(Zn) and a_gZIF-62(Zn)-5min. Data of ZIF-62(Zn) and a_gZIF-62(Zn) are taken from ref. 1. The local structure of the melt-quenched a_gZIF-62(Zn) is essentially identical to those of the ball-milled ZIF-62(Zn)-5min and the ball-milled and heated a_gZIF-62(Zn)-5min.

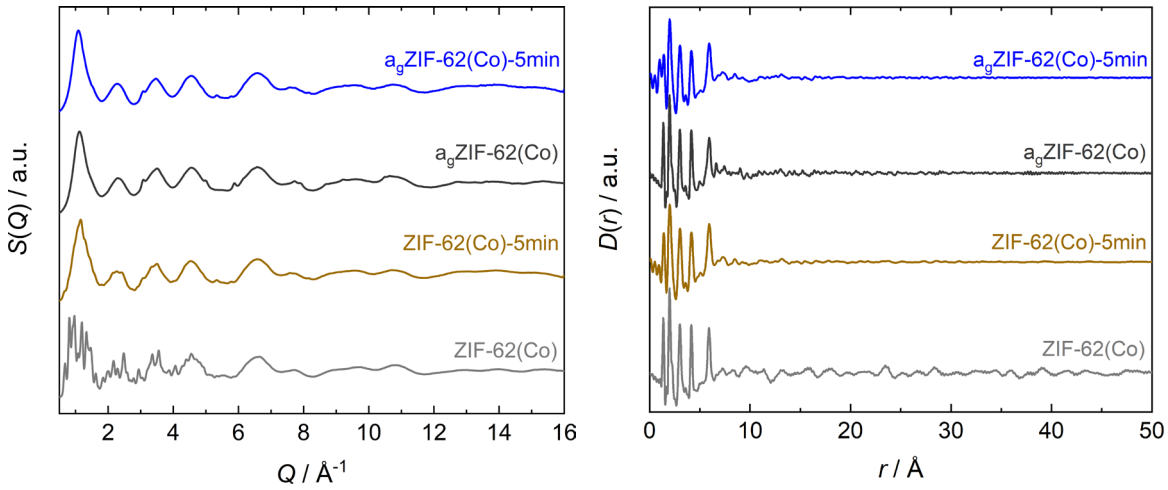

Figure A4.31. X-ray total scattering data in the form of $S(Q)$ and $D(r)$ of ZIF-62(Co), ZIF-62(Co)-5min, a_gZIF-62(Co) and a_gZIF-62(Co)-5min. Data of ZIF-62(Co) and a_gZIF-62(Co) are taken from ref. 7. The local structure of the melt-quenched a_gZIF-62(Co) is essentially identical to those of the ball-milled ZIF-62(Co)-5min and the ball-milled and heated a_gZIF-62(Co)-5min.

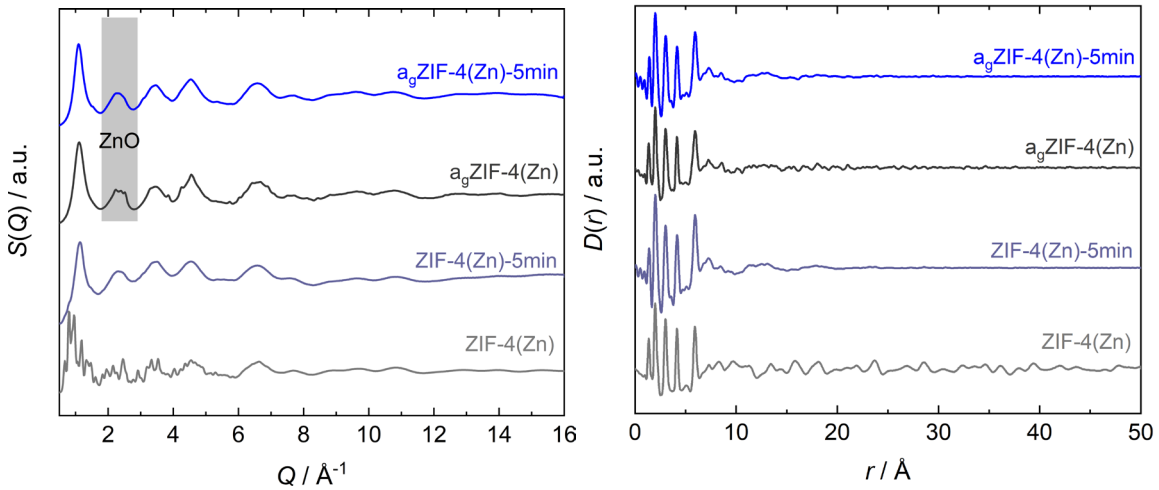

Figure A4.32. X-ray total scattering data in the form of $S(Q)$ and $D(r)$ of ZIF-4(Zn), ZIF-4(Zn)-5min, a_gZIF-4(Zn) and a_gZIF-4(Zn)-5min. Data of ZIF-4(Zn) and a_gZIF-4(Zn) are taken from ref. 6. The local structure of the melt-quenched a_gZIF-4(Zn) is essentially identical to those of the ball-milled ZIF-4(Zn)-5min and the ball-milled and heated a_gZIF-62(Co)-5min. Noteworthy, ZIF-4(Zn)-5min and the melt-quenched a_gZIF-4(Zn)-5min do not feature the ZnO impurities present in the melt-quenched a_gZIF-4(Zn). This is because ZIF-4(Zn)-5min and a_gZIF-4(Zn)-5min need a lower temperature for glass formation.

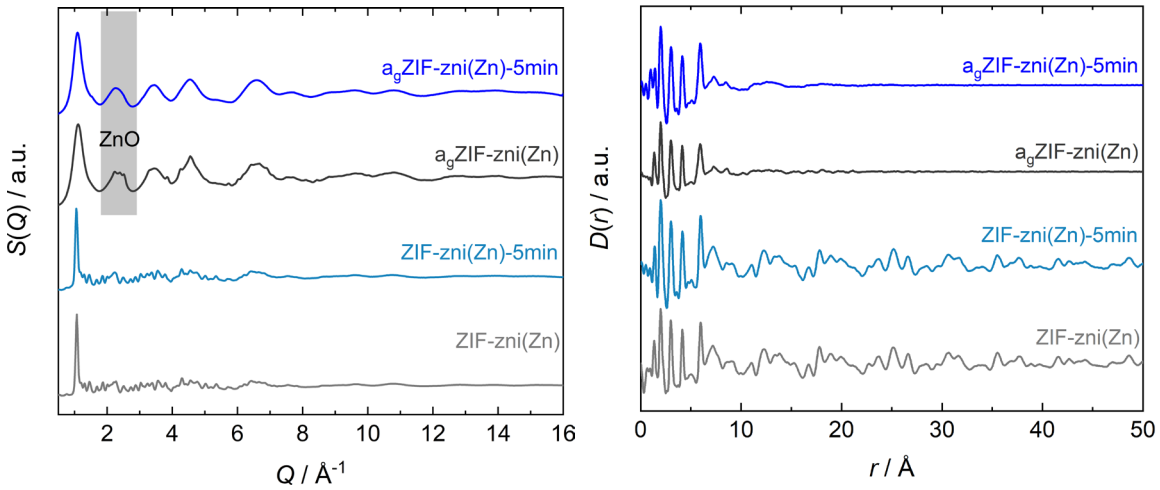

Figure A4.33. X-ray total scattering data in the form of $S(Q)$ and $D(r)$ of ZIF-zni(Zn), ZIF-zni(Zn)-5min, a_gZIF-zni(Zn) and a_gZIF-zni(Zn)-5min. Data of ZIF-zni(Zn) and a_gZIF-zni(Zn) are taken from ref. 6. The local structure of the melt-quenched a_gZIF-zni(Zn) is essentially identical to that of the ball-milled and heated a_gZIF-zni(Zn)-5min. Noteworthy, the melt-quenched a_gZIF-zni(Zn)-5min does not feature the ZnO impurities present in the melt-quenched a_gZIF-zni(Zn). This is because a_gZIF-zni(Zn)-5min needs a lower temperature for glass formation.

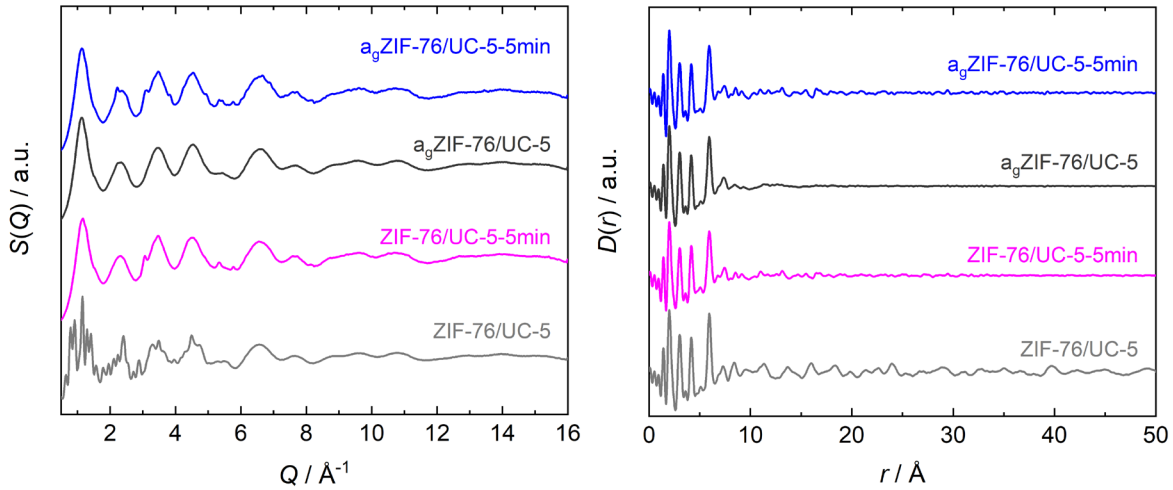

Figure A4.34. X-ray total scattering data in the form of $S(Q)$ and $D(r)$ of XPDF data of the ZIF-76/UC-5, ZIF-76/UC-5-5min, a$_g$ZIF-76/UC-5 and a$_g$ZIF-76/UC-5-5min.

A.4.2 – ^{1}H NMR spectroscopy data

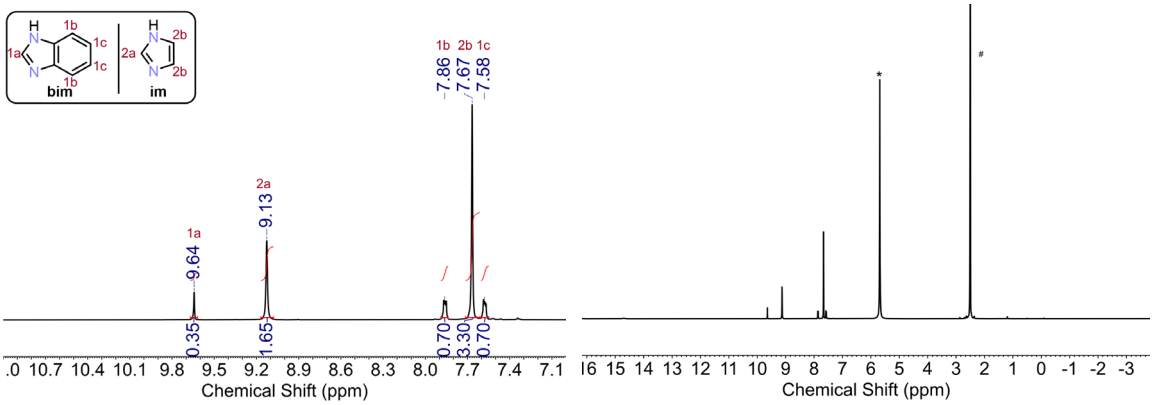

Figure A4.35. ^{1}H NMR spectrum of a digested sample of ZIF-62(Zn). Left: Zoom in the aromatic region (7.0 to 11.0 ppm). Right: Complete spectrum. Residual protons in DMSO at 2.5 ppm is marked with # and residual protons D_2O is marked with *.

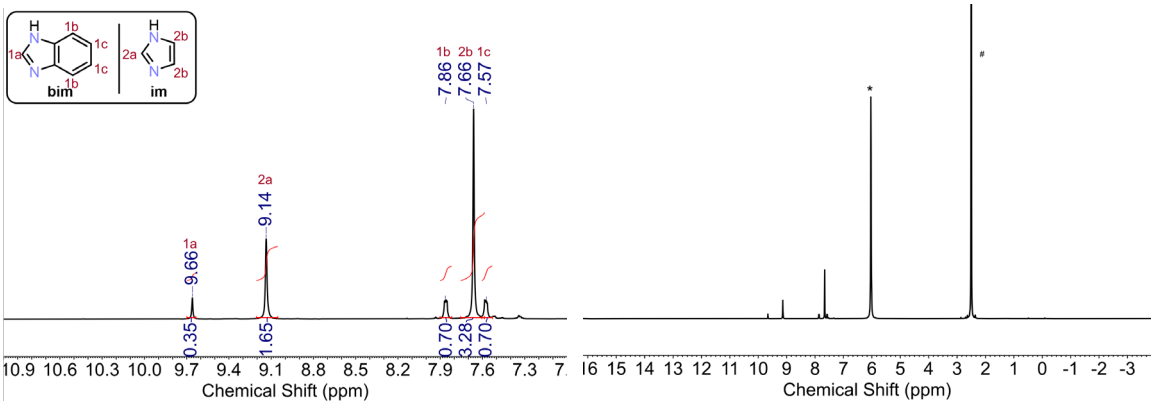

Figure A4.36. ^{1}H NMR spectrum of a digested sample of ZIF-62(Co). Left: Zoom in the aromatic region (7.0 to 11.0 ppm). Right: Complete spectrum. Residual protons in DMSO at 2.5 ppm is marked with # and residual protons D_2O is marked with *.

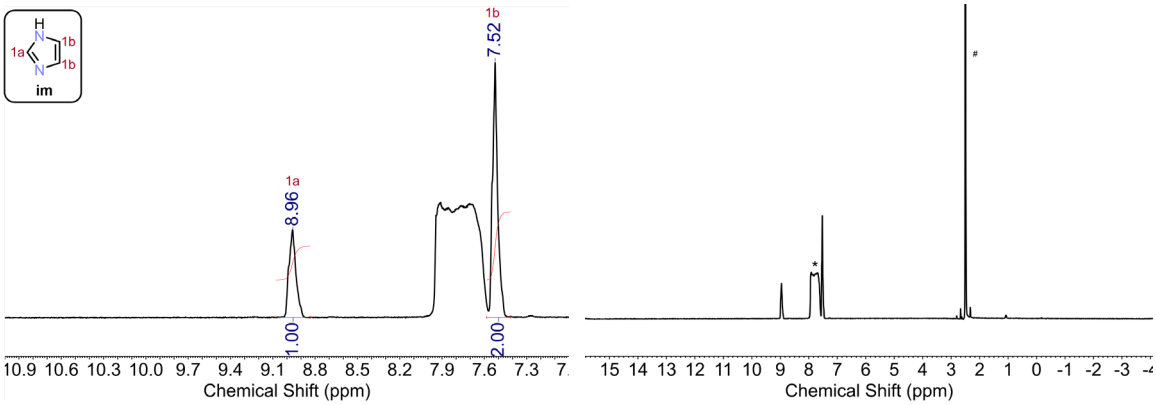

Figure A4.37. [1]H NMR spectrum of a digested sample of ZIF-4(Zn). Left: Zoom in the aromatic region (7.0 to 11.0 ppm). Right: Complete spectrum. Residual protons in DMSO at 2.5 ppm is marked with # and residual protons D_2O is marked with *.

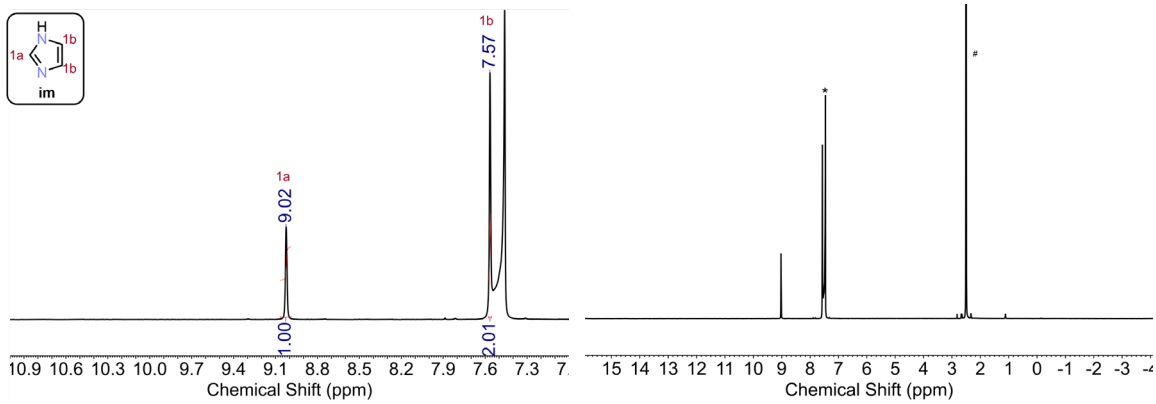

Figure A4.38. [1]H NMR spectrum of a digested sample of ZIF-4(Co). Left: Zoom in the aromatic region (7.0 to 11.0 ppm). Right: Complete spectrum. Residual protons in DMSO at 2.5 ppm is marked with # and residual protons D_2O is marked with *.

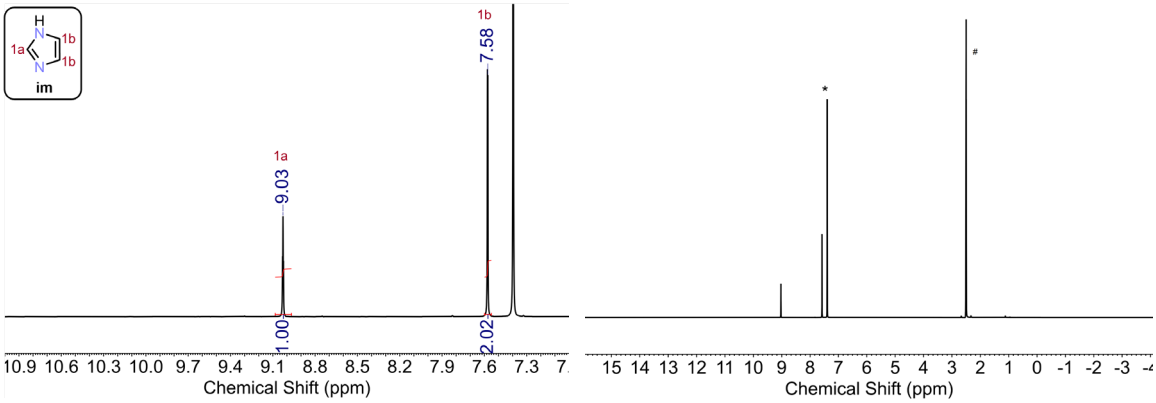

Figure A4.39.. [1]H NMR spectrum of a digested sample of ZIF-zni(Zn). Left: Zoom in the aromatic region (7.0 to 11.0 ppm). Right: Complete spectrum. Residual protons in DMSO at 2.5 ppm is marked with # and residual protons D_2O is marked with *.

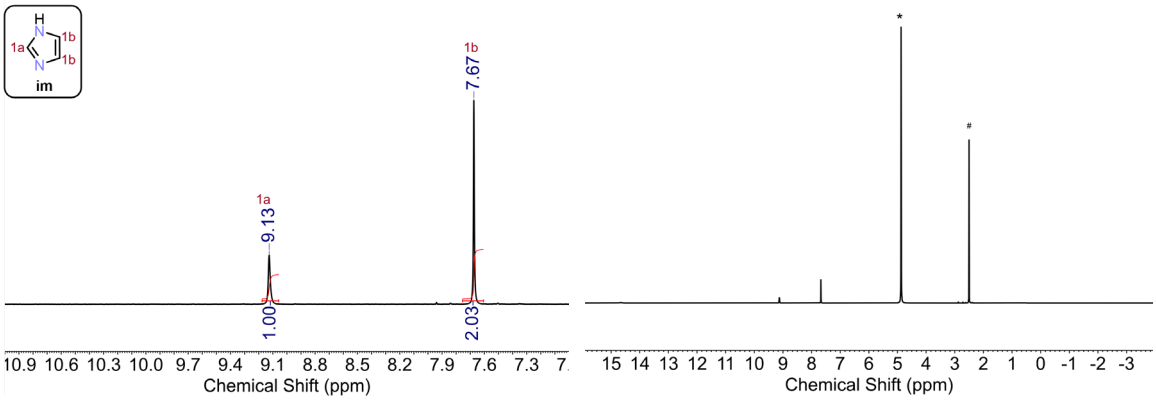

Figure A4.40. [1]H NMR spectrum of a digested sample of ZIF-zni(Co). Left: Zoom in the aromatic region (7.0 to 11.0 ppm). Right: Complete spectrum. Residual protons in DMSO at 2.5 ppm is marked with # and residual protons D_2O is marked with *.

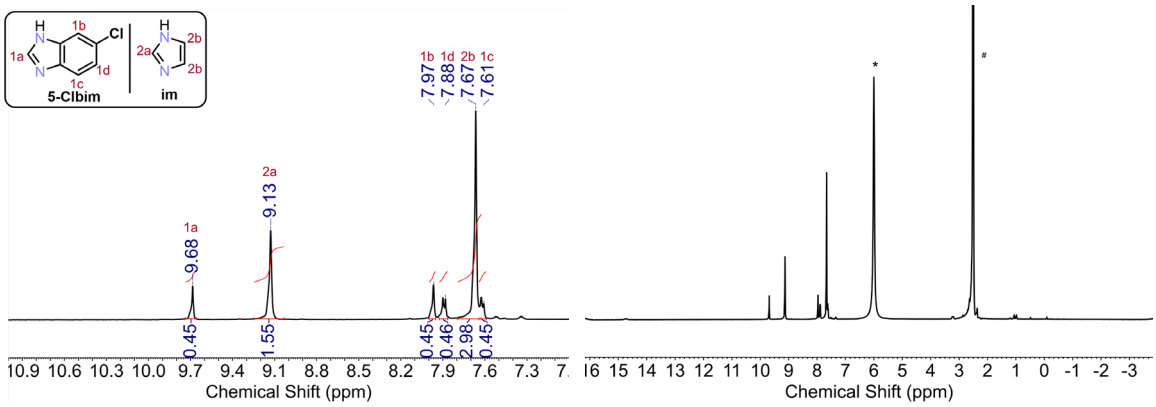

Figure A4.41. [1]H NMR spectrum of a digested sample of ZIF-76/UC-5. Left: Zoom in the aromatic region (7.0 to 11.0 ppm). Right: Complete spectrum. Residual protons in DMSO at 2.5 ppm is marked with # and residual protons D_2O is marked with *.

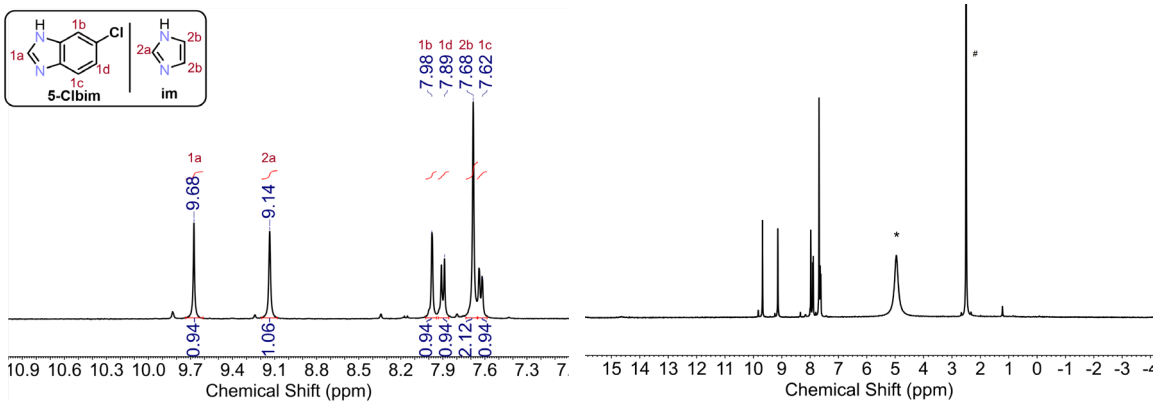

Figure A4.42. [1]H NMR spectrum of a digested sample of ZIF-76. Top: Zoom in the aromatic region (7.0 to 11.0 ppm). Bottom: Complete spectrum. Residual protons in DMSO at 2.5 ppm is marked with # and residual protons D_2O is marked with *.

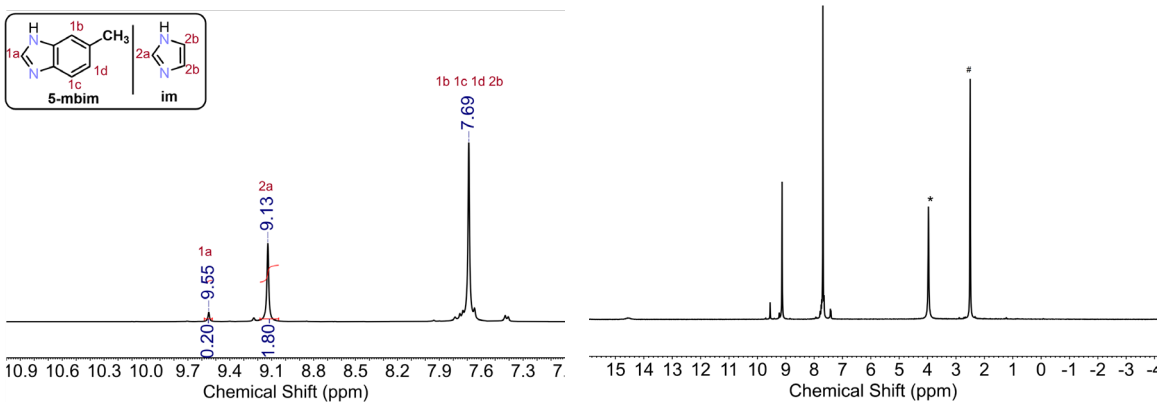

Figure A4.43. [1]H NMR spectrum of a digested sample of TIF-4. Top: Zoom in the aromatic region (7.0 to 11.0 ppm). Bottom: Complete spectrum. Residual protons in DMSO at 2.5 ppm is marked with # and residual protons D_2O is marked with *.

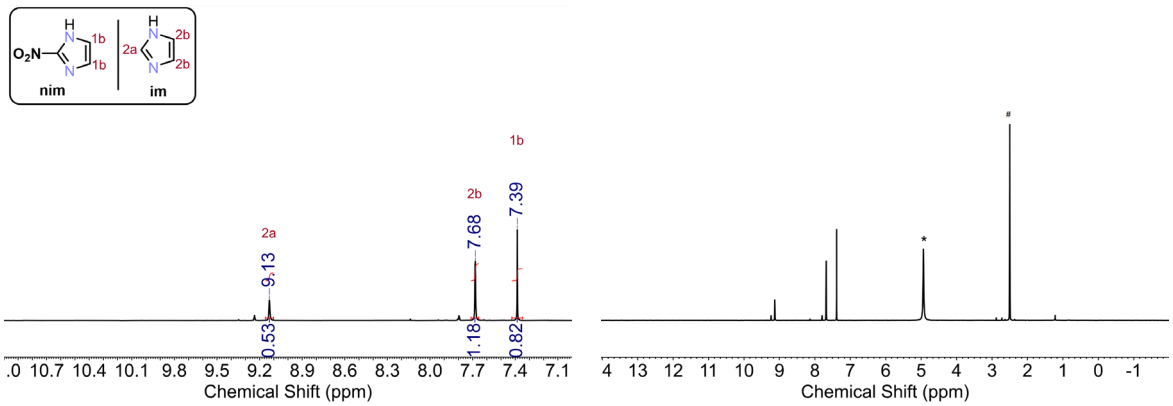

Figure A4.44. [1]H NMR spectrum of a digested sample of ZIF-70. Top: Zoom in the aromatic region (7.0 to 11.0 ppm). Bottom: Complete spectrum. Residual protons in DMSO at 2.5 ppm is marked with # and residual protons D_2O is marked with *.

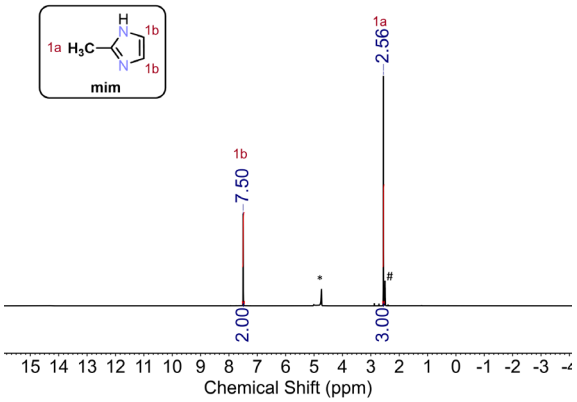

Figure A4.45.. Complete [1]H NMR spectrum of a digested sample of ZIF-8. Residual protons in DMSO at 2.5 ppm is marked with # and residual protons D_2O is marked with *.

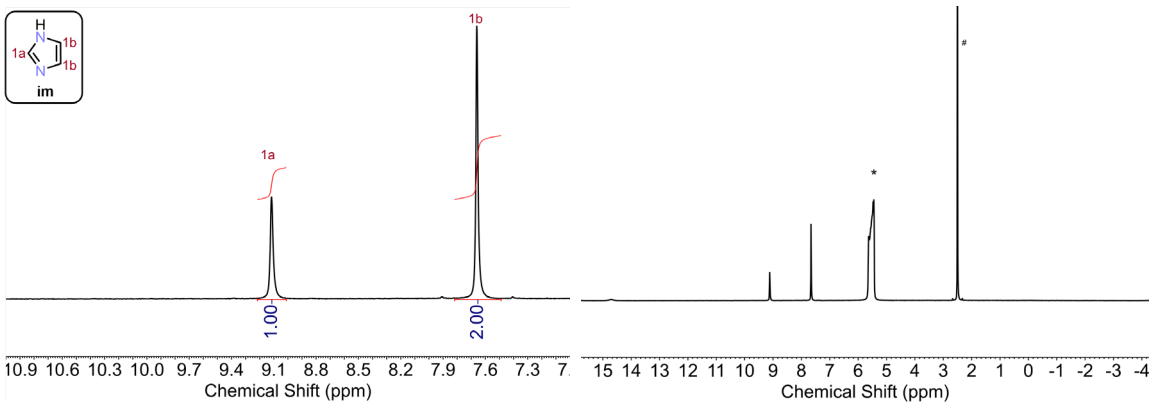

Figure A4.46. ^{1}H NMR spectrum of a digested sample of ZIF-Cu-1. Top: Zoom in the aromatic region (7.0 to 11.0 ppm). Bottom: Complete spectrum. Residual protons in DMSO at 2.5 ppm is marked with # and residual protons D_2O is marked with *.

A.4.3 – Fourier-transform infrared (FTIR) spectroscopy data

A.4.3.1 – Mid-infrared (mid-IR) spectra

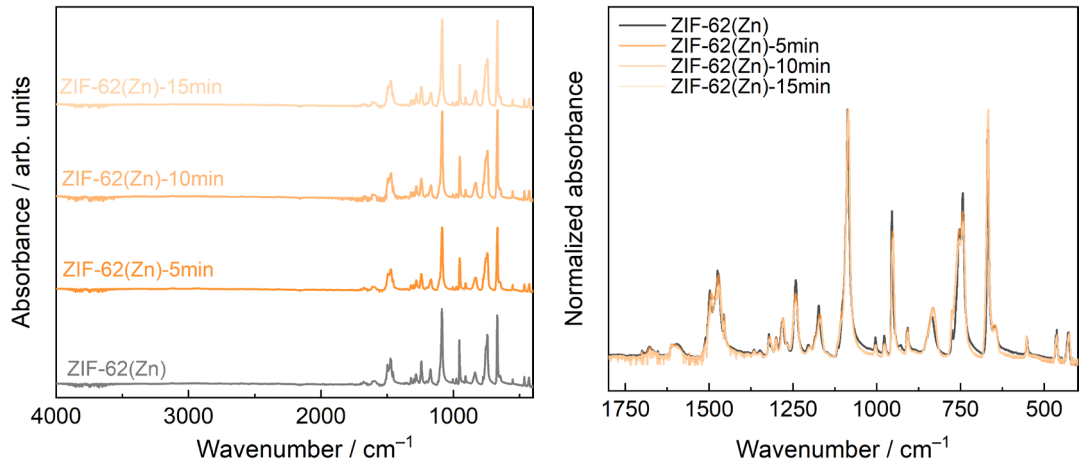

Figure A4.47. Left: Stacked plot of FTIR spectra of ZIF-62(Zn) and the corresponding samples derived via PSBM. Right: Overlapped plot of the normalized data zoomed into the 1800-400 cm^{-1} region.

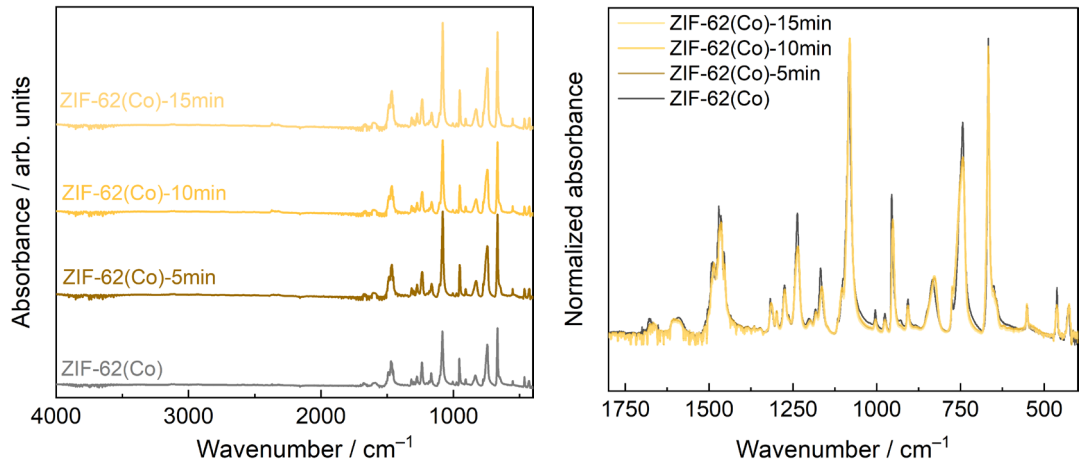

Figure A4.48. Left: Stacked plot of FTIR spectra of ZIF-62(Co) and the corresponding samples derived via PSBM. Right: Overlapped plot of the normalized data zoomed into the 1800-400 cm^{-1} region.

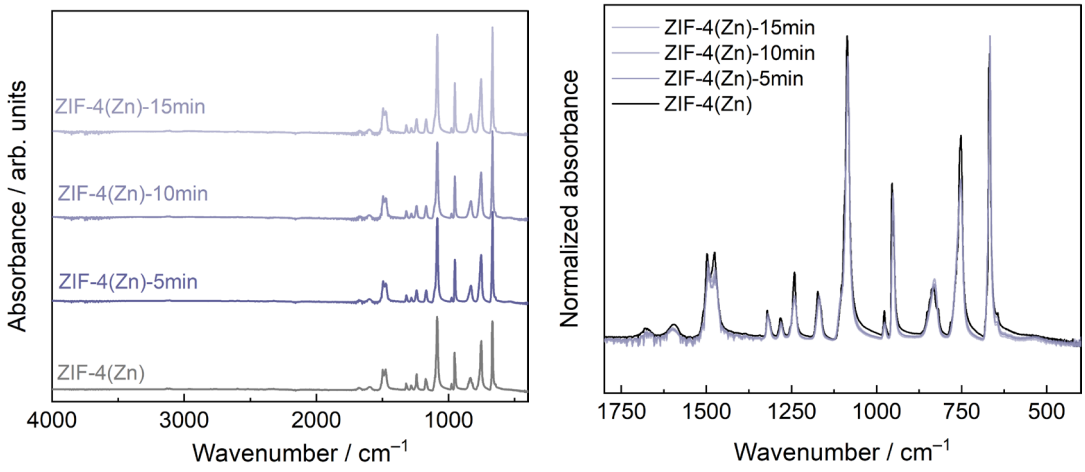

Figure A4.49. Left: Stacked plot of FTIR spectra of ZIF-4(Zn) and the corresponding samples derived via PSBM. Right: Overlapped plot of the normalized data zoomed into the 1800-400 cm^{-1} region.

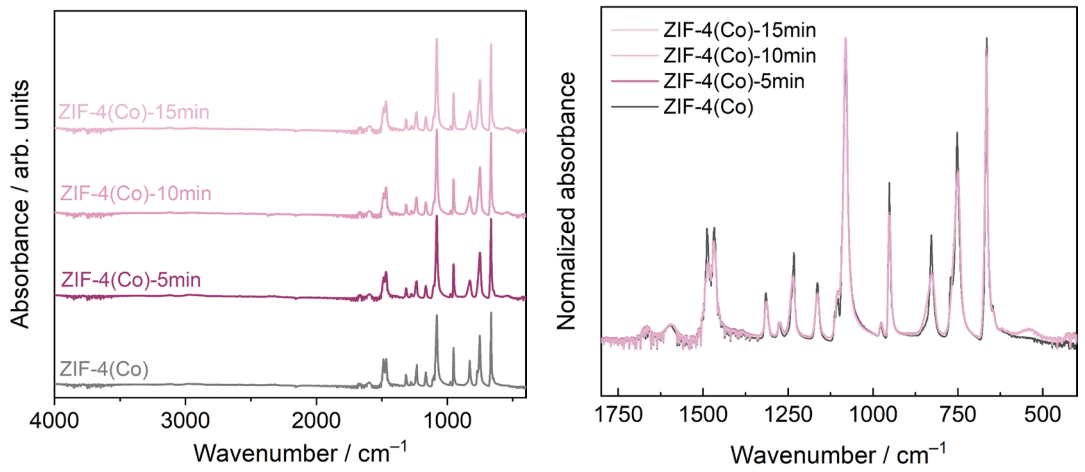

Figure A4.50. Left: Stacked plot of FTIR spectra of ZIF-4(Co) and the corresponding samples derived via PSBM. Right: Overlapped plot of the normalized data zoomed into the 1800-400 cm^{-1} region.

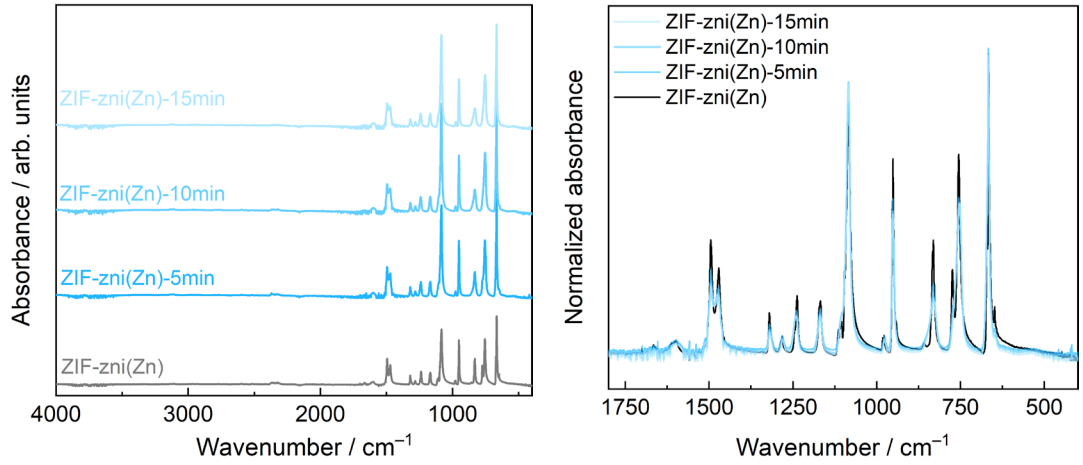

Figure A4.51. Left: Stacked plot of FTIR spectra of ZIF-zni(Zn) and the corresponding samples derived via PSBM. Right: Overlapped plot of the normalized data zoomed into the 1800-400 cm^{-1} region.

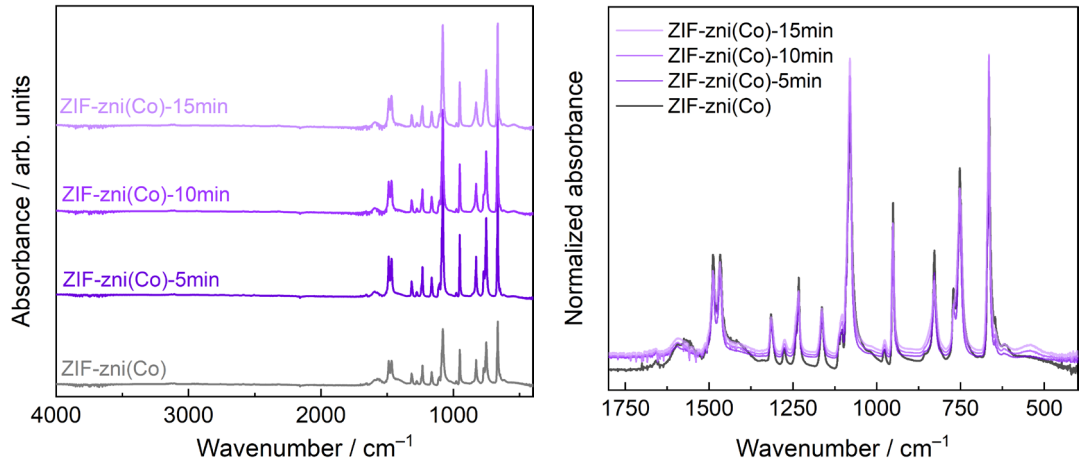

Figure A4.52. Left: Stacked plot of FTIR spectra of ZIF-zni(Co) and the corresponding samples derived via PSBM. Right: Overlapped plot of the normalized data zoomed into the 1800-400 cm^{-1} region.

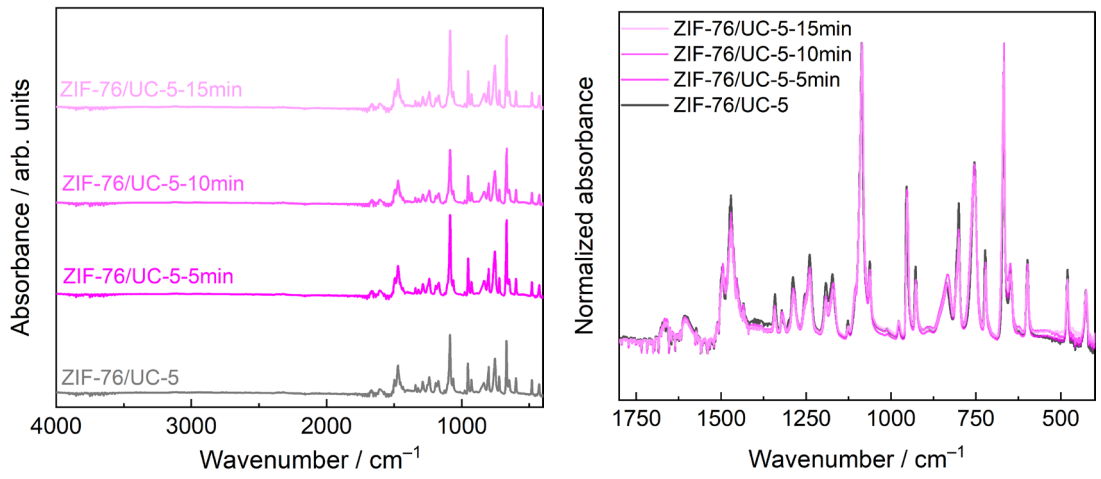

Figure A4.53. Left: Stacked plot of FTIR spectra of ZIF-76/UC-5 and the corresponding samples derived via PSBM. Right: Overlapped plot of the normalized data zoomed into the 1800-400 cm^{-1} region.

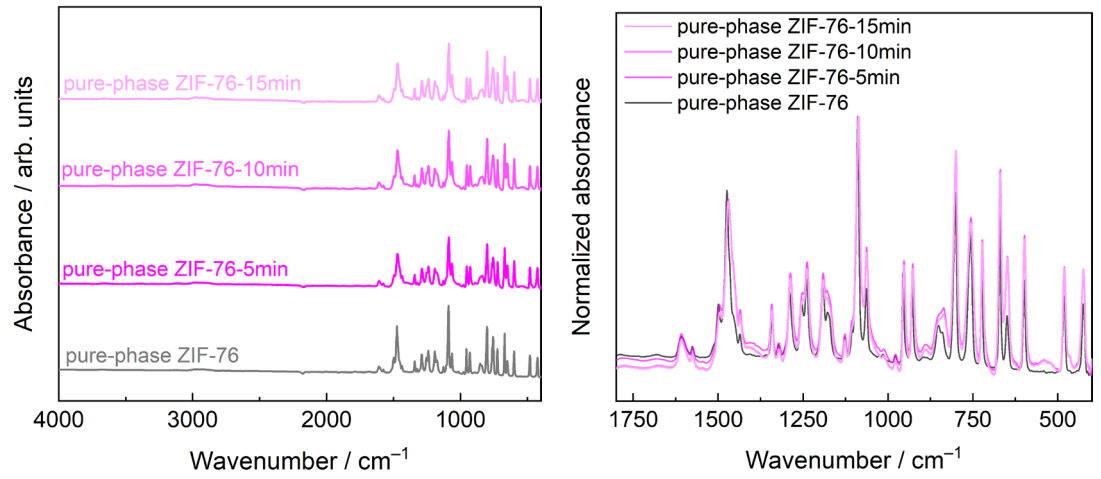

Figure A4.54. Left: Stacked plot of FTIR spectra of pure-phase ZIF-76 and the corresponding samples derived via PSBM. Right: Overlapped plot of the normalized data zoomed into the 1800-400 cm^{-1} region.

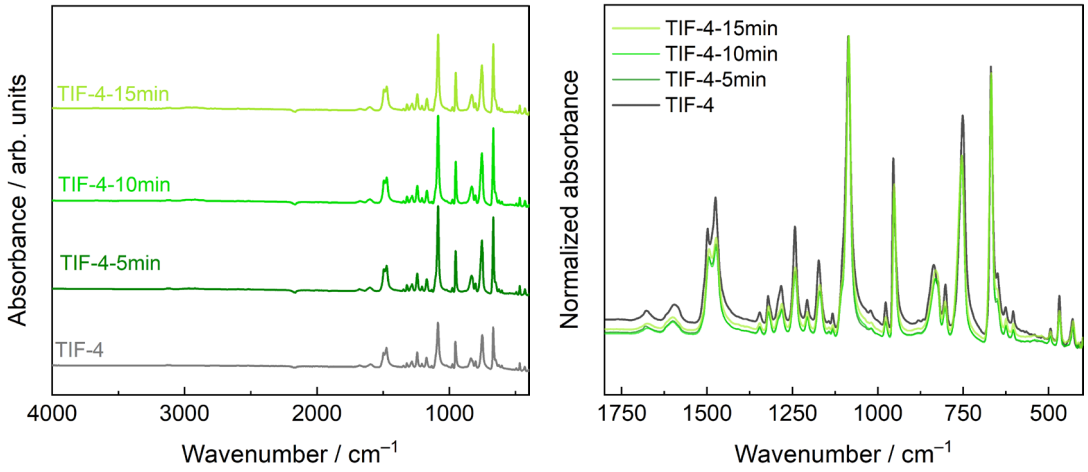

Figure A4.55. Left: Stacked plot of FTIR spectra of TIF-4 and the corresponding samples derived via PSBM. Right: Overlapped plot of the normalized data zoomed into the 1800-400 cm^{-1} region.

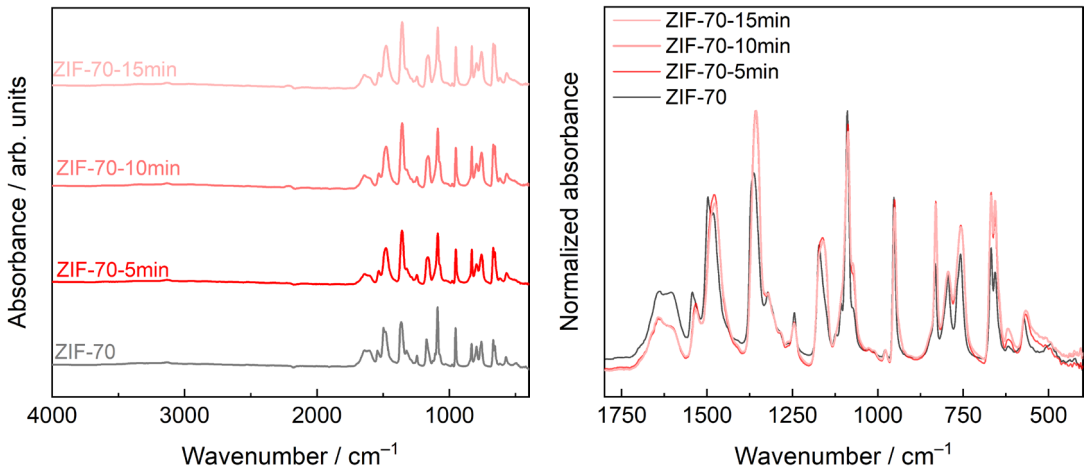

Figure A4.56. Left: Stacked plot of FTIR spectra of ZIF-70 and the corresponding samples derived via PSBM. Right: Overlapped plot of the normalized data zoomed into the 1800-400 cm^{-1} region.

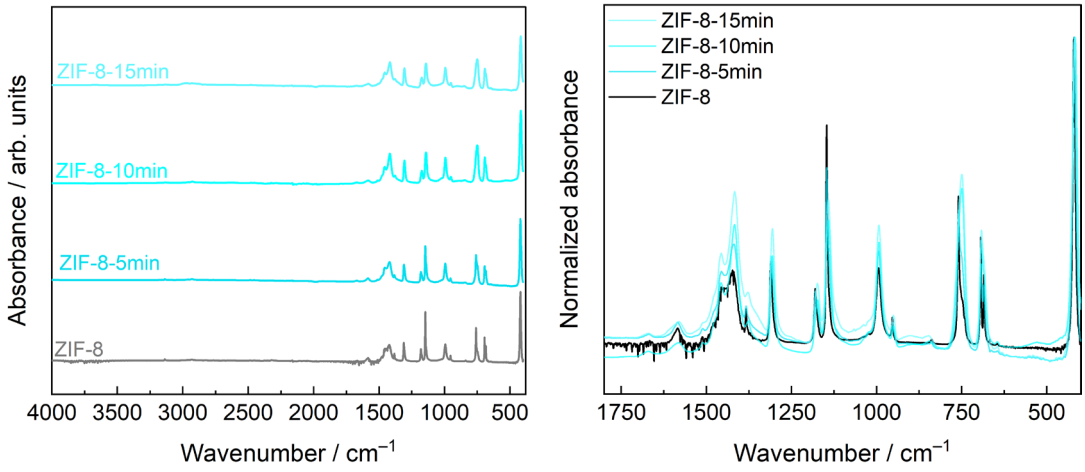

Figure A4.57. Left: Stacked plot of FTIR spectra of ZIF-8 and the corresponding samples derived via PSBM. Right: Overlapped plot of the normalized data zoomed into the 1800-400 cm^{-1} region.

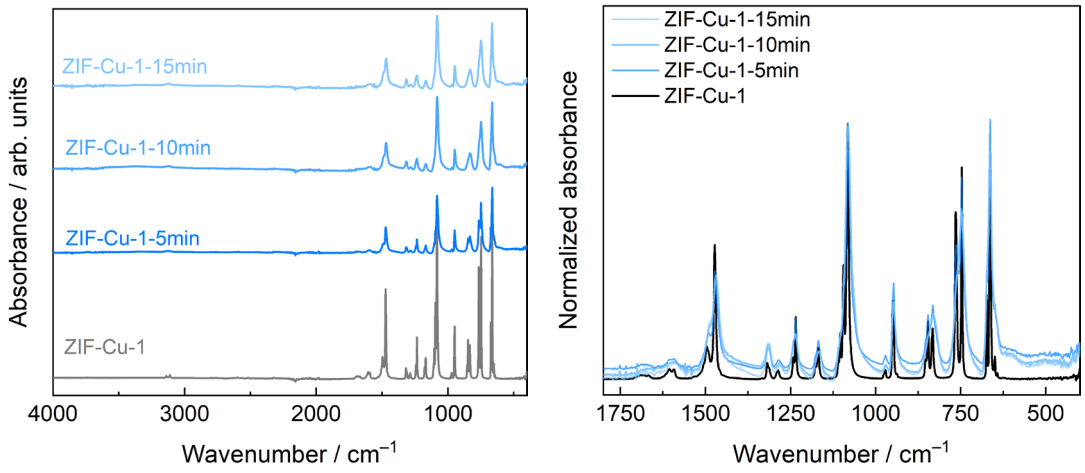

Figure A4.58. Left: Stacked plot of FTIR spectra of ZIF-Cu-1 and the corresponding samples derived via PSBM. Right: Overlapped plot of the normalized data zoomed into the 1800-400 cm^{-1} region.

A.4.3.2 – Far-infrared (far-IR) spectra

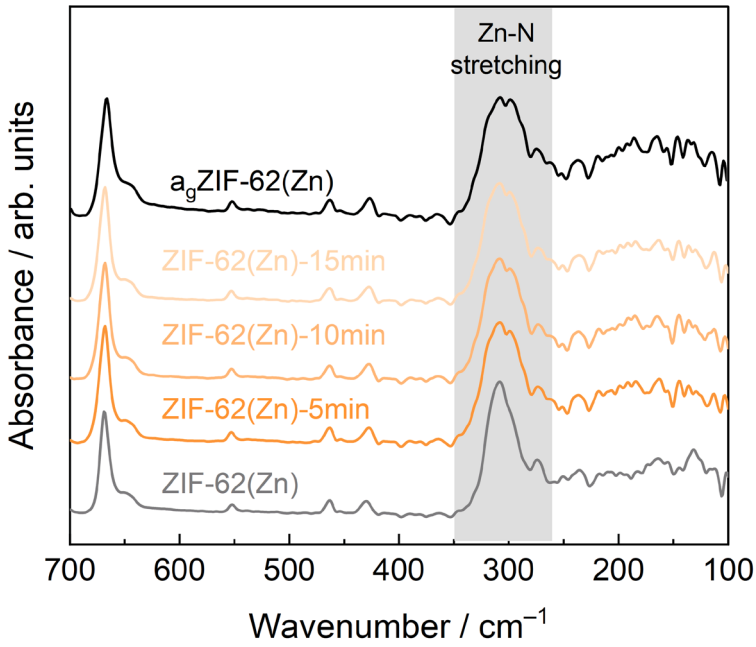

Figure A4.59. Stacked far-IR spectra of ZIF-62(Zn), a_gZIF-62(Zn) and the corresponding samples derived via PSBM. The band of the Zn–N stretching vibration is highlighted.

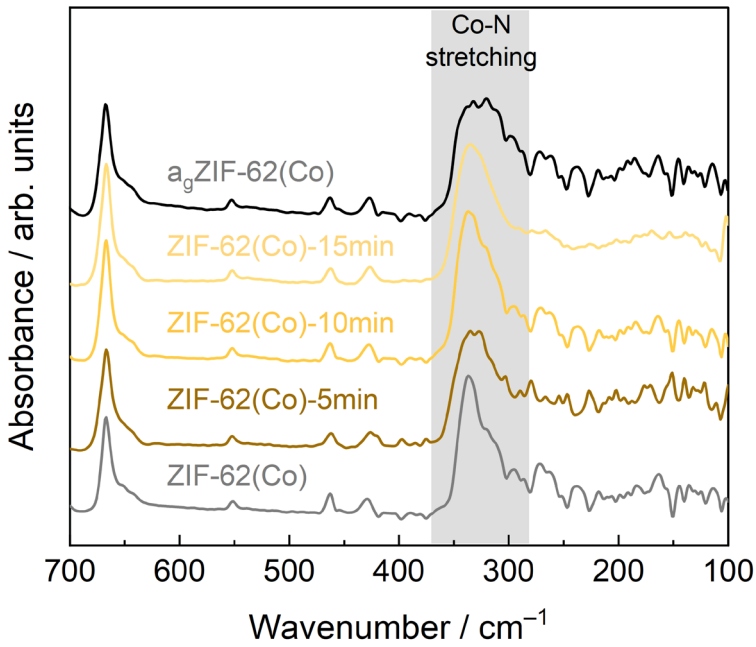

Figure A4.60. Stacked far-IR spectra of ZIF-62(Co), a_gZIF-62(Co), and the corresponding samples derived via PSBM. The band of the Co–N stretching vibration is highlighted.

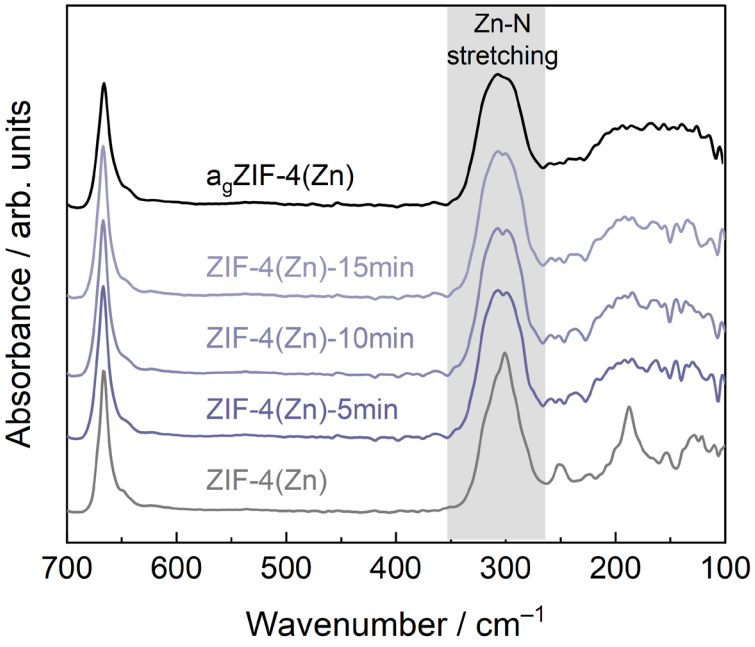

Figure A4.61. Stacked far-IR spectra of ZIF-4(Zn), a$_g$ZIF-4(Zn), and the corresponding samples derived via PSBM. The band of the Zn–N stretching vibration is highlighted.

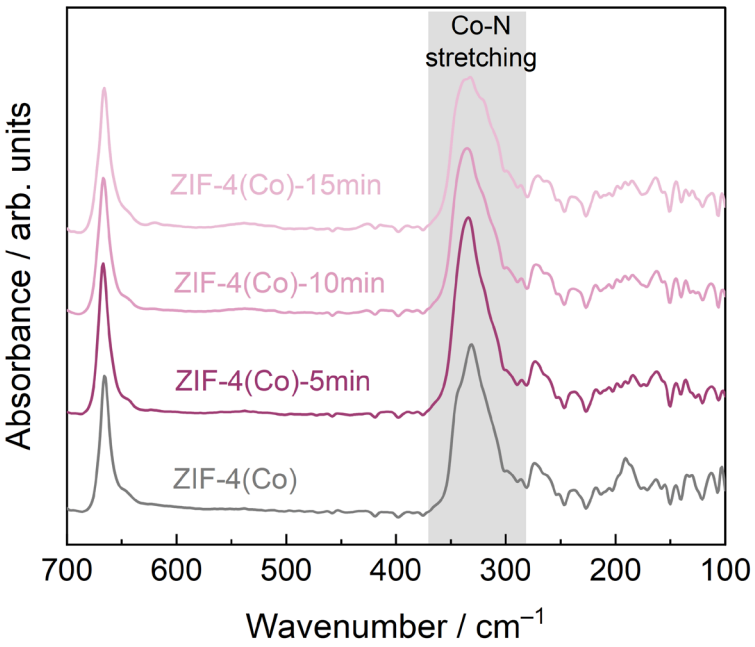

Figure A4.62. Stacked far-IR spectra of ZIF-4(Co) and the corresponding samples derived via PSBM. The band of the Co–N stretching vibration is highlighted.

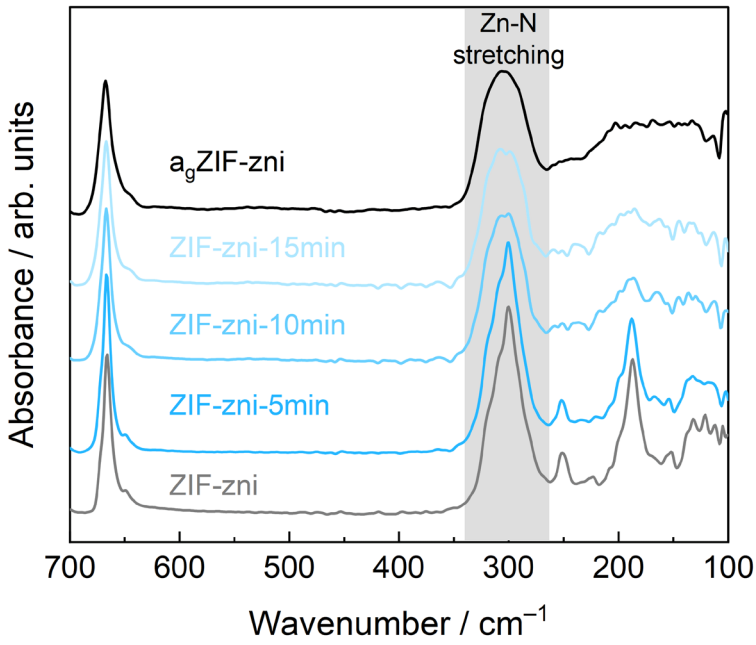

Figure A4.63. Stacked far-IR spectra of ZIF-zni(Zn), a_gZIF-zni(Zn) and the corresponding samples derived via PSBM. The band of the Zn–N stretching vibration is highlighted.

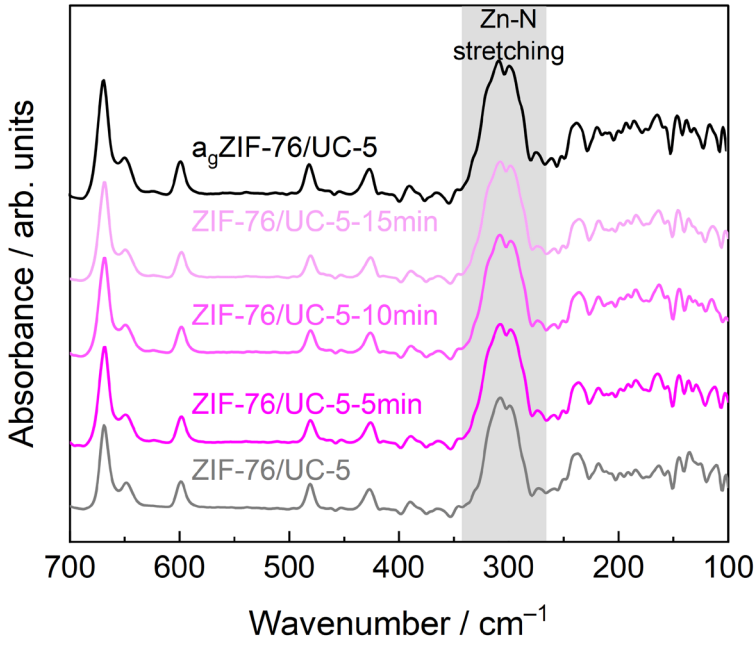

Figure A4.64. Stacked far-IR spectra of ZIF-76/UC-5, a_gZIF-76/UC-5, and the corresponding samples derived via PSBM. The band of the Zn–N stretching vibration is highlighted.

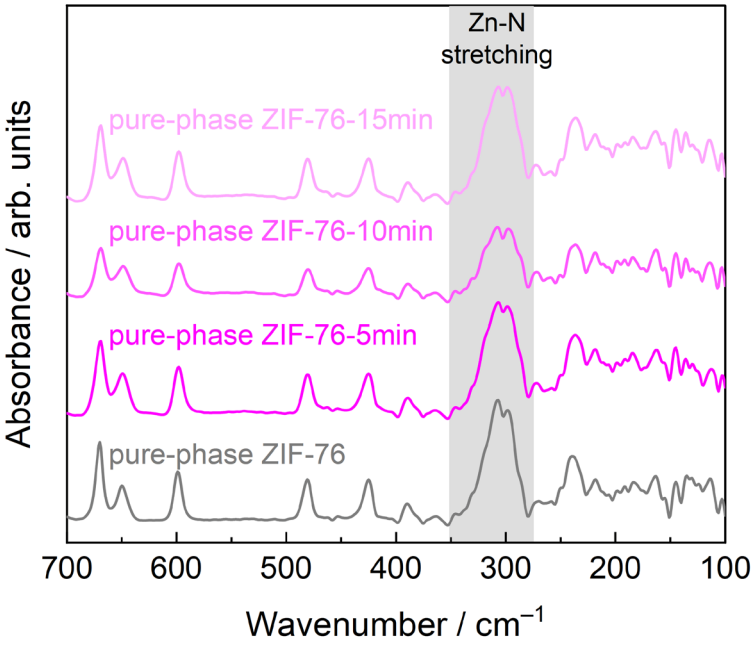

Figure A4.65. Stacked far-IR spectra of pure-phase ZIF-76 and the corresponding samples derived via PSBM. The band of the Zn–N stretching vibration is highlighted.

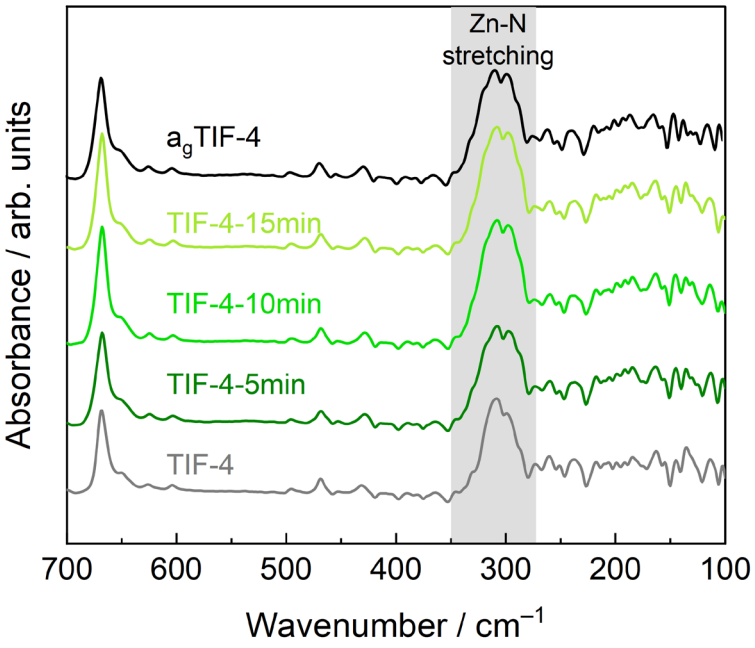

Figure A4.66. Stacked far-IR spectra of TIF-4, a$_g$TIF-4, and the corresponding samples derived via PSBM. The band of the Zn–N stretching vibration is highlighted.

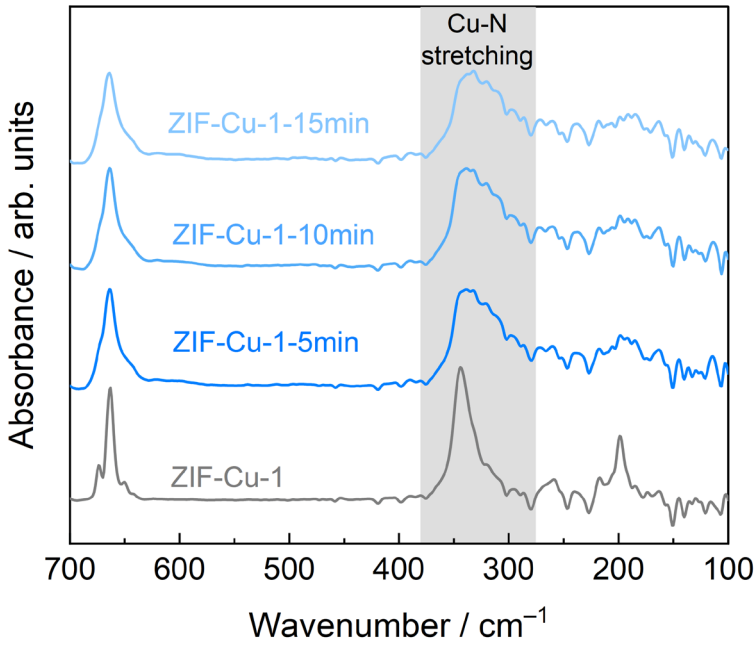

Figure A4.67. Stacked far-IR spectra of ZIF-Cu-1 and the corresponding samples derived via PSBM. The band of the Cu–N stretching vibration is highlighted.

Table A4.2. Summary of the parameters of the asymmetric metal–N stretching vibration for the ZIF microcrystals, MIGs, and corresponding MQGs.

Compound	Position of metal-N stretching band (cm^{-1})	FWHM (cm^{-1})
ZIF-62(Zn)	308	29.2
ZIF-62(Zn)-5min	308	36.3
ZIF-62(Zn)-10min	308	36.9
ZIF-62(Zn)-15min	308	38.6
a_gZIF-62(Zn)	307	39.5
ZIF-62(Co)	337	36.9
ZIF-62(Co)-5min	335	39.4
ZIF-62(Co)-10min	337	39.4
ZIF-62(Co)-15min	335	41.0
a_gZIF-62(Co)	320	47.7
ZIF-4(Zn)	301	31.3
ZIF-4(Zn)-5min	307	39.9
ZIF-4(Zn)-10min	307	39.9

ZIF-4(Zn)-15min	307	39.9
a_gZIF-4(Zn)	306	40.2
ZIF-4(Co)	331	33.8
ZIF-4(Co)-5min	334	36.8
ZIF-4(Co)-10min	332	38.7
ZIF-4(Co)-15min	335	43.7
ZIF-zni(Zn)	300	26.6
ZIF-zni(Zn)-5min	300	28.7
ZIF-zni(Zn)-10min	300	38.4
ZIF-zni(Zn)-15min	307	41.0
a_gZIF-zni(Zn)	306	41.3
ZIF-76	307	30.5
ZIF-76-5min	307	33.2
ZIF-76-10min	308	32.9
ZIF-76-15min	307	35.9
ZIF-76/UC-5	307	31.5
ZIF-76/UC-5-5min	308	35.9
ZIF-76/UC-5-5min	308	37.7
ZIF-76/UC-5-5min	308	36.2
a_gZIF-76/UC-5	308	37.1
TIF-4	308	31.4
TIF-4-5min	308	38.8
TIF-4-10min	308	37.7
TIF-4-15min	308	39.4
a_gTIF-4	308	38.5
ZIF-Cu-1	344	21.3
ZIF-Cu-1-5min	339	49.8
ZIF-Cu-1-10min	339	59.8
ZIF-Cu-1-15min	332	58.9

A.4.4 – CO_2 physisorption studies

The specific pore volumes (V_{pore}) were calculated according to the following formula[41]:

$$V_{pore} = \frac{n_{ads}^{max} \cdot M_{CO2}}{\rho_{sl}} \quad (2)$$

with n_{ads}^{max} the specific molar amount of gas adsorbed (mmol of gas/g material) at 195 K and 95 kPa, M_{CO2} the molar mass of CO_2, and ρ_{sl} the density of the supercooled liquid at 195 K (that is 1.258 g cm^{-3}). For these calculations the implemented routine in the Quantachrome ASIQwin version 5.2 software was used. The obtained values are summarized in **Table A4.3**.

BET analysis was performed with the Quantachrome ASIQwin version 5.2 software. The applied relative pressure ranges and quality factors are given in Table S6. The saturation pressure (p_0) amounts to 191 kPa.[166] As with the previous work[41], Brunauer–Emmett–Teller (BET) areas are only provided for reference, as the BET theory is strictly not applicable to such kind of microporous materials (**Table A4.4**).

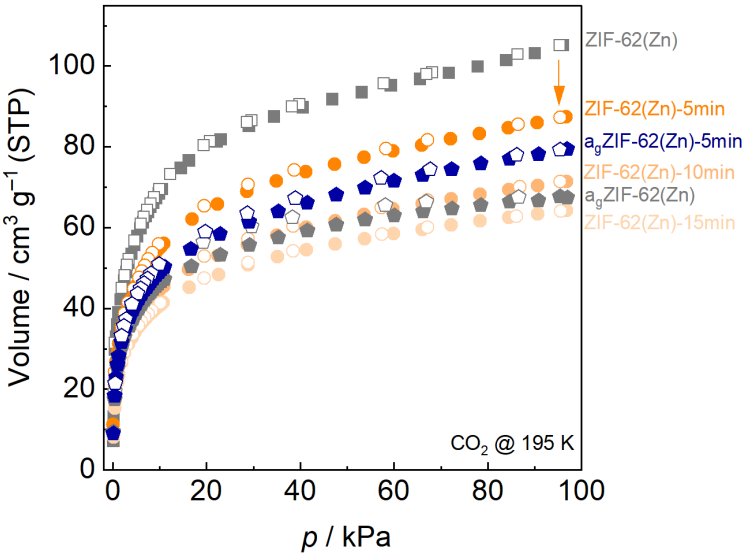

Figure A4.68. CO_2 sorption isotherms collected at 195 K for ZIF-62(Zn) and the amorphous sampled derived after varying PSBM times. a_gZIF-62(Zn) is the MQG of ZIF-62(Zn) derived by the traditional melt-quenching method. a_gZIF-62(Zn)-5min is the ball-milled material which has been additionally heated to 500 °C (i.e. above its T_g) and subsequently quenched.

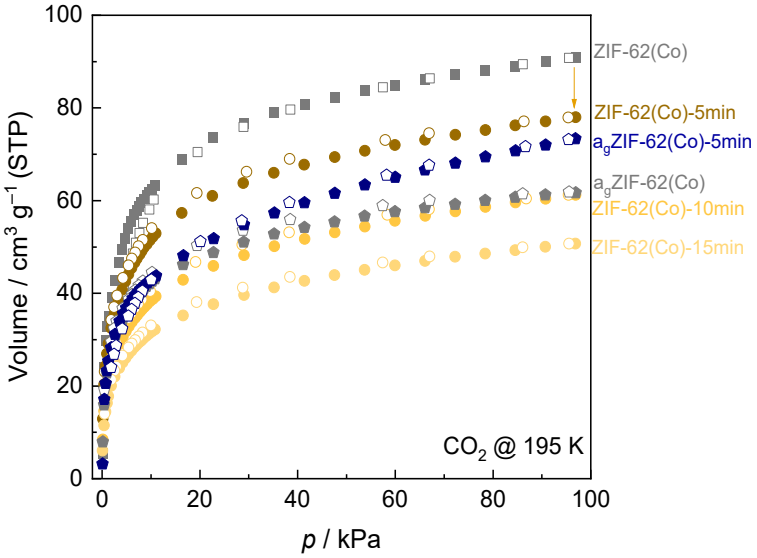

Figure A4.69. CO_2 sorption isotherms collected at 195 K for ZIF-62(Co) and the amorphous sampled derived after varying PSBM times. a_gZIF-62(Co) is the MQG of ZIF-62(Co) derived by the traditional melt-quenching method. a_gZIF-62(Co)-5min is the ball-milled material which has been additionally heated to 430 °C (i.e. above its T_g) and subsequently quenched.

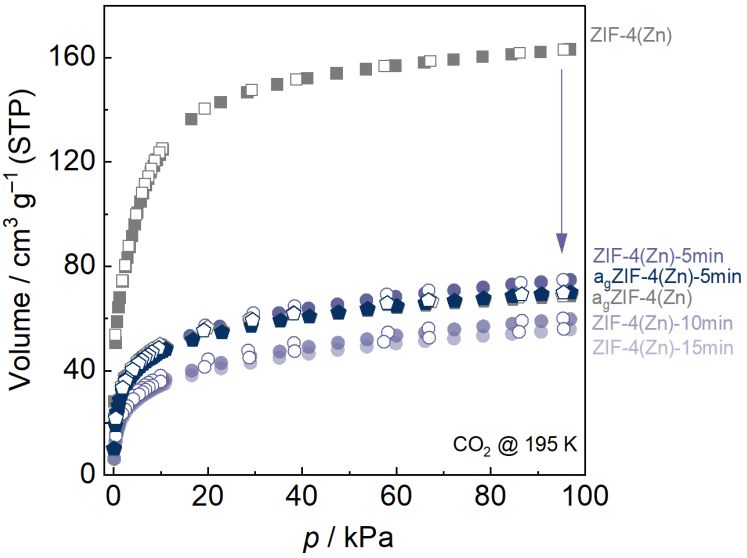

Figure A4.70. CO_2 sorption isotherms collected at 195 K for ZIF-4(Zn) and the amorphous sampled derived after varying PSBM times. a_gZIF-4(Zn) is the MQG of ZIF-4(Zn) derived by the traditional melt-quenching method. a_gZIF-4(Zn)-5min is the ball-milled material which has been additionally heated to 585 °C and subsequently melt-quenched.

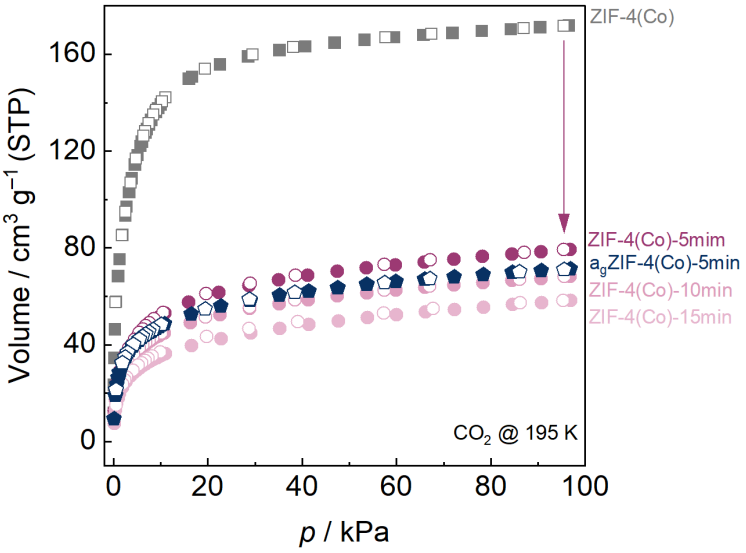

Figure A4.71. CO_2 sorption isotherms collected at 195 K for ZIF-4(Co) and the amorphous sampled derived after varying PSBM times. a_gZIF-4(Co)-5min is the ball-milled material which has been additionally heated to 340 °C (i.e. above its T_g but below the recrystallization temperature) and subsequently quenched.

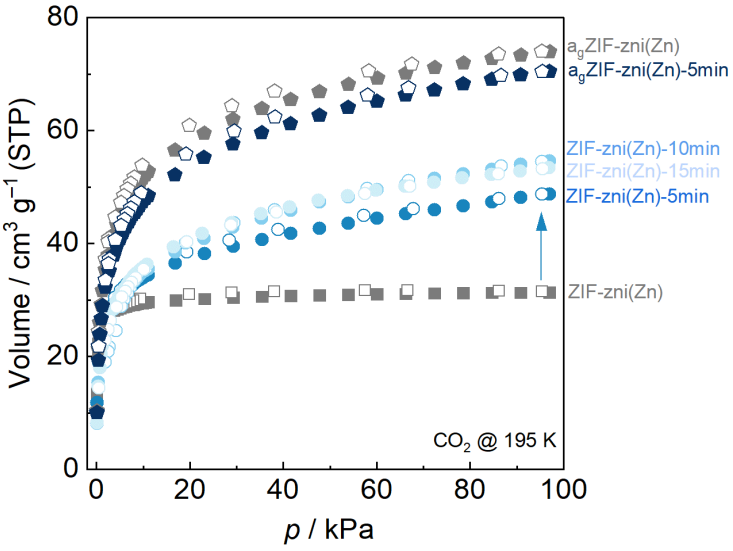

Figure A4.72. CO_2 sorption isotherms collected at 195 K for ZIF-zni(Zn) and the amorphous sampled derived after varying PSBM times. a_gZIF-zni(Zn) is the MQG of ZIF-zni(Zn) derived by the traditional melt-quenching method. a_gZIF-zni(Zn)-5min has been additionally heated to 580 °C and subsequently melt-quenched.

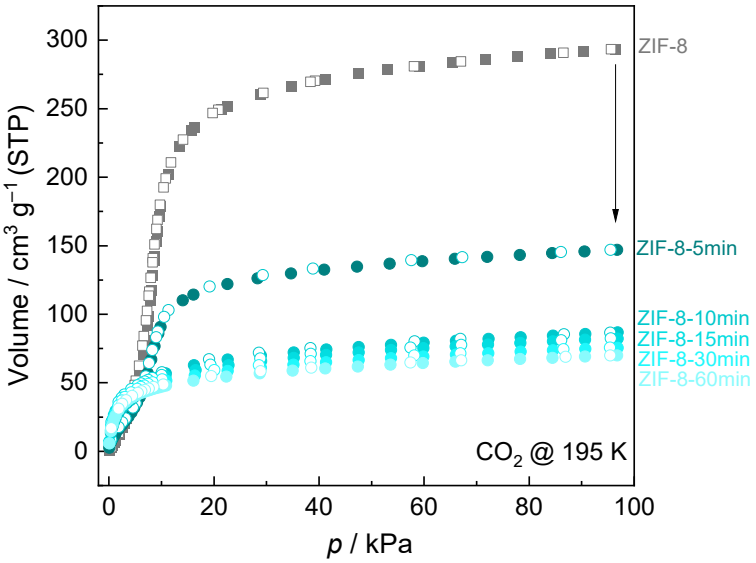

Figure A4.73. CO_2 sorption isotherms collected at 195 K for ZIF-8 and the amorphous samples derived after varying PSBM times.

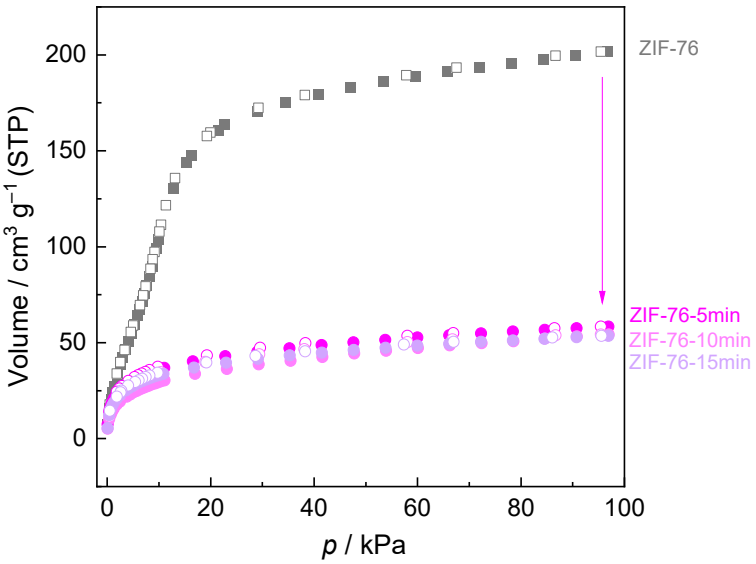

Figure A4.74. CO_2 sorption isotherms collected at 195 K for ZIF-76 and the amorphous samples derived after varying PSBM times.

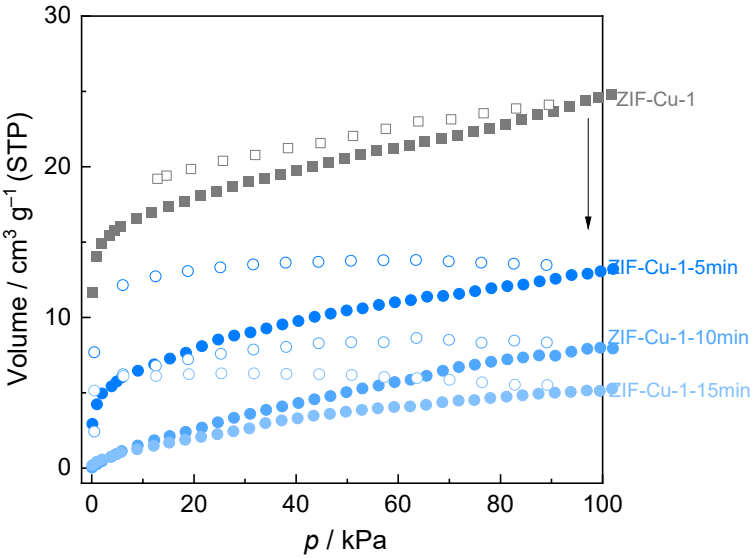

Figure A4.75. CO_2 sorption isotherms collected at 195 K for ZIF-Cu-1 and the amorphous samples derived after varying PSBM times.

Table A4.3. Summary of maximum gas capacities (V_{ads}^{max} and n_{ads}^{max}) and specific pore volumes (V_{pore}) derived from the CO_2 gas physisorption isotherms collected at 195 K for all investigated materials.

Compound	V_{ads}^{max} ($cm^3\ g^{-1}$ (STP))	n_{ads}^{max} (mmol g^{-1})	V_{pore} [a] ($cm^3\ g^{-1}$)
ZIF-62(Zn)	105.23	4.70	0.16
ZIF-62(Zn)-5min	87.33	3.90	0.14
ZIF-62(Zn)-10min	71.38	3.19	0.11
ZIF-62(Zn)-15min	64.18	2.87	0.10
a_gZIF-62(Zn)	67.29	3.00	0.11
a_gZIF-62(Zn)-5min	79.30	3.54	0.12
ZIF-62(Co)	90.92	4.06	0.14
ZIF-62(Co)-5min	77.99	3.48	0.12
ZIF-62(Co)-10min	61.21	2.73	0.10
ZIF-62(Co)-15min	50.69	2.26	0.08
a_gZIF-62(Co)	61.71	2.75	0.10
a_gZIF-62(Co)-5min	73.34	3.27	0.11
ZIF-4(Zn)	163.19	7.29	0.25
ZIF-4(Zn)-5min	74.83	3.34	0.12
ZIF-4(Zn)-10min	59.94	2.68	0.09
ZIF-4(Zn)-15min	55.92	2.50	0.09
a_gZIF-4(Zn)	68.56	3.06	0.11
a_gZIF-4(Zn)-5min	69.76	3.11	0.11
ZIF-4(Co)	171.81	7.67	0.27
ZIF-4(Co)-5min	79.25	3.54	0.12
ZIF-4(Co)-10min	68.14	3.04	0.11
ZIF-4(Co)-15min	58.26	2.60	0.09
a_gZIF-4(Co)-5min	71.17	3.18	0.11
ZIF-zni(Zn)	31.30	1.40	0.05
ZIF-zni(Zn)-5min	48.70	2.17	0.08
ZIF-zni(Zn)-10min	56.64	2.53	0.09
ZIF-zni(Zn)-15min	53.40	2.38	0.08
a_gZIF-zni(Zn)	73.94	3.30	0.12

a$_g$ZIF-zni(Zn)-5min	70.40	3.14	0.11
ZIF-76	201.89	9.01	0.32
ZIF-76-5min	58.39	2.61	0.09
ZIF-76-10min	54.26	2.42	0.08
ZIF-76-15min	53.59	2.39	0.08
ZIF-8	293.43	13.10	0.46
ZIF-8-5min	147.02	6.56	0.23
ZIF-8-10min	86.65	3.87	0.14
ZIF-8-15min	82.32	3.68	0.13
ZIF-8-30min	75.51	3.37	0.12
ZIF-8-60min	69.89	3.12	0.11
ZIF-Cu-1	24.79	1.11	0.04
ZIF-Cu-1-5min	13.22	0.59	0.02
ZIF-Cu-1-10min	7.93	0.35	0.01
ZIF-Cu-1-15min	5.27	0.24	0.01

[a] $p \approx 95$ kPa, applied value for the density of adsorbate in its supercooled liquid state $\rho_{liq}(CO_2\ @195K) = 1.258\ g\ cm^{-3}$.

Table A4.4. BET analysis data for the CO_2 gas physisorption studies performed at 195 K.

Compound	BET analysis[a]			
	p/p_0 range	C constant	correlation coefficient	BET surface area / $m^2\ g^{-1}$
ZIF-62(Zn)	0.0006-0.027	315.1	0.997	276
ZIF-62(Zn)-5min	0.0005-0.027	316.1	0.997	220
ZIF-62(Zn)-10min	0.0006-0.028	298.8	0.997	184
ZIF-62(Zn)-15min	0.0007-0.028	279.8	0.998	171
a_gZIF-62(Zn)	0.0006-0.026	323.2	0.998	188
a_gZIF-62(Zn)-5min	0.0005-0.026	302.0	0.998	200
ZIF-62(Co)	0.0006-0.028	201.3	0.995	275
ZIF-62(Co)-5min	0.0006-0.028	298.8	0.996	211
ZIF-62(Co)-10min	0.0006-0.027	310.9	0.997	154
ZIF-62(Co)-15min	0.0006-0.028	275.6	0.997	130
a_gZIF-62(Co)	0.0006-0.026	308.0	0.999	174
a_gZIF-62(Co)-5min	0.0006-0.027	211.2	0.995	192
ZIF-4(Zn)	0.0006-0.027	333.7	0.994	471
ZIF-4(Zn)-5min	0.0006-0.029	320.4	0.997	194
ZIF-4(Zn)-10min	0.0006-0.029	275.8	0.998	150
ZIF-4(Zn)-15min	0.0006-0.029	272.9	0.998	144
a_gZIF-4(Zn)	0.0006-0.027	333.2	0.998	200
a_gZIF-4(Zn)-5min	0.0006-0.027	337.1	0.998	195
ZIF-4(Co)	0.0002-0.027	362.1	0.993	549
ZIF-4(Co)-5min	0.0006-0.027	293.8	0.996	210
ZIF-4(Co)-10min	0.0006-0.027	320.6	0.997	178
ZIF-4(Co)-15min	0.0006-0.027	284.1	0.997	145
a_gZIF-4(Co)-5min	0.0006-0.025	198.3	0.998	198
ZIF-zni(Zn)	0.0006-0.027	1596.6	0.999	129
ZIF-zni(Zn)-5min	0.0006-0.027	584.0	0.999	143
ZIF-zni(Zn)-10min	0.0006-0.027	369.8	0.998	146
ZIF-zni(Zn)-15min	0.0006-0.027	340.0	0.998	149

a_gZIF-zni(Zn)	0.0006-0.027	333.2	0.998	216
a_gZIF-zni(Zn)-5min	0.0006-0.027	377.1	0.998	197
ZIF-76	0.04-0.12	12.5	0.961	1114
ZIF-76-5min	0.0004-0.026	315.1	0.997	146
ZIF-76-10min	0.0006-0.027	263.9	0.996	118
ZIF-76-15min	0.0004-0.026	286.8	0.998	134
ZIF-8	0.05-0.12	36.8	0.990	1242
ZIF-8-5min	0.05-0.12	20.5	0.960	700
ZIF-8-10min	0.0006-0.029	167.2	0.998	214
ZIF-8-15min	0.0006-0.029	218.8	0.998	231
ZIF-8-30min	0.0006-0.029	225.5	0.999	226
ZIF-8-60min	0.0006-0.029	204.1	0.999	210
ZIF-Cu-1	0.0007-0.029	1908.1	0.999	72
ZIF-Cu-1-5min	0.0006-0.026	705.3	0.998	26
ZIF-Cu-1-10min	0.0005-0.026	37.2	0.925	8
ZIF-Cu-1-15min	0.0006-0.025	167.4	0.960	5

[a] Applied value for cross sectional areas: $\sigma(CO_2\ @195\ K) = 17\ Å^2$/molecule.[167] $p_0(CO_2, 195K) = 191\ kPa$.[166]

A.4.5 – Thermal analysis

T_d was determined as the crossing points of tangents to the horizontal weight-loss line and the weight-loss line at the first decomposing step from TG/DTA data. All other thermal parameters were deducted from the DSC data. T_m is defined as the offset temperature of the endothermal melting peak and has been determined by the intersection of two tangents. T_a and T_{rc} are determine as the peak temperature of the exothermic peaks. $T_{rc,onset}$ is the onset temperature of the recrystallization signal. T_g is defined as the onset by the intersection of two tangents of the endothermic signal associated with the glass transition. ΔH_m is the integral area between the onset and offset of the melting peak in the DSC curve after baseline subtraction. ΔH_{rc} is the integral area between the onset and offset of the recrystallization peak in the DSC curve. For a better understanding of the abbreviations in this section, their definitions are given in **Table A4.5**. A compilation of all temperatures determined with TG/DTA and DSC is given in **Table A4.6**.

Table A4.5. Abbreviations for thermal analysis used in this section.

Abbreviations	Definitions
T_d	decomposition temperature (onset)
T_a	amorphization temperature (peak)
T_g	glass transition temperature (onset)
$T_{rc,onset}$	recrystallization temperature (onset)
T_{rc}	recrystallization temperature (peak)
T_m	melting temperature (offset)
ΔH_{rc}	enthalpy of recrystallization
ΔH_m	enthalpy of melting

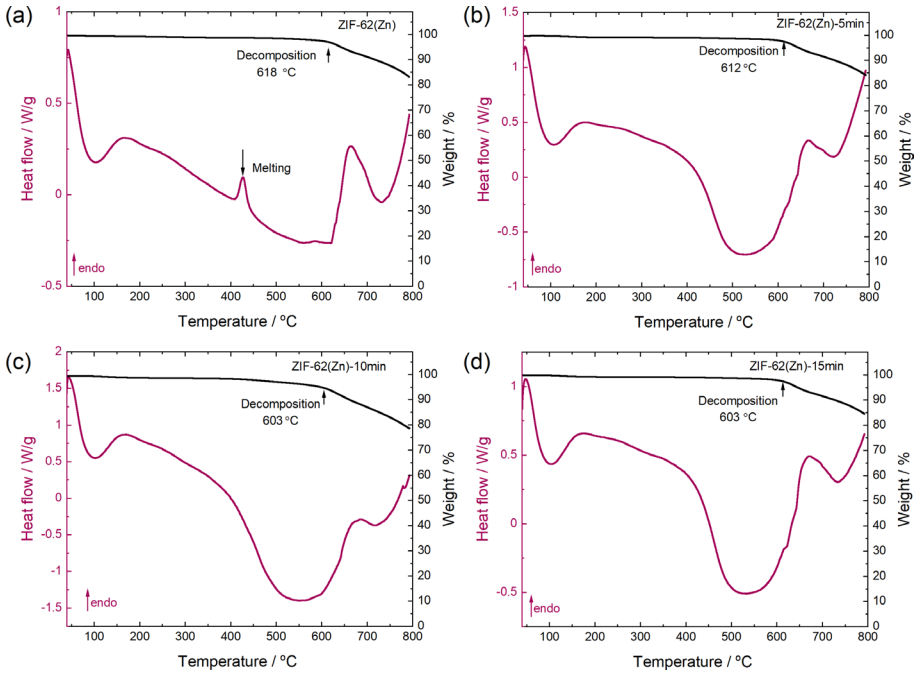

Figure A4.76. TG/DTA data of (a) activated ZIF-62(Zn), (b) ZIF-62(Zn)-5min, (c) ZIF-62(Zn)-10min and (d) ZIF-62(Zn)-15min. The heating rate was set to +10 °C min^{-1}.

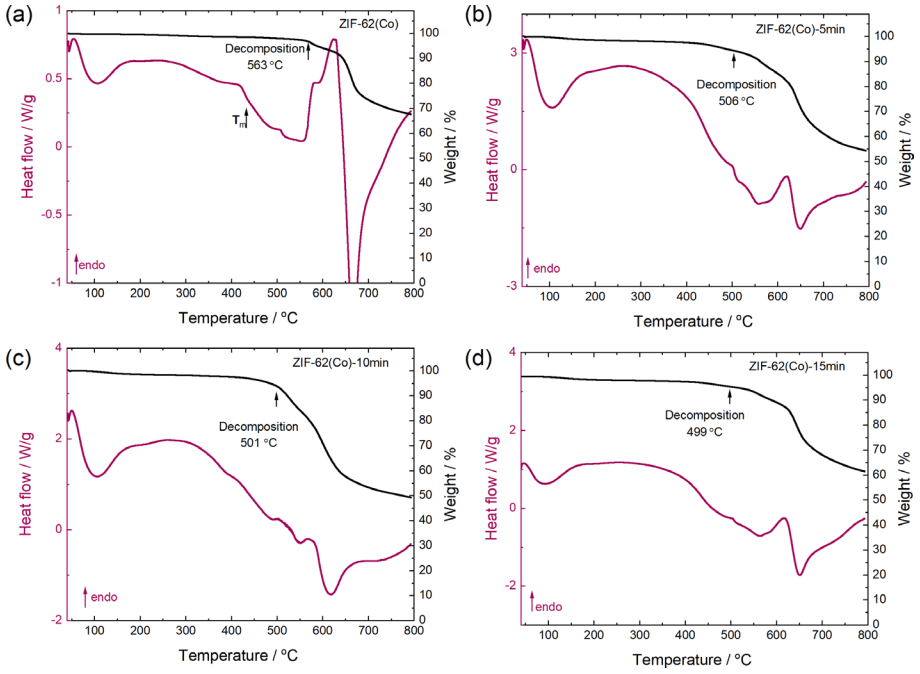

Figure A4.77. TG/DTA data of (a) activated ZIF-62(Co), (b) ZIF-62(Co)-5min, (c) ZIF-62(Co)-10min and (d) ZIF-62(Co)-15min. The heating rate was set to +10 °C min^{-1}.

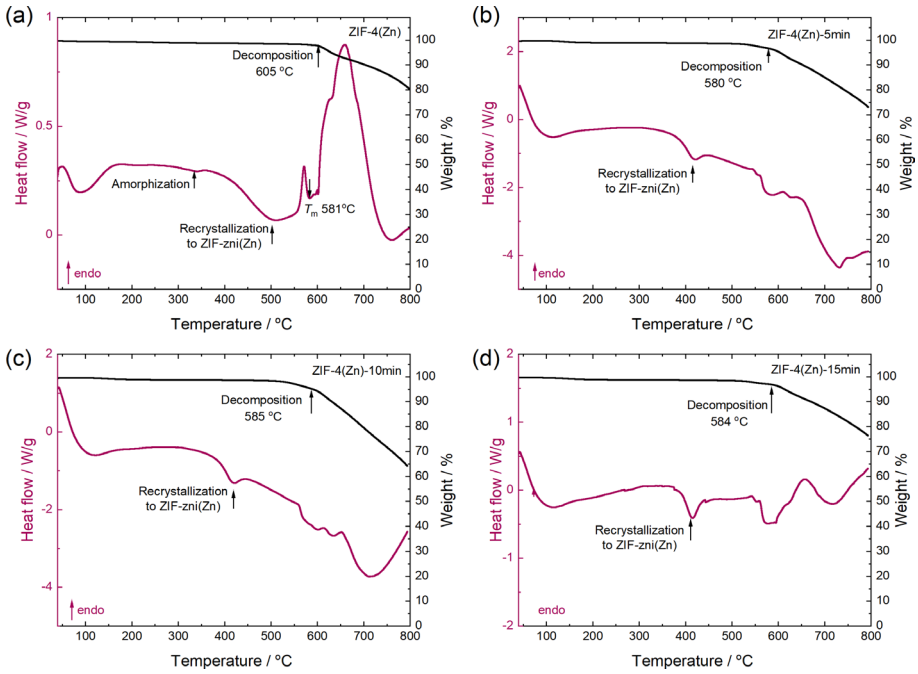

Figure A4.78. TG/DTA data of (a) activated ZIF-4(Zn), (b) ZIF-4(Zn)-5min, (c) ZIF-4(Zn)-10min and (d) ZIF-4(Zn)-15min. The heating rate was set to +10 °C min^{-1}.

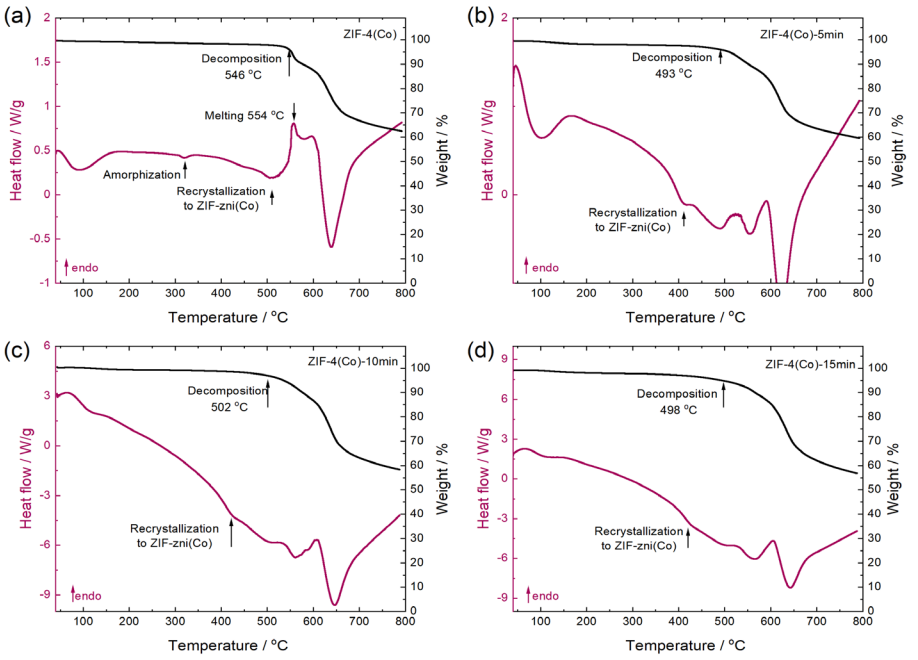

Figure A4.79. TG/DTA data of (a) activated ZIF-4(Co), (b) ZIF-4(Co)-5min, (c) ZIF-4(Co)-10min and (d) ZIF-4(Co)-15min. The heating rate was set to +10 °C min^{-1}.

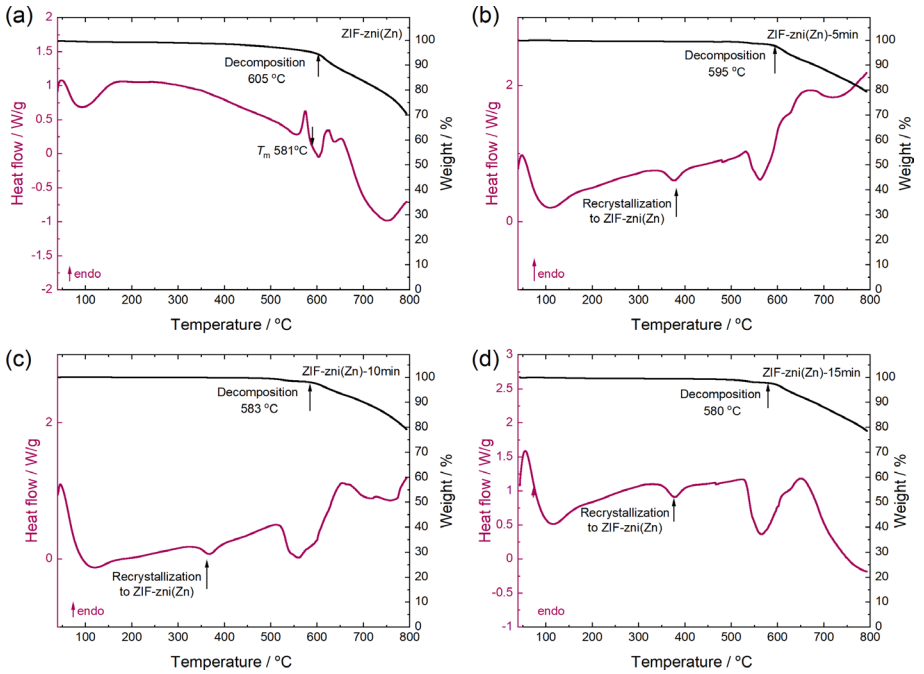

Figure A4.80. TG/DTA data of (a) activated ZIF-zni(Zn), (b) ZIF-zni(Zn)-5min, (c) ZIF-zni(Zn)-10min and (d) ZIF-zni(Zn)-15min. The heating rate was set to +10 °C min^{-1}.

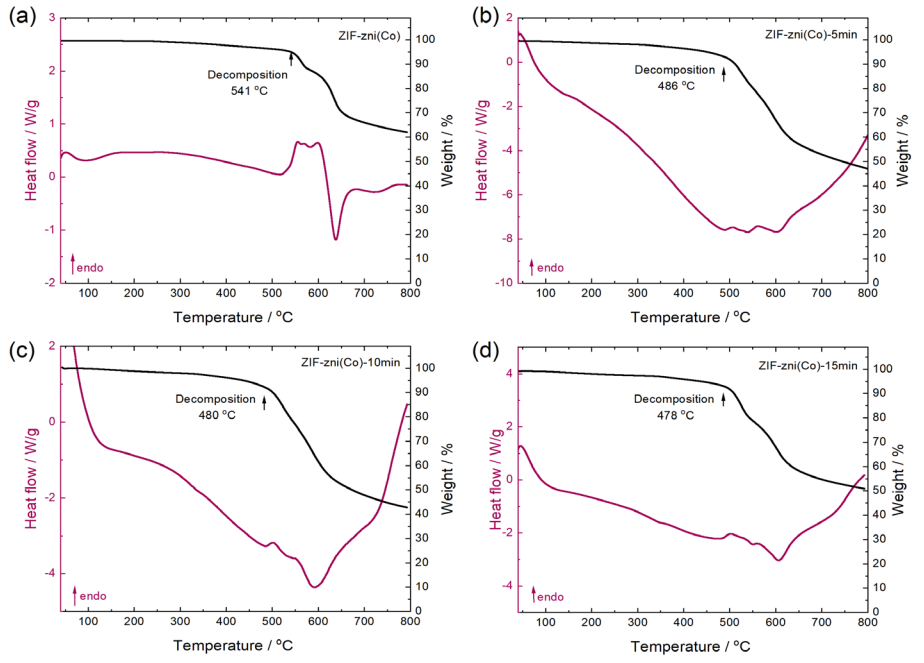

Figure A4.81. TG/DTA data of (a) activated ZIF-zni(Co), (b) ZIF-zni (Co)-5min, (c) ZIF-zni (Co)-10min and (d) ZIF-zni (Co)-15min. The heating rate was set to +10 °C min^{-1}.

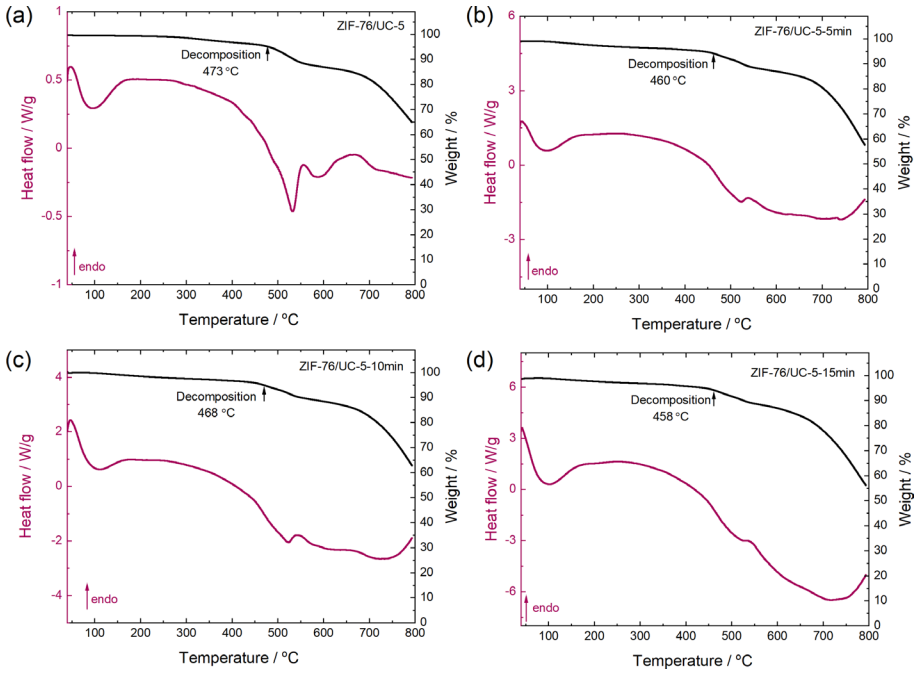

Figure A4.82. TG/DTA data of (a) activated ZIF-76/UC-5 (phase mixture), (b) ZIF-76/UC-5-5min, (c) ZIF-76/UC-5-10min and (d) ZIF-76/UC-5-15min. The heating rate was set to +10 °C min^{-1}.

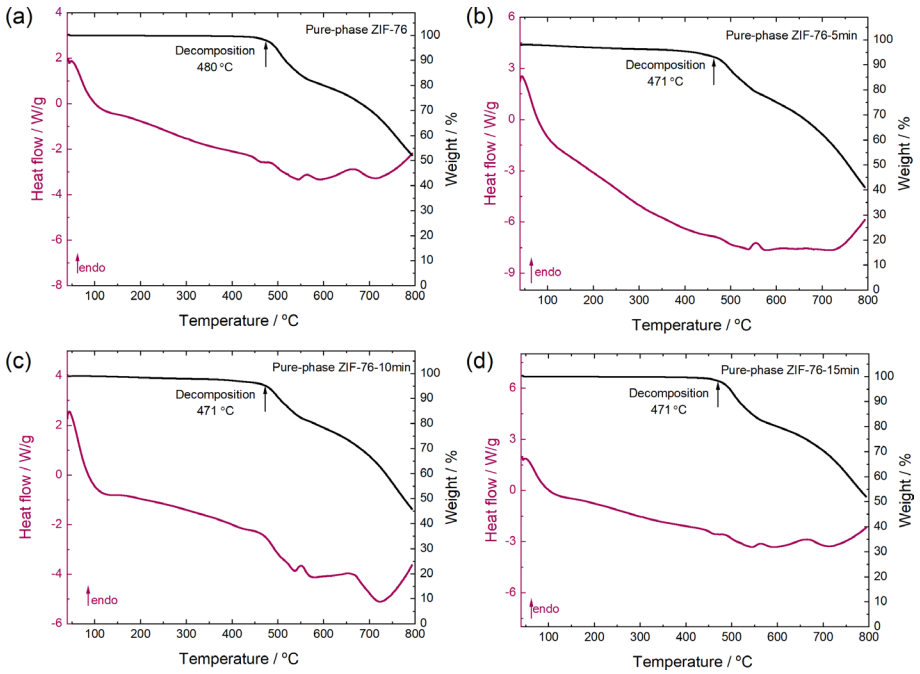

Figure A4.83. TG/DTA data of (a) activated phase pure ZIF-76, (b) ZIF-76-5min, (c) ZIF-76-10min and (d) ZIF-76-15min. The heating rate was set to +10 °C min–1.

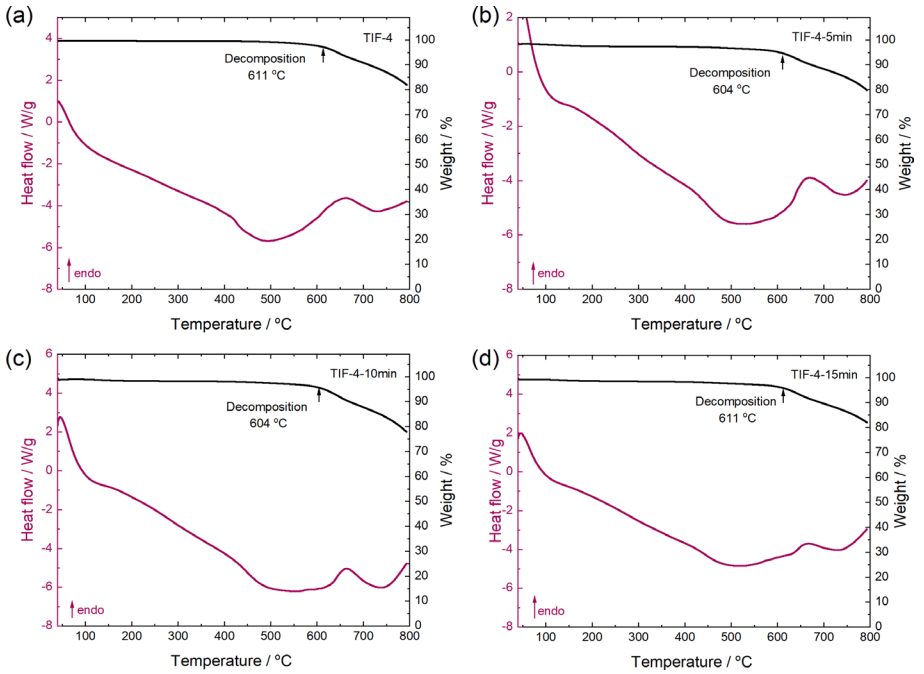

Figure A4.84. TG/DTA data of (a) activated TIF-4, (b) TIF-4-5min, (c) TIF-4-10min and (d) TIF-4-15min. The heating rate was set to +10 °C min^{-1}.

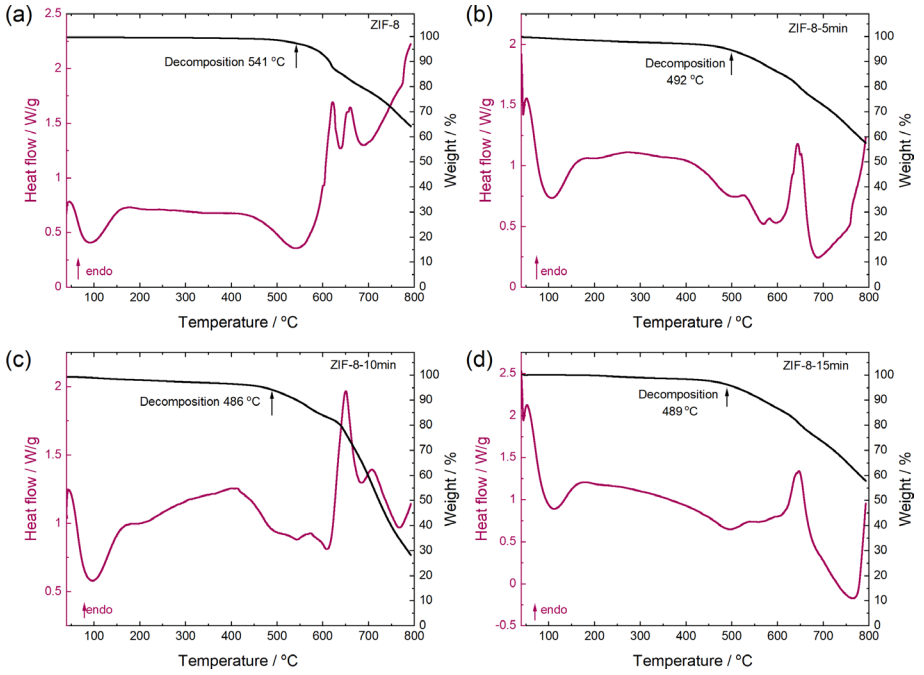

Figure A4.85. TG/DTA data of the (a) activated ZIF-8, (b) ZIF-8-5min, (c) ZIF-8-10min and (d) ZIF-8-15min. The heating rate was set to +10 °C min^{-1}.

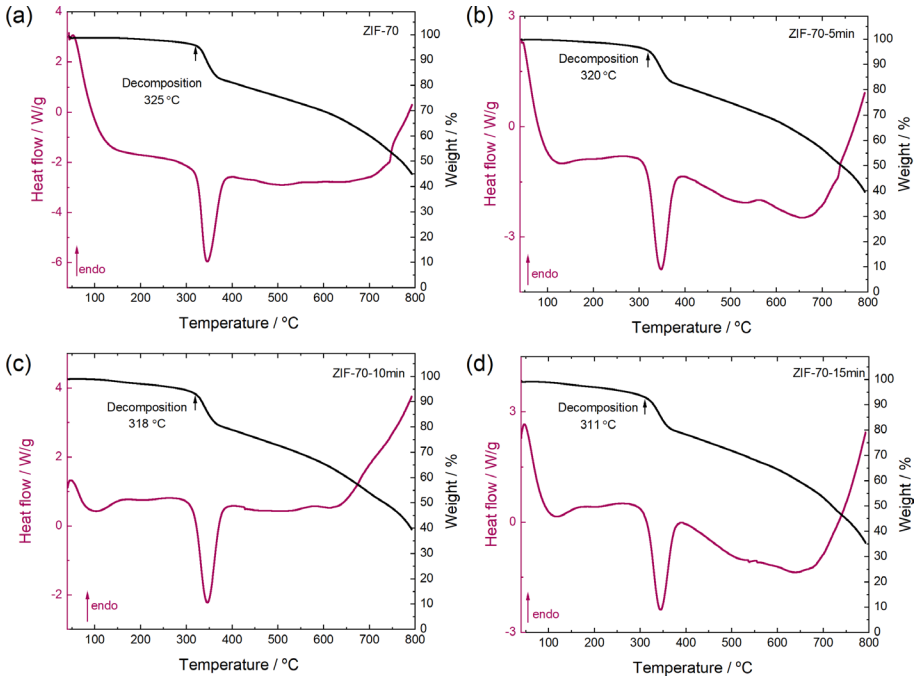

Figure A4.86. TG/DTA data of (a) activated ZIF-70, (b) ZIF-70-5min, (c) ZIF-70-10min and (d) ZIF-70-15min. The heating rate was set to +10 °C min^{-1}.

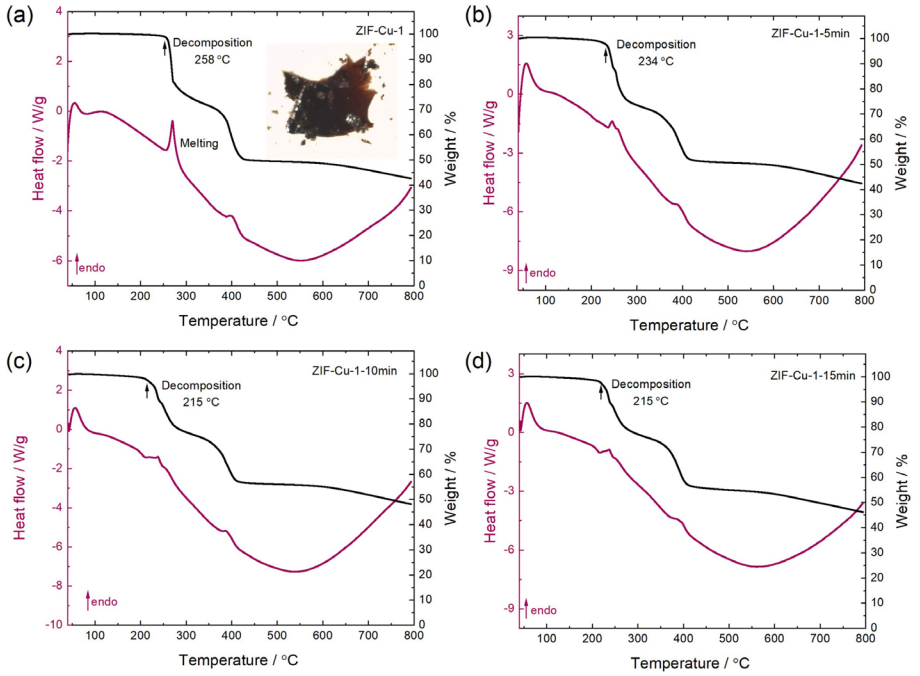

Figure A4.87. TG/DTA data of (a) activated ZIF-Cu-1, (b) ZIF-Cu-1-5min, (c) ZIF-Cu-1-10min and (d) ZIF-Cu-1-15min. The heating rate was set to +10 °C min^{-1}. The inset in (a) is the microscopic image of ZIF-Cu-1 after quenching to room temperature from 270 °C, i.e. the onset of melting and decomposition. The quenched sample shows features of flow indicative of melting. The brown color of the sample, however, signifies partial decomposition during the melting process.

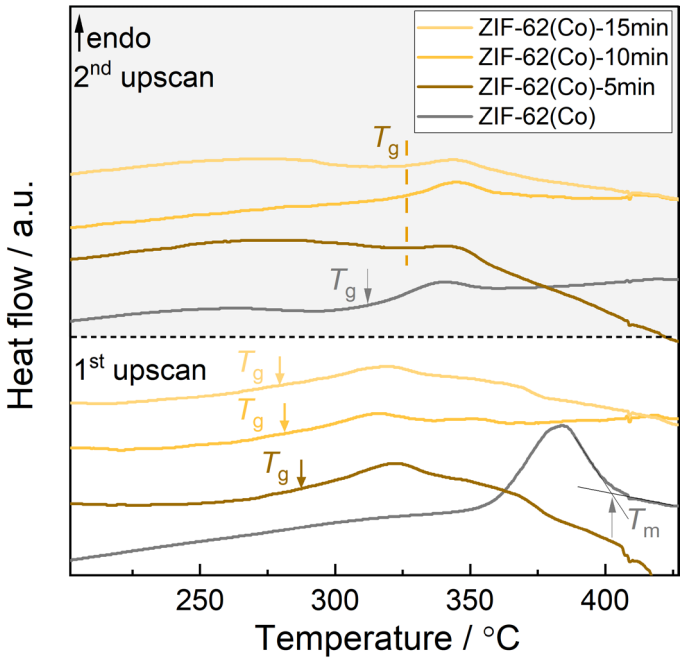

Figure A4.88. DSC data from two upscans of the activated ZIF-62(Co), ZIF-62(Co)-5min, ZIF-62(Co)-10min and ZIF-62(Co)-15min. The heating/cooling rate is ±10 °C min^{-1}.

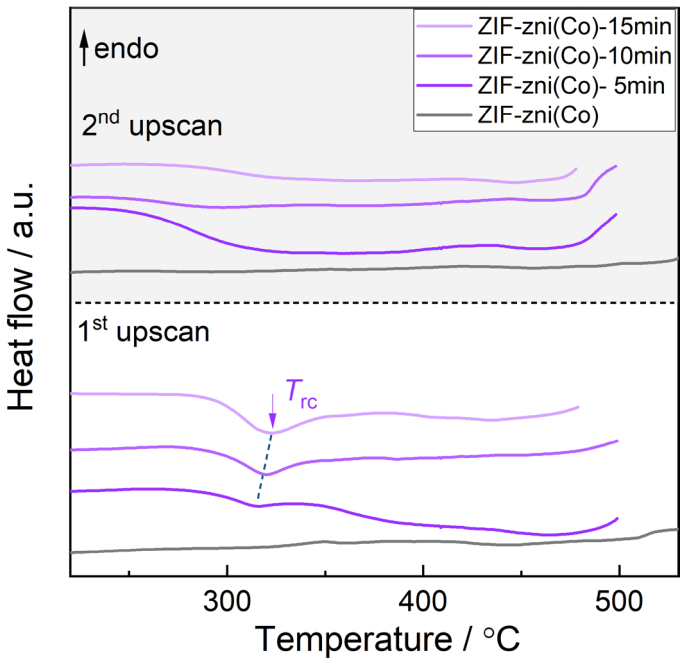

Figure A4.89. DSC data from two upscans of the activated ZIF-zni(Co), ZIF- zni(Co)-5min, ZIF-62(Co)-10min and ZIF-62(Co)-15min. The heating/cooling rate is ±10 °C min^{-1}. We speculate that a glass transition event must preceed the recrystallization during the first upscan of the PSBM samples, however, the glass transition is hidden underneath the exothermic recrystallization.

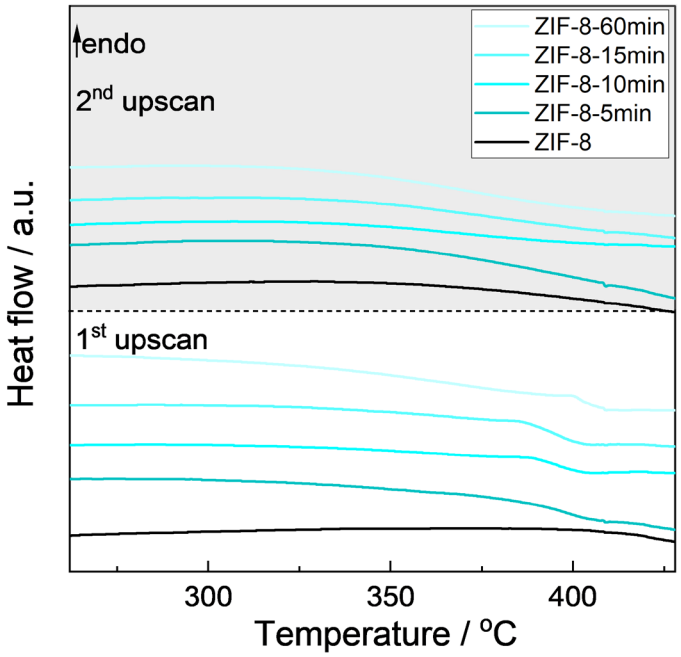

Figure A4.90. DSC data from two upscans of activated ZIF-8, ZIF-8-5min, ZIF-8-10min, ZIF-8-15min and ZIF-8-60min. The heating/cooling rate is ±10 °C min^{-1}.

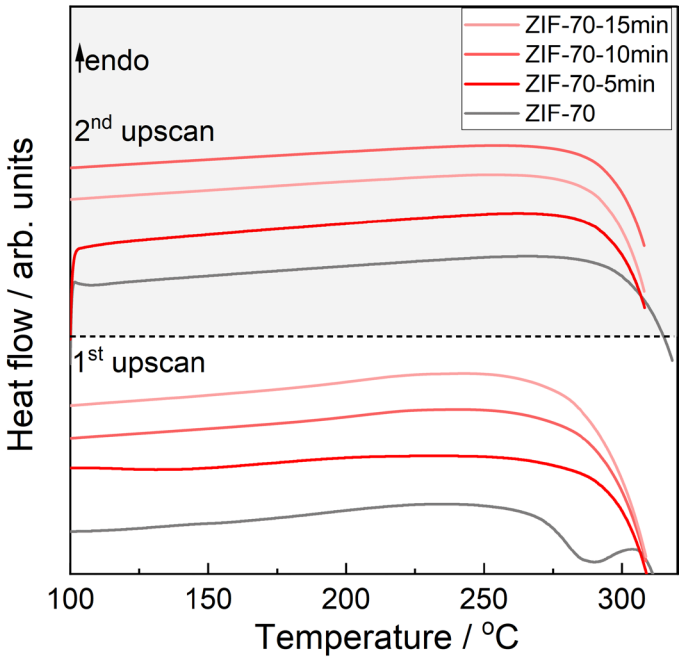

Figure A4.91. DSC data from two upscans of activated ZIF-70, ZIF-70-5min, ZIF-70-10min and ZIF-70-15min. The heating/cooling rate is ±10 °C min^{-1}.

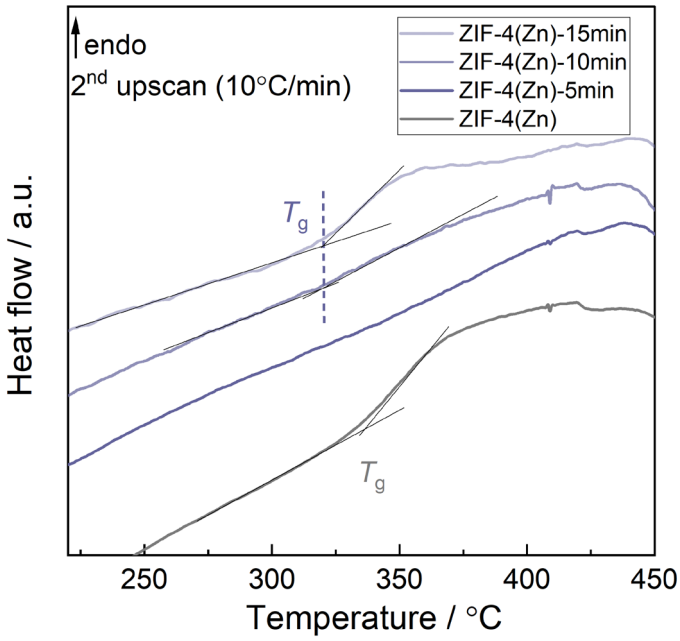

Figure A4.92. Zoomed DSC data of the second upscan of activated ZIF-4(Zn), ZIF-4(Zn)-5min, ZIF-4(Zn)-10min and ZIF-4(Zn)-15min. The ZIF-4(Zn) was heated to 590 °C and the PSBM samples were heated to 580 °C in the first upscan (i.e. beyond the melting point of the ZIF-zni(Zn) phase recrystallizing). Heating and cooling rates for both upscans were ±10 °C min^{-1}.

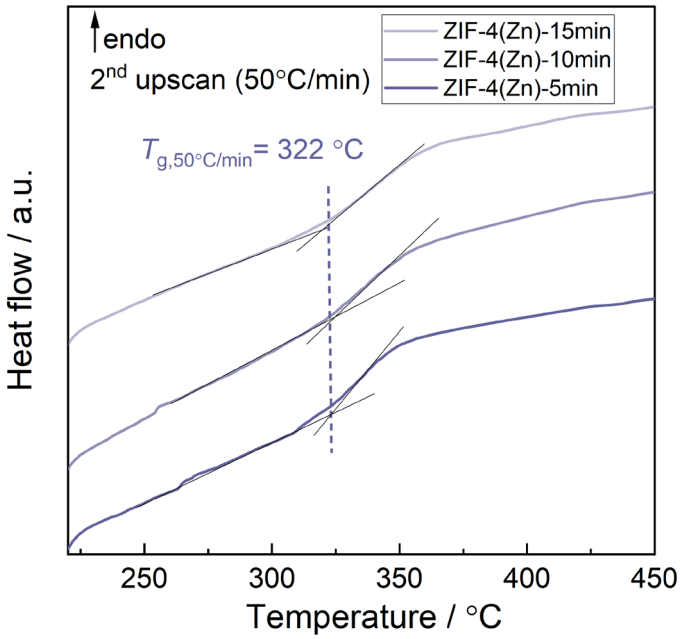

Figure A4.93. Zoomed DSC data of the second upscan with heating rete 50 °C mim^{-1} of ZIF-4(Zn)-5min, ZIF-4(Zn)-10min and ZIF-4(Zn)-15min. The samples were heated to 580 °C in the first upscan (i.e. beyond the melting point of the ZIF-zni(Zn) phase recrystallizing during the first upscan). Heating and cooling rates of the first up- and downscans were ±10 °C min^{-1}. Heating rate for the shown second upscans was +50 °C min^{-1}. The faster heating rate results in a much clearer heat flow signal for the glass transition.

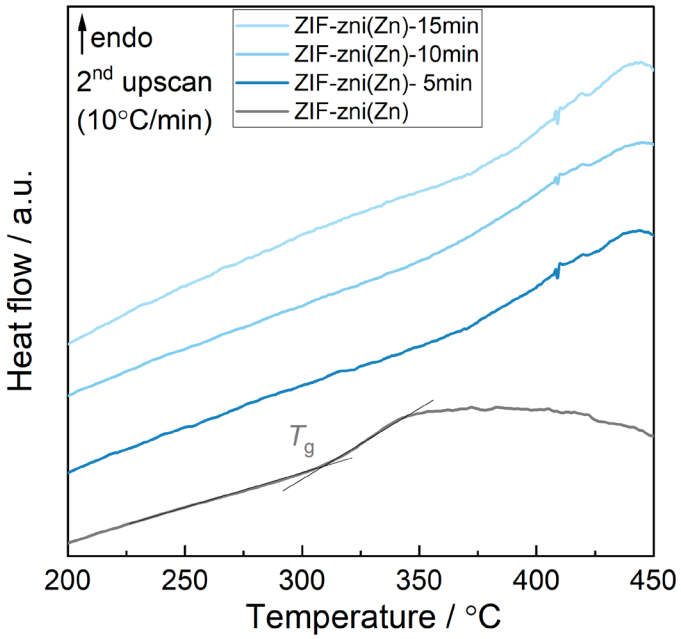

Figure A4.94. Zoomed DSC data of the second upscan of ZIF-zni(Zn), ZIF-zni(Zn)-5min, ZIF-zni(Zn)-10min and ZIF-zni(Zn)-15min. The ZIF-zni(Zn) was heated to 590 °C and the PSBM samples were heated to 580 °C in the first upscan (i.e. beyond the melting point of the ZIF-zni(Zn) phase recrystallizing during the first upscan). Heating and cooling rates for both upscans were ±10 °C min^{-1}.

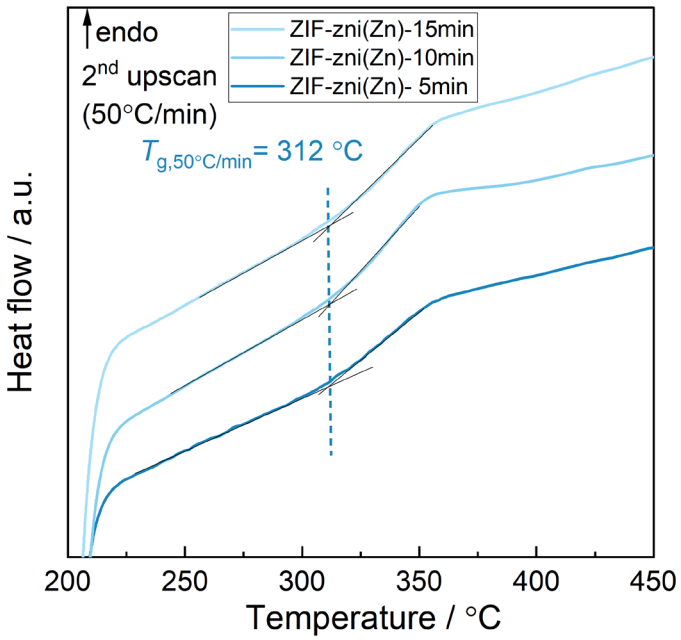

Figure A4.95. Zoomed DSC data of the second upscan of ZIF-zni(Zn)-5min, ZIF-zni(Zn)-10min and ZIF-zni(Zn)-15min. The samples were heated to 580 °C in the first upscan (i.e. beyond the melting point of the ZIF-zni(Zn) phase recrystallizing during the first upscan). Heating and cooling rates of the first up- and downscans were ±10 °C min^{-1}. Heating rate for the shown second upscans was +50 °C min^{-1}. The faster heating rate results in a much clearer heat flow signal for the glass transition.

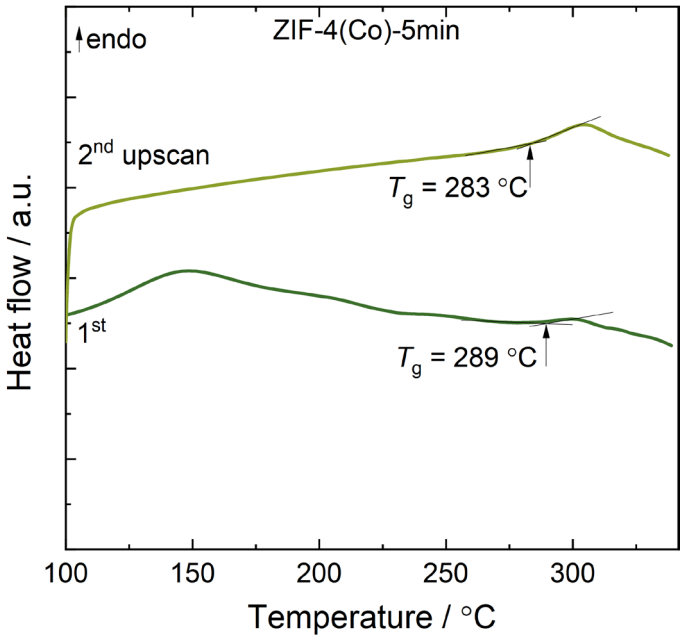

Figure A4.96. DSC data for two upscans of ZIF-4(Co)-5min. The heating/cooling rate is ±10 °C min^{-1}. To avoid recrystallization (T_{rc} = 414 °C), the first upscan was heated to 340 °C.

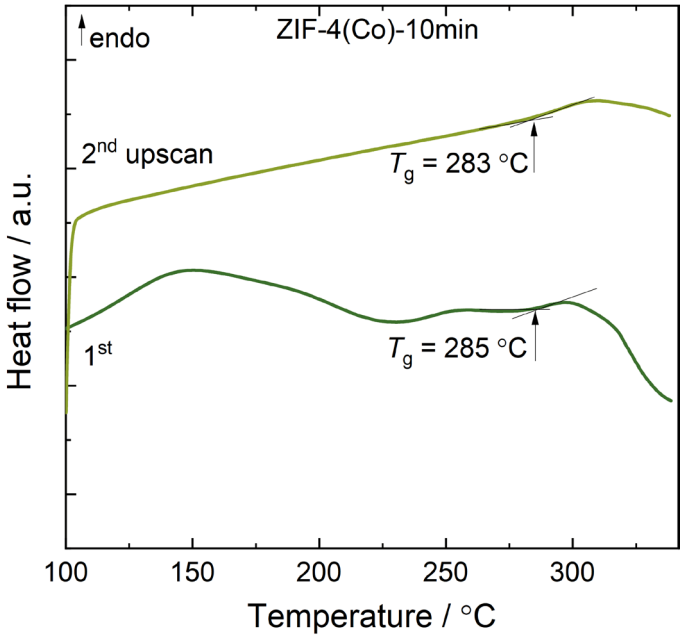

Figure A4.97. DSC data for two upscans of ZIF-4(Co)-10min. The heating/cooling rate is ±10 °C min^{-1}. To avoid recrystallization (T_{rc} = 414 °C), the first upscan was heated to 340 °C.

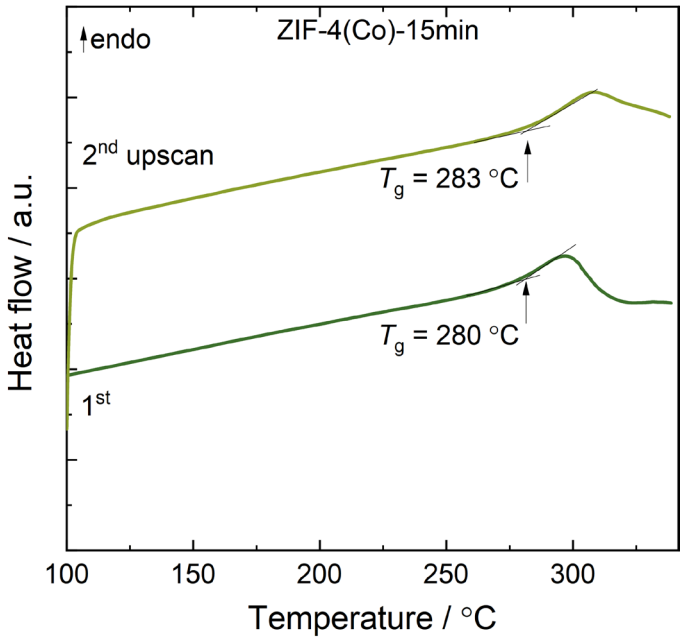

Figure A4.98. DSC data for 2 upscans of ZIF-4(Co)-15min. The heating/cooling rate is ±10 °C min^{-1}. To avoid recrystallization (T_{rc} = 412 °C), the first upscan was heated to 340 °C.

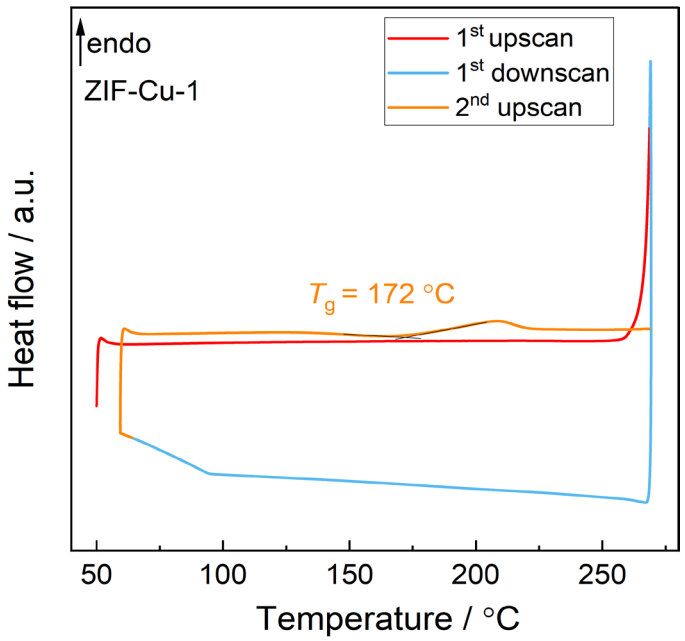

Figure A4.99. Cyclic DSC data for 2 upscans and 1 downscan of ZIF-Cu-1 (heating/cooling rate is ±10 °C min^{-1}), the upscans were heated to the onset of melting (270 °C) and then cooled in order to minimize decomposition.

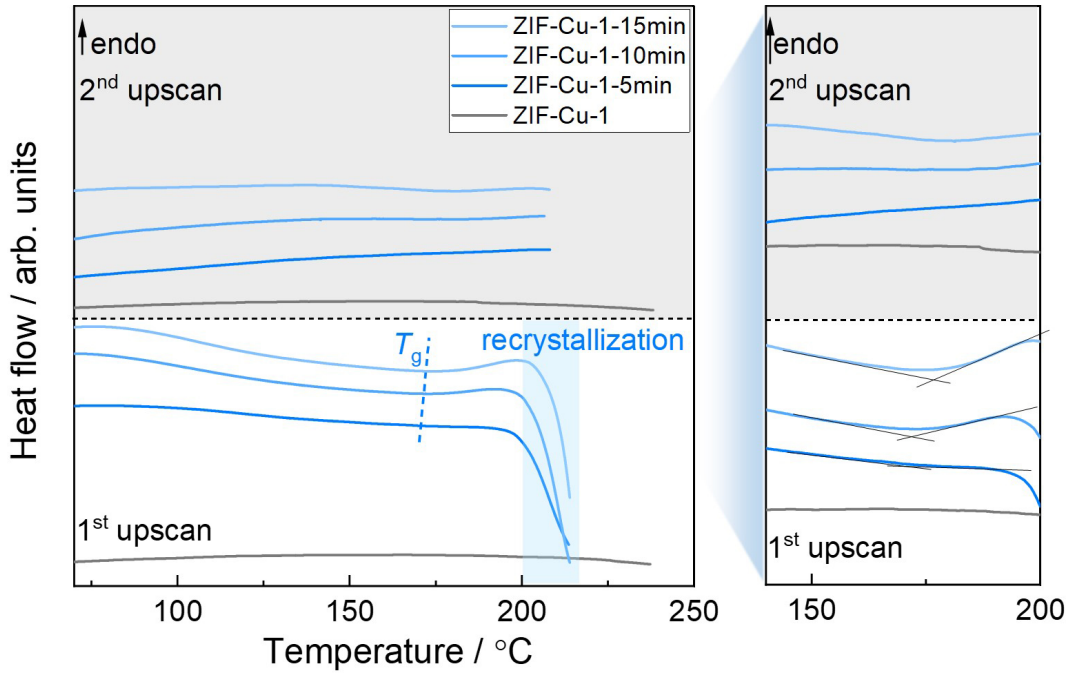

Figure A4.100. DSC data of the first upscan to 215 °C of crystalline ZIF-Cu-1 and PSBM amorphized ZIF-Cu-1-5min, ZIF-Cu-1-10min, ZIF-Cu-1-15min. The heating/cooling rate is ±10 °C min^{-1}. The PSBM materials show a glass transition around 170 °C and start to recrystallize at about 200 °C. There are no glass transition signals in the second DSC upscan (i.e. after thermal recrystallization).

Table A4.6. Summary of T_a, T_g, $T_{rc,onset}$, T_{rc}, and T_m in the 1st upscan, T_g in the 2nd upscan, and T_d of studied ZIFs materials.

Compound	T_a (1st upscan) (°C)	T_g (1st upscan) (°C)	T_g (2nd upscan) (°C)	$T_{rc,onset}$ (°C)	T_{rc} (°C)	T_m (°C)	T_d (°C)
ZIF-62(Zn)	-	-	325	-	-	437	618
ZIF-62(Zn)-5min	-	311	325	-	-	-	612
ZIF-62(Zn)-10min	-	307	325	-	-	-	603
ZIF-62(Zn)-15min	-	304	325	-	-	-	603
ZIF-62(Co)	-	-	313	-	-	401	563
ZIF-62(Co)-5min	-	288	326	-	-	-	506
ZIF-62(Co)-10min	-	279	326	-	-	-	501
ZIF-62(Co)-15min	-	280	326	-	-	-	499
ZIF-4(Zn)	326	-	336	450	501	581	605
ZIF-4(Zn)-5min	-	280	322[a]	398	419	570	580
ZIF-4(Zn)-10min	-	278	322[a]	396	416	570	585
ZIF-4(Zn)-15min	-	276	322[a]	393	412	570	584
ZIF-4(Co)	292	-	-	475	504	-	546
ZIF-4(Co)-5min	-	289	283[b]	383	414	-	493
ZIF-4(Co)-10min	-	285	283[b]	380	413	-	502
ZIF-4(Co)-15min	-	280	283[b]	379	412	-	498
ZIF-zni(Zn)	-	-	310	-	-	584	605
ZIF-zni(Zn)-5min	-	293	312[a]	333	366	565	595
ZIF-zni(Zn)-10min	-	291	312[a]	351	376	562	583
ZIF-zni(Zn)-15min	-	289	312[a]	368	401	564	580
ZIF-zni(Co)	-	-	-	-	-	-	541
ZIF-zni(Co)-5min	-	-[c]	-	296	314	-	486
ZIF-zni(Co)-10min	-	-[c]	-	298	319	-	480
ZIF-zni(Co)-15min	-	-[c]	-	297	321	-	478
ZIF-76/UC-5	-	-	339	-	-	448	473
ZIF-76/UC-5-5min	-	338	339	-	-	-	460
ZIF-76/UC-5-10min	-	331	339	-	-	-	468
ZIF-76/UC-5-15min	-	321	339	-	-	-	458
ZIF-76	-	-	-	-	-	-	480

ZIF-76-5min	-	347	351	-	-	-	471
ZIF-76-10min	-	334	357	-	-	-	471
ZIF-76-15min	-	278	357	-	-	-	471
TIF-4	-	-	323	-	-	427	611
TIF-4-5min	-	319	323	-	-	-	604
TIF-4-10min	-	314	323	-	-	-	604
TIF-4-15min	-	314	323	-	-	-	611
ZIF-70	-	-	-	-	-	-	325
ZIF-70-5min	-	-	-	-	-	-	320
ZIF-70-10-min	-	-	-	-	-	-	318
ZIF-70-15-min	-	-	-	-	-	-	311
ZIF-8	-	-	-	-	-	-	541
ZIF-8-5min	-	-	-	-	-	-	492
ZIF-8-10min	-	-	-	-	-	-	486
ZIF-8-15min	-	-	-	-	-	-	489
ZIF-Cu-1	-	-	-	-	-	-	258[d]
ZIF-Cu-1-5min	-	166	162[b]	202	-[e]	-	234
ZIF-Cu-1-10min	-	167	165[b]	203	-[e]	-	215
ZIF-Cu-1-15min	-	170	169[b]	208	-[e]	-	215

[a] The first upscan was heated to the melting temperature. These T_g values were determined from a scan with a heating rate of 50 °C min^{-1} in the second upscan.

[b] The maximum temperature of the first upscan was below the recrystallization temperature.

[c] Possibly due to the overlap of T_g and T_{rc}, a clear T_g signal is not detectable.

[d] Thermal decomposition and melting are overlapping.

[e] The peak temperature of T_{rc} cannot be reliably determined because it overlaps with decomposition.

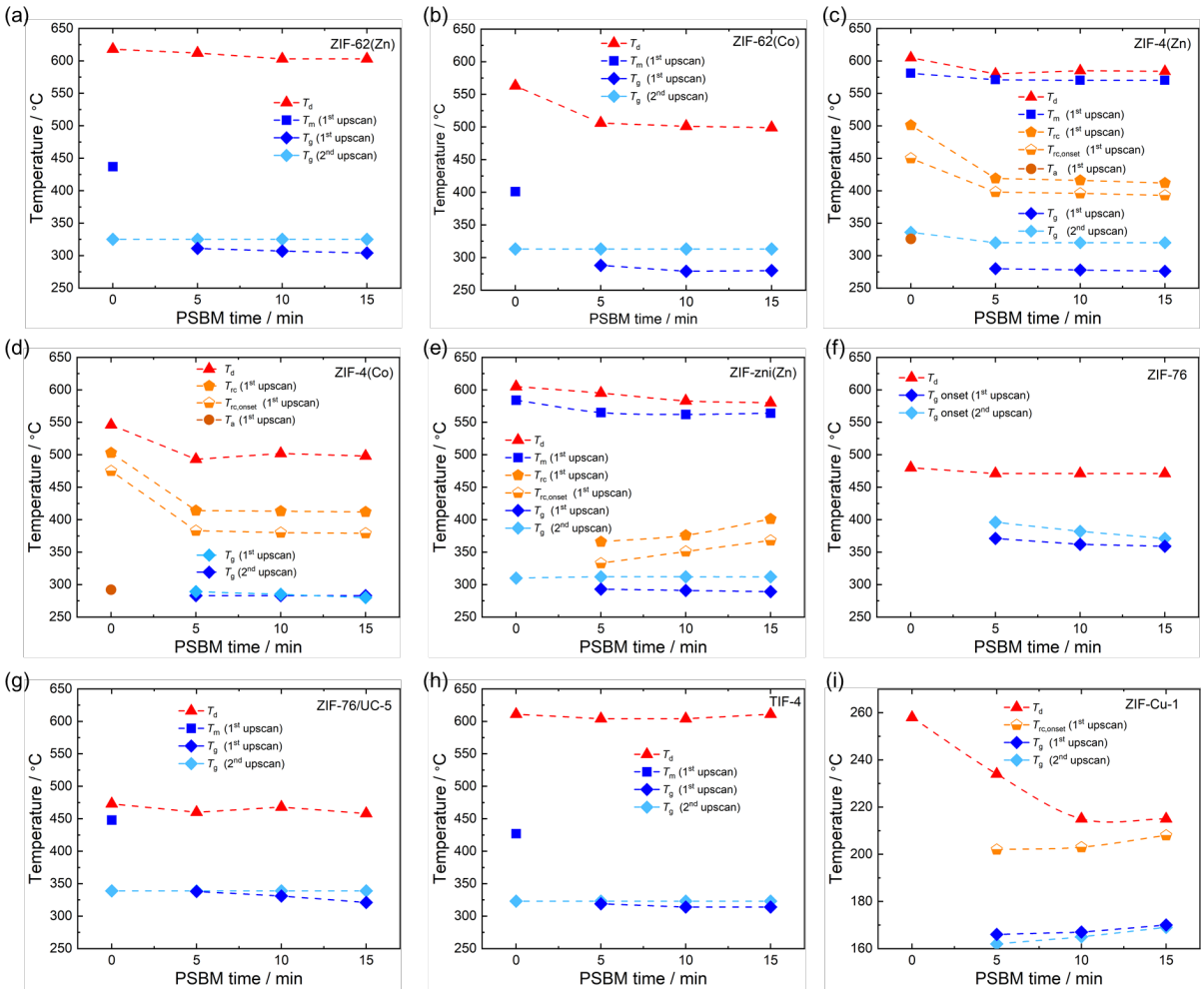

Figure A4.101. Summary of T_a, T_g, $T_{rc,onset}$, T_{rc} and T_m values derived from the first upscans and T_g values derived from the second upscans of the DSC measurement with T_d values derived from TG/DTA measurements as a function of PSBM time for various of the ZIFs under study here. Note that in order to detect the T_g in the 2nd upscan of ZIF-4(Co), the 1st upscan was only heated below the recrystallization temperature. Lines are just a guide to the eye.

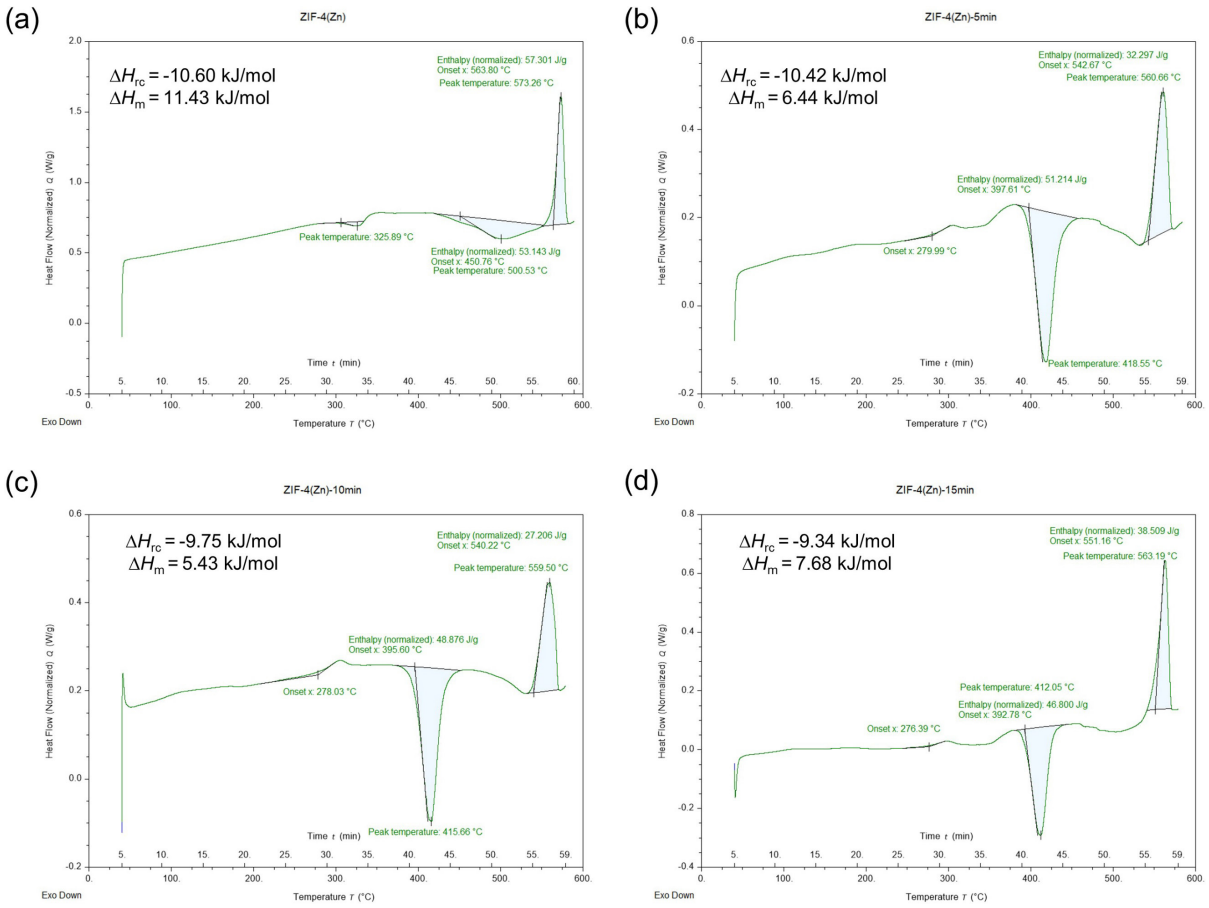

Figure A4.102. Phase transition enthalpies of ZIF-4(Zn), ZIF-4(Zn)-5min, ZIF-4(Zn)-10min and ZIF-4(Zn)-15min determined from the first upscan of DSC data.

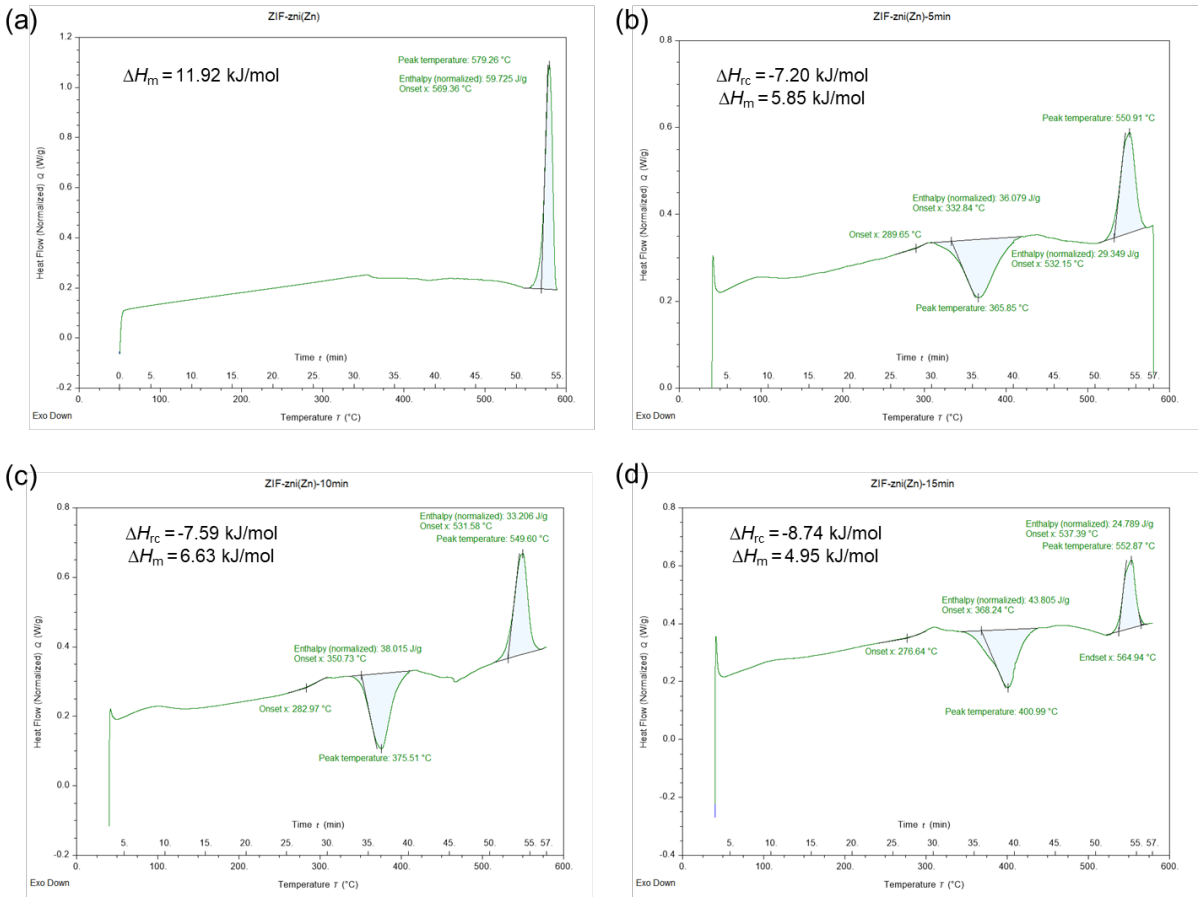

Figure A4.103. Phase transition enthalpies of ZIF-zni(Zn), ZIF-zni(Zn)-5min, ZIF-zni(Zn)-10min and ZIF-zni(Zn)-15min determined from the first upscan of DSC data.

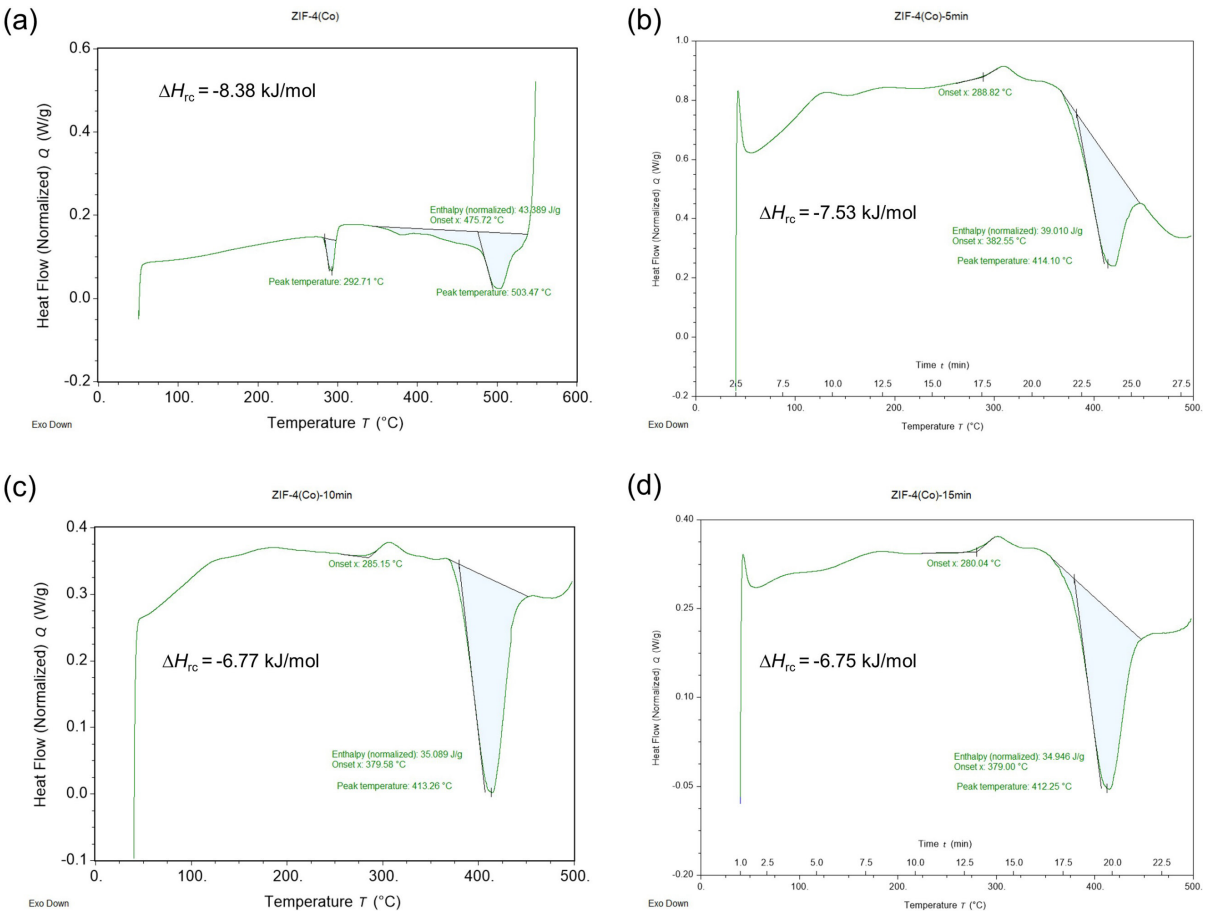

Figure A4.104. Phase transition enthalpies of ZIF-4(Co), ZIF-4(Co)-5min, ZIF-4(Co)-10min and ZIF-4(Co)-15min determined from the first upscan of DSC data.

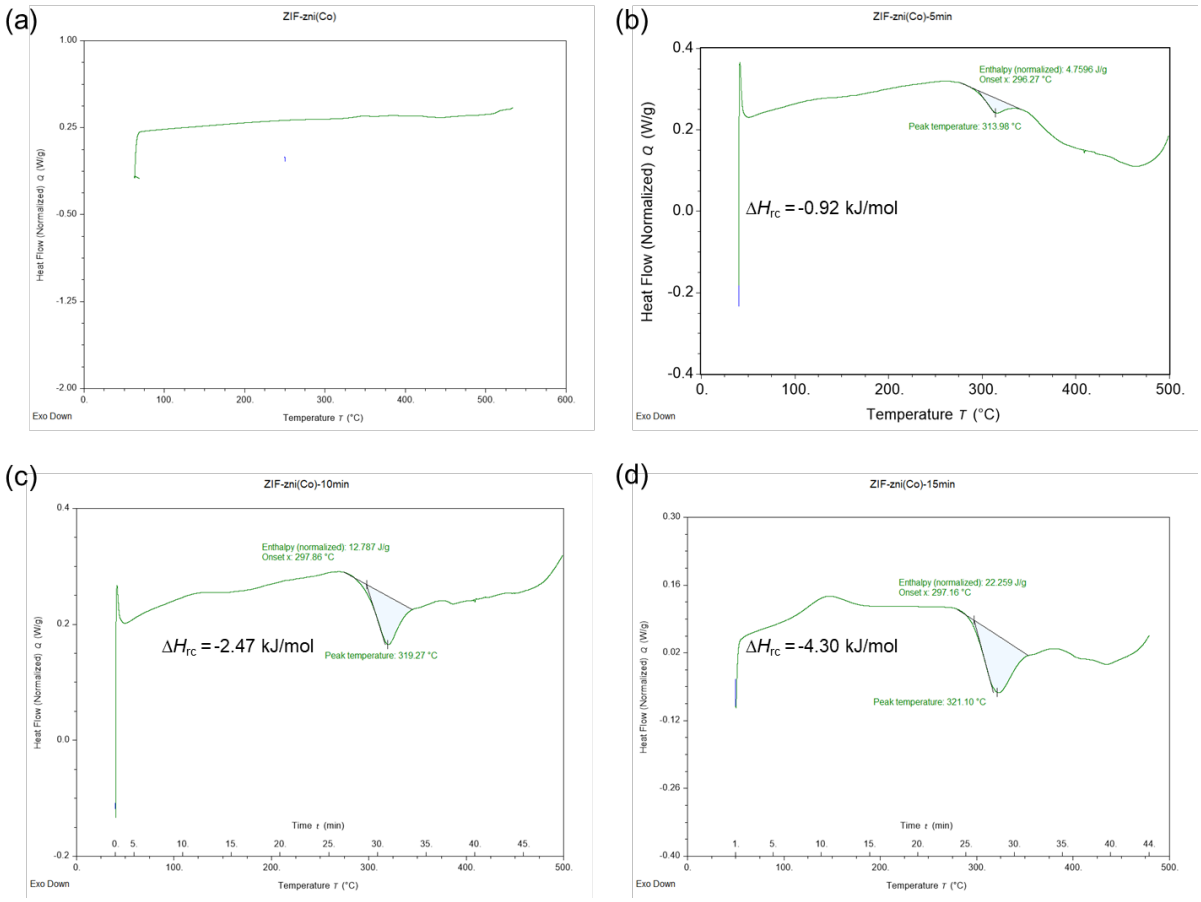

Figure A4.105. Phase transition enthalpies of ZIF-zni(Co), ZIF-zni(Co)-5min, ZIF-zni(Co)-10min and ZIF-zni(Co)-15min determined from the first upscan of DSC data.

Table A4.7. Summary of the phase transition enthalpies of ZIF-4(M) and ZIF-zni(M) as well as the corresponding PSBM samples determined from the first upscan of DSC data.

Compound	ΔH_{rc}		ΔH_{m}	
	J/g	kJ/mol	J/g	kJ/mol
ZIF-4(Zn)	–53.14	–10.60	57.30	11.43
ZIF-4(Zn)-5min	–51.21	–10.22	32.30	6.44
ZIF-4(Zn)-10min	–48.88	–9.75	27.21	5.43
ZIF-4(Zn)-15min	–46.80	–9.34	38.51	7.68
ZIF-zni(Zn)	/	/	59.73	11.92
ZIF-zni(Zn)-5min	–36.08	–7.20	29.33	5.85
ZIF-zni(Zn)-10min	–38.02	–7.59	33.21	6.63
ZIF-zni(Zn)-15min	–43.81	–8.74	24.79	4.95
ZIF-4(Co)	–43.39	–8.38	/	/
ZIF-4(Co)-5min	–39.01	–7.53	/	/
ZIF-4(Co)-10min	–35.09	–6.77	/	/
ZIF-4(Co)-15min	–34.95	–6.75	/	/
ZIF-zni(Co)	/	/	/	/
ZIF-zni(Co)-5min	–4.76	–0.92	/	/
ZIF-zni(Co)-10min	–12.79	–2.47	/	/
ZIF-zni(Co)-15min	–22.26	–4.30	/	/

A.4.6 – Scanning electron microscopy and optical microscopy

Scanning electron microscopy (SEM) imaging was performed with a Hitachi S-4500 instrument. For measurements, samples were placed on a conductive adhesive pad. Imaging was done with 1 kV accelerating voltage on a secondary electron detector. For the PSBM samples, the SEM morphologies are that of amorphous glassy agglomerates. In order to distinguish between the particle sizes of the PSBM samples, the particle sizes counted are those of the agglomerates (i.e. not the size of the primary particles). The particle size distributions were processed using the Nano Measurer 1.2 software (shareware developed by Department of Chemistry, Fudan University).

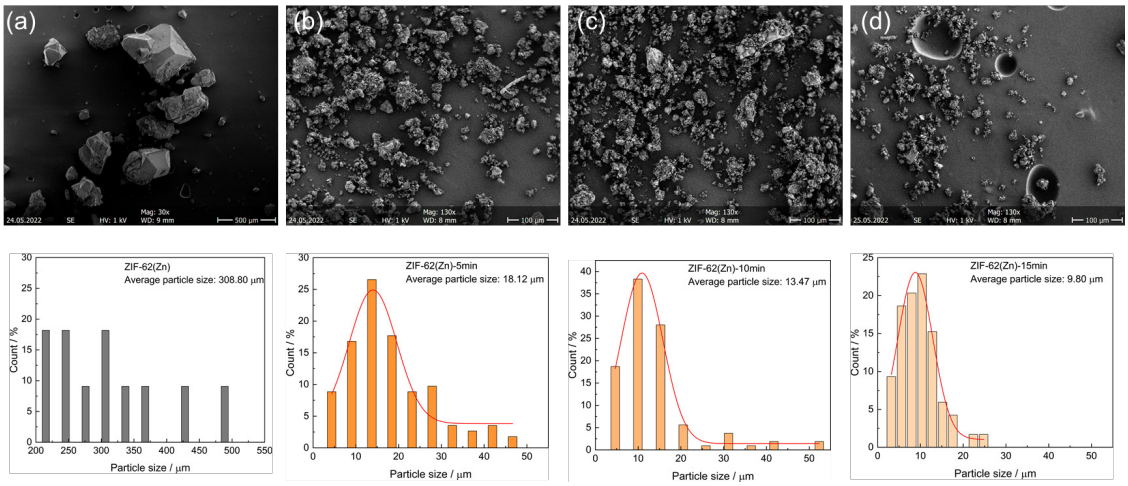

Figure A4.106. SEM images of ZIF-62(Zn) and the corresponding samples derived after PSBM.

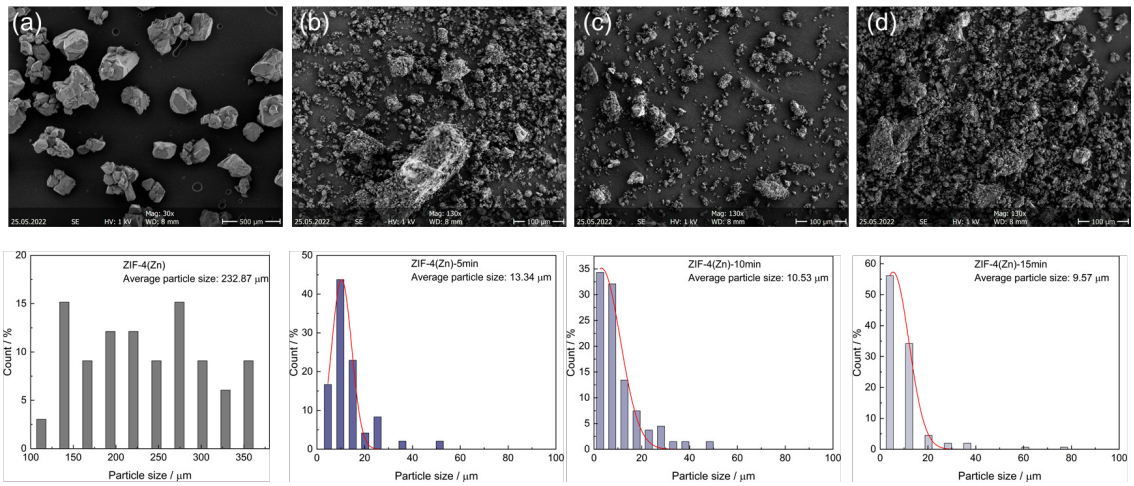

Figure A4.107. SEM images of ZIF-4(Zn) and the corresponding samples derived after PSBM.

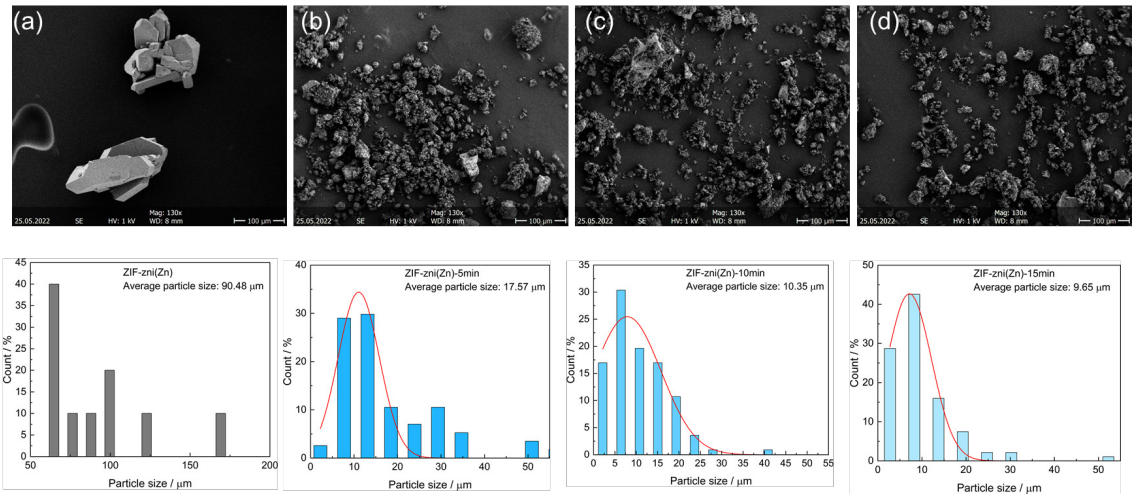

Figure A4.108. SEM images of ZIF-zni(Zn) and the corresponding samples derived after PSBM.

Table A4.8. Average particle sizes of selected ZIF samples and the corresponding materials derived by PSBM.

Compound	number of particles analyzed	Average particle size (µm)	standard deviation (µm)
ZIF-62(Zn)	11	308.8	93.4
ZIF-62(Zn)-5min	113	18.1	10.1
ZIF-62(Zn)-10min	117	13.5	9.2
ZIF-62(Zn)-15min	118	9.8	4.5
ZIF-4(Zn)	33	232.9	72.5
ZIF-4(Zn)-5min	48	13.3	8.7
ZIF-4(Zn)-10min	134	10.5	9.3
ZIF-4(Zn)-15min	155	9.6	9.5
ZIF-zni(Zn)	10	90.5	35.7
ZIF-zni(Zn)-5min	57	17.6	11.6
ZIF-zni(Zn)-10min	112	10.4	6.8
ZIF-zni(Zn)-15min	94	9.7	7.6

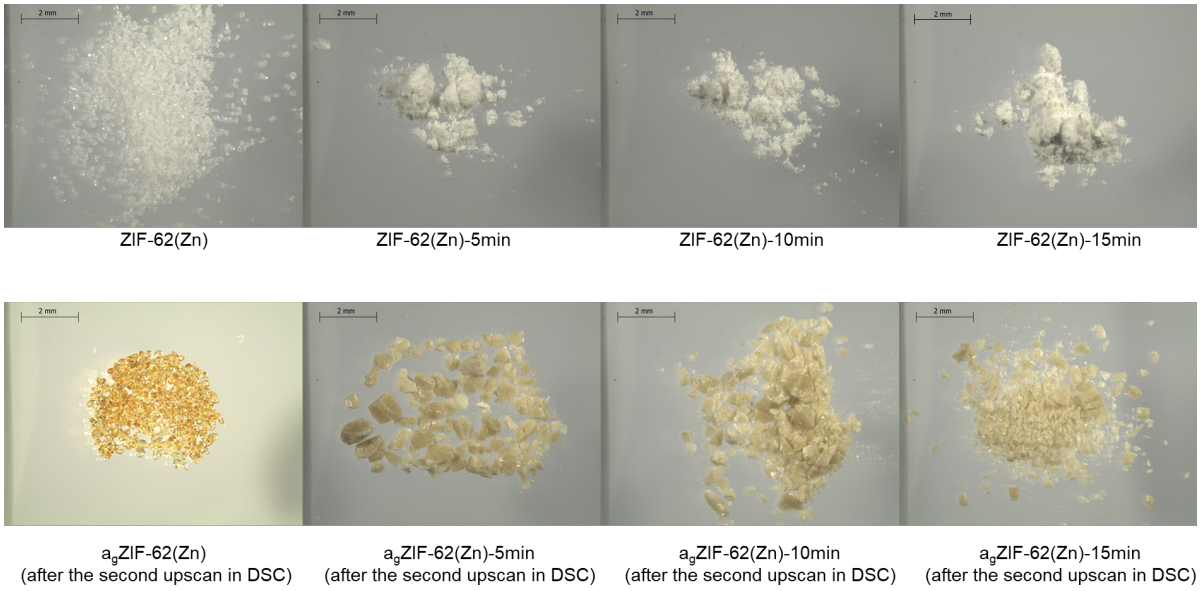

Figure A4.109. Optical microscopy images of ZIF-62(Zn), ZIF-62(Zn)-5min, ZIF-62(Zn)-10min, ZIF-62(Zn)-15min (top), and their corresponding samples after the second upscan in DSC (bottom). The four samples in the bottom were heated to 500 °C in the two upscans. Heating and cooling rates for both upscans were ±10 °C min^{-1}.

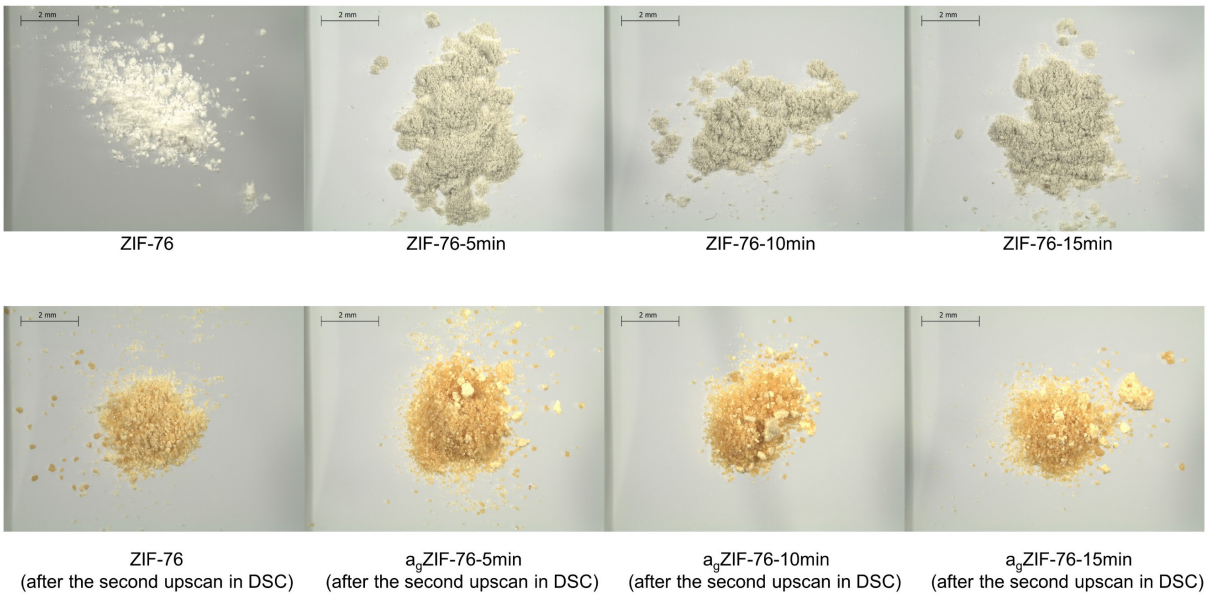

Figure A4.110. Optical microscopy images of ZIF-76, ZIF-76-5min, ZIF-76-10min, ZIF-76-15min (top). The corresponding samples after the second upscan in DSC (bottom). The ZIF-76 was heated to 450 °C and the PSBM samples were heated to 440 °C in two upscans. Heating and cooling rates for both upscans were ±10 °C min^{-1}.

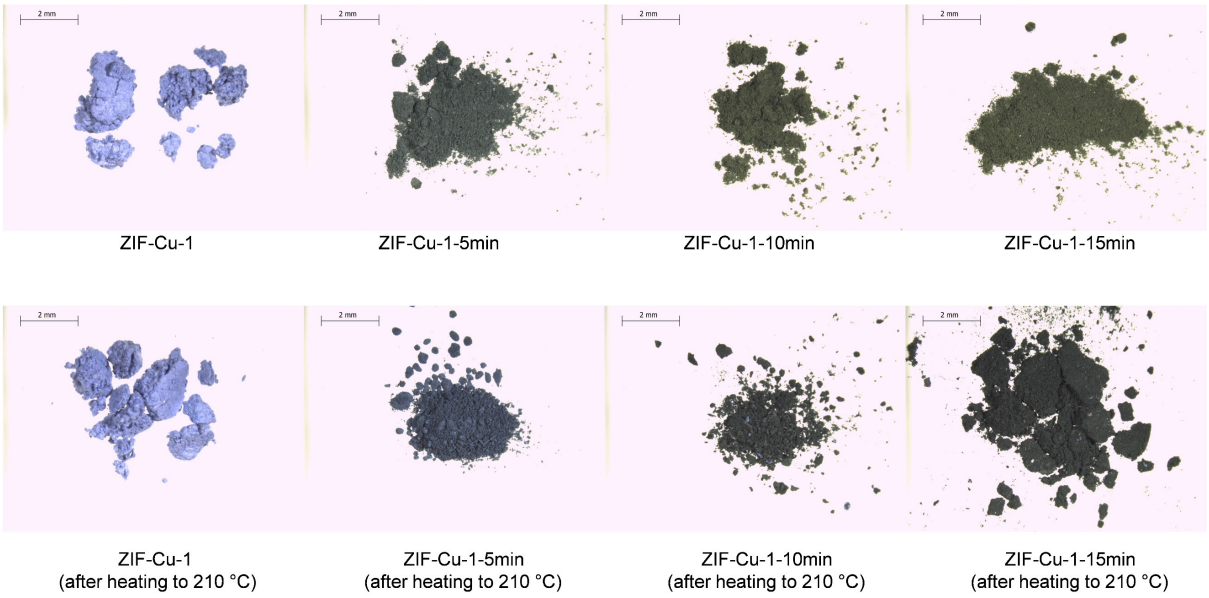

Figure A4.111. Optical microscopy images of ZIF-Cu-1, ZIF-Cu-1-5min, ZIF-Cu-1-10min, ZIF-Cu-1-15min, and their corresponding samples after heating to 210 °C. The color of ZIF-Cu-1 changed from blue to dark green after 5 min of PSBM. This is an indication that the coordination environment of the Cu^{2+} centers is distorted by PSBM (top). In addition, the color of the PSBM samples regains some blue features after heating the ball-milled samples to 210 °C, which is in agreement with the partial recrystallization of the materials (bottom).

Appendix to Section 5

A.5.1 – X-ray powder diffraction data and variable temperature XPDF

A.5.1.1 – X-ray powder diffraction data

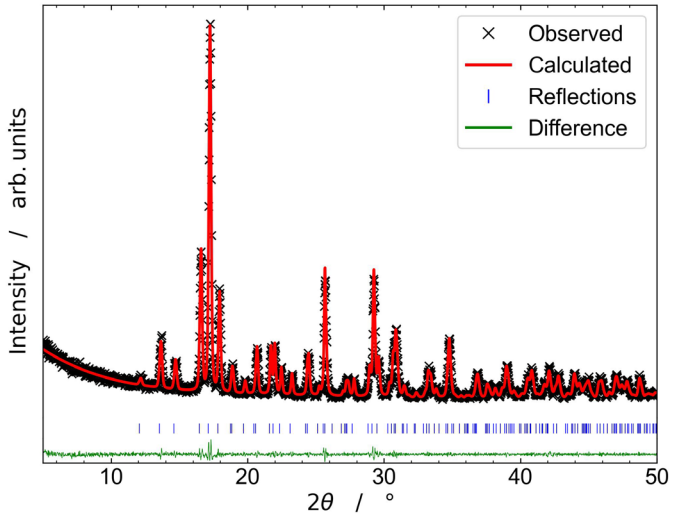

Figure A5.1. Profile fit (Pawley method) performed on the XRPD pattern of $Cd(im)_2$. The blue tick marks indicate the positions of allowed Bragg peaks. The corresponding crystallographic data can be found in **Table 5.2**. The same data can also be found in **Figure 5.2** in the main text. The data is also shown here for easier comparison with other samples. The diffraction pattern was recorded with an overall scan time of 16 h.

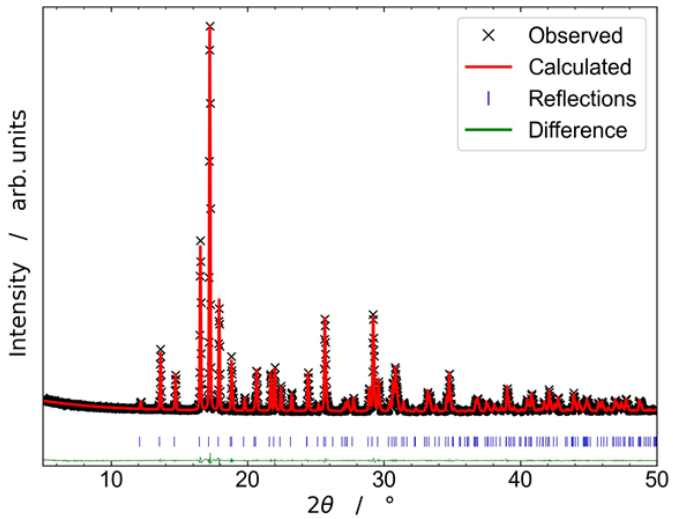

Figure A5.2. Profile fit (Pawley method) performed on the XRPD pattern of $Cd(im)_2$-*sol*. The blue tick marks indicate the positions of allowed Bragg peaks. The corresponding crystallographic data can be found in **Table 5.2**. The diffraction pattern was recorded with an overall scan time of 16 h. The same data can also be found in **Figure 5.2** in the main text.

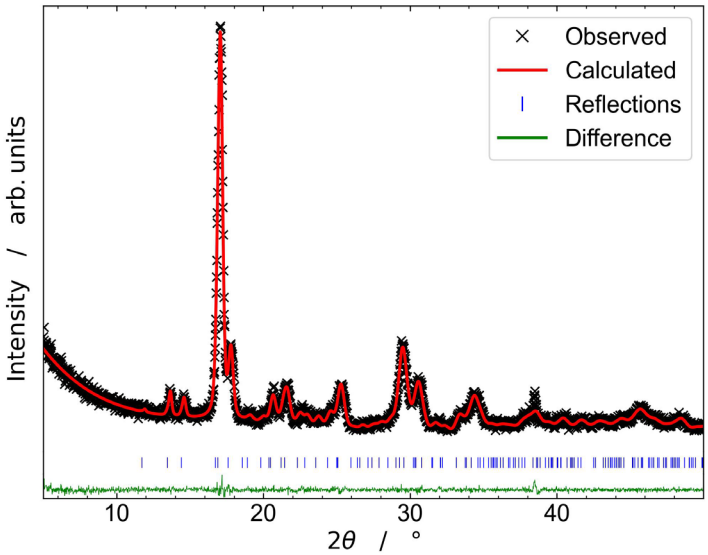

Figure A5.3. Profile fit (Pawley method) performed on the XRPD pattern of prcCd(im)$_2$. The blue tick marks indicate the positions of allowed Bragg peaks. The corresponding crystallographic data can be found in **Table 5.2**. Cd(im)$_2$ crystallizes in the expanded high-temperature configuration (CCDC: BAYQAU06)[153] from the supercooled liquid phase in the range from 200 °C to 300 °C. The expanded configuration with a unit cell volume of about 1610 Å^3 is fixed in a glass matrix and remains even after returning to room temperature. The diffraction pattern was recorded with an overall scan time of 16 h. The unfitted reflection at 38.4° 2θ is assigned to a small amount of metallic Cd.

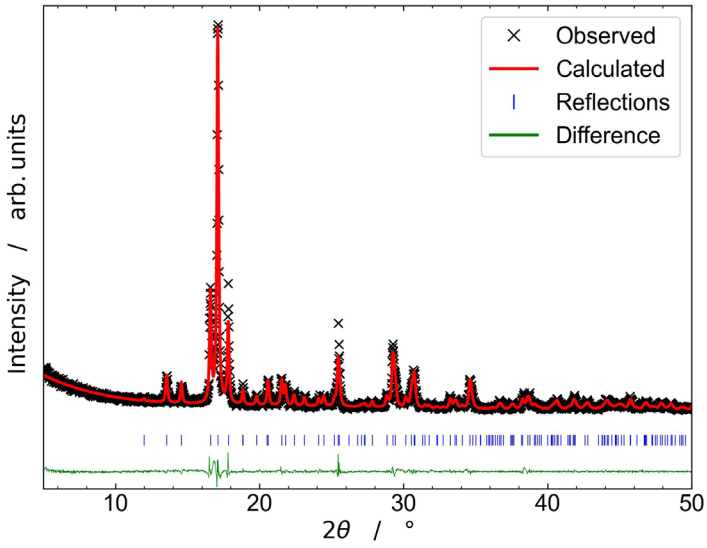

Figure A5.4. Profile fit (Pawley method) performed on the XRPD pattern of fully recrystallized frcCd(im)$_2$. The blue tick marks indicate the positions of allowed Bragg peaks. The corresponding crystallographic data can be found in **Table 5.2**. After complete recrystallization, the amorphous glass matrix that stabilizes Cd(im)$_2$ n its expanded high-temperature configuration is no longer present. As a result, frcCd(im)$_2$ adopts the denser room-temperature configuration of Cd(im)$_2$, with a unit cell volume of approximately 1563 Å^3. The diffraction pattern was recorded with an overall scan time of 16 h.

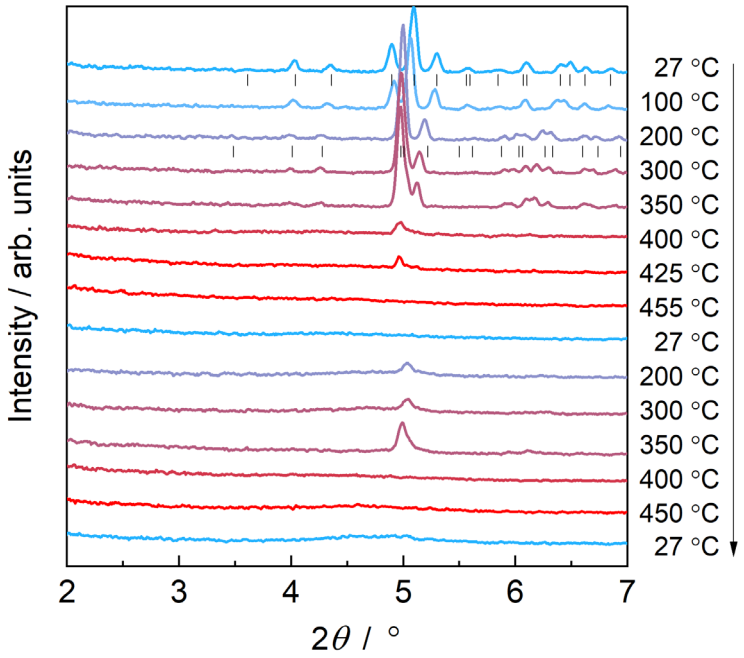

Figure A5.5. VT-XRPD patterns ($\lambda = 0.61992$ Å) of $Cd(im)_2$. The patterns are not normalized but vertically offset for clarity. Reflection positions for $Cd(im)_2$ at 300 K and 500 K (CCDC code BAYQAU11 and BAYQAU06)[153] are shown as black tick marks (300 K, BAYQAU11, upper ticks; 500 K, BAYQAU06, lower ticks).

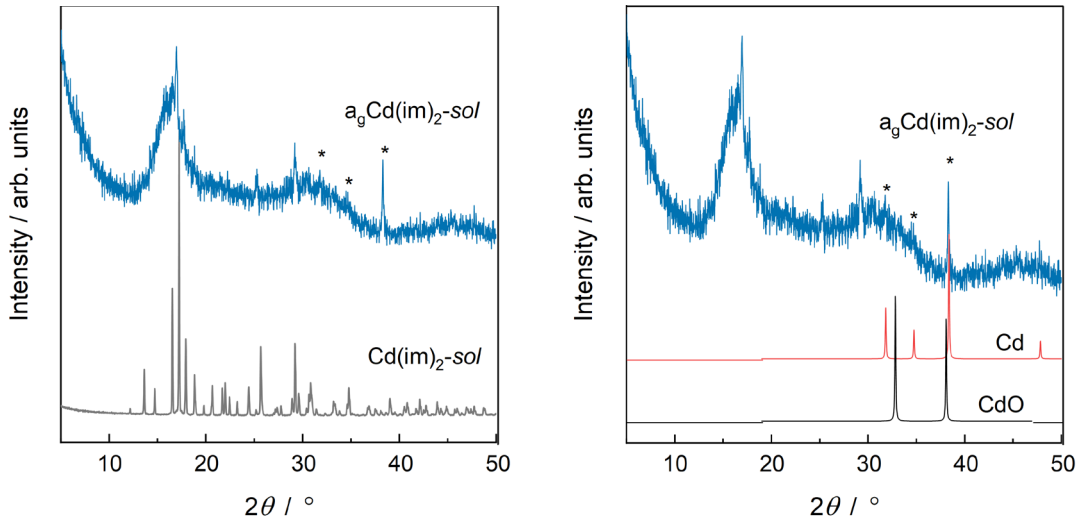

Figure A5.6. Left: XRPD patterns of crystalline pristine $Cd(im)_2$-*sol* and glassy $a_gCd(im)_2$-*sol*, which has been heated to 465 °C**.** The diffraction pattern of $a_gCd(im)_2$-*sol* was recorded with an overall scan time of 16 h, and the crystalline $Cd(im)_2$-*solv* with 37 min. Right: Determination of peaks marked with an asterisk are from Cd.

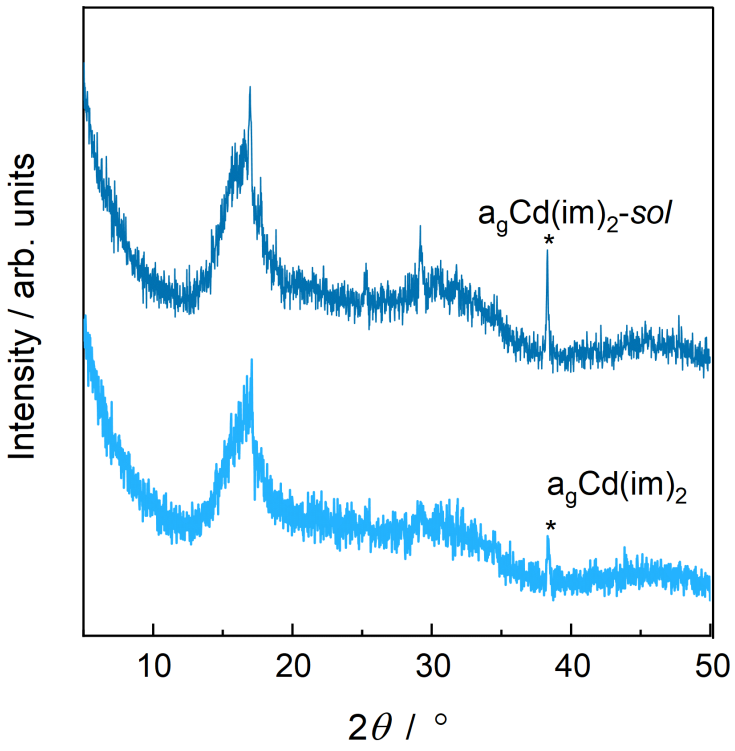

Figure A5.7. XRPD patterns a_gCd(im)$_2$-*sol* which has been heated to 465 °C and a_gCd(im)$_2$ which has been heated to 457 °C. The diffraction patterns were recorded with an overall scan time of 16 h. The reflection marked with an asterisk corresponds to the decomposition product Cd metal. The other peaks in the pattern of a_gCd(im)$_2$-*sol* are from recrystallized Cd(im)$_2$. In comparison to Cd(im)$_2$-*solv*, mechanically synthesized Cd(im)$_2$ avoids most of the decomposition during melting.

A.5.1.2 – X-ray total scattering data

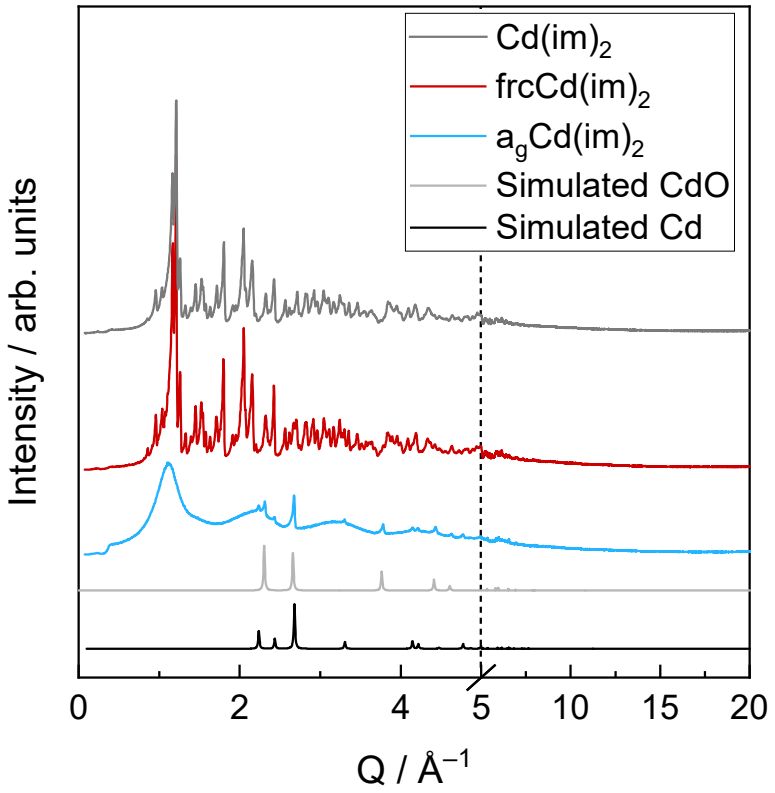

Figure A5.8. X-ray total scattering data in the form of $I(Q)$ of $Cd(im)_2$, $a_gCd(im)_2$, and $frcCd(im)_2$.

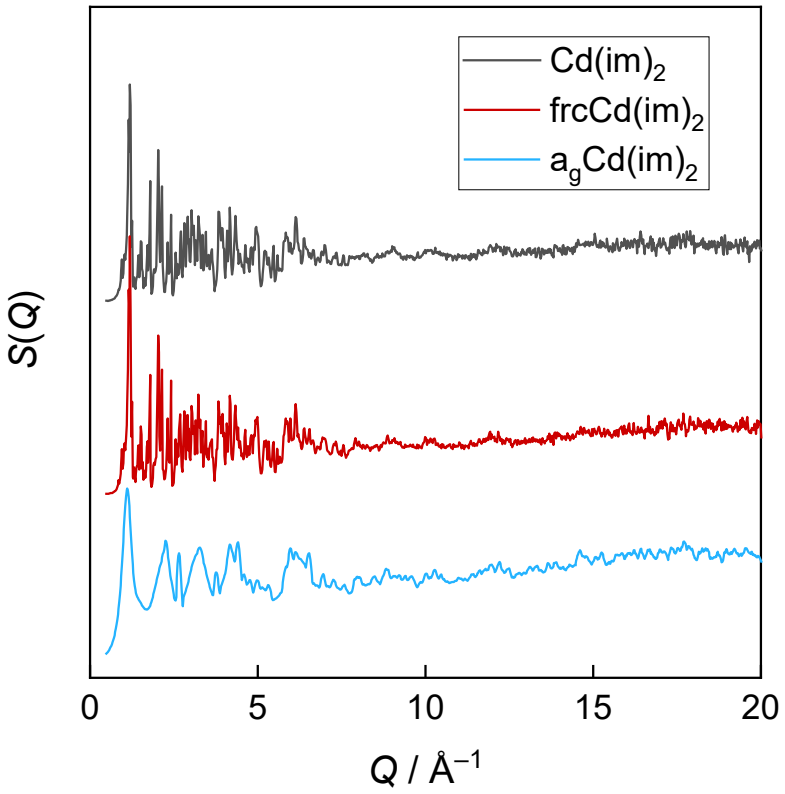

Figure A5.9. X-ray total scattering data in the form of $S(Q)$ of $Cd(im)_2$, $a_gCd(im)_2$, and $frcCd(im)_2$.

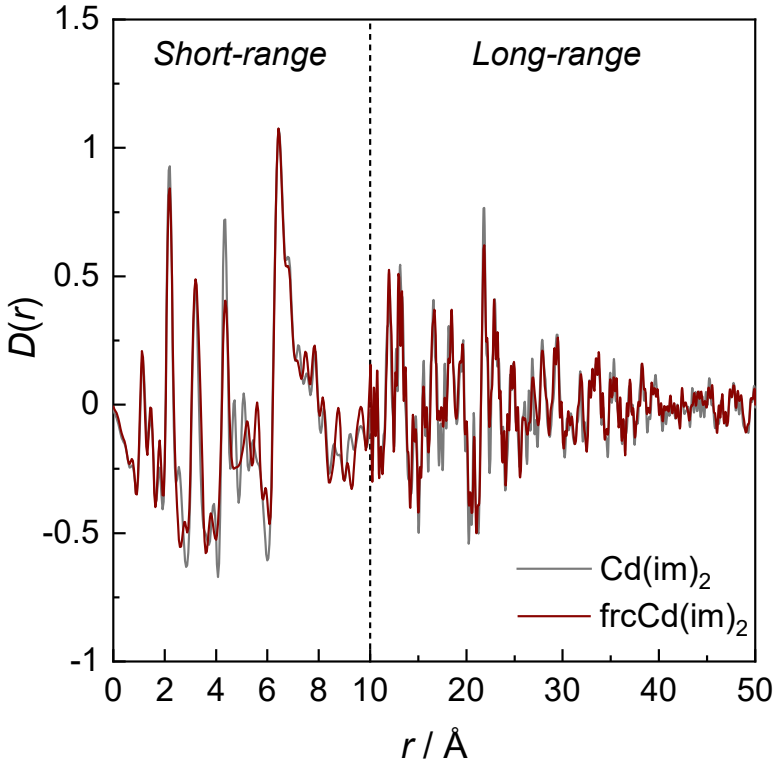

Figure A5.10. Comparison of PDFs data of $Cd(im)_2$ and $frcCd(im)_2$ derived from X-ray total scattering experiment.

A.5.2 – H NMR spectroscopy data

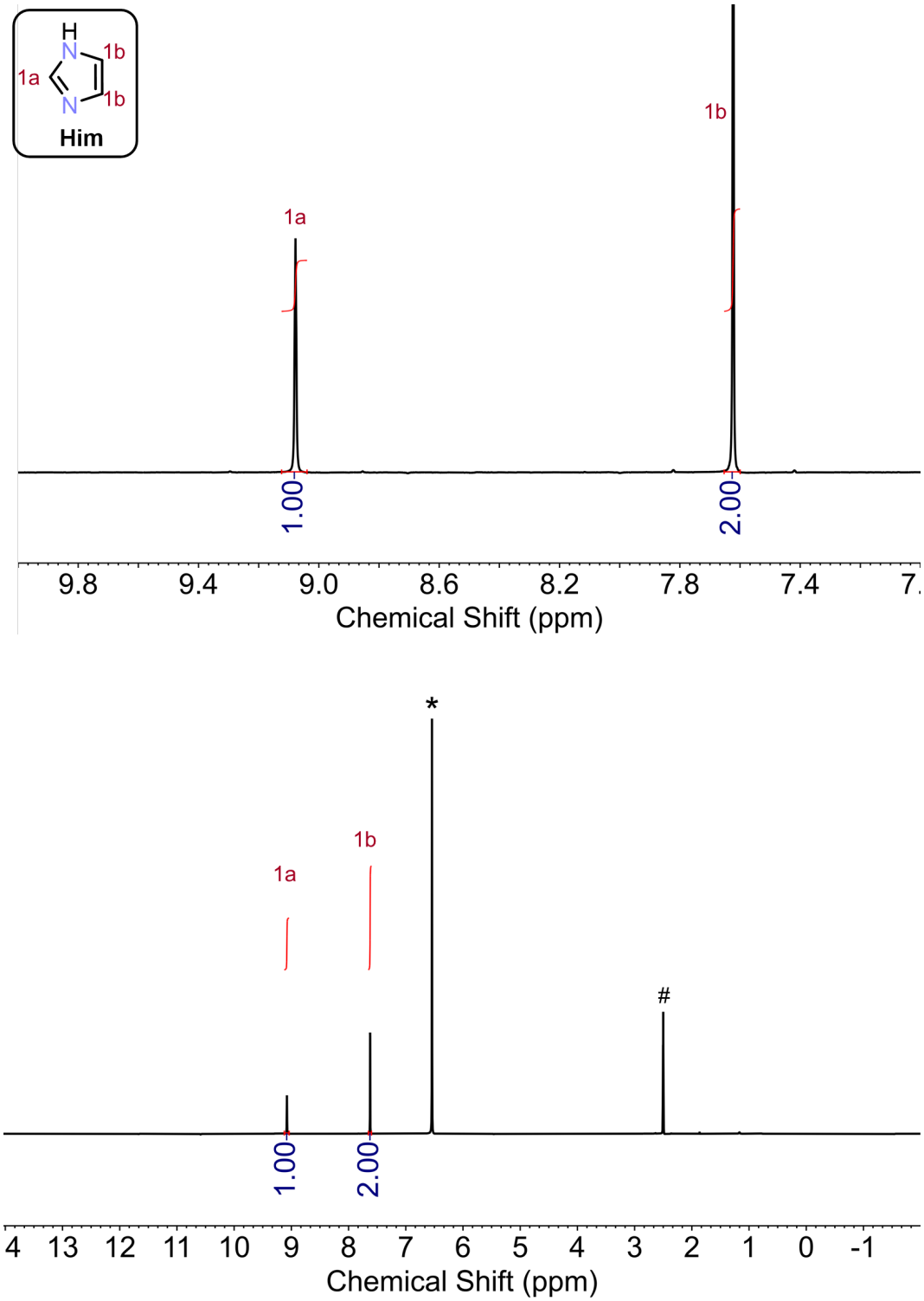

Figure A5.11. ^{1}H NMR spectrum of a digested sample of $Cd(im)_2$. Top: Zoom in the aromatic region (7.0 to 10.0 ppm). Bottom: Complete spectrum. Residual protons in DMSO at 2.5 ppm is marked with # and residual protons D_2O is marked with *.

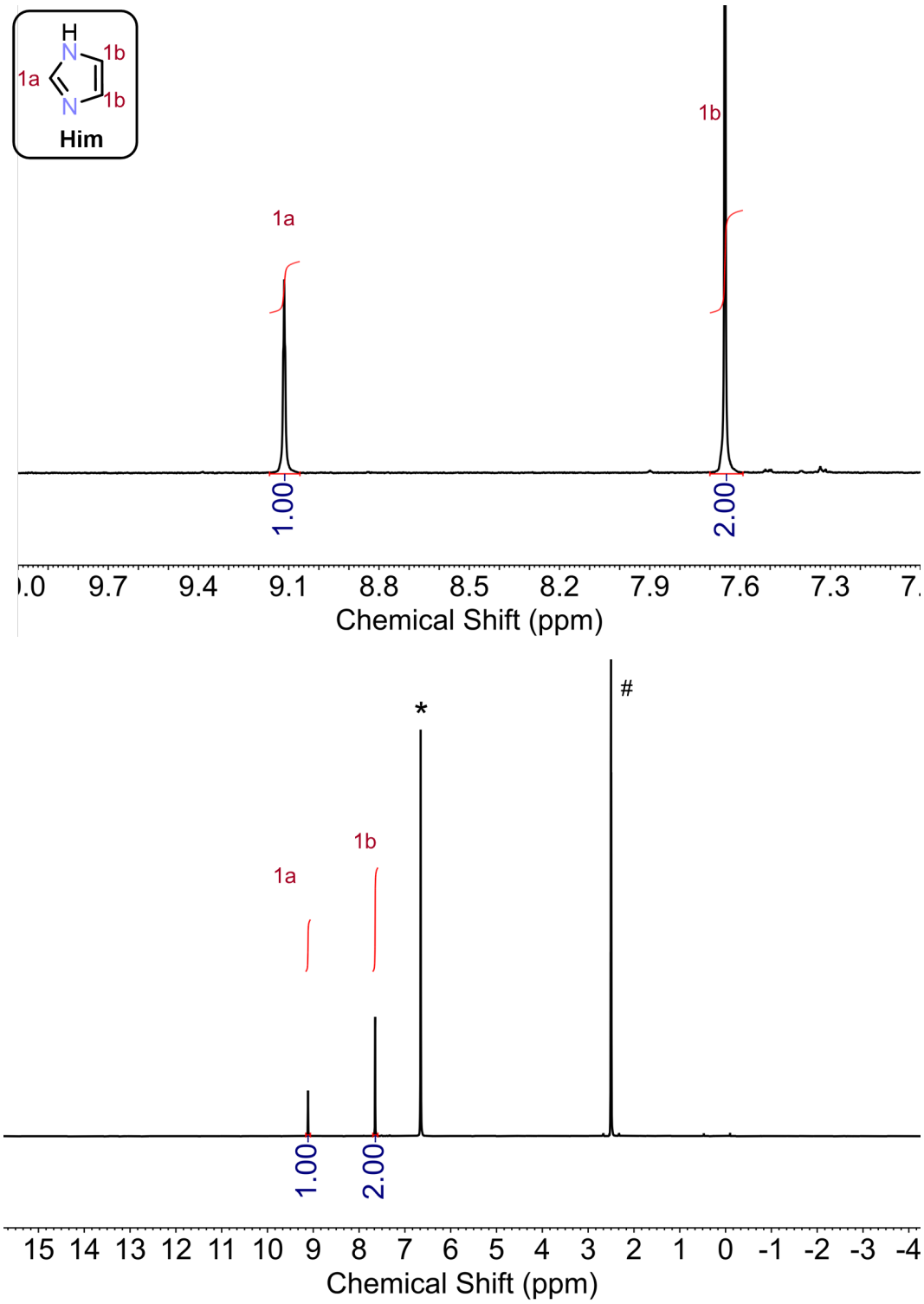

Figure A5.12. ^{1}H NMR spectrum of a digested sample of Cd(im)$_2$-*sol*. Top: Zoom in the aromatic region (7.0 to 10.0 ppm). Bottom: Complete spectrum. Residual protons in DMSO at 2.5 ppm is marked with # and residual protons D_2O is marked with *.

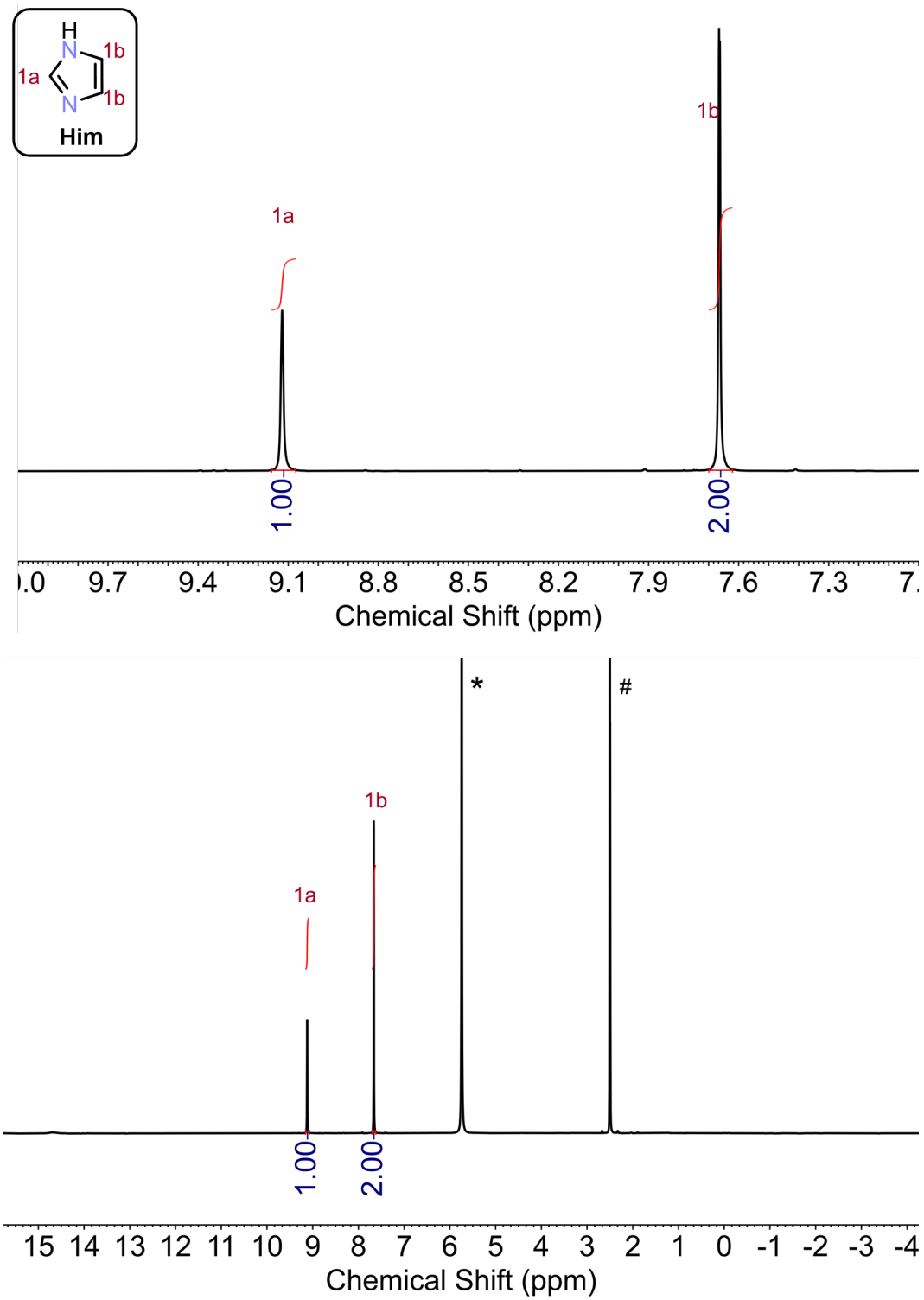

Figure A5.13. ^{1}H NMR spectrum of a digested sample of a_gCd(im)$_2$. Top: Zoom in the aromatic region (7.0 to 10.0 ppm). Bottom: Complete spectrum. Residual protons in DMSO at 2.5 ppm is marked with # and residual protons D_2O is marked with *.

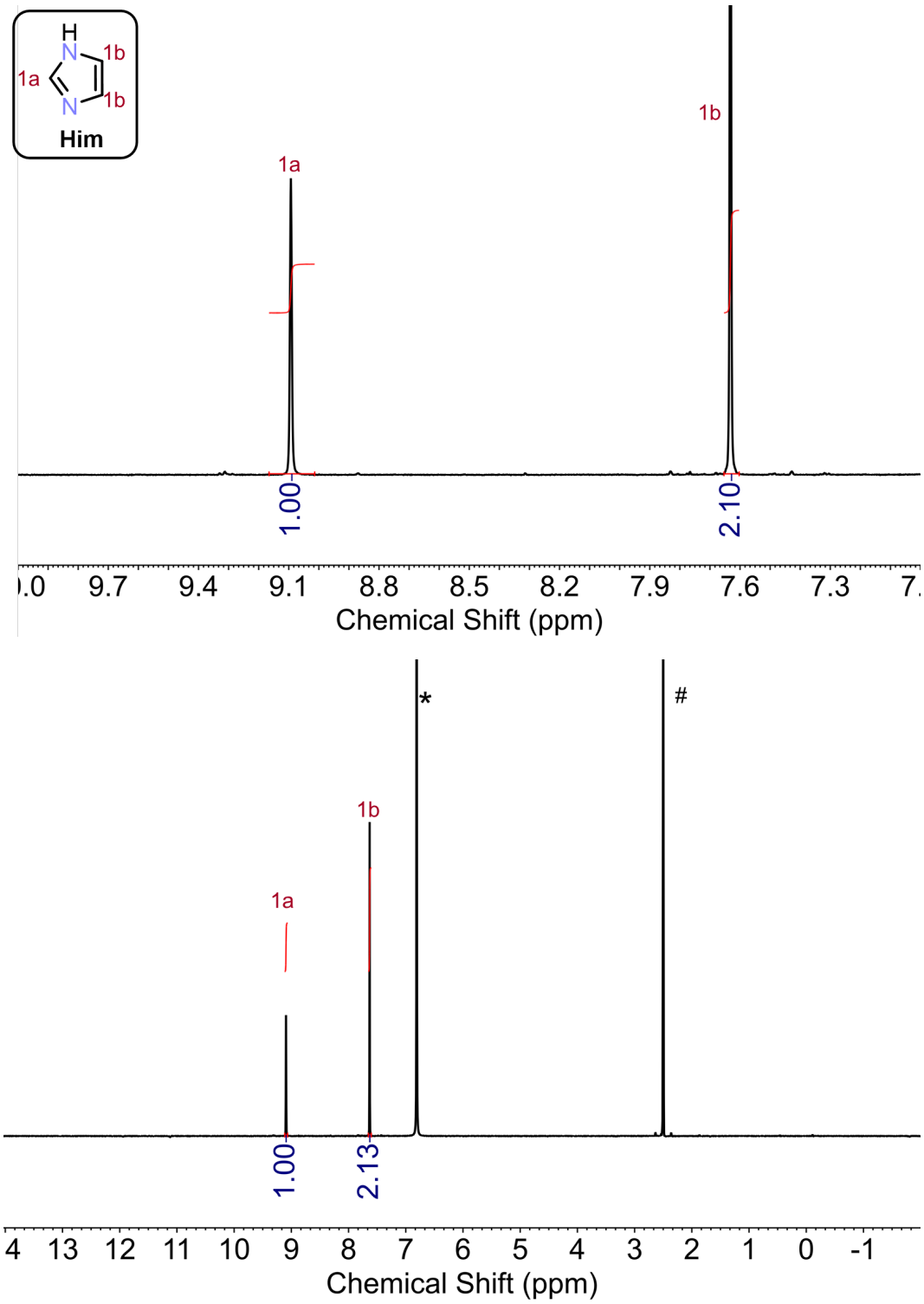

Figure A5.14. ^{1}H NMR spectrum of a digested sample of a_gCd(im)$_2$-*sol*. Top: Zoom in the aromatic region (7.0 to 10.0 ppm). Bottom: Complete spectrum. Residual protons in DMSO at 2.5 ppm is marked with # and residual protons D_2O is marked with *.

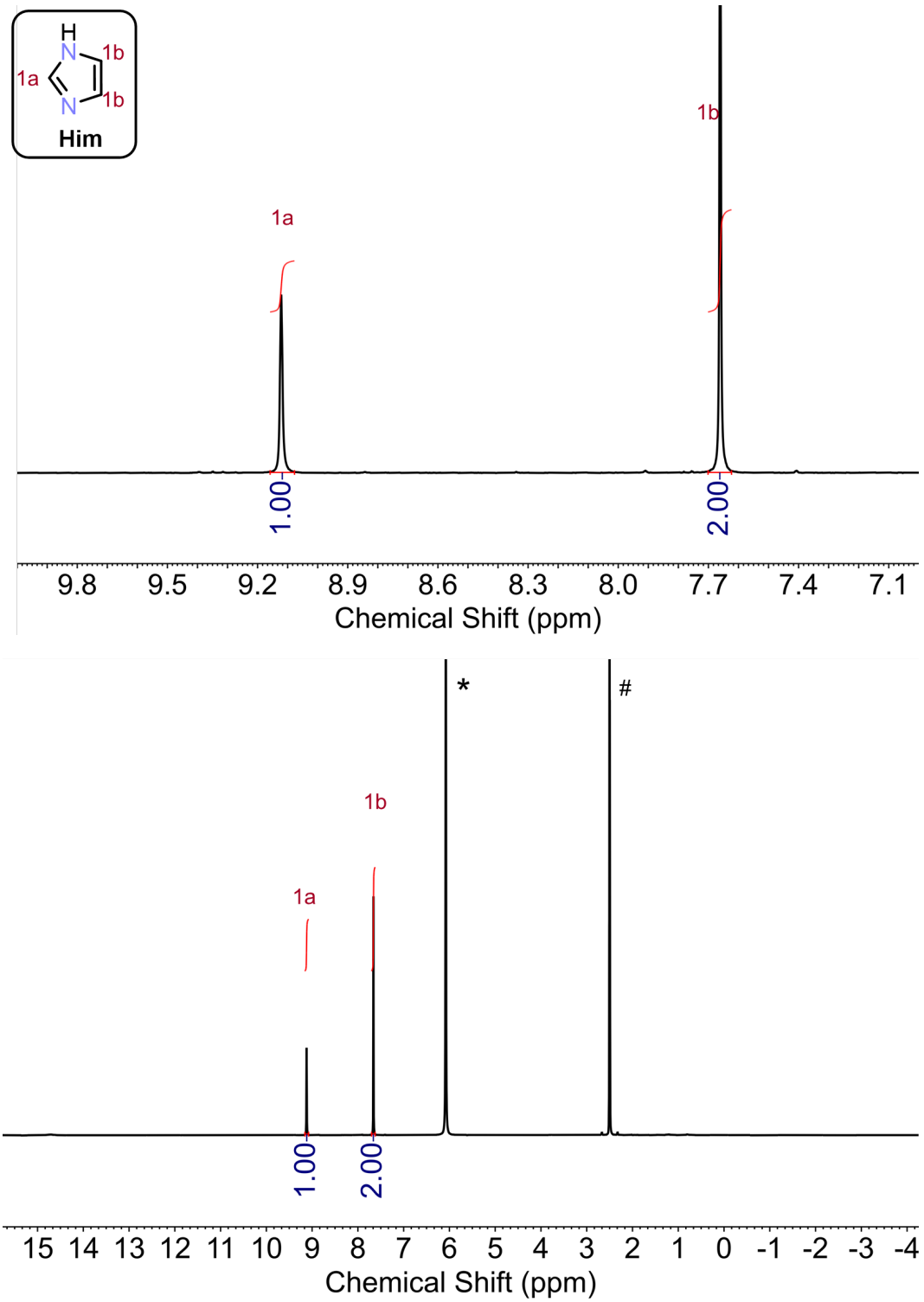

Figure A5.15. ^{1}H NMR spectrum of a digested sample of prcCd(im)$_2$. Top: Zoom in the aromatic region (7.0 to 11.0 ppm). Bottom: Complete spectrum. Residual protons in DMSO at 2.5 ppm is marked with # and residual protons D_2O is marked with *.

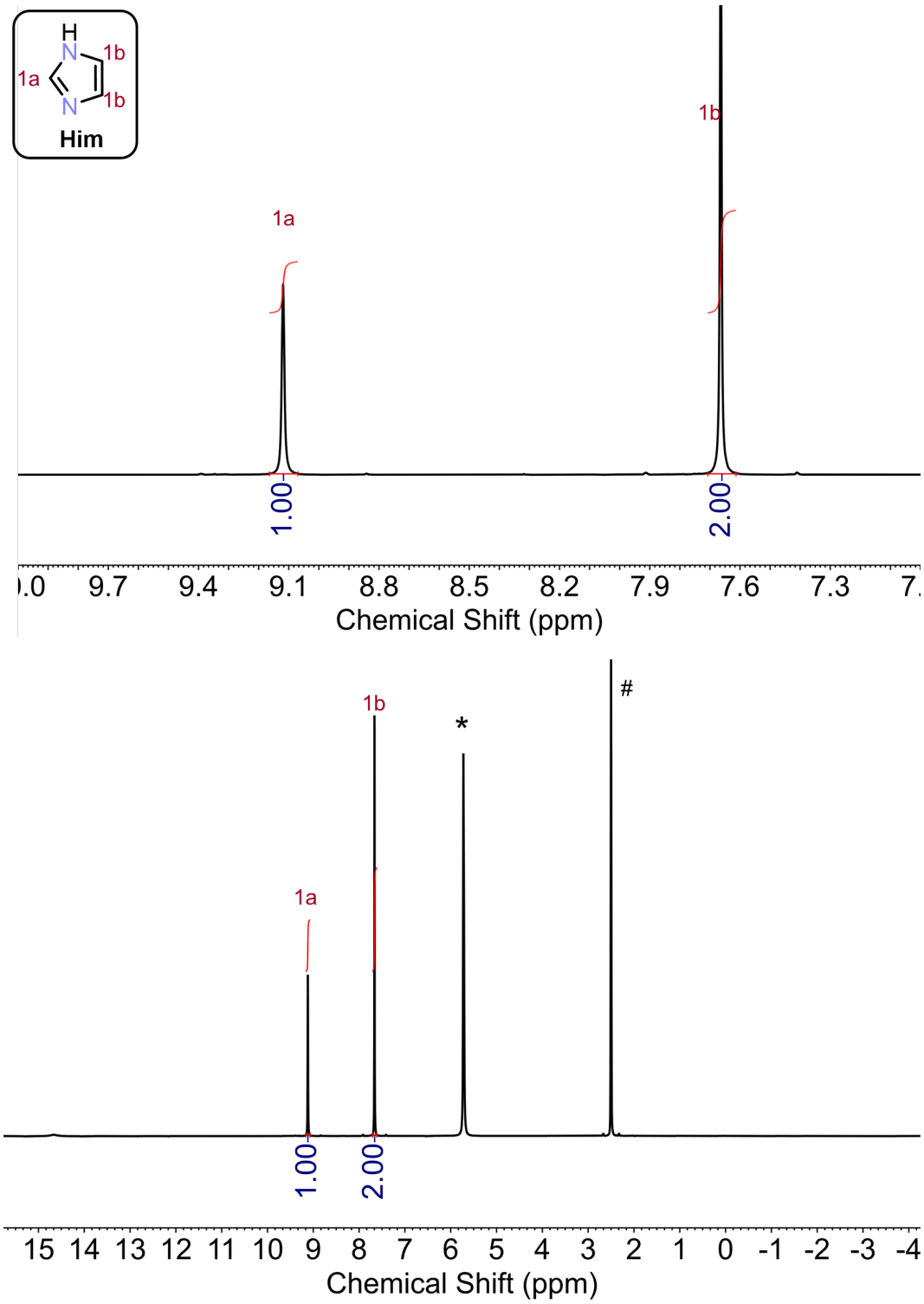

Figure A5.16. ^{1}H NMR spectrum of a digested sample of frcCd(im)$_2$. Top: Zoom in the aromatic region (7.0 to 11.0 ppm). Bottom: Complete spectrum. Residual protons in DMSO at 2.5 ppm is marked with # and residual protons D_2O is marked with *.

A.5.3 – Fourier-transform infrared (FTIR) spectroscopy data

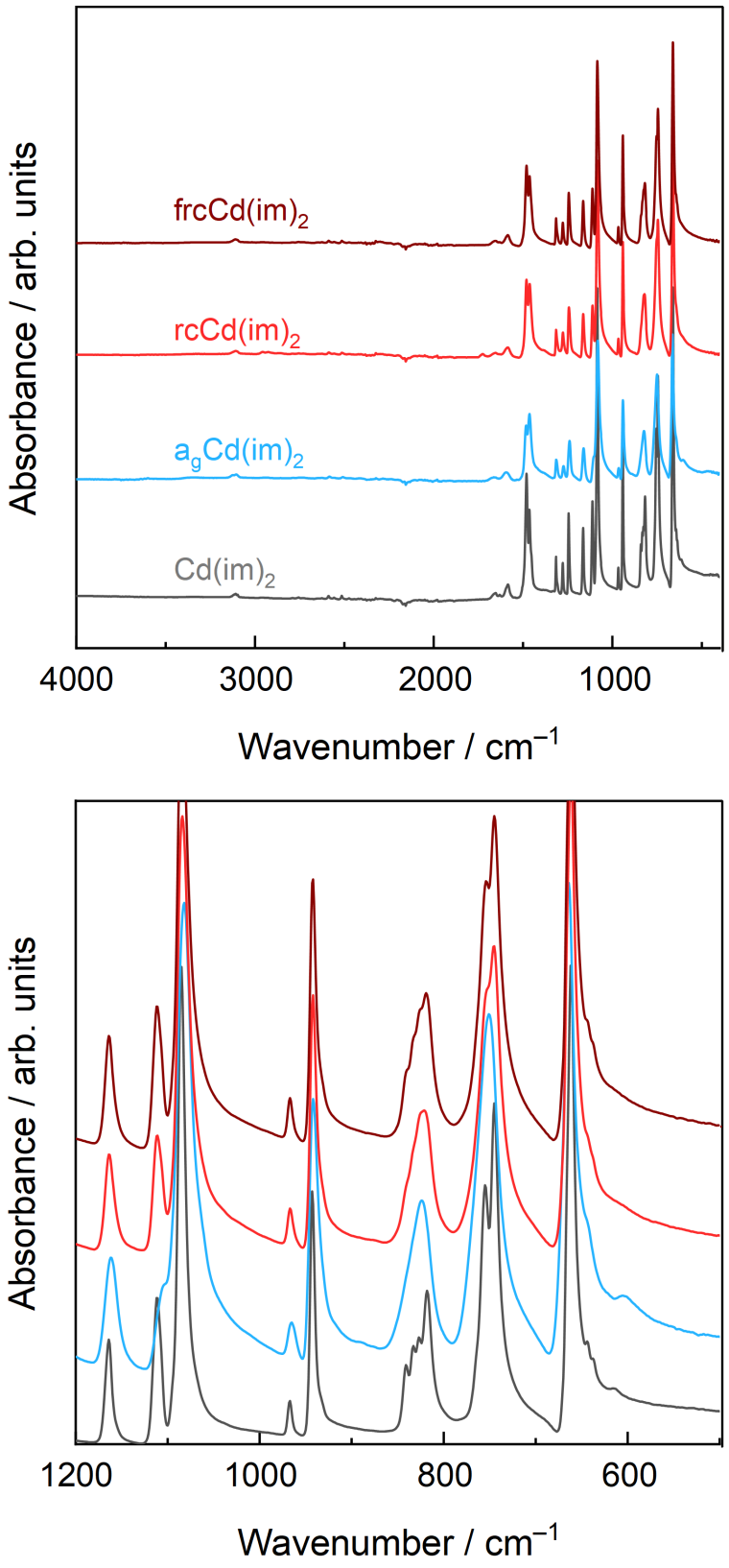

Figure A5.17. Top: FTIR spectra of of $Cd(im)_2$, $a_gCd(im)_2$, $prcCd(im)_2$, and $frcCd(im)_2$. Bottom: Zoom in the region of 500 to 1200 cm^{-1}.

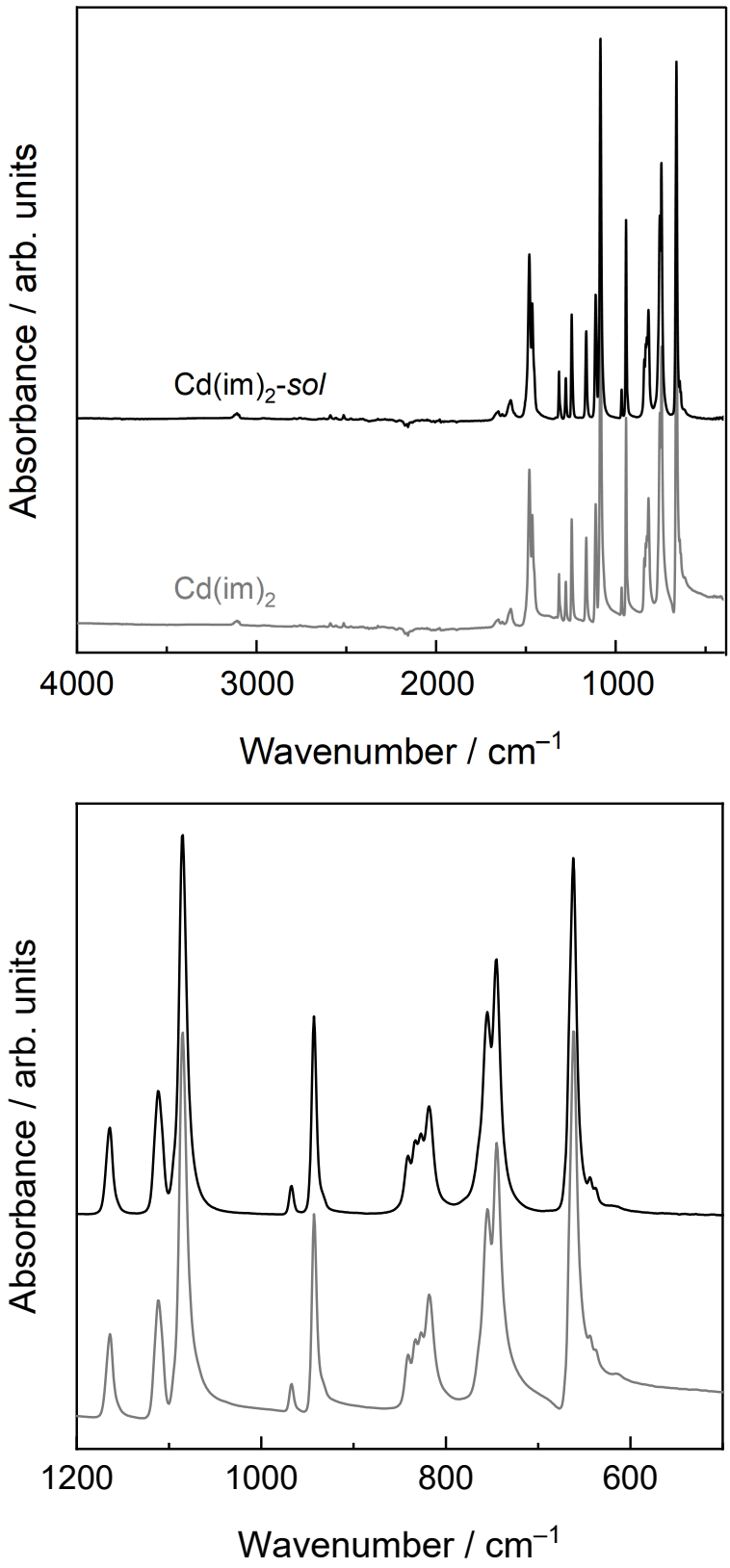

Figure A5.18. Top: FTIR spectra of $Cd(im)_2$ and $Cd(im)_2$-*sol*. Bottom: Zoom in the region of 500 to 1200 cm^{-1}.

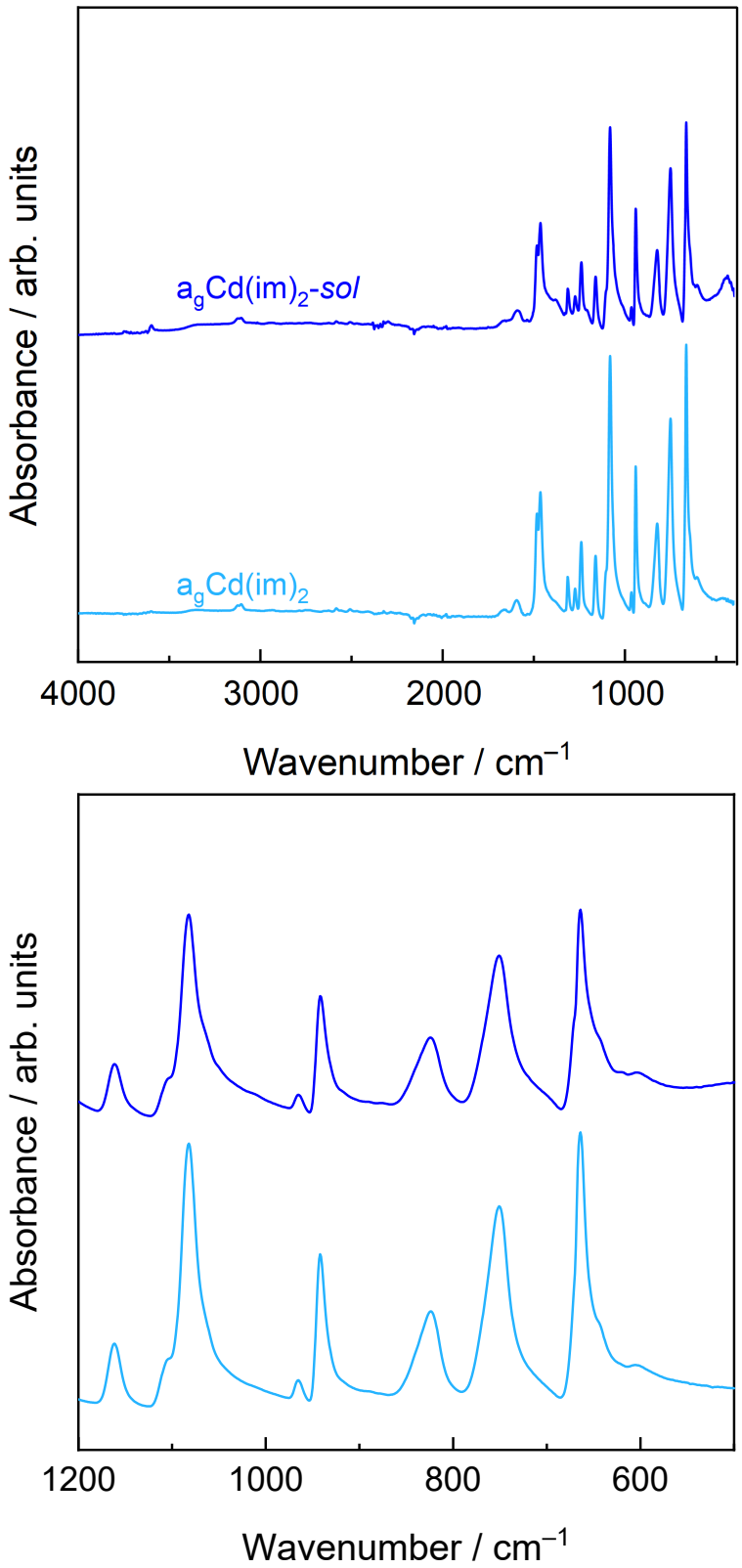

Figure A5.19. Top: FTIR spectra of a_gCd(im)$_2$ and a_gCd(im)$_2$-*sol*. Bottom: Zoom in the region of 500 to 1200 cm^{-1}.

A.5.4 – Thermal analysis

A.5.4.1 – TG/DTA and DSC data

T_d was determined as the crossing points of tangents to the horizontal weight-loss line and the weight-loss line at the first decomposing step from TG/DTA data. All other thermal parameters were deducted from the DSC data. T_m is defined as the offset temperature of the endothermal melting peak and has been determined by the intersection of two tangents. T_g is defined as the onset by the intersection of two tangents of the endothermic signal associated with the glass transition. T_{rc} are determined as the peak temperature of the exothermic peaks. ΔH_m is the integral area between the onset and offset of the melting peak in the DSC curve after baseline subtraction. ΔH_{rc} is the integral area between the onset and offset of the recrystallization peak in the DSC curve. For a better understanding of the abbreviations in this section, their definitions are given in **Table A5.1**. A compilation of all temperatures determined with TG/DTA and DSC is given in **Table A5.2**.

Table A5.1. Abbreviations for thermal analysis used in this section.

Abbreviations	Definitions
T_d	decomposition temperature (onset)
T_g	glass transition temperature (onset)
T_{rc}	recrystallization temperature (peak)
T_m	melting temperature (offset)
ΔH_{rc}	enthalpy of recrystallization
ΔH_m	enthalpy of melting

Table A5.2. Summary of T_g, T_{rc}, and T_m, and T_d of studied $Cd(im)_2$ materials.

Compound	T_g (°C)	T_{rc} (°C)	ΔH_{rc} (kJ/mol)	T_m (°C)	ΔH_m (kJ/mol)	T_d (°C)
$Cd(im)_2$	175	223	–9.8	455	16.6	473
$Cd(im)_2$-*sol*	185	261	–6.6	461	16.1	455

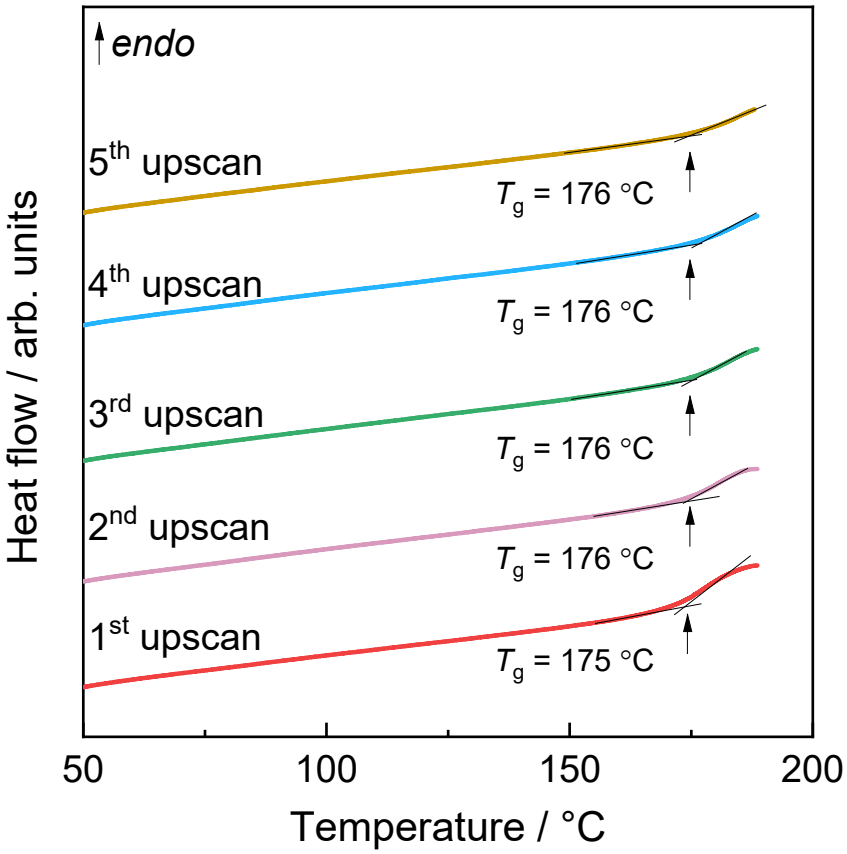

Figure A5.20. Five consecutive DSC cycles for a_gCd(im)$_2$ showcasing the stability of T_g. The heating and cooling rates for both scans were ±10 °C min^{-1}.

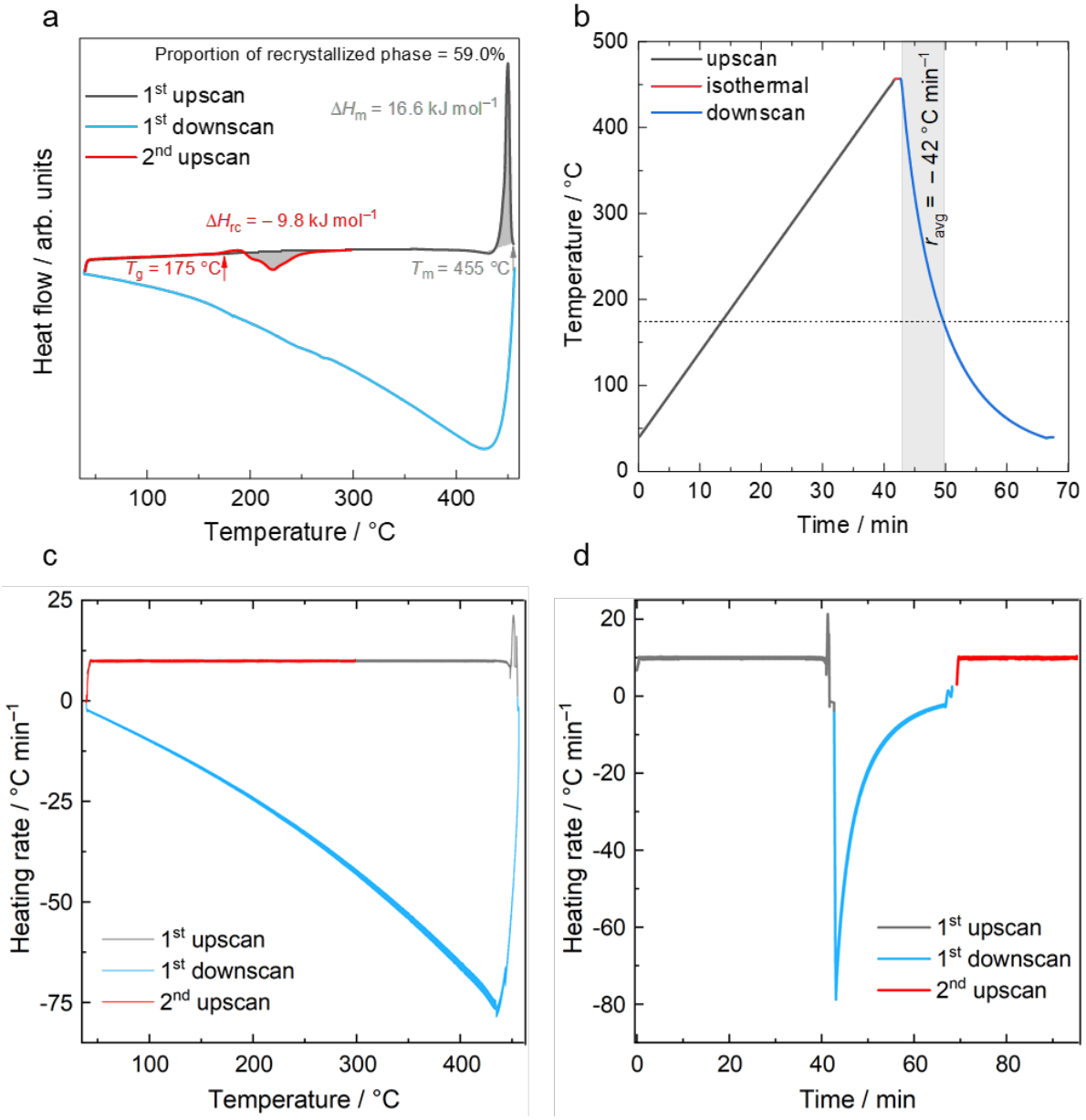

Figure A5.21. (a) DSC data for preparation of rcCd(im)$_2$. The heating rates for both upscans were +10 °C min^{-1}. The cooling rate for downscan was set to –100 °C min^{-1}. (b) Calculated actual average cooling rate from 456 °C (T_m) to 175 °C (T_g) is –42 °C min^{-1}. (c) The relationship between heating rate and temperature. (d) The relationship between heating rate and time.

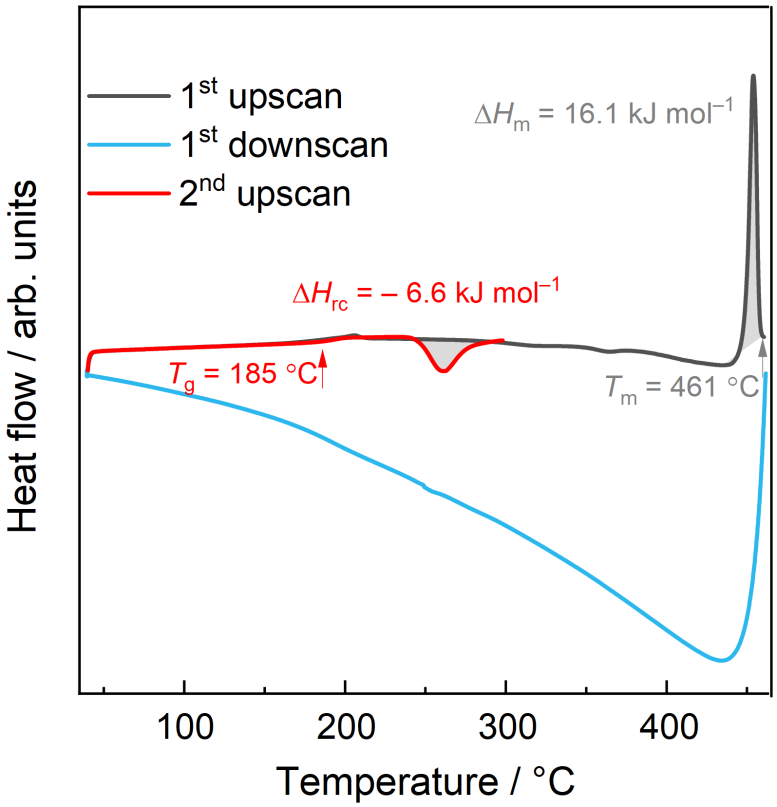

Figure A5.22. DSC data for preparation of a_gCd(im)$_2$-*sol*. The heating rates for both upscans were +10 °C min^{-1}. The cooling rate for downscan was set to –100 °C min^{-1}, the actual average cooling rate from 462 °C to 175°C is –42 °C min^{-1} as determined before.

A.5.4.2 – Heat capacity measurements

The evolution of heat capacity (C_p) of a_gCd(im)$_2$ in the range from 60 to 200 °C was determined by modulated DSC using a DSC 25 calorimeter (TA Instruments). In this measurement, a sinusoidal modulation with a temperature amplitude of ±1 °C and a modulation period of 120 s was overlaid on a linear heating ramp with an average heating rate of 2 °C min^{-1}. Baseline and sapphire reference scans were collected before the sample scan using the same temperature program.

A.5.4.3 – Determination of the calorimetric fragility

The fragility of the a_gCd(im)$_2$ was determined according to procedures published in previous work[93]. The melt-quenched ZIF glass was cycled from 50 °C to 430 °C, with varying heating and cooling rates from ±25 to ±5 °C/min. T_f is the fictive temperature of the glass sample prepared with different cooling rates (q_c). T_f at a heating/cooling rate of ±10 °C/min corresponds to T_g. The calorimetric fragility index m is determined as the slope of the plot of $\log_{10}(1/q_c)$ versus T_g/T_f (i.e. the T_g scaled reciprocal T_f, absolute temperatures in Kelvin).

$$m = \frac{\partial \log_{10}\left(\frac{1}{q_c}\right)}{\partial\left(\frac{T_g}{T_f}\right)}$$

The fragility index m is a measure for the activation energy of viscous flow at T_g. Glasses with a low fragility are called strong (for example vitreous silica with m = 20) while glasses with a fragility higher than about 40 are called fragile.

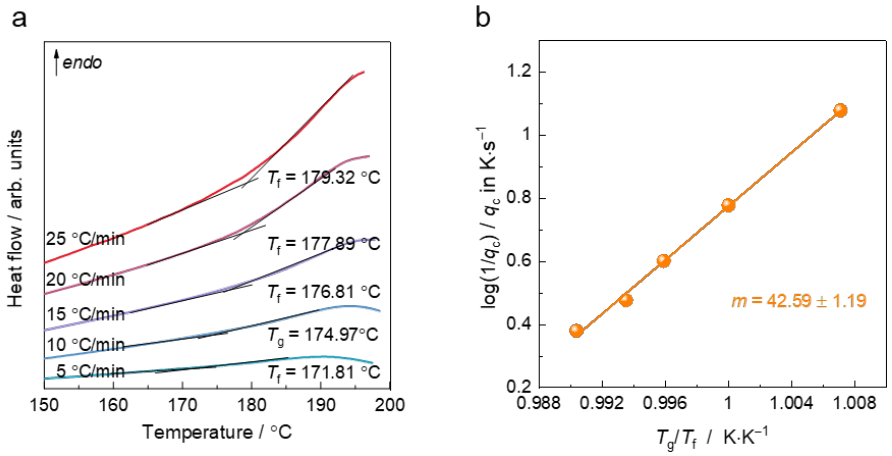

Figure A5.23. (a) DSC upscans of a_gCd(im)$_2$ with heating rates from 25 to 5 °C/min. The cooling rate before each of these scans has been identical to its heating rate. (b) Determination of the calorimetric fragility index m by a linear fit of $\log(1/q_c)$ against T_g/T_f.

A.5.5 – Thermal analysis CO_2 physisorption studies

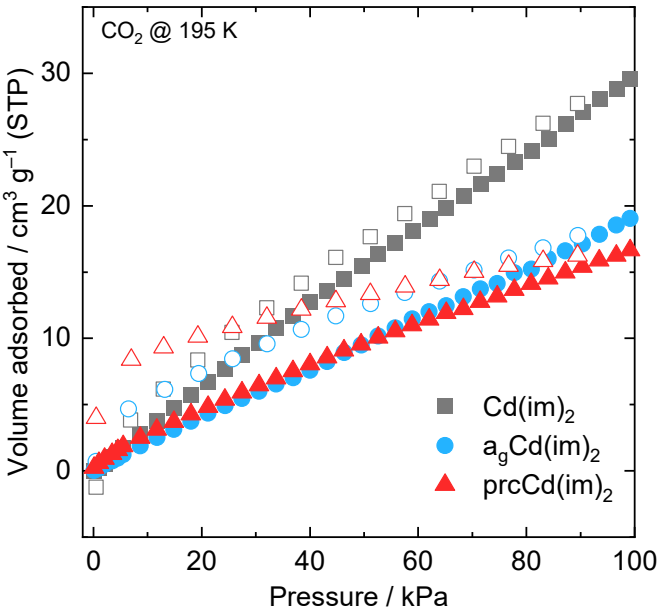

Figure A5.24. CO_2 sorption isotherms collected at 195 K for $Cd(im)_2$, $a_gCd(im)_2$, and $prcCd(im)_2$. Adsorption is predominantly assigned to the adsorption of CO_2 on the external particle surfaces.

A.5.6 – Optical Microscopy

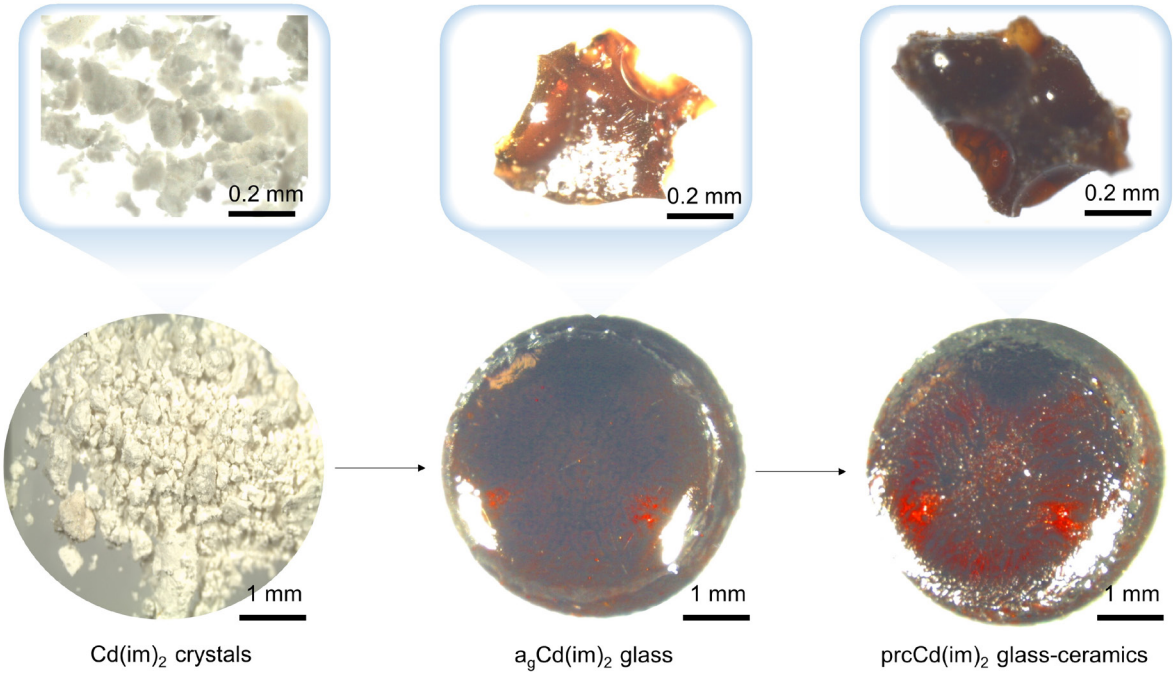

Figure A5.25. Micrographs of $Cd(im)_2$, $a_gCd(im)_2$, and $prcCd(im)_2$.

A.5.7 – Definition of geometry index

In coordination chemistry and crystallography, the geometry index or structural parameter (τ) is a number ranging from 0 to 1 that indicates what the geometry of the coordination center is.[132]

In 2007 Houser *et al.* developed the analogous τ_4 parameter to distinguish whether the geometry of the coordination center is square planar or tetrahedral.[132] The formula is:

$$\tau_4 = \frac{360° - (\varphi_1 + \varphi_2)}{360° - 2\theta}$$

where: φ_1 and φ_2 are the two greatest valence angles of coordination center; $\theta = \cos^{-1}(-1/3) \approx 109.5°$ is a tetrahedral angle. $\tau_4 = 1$ for tetrahedral and $\tau_4 = 0$ for square planar.

A.5.8 –Density functional theory calculations

Density functional theory (DFT) calculations were performed with ORCA 5.0.2.[168] Input structures were generated using Chem3D 19.0 and Avogadro (ORCA enhanced version).[169] Initial geometry optimization was carried out with a MM2 force field, implemented in Avogadro for small molecules and with the B97-3c functional and def2-SVP basis set for cobalt complexes. A second geometry optimization and frequency analysis were performed using the BP86 functional with the def2-TZVP ba- sis set. For all calculations, a frequency analysiswas performed to verify the absence of negative frequencies.

Bibliography

[1] S. Horike, S. S. Nagarkar, T. Ogawa, S. Kitagawa, *Angew. Chem. Int. Ed.* **2020**, *59*, 6652-6664.

[2] T. D. Bennett, S. Horike, *Nat. Rev. Mater* **2018**, *3*, 431-440.

[3] *Chem. Rev.* **2012**, *112*, 673-674.

[4] S. R. Batten, N. R. Champness, X.-M. Chen, J. Garcia-Martinez, S. Kitagawa, L. Öhrström, M. O'Keeffe, M. Paik Suh, J. Reedijk, *Pure Appl. Chem.* **2013**, *85*, 1715-1724.

[5] P. Z. Moghadam, A. Li, X. W. Liu, R. Bueno-Perez, S. D. Wang, S. B. Wiggin, P. A. Wood, D. Fairen-Jimenez, *Chem. Sci.* **2020**, *11*, 8373-8387.

[6] H. Furukawa, K. E. Cordova, M. O'Keeffe, O. M. Yaghi, *Science* **2013**, *341*, 1230444.

[7] O. M. Yaghi, M. O'Keeffe, N. W. Ockwig, H. K. Chae, M. Eddaoudi, J. Kim, *Nature* **2003**, *423*, 705-714.

[8] H. Li, M. Eddaoudi, M. O'Keeffe, O. M. Yaghi, *Nature* **1999**, *402*, 276-279.

[9] N. Stock, S. Biswas, *Chem. Rev.* **2012**, *112*, 933-969.

[10] J. Hwang, R. Yan, M. Oschatz, B. V. K. J. Schmidt, *J. Mater. Chem. A* **2018**, *6*, 23521-23530.

[11] V. F. Yusuf, N. I. Malek, S. K. Kailasa, *ACS Omega* **2022**, *7*, 44507-44531.

[12] X. Zhang, Z. Chen, X. Liu, S. L. Hanna, X. Wang, R. Taheri-Ledari, A. Maleki, P. Li, O. K. Farha, *Chem. Soc. Rev.* **2020**, *49*, 7406-7427.

[13] H. Deng, C. J. Doonan, H. Furukawa, R. B. Ferreira, J. Towne, C. B. Knobler, B. Wang, O. M. Yaghi, *Science* **2010**, *327*, 846-850.

[14] S. M. Cohen, *Chem. Rev.* **2012**, *112*, 970-1000.

[15] O. Karagiaridi, M. B. Lalonde, W. Bury, A. A. Sarjeant, O. K. Farha, J. T. Hupp, *J. Am. Chem. Soc.* **2012**, *134*, 18790-18796.

[16] O. Karagiaridi, W. Bury, J. E. Mondloch, J. T. Hupp, O. K. Farha, *Angew. Chem. Int. Ed.* **2014**, *53*, 4530-4540.

[17] M. Kim, J. F. Cahill, Y. Su, K. A. Prather, S. M. Cohen, *Chem. Sci.* **2012**, *3*, 126-130.

[18] J. H. Cavka, S. Jakobsen, U. Olsbye, N. Guillou, C. Lamberti, S. Bordiga, K. P. Lillerud, *J. Am. Chem. Soc.* **2008**, *130*, 13850-13851.

[19] O. M. Yaghi, Kalmutzki, M.J. and Diercks, C.S. (2019). in *Zeolitic Imidazolate Frameworks*, **2019**, pp. 463-479 https://doi.org/410.1002/9783527821099.ch9783527821020.

[20] R. Banerjee, A. Phan, B. Wang, C. Knobler, H. Furukawa, M. O'Keeffe, M. Yaghi Omar, *Science* **2008**, *319*, 939-943.

[21] M. F. Thorne, M. L. R. Gómez, A. M. Bumstead, S. Li, T. D. Bennett, *Green Chem.* **2020**, *22*, 2505-2512.

[22] J. Song, L. Frentzel-Beyme, R. Pallach, P. Kolodzeiski, A. Koutsianos, W.-L. Xue, R. Schmid, S. Henke, *J. Am. Chem. Soc.* **2023**, *145*, 9273-9284.

[23] P. J. Beldon, L. Fábián, R. S. Stein, A. Thirumurugan, A. K. Cheetham, T. Friščić, *Angew. Chem. Int. Ed.* **2010**, *49*, 9640-9643.

[24] K. Noh, J. Lee, J. Kim, *Isr. J. Chem* **2018**, *58*, 1075-1088.

[25] B. Chen, Z. Yang, Y. Zhu, Y. Xia, *J. Mater. Chem. A* **2014**, *2*, 16811-16831.

[26] H. Wang, X. Pei, M. J. Kalmutzki, J. Yang, O. M. Yaghi, *Acc. Chem. Res.* **2022**, *55*, 707-721.

[27] A. Phan, C. J. Doonan, F. J. Uribe-Romo, C. B. Knobler, M. O'Keeffe, O. M. Yaghi, *Acc. Chem. Res.* **2010**, *43*, 58-67.

[28] Z. Zheng, Z. Rong, H. L. Nguyen, O. M. Yaghi, *Inorg. Chem.* **2023**, *62*, 20861-20873.

[29] N. Ma, S. Horike, *Chem. Rev.* **2022**, *122*, 4163-4203.

[30] J. Fonseca, T. Gong, L. Jiao, H.-L. Jiang, *J. Mater. Chem. A* **2021**, *9*, 10562-10611.

[31] N. Ma, S. Kosasang, E. K. Berdichevsky, T. Nishiguchi, S. Horike, *Chem. Sci.* **2024**, *15*, 7474-7501.

[32] Y.-S. Wei, C. W. Ashling, T. Watcharatpong, Z. Fan, S. Horike, *Adv. Funct. Mater.* **2023**, *n/a*, 2307226.

[33] T. D. Bennett, J. C. Tan, Y. Yue, E. Baxter, C. Ducati, N. J. Terrill, H. H. Yeung, Z. Zhou, W. Chen, S. Henke, A. K. Cheetham, G. N. Greaves, *Nat. Commun.* **2015**, *6*, 8079.

[34] E. D. Zanotto, J. C. Mauro, *J. Non-Cryst. Solids* **2017**, *471*, 490-495.

[35] O. Smirnova, S. Hwang, R. Sajzew, L. Ge, A. Reupert, V. Nozari, S. Savani, C. Chmelik, M. R. Reithofer, L. Wondraczek, J. Kärger, A. Knebel, *Nat. Mater.* **2024**, *23*, 262-270.

[36] R. S. K. Madsen, A. Qiao, J. Sen, I. Hung, K. Chen, Z. Gan, S. Sen, Y. Yue, *Science* **2020**, *367*, 1473-1476.

[37] T. To, S. S. Sørensen, M. Stepniewska, A. Qiao, L. R. Jensen, M. Bauchy, Y. Yue, M. M. Smedskjaer, *Nat. Commun.* **2020**, *11*, 2593.

[38] Y. Wang, H. Jin, Q. Ma, K. Mo, H. Mao, A. Feldhoff, X. Cao, Y. Li, F. Pan, Z. Jiang, *Angew. Chem. Int. Ed.* **2020**, *59*, 4365-4369.

[39] M. Chai, R. Chen, K. Xu, Y. Chen, S. Ma, R. Lin, V. Chen, J. Hou, *J. Mater. Chem. A* **2023**, *11*, 20302-20314.

[40] T. D. Bennett, Y. Yue, P. Li, A. Qiao, H. Tao, N. G. Greaves, T. Richards, G. I. Lampronti, S. A. T. Redfern, F. Blanc, O. K. Farha, J. T. Hupp, A. K. Cheetham, D. A. Keen, *J. Am. Chem. Soc.* **2016**, *138*, 3484-3492.

[41] L. Frentzel-Beyme, P. Kolodzeiski, J.-B. Weiß, A. Schneemann, S. Henke, *Nat. Commun.* **2022**, *13*, 7750.

[42] Z. Yang, Y. Belmabkhout, L. N. McHugh, D. Ao, Y. Sun, S. Li, Z. Qiao, T. D. Bennett, M. D. Guiver, C. Zhong, *Nat. Mater.* **2023**, *22*, 888-894.

[43] L. Frentzel-Beyme, M. Kloss, P. Kolodzeiski, R. Pallach, S. Henke, *J. Am. Chem. Soc.* **2019**, *141*, 12362-12371.

[44] H. Tao, T. D. Bennett, Y. Yue, *Adv. Mater.* **2017**, *29*, 1601705.

[45] Z. Yin, Y.-B. Zhang, H.-B. Yu, M.-H. Zeng, *Sci. Bull.* **2020**, *65*, 1432-1435.

[46] M.-Z. Chen, J. Li, S. Liao, Y.-H. Guo, T. Liu, R.-F. Ma, T.-Y. Xie, W.-D. Liu, S.-X. Peng, X. Kuang, Z. Yin, Y. Zhao, M.-H. Zeng, *Angew. Chem. Int. Ed.* **2023**, *62*, e202305942.

[47] R. Gaillac, P. Pullumbi, K. A. Beyer, K. W. Chapman, D. A. Keen, T. D. Bennett, F. X. Coudert, *Nat. Mater.* **2017**, *16*, 1149-1154.

[48] L. B. McCusker, R. B. Von Dreele, D. E. Cox, D. Louer, P. Scardi, *J. Appl. Crystallogr.* **1999**, *32*, 36-50.

[49] G. Pawley, *J. Appl. Cryst.* **1981**, *14*, 357-361.

[50] A. Le Bail, *Powder Diffr.* **2005**, *20*, 316-326.

[51] P. Juhas, T. Davis, C. L. Farrow, S. J. L. Billinge, *J. Appl. Crystallogr.* **2013**, *46*, 560-566.

[52] D. Keen, *J. Appl. Crystallogr.* **2001**, *34*, 172-177.

[53] A. K. Soper, E. R. Barney, *J. Appl. Crystallogr.* **2011**, *44*, 714-726.

[54] M. W. Terban, S. J. L. Billinge, *Chem. Rev.* **2022**, *122*, 1208-1272.

[55] Q. Zheng, Y. Zhang, M. Montazerian, O. Gulbiten, J. C. Mauro, E. D. Zanotto, Y. Yue, *Chem. Rev.* **2019**, *119*, 7848-7939.

[56] J. C. Mauro, R. J. Loucks, P. K. Gupta, *J. Am. Ceram. Soc.* **2009**, *92*, 75-86.

[57] J. C. Mauro, Y. Yue, A. J. Ellison, P. K. Gupta, D. C. Allan, *Proc. Natl. Acad. Sci. U S A* **2009**, *106*, 19780-19784.

[58] T. D. Bennett, A. K. Cheetham, *Acc. Chem. Res.* **2014**, *47*, 1555-1562.

[59] A. F. Sapnik, I. Bechis, S. M. Collins, D. N. Johnstone, G. Divitini, A. J. Smith, P. A. Chater, M. A. Addicoat, T. Johnson, D. A. Keen, K. E. Jelfs, T. D. Bennett, *Nat. Commun.* **2021**, *12*, 2062.

[60] Z. Zeng, L. Yang, Q. Zeng, H. Lou, H. Sheng, J. Wen, D. J. Miller, Y. Meng, W. Yang, W. L. Mao, H.-k. Mao, *Nat. Commun.* **2017**, *8*, 322.

[61] A. W. Thornton, K. E. Jelfs, K. Konstas, C. M. Doherty, A. J. Hill, A. K. Cheetham, T. D. Bennett, *Chem. Commun.* **2016**, *52*, 3750-3753.

[62] T. F. Willems, C. H. Rycroft, M. Kazi, J. C. Meza, M. Haranczyk, *Microporous Mesoporous Mat.* **2012**, *149*, 134-141.

[63] C. F. Macrae, I. Sovago, S. J. Cottrell, P. T. A. Galek, P. McCabe, E. Pidcock, M. Platings, G. P. Shields, J. S. Stevens, M. Towler, P. A. Wood, *J. Appl. Crystallogr* **2020**, *53*, 226-235.

[64] K. A. Cychosz, M. Thommes, *Engineering* **2018**, *4*, 559-566.

[65] J. Hou, M. L. Ríos Gómez, A. Krajnc, A. McCaul, S. Li, A. M. Bumstead, A. F. Sapnik, Z. Deng, R. Lin, P. A. Chater, D. S. Keeble, D. A. Keen, D. Appadoo, B. Chan, V. Chen, G. Mali, T. D. Bennett, *J. Am. Chem. Soc.* **2020**, *142*, 3880-3890.

[66] A. Vishnyakov, P. I. Ravikovitch, A. V. Neimark, *Langmuir* **1999**, *15*, 8736-8742.

[67] S. Samios, A. K. Stubos, G. K. Papadopoulos, N. K. Kanellopoulos, F. Rigas, *J. Colloid Interface Sci.* **2000**, *224*, 272-290.

[68] D. P. Broom, *Adsorption* **2023**.

[69] A. L. Myers, J. M. Prausnitz, *AlChE J.* **1965**, *11*, 121-127.

[70] K. S. Walton, D. S. Sholl, *AlChE J.* **2015**, *61*, 2757-2762.

[71] X. Zheng, M. Kato, Y. Uemura, D. Matsumura, I. Yagi, K. Takahashi, S.-i. Noro, T. Nakamura, *Inorg. Chem.* **2023**, *62*, 1257-1263.

[72] M. Eddaoudi, D. B. Moler, H. Li, B. Chen, T. M. Reineke, M. O'Keeffe, O. M. Yaghi, *Acc. Chem. Res.* **2001**, *34*, 319-330.

[73] S. Kitagawa, R. Kitaura, S.-i. Noro, *Angew. Chem., Int. Ed.* **2004**, *43*, 2334-2375.

[74] H. Furukawa, K. E. Cordova, M. O'Keeffe, O. M. Yaghi, *Science* **2013**, *341*, 1230444.

[75] S. Li, R. Limbach, L. Longley, A. A. Shirzadi, J. C. Walmsley, D. N. Johnstone, P. A. Midgley, L. Wondraczek, T. D. Bennett, *J. Am. Chem. Soc.* **2019**, *141*, 1027-1034.

[76] T. D. Bennett, J.-C. Tan, Y. Yue, E. Baxter, C. Ducati, N. J. Terrill, H. H. M. Yeung, Z. Zhou, W. Chen, S. Henke, A. K. Cheetham, G. N. Greaves, *Nat. Commun.* **2015**, *6*, 8079.

[77] A. M. Bumstead, M. L. Ríos Gómez, M. F. Thorne, A. F. Sapnik, L. Longley, J. M. Tuffnell, D. S. Keeble, D. A. Keen, T. D. Bennett, *CrystEngComm* **2020**, *22*, 3627-3637.

[78] L. Longley, S. M. Collins, S. Li, G. J. Smales, I. Erucar, A. Qiao, J. Hou, C. M. Doherty, A. W. Thornton, A. J. Hill, X. Yu, N. J. Terrill, A. J. Smith, S. M. Cohen, P. A. Midgley, D. A. Keen, S. G. Telfer, T. D. Bennett, *Chem. Sci.* **2019**, *10*, 3592-3601.

[79] K. S. Park, Z. Ni, A. P. Côté, J. Y. Choi, R. Huang, F. J. Uribe-Romo, H. K. Chae, M. O'Keeffe, O. M. Yaghi, *Proc. Natl. Acad. Sci. U.S.A.* **2006**, *103*, 10186-10191.

[80] X.-C. Huang, Y.-Y. Lin, J.-P. Zhang, X.-M. Chen, *Angew. Chem. Int. Ed.* **2006**, *45*, 1557-1559.

[81] J. C. Tan, T. D. Bennett, A. K. Cheetham, *Proc. Natl. Acad. Sci. U.S.A.* **2010**, *107*, 9938-9943.

[82] D. Saliba, M. Ammar, M. Rammal, M. Al-Ghoul, M. Hmadeh, *J. Am. Chem. Soc.* **2018**, *140*, 1812-1823.

[83] H. Dai, X. Yuan, L. Jiang, H. Wang, J. Zhang, J. Zhang, T. Xiong, *Coord. Chem. Rev.* **2021**, *441*, 213985.

[84] Y. Pan, K. Sun, S. Liu, X. Cao, K. Wu, W.-C. Cheong, Z. Chen, Y. Wang, Y. Li, Y. Liu, D. Wang, Q. Peng, C. Chen, Y. Li, *J. Am. Chem. Soc.* **2018**, *140*, 2610-2618.

[85] C. L. Hobday, C. H. Woodall, M. J. Lennox, M. Frost, K. Kamenev, T. Düren, C. A. Morrison, S. A. Moggach, *Nat. Commun.* **2018**, *9*, 1429.

[86] P. Li, J. Li, X. Feng, J. Li, Y. Hao, J. Zhang, H. Wang, A. Yin, J. Zhou, X. Ma, B. Wang, *Nat. Commun.* **2019**, *10*, 2177.

[87] R. Gaillac, P. Pullumbi, F.-X. Coudert, *J. Phys. Chem. C* **2018**, *122*, 6730-6736.

[88] V. Nozari, C. Calahoo, J. M. Tuffnell, D. A. Keen, T. D. Bennett, L. Wondraczek, *Nat. Commun.* **2021**, *12*, 5703.

[89] R. A. Klein, S. Shulda, P. A. Parilla, P. Le Magueres, R. K. Richardson, W. Morris, C. M. Brown, C. M. McGuirk, *Chem. Sci.* **2021**, *12*, 15620-15631.

[90] G. Pawley, *J. Appl. Crystallogr.* **1981**, *14*, 357-361.

[91] G. N. Greaves, S. Sen, *Adv. Phys.* **2007**, *56*, 1-166.

[92] K. Ito, C. T. Moynihan, C. A. Angell, *Nature* **1999**, *398*, 492-495.

[93] A. Qiao, T. D. Bennett, H. Tao, A. Krajnc, G. Mali, C. M. Doherty, A. W. Thornton, J. C. Mauro, G. N. Greaves, Y. Yue, *Sci. Adv.* **2018**, *4*, eaao6827.

[94] J. Orava, A. L. Greer, *J. Chem. Phys.* **2014**, *140*, 214504.

[95] S. Li, S. Yu, S. M. Collins, D. N. Johnstone, C. W. Ashling, A. F. Sapnik, P. A. Chater, D. S. Keeble, L. N. McHugh, P. A. Midgley, D. A. Keen, T. D. Bennett, *Chem. Sci.* **2020**, *11*, 9910-9918.

[96] J. Hou, C. W. Ashling, S. M. Collins, A. Krajnc, C. Zhou, L. Longley, D. N. Johnstone, P. A. Chater, S. Li, M.-V. Coulet, P. L. Llewellyn, F.-X. Coudert, D. A. Keen, P. A. Midgley, G. Mali, V. Chen, T. D. Bennett, *Nat. Commun.* **2019**, *10*, 2580.

[97] L. N. McHugh, M. F. Thorne, G. Robertson, G. Divitini, T. D. Bennett, *Chem. Eur. J.* **2022**, *28*, e202104026.

[98] M. F. Thorne, A. F. Sapnik, L. N. McHugh, A. M. Bumstead, C. Castillo-Blas, D. S. Keeble, M. Diaz Lopez, P. A. Chater, D. A. Keen, T. D. Bennett, *Chem. Commun.* **2021**, *57*, 9272-9275.

[99] C. Zhou, L. Longley, A. Krajnc, G. J. Smales, A. Qiao, I. Erucar, C. M. Doherty, A. W. Thornton, A. J. Hill, C. W. Ashling, O. T. Qazvini, S. J. Lee, P. A. Chater, N. J. Terrill, A. J. Smith, Y. Yue, G. Mali, D. A. Keen, S. G. Telfer, T. D. Bennett, *Nat. Commun.* **2018**, *9*, 5042.

[100] M. R. Ryder, B. Civalleri, T. D. Bennett, S. Henke, S. Rudić, G. Cinque, F. Fernandez-Alonso, J.-C. Tan, *Phys. Rev. Lett.* **2014**, *113*, 215502.

[101] A. V. Neimark, Y. Lin, P. I. Ravikovitch, M. Thommes, *Carbon* **2009**, *47*, 1617-1628.

[102] Horv, Aacute, G. Th, Eacute, Za, K. Kawazoe, *J. Chem. Eng. Jpn.* **1983**, *16*, 470-475.

[103] N. Ramesh Rao, P. S. R. Krishna, S. Basu, B. A. Dasannacharya, K. S. Sangunni, E. S. R. Gopal, *J. Non-Cryst. Solids* **1998**, *240*, 221-231.

[104] K. Li, D. H. Olson, J. Seidel, T. J. Emge, H. Gong, H. Zeng, J. Li, *J. Am. Chem. Soc.* **2009**, *131*, 10368-10369.

[105] Y. Wang, H. Jin, Q. Ma, K. Mo, H. Mao, A. Feldhoff, X. Cao, Y. Li, F. Pan, Z. Jiang, *Angew. Chem. Int. Ed.* **2020**, *59*, 4365-4369.

[106] N. Ma, S. Kosasang, A. Yoshida, S. Horike, *Chem. Sci.* **2021**, *12*, 5818-5824.

[107] G. Jiang, C. Qu, F. Xu, E. Zhang, Q. Lu, X. Cai, S. Hausdorf, H. Wang, S. Kaskel, *Adv. Funct. Mater.* **2021**, *31*, 2104300.

[108] J. Hou, P. Chen, A. Shukla, A. Krajnc, T. Wang, X. Li, R. Doasa, H. G. Tizei Luiz, B. Chan, N. Johnstone Duncan, R. Lin, U. Schülli Tobias, I. Martens, D. Appadoo, S. Ari Mark, Z. Wang, T. Wei, S.-C. Lo, M. Lu, S. Li, B. Namdas Ebinazar, G. Mali, K. Cheetham Anthony, M. Collins Sean, V. Chen, L. Wang, D. Bennett Thomas, *Science* **2021**, *374*, 621-625.

[109] H. Tao, T. D. Bennett, Y. Yue, *Adv. Mater.* **2017**, *29*.

[110] C. Healy, K. M. Patil, B. H. Wilson, L. Hermanspahn, N. C. Harvey-Reid, B. I. Howard, C. Kleinjan, J. Kolien, F. Payet, S. G. Telfer, P. E. Kruger, T. D. Bennett, *Coord. Chem. Rev.* **2020**, *419*, 213388.

[111] R. Banerjee, H. Furukawa, D. Britt, C. Knobler, M. O'Keeffe, O. M. Yaghi, *J. Am. Chem. Soc.* **2009**, *131*, 3875-3877.

[112] S. Głowniak, B. Szczęśniak, J. Choma, M. Jaroniec, *Mater. Today.* **2021**, *46*, 109-124.

[113] W. Xu, H. Chen, K. Jie, Z. Yang, T. Li, S. Dai, *Angew. Chem. Int. Ed.* **2019**, *58*, 5018-5022.

[114] T. Panda, S. Horike, K. Hagi, N. Ogiwara, K. Kadota, T. Itakura, M. Tsujimoto, S. Kitagawa, *Angew. Chem. Int. Ed.* **2017**, *56*, 2413-2417.

[115] N. Ma, R. Ohtani, H. M. Le, S. S. Sørensen, R. Ishikawa, S. Kawata, S. Bureekaew, S. Kosasang, Y. Kawazoe, K. Ohara, M. M. Smedskjaer, S. Horike, *Nat. Commun.* **2022**, *13*, 4023.

[116] Y. Ohara, A. Hinokimoto, W. Chen, T. Kitao, Y. Nishiyama, Y.-l. Hong, S. Kitagawa, S. Horike, *Chem. Commun.* **2018**, *54*, 6859-6862.

[117] R. N. Widmer, G. I. Lampronti, S. Anzellini, R. Gaillac, S. Farsang, C. Zhou, A. M. Belenguer, C. W. Wilson, H. Palmer, A. K. Kleppe, M. T. Wharmby, X. Yu, S. M. Cohen, S. G. Telfer, S. A. T. Redfern, F. X. Coudert, S. G. MacLeod, T. D. Bennett, *Nat. Mater.* **2019**, *18*, 370-376.

[118] S.-X. Peng, Z. Yin, T. Zhang, Q. Yang, H.-B. Yu, M.-H. Zeng, *J. Chem. Phys.* **2022**, *157*, 104501.

[119] T. D. Bennett, S. Cao, J. C. Tan, D. A. Keen, E. G. Bithell, P. J. Beldon, T. Friscic, A. K. Cheetham, *J. Am. Chem. Soc.* **2011**, *133*, 14546-14549.

[120] E. F. Baxter, T. D. Bennett, A. B. Cairns, N. J. Brownbill, A. L. Goodwin, D. A. Keen, P. A. Chater, F. Blanc, A. K. Cheetham, *Dalton Trans.* **2016**, *45*, 4258-4268.

[121] T. D. Bennett, P. J. Saines, D. A. Keen, J.-C. Tan, A. K. Cheetham, *Chem. Eur. J.* **2013**, *19*, 7049-7055.

[122] S. Cao, T. D. Bennett, D. A. Keen, A. L. Goodwin, A. K. Cheetham, *Chem. Commun.* **2012**, *48*, 7805-7807.

[123] R. Lin, X. Li, A. Krajnc, Z. Li, M. Li, W. Wang, L. Zhuang, S. Smart, Z. Zhu, D. Appadoo, J. R. Harmer, Z. Wang, A. G. Buzanich, S. Beyer, L. Wang, G. Mali, T. D. Bennett, V. Chen, J. Hou, *Angew. Chem. Int. Ed.* **2022**, *61*, e202112880.

[124] L. Frentzel-Beyme, M. Kloß, R. Pallach, S. Salamon, H. Moldenhauer, J. Landers, H. Wende, J. Debus, S. Henke, *J. Mater. Chem. A* **2019**, *7*, 985-990.

[125] N. Masciocchi, S. Bruni, E. Cariati, F. Cariati, S. Galli, A. Sironi, *Inorg. Chem.* **2001**, *40*, 5897-5905.

[126] A. M. Bumstead, M. F. Thorne, A. F. Sapnik, C. Castillo-Blas, G. I. Lampronti, T. D. Bennett, *Dalton Trans.* **2022**, *51*, 13636-13645.

[127] J. C. Tan, T. D. Bennett, A. K. Cheetham, *Proc. Natl. Acad. Sci. U.S.A.* **2010**, *107*, 9938-9943.

[128] T. D. Bennett, A. L. Goodwin, M. T. Dove, D. A. Keen, M. G. Tucker, E. R. Barney, A. K. Soper, E. G. Bithell, J.-C. Tan, A. K. Cheetham, *Phys. Rev. Lett.* **2010**, *104*, 115503.

[129] W.-L. Xue, P. Kolodzeiski, H. Aucharova, S. Vasa, A. Koutsianos, R. Pallach, J. Song, L. Frentzel-Beyme, R. Linser, S. Henke, *Nat. Commun.* **2024**, *15*, 4420.

[130] J. Song, R. Pallach, L. Frentzel-Beyme, P. Kolodzeiski, G. Kieslich, P. Vervoorts, C. L. Hobday, S. Henke, *Angew. Chem. Int. Ed.* **2022**, *61*, e202117565.

[131] S.-i. Noro, X. Zheng, A. Wang, K. Suzuki, S. Kosasang, S. Horike, D. Padovan, K. Nakajima, H. Sato, K. Takahashi, T. Nakamura, *Inorg. Chem.* **2022**, *61*, 3379-3386.

[132] L. Yang, D. R. Powell, R. P. Houser, *Dalton Trans.* **2007**, 955-964.

[133] A. A. L. Michalchuk, F. Emmerling, *Angew. Chem. Int. Ed.* **2022**, *61*, e202117270.

[134] W. Wang, M. Chai, M. Y. Bin Zulkifli, K. Xu, Y. Chen, L. Wang, V. Chen, J. Hou, *Mol. Syst. Des. Eng.* **2023**, *8*, 560-579.

[135] C. Castillo-Blas, A. M. Chester, R. P. Cosquer, A. F. Sapnik, L. Corti, R. Sajzew, B. Poletto-Rodrigues, G. P. Robertson, D. J. M. Irving, L. N. McHugh, L. Wondraczek, F. Blanc, D. A. Keen, T. D. Bennett, *J. Am. Chem. Soc.* **2023**, *145*, 22913-22924.

[136] C. Suryanarayana, *Prog. Mater. Sci.* **2001**, *46*, 1-184.

[137] H. Jiang, K.-s. Moon, H. Dong, F. Hua, C. P. Wong, *Chem. Phys. Lett.* **2006**, *429*, 492-496.

[138] A. van Teijlingen, S. A. Davis, S. R. Hall, *Nanoscale Adv.* **2020**, *2*, 2347-2351.

[139] K. Li, H. Xiao, J. He, H. Jiang, *NANO* **2018**, *13*, 1850025.

[140] V. Nozari, O. Smirnova, J. M. Tuffnell, A. Knebel, T. D. Bennett, L. Wondraczek, *Adv. Mater. Technol.* **2022**, *7*, 2200343.

[141] L. León-Alcaide, R. S. Christensen, D. A. Keen, J. L. Jordá, I. Brotons-Alcázar, A. Forment-Aliaga, G. Mínguez Espallargas, *J. Am. Chem. Soc.* **2023**, *145*, 11258-11264.

[142] I. Luz, F. X. Llabrés i Xamena, A. Corma, *J. Catal.* **2010**, *276*, 134-140.

[143] Y. Ma, X. Han, S. Xu, Z. Wang, W. Li, I. da Silva, S. Chansai, D. Lee, Y. Zou, M. Nikiel, P. Manuel, A. M. Sheveleva, F. Tuna, E. J. L. McInnes, Y. Cheng, S. Rudić, A. J. Ramirez-Cuesta, S. J. Haigh, C. Hardacre, M. Schröder, S. Yang, *J. Am. Chem. Soc.* **2021**, *143*, 10977-10985.

[144] J. Park, A. C. Hinckley, Z. Huang, D. Feng, A. A. Yakovenko, M. Lee, S. Chen, X. Zou, Z. Bao, *J. Am. Chem. Soc.* **2018**, *140*, 14533-14537.

[145] X. Li, R. Lin, J. Hou, L. Wang, *Cell Rep. Phys. Sci.* **2022**, *3*, 100932.

[146] S. Li, R. Limbach, L. Longley, A. A. Shirzadi, J. C. Walmsley, D. N. Johnstone, P. A. Midgley, L. Wondraczek, T. D. Bennett, *J. Am. Chem. Soc.* **2019**, *141*, 1027-1034.

[147] M. Kim, H.-S. Lee, D.-H. Seo, S. J. Cho, E.-c. Jeon, H. R. Moon, *Nat. Commun.* **2024**, *15*, 1174.

[148] W.-L. Xue, G.-Q. Li, H. Chen, Y.-C. Han, L. Feng, L. Wang, X.-L. Gu, S.-Y. Hu, Y.-H. Deng, L. Tan, M. T. Dove, W. Li, J. Zhang, H. Dong, Z. Chen, W.-H. Deng, G. Xu, G. Wang, C.-Q. Wan, *Nat. Commun.* **2024**, *15*, 2040.

[149] R. Lin, M. Chai, Y. Zhou, V. Chen, T. D. Bennett, J. Hou, *Chem. Soc. Rev.* **2023**, *52*, 4149-4172.

[150] E. C. Constable, C. E. Housecroft, *Chem. Soc. Rev.* **2013**, *42*, 1429-1439.

[151] L. N. McHugh, T. D. Bennett, *J. Mater. Chem. A* **2022**.

[152] O. Smirnova, R. Sajzew, S. J. Finkelmeyer, T. Asadov, S. Chattopadhyay, T. Wieduwilt, A. Reupert, M. Presselt, A. Knebel, L. Wondraczek, *Nat. Commun.* **2024**, *15*, 5079.

[153] I. E. Collings, A. B. Cairns, A. L. Thompson, J. E. Parker, C. C. Tang, M. G. Tucker, J. Catafesta, C. Levelut, J. Haines, V. Dmitriev, P. Pattison, A. L. Goodwin, *J. Am. Chem. Soc.* **2013**, *135*, 7610-7620.

[154] W.-L. Xue, C. Das, J.-B. Weiß, S. Henke, *Angew. Chem. Int. Ed.* **2024**, e202405307.

[155] W. Holand, G. H. Beall, *Glass-ceramic technology*, John Wiley & Sons, **2019**.

[156] C. L. Farrow, P. Juhas, J. W. Liu, D. Bryndin, E. S. Božin, J. Bloch, T. Proffen, S. J. L. Billinge, *J. Phys.: Condens. Matter* **2007**, *19*, 335219.

[157] D. H. Brouwer, in *Compr. Inorg. Chem. III* (Eds.: J. Reedijk, K. R. Poeppelmeier), Elsevier, Oxford, **2023**, pp. 107-137.

[158] J. Deubener, M. Allix, M. J. Davis, A. Duran, T. Höche, T. Honma, T. Komatsu, S. Krüger, I. Mitra, R. Müller, S. Nakane, M. J. Pascual, J. W. P. Schmelzer, E. D. Zanotto, S. Zhou, *J. Non-Cryst. Solids* **2018**, *501*, 3-10.

[159] A. Coelho, *J. Appl. Crystallogr.* **2018**, *51*, 210-218.

[160] M. Basham, J. Filik, M. T. Wharmby, P. C. Y. Chang, B. El Kassaby, M. Gerring, J. Aishima, K. Levik, B. C. A. Pulford, I. Sikharulidze, D. Sneddon, M. Webber, S. S. Dhesi, F. Maccherozzi, O. Svensson, S. Brockhauser, G. Naray, A. W. Ashton, *J. Synchrotron Rad.* **2015**, *22*, 853-858.

[161] H. Walba, R. W. Isensee, *J. Org. Chem.* **1961**, *26*, 2789-2791.

[162] Y. Du, B. Wooler, M. Nines, P. Kortunov, C. S. Paur, J. Zengel, S. C. Weston, P. I. Ravikovitch, *J. Am. Chem. Soc.* **2015**, *137*, 13603-13611.

[163] W. Morris, C. J. Stevens, R. E. Taylor, C. Dybowski, O. M. Yaghi, M. A. Garcia-Garibay, *J. Phys. Chem. C* **2012**, *116*, 13307-13312.

[164] J. Runt, M. Kanchanasopa, in *Encyclopedia of Polymer Science and Technology*, **2004**, p. https://doi.org/10.1002/0471440264.pst0471440502.

[165] S. Venkatram, J. McCollum, N. Stingelin, B. Brettmann, *Polym. Int.* **2023**, *72*, 855-860.

[166] P. J. Branton, P. G. Hall, M. Treguer, K. S. W. Sing, *J. Chem. Soc., Faraday Trans.* **1995**, *91*, 2041-2043.

[167] W. Yang, A. J. Davies, X. Lin, M. Suyetin, R. Matsuda, A. J. Blake, C. Wilson, W. Lewis, J. E. Parker, C. C. Tang, M. W. George, P. Hubberstey,

S. Kitagawa, H. Sakamoto, E. Bichoutskaia, N. R. Champness, S. Yang, M. Schröder, *Chem. Sci.* **2012**, *3*, 2993-2999.

[168] F. Neese, F. Wennmohs, U. Becker, C. Riplinger, *J. Chem. Phys.* **2020**, *152*, 224108.

[169] M. D. Hanwell, D. E. Curtis, D. C. Lonie, T. Vandermeersch, E. Zurek, G. R. Hutchison, *J. Cheminf.* **2012**, *4*, 17.

.

List of Publications

Publications:

1. Wen-Long Xue, Pascal Kolodzeiski, Hanna Aucharova, Suresh Vasa, Athanasios Koutsianos, Roman Pallach, Jianbo Song, Louis Frentzel-Beyme, Rasmus Linser, Sebastian Henke*., "Highly Porous Metal-Organic Framework Liquids and Glasses via a Solvent-Assisted Linker Exchange Strategy of ZIF-8", *Nat. Commun.* **2024**, 15, 4420.

2. Wen-Long Xue, Chinmoy Das, Jan-Benedikt Weiß, Sebastian Henke*., "Insights into The Mechanochemical Glass Formation of Zeolitic Imidazolate Frameworks", *Angew. Chem. Int. Ed.* **2024**, e202405307.

Manuscripts under preparation:

1. Wen-Long Xue, Sebastian Henke*., "Solvent-free Direct Synthesis of Super-Sized Uni/Multivariate Zeolitic Imidazolate Framework Glasses".

2. Wen-Long Xue, Sebastian Henke*., "Cadmium Zeolitic Imidazolate Framework Glass and Ceramics".

3. Wen-Long Xue, Sebastian Henke*., "Quantification and Tailoring of Porosity in Metal-Organic Framework Glasses". (Review article)

Contributions to other projects:

1. Chumei Ye, Giulio I Lampronti, Lauren N McHugh, Celia Castillo-Blas, Ayano Kono, Celia Chen, Georgina P Robertson, Liam AV Nagle-Cocco, Weidong Xu, Samuel D Stranks, Valentina Martinez, Ivana Brekalo, Bahar Karadeniz, Krunoslav Užarević, Wen-Long Xue, Pascal Kolodzeiski, Chinmoy Das, Philip Chater, David A Keen, Siân E Dutton, Thomas D Bennett*., "Mechanochemically-Induced Glass Formation from Two-Dimensional Hybrid Organic–Inorganic Perovskites", *Chem. Sci.,* **2024**, *15, 7198-7205.*

2. Jianbo Song, Louis Frentzel-Beyme, Roman Pallach, Pascal Kolodzeiski, Athanasios Koutsianos, Wen-Long Xue, Rochus Schmid, and Sebastian Henke*., "Modulating liquid-liquid transitions and glass formation in zeolitic imidazolate frameworks by decoration with electron withdrawing cyano groups", *J. Am. Chem. Soc.*, **2023***, 145, 16, 9273–9284.*

3. Joohan Nam, Eunji Jin, Leila Abylgazina, Jürgen Getzschmann, Wen-Long Xue, Hong Kyu Lee, Hyunchul Oh, Hoi Ri Moon, Sebastian Henke, Andreas Schneemann*, Wonyoung Choe*., "Molecularly-Engineered Kirigami Responses to External Stimuli", *ChemRxiv*, **2024**, *DOI: 10.26434/chemrxiv-2024-ffwgh.*

Publications in the previous working group:

1. Wen-Long Xue, Guo-Qiang Li, Hui Chen, Yu-Chen Han, Li Feng, Lu Wang, Xiao-Ling Gu, Si-Yuan Hu, Yu-Heng Deng, Lei Tan, Martin T. Dove, Wei Li*, Jiangwei Zhang*, Hongliang Dong, Zhiqiang Chen, Wei-Hua Deng, Gang Xu*, Guo Wang, Chong-Qing Wan*., "Melt-Quenched Glass Formation of a Family of Metal-Carboxylate Frameworks", *Nat. Commun.,* **2024**, *15, 2040.*

2. Jiao-Rong Li, Yu-Chen Han, Wen-Long Xue, Zhong-Feng Li*, Yu-Heng Deng*, Chong-Qing Wan*., "Solid Ionic Liquids with Macro–Microporous Structure for Efficient Heterogeneous Catalysis of Biodiesel" *New J. Chem.,* **2023**, *47, 7701-7707.*

3. Nan Wang, Wen-Long Xue, Chong-Qing Wan, Ying-Feng Wang, Ya-Ping Li*., "Hydrophobic Polymer Tethered Magnetic Zirconium-Based Metal-Organic Framework as Advance and Recyclable Adsorbent for Microwave-Assisted Extraction of Polycyclic Aromatic Hydrocarbons from Environmental Water Samples" *Microchemical Journal,* **2021***,168,106361.*

4. Wen-Long Xue, Wei-Hua Deng, Hui Chen, Rui-Heng Liu, Jared M. Taylor, Yu-Kun Li, Lu Wang, Yu- Heng Deng, Wen-Hua Li, Ying-Yi Wen, Guan-E Wang, Chong-Qing Wan*, and Gang Xu*., "MOF-Directed Synthesis of Crystalline Ionic Liquids with Enhanced Proton Conduction", *Angew. Chem. Int. Ed.* **2021**, *60, 1290–1297.*

5. Wen-Long Xue, Lu Wang, Yu-Kun Li, Hui Chen, Ke Xin Fu, Fan Zhang, Tao He, Yu-Heng Deng*, Jian-Rong Li, and Chong-Qing Wan*., "Reticular Chemistry for Ionic Liquid-Functionalized Metal−Organic Frameworks with High Selectivity for CO_2", *ACS Sustainable Chem. Eng.* **2020***, 8, 18558−18567.*

List of Presentations

Oral presentations

1. "Modulation of Porosity, Melting and Glass formation in Zeolitic Imidazolate Frameworks via Post-synthetic Strategy", Inorganic chemistry PhD Seminar, TU Dortmund, January **2024**.

2. "Solvent-free Direct Synthesis of Super-Sized Uni/Multivariate Zeolitic Imidazolate Framework Glasses". Inorganic chemistry PhD Seminar, TU Dortmund, July **2024**.

Poster Presentations

1. "ZIF-8 glasses with high microporosity", 57th Course of International School of Crystallography, Erice, Italy, June **2022**.

2. "ZIF-8 derived MOF glasses with high microporosity", 8th International Conference on Metal-Organic Frameworks and Open Framework Compounds (MOF2022), Dresden, Germany, September **2022**.

3. "ZIF-8 derived MOF glasses with high microporosity", 11th Young Chemists Symposium Ruhr, Dortmund, Germany, March **2023**.

4. "Highly porous melt-quenched metal-organic framework glasses via a solvent assisted linker exchange strategy of ZIF-8", 5th European Conference on Metal Organic Frameworks and Porous Polymers (EuroMOF2023), Granada, Spain, September **2023**.

5. "Insights into the Mechanochemical Glass Formation of Zeolitic Imidazolate Frameworks", 9th International Conference on Metal–Organic Frameworks and Open Framework Compounds (MOF2024), Singapore, July **2024**.

Eidesstattliche Versicherung (Affidavit)

Xue, Wenlong
Name, Vorname
(Surname, first name)

231296
Matrikel-Nr.
(Enrolment number)

Belehrung:

Wer vorsätzlich gegen eine die Täuschung über Prüfungsleistungen betreffende Regelung einer Hochschulprüfungsordnung verstößt, handelt ordnungswidrig. Die Ordnungswidrigkeit kann mit einer Geldbuße von bis zu 50.000,00 € geahndet werden. Zuständige Verwaltungsbehörde für die Verfolgung und Ahndung von Ordnungswidrigkeiten ist der Kanzler/die Kanzlerin der Technischen Universität Dortmund. Im Falle eines mehrfachen oder sonstigen schwerwiegenden Täuschungsversuches kann der Prüfling zudem exmatrikuliert werden, § 63 Abs. 5 Hochschulgesetz NRW.

Die Abgabe einer falschen Versicherung an Eides statt ist strafbar.

Wer vorsätzlich eine falsche Versicherung an Eides statt abgibt, kann mit einer Freiheitsstrafe bis zu drei Jahren oder mit Geldstrafe bestraft werden, § 156 StGB. Die fahrlässige Abgabe einer falschen Versicherung an Eides statt kann mit einer Freiheitsstrafe bis zu einem Jahr oder Geldstrafe bestraft werden, § 161 StGB.

Die oben stehende Belehrung habe ich zur Kenntnis genommen:

Official notification:

Any person who intentionally breaches any regulation of university examination regulations relating to deception in examination performance is acting improperly. This offence can be punished with a fine of up to EUR 50,000.00. The competent administrative authority for the pursuit and prosecution of offences of this type is the chancellor of the TU Dortmund University. In the case of multiple or other serious attempts at deception, the candidate can also be unenrolled, Section 63, paragraph 5 of the Universities Act of North Rhine-Westphalia.

The submission of a false affidavit is punishable.

Any person who intentionally submits a false affidavit can be punished with a prison sentence of up to three years or a fine, Section 156 of the Criminal Code. The negligent submission of a false affidavit can be punished with a prison sentence of up to one year or a fine, Section 161 of the Criminal Code.

I have taken note of the above official notification.

Dortmund, 12.08.2024
Ort, Datum
(Place, date)

Unterschrift
(Signature)

Titel der Dissertation:
(Title of the thesis):

Modulation of Porosity, Melting and Glass Formation in Zeolitic Imidazolate Frameworks

Ich versichere hiermit an Eides statt, dass ich die vorliegende Dissertation mit dem Titel selbstständig und ohne unzulässige fremde Hilfe angefertigt habe. Ich habe keine anderen als die angegebenen Quellen und Hilfsmittel benutzt sowie wörtliche und sinngemäße Zitate kenntlich gemacht.
Die Arbeit hat in gegenwärtiger oder in einer anderen Fassung weder der TU Dortmund noch einer anderen Hochschule im Zusammenhang mit einer staatlichen oder akademischen Prüfung vorgelegen.

I hereby swear that I have completed the present dissertation independently and without inadmissible external support. I have not used any sources or tools other than those indicated and have identified literal and analogous quotations.

The thesis in its current version or another version has not been presented to the TU Dortmund University or another university in connection with a state or academic examination.*

*Please be aware that solely the German version of the affidavit ("Eidesstattliche Versicherung") for the PhD thesis is the official and legally binding version.

Dortmund, 12.08.2024
Ort, Datum
(Place, date)

Unterschrift
(Signature)